Molecular Design of Organometallic Ni, Pd and Pt Complexes Aiming for Ni(II)-based Triplet Emission

Inaugural-Dissertation

zur

Erlangung des Doktorgrades

der Mathematisch-Naturwissenschaftlichen Fakultät

der Universität zu Köln

vorgelegt von

Rose Jordan

angenommen im Jahr 2025

Abstract

The present work approaches the challenge of replacing Pt with the cheaper and more abundant Ni in optoelectronic applications from multiple angles. The effect of heavy phosphine analogue ancillary ligands $PnPh_3$, Pn = As and Sb, on the photophysical properties of tridentate, cyclometalated pincer complexes is explored as one strategy to enhance or facilitate their triplet emission. To elucidate the structure-property-relationships in our chosen model system, the doubly cyclometalated Pt(II) complexes [Pt(C^N^C)($PnPh_3$)], UV/vis absorption and emission spectroscopy, as well as transient absorption spectroscopy were used among others.

Encouraging results showing enhanced phosphorescence in the $AsPh_3$ and $SbPh_3$ derivatives of the Pt(II) complexes motivated us to proceed to the Pd(II) system [Pd(C^N^C)($PnPh_3$)]. The investigations of these compounds notably included the exploration of their synthesis and reactivity in addition to the in-depth spectroscopic study. The results represent the first ever comprehensive characterization of doubly cyclometalated Pd(C^N^C) complexes. We find that the effect of the $PnPh_3$ variation is multifaceted, affecting not only spin-orbit coupling, but also the character of the emissive T_1 state, the ligand field, and vibronic coupling. Overall, the study establishes heavy $PnPh_3$ ancillary ligands as a useful tool for emitter design to fine-tune said properties in tridentate pincer complexes, both in the not yet accessible Ni(C^N^C) system and beyond.

Concurrently, a second approach is explored, probing the ability of the strongly σ donating, monodentate perfluorophenyl ligand to promote phosphorescence from Ni(II) complexes in place of double cyclometalation. Two emissive [Ni(C_6F_5)$_2$(N^N)] complexes containing phenanthroline derivatives were identified, while the N^N = dipyridophenazine (dppz) derivative was found to be non-emissive. This is attributed to stacking-related quenching processes, leaving room for future improvement by ligand modifications suppressing stacking interactions.

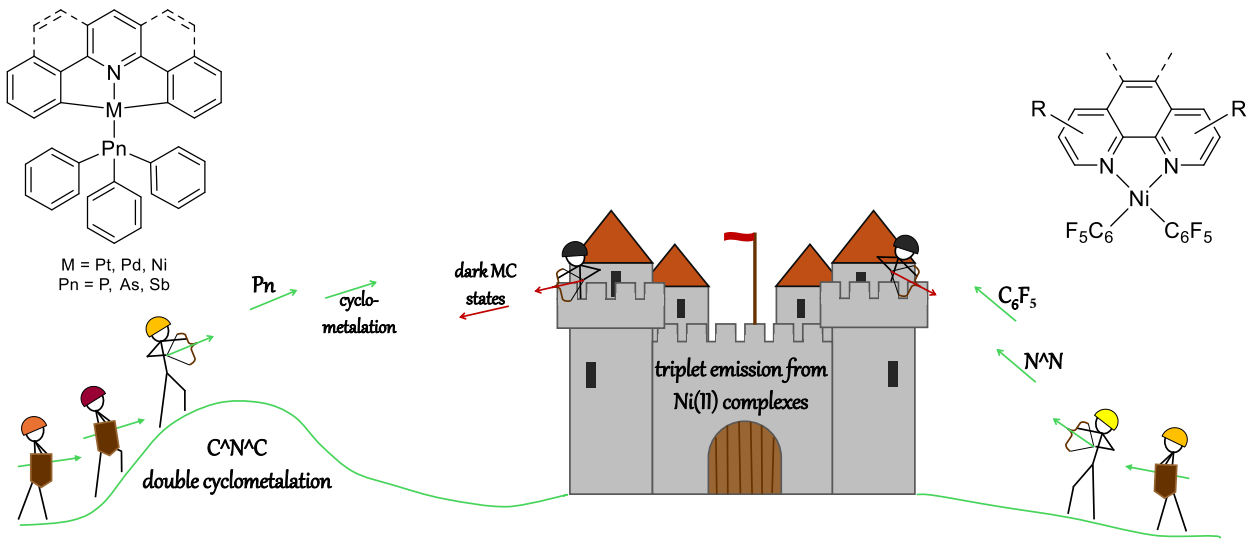

Kurzzusammenfassung

Die vorliegende Arbeit nähert sich dem Ziel der Substitution von Pt durch das günstigere und reichlicher vorhandene Ni im Kontext optoelektronischer Anwendungen aus mehreren Richtungen. Der Effekt von schweren phosphin-analogen Hilfsliganden $PnPh_3$, Pn = As und Sb, auf die photophysikalischen Eigenschaften von tridentaten, cyclometallierten Pincerkomplexen als Strategie zur Förderung ihrer Tripletemission wurde untersucht. UV/Vis-Absorptions- und Emissionsspektroskopie sowie ultraschnelle transiente Absorptionsspektroskopie wurden verwendet, um Struktur-Eigenschafts-Beziehungen in den zweifach cyclometallierten Pt(II)-Komplexen [Pt(C^N^C)($PnPh_3$)], welche als Modellsystem herangezogen wurden, zu beleuchten.

Auf die vielversprechende Beobachtung verbesserter Phosphoreszenz bei den $AsPh_3$- und $SbPh_3$-Derivaten der Pt(II)-Komplexe folgte die Untersuchung des Pd(II)-Systems [Pd(C^N^C)($PnPh_3$)]. Diese beinhaltete neben der tiefgreifenden photophysikalischen Charakterisierung der Pd(II)-Komplexe auch die Exploration ihrer Synthese und Reaktivität. Bei den Ergebnissen handelt es sich um die erste umfassende Beschreibung der Eigenschaften zweifach cyclometallierter Pd(C^N^C)-Komplexe überhaupt. Der Effekt der $PnPh_3$-Variation erweist sich als facettenreich und betrifft nicht nur die Spin-Bahn-Kopplung, sondern auch den Charakter des T_1-Zustandes, das Ligandenfeld und vibronische Kopplungen. Die Studie etabliert schwere $PnPh_3$-Hilfsliganden als nützliches Werkzeug beim Emitterdesign zum Finetuning der genannten Eigenschaften in tridentaten Pincerkomplexen, sowohl für das noch nicht zugängliche Ni(C^N^C)-System als auch darüber hinaus.

Zugleich wird als weitere Strategie die Eignung des stark σ-donierenden Perfluorophenylliganden, die Phosphoreszenz von Ni(II)-Komplexen anstelle von Cyclometallierung zu fördern, erprobt. Zwei lumineszente [Ni(C_6F_5)$_2$(N^N)]-Komplexe mit Phenanthrolinderivaten wurden identifiziert, während das Derivat mit N^N = Dipyridophenazin (dppz) sich als emissionslos erwies. Dies wird auf Deaktivierungsprozesse im Zusammenhang mit Stapelungseffekten zurückgeführt, weshalb Raum für zukünftige Verbesserung durch Ligandenmodifikationen bleibt, welche das Stapeln der Komplexe verhindern.

Contents

1 Introduction

1.1 Fundamentals of photoluminescence

Luminescent transition metal complexes see widespread use in optoelectronic and medical applications.[1–6] In general, luminescence is the emission of light during the relaxation of a system, e.g. a transition metal complex molecule, from an electronically excited state to the electronic ground state. If the electronically excited state is generated through the absorption of light, the resulting emission is more specifically termed photoluminescence.[7] Typical properties to describe the emission include the photoluminescence lifetime τ_{PL} and the photoluminescence quantum yield Φ_{PL}.[8,9] There are several different types of luminescence, including fluorescence, phosphorescence and thermally activated delayed fluorescence (TADF), whose different characteristics make them advantageous for different types of applications.[7,10]

Fluorescence, which is radiative electronic relaxation without a change in spin multiplicity, e.g. from S_1 to S_0 in a system with a singlet ground state (Figure 1.1 left), is characterized by comparatively short lifetimes in the ns range, which is useful for e.g. biomedical probes requiring a fast luminescent response.[10–12] However, for optoelectronic devices such as organic light-emitting diodes (OLEDs), fluorescent emitters are less useful because their quantum yields are limited to 25% due to spin statistics for the recombination of charge carriers in the device.[10,13]

Phosphorescence in contrast is the radiative decay of an electronically excited state that differs in spin multiplicity from the ground state, e.g. from T_1 to S_0 (Figure 1.1 right). Therefore, it necessarily involves intersystem crossing (ISC), which is why phosphorescence lifetimes are comparatively longer than fluorescence lifetimes.[7,10] Furthermore, as the T_1 state for a given molecule is lower in energy than the S_1 state according to *Hund*'s rule (or more precisely, due to the attractive exchange interaction between electrons of parallel spin as well as decreased repulsive *Coulomb* interaction),[14] the emission is shifted to lower energies. Both of these characteristics make phosphorescent emitters very suitable for optoelectronic applications.[10]

Thermally activated delayed fluorescence can occur when the energy gap between (in our S_0 ground state example) S_1 and T_1 is small (typically ≤ 0.1 eV), allowing for thermal repopulation of S_1 from T_1 followed by fluorescent decay of the S_1 state (Figure 1.1 middle).[10,15–17] Because it involves ISC like phosphorescence, this process is also significantly slower ("delayed") than regular fluorescence without intermediary population of the T_1 state, and avoids the spin-statistical limitations of regular fluorescence.[15,16,18]

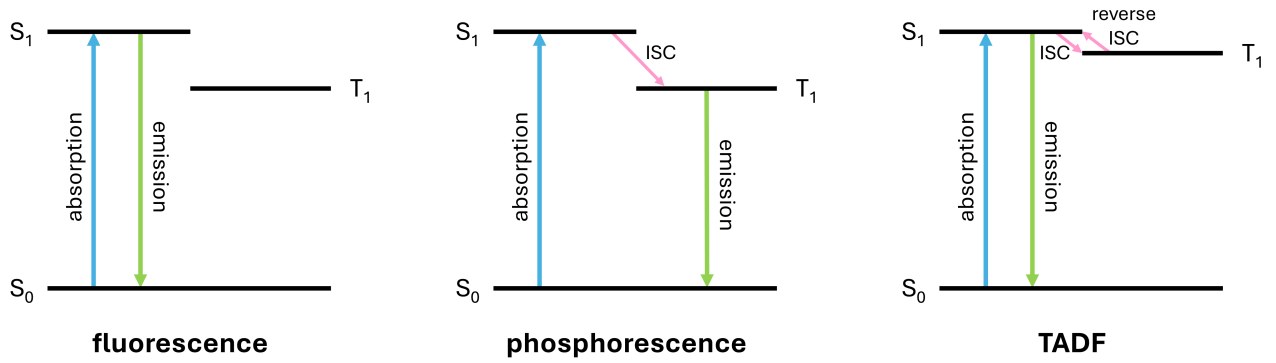

Figure 1.1: Simplified illustration of different photoluminescence mechanisms in a system with a singlet ground state.

1.2 Photoluminescent transition metal complexes

Transition metal complexes are excellent candidates for both phosphorescence and TADF due to their large spin-orbit coupling (SOC), which facilitates ISC, compared to purely organic chromophores.[2,10] SOC is the relativistic magnetic interaction between an electron's orbital angular momentum l, which acts similarly to a coil, and its spin s, which acts similarly to a bar magnet, leading to a finesplitting of its energy levels.[19] In the case of strong SOC, the interaction creates a situation where the system must be described by its total angular momentum J rather than by orbital angular momentum L and spin S separately due to mixing of states of different multiplicities.[10,19] The conservation principle then only applies to J instead of L and S individually, making multiplicity changes no longer strictly quantum mechanically forbidden.[19] A measure for the SOC of any specific element in a given oxidation state is their SOC constant ξ.[20,21] The magnitude of SOC scales with Z^4 where Z is the atomic number, meaning that among the transition metals, the 5d elements have the largest SOC constants.[22,23]

However, relatively facile ISC is necessary, but not sufficient for efficient phosphorescence, because of the competition of radiative decay with non-radiative decay pathways.[10] To describe this in quantitative terms, the radiative and non-radiative rate constants k_r and k_{nr} are useful quantities, which are related to τ_{PL} and Φ_{PL} as follows:[23]

$$\Phi_{PL} = \frac{k_r}{k_r + k_{nr}} \tag{1.1}$$

$$\tau_{PL} = \frac{1}{k_r + k_{nr}} \tag{1.2}$$

Therefore, a fundamental aspect of emitter design is maximizing k_r and minimizing k_{nr}.[23] This essentially involves tuning the energy and properties of the electronic states involved in the intended emissive decay pathway, as well as of any other states through which non-radiative decay may proceed, the latter being commonly called "dark states".[10,24]

In (organometallic) complexes containing multidentate heteroaromatic ligands, emissive states typically have metal-to-ligand charge transfer (MLCT) character, π-π* (ligand-centered, LC, ligand-to-ligand charge transfer, LL'CT, or intraligand charge transfer, ILCT) character, or a combination thereof, while d-d* (metal-centered, MC) states are typically dark.[24,25] This is directly related to the observation that non-radiative decay of an excited state is more efficient the more distorted its geometry compared to the ground state.[24] This principle can be rationalized by visualizing the potential energy surfaces of the relevant states, as shown in Figure 1.2 in a schematic 2D representation.[25] If the geometric differences between an excited state and the ground state are large, their potential energy surfaces intersect at a lower energy, increasing the probability of thermal deactivation, i.e. vibrational dissipation of energy, over radiative relaxation. This reinforces the notion that the population of MC states is likely to quench luminescence, since they are usually significantly distorted relative to the ground state, motivating the use of strong-field ligands to increase their energy and make them thermally inaccessible.[24–26] Furthermore, this gives rise to molecular rigidification as a powerful tool for emitter design with a significant potential to minimize non-radiative decay.[24,27–32]

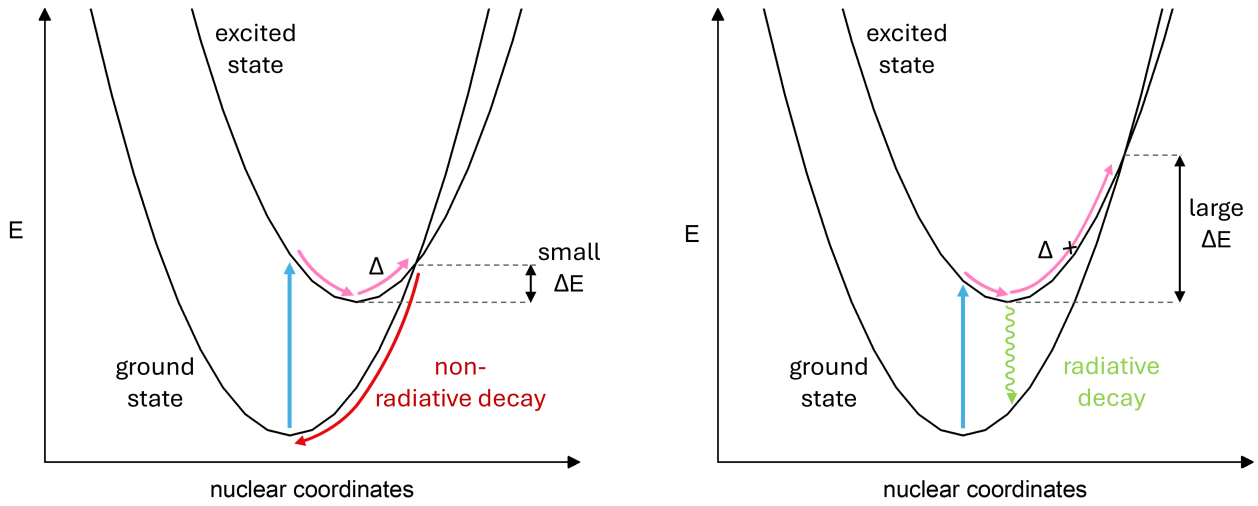

Figure 1.2: Schematic 2D projection of potential energy surfaces for a molecule with a more (left) or less strongly distorted (right) excited state, illustrating the effect on the energy at which the surfaces intersect.

1.3 Emitter design in Pt(II), Pd(II) and Ni(II) complexes

The group 10 transition metals Ni, Pd and Pt in their +II oxidation state feature a d^8 valence electron configuration. Pd(II) and Pt(II) complexes are almost exclusively square planar in geometry, whereas Ni(II) complexes of weak ligands may also be tetrahedral or octahedral due to the influence of the metal ion on the ligand field splitting, which increases down the group.[24,33] The ligand field splitting pattern in a square planar complex features a strongly antibonding, vacant $d_{x^2-y^2}$ orbital which is significantly destabilized compared to the d_{z^2}, d_{xy}, d_{xz} and d_{yx} orbitals, making the electronic ground state of planar d^8 complexes a singlet (S_0) state (Figure 1.3).[25,34] Compared to octahedral and even more so tetrahedral complexes with equivalent ligands, the ligand field splitting in a square planar complex is significantly larger.[35] From an emitter design perspective, this makes the

group 10 transition metals attractive candidates to work with, as their dark MC states are already comparatively high in energy and may thus realistically be rendered inaccessible by the introduction of sufficiently strong ligands.[26,36]

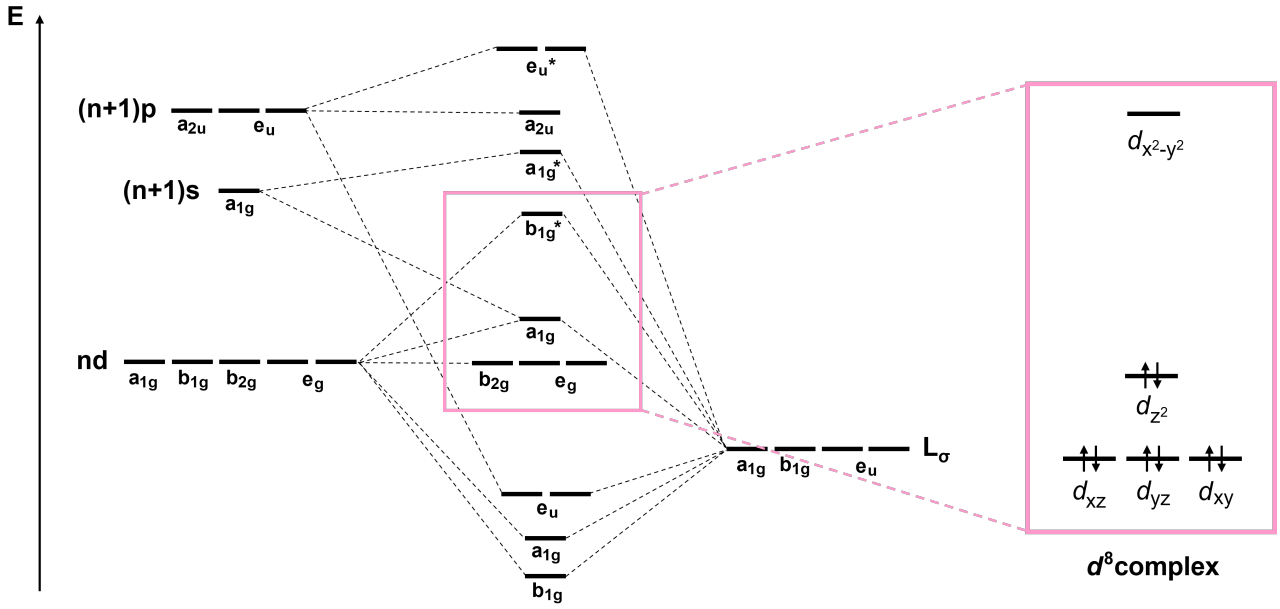

Figure 1.3: Molecular orbital scheme for an ideal square planar (D_{4h}), σ-bonding only transition metal complex highlighting the resulting d-orbital splitting, adapted from *Deeth et al.*.[34] Note that in many real systems the d_{xz} and d_{yz} and the d_{xy} orbitals may be non-degenerate due to π interactions, and the energetic ordering of the d_π and d_{z^2} orbitals may vary.

In the case of Pt(II), the favourable combination of strong SOC (ξ = 4253 cm^{-1} for Pt(II))[37] and intrinsically large ligand field splitting makes Pt(II)-based triplet emitters a popular and rewarding research subject.[38] Especially the use of rigid tri- and tetradentate heteroaromatic ligands allows for the realization of high quantum yields and long emission lifetimes due to their rigidity and strong ligand field.[26,39] While tetradentate ligands provide maximum rigidity, tridentate pincers allow for fine-tuning of the complex properties *via* the fourth, so-called ancilliary ligand or coligand.[32,40–42] Overall, a very large number of Pt(II) triplet emitters which are luminescent at low temperatures in the solid state (typically 77 K in glassy matrices of frozen solvents), and in many cases also at room temperature in fluid solution, have been reported and extensively characterized to date.[23–25,42–46]

These also include many examples of systems emitting from metal-metal-to-ligand charge transfer (MMLCT) excited states.[24,47–52] MMLCT emission is frequently observed where short Pt···Pt distances (typically 2.9 to 3.5 Å) lead to interactions between the d_{z^2} orbitals.[23,53] Such close Pt···Pt contacts may occur in concentrated solutions in the form of ground state aggregates or excimers of mononuclear Pt(II) complexes, in the solid state, and in polynuclear Pt(II) complexes.[23,43,54] The axial interaction of the metal-centred orbitals results in an elevated, combined ("metal-metal") highest occupied molecular orbital (HOMO) level for the system. At the same time, interactions between the π orbitals of the ligands may lower the lowest unoccupied molecular orbital (LUMO) energy. Thus the HOMO-LUMO gap is overall narrowed and the MMLCT emission is red-shifted compared to the MLCT emission of the single non-interacting complex molecule.[23,53]

In contrast to Pt(II), a vast majority of reported examples of Pd(II) triplet emitters are only luminescent at low temperatures in the solid state but remain non-emissive at room temperature.[55–60] Compared to their Pt(II) analogues, the character of their emissive states tends to be even more ligand-centred, e.g. LC or ILCT in character, with only small MLCT contributions.[23,60] This is linked to long excited state lifetimes, but also diminished radiative rates due to the weaker metal participation moderating the SOC effect.[23] However, while the SOC constant ξ for Pd(II) is at 1460 cm^{-1} already considerably lower than that of Pt(II),[20,21] it is not the main reason for the weaker performance of Pd(II) triplet emitters. Rather, the accessibility of geometrically distorted MC states due to the significantly lower ligand splitting compared to Pt(II) is identified as the principal factor in most reports.[56–59] Therefore, the requirements for rigid strong-field ligands to achieve less distorted, high-lying MC states are even higher for the design of Pd(II) triplet emitters.[56] Increasingly, the role of Pd$\cdots$Pd contacts enabling MMLCT emission also from Pd(II) complexes is being explored as well.[23,59]

Reports of emissive Ni(II) complexes are even more sparse, with only a handful of published examples so far.[61–69] In a number of cases, the emission is essentially identified as metal-perturbed ligand fluorescence barely differing from the emission of the non-coordinated ligands, i.e. emission from ^{1}LC states.[61,64,65] This applies to a series of heteroleptic five-coordinated Ni(II) complexes containing substituted 8-hydroxyquinoline ligands reported by *Santana* and coworkers in 2010, as well as to the tetradentate Ni(II) complexes containing O^N^N^O coordinating phenazine-based Schiff base-like ligands reported by *Weber et al.* in 2021 (Figure 1.4 a). In both cases, the complexes are weakly emissive in solution at room temperature, with Φ_{PL} up to 1.6% for the five-coordinated complexes from the *Santana* group and up to 4.8% for the tetradentate complexes from the *Weber* group.[61,64] *Chen* and coworkers reported an emission from bis-carbene Ni(II) complexes contaning a bidentate ligand with alkyl bridged benzimidazolylidene moieties in the solid state in 2024, which they attribute to ^{1}LLCT states (Figure 1.4 b). The singlet nature of the emissive state is evidenced by the fact that iodido coligands, which increase SOC and enhance ISC, quench the luminescence, and that the emission is not sensitive to the presence of oxygen, which can also quench phosphorescence.[66]

Similarly to the situation with Pd(II), a major obstacle for triplet emission from Ni(II) complexes is the rapid decay of MLCT states to dark ^{3}MC states, as the ligand field splitting in Ni(II) complexes is again drastically smaller than in Pd(II) complexes.[65] This was demonstrated for the cyclometalated N^C^N Ni(II) complex [Ni(dpb)(Cl)] (Hdpb = dipyridylbenzene) in a 2023 study by *Wenger* and coworkers, who showed that the initially populated ^{1}MLCT states decay to dark ^{3}MC states within $<$ 1 ps. However, the group was also able to show that ^{3}MLCT state lifetimes in Ni(II) complexes can be systematically elongated using molecular design in a separate study published in 2022.[70,71] In both studies, they identified the most promising design strategies as increasing the ligand field strength by using strong σ donors and π acceptors and increasing the molecular rigidity against geometrical distortion, as well as control of the second coordination sphere through sterical hindrance.[70,71]

A first example of a phosphorescent Ni(II) complex was published by *Yam* and coworkers in 2020. The complex [Ni(dpb)(cbz)] is closely related to [Ni(dpb)(Cl)], but contains a carbazolyl (cbz) instead of a chlorido coligand (Figure 1.4 c). [Ni(dpb)(cbz)] shows weak luminescence at room temperature in addition to intense emission at 77 K. The assignment of the emissive state as metal-perturbed ^{3}LC (^{3}MP-LC) localized on the N^C^N ligand with possible weak ^{3}MLCT mixing is supported by the observed τ_{PL} in the submicrosecond range and the characteristic vibrational progression spacing at low temperature.[63] A key difference setting [Ni(dpb)(cbz)] apart from [Ni(dpb)(Cl)] is the stronger σ donation of the cbz coligand, matching the principles that were later delineated systematically by *Wenger et al.*,[63,70,71] however, it may be noted that carbazole is also a fluorophore.[72]

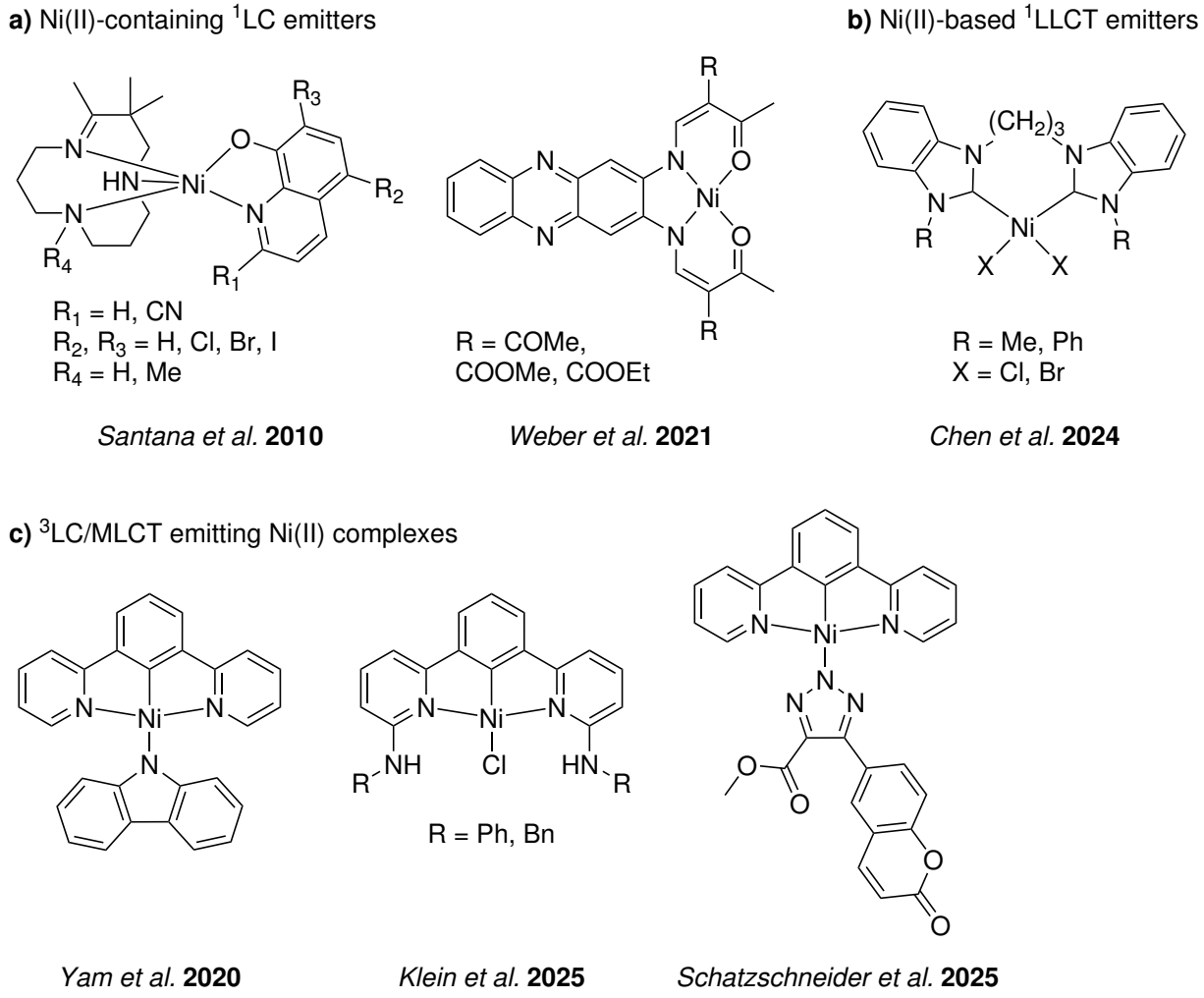

Figure 1.4: Published examples of photoluminescent Ni(II) complexes.[61,63,64,66,68,69]

Recently in 2025, *Schatzschneider* and coworkers reported another weakly phosphorescent Ni(dpb) derivative bearing a coumarin-functionalized triazolato coligand (Figure 1.4 c). Similarly to the example from the *Yam* group, the long-lived (μs range) emission of the complex at 77 K was assigned primarily ^{3}LC character with weak MLCT perturbation.[68] The two reports exemplify that engineering excited states to have essentially LC character with small MLCT contributions can allow to retain the long lifetimes of LC states while also accessing the triplet manifold,[63] despite the small SOC constant of the Ni(II) ion (ξ = 630 cm^{-1}).[20,21]

Also in 2025, *Klein et al.* reported two Ni(II) complexes containing dpb-derived N^C^N ligands which bear phenyl- or benzylamino groups *ortho* to the N positions (Figure 1.4 c). They observed emissions in the ms lifetime range in glassy matrices at 77 K and in poly(methyl methacrylate) (PMMA) matrices at up to 300 K, which were tentatively interpreted to stem from triplet states with Ni(II) involvement. The exceptionally long lifetimes were attributed to the steric strain introduced by the *ortho*-to-1N phenyl- and benzylamino groups, representing another successful application of a promising molecular design principle, namely molecular rigidification.[69]

2 Project Concept and Objectives

Replacing Pt with its lighter sister elements Pd and ultimately Ni for the use of transition metal complexes in optoelectronics, such as OLEDs, is an important goal both from an economical as well as ecological perspective.[2] Research aiming for this is focused on finding strategies to overcome the aforedescribed limitations of Pd(II) and Ni(II) complexes as emitter materials through sophisticated emitter design. As argued in the preceding sections, the key prerequisites for efficient triplet emission can be summarized as sufficient SOC, inaccessibility of MC states (i.e. strong ligand field splitting), and molecular rigidity.[23,24] The present work is comprised of essentially two sub-projects which approach the task from different angles based on these molecular design principles.

2.1 Effect of heavy atom containing ancillary ligands on triplet emission from Pt(II), Pd(II) and Ni(II) C^N^C complexes

The first sub-project is primarily focused on the aspect of SOC, and addresses the dichotomy that sufficient participation of the metal in the relevant excited states is required for efficient ISC, but also associated with rapid and often non-radiative decay especially in the case of Ni.[23,70] A potential strategy to ensure sufficient SOC and thus ISC rates in systems with potentially emissive MP-LC states might be the introduction of additional heavy atoms *via* the ligands. For example in the Ni(II) complexes reported by *Chen et al.* in 2023, this principle is already operational in the derivatives containing iodido coligands (compare Figure 1.4 b), albeit the heavy atom effect of the iodido ligands merely quenches the fluorescence but does not give rise to phosphorescence, probably due to the population of ^{3}MC states.[66]

Aiming to investigate the effect of introducing heavier donor atoms into triplet emitter candidates in depth in a controlled manner, we chose to focus on tridentate complexes with triphenylpnictane ($PnPh_3$, Pn = P, As, Sb, (Bi)) coligands. A first study of this type with promising results was published in 2020 by our close collaborators from the *Strassert* group. In their project, they worked with derivatives of the dianionic N^N^N ligand 2,6-bis(1H-1,2,4-triazol-5-yl)pyridine, and focused especially on the compensation of hybridization defects at the Pn donor atoms upon coordination to Pt(II) in addition to their study of the photophysics of the complexes.[73] Another contribution from the *Strassert* group to the collaborative triphenylpnictane ancillary ligand project was published in 2024, utilizing a mono-cyclometalated C^N^N ligand platform.[74] The triphenylpnictanes PPh_3, $AsPh_3$ and $SbPh_3$ are relatively strong σ donors, with the donor strength increasing slightly down the group along with the increasing *s* character of the lone pair.[75,76] The even heavier derivative containing the non-toxic main group metal bismuth is not known as a classical ligand, with examples of decently stable $BiPh_3$ transition metal complexes being essentially restricted to the early transition metal carbonyl complexes $[M(CO)_5(BiPh_3)]$ (M = Cr, Mo, W).[75] However, density functional theory (DFT) calculations accompanying the 2020 study by *Strassert* and coworkers on the aforementioned

[Pt(N^N^N)($PnPh_3$)] complexes suggested that the Bi-containing derivatives might be stable species with attractive photophysical properties.[73] Therefore, we tentatively decided to also include $BiPh_3$ in our study and attempt syntheses with it, despite having reason to doubt the isolability of the hypothesized species.[77]

For our in-depth follow-up on the pioneering work published by *Strassert et al.* in 2020, we chose to work with doubly cyclometalated C^N^C ligands (Figure 2.1 a). Touching also on the other two pillars of emitter design, a tridentate, doubly cyclometalated ligand can be expected to provide both an exceptionally strong ligand field and molecular rigidity, the degree of which depending on the specific structure. In order to minimize additional, complicating effects of specific functional groups, we selected two of the the most plain examples satisfying these characteristics, namely 2,6-di(phenid-2'-yl)pyridine (dpp), and its more rigid derivative dibenzo[*c,h*]acridine (dba), where the three rings are kept in plane by additional annulation.

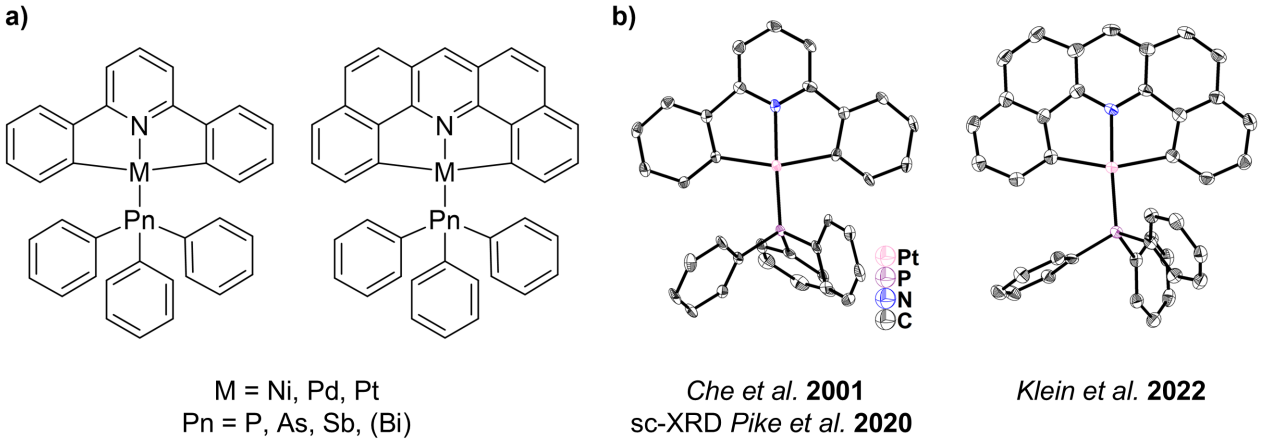

Figure 2.1: a) General structure of the complexes [M(dpp)($PnPh_3$)] and [M(dba)($PnPh_3$)] envisioned for our study on the effect of the introduction of additional heavy atoms through the ligand on the phosphorescence. b) Molecular structures from *sc*-XRD of the previously reported examples [Pt(dpp)(PPh_3)] and [Pt(dba)(PPh_3)].[40,78,79] Thermal ellipsoids shown at 50% probability, H atoms omitted for clarity.

Of the complexes thus envisioned for our studies, the Pt(II) and PPh_3 containing examples [Pt(dpp)(PPh_3)] and [Pt(dba)(PPh_3)] were previously reported (Figure 2.1 b).[40,78] Also reported, including by the *Klein* group, were the complexes [Pt(dpp)(dmso)], [Pt(dpp)(MeCN)] and [Pt(dba)(dmso)], which contain easily displaceable solvent coligands and may thus be useful precursors for the new target complexes.[28,80] The synthesis and properties of doubly cyclometalated Pt(II) complexes [Pt(C^N^C)(L)] (L = neutral ligand) are generally well documented in the literature.[28,40,78–82] Therefore, the system is quite attractive for our study since a broad range of reference data is available, which helps to contextualize any observed variations between the complexes containing different $PnPh_3$ coligands. While Pt(II) complexes are already established as efficient triplet emitters for the use in optoelectronic devices,[1,46] they may still serve as model systems for studies such as ours. Specifically the performance of the complex [Pt(dpp)(PPh_3)] does leave room for improvement, as it was reported to be non-emissive in fluid solution by *Che* and coworkers, and its Φ_{PL} in the solid or at low temperatures in glassy matrices does not reach unity. Furthermore, *Che et al.* concluded from their study that even at a concentration of

1 mmol/L, [Pt(dpp)(PPh_3)] does not form ^{3}MMLCT-emitting excimers due to the bulky arylphosphine coligand.[78] Therefore, we can expect that our study will not be unnecessarily complicated by another layer of complexity, i.e. concentration-dependent differences in the excited states of the chosen complexes.

In contrast, only two examples of doubly cyclometalated [Pd(C^N^C)(L)] derivatives have been previously reported, namely [Pd(dpp)(py)] (py = pyridine) by *von Zelewsky et al.* in 1988, and [Pd(dpp)(PPh_3)] by *Baya et al.* in 2022 (Figure 2.2 a). The report by *von Zelewsky et al.* states a very low yield of only 1.6% for a synthesis route *via* a lithiated dpp species, and includes very limited analytical data, e.g. no nuclear magnetic resonance (NMR) spectra.[83] The work of *Baya* and coworkers describes a more realistic and efficient synthesis protocol and does include NMR spectra of [Pd(dpp)(PPh_3)].[84] However, [Pd(dpp)(PPh_3)] has not been photophysically characterized.[59]

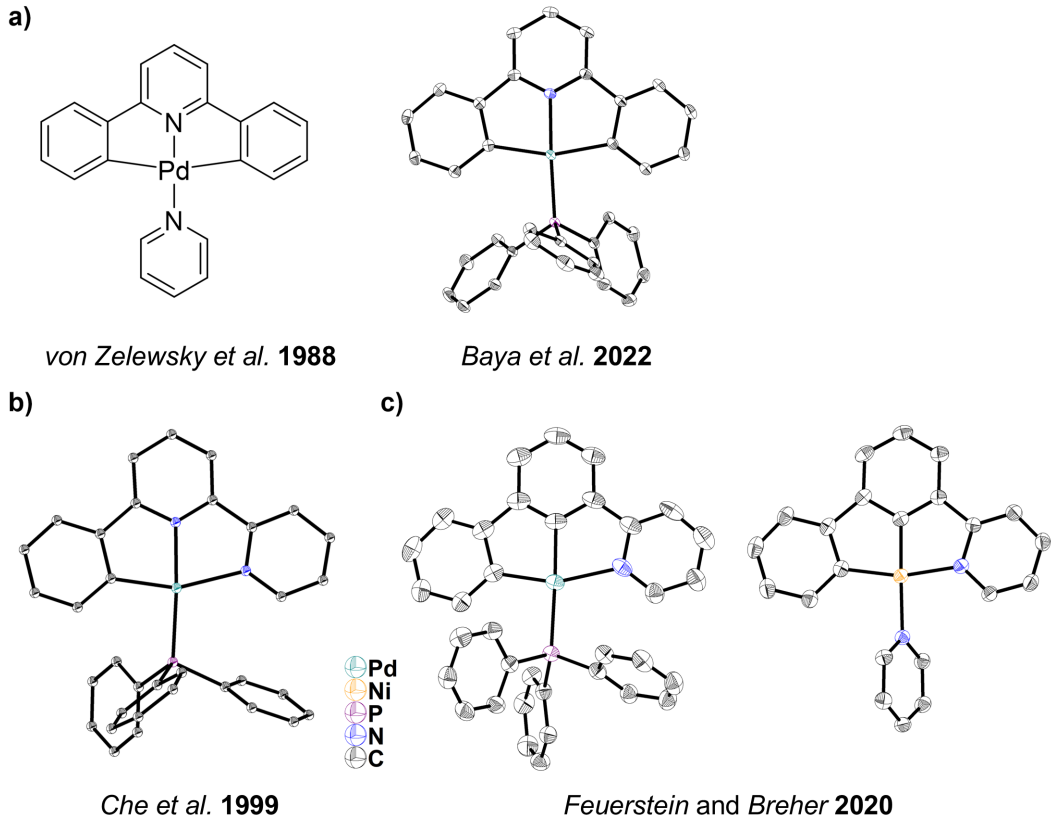

Figure 2.2: a) Structure and molecular structure from *sc*-XRD of the previously reported [Pd(dpp)(L)] derivatives with L = py and PPh_3.[83,84] b) Molecular structure from *sc*-XRD of the luminescent complex $[Pd(phbpy)(PPh_3)]^+$ (phbpy = 3-(phenid-2-yl)-2,2'-bipyridine).[58] c) Molecular structures from *sc*-XRD of the doubly cyclometalated complexes [Pd(bphpy)(PPh_3)] and [Ni(bphpy)(py)] (bphpy = 2-(biphen-2,2'-id-3-yl)pyridine)).[85] Thermal ellipsoids shown at 50% (a and b) or 30% (c) probability, H atoms and counteranions omitted for clarity.

Two examples of very similar literature-reported complexes are $[Pd(phbpy)(PPh_3)]^+$ and [Pd(bphpy)(PPh_3)] (phbpy = 3-(phenid-2-yl)-2,2'-bipyridine, bphpy = 2-(biphen-2,2'-id-3-yl)pyridine), the latter being the C^C^N coordinated constitutional isomer of [Pd(dpp)(PPh_3)] (Figure 2.2 b and c).[58,85] $[Pd(phbpy)(PPh_3)]^+$ shows an emission at 77 K in the solid state and in glassy matrices, whereas [Pd(bphpy)(PPh_3)] in the solid state is even emissive at room temperature, in both

cases from ^{3}MP-LC states.[58,85] While the emission properties of these complexes are at least partly tied to the non-palindromic nature of the tridentate ligands,[59,85] we expect the [Pd(dpp)($PnPh_3$)] (Pn = P, As, Sb) complexes to be at least weakly emissive at 77 K and thus suited to study the effect of the $PnPh_3$ ligand variation on them.

Naturally, the ultimate goal is to study directly whether triplet emission from [Ni(dpp)($PnPh_3$)] (Pn = P, As, Sb) can be facilitated or enhanced by the presence of heavy donor atoms, alas, no examples of doubly cyclometalated [Ni(C^N^C)(L)] complexes are known to date. Along with [Pd(bphpy)(PPh_3)], *Feuerstein* and *Breher* reported the isolation of several crystals of [Ni(bphpy)(py)], in both cases using a double C–X activation procedure (Figure 2.2 c).[85] Judging from this, the feasibility of isolating [Ni(dpp)(PPh_3)] after finding a suitable synthesis method, involving C–H activation, C–X activation, or both, must not be ruled out categorically. However, Ni(II) C^N^C complexes are probably even more reactive than their C^C^N isomers due to the *trans* configuration of the strong σ donors.[85,86] This reinforces the value of thoroughly studying the effect of heavy ancillary donor atoms on the photophysics of the Pt(II) and Pd(II) C^N^C systems first to gauge the balance between effort and effect for the Ni(II) system.

2.2 Luminescent Ni(II) perfluorophenyl complexes with α-diimine ligands

The second sub-project is most focused on the design principle of creating a strong ligand field, and picks up on the exact issue that the doubly cyclometalated [Ni(C^N^C)(L)] system is anticipated to be synthetically difficult to access and extremely reactive. Due to the exceptional difficulties expected for the potential preparation and handling of [Ni(C^N^C)(L)] derivatives such as [Ni(dpp)(PPh_3)], we decided to concurrently explore a different system that includes the most desirable structural characteristics of [Ni(C^N^C)(L)], but is significantly more stable and accessible. With the long-term perspective of applications of new emitter materials for example in OLED devices, stability and accessibility of the compounds are important considerations right along with their photophysical performance.[87]

The perfluorophenyl ligand C_6F_5 is a monodentate C-coordinating aryl ligand, and as such a very strong σ donor. Additionally, it is a potentially strong π acceptor due to the electron withdrawing effect of the fluoro substituents, which lowers the energy of the π* orbitals.[88,89] Therefore, complexes of the type [Ni(C_6F_5)$_2$$L_2$] feature two very strong carbanionic ligands like the hypothetical [Ni(C^N^C)(L)]. While *trans*-configured examples do exist,[90,91] most examples are *cis*-configured,[91–95] making them more similar to [Ni(C^C^N)(L)] electronically, which according to *Feuerstein* and *Breher* might be even more favourable.[85]

Most commonly, [Ni(C_6F_5)$_2$$L_2$] derivatives are synthesized from Ni(C_6F_5)$_2$ solvent complexes [Ni(C_6F_5)$_2$(solv)$_2$] as precursors from which the labile solvent ligands can be displaced by mono- or bidentate ligands.[91,93,94,96–98] An early method for the synthesis of a Ni(C_6F_5)$_2$ solvent complex was presented in 1978 by *Arcas* and *Royo*.[96,97] They described the preparation of a solution containing

a $Ni(C_6F_5)_2$ species *via* a Grignard reaction of F_5C_6MgBr with $NiBr_2$ in THF and 1,4-dioxane (Figure 2.3 a).[96] The resulting $Ni(C_6F_5)_2$ complex was identified as $[Ni(C_6F_5)_2(1,4\text{-dioxane})_2]$ based on elemental analysis later that year.[97] In the late 1980s and 1990s, *López* and coworkers established *cis*-$[Ni(C_6F_5)_2(PhCN)_2]$ as another synthetically useful precursor for $[Ni(C_6F_5)_2L_2]$ complexes.[93,99,100] Its synthesis is based directly on the synthesis of $[Ni(C_6F_5)_2(1,4\text{-dioxane})_2]$, which can be converted to *cis*-$[Ni(C_6F_5)_2(PhCN)_2]$ by adding benzonitrile after complete removal of magnesium salts (Figure 2.3 b). The subsequent popularity of *cis*-$[Ni(C_6F_5)_2(PhCN)_2]$ as a precursor for $Ni(C_6F_5)_2$ complexes over $[Ni(C_6F_5)_2(1,4\text{-dioxane})_2]$ is probably due to its higher stability and thus more convenient handling.[93,94,98]

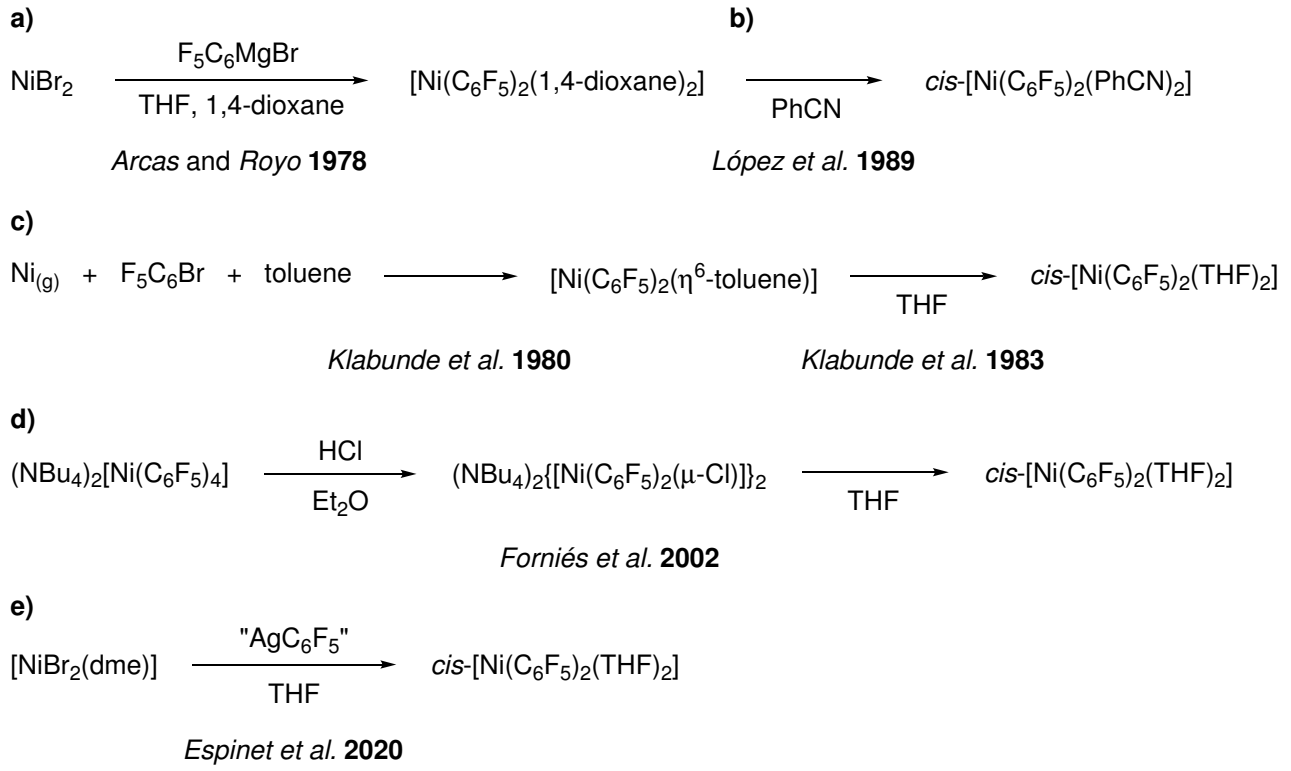

Figure 2.3: Previously reported synthesis routes for common $Ni(C_6F_5)_2$ solvent complexes $[Ni(C_6F_5)_2(solv)_2]$, which are precursors for $[Ni(C_6F_5)_2L_2]$.[91,92,97,99,101,102]

Another $Ni(C_6F_5)_2$ solvent complex reported by multiple groups is $[Ni(C_6F_5)_2(THF)_2]$.[91,92,102] In 1980, the group of *Klabunde* reported the synthesis of $[Ni(C_6F_5)_2(\eta^6\text{-toluene})]$ through the reaction of vaporized elemental Ni with F_5C_6Br and toluene (Figure 2.3 c).[101] In 1983, they reported the subsequent synthesis of $[Ni(C_6F_5)_2(THF)_2]$ by treating $[Ni(C_6F_5)_2(\eta^6\text{-toluene})]$ with THF. Based on IR spectroscopy, *Klabunde et al.* assigned their product as *trans*-$[Ni(C_6F_5)_2(THF)_2]$.[102] However, in 2002, *Forniés* and coworkers reported the solid state structure of *cis*-$[Ni(C_6F_5)_2(THF)_2]$, which showed an identical IR spectrum to the material obtained by *Klabunde et al.*, proving that the previous assignment of the configuration was erroneous.[92] Differing from the route described by *Klabunde*, *Forniés* and coworkers obtained *cis*-$[Ni(C_6F_5)_2(THF)_2]$ by treating $[Ni(C_6F_5)_4]^{2-}$ with anhydrous HCl in Et_2O and reacting the resulting complex $[Ni(C_6F_5)_2(\mu\text{-Cl})]_2^{2-}$ with $AgClO_4$ in THF (Figure 2.3 d). Most recently, *Espinet* and coworkers synthesized *cis*-$[Ni(C_6F_5)_2(THF)_2]$ *via* transmetalation of C_6F_5 ligands from "AgC_6F_5" to Ni(II) in THF (Figure 2.3 e).[91]

The stability of *cis*-Ni(C_6F_5)$_2$ complexes is strongly dependent on the ligand(s) occupying the remaining two coordination sites. The two dominant, competing decomposition pathways are C–C coupling (reductive elimination) and hydrolysis, forming $C_{12}F_{10}$ and F_5C_6H, respectively.[91] Hydrolysis is more prominent for [Ni(C_6F_5)$_2$L$_2$] derivatives where L$_2$ is two monodentate ligands, as it is primarily promoted by coordination of H_2O in place of L. Axial coordination and hydrolytic attack of H_2O is hindered by the hydrophobic shielding of of the Ni(II) center by the C_6F_5 ligands, which are typically oriented approximately perpendicular to the coordination plane (Figure 2.4 a).[91,92,94] This is a major reason for the strikingly higher stability of C_6F_5 complexes compared to C_6H_5 complexes. Furthermore, the presence of fluorine substituents specifically in the *ortho* position of aryl ligands is positively correlated with the metal–C bond strength, which translates into decreased reductive elimination rates compared to non-*ortho*-fluorinated aryl ligands.[91,103] The reductive elimination of $C_{12}F_{10}$ is generally promoted thermally and in non-coordinating solvents, as well as by the presence of atmospheric oxygen.[91] While complexes containing bipyridines do not undergo reductive elimination at room temperature, as noted already by *Yamamoto* and coworkers in 2002, *Espinet et al.* have demonstrated that phosphine-electron withdrawing olefin (PEWO) ligands induce instantaneous F_5C_6–C_6F_5 coupling, with various mono- and bidentate phosphine ligands falling somwhere on the scale between these two extremes.[89,91,95]

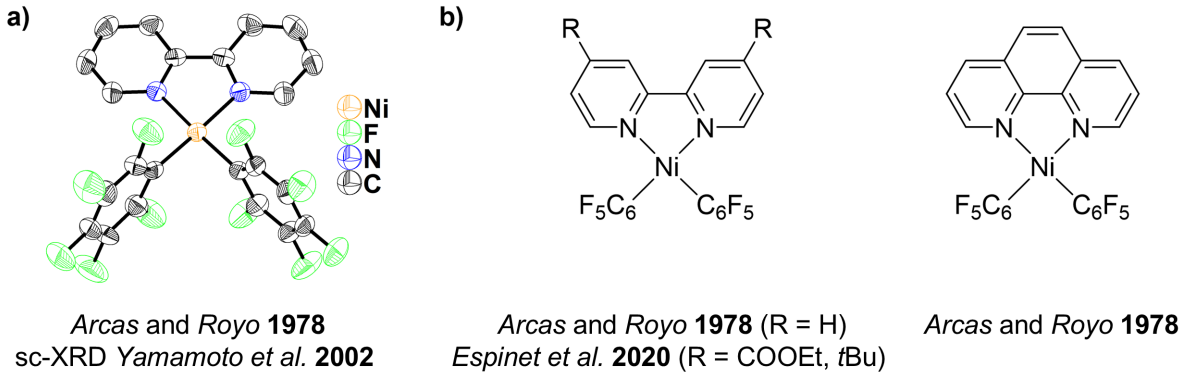

Figure 2.4: a) Molecular structure from *sc*-XRD of the stable Ni(C_6F_5)$_2$ complex [Ni(C_6F_5)$_2$(bpy)],[89,96] exhibiting the typical near-perpendicular orientation of the perfluorophenyl ligands to the coordination plane. Thermal ellipsoids shown at 50% probability, H atoms omitted for clarity. b) Further examples of previously reported Ni(C_6F_5)$_2$ complexes with α-diimine ligands on which the development of emissive Ni(C_6F_5)$_2$ derivatives may be based.[91,96,97]

For the purpose of C–C coupling catalysis, high rates of reductive elimination are desirable, but in triplet emitter candidates, both hydrolysis and reductive elimination should ideally be suppressed. Therefore, Ni(C_6F_5)$_2$ complexes with chromophoric α-diimine ligands derived from the published examples shown in Figure 2.4 b appear to be an excellent starting point, both due to the high stability of [Ni(C_6F_5)$_2$(bpy)] and its derivatives noted by *Yamamoto* and *Espinet*, and the concurrent suitability of bpy-derived chromophores as ligands for luminescent transition metal complexes.[104–107] Exploring whether [Ni(C_6F_5)(N^N)] complexes are indeed ideal Ni(II) emitter candidates is therefore another core objective of this work.

3 Results and Discussion

3.1 Enhanced Luminescence Properties Through Heavy Ancillary Ligands in [Pt(C^N^C)(L)] Complexes, L = $AsPh_3$ and $SbPh_3$ (Publication 1)

We started our investigations of the effects of $PnPh_3$ ancillary ligands on the photophysics of group 10 doubly cyclometalated C^N^C complexes with the third row transition metal Pt. The focus of the work are in-depth spectroscopic studies on the compounds [Pt(dpp)($PnPh_3$)] and [Pt(dba)($PnPh_3$)] (dpp = 2,6-di(phenid-2'-yl)pyridine, dba = dibenzo[*c*:*h*]acridine, Pn = P, As, Sb), which are privileged by their facile synthesis and high stability. All results are presented and discussed in the following **Publication 1**, which is reprinted from Ref.[108] with permission from the Royal Society of Chemistry.

The author's contributions to the work include the synthesis and characterization of the discussed compounds, the (TD-)DFT calculations, and the autonomous preparation of the manuscript for revision in collaboration with the co-authors. Emission spectroscopy and transient absorption spectroscopy were conducted at the labs of Prof. Dr. Cristian A. Strassert and Prof. Dr. Benjamin Dietzek-Ivanšić, respectively. The individual contributions of all co-authors are described in detail in section "Author contributions" in the publication. The Supporting Information (experimental details, spectra and tables) for **Publication 1** is provided in section 6.1.

Dalton Transactions

ROYAL SOCIETY OF CHEMISTRY

PAPER

View Article Online
View Journal | View Issue

Check for updates

Cite this: *Dalton Trans.*, 2023, **52**, 18220

Enhanced luminescence properties through heavy ancillary ligands in [Pt(C^N^C)(L)] complexes, L = $AsPh_3$ and $SbPh_3$†

Rose Jordan, [a] Iván Maisuls, [b] Shruthi S. Nair, [c,d] Benjamin Dietzek-Ivanšić, *[c,d] Cristian A. Strassert *[b] and Axel Klein *[a]

Received 1st October 2023,
Accepted 20th November 2023

DOI: 10.1039/d3dt03225f

rsc.li/dalton

In the frame of our research aiming to develop efficient triplet-emitting materials, we are exploring the concept of introducing additional heavy atoms into cyclometalated transition metal complexes to enhance intersystem-crossing (ISC) and thus triplet emission through increased spin–orbit coupling (SOC). In an in-depth proof-of-principle study we investigated the double cyclometalated Pt(II) complexes [Pt(C^N^C)($PnPh_3$)] (HC^N^CH = 2,6-diphenyl-pyridine (H_2dpp) or dibenzoacridine (H_2dba); Pn = pnictogen atoms P, As, Sb, or Bi) through a combined experimental and theoretical approach. The derivatives containing Pn = P, As, and Sb were synthesised and characterised comprehensively using single crystal X-ray diffraction (scXRD), UV-vis absorption and emission spectroscopy, transient absorption (TA) spectroscopy and cyclic voltammetry (CV). Across the series P < As < Sb, a red-shift is observed concerning absorption and emission maxima as well as optical and electrochemical HOMO–LUMO gaps. Increased photoluminescence quantum yields Φ_L and radiative rates k_r from mixed metal-to-ligand charge transfer (MLCT)/ligand centred (LC) triplet states are observed for the heavier homologues. Transient absorption spectroscopy showed processes in the ps range that were assigned to the population of the T_1 state by ISC. The heavy $PnPh_3$ ancillary ligands are found to enhance the emission efficiency due to both higher Pt–Pn bond strength and stronger SOC related to increased MLCT character of the excited states. The experimental findings are mirrored in hybrid (TD-)DFT calculations. This allowed for extrapolation to the rather elusive Bi derivatives, which were synthetically not accessible. This shortcoming is attributed to the transmetalation of phenyl groups from $BiPh_3$ to Pt, as supported by experimental NMR/MS as well as DFT studies.

Introduction

Luminescent organometallic transition metal complexes with efficient phosphorescence at ambient temperature are the subject of academic and technological interest with promising applications in illumination, display technology, sensors, therapeutic agents, and biological probes.[1–15] High quantum efficiency of such materials is due to strong spin–orbit coupling (SOC), which allows for triplet (electro)luminescence.[5,7] However, many transition metal complexes are scarcely emissive at room temperature, often because their excited metal-centred (d–d*) states are subject to efficient non-radiative deactivation.[5,8,9,11] Cyclometalated heteroaromatic ligands appear to be a good strategy towards effective emitters in many regards. The very strong ligand field of the cyclometalated carbanions raises the energy of the dissociative d–d* states impeding the population of these non-emissive, so-called dark states.[8,11] The rigidity introduced by these ligands prohibits large distortions of the excited state compared with the electronic ground state. High rigidity of both the organic ligand and the coordination polyhedron around the metal are considered to be important to generate long-lived and efficient triplet emitting complexes.[5,9,16–42] Such a strategy has led to many cyclometalated Pt(II) and a number of related Pd(II) com-

[a]*University of Cologne, Faculty for Mathematics and Natural Sciences, Department of Chemistry, Institute for Inorganic Chemistry, Greinstrasse 6, D-50939 Köln, Germany. E-mail: rjordan1@uni-koeln.de, axel.klein@uni-koeln.de*
[b]*Universität Münster, Institut für Anorganische und Analytische Chemie, CiMIC, CeNTech, Heisenbergstraße 11, D-48149 Münster, Germany. E-mail: maisuls@uni-muenster.de, cstra_01@uni-muenster.de*
[c]*Friedrich Schiller University Jena, Institute for Physical Chemistry (IPC), Helmholtzweg 4, 07743 Jena, Germany. E-mail: benjamin.dietzek@uni-jena.de*
[d]*Leibniz Institute for Photonic Technologies Jena (IPHT), Research Department Functional Interfaces, Albert-Einstein-Str. 9, 07745 Jena, Germany. E-mail: shruthi.santoshnair@leibniz-ipht.de, benjamin.dietzek@leibniz-ipht.de*

†Electronic supplementary information (ESI) available: All other data including experimental procedures and characterisation data for all new compounds. CCDC 2149899, 2257280, 2194357 and 2208288 for [Pt(dpp)($AsPh_3$)], [Pt(dpp)($SbPh_3$)], [Pt(dba)($AsPh_3$)] and [Pt(dba)($SbPh_3$)]. For ESI and crystallographic data in CIF or other electronic format see DOI: https://doi.org/10.1039/d3dt03225f

This journal is © The Royal Society of Chemistry 2023

plexes, which are emissive either from triplet states with primarily ligand-centred ^{3}LC ($^3\pi$–π^*) character, from metal-to-ligand charge transfer ^{3}MLCT states, or mixtures thereof.[5,8,16–29]

On the way to introducing Ni(II) to the field, replacing Pt or Pd, the intrinsically much smaller spin–orbit coupling (SOC) and ligand field splitting of Ni(II) pose an obstacle to the realisation of efficient phosphorescence.[29,34,42–46] Considering the question of how to facilitate spin-forbidden transitions and to also reach significant phosphorescence rates in Ni(II) complexes has led us to the idea of introducing additional heavy main group elements into the compounds, specifically in the form of $PnPh_3$ (Pn = P, As, Sb, Bi) ancillary ligands for tridentate ligand systems. The ancillary ligand or coligand represents an important point of access for tuning the properties of square planar complexes with tridentate ligands.[17,26,47–49] In order to evaluate whether our concept of improving phosphorescence using heavy ancillary ligands for tridentate ligand systems is viable, we initially resorted to Pt(II) complexes as a synthetically well-accessible model system. After a first study on a series of Pt(II) complexes [Pt(N^N^N)($PnPh_3$)] (Pn = P, As, Sb) containing the tridentate N^N^N = 2,6-bis(3-(trifluoromethyl)-1*H*-1,2,4-triazol-5-yl)pyridine and 2,6-bis(3-(*tert*-butyl)-1*H*-1,2,4-triazol-5-yl)pyridine ligands found little systematic variation between the $PnPh_3$ homologues due to a saturation effect from Pt on the emission efficiency in this N^N^N system,[30] we moved on to cyclometalated C^N^C ligand systems.[31]

Herein, we report two series of double cyclometalated Pt(II) complexes [Pt(C^N^C)($PnPh_3$)] (Pn = P, As, Sb) based on the two established C^N^C ligand systems dpp (H_2dpp = 2,6-diphenyl-pyridine)[31,50] and dba (H_2dba = dibenzo[*c*,*h*]acridine)[31,51] which showed an enhancement of the phosphorescence quantum yields for their heavier congeners. The role of radiative and radiationless deactivation rates was studied by combining extensive photoluminescence (PL) and transient absorption spectroscopy (TAS) with density functional theory (DFT) calculations.

Results and discussion

Synthesis and structural characterisation

The new complexes [Pt(C^N^C)($AsPh_3$)] and [Pt(C^N^C)($SbPh_3$)] were synthesised in the same way as the previously reported lighter congeners [Pt(C^N^C)(PPh_3)][50,51] *via* a facile ligand exchange reaction from the corresponding [Pt(C^N^C)(dmso)] precursors as shown in Scheme 1 in good yields ranging from 64% to 84% (more information in the ESI†). The new complexes were characterised by nuclear magnetic resonance (NMR) spectroscopy (see Fig. S1–S20 in the ESI†) as well as high-resolution electrospray ionisation mass spectrometry (HR-ESI-MS) and single-crystal X-ray diffraction (scXRD).

Similar to our previous report on a series of Pt(II) complexes [Pt(N^N^N)($PnPh_3$)] (N^N^N = 2,6-bis(3-(trifluoromethyl)-1*H*-1,2,4-triazol-5-yl)pyridine and 2,6-bis(3-(*tert*-butyl)-1*H*-1,2,4-triazol-5-yl)pyridine; Pn = P, As, Sb)[30] the $BiPh_3$ derivatives of the dpp and dba complexes were not isolated, but MS and NMR evidence suggests their transient formation. Based on our observation of progressively de-phenylated fragments of $BiPh_3$ and progressively phenylated derivatives of the dpp ligand in ESI-MS reaction control samples as well as the relative depletion of $BiPh_3$ next to [Pt(dpp)(dmso)] during *in situ* ^{1}H NMR studies (Fig. S21, ESI†), we suspect that the reason for our failure to isolate [Pt(dpp)($BiPh_3$)] lies in the catalytic decomposition of $BiPh_3$ in the presence of [Pt(dpp)(dmso)]. A free DFT geometry optimisation of the postulated structure of [Pt(dpp)($BiPh_3$)] yielded a pentacoordinate geometry [Pt(C^N^C)(Ph)($BiPh_2$)] where a phenyl group from $BiPh_3$ moved to the Pt centre in the C^N^C coordination plane while the remaining $BiPh_2$ fragment is displaced into a distal position with a Pt···Bi distance of 2.72 Å (Fig. S26 and Table S5, ESI†). This further supports the assumption that the decomposition of $BiPh_3$ under the reaction conditions is triggered by the transmetalation of phenyl groups to Pt as initial reaction, which is then followed by a cascade of decomposition reactions. Detailed information on our experimental studies leading to this conclusion as well as computational details can be found in the ESI.† For further DFT calculations on the elusive [Pt(dpp)($BiPh_3$)] and [Pt(dba)($BiPh_3$)] complexes, the predicted transmetalation of a phenyl group was suppressed during the geometry optimisation by excluding the N-Pt-Bi angle from the optimisation process (Fig. S26 and Table S5, ESI†).

Crystal structures and DFT-calculated molecular structures

The structures of the four new complexes [Pt(C^N^C)($AsPh_3$)] and [Pt(C^N^C)($SbPh_3$)] (C^N^C = dpp, dba) were determined by scXRD (Fig. 1 and Figs. 22–24, ESI†). Details on data collection, structure solution and refinement as well as selected structural parameters are listed in Tables S1–S3 (ESI†) alongside with the data for the previously reported [Pt(dpp)(PPh_3)] and [Pt(dba)(PPh_3)].[50,51] The crystal structures feature long

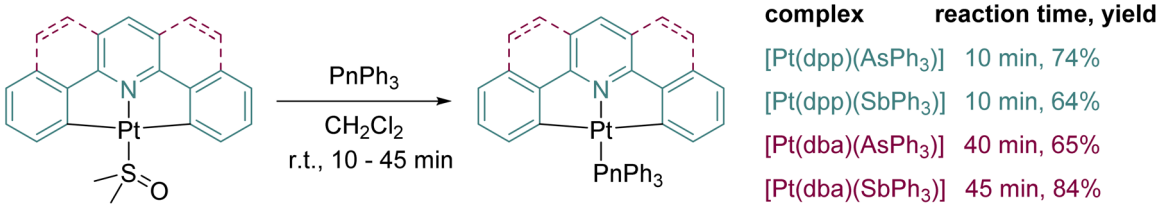

Scheme 1 General synthetic procedure for the complexes.

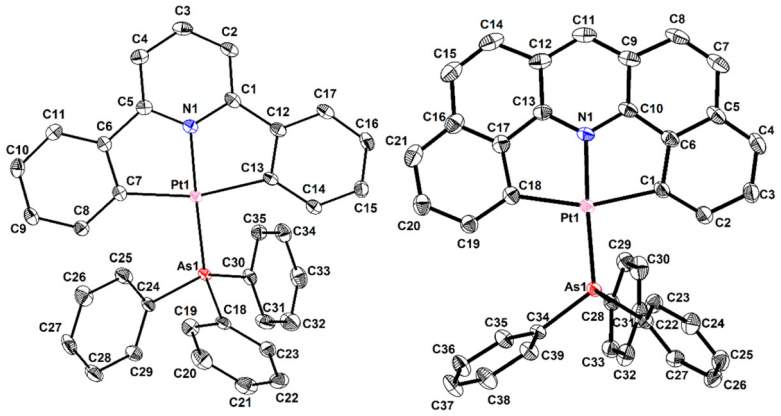

Fig. 1 Molecular structures of the complexes [Pt(dpp)($AsPh_3$)] (left) and [Pt(dba)($AsPh_3$)] (right) with numbering, as obtained from scXRD. Displacement ellipsoids are shown at 50% probability, H atoms omitted for clarity.

Pt···Pt distances ranging from about 7 to 10 Å (far beyond a significant interaction between the Pt atoms, typically below 3.5 Å); thus, no significant Pt···Pt interactions nor π-stacking interactions were found.[52,53] In contrast, the dba containing structures show pronounced π-stacking of the acridine moieties with centroid distances between 3.5 and 3.6 Å. However, due to the antiparallel alignment of the [Pt(dba)] fragments as dictated by the bulky $PnPh_3$ ancillary ligands, significant Pt···Pt interactions can still be ruled out from large Pt···Pt distances ranging from 6.9 to 7.7 Å (Fig. 1).

As expected from the increasing radii of the progressively heavier pnictogens, the Pt–Pn bond lengths increase by about 0.11 Å from the P to the As derivatives and by another 0.15 to 0.18 Å from the As to the Sb derivatives for both C^N^C ligands. This aligns with our findings for the previously reported [Pt(N^N^N)($PnPh_3$)] series. However, the Pt–Pn distances are overall slightly shorter in the herein reported C^N^C complexes by about 0.07 to 0.02 Å.[30] This indicates a slightly higher bond strength, possibly due to an increased covalent character of the Pt–Pn bond in the herein studied system. The differences between Pt–Pn bond lengths (if comparing the C^N^C *versus* N^N^N complexes) are largest for the PPh_3 complexes and smallest for the $SbPh_3$ derivatives. This may be related to the Pt–Sb bond being generally more covalent than the Pt–P or Pt–As bond due to better orbital overlap between atoms of more similar atomic or ionic radii and polarisability. The averaged C–Pn–C angles decrease slightly along P > As > Sb for both series of complexes, from P (~104°) to As (~103°) and more markedly to Sb (99° for dpp, 101° for dba) (data in Tables S2 and S3, ESI†), exceeding the C–Pn–C angles of the free ligands by around 3 to 4°. We have previously described this widening of the angles upon binding to Pt as compensation of the hybridisation defect at the Pn atom.[30]

Notably for the complexes with the more flexible dpp ligand, a significant deviation from a coplanar orientation between the pyridine moiety and one of the phenyl moieties is observed in the solid state, with dihedral angles reaching up to 12° in the PPh_3 derivative.[50] This pronounced unilateral twist is not predicted by DFT geometry optimisations using BP86/def2-TZVP/CPCM(CH_2Cl_2)[54–58] (Tables S2 and S3, ESI†) and the underlying reason are likely packing effects in the solid state. Apart from this deviation, the experimentally observed structural trends in the solid state are well reproduced by DFT. The optimised structures were used as the basis for all further calculations using the hybrid functional TPSSh, which was found to provide qualitatively good to excellent results for organometallic transition metal complexes in previous studies.[34,59–62]

Electrochemistry and DFT-calculated frontier orbitals

Cyclic voltammograms showed irreversible oxidations at around +0.6 V (Fig. 2, Fig. S27–S32 and Table S6, ESI†) for all complexes with slightly higher values for the dba derivatives and almost no variation within the dpp and dba series. They are assigned to essentially metal centred Pt(II)/Pt(III) couples. The DFT-calculated frontier molecular orbital (FMO) landscapes (Fig. S33 and S34, ESI†), which show energetically virtually invariant highest occupied molecular orbitals (HOMOs) with strong metal centred character for the complexes within each series, support this assignment.

Two reduction processes were observed for all complexes (Fig. 2). Interestingly, their potentials are virtually identical for [Pt(dpp)(PPh_3)] and [Pt(dpp)($AsPh_3$)] and appear at −2.36 and −2.96 V (*vs.* ferrocene/ferrocenium). For the dba complexes three reduction waves were observed, the first ones at markedly less negative potentials. In both series the $SbPh_3$ complexes exhibit the least negative values. The DFT-calculated lowest unoccupied molecular orbitals (LUMO) represent exclusively the π* levels of the C^N^C ligands. This fits well to the general separation of the reduction potential of the two systems into dpp and dba complexes. The observed $PnPh_3$ ancillary ligand-dependent differences (with the Sb derivatives having the least negative potentials) are fully in line with the DFT-calculated LUMO+1 showing contributions from the $PnPh_3$ ligands. These assignments are further substantiated through spectro-electrochemical (UV-vis-SEC) studies (Fig. S39–S42, ESI†).

This journal is © The Royal Society of Chemistry 2023

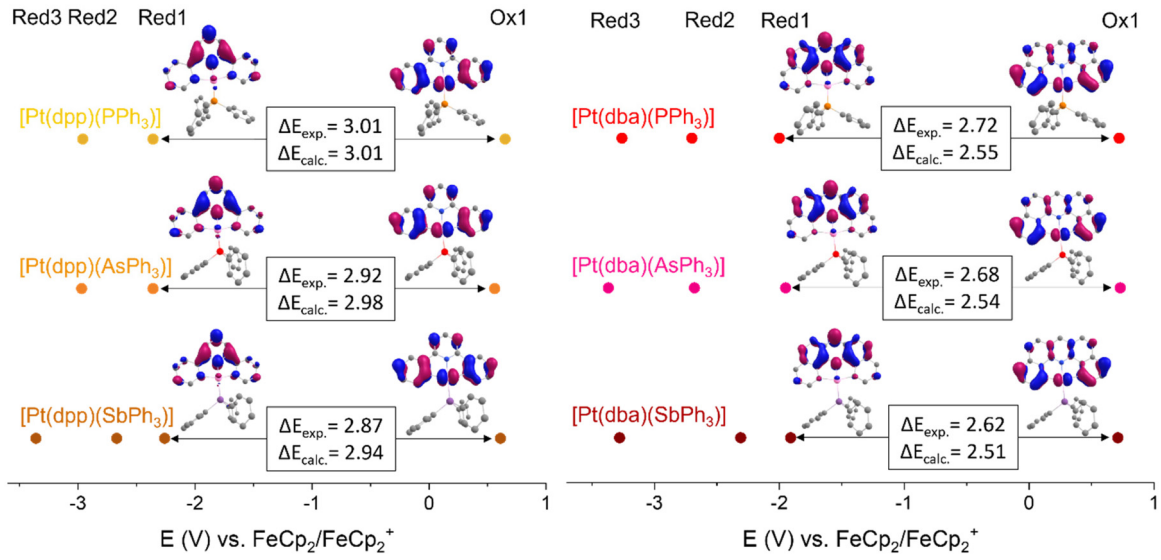

Fig. 2 Electrochemical data from cyclic voltammetry in 0.1 M n-Bu_4NPF_6 THF solutions at a scan rate of 50 mV s^{-1} (dots); DFT-calculated frontier orbitals, and energies for [Pt(dpp)(PnPh$_3$)] (left) and [Pt(dba)(PnPh$_3$)] (right; Pn = P, As, Sb). Values for the redox potentials are half half-wave potentials $E_{1/2}$ for the reversible first reduction and potentials E_p for the irreversible oxidations and second and third reductions (Table S6, ESI†).

Upon reduction, the complexes show several bands indicative of reduced phenyl-pyridine or acridine moieties, and pointing to ligand-centred LUMOs mirroring what has been reported for related complexes.[25,34,51,63,64] Oxidation of the dpp complexes leads to a general bleaching of the long-wavelength bands in line with a depopulation of the metal-dominated HOMO. For the dba derivatives, the long-wavelength bands also bleach upon oxidation, but also a broad absorption band ranging from 500 to 350 nm appears. This slightly resembles the acridinyl radical (also called "C radical"), which absorbs in this range[65,66] and agrees with the more pronounced contribution of the dba ligand to the HOMO of the complex, particularly when compared with dpp.

The electrochemical HOMO–LUMO gaps range from about 3.0 to 2.6 eV narrowing along the series P > As > Sb for both the dpp and the dba complexes. The smaller gaps for the dba complexes (2.72 to 2.62 eV) compared with the dpp derivatives (3.01 to 2.87 eV) by about 0.2 to 0.3 eV can be rationalised by the more extended π-system in the dba complexes and are reproduced by the DFT-calculations (Fig. 2, Fig. S33 and S34, ESI†). Parallel trends are predicted by DFT, which shows a decrease in the HOMO–LUMO gaps between the PPh_3 and $SbPh_3$ derivatives by 0.07 eV for the dpp complexes and 0.06 eV for the dba complexes. The DFT calculated values are generally slightly smaller than the experimental values. It should be noted that the predictive power of DFT reproduces trends much better than absolute numbers, as specifically the HOMO–LUMO gap depends strongly on how much Hartree–Fock exchange is included in the functional.[67,68] Energetically above the strongly ligand-centred LUMOs (LUMO and LUMO+1 for dpp; LUMO to LUMO+2 for dba), a metal centred MO of strong $d_{x^2-y^2}$ character is found in the DFT calculated FMO landscapes. This orbital is significantly destabilised across both series from P to Sb, indicating that the ligand-field splitting increases down the group 15 elements due to their increasing polarisability and atomic radii, as discussed earlier. The described trends for the PPh_3, $AsPh_3$, and $SbPh_3$ derivatives of both the dpp and dba complexes are continued in the calculated FMO landscapes for the hypothetical $BiPh_3$ derivatives.

UV-vis absorption spectroscopy and TD-DFT calculations

The UV-vis absorption spectra of the dba complexes [Pt(dba)(PnPh$_3$)] (Pn = P, As, Sb) feature absorption bands down to almost 600 nm, which are structured into four double bands around 290, 340, 400 and 520 nm (Fig. 3, Table 1, Fig. S35 and S37, ESI†). The dpp complexes [Pt(dpp)(PnPh$_3$)] (Pn = P, As, Sb) show only two intense, structured absorption bands, one at about 250 to 300 nm and a second at around 350 nm. Additionally, very weak absorption bands trail down to about 500 nm. UV-bands in both systems have been previously assigned to transitions into LC (π–π*) states, whereas mixed LC/metal-to-ligand charge transfer (MLCT) states were discussed for increasingly long-wavelength bands.[31,51,69,70]

TD-DFT calculated absorption spectra excellently match the experimental results and support these assignments (Fig. 3, Table 1, Fig. S35–S38, Tables S6 and S7, ESI†). Fig. 3 (right) shows selected transition difference densities for the TD-DFT calculated transitions for [Pt(dba)(SbPh$_3$)] as a representative example, while illustrating their mixed yet predominantly ^{1}LC and ^{1}MLCT character, in agreement with previously reported data for related compounds.[25,28–31,34,35,51,52] Across the series P > As > Sb, a slight red-shift of the UV-vis absorption energies is both observed experimentally and predicted theoretically, matching the electrochemical data and the electronic structure modelled by DFT.

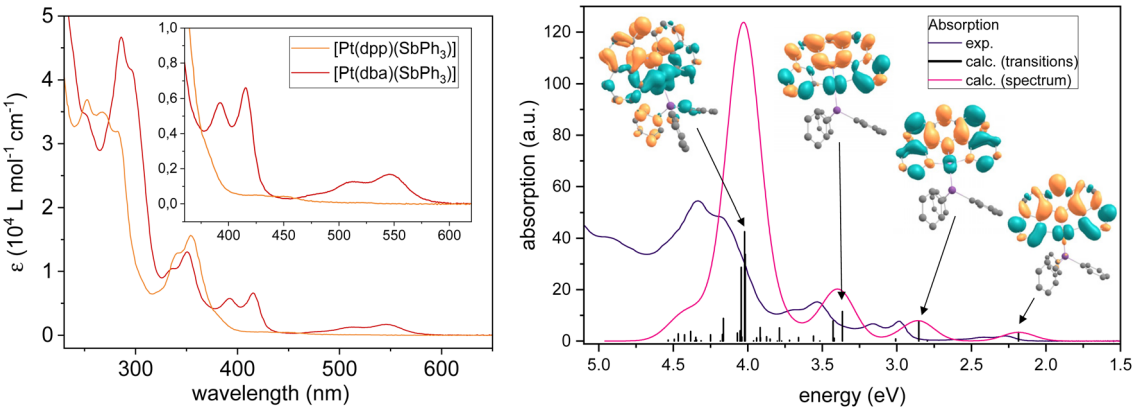

Fig. 3 Left: experimental UV-vis absorption spectra (molar absorption coefficient ε as a function of wavelength) of [Pt(C^N^C)($SbPh_3$)] in CH_2Cl_2 solution at 298 K. Inset: magnification of the 350–630 nm region. Right: experimental UV-vis absorption spectrum in CH_2Cl_2 solution at 298 K and TD-DFT-calculated spectrum with selected transition difference densities for [Pt(dba)($SbPh_3$)].

Table 1 Experimental and TD-DFT-calculated UV-vis absorption maxima for the complexes [Pt(dba)($PnPh_3$)] (Pn = P, As, Sb, Bi)[a,b]

		λ_1	λ_2	λ_3	λ_4	λ_5	λ_6	λ_7	λ_8
[Pt(dba)(PPh_3)]	Exp.[a]	286	296	333	348	387	409	499	533
	Calc.[b]	306		363		430		552	
[Pt(dba)($AsPh_3$)]	Exp.[a]	285	296	333	354	390	412	505	539
	Calc.[b]	307		364		432		560	
[Pt(dba)($SbPh_3$)]	Exp.[a]	286	296	335	351	392	416	511	546
	Calc.[b]	308		365		434		567	

[a] In CH_2Cl_2; absorption maxima λ in nm. [b] TPSSh/def2-TZVP/CPCM(CH_2Cl_2), maxima from convoluted spectrum.

The absorption cut-off extrapolated from the low-energy slope of the lowest energy absorption band, representing the optical HOMO–LUMO gap, is about 565 nm (2.19 eV) for [Pt(dba)(PPh_3)] to 580 nm (2.14 eV) for [Pt(dba)($SbPh_3$)]. While the optical HOMO–LUMO gap is expected to exceed the electrochemical HOMO–LUMO gap (which probes the molecule in its geometric ground state), the opposite is the case here, as the electrochemical HOMO–LUMO gaps determined from CVs are larger by about 0.5 eV than the optical gaps obtained from UV-vis absorption spectroscopy. Since negative reorganisation energy (*i.e.*, reorganisation into a higher energy conformation upon oxidation/reduction) is physically not reasonable, we have to consider the contribution of direct absorption from the S_0 ground state into lowest ^{3}MLCT states producing the low-energy absorption bands and thus the low optical gaps. This is discussed for Pt(II) systems in the literature,[71–74] with a lower energy and weakly intense band related to a ^{3}MLCT state mirroring the absorption into the ^{1}MLCT state. Remarkably, our TD-DFT calculations also predict these very low energy transitions, even if they do not include such triplet admixtures. DFT calculated T_1–S_0 energy gaps of 1.97 eV for [Pt(dba)(PPh_3)] and 1.95 eV for the As and Sb derivatives (Table 2) are roughly consistent with this assumption and reinforcing the assumed correlation between optical and actual HOMO–LUMO gaps.

Time-resolved and steady-state photoluminescence spectroscopy

Photoluminescence spectroscopy showed the dpp complexes [Pt(dpp)($PnPh_3$)] (Pn = P, As, Sb) to be emissive at 77 K in frozen CH_2Cl_2/MeOH (1 : 1) glassy matrices, but not in solution at 298 K. The spectra (Fig. S43–S45, ESI†) show two sharp emission bands around 515 and 560 nm and a shoulder around 590 nm. This corresponds to an approximate energy of around 2.4 eV for the 0–0 transitions, which is markedly larger than the DFT calculated $\Delta E(T_1$–$S_0)$ values (around 2.05 eV, see Table 2). The dba derivatives [Pt(dba)($PnPh_3$)] (Pn = P, As, Sb) are emissive both at 77 K in frozen glassy matrices and, albeit weakly, at 298 K in solution (spectra in Fig. 4 and Fig. S46–S48, ESI†). At 77 K, three sharp bands with emission maxima around 580, 630 and 690 nm are found. At 298 K, these maxima are shifted to around 595, 640 and 700 nm, where the latter two are not sharp bands but shoulders. Also in this case, the energy of the 0–0 transitions according to spectroscopy (around 2.1 eV) exceeds the DFT calculated $\Delta E(T_1$–$S_0)$ values discussed above, but not as markedly as for the dpp series. Like for the absorption spectra, a red-shift is observed for the emission spectra across the series P < As < Sb for both systems, whereas the calculated $\Delta E(T_1$–$S_0)$ values show a marginal (and in the case of dpp imperfect) downwards trend on the second decimal place. All data is compiled in Table 2.

This journal is © The Royal Society of Chemistry 2023

Table 2 Experimental and calculated photophysical data for the complexes [Pt(C^N^C)($PnPh_3$)] (Pn = P, As, Sb)[a]

	T	λ_{max} (nm)	$\Phi_L \pm 0.02$	τ (μs)[e]	k_r (10^{-4} s^{-1})	k_{nr} (10^{-4} s^{-1})	$\langle S_n\|H_{SO}\|T_1\rangle^2$ (cm^{-2})[f]	$\Delta E(T_1–S_0)$ (eV / nm)[f]
[Pt(dpp)(PPh_3)]	77 K[b]	511, 550, 590[d]	0.48	12.70 ± 0.01	3.8 ± 0.2	4.1 ± 0.2	9.18×10^5 ($n = 0$) 1.23×10^4 ($n = 2$)	2.06 / 602
[Pt(dpp)($AsPh_3$)]	77 K[b]	517, 557, 588[d]	0.70	11.80 ± 0.01	5.9 ± 0.2	2.5 ± 0.2	9.06×10^5 ($n = 0$) 1.41×10^4 ($n = 2$)	2.04 / 608
[Pt(dpp)($SbPh_3$)]	77 K[b]	521, 562, 592[d]	0.68	11.60 ± 0.01	5.6 ± 0.2	3.0 ± 0.2	8.14×10^5 ($n = 0$) 1.11×10^4 ($n = 2$)	2.05 / 605
[Pt(dba)(PPh_3)]	77 K[b]	576, 625, 684	0.90	27.90 ± 0.06	3.2 ± 0.1	0.5 ± 0.1	2.99×10^5 ($n = 0$)	1.97 / 629
	298 K[c]	590, 635[d], 695[d]	0.03	0.81 ± 0.01	0.4 ± 0.2	12.0 ± 0.3	1.20×10^5 ($n = 2$)	
[Pt(dba)($AsPh_3$)]	77 K[b]	580, 632, 692	0.90	23.70 ± 0.07	3.8 ± 0.1	0.4 ± 0.1	2.94×10^5 ($n = 0$)	1.95 / 636
	298 K[c]	594, 636[d], 700[d]	0.04	0.270 ± 0.001	1.5 ± 0.7	35.4 ± 0.8	1.38×10^5 ($n = 2$)	
[Pt(dba)($SbPh_3$)]	77 K[b]	584, 635, 694	0.94	21.90 ± 0.02	4.3 ± 0.1	0.3 ± 0.1	2.22×10^5 ($n = 0$)	1.95 / 636
	298 K[c]	598, 640[d], 702[d]	0.07	0.470 ± 0.001	1.5 ± 0.4	19.8 ± 0.4	1.41×10^5 ($n = 2$)	

[a] Excitation wavelength λ_{exc} = 350 nm. [b] Measured in a frozen glassy matrix of CH_2Cl_2/MeOH (1 : 1) at 77 K. [c] Measured in fluid CH_2Cl_2 solution upon purging with Ar. [d] Shoulder. [e] For bi-exponential photoluminescence decays, amplitude-weighted average lifetimes are shown. Raw time-resolved photoluminescence decays along with the fitting parameters are shown in the ESI.† [f] (TD-)DFT calculated, computational details in the ESI.†

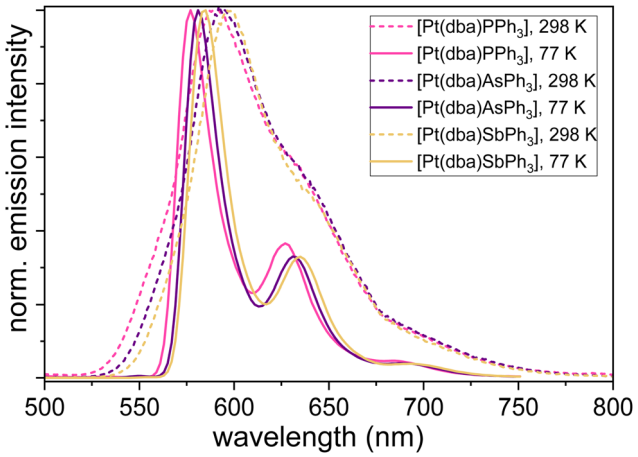

Fig. 4 Photoluminescence spectra of the complexes [Pt(dba)($PnPh_3$)] (Pn = P, As, Sb) at 77 K in a frozen glassy matrix of MeOH/CH_2Cl_2 (1 : 1) (solid lines) and in CH_2Cl_2 solution at 298 K (dashed lines).

For the dpp series, photoluminescence quantum yields (Φ_L) of 0.70 and 0.68 were found for the $AsPh_3$ and $SbPh_3$ derivatives, significantly exceeding the value of 0.48 for [Pt(dpp)(PPh_3)]. The Φ_L are in concordance with literature reported values for similar Pt(II) complexes with flexible double cyclometalated C^N^C ligands.[49,51,64,69,75,76] For the dba series at 77 K, values of Φ_L near unity (0.90 for PPh_3 and $AsPh_3$, 0.94 for $SbPh_3$) were determined. For similar complexes bearing several different ancillary ligands on the [Pt(dba)] fragment, we recently reported Φ_L at 77 K between 0.80 and 0.90.[51] At 298 K, the dba complexes exhibit much lower Φ_L with values (below 0.1, see Table 2). At room temperature (298 K), all three dba complexes are practically non-emissive, with their Φ_L values approaching the experimental uncertainty (except for the $SbPh_3$ complex, which exhibits a modest yet measurable Φ_L). The excited state lifetimes (τ) determined for both series at 77 K are within the range typically reported for similar C^N^C Pt(II) complexes at 77 K (ref. 47–49, 51, 64, 69, 75 and 76) and decrease across the series P > As > Sb.

Based on the obtained Φ_L and excited-state lifetimes, we estimated the average radiative (k_r) and non-radiative (k_{nr}) rate constants, as detailed in Table 2 and Fig. 5.

At 77 K, we see a trend of increasing k_r values and decreasing k_{nr} values from P to Sb in both the dpp and the dba series (Fig. 5A and B). We assume that the observed deviations from the linear trend (especially for k_{nr}) are due to 3d-contraction anomaly related to the first filling of a d-shell before the element As.[77,78] At 298 K, k_r for the dba complexes also increases from P to Sb, but no clear trend can be deduced from the k_{nr} values, which we attribute to more complex roto-vibronic relaxation pathways between T_1 and S_0 or possibly *via* the population of dissociative ^{3}MC states at ambient temperature (Fig. 5C).

To further our understanding of the interplay between SOC and roto-vibronic aspects in the photophysics of the two series of complexes, we expanded our computational work to include TD-DFT spin–orbit coupling calculations at the DFT optimised T_1 geometries (Table S4, ESI†).[79–81] The results indicate significant mixing of the T_1 states with the S_0 and S_2 states. Surprisingly, the S_1 states only marginally couple with the T_1 states. The corresponding SOC matrix elements $\langle S_n|H_{SO}|T_1\rangle^2$ are listed in Table 2. In general, the values of $\langle S_2|H_{SO}|T_1\rangle^2$ are larger for the dba series than in the dpp series by a factor of 10. This may be related to the rigidity of the dba framework, thus allowing for a stronger coupling with higher excited states as more geometric overlap is preserved.

For the dba complexes, an increase in $\langle S_2|H_{SO}|T_1\rangle^2$ across the P < As < Sb series is predicted alongside a decrease in $\langle S_0|H_{SO}|T_1\rangle^2$. For the dpp derivatives, the $\langle S_0|H_{SO}|T_1\rangle^2$ values again decrease when moving down the pnictogen group. Interestingly, an unexpected trend in $\langle S_2|H_{SO}|T_1\rangle^2$ is observed for the dpp series, namely Sb < P < As. Thus, in the particular case of [Pt(dpp)($SbPh_3$)], our calculations predict a counterintuitively diminished SOC.

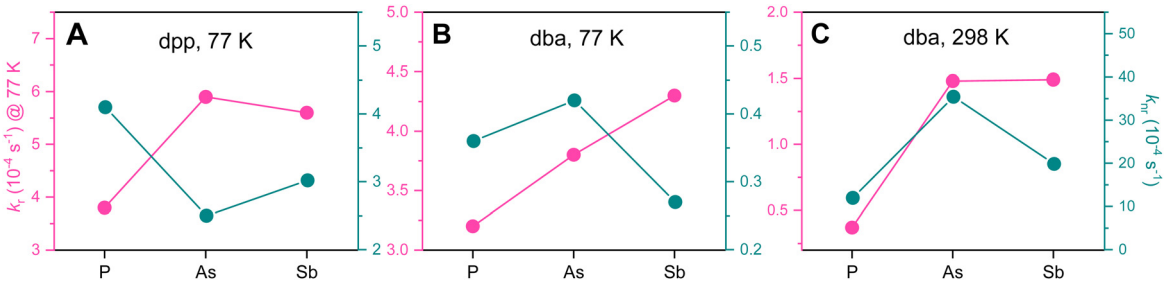

Fig. 5 Visualisation of k_r (pink) and k_{nr} (green) for the complexes [Pt(dpp)($PnPh_3$)] (A) and [Pt(dba)($PnPh_3$)] at 77 K (B) and 298 K (C) (Pn = P, As, Sb).

A possible explanation for these differences between the dpp and dba complexes lies in the character of the emissive states. The MLCT character of the emissive state is expected to decrease in frozen matrix at 77 K. Furthermore, the extended π-system of the dba ligand leads to smaller MLCT and larger LC contributions compared with the dpp system. We assume that for the dpp complexes at 77 K and for the dba derivatives at 298 K we have a larger MLCT contribution compared with dba at 77 K. With a higher MLCT character in the excited state, the heavier $SbPh_3$ ligand is not able to develop its potential for higher SOC as the effect is already strong due to the participation of the Pt centre.[30] Only in case of the LC-dominated dba systems at 77 K, $SbPh_3$ reveals its superior SOC capacity over the lighter homologues.

To confirm this, we assessed the character of the emissive T_1 states for both series of complexes as well as for the hypothetical $BiPh_3$ theoretically *via* exciton analysis using the open-source software TheoDORE (Fig. 6, see ESI† for details).[82] On first view, they confirm that for the dpp series that MLCT character of the T_1 excited state is higher than for the dba complexes (~22% *vs.* ~17%) and the LC character dominates the latter (~65% *vs.* ~75%).

In both series, the LC character decreases slightly down the series from P to Sb, while the MLCT contribution increases. This is in line with the above discussed higher polarisability of the $PnPh_3$ ligands leading to the observed red-shifts in absorption and emission as well as to the reduced electrochemical gaps.

Femtosecond transient absorption spectroscopy

The excited state dynamics of the two series of complexes [Pt(dpp)($PnPh_3$)] and [Pt(dba)($PnPh_3$)] (Pn = P, As, Sb) were studied further using femtosecond transient absorption (fsTA) spectroscopy under ambient conditions. A particular focus was on observing the ISC from the singlet to the triplet manifold and obtaining time constants for this process in the different $PnPh_3$ derivatives. The ISC from singlet excited states into the triplet manifold is an ultrafast process for Pt(II) complexes, with reported ISC time constants for organometallic Pt(II) complexes being typically <5 ps and often even <1 ps.[83–86]

When exciting the dpp complexes at 340 nm we observed intense excited state absorption (ESA) with broad features around 430 and 550 nm and no ground state bleach (spectra in Fig. 7a and Fig. S49, ESI†). Global analysis of the TA data

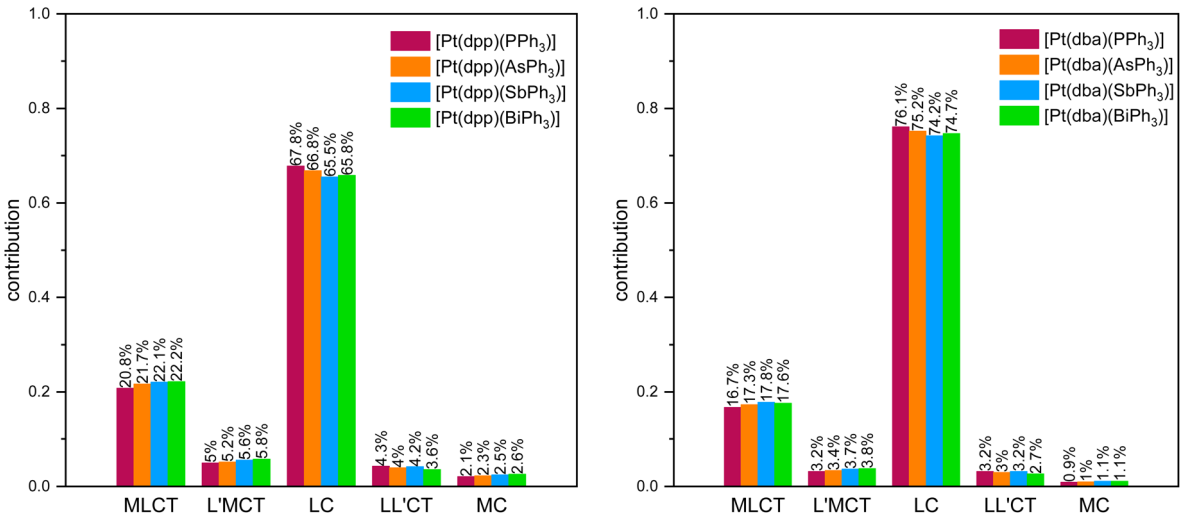

Fig. 6 Decomposition of the emissive T_1 states into MLCT, L'MCT, LL'CT, LC and MC contributions for [Pt(dpp)($PnPh_3$)] (left) and [Pt(dba)($PnPh_3$)] (right; Pn = P, As, Sb, Bi) based on TD-DFT calculations (TPSSh/def2-TZVP/CPCM(CH_2Cl_2)).[82]

This journal is © The Royal Society of Chemistry 2023

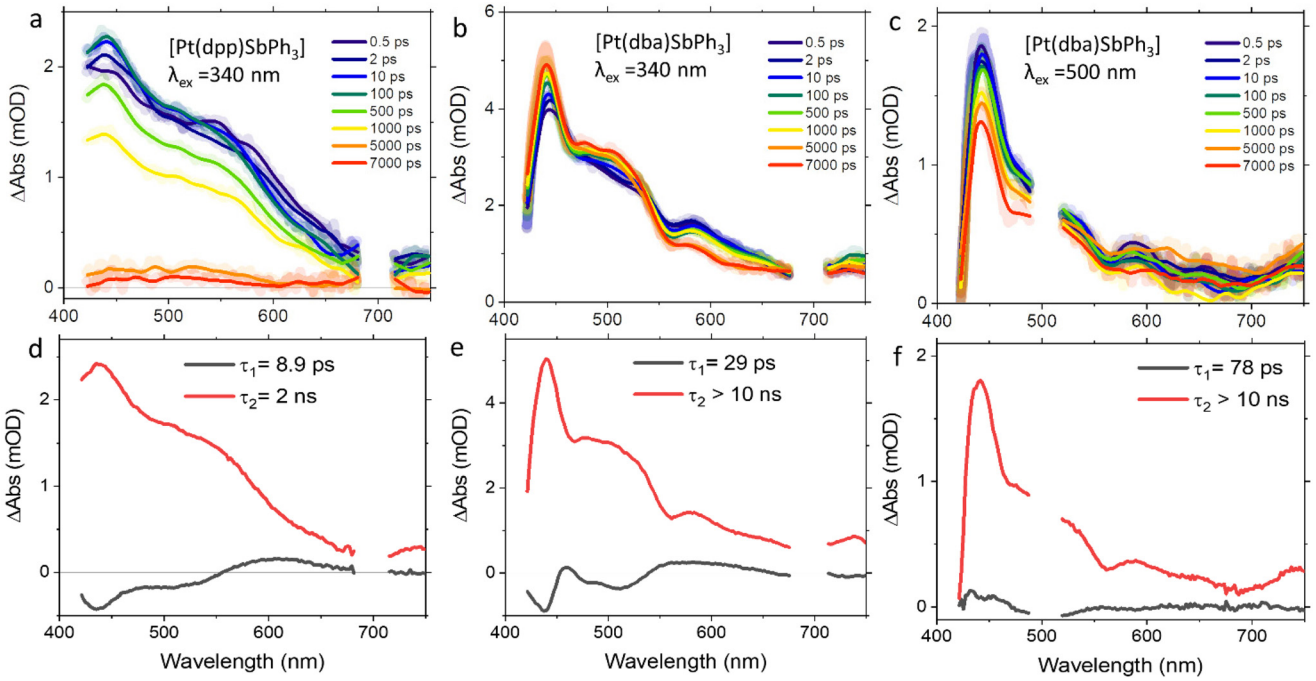

Fig. 7 Transient absorption spectra (TAS) at selected delay times (a–c) and decay-associated spectra (d–f) for [Pt(dpp)($SbPh_3$)] following excitation at 340 nm (a and d), [Pt(dba)($SbPh_3$)] upon excitation at 340 nm (b and e) and 500 nm (c and f) in THF. The thicker lines in TAS shows smoothed data.

using an exponential kinetic scheme reveals two characteristic time constants, one very fast (<10 ps) and one slower process beyond 10 ns after excitation. The first process is fastest in the PPh_3 derivative and significantly slower in the $SbPh_3$ complex. We assign this to an ISC in accordance with literature values for similar complexes.[83–86] The counterintuitive trend in the <10 ps time constants (P ≈ As < Sb) roughly parallel the trend in decreasing SOC calculated by TD-DFT for the dpp series. Another concurring factor is probably the increasing Pt–Pn bond strength slowing down all radiationless processes (including ISC). The second process with time constants around 1.7 to 2.9 ns can be assigned to the relaxation from the T_1 state to the ground state. This is consistent with absence of phosphorescence in the μs time range at 298 K. For [Pt(dpp)(dmso)], a relaxation pathway *via* T_2 is described in the literature based on detailed theoretical analysis.[72] It is therefore in principle also possible that the observed ISC occurs between S_1 and T_2 followed by a rapid decay from T_2 to T_1, even though we did not make any experimental observations specifically pointing in that direction.

For the dba complexes, we performed transient absorption experiments upon excitation at 340 and 500 nm. In all cases, we also observed intense ESA with maxima at 430 nm and shoulders at 500 and 580 nm. The evolution of signals could be fitted to a model taking into account two distinct processes (see Fig. 7 and Fig. S50 and S51, ESI†), with a slower process that is assigned to the decay of the emissive T_1 state exceeding the 10 ns window.

Upon 340 nm excitation, we observed a fast process characterised by time constants around 30 ps for all complexes Pn = P, As, and Sb. We again assign this sub-100 ps kinetics to ISC, based on the characteristic time constants and the similar shapes regarding the decay-associated spectra for the fast process in the dpp derivatives (*i.e.* decrease of ESA at 580 nm and increase of ESA at 430 and 500 nm). For the dba derivatives, this process is overall slower than in the dpp complexes due to the larger LC contributions to the excited states.

Upon excitation at 500 nm, we see less pronounced spectral changes in the process represented by the first component, if compared to that observed at 340 nm excitation, leading us to assume the population of a different state (with significant triplet admixtures already upon initial excitation). It is possible that intermediate steps (like partial ISC) are not resolved from the relatively slow effective τ_1. The slower ISC rate could be attributed to increased LC character. The second component is longer-lived and its spectral profile resembles that observed upon 340 nm excitation.

Generally, the lifetimes of the S_1 states for the more rigid dba complexes are significantly longer than for the dpp derivatives, pointing to a slower ISC. For both series, the ISC under ambient conditions is not significantly faster for the heavy $SbPh_3$ derivatives compared to their lighter PPh_3 and $AsPh_3$ congeners as originally expected. As discussed above, the effect of the $PnPh_3$ variation is multifaceted. The initially predicted enhancement of SOC for the heavier derivatives is observed only in the dba series, due to the predominant LC character of their emissive triplet states. With increasing MLCT character of the emissive triplet state, the heavy atom effect is progressively masked by the dominating effect of the

5d metal, as seen in the dpp complexes. Furthermore, the variation of the Pn atom induces not only changes in SOC, but also in the Pt–Pn bond strength, influencing the photophysical properties by affecting the vibronic properties.

Conclusions

The effects of progressively heavy pnictogen-based ancillary ligands $PnPh_3$ on the electronic and photophysical properties two series of Pt(II) C^N^C cyclometalated complexes [Pt(dpp)$PnPh_3$] and [Pt(dba)$PnPh_3$] (Pn = P, As, Sb; H_2dpp = 2,6-diphenyl-pyridine, H_2dba = dibenzoacridine) were explored. The electrochemical HOMO–LUMO gaps and the long-wavelength UV-vis absorption and emission maxima are red-shifted along the series P < As < Sb for both the dpp and the dba framework, in line with increasing electron density at the Pt centre, which we interpret as stronger σ-donation of the heavier $PnPh_3$ ligands to Pt. The latter correlates with an increasing ligand-field splitting along P < As < Sb. The photoluminescence quantum yields Φ_L are increased for the heavy congeners reaching almost unity for the dba complex. The radiative rate constants k_r are increased by introduction of the heavier homologues while the non-radiative rate constants k_{nr} are reduced. As an important factor for this behaviour we identify increased Pt–Pn bond strength in the heavier derivatives, especially with $SbPh_3$, due to better orbital overlap resulting from more similar atomic/ionic radii and polarisability. The initially sought-after heavy atom effect with increased spin orbit coupling (SOC) for the heavier $PnPh_3$ ancillary ligands is modulated by the character of the excited states. In our two series of complexes the increased SOC is most evident for the dba complexes at 77 K, where the LC character of the excited state is dominant over the MLCT character. Thus, the enhancement of phosphorescence *via* introduction of heavy ligands is less prominent in systems with emissive states of strong MLCT character.

Based on this analysis, we are confident that the present design principle of combining a cyclometalating, rigid tridentate ligand with a heavy element containing ancillary ligand can be applied to further systems, especially with LC-dominated excited states to enhance triplet emission. For the present series of complexes, we were unable to obtain the Bi derivative, which therefore remains an open synthetic challenge. In the future, the isolation of this or related Bi-containing complexes will show whether its heavy atom effect can further enhance k_r in complexes with weak SOC. Further promising candidates for heavy ancillary ligands may also include the anionic tetrelate derivatives GeR_3^-, SnR_3^-, and PbR_3^-.

Author contributions

R.J. carried out syntheses, cyclic voltammetry, UV-vis absorption spectroscopy and spectroelectrochemistry measurements as well as the computational work. I.M. carried out the emission spectroscopy. S.S.N and R.J. carried out the transient absorption spectroscopy measurements. A.K., B.D.-I., and C.A. S. supervised the project. R.J. and A.K. wrote the original draft, all authors revised the manuscript. All authors agreed with the final version.

Data availability

All relevant data are available from the corresponding authors upon request.

Conflicts of interest

There are no conflicts to declare.

Acknowledgements

We thank the Deutsche Forschungsgemeinschaft [DFG Priority Programme 2102 “Light-controlled Reactivity of Metal Complexes” STR 1186/6-1 and 6-2 (C. A. S.), KL1194/16-1 and 16-2 (A. K.), and DI1517/19-1 (B. D.-I.)] and the Studienstiftung des Deutschen Volkes e.V. (R. J.) for funding of this project. We would also like to thank the Regional Computing Center of the University of Cologne (RRZK) for providing computing time on the DFG-funded High Performance Computing (HPC) system CHEOPS as well as for technical support.

References

1 K. Mori and H. Yamashita, Metal Complexes Supported on Solid Matrices for Visible–Light–Driven Molecular Transformations, *Chem. – Eur. J.*, 2016, **22**, 11122–11137, DOI: **10.1002/chem.201600441**.
2 M. Parasram and V. Gevorgyan, Visible light-induced transition metal-catalyzed transformations: beyond conventional photosensitizers, *Chem. Soc. Rev.*, 2017, **46**, 6227–6240, DOI: **10.1039/C7CS00226B**.
3 Q. Zhao, F. Li and C. Huang, Phosphorescent chemosensors based on heavy-metal complexes, *Chem. Soc. Rev.*, 2010, **39**, 3007–3030, DOI: **10.1039/B915340C**.
4 A. S.-Y. Law, L. C.-C. Lee, K. K.-W. Lo and V. W.-W. Yam, Aggregation and Supramolecular Self-Assembly of Low-Energy Red Luminescent Alkynylplatinum(II) Complexes for RNA Detection, Nucleolus Imaging, and RNA Synthesis Inhibitor Screening, *J. Am. Chem. Soc.*, 2021, **143**, 5396–5405, DOI: **10.1021/jacs.0c13327**.
5 K. Li, G. S. M. Tong, Q. Wang, G. Cheng, W.-Y. Tong, W.-H. Ang, W.-L. Kwong and C.-M. Che, Highly phosphorescent platinum(II) emitters: photophysics, materials and biological applications, *Chem. Sci.*, 2016, **7**, 1653–1673, DOI: **10.1039/C5SC03766B**.
6 S. Fantacci and F. De Angelis, A computational approach to the electronic and optical properties of Ru(II) and Ir(III)

 This journal is © The Royal Society of Chemistry 2023

polypyridyl complexes: Applications to DSC, OLED and NLO, *Coord. Chem. Rev.*, 2011, **255**, 2704–2726, DOI: 10.1016/j.ccr.2011.03.008.
7 C. E. Housecroft and E. C. Constable, Over the LEC rainbow: Colour and stability tuning of cyclometallated iridium(III) complexes in light-emitting electrochemical cells, *Coord. Chem. Rev.*, 2017, **350**, 155–177, DOI: 10.1016/j.ccr.2017.06.016.
8 H. Yersin, *Highly Efficient OLEDs with Phosphorescent Materials*, Wiley-VCH, Weinheim, Germany, 2008. DOI: 10.1002/9783527621309.
9 C. Bizzarri, E. Spuling, D. M. Knoll, D. Volz and S. Bräse, Sustainable metal complexes for organic light-emitting diodes (OLEDs), *Coord. Chem. Rev.*, 2018, **373**, 49–82, DOI: 10.1016/j.ccr.2017.09.011.
10 L. Ravotto and P. Ceroni, Aggregation induced phosphorescence of metal complexes: From principles to applications, *Coord. Chem. Rev.*, 2017, **346**, 62–76, DOI: 10.1016/j.ccr.2017.01.006.
11 H. Yersin, A. F. Rausch, R. Czerwieniec, T. Hofbeck and T. Fischer, The triplet state of organo-transition metal compounds. Triplet harvesting and singlet harvesting for efficient OLEDs, *Coord. Chem. Rev.*, 2011, **255**, 2622–2652, DOI: 10.1016/j.ccr.2011.01.042.
12 X. Zhen, R. Qu, W. Chen, W. Wu and X. Jiang, The development of phosphorescent probes for in vitro and in vivo bioimaging, *Biomater. Sci.*, 2021, **9**, 285–300, DOI: 10.1039/d0bm00819b.
13 Y. Chen, R. Guan, C. Zhang, J. Huang, L. Ji and H. Chao, Two-photon luminescent metal complexes for bioimaging and cancer phototherapy, *Coord. Chem. Rev.*, 2016, **310**, 16–40, DOI: 10.1016/j.ccr.2015.09.010.
14 C. Balachandran, K. Yokoi, K. Naito, J. Haribabu, Y. Tamura, M. Umezawa, K. Tsuchiya, T. Yoshihara, S. Tobita and S. Aoki, Cyclometalated Iridium(III) Complex–Cationic Peptide Hybrids Trigger Paraptosis in Cancer Cells via an Intracellular Ca^{2+} Overload from the Endoplasmic Reticulum and a Decrease in Mitochondrial Membrane Potential, *Molecules*, 2021, **26**, 7028, DOI: 10.3390/molecules26227028.
15 J. Haribabu, Y. Tamura, K. Yokoi, C. Balachandran, M. Umezawa, K. Tsuchiya, Y. Yamada, R. Karvembu and S. Aoki, Synthesis and Anticancer Properties of Bis- and Mono(cationic peptide) Hybrids of Cyclometalated Iridium (III) Complexes: Effect of the Number of Peptide Units on Anticancer Activity, *Eur. J. Inorg. Chem.*, 2021, **2021**, 1796–1814, DOI: 10.1002/ejic.202100154.
16 J. Kalinowski, V. Fattori, M. Cocchi and J. A. G. Williams, Light-emitting devices based on organometallic platinum complexes as emitters, *Coord. Chem. Rev.*, 2011, **255**, 2401–2425, DOI: 10.1016/j.ccr.2011.01.049.
17 I. O. Koshevoy, M. Krause and A. Klein, Non-covalent intramolecular interactions through ligand-design promoting efficient photoluminescence from transition metal complexes, *Coord. Chem. Rev.*, 2020, **405**, 213094, DOI: 10.1016/j.ccr.2019.213094.
18 L. M. Cinninger, L. D. Bastatas, Y. Shen, B. J. Holliday and J. D. Slinker, Luminescent properties of a 3, 5-diphenylpyrazole bridged Pt(II) dimer, *Dalton Trans.*, 2019, **48**, 9684–9691, DOI: 10.1039/C9DT00795D.
19 V. W.-W. Yam, V. K.-M. Au and S. Y.-L. Leung, Light-Emitting Self-Assembled Materials Based on d^8 and d^{10} Transition Metal Complexes, *Chem. Rev.*, 2015, **115**, 7589–7728, DOI: 10.1021/acs.chemrev.5b00074.
20 M. Cnudde, D. Brünink, N. L. Doltsinis and C. A. Strassert, Tetradentate N^N°N^N-type luminophores for Pt(II) complexes: Synthesis, photophysical and quantum-chemical investigation, *Inorg. Chim. Acta*, 2021, **518**, 120090, DOI: 10.1016/j.ica.2020.120090.
21 G. Li, L. Ameri, T. Fleetham, Z.-Q. Zhu and J. Li, Stable and efficient blue and green organic light emitting diodes employing tetradentate Pt(II) complexes, *Appl. Phys. Lett.*, 2020, **117**, 253301, DOI: 10.1063/5.0033023.
22 F. Yu, Y. Sheng, D. Wu, K. Qin, H. Li, G. Xie, Q. Xue, Z. Sun, Z. Lu, H. Ma and X.-C. Hang, Blue-Phosphorescent Pt(II) Complexes of Tetradentate Pyridyl–Carbolinyl Ligands: Synthesis, Structure, Photophysics, and Electroluminescence, *Inorg. Chem.*, 2020, **59**, 14493–14500, DOI: 10.1021/acs.inorgchem.0c02244.
23 G. Cheng, Y. Kwak, W.-P. To, T.-L. Lam, G. S. M. Tong, M.-K. Sit, S. Gong, B. Choi, W. Choi, C. Yang and C.-M. Che, High-efficiency solution-processed organic light-emitting diodes with tetradentate platinum(II) emitters, *ACS Appl. Mater. Interfaces*, 2019, **11**, 45161–45170, DOI: 10.1021/acsami.9b11715.
24 T. Fleetham, G. Li and J. Li, Phosphorescent Pt(II) and Pd (II) complexes for efficient, high–color–quality, and stable OLEDs, *Adv. Mater.*, 2016, **29**, 1601861, DOI: 10.1002/adma.201601861.
25 M. Krause, R. von der Stück, D. Brünink, S. Buss, N. L. Doltsinis, C. A. Strassert and A. Klein, Platinum and palladium complexes of tridentate C^N^N (phen-ide)-pyridine-thiazol ligands – A case study involving spectroelectrochemistry, photoluminescence spectroscopy and TD-DFT calculations, *Inorg. Chim. Acta*, 2021, **518**, 120093, DOI: 10.1016/j.ica.2020.120093.
26 M. Hebenbrock, D. González-Abradelo, A. Hepp, J. Meadowcroft, N. Lefringhausen, C. A. Strassert and J. Müller, Influence of the ancillary ligands on the luminescence of platinum(II) complexes with a triazole-based tridentate C^N^N luminophore, *Inorg. Chim. Acta*, 2021, **516**, 119988, DOI: 10.1016/j.ica.2020.119988.
27 V. Sivchik, A. Kochetov, T. Eskelinen, K. S. Kisel, A. I. Solomatina, E. V. Grachova, S. P. Tunik, P. Hirva and I. O. Koshevoy, Modulation of metallophilic and π–π interactions in platinum cyclometalated luminophores with halogen bonding, *Chem. – Eur. J.*, 2021, **27**, 1787–1794, DOI: 10.1002/chem.202003952.
28 E. V. Puttock, J. Sturala, J. C. M. Kistemaker and J. A. G. Williams, Platinum(II) Complexes of Tridentate–Coordinating Ligands Based on Imides, Amides, and Hydrazides: Synthesis and Luminescence Properties,

Eur. J. Inorg. Chem., 2021, **2021**, 335–347, DOI: 10.1002/ejic.202000879.

29 T. Eskelinen, S. Buss, S. K. Petrovskii, E. V. Grachova, M. Krause, L. Kletsch, A. Klein, C. A. Strassert, I. O. Koshevoy and P. Hirva, Photophysics and Excited State Dynamics of Cyclometalated [M (Phbpy)(CN)](M = Ni, Pd, Pt) Complexes: A Theoretical and Experimental Study, *Inorg. Chem.*, 2021, **60**, 8777–8789, DOI: 10.1021/acs.inorgchem.1c00680.

30 S. C. Gangadharappa, I. Maisuls, D. A. Schwab, J. Kösters, N. L. Doltsinis and C. A. Strassert, Compensation of Hybridization Defects in Phosphorescent Complexes with Pnictogen-Based Ligands—A Structural, Photophysical, and Theoretical Case-Study with Predictive Character, *J. Am. Chem. Soc.*, 2020, **142**, 21353–21367, DOI: 10.1021/jacs.0c09467.

31 S. Garbe, M. Krause, A. Klimpel, I. Neundorf, P. Lippmann, I. Ott, D. Brünink, C. A. Strassert, N. L. Doltsinis and A. Klein, Cyclometalated Pt Complexes of CNC Pincer Ligands: Luminescence and Cytotoxic Evaluation, *Organometallics*, 2020, **39**, 746–756, DOI: 10.1021/acs.organomet.0c00015.

32 A. Iwakiri, Y. Konno and K. Shinozaki, Determination of excimer emission quantum yield of Pt(dpb)Cl (dpbH = 1,3-di(2-pyridyl)benzene and its analogues in solution, *J. Lumin.*, 2019, **207**, 482–490, DOI: 10.1016/j.jlumin.2018.11.042.

33 E. Garoni, J. Boixel, V. Dorcet, T. Roisnel, D. Roberto, D. Jacquemin and V. Guerchais, Controlling the emission in flexibly-linked (N^C^N) platinum dyads, *Dalton Trans.*, 2018, **47**, 224–232, DOI: 10.1039/C7DT03695G.

34 L. Kletsch, R. Jordan, A. S. Köcher, S. Buss, C. A. Strassert and A. Klein, Photoluminescence of Ni(II), Pd(II), and Pt(II) Complexes [M(Me_2dpb)Cl] Obtained from C-H Activation of 1,5-Di(2-pyridyl)-2,4-dimethylbenzene (Me_2dpbH), *Molecules*, 2021, **26**, 5051, DOI: 10.3390/molecules26165051.

35 B. Schulze, C. Friebe, M. Jäger, H. Görls, E. Birckner, A. Winter and U. S. Schubert, Pt^{II} Phosphors with Click-Derived 1,2,3-Triazole-Containing Tridentate Chelates, *Organometallics*, 2018, **37**, 145–155, DOI: 10.1021/acs.organomet.7b00777.

36 M. Hebenbrock, L. Stegemann, J. Kösters, N. L. Doltsinis, J. Müller and C. A. Strassert, Phosphorescent Pt(II) complexes bearing a monoanionic C^N^N luminophore and tunable ancillary ligands, *Dalton Trans.*, 2017, **46**, 3160–3169, DOI: 10.1039/C7DT00393E.

37 A. Rodrigue-Witchel, D. L. Rochester, S.-B. Zhao, K. B. Lavelle, J. A. G. Williams, S. Wang, W. B. Connick and C. Reber, Pressure-induced variations of MLCT and ligand-centered luminescence spectra in square-planar platinum (II) complexes, *Polyhedron*, 2016, **108**, 151–155, DOI: 10.1016/j.poly.2015.12.011.

38 A. F. Rausch, L. Murphy, J. A. G. Williams and H. Yersin, Improving the performance of Pt(II) complexes for blue light emission by enhancing the molecular rigidity, *Inorg. Chem.*, 2012, **51**, 312–319, DOI: 10.1021/ic201664v.

39 P. Pander, A. V. Zaytsev, A. Sil, J. A. G. Williams, V. N. Kozhevnikov and F. B. Dias, Enhancement of thermally activated delayed fluorescence properties by substitution of ancillary halogen in a multiple resonance-like diplatinum(II) complex, *J. Mater. Chem. C*, 2022, **10**, 4851–4860, DOI: 10.1039/d1tc05026e.

40 G. Li, J. Wen, F. Zhan, W. Lou, Y.-F. Yang, Y. Hu and Y. She, Fused 6/5/6 metallocycle-based tetradentate Pt(II) emitters for efficient green phosphorescent OLEDs, *Inorg. Chem.*, 2022, **61**, 11218–11231, DOI: 10.1021/acs.inorgchem.2c01202.

41 L. Zhu, C. Sha, A. Lv, W. Xie, K. Shen, Y. Chen, G. Xie, H. Ma, H. Li and X.-C. Hang, Tetradentate Pt(II) complexes with peripheral hindrances for highly efficient solution-processed blue phosphorescent OLEDs, *Inorg. Chem.*, 2022, **61**, 10402–10409, DOI: 10.1021/acs.inorgchem.2c01063.

42 K. A. Van Houte, D. C. Heath, C. A. Barringer, A. L. Rheingold and R. S. Pilato, Functionalized 2-Pyridyl-Substituted Metallo-1,2-enedithiolates. Synthesis, Characterization, and Photophysical Properties of (dppe)M{S_2C_2(2-pyridine(ium))(CH_2CH_2OR'')} and (dppe)M[{S_2C_2(CH_2CH_2-*N*-2-pyridinium)}]$^+$ (R″ = H, Acetyl, Lauroyl; M = Pd, Pt; dppe = 1,2-Bis(diphenylphosphino)ethane), *Inorg. Chem.*, 1998, **37**, 4647–4653, DOI: 10.1021/ic980273j.

43 N. Vogt, A. Sandleben, L. Kletsch, S. Schäfer, M. T. Chin, D. A. Vicic, G. Hörner and A. Klein, Role of the X Coligands in Cyclometalated [Ni(Phbpy)X] Complexes (HPhbpy = 6-Phenyl-2,2′-bipyridine), *Organometallics*, 2021, **40**, 1776–1785, DOI: 10.1021/acs.organomet.1c00237.

44 C. Hamacher, N. Hurkes, A. Kaiser, A. Klein and A. Schüren, Electrochemistry and spectroscopy of organometallic terpyridine nickel complexes, *Inorg. Chem.*, 2009, **48**, 9947–9951, DOI: 10.1021/ic900753r.

45 H. Houjou, Y. Hoga, M. Yi-Lan, H. Achira, I. Yoshikawa, T. Mutai and K. Matsumura, Dinuclear fused salen complexes of group-10 metals: Peculiarity of the crystal structure and near-infrared luminescence of a bis (Pt-salen) complex, *Inorg. Chim. Acta*, 2017, **461**, 27–34, DOI: 10.1016/j.ica.2017.01.031.

46 Y.-S. Wong, M.-C. Tang, M. Ng and V. W.-W. Yam, Toward the design of phosphorescent emitters of cyclometalated earth-abundant nickel(II) and their supramolecular study, *J. Am. Chem. Soc.*, 2020, **142**(16), 7638–7646, DOI: 10.1021/jacs.0c02172.

47 W. Lu, M. C. W. Chan, K.-K. Cheung and C.-M. Che, π–π Interactions in Organometallic Systems. Crystal Structures and Spectroscopic Properties of Luminescent Mono-, Bi-, and Trinuclear Trans-cyclometalated Platinum(II) Complexes Derived from 2,6-Diphenylpyridine, *Organometallics*, 2001, **20**, 2477–2486, DOI: 10.1021/om0009839.

48 V. W.-W. Yam, R. P.-L. Tang, K. M.-C. Wong, X.-X. Lu, K.-K. Cheung and N. Zhu, Syntheses, Electronic Absorption, Emission, and Ion-Binding Studies of Platinum(II) C^N^C and Terpyridyl Complexes Containing Crown Ether Pendants, *Chem. – Eur. J.*, 2002, **8**, 4066–4076,

This journal is © The Royal Society of Chemistry 2023

DOI: 10.1002/1521-3765(20020902)8:17<4066::AID-CHEM4066>3.0.CO;2-O.
49 S. C. F. Kui, F.-F. Hung, S.-L. Lai, M.-Y. Yuen, C.-C. Kwok, K.-H. Low, S. S.-Y. Chui and C.-M. Che, Luminescent organoplatinum(II) complexes with functionalized cyclometalated C^N^C ligands: structures, photophysical properties, and material applications, *Chem. – Eur. J.*, 2012, **18**, 96–109, DOI: 10.1002/chem.201101880.
50 A. Kergreis, R. M. Lord and S. J. Pike, Influence of ligand and nuclearity on the cytotoxicity of cyclometallated C^N^C platinum(II) complexes, *Chem. – Eur. J.*, 2020, **26**, 14938–14946, DOI: 10.1002/chem.202002517.
51 J. N. Friedel, M. Krause, R. Jordan, I. Maisuls, D. Bruenink, D. Schwab, N. L. Doltsinis, C. A. Strassert and A. Klein, Triplet Emitting C^N^C Cyclometalated Dibenzo[c,h] Acridine Pt(II) Complexes, *Molecules*, 2022, **27**, 8054, DOI: 10.3390/molecules27228054.
52 V. W.-W. Yam and A. S. Y. Law, Luminescent d^8 metal complexes of platinum(II) and gold(III): From photophysics to photofunctional materials and probes, *Coord. Chem. Rev.*, 2020, **414**, 213298, DOI: 10.1016/j.ccr.2020.213298.
53 C. Janiak, A critical account on π–π stacking in metal complexes with aromatic nitrogen-containing ligands, *J. Chem. Soc., Dalton Trans.*, 2000, **21**, 3885–3896, DOI: 10.1039/B003010O.
54 F. Weigend and R. Ahlrichs, Balanced basis sets of split valence, triple zeta valence and quadruple zeta valence quality for H to Rn: Design and assessment of accuracy, *Phys. Chem. Chem. Phys.*, 2005, **7**, 3297, DOI: 10.1039/b508541a.
55 A. D. Becke, Density-functional exchange-energy approximation with correct asymptotic behavior, *Phys. Rev. A*, 1988, **38**, 3098–3100, DOI: 10.1103/PhysRevA.38.3098.
56 J. P. Perdew and W. Yue, Accurate and simple density functional for the electronic exchange energy: Generalized gradient approximation, *Phys. Rev. B: Condens. Matter Mater. Phys.*, 1986, **33**, 8800–8802, DOI: 10.1103/PhysRevB.33.8800.
57 V. Barone and M. Cossi, Quantum calculation of molecular energies and energy gradients in solution by a conductor solvent model, *J. Phys. Chem. A*, 1998, **102**, 1995–2001, DOI: 10.1021/jp9716997.
58 M. Cossi, N. Rega, G. Scalmani and V. Barone, Energiesstructures, and electronic properties of molecules in solution with the C–PCM solvation model, *J. Comput. Chem.*, 2003, **24**, 669–681, DOI: 10.1002/jcc.10189.
59 J. Tao, J. P. Perdew, V. N. Stavoverov and G. E. Scuseria, Climbing the density functional ladder: Nonempirical meta–generalized gradient approximation designed for molecules and solids, *Phys. Rev. Lett.*, 2003, **91**, 146401, DOI: 10.1103/PhysRevLett.91.146401.
60 R. Jordan, M. Niazi, S. Schäfer, W. Kaim and A. Klein, Rhenium Tricarbonyl Complexes of Azodicarboxylate Ligands, *Molecules*, 2022, **27**, 8159, DOI: 10.3390/molecules27238159.
61 L. Kletsch, G. Hörner and A. Klein, Cyclometalated Ni(II) Complexes [Ni(N^C^N)X] of the Tridentate 2,6-di(2-pyridyl) phen-ide Ligand, *Organometallics*, 2020, **39**, 2820–2829, DOI: 10.1021/acs.organomet.0c00355.
62 R. Alrefai, G. Hörner, H. Schubert and A. Berkefeld, Broadly versus Barely Variable Complex Chromophores of Planar Nickel(II) from κ^3-*N,N′,C* and κ^3-*N,N′,O* Donor Platforms, *Organometallics*, 2021, **40**, 1163–1177, DOI: 10.1021/acs.organomet.1c00121.
63 R. von der Stück, M. Krause, D. Brünink, S. Buss, N. L. Doltsinis, C. A. Strassert and A. Klein, Luminescent Pd(II) Complexes with Tridentate $^{-}$C^N^N Arylpyridine-(benzo)thiazole Ligands, *Z. Anorg. Allg. Chem.*, 2022, **648**, e202100278, DOI: 10.1002/zaac.202100278.
64 M. Krause, D. Kourkoulos, D. González-Abradelo, K. Meerholz, C. A. Strassert and A. Klein, Luminescent Pt^{II} Complexes of Tridentate Cyclometalating 2,5-Bis(aryl)-pyridine Ligands, *Eur. J. Inorg. Chem.*, 2017, **2017**, 5215–5223, DOI: 10.1002/ejic.201700792.
65 A. Kellmann and F. Tfibel, Radicals Produced from the Laser-Induced Photoionization of Acridine in Solution, *J. Photochem.*, 1982, **18**, 81–88, DOI: 10.1016/0047-2670(82)80009-9.
66 X. Liu, T. N. V. Karsili, A. L. Sobolewski and W. Domcke, Photocatalytic Water Splitting with the Acridine Chromophore: A Computational Study, *J. Phys. Chem. B*, 2015, **119**, 10664–10672, DOI: 10.1021/acs.jpcb.5b04833.
67 G. Zhang and C. B. Musgrave, Comparison of DFT methods for molecular orbital eigenvalue calculations, *J. Phys. Chem. A*, 2007, **111**, 1554–1561, DOI: 10.1021/jp061633o.
68 E. J. Baerends, O. V. Gritsenko and R. van Meer, The Kohn–Sham gap, the fundamental gap and the optical gap: the physical meaning of occupied and virtual Kohn–Sham orbital energies, *Phys. Chem. Chem. Phys.*, 2013, **15**, 16408–16425, DOI: 10.1039/C3CP52547C.
69 Q. Zhang, S. Wang, Y. Zhu, C. Zhang, W. M. Cao, X. Tian, J. Wu, H. Zhou and Y. Tian, Functional Platinum(II) complexes with four-photon absorption activity, lysosome specificity, and precise cancer therapy, *Inorg. Chem.*, 2021, **60**, 2362–2371, DOI: 10.1021/acs.inorgchem.0c03245.
70 R. Zhu, X. Chen, N. Shu, Y. Shang, Y. Wang, P. Yang, Y. Tang, F. Wang and J. Xu, Computational study of photochemical relaxation pathways of platinum(II) complexes, *J. Phys. Chem. A*, 2021, **125**, 10144–10154, DOI: 10.1021/acs.jpca.1c07017.
71 M. Wang and K. Ishii, Photochemical properties of phthalocyanines with transition metal ions, *Coord. Chem. Rev.*, 2022, **468**, 214626, DOI: 10.1016/j.ccr.2022.214626.
72 S. Záliš, Y.-C. Lam, H. B. Gray and A. Vlček, Spin–Orbit TDDFT Electronic Structure of Diplatinum(II, II) Complexes, *Inorg. Chem.*, 2015, **54**, 3491–3500, DOI: 10.1021/acs.inorgchem.5b00063.
73 T. J. McKay, J. A. Bolger, J. Staromlynska and J. R. Davy, Linear and nonlinear optical properties of platinum-ethynyl, *J. Chem. Phys.*, 1998, **108**, 5537–5541, DOI: 10.1063/1.475943.
74 V. M. Miskowski and V. H. Houlding, Linear and nonlinear optical properties of platinum-ethynyl, *Inorg. Chem.*, 1989, **28**, 1529–1533, DOI: 10.1021/ic00307a021.

75 J. S. Wilson, N. Chawdhury, M. R. A. Al-Mandhary, M. Younus, M. S. Khan, P. R. Raithby, A. Köhler and R. H. Friend, The energy gap law for triplet states in Pt-containing conjugated polymers and monomers, *J. Am. Chem. Soc.*, 2001, **123**, 9412–9417, DOI: **10.1021/ja010986s**.

76 G. S.-M. Tong and C.-M. Che, Emissive or nonemissive? A theoretical analysis of the phosphorescence efficiencies of cyclometalated platinum(II) complexes, *Chem. – Eur. J.*, 2009, **15**, 7225–7237, DOI: **10.1002/chem.200802485**.

77 J. E. Huheey and C. L. Huheey, Anomalous Properties of Elements that Follow "Long Periods" of Elements, *J. Chem. Educ.*, 1972, **49**, 227–230, DOI: **10.1021/ed049p227**.

78 S. Haupt and K. Seppelt, Solid State Structures of $AsCl_5$ and $SbCl_5$, *Z. Anorg. Allg. Chem.*, 2002, **628**, 729–734, DOI: **10.1002/1521-3749(200205)628:4<729::AID-ZAAC729>3.0.CO;2-E**.

79 D. Hernández-Castillo, R. E. P. Nau, M.-A. Schmid, S. Tschierlei, S. Rau and L. González, Multiple Triplet Metal-Centered Jahn-Teller Isomers Determine Temperature-Dependent Luminescence Lifetimes in $[Ru(bpy)_3]^{2+}$, *Angew. Chem., Int. Ed.*, 2023, e202308803, DOI: **10.1002/anie.202308803**.

80 K. Li, G. S. M. Tong, J. Yuan, C. Ma, L. Du, C. Yang, W.-M. Kwok, D. L. Phillips and C.-M. Che, Excitation-Wavelength-Dependent and Auxiliary-Ligand-Tuned Intersystem-Crossing Efficiency in Cyclometalated Platinum(II) Complexes: Spectroscopic and Theoretical Studies, *Inorg. Chem.*, 2020, **59**, 14654–14665, DOI: **10.1021/acs.inorgchem.0c01192**.

81 W. H. Lam, E. S.-H. Lam and V. W.-W. Yam, Computational Studies on the Excited States of Luminescent Platinum(II) Alkynyl Systems of Tridentate Pincer Ligands in Radiative and Nonradiative Processes, *J. Am. Chem. Soc.*, 2013, **135**, 15135–15143, DOI: **10.1021/ja406810a**.

82 F. Plasser, TheoDORE: A toolbox for a detailed and automated analysis of electronic excited state computations, *J. Chem. Phys.*, 2020, **152**, 084108, DOI: **10.1063/1.5143076**.

83 A. Lázaro, C. Cunha, R. Bosque, J. Pina, J. S. Ward, K.-N. Truong, K. Rissanen, J. C. Lima, M. Crespo, J. S. S. de Melo and L. Rodríguez, Room-temperature phosphorescence and efficient singlet oxygen production by cyclometalated Pt(II) complexes with aromatic alkynyl ligands, *Inorg. Chem.*, 2020, **59**, 8220–8230, DOI: **10.1021/acs.inorgchem.0c00577**.

84 K. Li, G. S. M. Tong, J. Yuan, C. Ma, L. Du, C. Yang, W.-M. Kwok, D. L. Phillips and C.-M. Che, Excitation-Wavelength-Dependent and Auxiliary-Ligand-Tuned Intersystem-Crossing Efficiency in Cyclometalated Platinum(II) Complexes: Spectroscopic and Theoretical Studies, *Inorg. Chem.*, 2020, **59**, 14654–14665, DOI: **10.1021/acs.inorgchem.0c01192**.

85 P. K. Chow, C. Ma, W.-P. To, G. S. M. Tong, S. L. Lai, S. C. F. Kui, W.-M. Kwok and C.-M. Che, Strongly Phosphorescent Palladium(II) Complexes of Tetradentate Ligands with Mixed Oxygen, Carbon, and Nitrogen Donor Atoms: Photophysics, Photochemistry, and Applications, *Angew. Chem., Int. Ed.*, 2013, **52**, 11775–11779, DOI: **10.1002/anie.201305590**.

86 T. Theiss, S. Buss, I. Maisuls, R. López-Arteaga, D. Brünink, J. Kösters, A. Hepp, N. L. Doltsinis, E. A. Weiss and C. A. Strassert, Room-Temperature Phosphorescence from Pd(II) and Pt(II) Complexes as Supramolecular Luminophores: The Role of Self-Assembly, Metal–Metal Interactions, Spin–Orbit Coupling, and Ligand-Field Splitting, *J. Am. Chem. Soc.*, 2023, **145**, 3937–3951, DOI: **10.1021/jacs.2c09775**.

This journal is © The Royal Society of Chemistry 2023

3.2 Synthesis and Photophysics of the Doubly Cyclometalated Pd(II) Complexes [Pd(C^N^C)(L)], L = PPh_3, $AsPh_3$ and $SbPh_3$ (Publication 2)

Encouraged by the promising results from **Publication 1**, the Pd(C^N^C) system was targeted next in our project aiming to elucidate whether and how phosphorescence can be enhanced by heavy $PnPh_3$ (Pn = As, Sb) ancillary ligands. A major aspect of the work towards this goal concerned the synthesis and reactivity of the target compounds, as the synthesis of Pd(C^N^C) complexes is significantly less facile and well studied than for Pt(C^N^C).[59,83,84] Multiple approaches were explored, including both C–H and C–X activation methods. We ultimately found that a pathway using two successive C–H activation steps is the most successful and convenient, building on the pioneering work of *Baya* and coworkers. On the thus obtained complexes [Pd(dpp)($PnPh_3$)] (dpp = 2,6-di(phenid-2'-yl)pyridine, Pn = P, As, Sb), we conducted expansive structural, electrochemical and photophysical studies. These represent the first systematic and in-depth investigation of Pd(C^N^C) complexes, as the small number of previous appearances of such compounds in the literature were accompanied only by sparse data. The results are laid out and discussed, as well as compared to the Pt(C^N^C) system, in the following **Publication 2**, which is reprinted with permission from Ref.[109]. Copyright © 2025, American Chemical Society.

The author's contributions to the work include the synthesis and characterization of the discussed compounds except for NMR spectroscopy of $\{[Pd(Hdpp)(\mu\text{-}Cl)]\}_2$. Furthermore, they include the (TD-)DFT calculations and the preparation of the manuscript for revision in collaboration with the co-authors. The 600 MHz ^{1}H NMR data of $\{[Pd(Hdpp)(\mu\text{-}Cl)]\}_2$ was provided by Dr. René von der Stück. Emission spectroscopy and transient absorption spectroscopy were conducted at the labs of Prof. Dr. Cristian A. Strassert and Prof. Dr. Benjamin Dietzek-Ivanšić, respectively. The individual contributions of all co-authors are described in detail in section "Author information" in the publication. The Supporting Information (spectra and tables) for **Publication 2** is provided in section 6.2.

Inorganic Chemistry

pubs.acs.org/IC Article

Synthesis and Photophysics of the Doubly Cyclometalated Pd(II) Complexes [Pd(C^N^C)(L)], L = PPh_3, $AsPh_3$, and $SbPh_3$

Rose Jordan,* Sam Kler, Iván Maisuls, Niklas Klosterhalfen, Benjamin Dietzek-Ivanšić,* Cristian A. Strassert,* and Axel Klein*

Cite This: *Inorg. Chem.* 2025, 64, 6561−6574 Read Online

ACCESS | Metrics & More | Article Recommendations | Supporting Information

ABSTRACT: While Pt(II) complexes containing doubly cyclometalated ligands as tridentate luminophores are well studied, the synthetic accessibility of their Pd(II) counterparts was lacking for a long time. Inspired by a recent report on the synthesis of [Pd(dpp)(PPh_3)] involving the C^N^C coordination mode (with dpp^{2-} = 2,6-di(phenid-2-yl)pyridine) and following our own work on closely related Pt(II)-based compounds, we produced the series of complexes [Pd(dpp)($PnPh_3$)] (Pn = P, As, Sb) by optimizing the synthetic procedure and exploring their reactivity in the process. Our study of the electrochemical (cyclic voltammetry) and photophysical (UV−vis absorption and emission, transient absorption (TA) spectroscopy) properties of the Pd(C^N^C) complexes represents the first report on their characterization. We observed UV−vis absorption bands down to 450 nm and electrochemical HOMO−LUMO gaps around 3.2 V, which show minimal variation with different $PnPh_3$ coligands. A more pronounced influence of the coligand was observed in time-resolved emission and TA spectroscopy. The highest photoluminescence quantum yield (Φ_L) in the series was found for [Pd(dpp)($AsPh_3$)], reaching 0.06. The interpretation of the spectroscopic data is supported by (TD-)DFT calculations. Additionally, we report structural and spectroscopic data for several dinuclear Pd(II) complexes, including the precursor {[Pd(dppH)(μ-Cl)]}$_2$ and multiple decomposition products of the sensitive compounds [Pd(dpp)($PnPh_3$)].

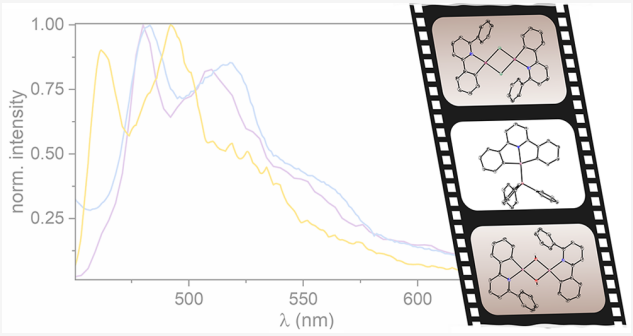

INTRODUCTION

Pd(II) complexes have long been a staple in synthetic chemistry due to their exceptional efficiency in catalyzing cross-coupling reactions, a contribution recognized by the 2010 Nobel prize awarded to *Heck*, *Negishi* and *Suzuki* for pioneering these methods.[1] Less prominently, Pd(II) complexes also show significant potential as triplet emitters, similar to their heavier congener Pt(II).[2−13] Pt(II)-based triplet emitters are an established and extensively studied class of compounds in the field of phosphorescent materials for optoelectronic and biomedical applications.[8−17] As a 5d transition metal, platinum offers favorable properties, including intrinsically high ligand field splitting and strong spin−orbit coupling (SOC).[17] Compared to similarly established octahedral Ir(III)-based coordination compounds, square-planar Pt(II) complexes exhibit even larger ligand field splitting but comparatively lower SOC.[17] Both Pt and Ir are united by their scarcity and high cost, driving research into diversified alternatives.[18] While Pd is also expensive and in high demand due to its critical role in organic synthesis,[19] achieving triplet emission from Pd(II) complexes may be a key step toward developing phosphorescent Ni(II) complexes.[13,20−24]

Novel organopalladium complexes at the interface of photochemistry and catalysis are thus highly relevant to modern organometallic chemistry. Investigating the relationships and trends in properties among group 10 transition metals - Ni, Pd and Pt - can facilitate the transfer of proven strategies from Pt and Pd to Ni. This applies not only to photochemistry but also to catalysis, as the frontiers of synthetic feasibility are continually pushed.[8,13]

One well-studied group of Pt(II) complexes is the doubly cyclometalated [Pt(C^N^C)(L)] system, which features a robust tridentate chromophore acting as a tridentate tri(hetero)aryl ligand (C^N^C), along with a variable coligand (or ancillary ligand) L that serves as an access point for fine-tuning of properties.[25−31] Surprisingly, the Pd counterparts of these complexes have remained virtually unexplored as triplet emitters, primarily due to their synthetic inaccessibility until

Received: December 20, 2024
Revised: February 21, 2025
Accepted: March 6, 2025
Published: March 27, 2025

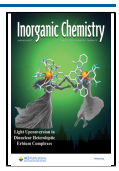

ACS Publications

© 2025 The Authors. Published by American Chemical Society

https://doi.org/10.1021/acs.inorgchem.4c05436
Inorg. Chem. 2025, 64, 6561−6574

Chart 1. Published Reaction Conditions for the Syntheses of [Pt(C^N^C)(DMSO)] (A), [Pd(C^C^N)(PPh$_3$)] (B) and [Pd(C^N^C)(PPh$_3$)] (C)[29,31−34]

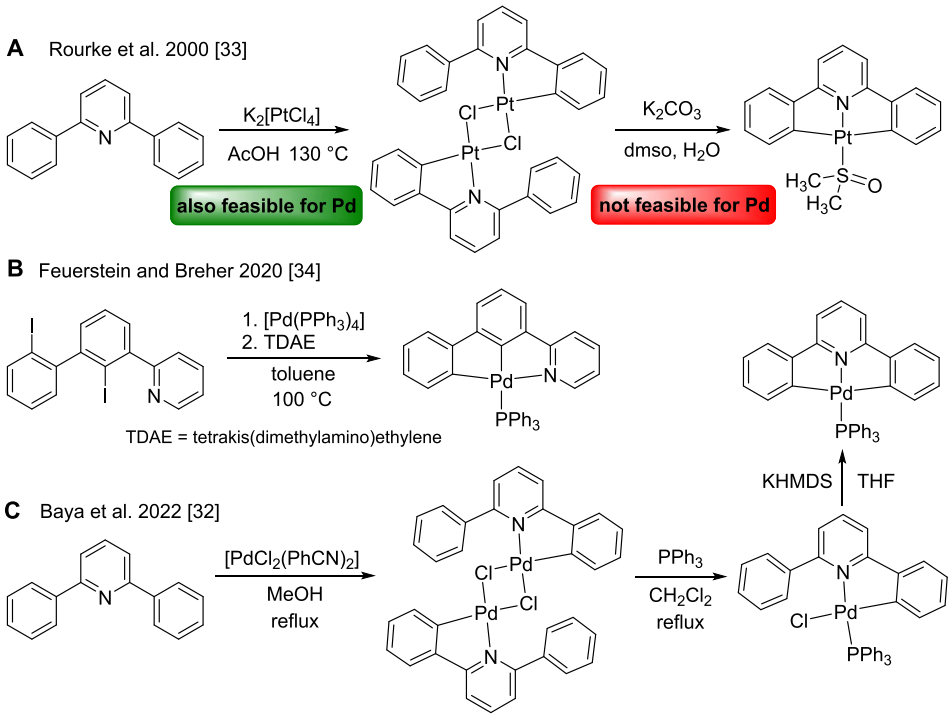

Chart 2. Synthesis Routes for [Pd(dpp)(PPh$_3$)] (3a, A) and [Pd(dpp)(PnPh$_3$)] with Pn = As, Sb (3b and 3c, B)

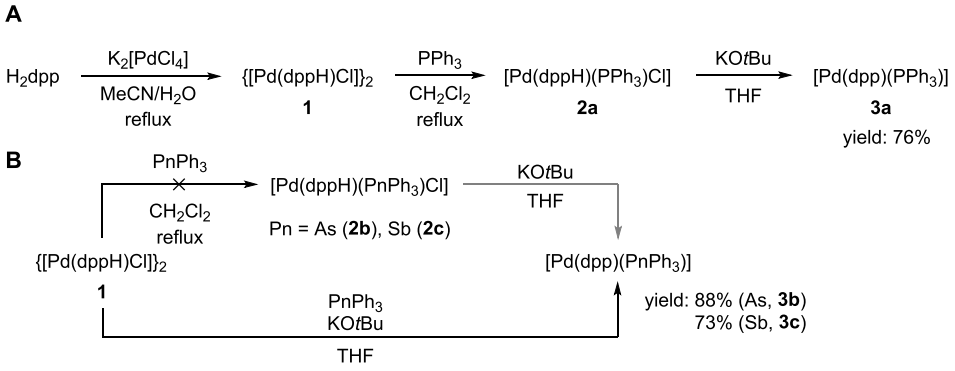

recently.[32] In contrast to the high similarity in methods for accessing singly cyclometalated N^C^N or C^N^N complexes with Pt(II) and Pd(II) centers, the synthesis conditions for [Pt(C^N^C)(L)] derivatives (Chart 1) are not applicable to the Pd system.[8,26−34]

The first example of doubly cyclometalated Pd(dpp) complexes (dpp = 2,6-di(phenid-2-yl)pyridine), was reported in 1988 by *von Zelewsky et al.* with the complex [Pd(dpp)(Py)]. However, very little analytical data accompanied this report.[35] Later studies were unable to confirm the viability of the described synthetic strategy, which involved dilithiation of H_2dpp and subsequent transmetalation of dpp^{2-}. A 1991 publication from the same group contains some additional data for [Pd(dpp)(Py)], including an emission spectrum of the complex in a glassy matrix of MeOH/EtOH at 77 K.[36] For the nonpalindromic derivative [Pd(C^C^N)(PPh$_3$)] reported in 2020, *Feuerstein* and *Breher* adopted a completely different route, relying on C−I oxidative addition rather than C−H activation (Chart 1B).[34] [Pd(C^C^N)(PPh$_3$)] is reported to be emissive at room temperature in the solid state.[34] More recently, in 2022, *Baya* and co-workers reported a three-step route to [Pd(dpp)(PPh$_3$)] as part of their research on heteropolymetallic architectures as models for transmetalation processes (Chart 1C).[32]

This pioneering work inspired us to explore the [Pd(dpp)(L)] system in our quest for emission enhancement through heavy ancillary ligands, building on the recently reported Pt(II) homologues [Pt(dpp)(PnPh$_3$)] (Pn = P, As, Sb).[31] In this previous study, we gained valuable insights into the effect of pnictogen variation on phosphorescence, with particularly promising results for the heavier PnPh$_3$-containing Pt(II) complexes where Pn = As or Sb.[31,37]

The present study aims not only to elucidate the challenging synthetic aspects of double cyclometalation chemistry required to access the [Pd(dpp)(L)]-type complexes, but also to investigate the impact of heavy ancillary ligands on phosphorescence in the [Pd(dpp)(L)] system. This research adds a crucial component to our understanding of this class of

https://doi.org/10.1021/acs.inorgchem.4c05436
Inorg. Chem. 2025, 64, 6561−6574

compounds. To achieve this, we conducted an extensive photophysical and (time-dependent) density functional theory ((TD-)DFT) calculations, which to our knowledge represents the first ever comprehensive characterization of this compound class.[31,34,35]

RESULTS AND DISCUSSION

Synthesis and Reactivity of the Complexes. [Pd(dpp)(PPh_3)] (**3a**) was synthesized in a modified procedure adapted from *Baya et al.* (Chart 2A).[32] Similar to the [Pt(C^N^C)(L)] derivatives, the Pd(dpp) platform is accessed through the singly cyclometalated, dimeric intermediate {[Pd(dppH)(μ-Cl)]}$_2$ (**1**). Unfortunately, by following the exact conditions reported by *Baya et al.*, we were unable to obtain **1**. Therefore, we adapted the synthesis of **1** from our protocol for [Pd(C^N^N)X] complexes using $K_2[PdCl_4]$ in a 1:1 MeCN/H_2O mixture, which provides satisfactory yields (for details, see Experimental Section). Since no analytical data for **1** has been available in the literature (most likely due to its poor solubility), we herein provide the first report its structure in the solid state (Figure S16, Supporting Information, SI) as well as ^{1}H NMR and optical spectra (Figure S29, SI) for the compound. Furthermore, we changed the base in the crucial second cyclometalation step from KHMDS to KO*t*Bu, which gave an improved yield of 76% (Chart 2A) compared to the reported 59%.[32]

For the heavier homologues [Pd(dpp)($AsPh_3$)] (**3b**) and [Pd(dpp)($SbPh_3$)] (**3c**), we observed no formation of [Pd(dppH)($PnPh_3$)Cl] (Pn = As, Sb, **2b** and **2c**) under the conditions used to prepare the second intermediate [Pd(dppH)(PPh_3)Cl] (**2a**, Chart 2A). We attribute this to the lower Lewis basicity and ligand strength for Pd(II), as herein reflected in ligand displacement potential when comparing $AsPh_3$ and $SbPh_3$ with PPh_3.[38,39] In contrast to reports suggesting that the Lewis basicity of $AsPh_3$ is approximately similar to that of PPh_3,[40] we have consistently observed that the tipping point for the ligand exchange (X→ $PnPh_3$) within the $PnPh_3$ series (in terms of speed and success under comparable conditions) lies between PPh_3 and $AsPh_3$.[28] Instead, we synthesized **3b** and **3c** through a combined reaction involving **1**, KO*t*Bu, and $AsPh_3$ or $SbPh_3$ (Chart 2B). This protocol was also applicable to **3a**. To clarify whether the presence of the $PnPh_3$ ligand is required for the second C−H activation or if the reaction might proceed sequentially through an already doubly cyclometalated intermediate, e.g., [Pd(dpp)(THF)], with subsequent ligand exchange, we performed the experiment again in the absence of any $PnPh_3$ (for details, see Experimental Section). Analysis of the reaction solution via ^{1}H NMR revealed the presence of a [Pd(dpp)(L)] species, most likely [Pd(dpp)(THF)], even though it was not possible to verify this spectroscopically during our experiment as the reaction was conducted in nondeuterated THF (Figure S14). Regardless, our observation of the formation of [Pd(dpp)(L)] upon the reaction of **1** with KO*t*Bu in THF suggests that the synthetic scope is not limited to the $PnPh_3$ ligands, with the possibility of facile further variation of the monodentate ligand in the future. While our qualitative experiment does not allow for conclusions about the yield of the transformation in the absence of $PnPh_3$, the presence of a monodentate ligand other than THF probably facilitates high yields as the presumed intermediate [Pd(dpp)(THF)] is removed from the equilibrium, as indicated by the good yields of **3b** and **3c**.

We found that the [Pd(dpp)(L)] complexes are highly sensitive to hydrolysis. This is probably the primary reason for the failure of the second cyclometalation under aqueous conditions, as typically used for the preparation of the related [Pt(dpp)(DMSO)] from {[Pt(dppH)(μ-Cl)]}$_2$ (Chart 1A).[29] Another possible factor is the suitability of DMSO as a coligand for Pt, but less for Pd. Additionally, the workup of [Pd(dpp)(PPh_3)] in air, as previously described,[32] resulted repeatedly in complete decomposition. Therefore, the workup must be carried out under inert conditions, excluding humidity, and ideally also excluding ambient light. Purified, dry solid samples of the complexes are stable and can be stored under Ar for several months.

Hydrolysis in solution yields defined products, namely {[Pd(dppH)(μ−OH)]}$_2$ (**4**, molecular structures shown in Figure S17) and free $PnPh_3$ (Pn = P, As, Sb). Further illustrating the reactivity of the complexes, we also identified other {[Pd(dppH)(μ-X)]}$_2$ derivatives, such as {[Pd(dppH)-(μ-κ^2-$NCCH_2$)]}$_2$ (**5**) which contains bridging deprotonated CH_3CN (crystal structure shown in Figure S18). Both compounds were found in samples aimed at crystallizing [Pd(dpp)($SbPh_3$)] (**3c**), from CH_2Cl_2 and from CH_3CN and Et_2O, respectively.

The ability of **3c** to abstract a proton from CH_3CN and to form the stable species {[Pd(dppH)(μ-κ^2-$NCCH_2$)]}$_2$ (**5**) suggests that the coordinating carbon sites in **3c** exhibit stronger basicity than the coordinating C-site of $NCCH_2^-$ in **5**. We assume that in **5**, the basicity of the carbanionic site in $NCCH_2^-$ is reduced due to the concurrent N-coordination to the second Pd(II) center, explaining the relative thermodynamic stability of **5**, which might otherwise be expected to rapidly undergo the reverse reaction. Conversely, this suggests that the loss of the $SbPh_3$ ligand is necessary for the reaction of **3c** with H_3CCN resulting in **5**. The formation of **5** might involve a transition state featuring agostic interactions, i.e., Pd···H−CH_2CN−Pd, similarly to the transition states that are well documented for C−H activation reactions with Pt.[41] The fact that the crystal structure of **5** reveals a *cis* configuration with respect to the phenidyl and $NCCH_2^-$ ligands suggests that a hypothetical initially formed *trans* isomer isomerizes to the more stable *cis* configuration due to the strong *trans* influence of the carbanionic ligands.

The remarkable reactivity especially of **3c** is particularly noteworthy when contrasted with the high stability of [Pt(dpp)(L)], including [Pt(dpp)($PnPh_3$)].[31] Potential explanations for these striking differences in reactivity will be discussed later, alongside the structural data.

In parallel, we also attempted to adapt the double oxidative addition route reported for the C^C^N system, namely [Pd(C^C^N)(PPh_3)],[34] to the dpp derivatives (Figure S23A). A limiting factor in this process was the availability of the iodinated protoligand I_2dpp. We approached the synthesis of I_2dpp through several different routes, including *Kröhnke* pyridine synthesis, *Suzuki* coupling reactions, and aryl-*Finkelstein* or *Sandmeyer* reactions starting from other X_2dpp derivatives (X = Br, F, NH_2). However, I_2dpp appears to be highly prone to deiodination, leading to the isolation of IHdpp or H_2dpp instead of the target compound in many cases. Furthermore, it was difficult to separate I_2dpp from Br_2dpp, from which it can be derived via an aryl-*Finkelstein* protocol, but only in poor yields due to the competition of the desired transformation with deiodination.

https://doi.org/10.1021/acs.inorgchem.4c05436
Inorg. Chem. 2025, 64, 6561−6574

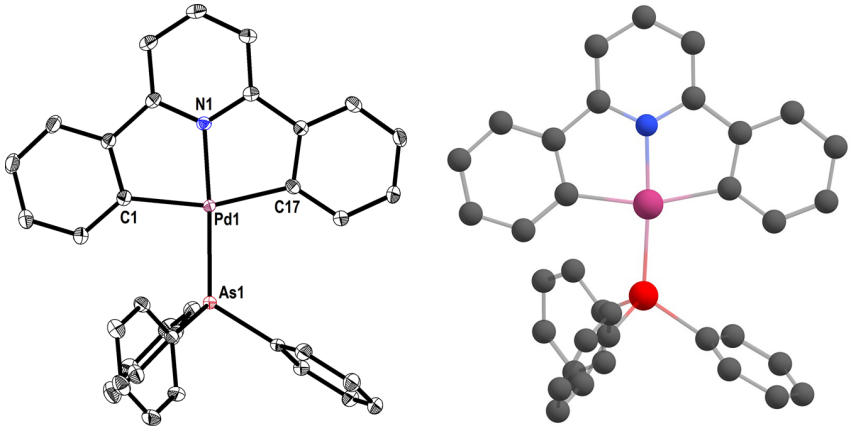

Figure 1. Left: Molecular structure of the complex [Pd(dpp)($AsPh_3$)] (**3b**) from scXRD; displacement ellipsoids are shown at 50% probability, H atoms omitted for clarity. Right: DFT-optimized structure of **3b**.

With the very small quantities of Br_2dpp-contaminated I_2dpp that we managed to obtain, we performed experiments mirroring the synthesis of [Pd(C^C^N)(PPh_3)]. They yielded product mixtures containing only traces of the desired compound [Pd(dpp)(PPh_3)] (**3a**), along with various side products according to the ^{1}H NMR spectra. One major product was isolated by fractioned crystallization and identified as what can be described as [(PPh_3)Pd(μ-(κ^3-C^N^C-κ^1-C)dpp)Pd(PPh_3)$_2$Br] (**8**), according to X-ray diffraction on single crystals (scXRD, Figure S21) and ^{1}H NMR spectroscopy (Figure S22). In the dinuclear complex **6**, the dpp moiety is triply metalated, forming the desired C^N^C motive with a [Pd(PPh_3)] fragment and bearing another unsupported [Pd(PPh_3)$_2$Cl] unit at the outward C-α position of one of the peripheral rings. One of the three metalation steps must be assumed to have occurred via C−H rather than C−X activation. Considering our knowledge of **3a** through deprotonation of {[Pd(dppH)(μ-Cl)]}$_2$ (**1**) with KO*t*Bu or KHMDS, we hypothesize that **8** is formed from an intermediate [Pd(dppBr)(PPh_3)Br] (**6**) which results from the reaction of [Pd(PPh_3)$_4$] with Br_2dpp. Due to the lower reactivity of the C−Br bond compared to the C−I bond with respect to oxidative addition, the first C−Br activation is probably not followed by a second oxidative addition to the same Pd center. Instead, the intended reductant tetrakis-(dimethylamino)ethylene (TDAE) might act as a base to facilitate a C−H activation. This would produce [Pd(dppBr)-(PPh_3)] (**7**), which still carries the second bromine substituent on the outward phenid-2-yl C-α position. This remaining C−Br bond can undergo oxidative addition to another Pd^0, forming [(PPh_3)Pd(μ-(κ^3-C^N^C-κ^1-C)dpp)Pd(PPh_3)$_2$Br] (**8**). This proposed mechanism for the formation of **8** is shown in Figure S23B.

Crystal Structures and DFT-Calculated Molecular Structures. The unprecedented complex [Pd(dpp)($AsPh_3$)] (**3b**) was crystallized and studied by X-ray diffractometry on single crystals (scXRD), both as a nonsolvate and as [Pd(dpp)($AsPh_3$)]·EtOAc. Due to superior data quality, the latter is used as the basis for discussion of the molecular structure (Figure 1). The structure of [Pd(dpp)(PPh_3)] (**3a**) was already reported by Baya *et al.*[32] We were unable to obtain single crystals of [Pd(dpp)($SbPh_3$)] (**3c**), which we attribute to the unfavorable combination of both high solubility and reactivity, as discussed earlier (*vide supra*).

The crystal structures of **3a** and **3b** differ significantly in cell parameters and symmetry. Interestingly, while **3a**[32] and its Pt congener [Pt(dpp)(PPh_3)][28] are isostructural, this is not the case for **3b** and [Pt(dpp)($AsPh_3$)][31] (see Table S2). As observed before for the [Pt(dpp)($PnPh_3$)] derivatives, there seems to be no common determining factor for the packing of the complexes, as the metal···metal and $\pi\cdots\pi$ distances are long and the head-to-tail stacking, which is frequently observed for complexes of this type,[8−13,16,24,26] is not very pronounced in either of the structures.

DFT-optimized geometries of **3b** and the reported **3a**[32] are very similar to those from scXRD (data in Table S3). Especially the E−Pd and N−Pd bond distances as well as the C−Pd−C and the Pd−Pn−C angles are in excellent agreement. This makes us confident that the DFT calculations also provide an outstanding model for the structure of **3c**.

Compared with the isoleptic Pt(II) derivatives,[28,31] the three Pd(II) complexes feature quite similar bond lengths and angles around the central metal. While the M−N bond is slightly shorter by about 0.01 Å in the Pd(II) complexes than in the Pt(II) derivatives, the other bonds around Pd are about 0.01 Å longer for the Pd(II) complexes, depending on the environment and in accordance with the dependence on the environment, virtually identical or even slightly larger ionic radius of Pd(II) as compared to Pt(II).[42] Both the Pd(II) and Pt(II) complexes show a sideways tilt of the $PnPh_3$ ancillary ligand from the coordination plane, accommodating its asymmetric steric demand.

The averaged Pd−Pn−C and C−Pn−C angles are in a very similar range to the corresponding angles in the Pt congeners, namely from 114 to 117° (M−Pn−C) and from 104 to 101° (C−Pn−C). This overall small variation reflects the compensation of the hybridization defect at Pn upon bond formation with Pd, as we have reported previously for Pt.[31,37] The Pd−Pn−C angle increases by 2° from **3a** to **3b**, and DFT predicts an increase by another 1° from **3b** to **3c**. Interestingly, in the Pt derivatives, the values are even more similar between P and As with a larger jump to Sb, opposite to the behavior seen here.

When comparing series of isoleptic Ni/Pd/Pt complexes, a frequent finding is that the Pd(II) complexes show the lowest covalency of the metal−ligand bonds and Pd behaves as the "hardest" of the three metals from an HSAB perspective, thus providing the least backbonding.[8,43−45] The strong basicity of

https://doi.org/10.1021/acs.inorgchem.4c05436
Inorg. Chem. 2025, 64, 6561−6574

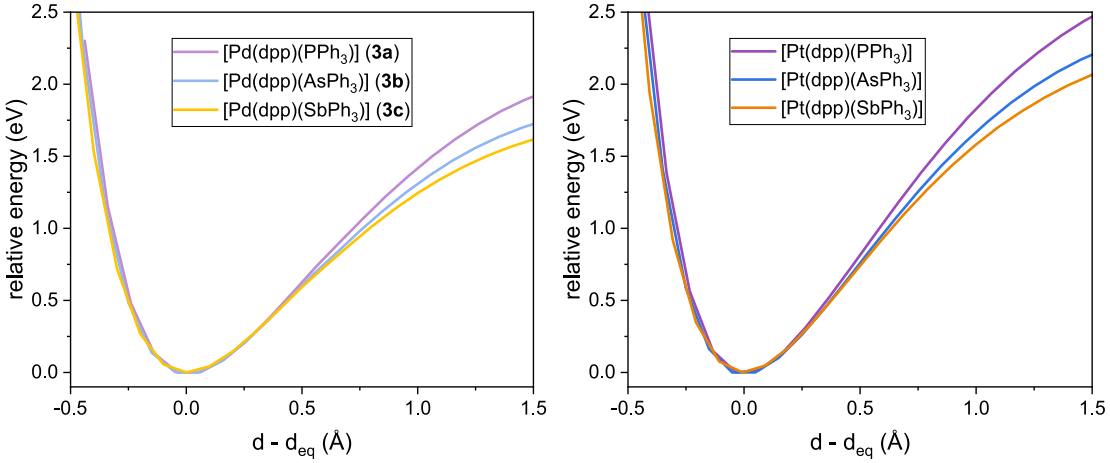

Figure 2. DFT-relaxed scans along the M−Pn bonds in [Pd(dpp)($PnPh_3$)] (**3a−c**, left) and [Pt(dpp)($PnPh_3$)] (right); Pn = P, As, Sb.

Table 1. Electrochemical Data for the Ligand Precursor H_2dpp and the Complexes [Pd(dpp)($PnPh_3$)] (3a−c, Pn = P, As, Sb)[a]

	Red3 E_p (V)	Red2 E_p (V)	Red1 $E_{1/2}$ (V)	Ox1 E_p (V)	ΔRed1−Ox1 (V)
H_2dpp			−2.85		
[Pd(dpp)(PPh_3)] (**3a**)	−3.37	−3.09	−2.46	0.72	3.18
[Pd(dpp)($AsPh_3$)] (**3b**)		−3.18	−2.52	0.71	3.23
[Pd(dpp)($SbPh_3$)] (**3c**)	−3.44	−2.75	−2.43	0.78	3.21

[a]Measured in a 0.1 M *n*-Bu_4NPF_6 THF solution at a scan rate of 50 mV/s. Potentials *E* (V) referenced against the $FeCp_2/FeCp_2^+$ redox pair. $E_{1/2}$: half-wave potential for reversible processes. E_p: peak potential for irreversible processes. Experimentally accessible potential range: 1.5 to −3.5 V vs. $FeCp_2/FeCp_2^+$.

the coordinating C-sites in the complexes **3a−c** matches this expectation, pointing to poorer stabilization of the formal carbanions due to weaker electron acceptance into the Pd orbitals, if compared to the Pt congeners (*i.e.*, a lower covalency). Combined with the similarly pronounced compensation of hybridization defects in the [Pd(dpp)($PnPh_3$)] and [Pt(dpp)($PnPh_3$)] (Pn = P, As, Sb) series, this supports the notion that the latter is essentially due to polarization of the Pn atom upon coordination, and largely independent of the extent of covalent interaction.[37]

To compare the overall Pd−Pn bond strengths (both within the [Pd(dpp)($PnPh_3$)] series and with respect to the Pt derivatives) regardless of the extent of covalent contributions, we performed DFT relaxed surface scans along the M−Pn bonds for both the Pd and Pt series (Figure 2). Judging from the slopes of the energy increase upon elongation of the M−Pn bonds, the results align with our experimental observation of decreasing stability (here specifically: M−Pn bond strength) of the complexes along *P* > As > Sb, as well as Pt > Pd.

Electrochemistry and DFT-Calculated Frontier Molecular Orbitals. Cyclic voltammetry on the three complexes [Pd(dpp)($PnPh_3$)] (**3a−c**, Pn = P, As, Sb) revealed irreversible oxidation waves at peak potentials around +0.7 to +0.8 V vs the ferrocene/ferrocenium couple. On the cathodic side, reversible (Pn = P) or partially reversible (Pn = As or Sb) reduction waves at around −2.4 V are followed by further, irreversible waves reaching up to −3.5 V (Table 1, Figures 3 and S24).

The oxidation potentials do not change significantly upon variation of the ancillary $PnPh_3$ ligand, indicating a process with little monodentate coligand involvement. As for the analogous Pt(II) complexes [Pt(dpp)($PnPh_3$)] (Pn = P, As, Sb),[31] we assign the oxidation waves to essentially metal-

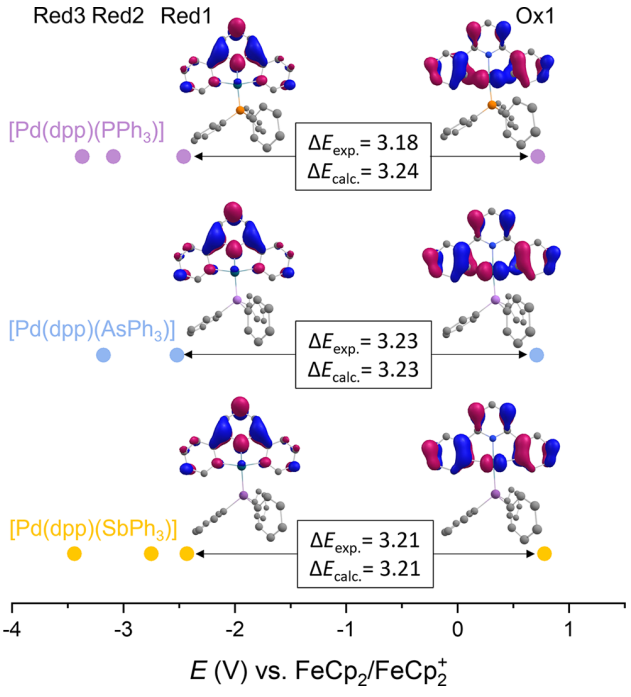

Figure 3. Electrochemical potentials from cyclic voltammetry (data in Table 1) as well as DFT-calculated frontier orbitals and their energies for [Pd(dpp)($PnPh_3$)] (**3a−c**, Pn = P, As, Sb). Shown as colored dots are the half-wave potentials $E_{1/2}$ for the reversible first reduction, and the peak potentials E_p for the irreversible oxidation waves as well as for the second and third reduction processes (Table 1). Electrochemical gaps $\Delta E_{exp} = E_{ox1} - E_{red1}$ as well as calculated gaps between highest occupied molecular orbitals (HOMO) and lowest unoccupied molecular orbitals (LUMO) ΔE_{calc} are indicated in eV.

https://doi.org/10.1021/acs.inorgchem.4c05436
Inorg. Chem. 2025, 64, 6561−6574

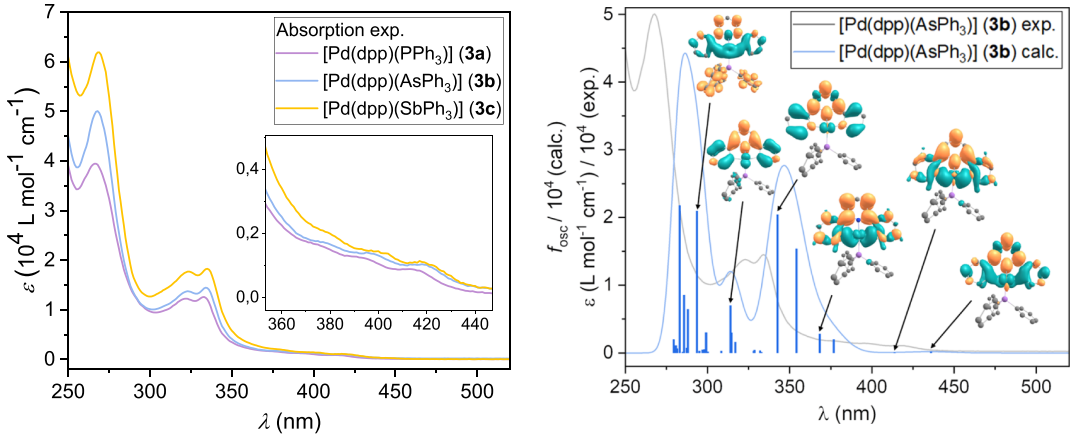

Figure 4. Left: Experimental UV−vis absorption spectra of [Pd(dpp)($PnPh_3$)] (**3a−c**, Pn = P, As, Sb) in THF. Right: TD-DFT-calculated individual transitions (blue bars), calculated UV−vis absorption spectrum (blue line), and experimental UV−vis absorption spectrum (gray) for **3b** with difference densities (blue = negative, orange = positive) for selected transitions.

Table 2. Experimental and TD-DFT-Calculated UV−vis Absorption Maxima for the Complexes [Pd(dpp)($PnPh_3$)] (3a−c, Pn = P, As, Sb)

		λ_1 (ε)	λ_2 (ε)	λ_3 (ε)	λ_4 (ε)	λ_5 (ε)	λ_6 (ε)
[Pd(dpp)(PPh_3)] (**3a**)	exp.[a]	267 (3.95)	322 (1.23)	333 (1.26)	374 (0.17)	391 (0.12)	414 (0.09)
	calc.[b]	286	314	345	373[c]	432	
[Pd(dpp)($AsPh_3$)] (**3b**)	exp.[a]	268 (5.00)	323 (1.38)	334 (1.45)	377 (0.17)	396 (0.14)	418 (0.10)
	calc.[b]	286	314	347	377[c]	434	
[Pd(dpp)($SbPh_3$)] (**3c**)	exp.[a]	268 (6.19)	324 (1.77)	335 (1.83)	378 (0.20)	398 (0.15)	418 (0.11)
	calc.[b]	288	314	349	438		

[a]In THF; absorption maxima (wavelength λ in nm); molar absorption coefficients ε in 10^4 L mol^{-1} cm^{-1}. [b]TPSSh/def2-TZVP/CPCM(THF), maxima from convoluted spectrum. [c]Shoulder.

centered Pd(II)/Pd(III) couples. This is further supported by the large d-orbital contributions to the highest occupied molecular orbitals (HOMOs, Figures 3 and S25) predicted by DFT. Overall, the Pd complexes **3a−c** were oxidized at higher potentials by about 100 to 150 mV compared with the Pt congeners,[31] in agreement with other studies comparing homoleptic Pt(II) and Pd(II) complexes.[8,10,13,24]

Compared to the protoligand H_2dpp, the first reduction processes of the Pd(II) complexes are facilitated by about 0.3 to 0.4 V (as previously observed for the Pt derivatives, which are reduced at overall slightly milder potentials than the Pd complexes by 0.1 to 0.2 V).[31] Also like in the Pt(II) case, the $SbPh_3$ complex **3c** undergoes a second reduction at a significantly milder potential than the PPh_3 and $AsPh_3$ complexes **3a** and **3b**. Furthermore, **3a** and **3c** show a third, irreversible reduction wave around −3.4 V, near the lower limit of the measurement window. Considering that both the first and second reduction occurs at the most cathodically shifted potential for **3b** (*i.e.*, among the three Pd complexes **3a−c**), its corresponding third reduction probably exceeds the measurement window. We assign these cathodic waves to ligand-centered reduction processes based on the strong π^* character of the DFT-calculated lowest unoccupied molecular orbitals (LUMOs, Figures 3 and S23), as well as on our previous findings from UV−vis-spectroelectrochemical (UV-vis-SEC) studies on the Pt(II) derivatives.[31] Due to the overall very similar electrochemical behavior observed for the Pd and Pt congeners, we are confident that the SEC conclusions for [Pt(dpp)($PnPh_3$)] (Pn = P, As, Sb) are transferrable to the Pd series.

With values around 3.2 eV, the electrochemical HOMO−LUMO gaps ($\Delta E_{exp} = E_{ox1} - E_{red1}$) of the Pd(II) complexes **3a−c** are significantly wider than those of their Pt(II) congeners, namely by 0.2 to 0.3 eV. This is typical, as the HOMO−LUMO gaps of homologous complexes within the Ni/Pd/Pt triad usually increase along the series Ni < Pt < Pd.[8,13,43−46] Interestingly, the pronounced trend of decreasing ΔE_{exp} observed for the Pt(II) complexes[31] along the $PnPh_3$ series (P > As > Sb) is not found for the Pd(II) derivatives; in fact, the values are somewhat more uniform, with the largest deviation being a 0.05 eV increase from **3a** to **3b**. We interpret this in terms of weaker participation of the $PnPh_3$ in the frontier molecular orbitals (FMOs), which is consistent with our assumption of significantly lower covalency of the coordinative bonds within the Pd(II) complexes as compared to the analogous Pt(II) species. Our DFT calculations predict also very uniform ΔE_{calc} values for the HOMO−LUMO gaps, in a very similar range to the measured ΔE_{exp}. However, they do not mirror the experimental finding of the smallest ΔE_{exp} found for the PPh_3 complex, albeit the differences are overall barely significant.

Comparing the wider DFT-calculated FMO landscapes for the three Pd(II) complexes **3a−c** (Figure S25), we find barely any variation in the HOMOs as well as the LUMO and LUMO+1, in accordance with a lack of $PnPh_3$ contributions to these MOs. The LUMO+2 to LUMO+4 distributions exhibit strong $PnPh_3$ and minor $d_{x^2-y^2}$ contributions. The energies of the LUMO+2 and LUMO+3 vary somewhat more between the three complexes, each within a range of up to 0.2 eV. While the energy of the LUMO+3 increases linearly along P < As <

https://doi.org/10.1021/acs.inorgchem.4c05436
Inorg. Chem. 2025, 64, 6561−6574

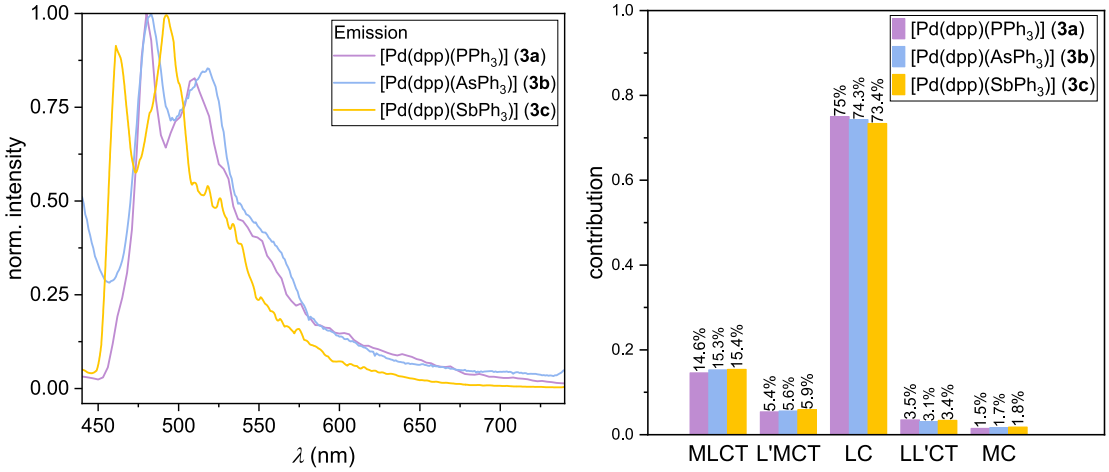

Figure 5. Left: Photoluminescence emission spectra of the complexes [Pd(dpp)(PnPh$_3$)] (**3a–c**, Pn = P, As, Sb) at 77 K in a glassy matrix of frozen 2-MeTHF (λ_{ex} = 350 nm). Right: Decomposition of the emissive T_1 states into MLCT, L'MCT, LL'CT, LC and MC contributions for **3a–c** based on TD-DFT calculations; L = dpp, L' = PnPh$_3$.[49]

Table 3. Experimental and Calculated Photophysical Data for the Complexes [Pd(dpp)(PnPh$_3$)] (3a–c, Pn = P, As, Sb)[a]

Pn	λ_{max} (nm)	Φ_L	τ (μs)[c]	k_r (10^4 s^{-1})[d]	k_{nr} (10^4 s^{-1})[d]	ΔE (T_1–S_0) (eV/nm)[e]	$\langle S_n\|H_{SO}\|T_1\rangle^2$ (cm^{-2})[e]
P (3a)	480, 510, 549[b]	<0.03	473.5 ± 0.8	≤0.006	0.20 ≤ k_{nr} ≤ 0.21	2.016/615	1.49×10^4 (n = 0)
							1.40×10^2 (n = 1)
							4.45×10^2 (n = 2)
As (3b)	483, 518, 554[b]	0.06 ± 0.02	665 ± 8	≤0.06	0.09 ≤ k_{nr} ≤ 0.19	2.004/617	1.36×10^4 (n = 0)
							3.16×10^2 (n = 1)
							4.31×10^2 (n = 2)
Sb (3c)	461, 492, 526[b]	<0.03	223.2 ± 0.5	≤0.001	0.03 ≤ k_{nr} ≤ 0.05	1.989/623	1.48×10^4 (n = 0)
							4.61×10^2 (n = 1)
							6.34×10^2 (n = 2)

[a]Measured at 77 K in a glassy matrix of frozen 2-MeTHF. Excitation wavelength λ_{exc} = 350 nm. [b]Shoulder. [c]For multiexponential photoluminescence decays, amplitude-weighted average lifetimes are indicated. Raw time-resolved photoluminescence decays along with the fitting parameters are shown in the SI, Figures S30–S32. [d]Average k_r, k_{nr} and the respective uncertainties were calculated based on eqs 1–4 (see Experimental Section) [e]Calculated by (TD-)DFT.

Sb, the energy of the LUMO+2 peaks for As. This unclear trend points toward a complex effect of the PnPh$_3$ variation on the bonding situation with Pd. Compared to their Pt(II) congeners, DFT predicts essentially the same FMO shapes for the Pd(II) complexes.[31] Key differences include the LUMOs with PnPh$_3$ involvement, which did show a uniform increase in energy along the trend P < As < Sb for the Pt(II) derivatives, as well as the energy of the d_{z^2} (HOMO−2), which is markedly destabilized in the Pd(II) complexes (as compared to the Pt(II) homologues).[31]

UV–vis Absorption Spectroscopy and TD-DFT Calculations. The three complexes [Pd(dpp)(PnPh$_3$)] (**3a–c**, Pn = P, As, Sb) show an intense absorption band at 267 nm, a structured system of medium intensity with maxima at 314 and 334 nm, and a broad profile with several weak maxima in the range of 360 to 450 nm (Figure 4). Closer inspection reveals a pronounced hyperchromic shift and a very small bathochromic shift of the maxima along the Pn series (*i.e.*, P < As < Sb, see Table 2). The latter was previously also observed for the Pt(II) derivatives [Pt(dpp)(PnPh$_3$)].[31]

The TD-DFT-calculated maxima agree well with the experimental data (Figure 2 right, Table 2, Figures S26–S28) and suggest essentially ligand-centered (LC, *i.e.*, π–π^*) character with LL'CT contributions (L = dpp, L′ = PnPh$_3$) for the excited states corresponding to the UV bands at 287 nm. The structured bands at 300 to 350 nm can be assigned to transitions into states with mixed LC/metal-to-ligand charge transfer (MLCT) character, based on the TD-DFT results as well as on our previous conclusions for the analogous Pt(II) complexes.[31] The weak absorption bands between 360 and 450 nm represent transitions into MLCT states, with almost exclusive participation of the LUMO (according to TD-DFT calculations). Extrapolation of the absorption cutoff from the slope of the lowest energy absorption bands gives values of 440, 445, and 455 nm for **3a**, **3b** and **3c**, respectively. This corresponds to optical HOMO–LUMO gaps (ΔE_{opt}) ranging from 2.82 to 2.72 eV. For the analogous Pt(II) complexes, we observed the same phenomenon with optical gaps being counterintuitively smaller than the electrochemical gaps.[31] In the Pt(II) case, we rationalized our findings in terms of ^{3}MLCT contributions to the states associated with the lowest energy absorption bands, as based on TD-DFT and transient absorption (TA) spectroscopic studies.[31] It seems reasonable to assume the same for the presently studied Pd(II) complexes, as will be elaborated later.

Time-Resolved and Steady-State Photoluminescence Spectroscopy. In liquid solutions at room temperature, no luminescence from the Pd(II) complexes **3a–c** was observed. The same is true for their Pt(II) congeners,[31] therefore, we essentially attribute this to insufficient rigidity of the dpp ligand

https://doi.org/10.1021/acs.inorgchem.4c05436
Inorg. Chem. 2025, 64, 6561–6574

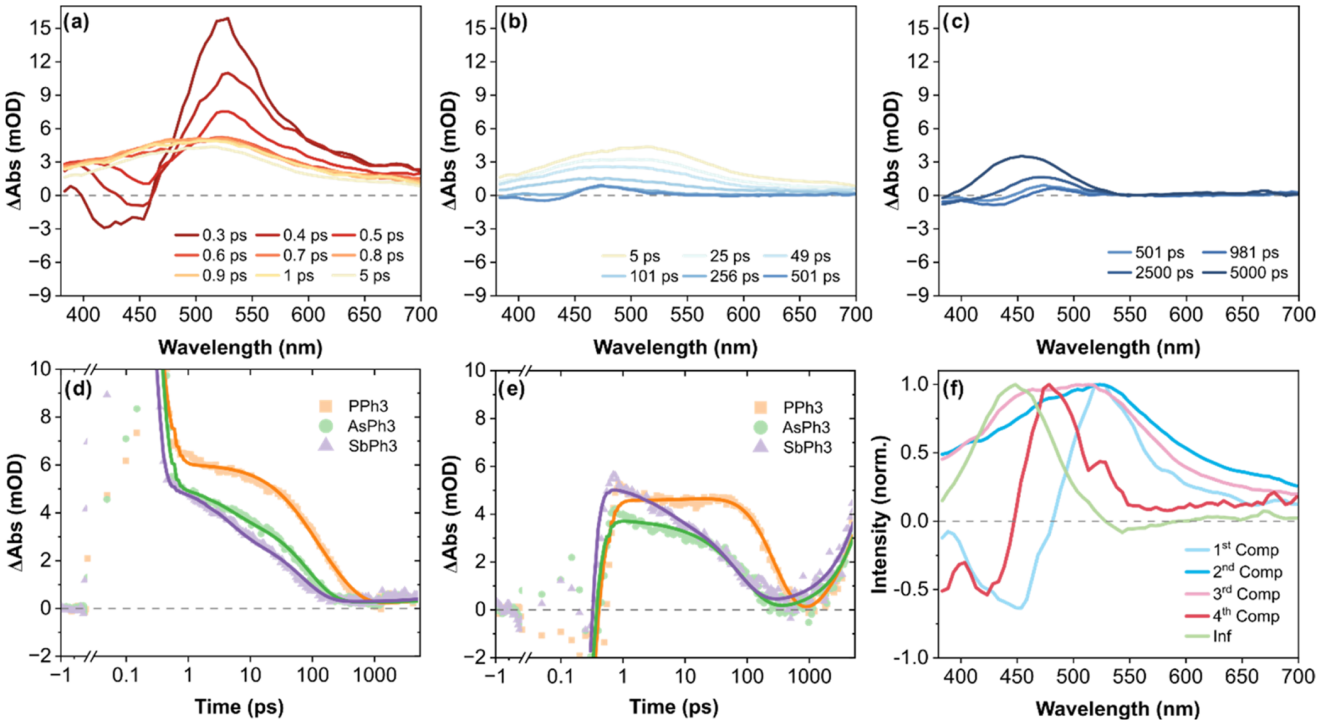

Figure 6. Transient absorption spectra of [Pd(dpp)($AsPh_3$)] (**3b**) measured in THF following excitation at 350 nm. Excitation powers were set to 450 μW. Transient absorption spectra recorded at delay times ranging from (a) 0.3 to 5 ps; (b) 5 to 500 ps; (c) 500 to 5000 ps. The transient absorption kinetics recorded at 525 and 445 nm are shown in (d) and (e), respectively. The kinetics of the other complexes with Pn = P (**3a**), Sb (**3c**) are also shown for comparison. (f) Normalized species associated spectra (SAS) obtained from a consecutive fit.

in a nonrigid environment. The problem is probably aggravated by the relatively stabilized ^{3}MC states in a Pd(II) complex, as compared to the analogous Pt(II) compound (with nonradiative deactivation through thermally accessible ^{3}MC states being the most commonly cited reason for the lack of emission in Pd(II) complexes at room temperature).[47] However, photoluminescence spectroscopy showed that the compounds [Pd(dpp)($PnPh_3$)] (**3a–c**, Pn = P, As, Sb) are moderately emissive at 77 K in glassy matrices of frozen 2-MeTHF. The emission spectra (Figure 5, left, and Figure S33 together with excitation spectra) feature pronounced vibrational progressions, with two distinct maxima and a shoulder for each complex (data compiled in Table 3). The spectra of **3a** and **3b** resemble each other, with only a very small red shift for **3b** compared to **3a** (with respect to the first maximum around 480 nm), and a more pronounced red shift for the second and third maxima (at 510/518 nm and 549/554 nm, respectively). For the homoleptic Pt(II) complexes, we had found a similarly progressive red shift across the full series P < As < Sb.[31] However, for the Pd(II) homologues reported herein, the trend is not continued for **3c**, which shows a significantly blue-shifted emission with the first maximum peaking at 461 nm. At around 450 nm, the onsets of the emission bands of the three complexes coincide with the absorption cutoff in their absorption spectra. This supports our attribution of significant ^{3}MLCT contributions to the very weak absorption bands between 380 and 460 nm discussed above, thus paralleling the behavior of the Pt(II) congeners.[31]

As detailed in Table 3, the photoluminescence lifetimes are in the μs range, which is within a typical range for triplet emission from Pd(II) complexes.[6,9−13,48] In addition, based on the photoluminescence quantum yields (Φ_L) and amplitude-weighted average lifetimes (τ), both the average radiative (k_r) and nonradiative (k_{nr}) rate constants were estimated (Table 3). It should be noted that finding a clear trend regarding the values of k_r and k_{nr} is challenging due to the low quantum yields, which result in significant uncertainties in the calculation of these parameters (see Experimental Section, eqs 1−4). Nevertheless, as in the homoleptic Pt(II) analogs, we observe that the highest k_r is found for the $AsPh_3$ complex, correlating with the scandide contraction (*i.e.*, the 3d anomaly related to the first filling of a d shell before the element As).[31] For the k_{nr}, while the complexes with PPh_3 and $AsPh_3$ are practically within the same uncertainty range, the complex with $SbPh_3$ has a smaller k_{nr}.

Exciton decomposition analysis of the T_1 states of **3a–c** indicates up to 75% LC and around 15% MLCT contributions (Figure 5). Across the Pn series from P to Sb, a decreasing LC character is predicted whereas the MLCT involvement increases. Minor L'MCT contributions are predicted to increase across the series as well. The same trends were observed for the previously studied [Pt(dpp)($PnPh_3$)] series; however, the Pt(II) derivatives showed a stronger MLCT character, with contributions estimated at 20 to 22%, and a smaller LC participation (around 66 to 68%).[31] Strong LC character of the emissive state is typical for Pd(II) complexes and associated with small k_r.[50,51] Comparison of TD-DFT-calculated SOC matrix elements within the Pd complex series showed an upward trend along P < As < Sb for $\langle S_2|H_{SO}|T_1\rangle^2$ and $\langle S_1|H_{SO}|T_1\rangle^2$. From our study of the homologous Pt(II) complexes, we concluded that the emission efficiency was progressively more dependent on the SOC as the LC contributions to the emissive state increased.[31] Thus, the opposing trends regarding SOC (*i.e.*, increasing along P < As <

https://doi.org/10.1021/acs.inorgchem.4c05436
Inorg. Chem. 2025, 64, 6561−6574

Table 4. Fit Parameters for the Transient Absorption Measurements on [Pd(dpp)($PnPh_3$)] (3a–c, Pn = P, As, Sb)[a]

	τ_1 (ps)	τ_2 (ps)	τ_3 (ps)	τ_4 (ns)	inf
[Pd(dpp)(PPh_3)] (**3a**)	0.20 ± 0.05	62 ± 5	250 ± 10	13 ± 1	Yes
[Pd(dpp)($AsPh_3$)] (**3b**)	0.10 ± 0.02	5.0 ± 0.5	87 ± 4	Long	Yes
[Pd(dpp)($SbPh_3$)] (**3c**)	0.10 ± 0.03	5.0 ± 0.5	67 ± 5	Long	Yes

[a]For the fits, all data points after 300 fs were considered and a model with four consecutive and one infinite component was applied.

Sb) and LC character of the T_1 states suggested by our calculations (*i.e.*, decreasing along P > As > Sb) may explain unclear correlation with the emission behavior of the three Pd(II) complexes **3a–c**. During our previous study, we also identified the M–Pn bond as a source for the differences within the $PnPh_3$ (Pn = P, As, Sb) series in a broader sense.[31] For instance, the variation of the Pn atom may also influence k_r and k_{nr} through changes in the energies of vibrational modes with M–Pn involvement and the shape of the potential energy surfaces of the states involved in the respective decay pathways.

During the photoluminescence measurements of **3b** and **3c**, we observed another emission band at 395 nm, depending on the sample preparation and duration of the measurements. We were able to trace the origin of these bands to {[Pd(dppH)-X]}$_2$ by measuring the emission of {[Pd(dppH)(μ-Cl)]}$_2$ (**1**, Figure S29), which is surprisingly intense, giving rise to a considerably lower detection limit for traces of {[Pd(dppH)(μ-X)]}$_2$ species by emission spectroscopy, as compared to the other spectroscopic methods employed herein (*e.g.*, NMR). However, assuming the emission does not differ depending on the bridging anionic ligand X^-, it is unclear whether we are observing residual **1** or a newly formed species, such as {[Pd(dppH)(μ–OH)]}$_2$ (**4**), *i.e.*, whether any {[Pd(dppH)(μ-X)]}$_2$ is present still from preparation or again after initial hydrolysis. For **3a**, the problem is not encountered. An obvious difference between **3a** vs **3b** and **3c** complexes lies in the synthesis in three vs. two steps. However, there is no evident basis to assume that the identical workup steps for all three complexes (including extraction of the target compounds from the crude product with CH_2Cl_2 or toluene and subsequent filtration) should systematically lead to contamination with **1** (*e.g.*, due to residual solubility in these solvents) for $AsPh_3$ and $SbPh_3$ yet not for PPh_3. This rather points to the assignment of the observed bands to **4**. In that case, the absence of this band for the PPh_3 complex is due to its slightly higher stability in solutions, which was also indicated by our DFT calculations, as discussed above.

Femtosecond Transient Absorption Spectroscopy. To investigate the excited-state relaxation cascades, transient absorption (TA) experiments were performed in dry and oxygen-free THF solutions at room temperature. The complexes [Pd(dpp)($PnPh_3$)] (**3a–c**, Pn = P, As, Sb) were excited at 350 nm using excitation powers of 450 μW. Again, **3c** proved to be the most reactive compound, showing signs of photodegradation even at excitation powers as low as 200 μW. Figure 6 shows the transient spectra upon excitation into the LC/MLCT state of **3b**. To better illustrate the complexes' excited-state deactivation kinetics, the data recorded within the experimentally accessible delay-time window of 5 ns are depicted in different panels: (a) 0.3 to 5 ps, (b) 5 to 500 ps and (c) 500 to 5000 ps.

Following the initial excitation, a fast conversion process is visible. The associated spectral changes show an isosbestic point at 475 nm on a time scale of approximately 1 ps. The initial state still features a sharp excited-state absorption (ESA) band at 525 nm. This feature evolves into an ESA spanning the spectral range between 380 and 700 nm. This band then gradually decays over the course of several hundred ps, only to be slowly replaced by another ESA signature centered around 445 nm. The rise kinetics of the latter ESA band indicate a comparably slow formation of the corresponding species, which is not completed within the range of experimentally accessible delay times. While qualitatively similar features are observed for **3a** and **3c** (see Figure S34), notable differences concerning the kinetics are observed. This can be visualized by considering the intermediate decay of the ESA band at 525 nm, displayed in Figure 6d. This process is considerably slower for **3a** than for **3c**. Furthermore, the population of the long-lived ESA feature at 445 nm occurs in the order of decreasing atomic number, namely Sb < As < P, as depicted in Figure 6e.

Due to the absence of both red shifted absorption bands (typical for aggregate formation[50]) and broad emission features in the steady-state emission spectra (typical for excimer phosphorescence based on metal-metal-to-ligand charge transfer, *i.e.*, MMLCT, states[52]) we interpret our transient absorption data in the context of isolated Pd(II) complexes. The analysis of the data requires four kinetic components in a consecutive decay mechanism. An additional nondecaying component is added to account for the long-lived species. Table 4 displays the resulting fit constants. The obtained species associated spectra (SAS) are shown in Figure 6f. The components τ_2 and τ_3 show a strong dependence on the Pn in the ancillary ligand (see Figure S34), with significantly shorter values for **3b** and **3c**. Therefore, we associate these components with ISC, the rate of which depends on the SOC coupling elements. The heavier Pt(II)-containing homologues show much larger SOC matrix elements as compared to the Pd(II) complexes,[31] which translate into higher ISC rates. While the corresponding spectral changes take place within less than 1 ps for Pt(II), time constants on the order of 10 ps are indeed realistic for Pd(II) complexes as demonstrated for Pd(II)/Pt(II) O^N^C^N systems.[43] Regarding the nature of the states involved in the ISC process, larger $\langle S_2|H_{SO}|T_1\rangle^2$ than $\langle S_1|H_{SO}|T_1\rangle^2$ elements are found for all complexes (see Table 3). Nevertheless, ISC is presumably happening from the S_1 state due to fast internal conversion from higher S_n states to the S_1 state. Indeed, there is a clear trend in the magnitude of the calculated $\langle S_1|H_{SO}|T_1\rangle^2$ SOC elements in the order Sb > As > P, which correlates with the presumed ISC rates.

For the aforementioned Pd(II) O^N^C^N compounds, a long-lived (emissive) state of ^{3}LC character has also been observed on the order of several μs.[46] We postulate that a dark state of similar nature (^{3}LC or ^{3}LLCT) might also be responsible for the long-lived kinetics in our [Pd(dpp)-($PnPh_3$)] systems. We further note that this would again be a different LC state than the one responsible for the phosphorescent decay observed at 77 K.

https://doi.org/10.1021/acs.inorgchem.4c05436
Inorg. Chem. 2025, 64, 6561–6574

CONCLUSIONS

A series of only very recently accessible doubly cyclometalated Pd(II) complexes [Pd(dpp)($PnPh_3$)] (**3a−c**, dpp = 2,6-di(phenid-2-yl)pyridine; Pn = P, As, Sb), including the two new complexes [Pd(dpp)($AsPh_3$)] (**3b**) and [Pd(dpp)-($SbPh_3$)] (**3c**), was synthesized. For the unprecedented As and Sb derivatives, we found that adjustment of the synthesis route was necessary to obtain the target compounds due to divergent ligand displacement behavior of P vs As and Sb. The doubly cyclometalated complexes are particularly sensitive to hydrolysis, and in the case of **3c** even solvolysis in protic solvents.

The three complexes were subsequently characterized electrochemically, spectroscopically and theoretically. We found very small variations in the electrochemical profiles and UV−vis absorption spectra, as well as for the (TD-)DFT-calculated FMOs and spectra across the series **3a−c**. This suggests a marginal contribution from the $PnPh_3$ ancillary ligands to the relevant orbitals and states. However, we observed more significant differences between the complexes using time-resolved emission and ultrafast transient absorption (TA) spectroscopy, especially regarding their excited-state relaxation kinetics. The complexes show a very weak (Φ_L < 0.1) emission around 500 nm in frozen glassy matrix at 77 K, with **3b** providing the highest quantum yield and radiative rate constant. TA spectroscopy revealed a relatively complex picture with four processes: In fact, we observed a strong dependence of the fit components τ_2 and τ_3 on the Pn, which points toward processes involving ISC, as TD-DFT calculations predicted significantly increased SOC matrix elements for the heavier derivatives. Additionally, a long-lived state of presumably ^{3}LC or ^{3}LLCT character is observed for all complexes. The rate at which this state is populated differs, as it seems to correlate with the time constant of the preceding ISC process (*i.e.*, the long-lived state is populated faster for Pn = Sb).

Similarly to the previously studied Pt(II) complexes, the overall influence of the Pn variation is probably due to the interplay of numerous effects, which appears to be even more complex for the Pd(II) derivatives. Even though the predictive capacity is restricted, a clear improvement of the emission efficiency can be demonstrated upon replacement of Pn = P for Pn = As in [Pd(dpp)($PnPh_3$)]. Furthermore, as the present study represents a pioneering characterization of such doubly cyclometalated [Pd(C^N^C)(L)] complexes with tridentate luminophores as chelating ligands, we envision a significant potential for the improvement and tuning of this class of compounds by exchange of the ancillary ligand and tweaking of the C^N^C scaffold. For future studies, a solid basis is established for experimental and theoretical work.

EXPERIMENTAL SECTION

Syntheses. The [Pd(dpp)($PnPh_3$)] complexes **3a−c** were synthesized and subsequently handled in an argon atmosphere using *Schlenk* techniques. Solvents were degassed over three freeze-pump-thaw cycles and dried over activated molecular sieves. 2,6-diphenylpyridine (H_2dpp) was prepared under typical *Suzuki* conditions.[29]

*{[Pd(dppH)(μ-Cl)]}$_2$ (**1**).* 354.3 mg (1.53 mmol, 1.0 equiv) H_2dpp were dissolved in 40 mL MeCN. To this solution, a solution of 500 mg (1.53 mmol, 1.0 equiv) $K_2[PdCl_4]$ in 40 mL H_2O was added. The solution was heated to 90 °C for 24 h, during which a bright yellow precipitate was formed. After cooling to room temperature, the yellow solid was filtered off, washed sequentially with H_2O and MeCN, and dried. Yield: 396.9 mg (0.53 mmol, 70%). ^{1}H NMR (600 MHz, DMF-d_7): δ (ppm) = 8.17 (t, J = 7.7 Hz, 1H, H9), 8.12 (dd, J = 8.1, 1.3 Hz, 1H, H8), 8.02−7.99 (m, 2H, H14), 7.85 (dd, J = 7.9, 1.2 Hz, 1H, H2), 7.71 (dd, J = 7.7, 1.6 Hz, 1H, H5), 7.59 (dd, J = 7.6, 1.4 Hz, 1H, H10), 7.57−7.49 (m, 3H, H13, H15), 7.12 (td, J = 7.4, 1.2 Hz, 1H, H3), 6.99 (ddd, J = 8.0, 7.2, 1.5 Hz, 1H, H4). ^{13}C NMR (151 MHz, DMF-d_7): δ (ppm) = 165.8, 161.6, 149.9, 147.3, 140.6, 140.6, 138.3, 130.0, 129.6, 129.2, 128.7, 125.3, 125.3, 124.8, 118.4. Elemental analysis ($C_{34}H_{24}N_2Cl_2Pd_2$, 744.32 g/mol) found (calculated): C, 54.91 (54.87); H, 3.21 (3.25); N, 3.74 (3.76).

*[Pd(dppH)(PPh_3)Cl] (**2a**).* 74.4 mg (0.1 mmol, 1.0 equiv) **1** and 59 mg (0.225 mmol, 2.25 equiv) PPh_3 were dissolved in 12 mL CH_2Cl_2. The solution was heated to reflux for 1 h. After cooling to room temperature, the solution was filtered through a syringe filter and the filtrate was evaporated to dryness. The residue was washed with Et_2O, affording a yellow powder. NMR data agrees with reported values.[32] Yield: 120.1 mg (0.189 mmol, 95%). ^{1}H NMR (300 MHz, CD_2Cl_2, see Figure S15 for numbering scheme): δ (ppm) = 8.10−8.04 (m, 2H, H13), 7.95 (t, J = 7.9 Hz, 1H, H9), 7.82 (d, J = 8.0 Hz, 1H, H8), 7.75 (dd, J = 11.5, 7.8 Hz, 6H, H17), 7.60 (d, J = 7.8 Hz, 1H, H5), 7.52 (d, J = 7.7 Hz, 1H, H10), 7.47−7.39 (m, 6H, H14, H15 and H19), 7.39−7.32 (m, 6H, H18), 6.97 (t, J = 7.4 Hz, 1H, H4), 6.53 (p, J = 7.7 Hz, 2H, H2 and H3).

*[Pd(dpp)(PPh_3)] (**3a**).* 63.4 mg (0.1 mmol, 1.0 equiv) **2a** were suspended in 5.5 mL THF. 0.092 mL (0.11 mmol, 1.1 equiv) of a KO*t*Bu stock solution (1.2 M in THF) were added, turning the previously yellow suspension into an orange solution. After 1 h, the solvent was removed. The residue was dissolved in 6 mL CH_2Cl_2 and filtered through a syringe filter. The filtrate was evaporated to dryness. The residue was washed with *n*-pentane thrice and dried, affording a pale-yellow powder. NMR results agree with the reported values.[32] Yield: 45.2 mg (0.076 mmol, 76%). ^{1}H NMR (500 MHz, CD_2Cl_2, see Figure S15 for numbering scheme): δ (ppm) = 7.83 (m, 6H, H11), 7.74 (t, J = 8.0 Hz, 1H, H9), 7.51−7.43 (m, 5H, H5 and H13), 7.43−7.35 (m, 8H, H8 and H12), 6.89 (td, J = 7.5, 1.3 Hz, 2H, H4), 6.57 (td, J = 7.4, 1.4 Hz, 2H, H3), 6.16 (dd, J = 7.5, 1.3 Hz, 2H, H2). ^{31}P NMR (121 MHz, CD_2Cl_2): δ (ppm) = 45.1. Elemental analysis ($C_{35}H_{26}NPPd$, 597.99 g/mol) found (calculated): C, 69.99 (70.30); H, 4.31 (4.38); N, 2.31 (2.34).

*[Pd(dpp)($AsPh_3$)] (**3b**).* 74.4 mg (0.1 mmol, 1.0 equiv) **1** and 67.9 mg (0.22 mmol, 2.2 equiv) $AsPh_3$ were suspended in 10 mL THF. 0.183 mL (0.22 mmol, 2.2 equiv) of a KO*t*Bu stock solution (1.2 M in THF) were added. After stirring for 3 d, the previously yellow suspension had turned into an orange solution. The solvent was removed and the residue was dissolved in 6 mL CH_2Cl_2. The solution was filtered through a syringe filter and the filtrate was evaporated to dryness. The residue was washed with *n*-pentane thrice and dried, affording a bright yellow powder. Yield: 113.2 mg (0.18 mmol, 88%). ^{1}H NMR (500 MHz, CD_2Cl_2, see Figure S15 for numbering scheme): δ (ppm) = 7.78−7.69 (m, 7H, H9 and H11), 7.47 (td, J = 7.4, 1.4 Hz, 5H, H8 and H13), 7.40 (m, 8H, H12 and H5), 6.90 (td, J = 7.5, 1.3 Hz, 2H, H4), 6.57 (td, J = 7.3, 1.4 Hz, 2H, H3), 6.41 (dd, J = 7.4, 1.3 Hz, 2H, H2). ^{13}C NMR (126 MHz, CD_2Cl_2): δ (ppm) = 168.7, 165.8, 151.4, 139.5, 139.5, 134.6, 130.1, 128.7, 128.6, 124.0, 123.3, 115.2. Elemental analysis ($C_{35}H_{26}NAsPd$, 641.94 g/mol) found (calculated): C, 65.50 (65.49); H, 4.04 (4.08); N, 2.12 (2.18). (+)-HR-ESI-MS: m/z = 641.04122 ([M + H]$^+$, calc. 641.04048).

*[Pd(dpp)($SbPh_3$)] (**3c**).* 104.2 mg (0.14 mmol, 1.0 equiv) **1** and 105.9 mg (0.3 mmol, 2.1 equiv) $SbPh_3$ were suspended in 10 mL THF. 0.33 mL (0.30 mmol, 2.2 equiv) of a KO*t*Bu stock solution (0.9 M in THF) were added. After stirring for 1.5 h, the solvent was removed and the residue was extracted with CH_2Cl_2. The extract was filtered through a syringe filter and filtrate was evaporated to dryness. The residue was dissolved in toluene and *n*-pentane was added while stirring to precipitate a yellow powder. The solution was decanted and the yellow powder was washed with *n*-pentane four times. Yield: 141.4 mg (0.21 mmol, 73%). ^{1}H NMR (500 MHz, CD_2Cl_2, see Figure S15 for numbering scheme): δ (ppm) = 7.78−7.71 (m, 7H, H9 and H11), 7.54−7.44 (m, 5H, H8 and H13), 7.42 (m, 8H, H12 and H5), 6.94 (td, J = 7.5, 1.3 Hz, 2H, H4), 6.90 (dd, J = 7.3, 1.6 Hz, 2H, H2), 6.63

https://doi.org/10.1021/acs.inorgchem.4c05436
Inorg. Chem. 2025, 64, 6561−6574

(tt, J = 7.3, 1.2 Hz, 2H, H3). ^{13}C NMR (126 MHz, CD_2Cl_2): δ (ppm) = 168.5, 166.3, 152.2, 142.2, 140.2, 137.2, 132.1, 130.7, 129.7, 124.6, 124.3, 116.0. Elemental analysis ($C_{35}H_{26}NSbPd$, 688.78 g/mol) found (calculated): C, 60.91 (61.03); H, 3.77 (3.80); N, 1.95 (2.03). (+)-HR-ESI-MS: m/z = 687.02337 ($[M + H]^+$, calc. 687.02270).

Reaction of 1 with KO*t*Bu in the Absence of $PnPh_3$. 48.7 mg (0.065 mmol, 1.0 equiv) **1** were suspended in 4 mL THF. 0.16 mL (0.144 mmol, 2.2 equiv) of a KO*t*Bu stock solution (0.9 M in THF) were added. After stirring for 30 min, an aliquot of the reaction mixture was analyzed via ^{1}H NMR, using a sealed glass ampule containing DMSO-d_6 as an internal standard and for shimming. ^{1}H NMR (300 MHz, THF/DMSO-d_6): δ (ppm) = 7.62 (d, J = 7.1 Hz, 2H), 7.42 (t, J = 7.9 Hz, 1H), 7.26 (d, J = 7.9 Hz, 2H), 7.14 (d, J = 7.9 Hz, 2H), 6.89 (t, J = 7.3 Hz, 2H), 6.74 (t, J = 7.3 Hz, 2H).

Instrumentation and Software. NMR spectra were recorded on a Bruker Avance II 300 (^{1}H: 300, ^{13}C: 75, ^{19}F: 282 MHz), Bruker Avance 400 (^{1}H: 400.13, ^{13}C: 100.61, ^{19}F: 376.50 MHz), Bruker Avance III 499 (^{1}H: 500, ^{13}C: 125, ^{19}F: 470 MHz), Bruker Avance III 500 (^{1}H: 500, ^{13}C: 125, ^{19}F: 470 MHz) or Bruker Avance II+ 600 (^{1}H: 600 MHz) spectrometer. ^{1}H chemical shifts were referenced to $SiMe_4$ (0 ppm) unless otherwise specified.

scXRD measurements were performed on a Bruker D8 Venture diffractometer including a Bruker Photon 100 CMOS detector using Mo Kα (λ = 0.71073 Å) radiation. The crystal data was collected using APEX4 v2021.10−0.[53] The structures were solved by dual space methods using SHELXT, and the refinement was carried out with SHELXL employing the full-matrix least-squares methods on $F_O^2 < 2\sigma(F_O^2)$ as implemented in ShelXle.[54−56] The non-hydrogen atoms were refined with anisotropic displacement parameters without any constraints. The hydrogen atoms were included by using appropriate riding models.

UV−vis-NIR absorption spectra were recorded on an Agilent Cary60 spectrophotometer. Cyclic voltammetry was carried out at 100 mV/s scan rate in 0.1 M n-Bu_4NPF_6 solutions using a three-electrode configuration (glassy carbon working electrode, Pt counter electrode, Ag/AgCl reference) and a Metrohm Autolab PG STAT 30 potentiostat with ferrocene/ferrocenium as internal reference.

Photoluminescence quantum yields were measured with a Hamamatsu Photonics absolute PL quantum yield measurement system (C9920−02) equipped with a L9799−01 CW Xe light source (150 W), a monochromator, a C7473 photonic multichannel analyzer, an integrating sphere and employing U6039−05 software (Hamamatsu Photonics, Ltd., Shizuoka, Japan). Steady-state excitation and emission spectra were recorded on a FluoTime 300 spectrometer from PicoQuant equipped with a 300 W ozone-free Xe lamp (200−1100 nm), a 10 W Xe flash-lamp (200−1100 nm, pulse width ca. 1 μs) with repetition rates of 1 − 300 Hz, a double-grating excitation monochromator (Czerny-Turner type, grating with 1200 lines/mm, blaze wavelength: 300 nm), diode lasers (pulse width <20 ps) operated by a computer-controlled laser driver PDL-820 "Sepia II" (repetition rate up to 80 MHz, burst mode for slow and weak decays), two emission monochromators (Czerny-Turner, selectable between double-grating blazed at 500 nm with 2.7 nm/mm dispersion and 1200 lines/mm, or single-grating blazed at 1250 nm with 5.4 nm/mm dispersion and 600 lines/mm) with adjustable slit width between 25 μm and 7 mm, Glan-Thompson polarizers for excitation (after the Xe-lamps) and emission (after the sample). Different sample holders (Peltier-cooled mounting unit ranging from −15 to 110 °C or an adjustable front-face sample holder), along with two detectors (namely a PMA Hybrid-07 from PicoQuant with transit time spread fwhm <50 ps, 220 − 850 nm, or a H10330C-45-C3 NIR detector with transit time spread fwhm 0.4 ns, 950−1400 nm from Hamamatsu) were used. Steady-state spectra and photoluminescence lifetimes were recorded in TCSPC mode by a PicoHarp 300 (minimum base resolution 4 ps) or in MCS mode by a TimeHarp 260 (where up to several ms can be traced). Emission and excitation spectra were corrected for source intensity (lamp and grating) by standard correction curves. For samples with lifetimes in the ns order, an instrument response function calibration (IRF) was performed using a diluted Ludox dispersion. Lifetime analysis was performed using the commercial EasyTau 2 software (PicoQuant). The quality of the fit was assessed by minimizing the reduced chi squared function (χ2) and visual inspection of the weighted residuals and their autocorrelation. All solvents used were of spectrometric grade (Uvasol, Merck).

Average radiative (k_r) and nonradiative (k_{nr}) rate constants were calculated following eqs 1 and 2. Absolute uncertainties were estimated by eqs 3 and 4.

$$k_R = \frac{\Phi_L}{\tau_{av}} \tag{1}$$

$$\Delta k_R = \left(\frac{\Delta\Phi_L}{\tau_{av}}\right) + \left(\frac{\Delta\tau_{av}}{\tau_{av}^2}\cdot\Phi_L\right) \tag{2}$$

$$k_{NR} = \frac{1-\Phi_L}{\tau_{av}} \tag{3}$$

$$\Delta k_{NR} = \left(\frac{\Delta\Phi_L}{\tau_{av}}\right) + \left(\frac{(1+\Phi_L)\Delta\tau_{av}}{\tau_{av}^2}\right) \tag{4}$$

Computational Details. All DFT calculations were performed using ORCA 5.0.2.[57,58] For all atoms, def2-TZVP basis sets, as well as the corresponding def2-ECPs for Pd and Sb, were used unless stated otherwise.[59] The S_0 and T_1 geometries of all compounds were optimized at the BP86 level of theory, using Grimme's D3 dispersion correction and the conductor-like polarizable continuum model (CPCM) parametrized for THF as an approximate solvation model.[60−65] The geometry optimizations were followed up with numerical frequency calculations in order to confirm the energetic minimum nature of the optimized structure as indicated by the absence of imaginary modes. On the optimized geometries, single point and TD-DFT calculations were performed using the TPSSh functional, Grimme's D3 dispersion correction and CPCM parametrized for THF.[66] Orbital isosurfaces were extracted from the S_0 single point calculations using the ORCA module orca_plot and plotted with the visualization software CHEMCRAFT at a contour value of 0.04.[67,68] For the TD-DFT calculations of absorption spectra, 30 roots (transitions) for singlets and triplets each were included for every complex. Broadened spectra were obtained using the orca_mapspc module with 2000 cm^{-1} full width at half-maximum band broadening. The TD-DFT calculation output was further evaluated using the software package TheoDORE to analyze relative MLCT, L′MCT, LC, LL′CT, and MC contributions to the emissive T_1 states, using the implemented standard algorithm for molecular partitioning of transition metal complexes employing Openbabel.[49] At the T_1 geometries, spin−orbit (SO) calculations were performed using the Zeroth-Order Regular Approximation (ZORA), the TPSSh functional, SARC-ZORA-TZVP basis sets for Pd and Sb, and the CPCM parametrized for THF.[69,70] Spin-restricted relaxed surface scans along the M−Pn bonds in $[M(dpp)(PnPh_3)]$ (M = Pd, Pt; Pn = P, As, Sb) were performed using the TPSSh functional, Grimme's D3 dispersion correction, CPCM parametrized for THF, and def2-TZVP basis sets for all atoms as well as the corresponding def2-ECPs for Pd, Sb and Pt. To confirm that the ground state remains a singlet at d(Pd−Pn) = 4.0 Å, we optimized the structures at this point as triplet states and afterward compared the energies between singlet and triplet states. In all cases, we found that the singlet state is lower in energy than the triplet state by around 1.1 eV and thus represents the ground state.

■ ASSOCIATED CONTENT

Data Availability Statement

All relevant data are available from the corresponding authors upon request.

Supporting Information

The Supporting Information is available free of charge at https://pubs.acs.org/doi/10.1021/acs.inorgchem.4c05436.

https://doi.org/10.1021/acs.inorgchem.4c05436
Inorg. Chem. 2025, 64, 6561−6574

Detailed structural data and figures, NMR spectra, cyclic voltammograms, UV−vis absorption, emission and TA spectra, computational data for all new complexes (PDF)

Accession Codes

Deposition Numbers 2201141, 2309500, 2331260, 2364152, and 2381835 contain the supplementary crystallographic data for this paper. Crystallographic data has been deposited at the Cambridge Crystallographic Data Centre for [Pd(dpp)-($AsPh_3$)].EtOAc (CCDC 2331260), {[Pd(dppH)(μ-Cl)]}$_2$ (2381835), {[Pd(dppH)(μ−OH)]}$_2$ (2309500), {[Pd-(dppH)(μ-κ_2-$NCCH_2$)]}$_2$ (2364152), and [(PPh_3)Pd(dpp)-Pd(PPh_3)$_2$Br] (2201141) These data can be obtained free of charge via the joint Cambridge Crystallographic Data Centre (CCDC) and Fachinformationszentrum Karlsruhe Access Structures service.

AUTHOR INFORMATION

Corresponding Authors

Rose Jordan − *Faculty for Mathematics and Natural Sciences, Department of Chemistry and Biochemistry, Institute for Inorganic and Materials Chemistry, University of Cologne, D-50939 Köln, Germany*; Email: rose.jordan@uni-koeln.de

Benjamin Dietzek-Ivanšić − *Institute for Physical Chemistry (IPC), Friedrich Schiller University Jena, 07743 Jena, Germany; Research Department Functional Interfaces, Leibniz Institute for Photonic Technologies Jena (IPHT), 07745 Jena, Germany*; Email: benjamin.dietzek@leibniz-ipht.de

Cristian A. Strassert − *Institut für Anorganische und Analytische Chemie, CiMIC, SoN, CeNTech, Universität Münster, D-48149 Münster, Germany*; orcid.org/0000-0002-1964-0169; Email: cstra_01@uni-muenster.de

Axel Klein − *Faculty for Mathematics and Natural Sciences, Department of Chemistry and Biochemistry, Institute for Inorganic and Materials Chemistry, University of Cologne, D-50939 Köln, Germany*; Email: axel.klein@uni-koeln.de

Authors

Sam Kler − *Faculty for Mathematics and Natural Sciences, Department of Chemistry and Biochemistry, Institute for Inorganic and Materials Chemistry, University of Cologne, D-50939 Köln, Germany*

Iván Maisuls − *Institut für Anorganische und Analytische Chemie, CiMIC, SoN, CeNTech, Universität Münster, D-48149 Münster, Germany*

Niklas Klosterhalfen − *Institute for Physical Chemistry (IPC), Friedrich Schiller University Jena, 07743 Jena, Germany; Research Department Functional Interfaces, Leibniz Institute for Photonic Technologies Jena (IPHT), 07745 Jena, Germany*

Complete contact information is available at: https://pubs.acs.org/10.1021/acs.inorgchem.4c05436

Author Contributions

R.J. and S.K. carried out syntheses, cyclic voltammetry and UV−vis absorption spectroscopy. R.J. provided the computational work. I.M. carried out the emission spectroscopy. N.K. carried out the transient absorption spectroscopy measurements. A.K., B.D.-I., and C.A.S. supervised the project. R.J. and A.K. wrote the original draft, R.J., A.K., I.M., N.K., B.D.-I. and C.A.S. revised the manuscript. All authors agreed with the final version.

Notes

The authors declare no competing financial interest.

ACKNOWLEDGMENTS

We thank the Deutsche Forschungsgemeinschaft [DFG Priority Programme 2102 "Light-controlled Reactivity of Metal Complexes" STR 1186/6-1 and 6-2 (C.A.S.), KL1194/16-1 and 16-2 (A.K.), and DI1517/19-1 (B.D.-I.)] and the Studienstiftung des Deutschen Volkes e.V. (R.J.) for funding of this project. This work was also supported by the DFG/Land NRW (INST 211/915-1 FUGG: "Integrated confocal luminescence spectrometer with spatiotemporal resolution and multiphoton excitation", C.A.S.). We would also like to thank the Regional Computing Center of the University of Cologne (RRZK) for providing computing time on the DFG-funded High Performance Computing (HPC) system CHEOPS, as well as Prof. Dr. Michael Hanrath from the Theoretical Chemistry group of the University of Cologne for providing computing time on the group's cluster.

REFERENCES

(1) Johansson Seechurn, C. C. C.; Kitching, M. O.; Colacot, T. J.; Snieckus, V. Palladium-Catalyzed Cross-Coupling: A Historical Contextual Perspective to the 2010 Nobel Prize. *Angew. Chem., Int. Ed.* **2012**, *51*, 5062−5085.

(2) Lin, J.; Zou, C.; Zhang, X.; Gao, Q.; Suo, S.; Zhuo, Q.; Chang, X.; Xie, M.; Lu, W. Highly phosphorescent organopalladium(II) complexes with metal−metal-to-ligand charge-transfer excited states in fluid solutions. *Dalton Trans.* **2019**, *48*, 10417−10421.

(3) Ghedini, M.; Aiello, I.; La Deda, M.; Grisolia, A. Mixed 2-phenylpyridine and 5-substitued-8-hydroxyquinolines palladium(II) complexes: new emitters in solutions at room temperature. *Chem. Commun.* **2003**, 2198−2199.

(4) Ghedini, M.; Pugliese, T.; La Deda, M.; Godbert, N.; Aiello, I.; Amati, M.; Belviso, S.; Lelj, F.; Accorsi, G.; Barigelletti, F. Spectroscopy and electrochemical properties of a homologous series of acetylacetonato and hexafluoroacetylacetonato cyclopalladated and cycloplatinated complexes. *Dalton Trans.* **2008**, 4303−4318.

(5) Kuwabara, J.; Ogawa, Y.; Taketoshi, A.; Kanbara, T. Enhancement of the photoluminescence of a thioamide-based pincer palladium complex in the crystalline state. *J. Organomet. Chem.* **2011**, *696*, 1289−1293.

(6) Fleetham, T.; Li, G.; Li, J. Phosphorescent Pt(II) and Pd(II) Complexes for Efficient, High-Color-Quality, and Stable OLEDs. *Adv. Mater.* **2017**, *29*, 1601861.

(7) Emami, M.; Shahroosvand, H.; Bikas, R.; Lis, T.; Daneluik, C.; Pilkington, M. Synthesis, Study, and Application of Pd(II) Hydrazone Complexes as the Emissive Components of Single-Layer Light-Emitting Electrochemical Cells. *Inorg. Chem.* **2021**, *60*, 982−994.

(8) Kletsch, L.; Jordan, R.; Köcher, A. S.; Buss, S.; Strassert, C. A.; Klein, A. Photoluminescence of Ni(II), Pd(II), and Pt(II) Complexes [M(Me_2dpb)Cl] Obtained from C−H Activation of 1,5-Di(2-pyridyl)-2,4-dimethylbenzene (Me_2dpbH). *Molecules* **2021**, *26*, 5051.

(9) Von der Stück, R.; Krause, M.; Brünink, D.; Buss, S.; Doltsinis, N. L.; Strassert, C. A.; Klein, A. Luminescent Pd(II) Complexes with Tridentate $^-$C^N^N Aryl-pyridine-(benzo)thiazole Ligands. *Z. Anorg. Allg. Chem.* **2022**, *648*, e202100278.

(10) Krause, M.; von der Stück, R.; Brünink, D.; Buss, S.; Doltsinis, N. L.; Strassert, C. A.; Klein, A. Platinum and palladium complexes of tridentate $^-$C^N^N (phen-ide)-pyridine-thiazol ligands − A case study involving spectroelectrochemistry, photoluminescence spectroscopy and TD-DFT calculations. *Inorg. Chim. Acta* **2021**, *518*, 120093.

(11) Theiss, T.; Buss, S.; Maisuls, I.; López-Arteaga, R.; Brünink, D.; Kösters, J.; Hepp, A.; Doltsinis, N. L.; Weiss, E. A.; Strassert, C. A.

Room-Temperature Phosphorescence from Pd(II) and Pt(II) Complexes as Supramolecular Luminophores: The Role of Self-Assembly, Metal−Metal Interactions, Spin−Orbit Coupling, and Ligand-Field Splitting. *J. Am. Chem. Soc.* **2023**, *145*, 3937−3951.
(12) Maisuls, I.; Wang, C.; Gutierrez Suburu, M. E.; Wilde, S.; Daniliuc, C.-G.; Brünink, D.; Doltsinis, N. L.; Ostendorp, S.; Wilde, G.; Kösters, J.; Resch-Genger, U.; Strassert, C. A. Ligand-controlled and nanoconfinement-boosted luminescence employing Pt(II) and Pd(II) complexes: from color-tunable aggregation-enhanced dual emitters towards self-referenced oxygen reporters. *Chem. Sci.* **2021**, *12*, 3270−3281.
(13) Eskelinen, T.; Buss, S.; Petrovskii, S. K.; Grachove, E. V.; Krause, M.; Kletsch, L.; Klein, A.; Strassert, C. A.; Koshevoy, I. O.; Hirva, P. Photophysics and Excited State Dynamics of Cyclometalated [M(Phbpy)(CN)] (M = Ni, Pd, Pt) Complexes: A Theoretical and Experimental Study. *Inorg. Chem.* **2021**, *60*, 8777−8789.
(14) Zhao, Q.; Li, F.; Huang, C. Phosphorescent chemosensors based on heavy-metal complexes. *Chem. Soc. Rev.* **2010**, *39*, 3007−3030.
(15) Law, A. S.-Y.; Lee, L. C.-C.; Lo, K. K.-W.; Yam, V. W.-W. Aggregation and Supramolecular Self-Assembly of Low-Energy Red Luminescent Alkynylplatinum(II) Complexes for RNA Detection, Nucleolus Imaging, and RNA Synthesis Inhibitor Screening. *J. Am. Chem. Soc.* **2021**, *143*, 5396−5405.
(16) Li, K.; Tong, G. S. M.; Wang, Q.; Cheng, G.; Tong, W.-Y.; Ang, W.-H.; Kwong, W.-L.; Che, C.-M. Highly phosphorescent platinum(II) emitters: photophysics, materials and biological applications. *Chem. Sci.* **2016**, *7*, 1653−1673.
(17) Yersin, H.; Rausch, A. F.; Czerwieniec, R.; Hofbeck, T.; Fischer, T. The triplet state of organo-transition metal compounds. Triplet harvesting and singlet harvesting for efficient OLEDs. *Coord. Chem. Rev.* **2011**, *255*, 2622−2652.
(18) Bizzarri, C.; Spuling, E.; Knoll, D. M.; Volz, D.; Bräse, S. Sustainable metal complexes for organic light-emitting diodes (OLEDs). *Coord. Chem. Rev.* **2018**, *373*, 49−82.
(19) Chernyshev, V. M.; Ananikov, V. P. Nickel and Palladium Catalysis: Stronger Demand than Ever. *ACS Catal.* **2022**, *12*, 1180−1200.
(20) Vogler, A. Nickel(II) complexes as triplet emitters? IL phosphorescence of Ni(II)(binap)Cl_2 under ambient conditions. *Inorg. Chem. Commun.* **2016**, *65*, 39−40.
(21) Wong, Y.-S.; Tang, M.-C.; Ng, M.; Yam, V. W.-W. Toward the design of phosphorescent emitters of cyclometalated earth-abundant nickel(II) and their supramolecular study. *J. Am. Chem. Soc.* **2020**, *142*, 7638−7646.
(22) Ogawa, T.; Wenger, O. S. Nickel(II) Analogues of Phosphorescent Platinum(II) Complexes with Picosecond Excited-State Decay. *Angew. Chem., Int. Ed.* **2023**, *62*, e202312851.
(23) Ogawa, T.; Sinha, N.; Pfund, B.; Prescimone, A.; Wenger, O. S. Molecular Design Principles to Elongate the Metal-to-Ligand Charge Transfer Excited-State Lifetimes of Square-Planar Nickel(II) Complexes. *J. Am. Chem. Soc.* **2022**, *144*, 21948−21960.
(24) Niazi, M.; Maisuls, I.; Strassert, C. A.; Klein, A. Molecular Rigidification of Cyclometalated N^C^N Pt(II)- and Pd(II)-Based Triplet Emitters. *Organometallics* **2024**, *43*, 1547−1556.
(25) Lu, W.; Chan, M. C. W.; Cheung, K.-K.; Che, C.-M. $\pi-\pi$ Interactions in Organometallic Systems. Crystal Structures and Spectroscopic Properties of Luminescent Mono-, Bi-, and Trinuclear Trans-cyclometalated Platinum(II) Complexes Derived from 2,6-Diphenylpyridine. *Organometallics* **2001**, *20*, 2477−2486.
(26) Kui, S. C. F.; Hung, F.-F.; Lai, S.-L.; Yuen, M.-Y.; Kwok, C.-C.; Low, K.-H.; Chui, S. S.-Y.; Che, C.-M. Luminescent organoplatinum(II) complexes with functionalized cyclometalated C^N^C ligands: structures, photophysical properties, and material applications. *Chem.−Eur. J.* **2012**, *18*, 96−109.
(27) Yam, V. W.-W.; Tang, R. P.-L.; Wong, K. M.-C.; Lu, X.-X.; Cheung, K.-K.; N Syntheses, Zhu. Electronic Absorption, Emission, and Ion-Binding Studies of Platinum(II) C^N^C and Terpyridyl Complexes Containing Crown Ether Pendants. *Chem.−Eur. J.* **2002**, *8*, 4066−4076.
(28) Kergreis, A.; Lord, R. M.; Pike, S. J. Influence of ligand and nuclearity on the cytotoxicity of cyclometallated C^N^C platinum(II) complexes. *Chem.−Eur. J.* **2020**, *26*, 14938−14946.
(29) Garbe, S.; Krause, S.; Klimpel, M.; Neundorf, A.; Lippmann, I.; Ott, P.; Brünink, I.; Strassert, D.; Doltsinis, C. A.; Klein, N. L. A. Cyclometalated Pt Complexes of CNC Pincer Ligands: Luminescence and Cytotoxic Evaluation. *Organometallics* **2020**, *39*, 746−756.
(30) Friedel, J. N.; Krause, M.; Jordan, R.; Maisuls, I.; Bruenink, D.; Schwab, D.; Doltsinis, N. L.; Strassert, C. A.; Klein, A. Triplet Emitting C^N^C Cyclometalated Dibenzo[c,h]Acridine Pt(II) Complexes. *Molecules* **2022**, *27*, 8054.
(31) Jordan, R.; Maisuls, I.; Nair, S. S.; Dietzek-Ivanšić, B.; Strassert, C. A.; Klein, A. Enhanced luminescence properties through heavy ancillary ligands in [Pt(C^N^C)(L)] complexes, L = $AsPh_3$ and $SbPh_3$. *Dalton Trans.* **2023**, *52*, 18220−18232.
(32) Campillo, D.; Escudero, D.; Baya, M.; Martín, A. Heteropolymetallic Architectures as Snapshots of Transmetallation Processes at Different Degrees of Transfer. *Chem.−Eur. J.* **2022**, *28*, e202104538.
(33) Cave, G. W. V.; Fanizzi, F. P.; Deeth, R. J.; Errington, W.; Rourke, J. P. C−H Activation Induced by Water. Monocyclometalated to Dicyclometalated: C^N^C Tridentate Platinum Complexes. *Organometallics* **2000**, *19*, 1355−1364.
(34) Feuerstein, W.; Breher, F. Synthetic access to a phosphorescent non-palindromic pincer complex of palladium by a double oxidative addition − comproportionation sequence. *Chem. Commun.* **2020**, *56*, 12589.
(35) Cornioley-Deuschel, C.; Ward, T.; von Zelewsky, A. Complexes with a Pincers. 2,6-Diphenylpyridine as Twofold-Deprotonated (C^N^C) Terdentate Ligand in C,C-*trans*-, and as Mono-deprotonated (C^N) Chelate Ligand in Chiral C,C-*cis*-Complexes of Platinum(II) and Palladium(II). *Helv. Chim. Acta* **1988**, *71*, 130−133.
(36) Maestri, M.; Cornioley-Deuschel, C.; von Zelewsky, A. Spectroscopic properties of Pt(II) and Pd(II) complexes with aromatic terdendate (C″>N^C) cyclometallating ligands. *Coord. Chem. Rev.* **1991**, *111*, 117−123.
(37) Gangadharappa, S. C.; Maisuls, I.; Schwab, D. A.; Kösters, J.; Doltsinis, N. L.; Strassert, C. A. Compensation of Hybridization Defects in Phosphorescent Complexes with Pnictogen-Based Ligands—A Structural, Photophysical, and Theoretical Case-Study with Predictive Character. *J. Am. Chem. Soc.* **2020**, *142*, 21353−21367.
(38) Heckel, A.; Bendt, G.; John, L.; Wölper, C.; Schulz, S. Synthesis and solid-state structures of *t*-Bu_3Ga−EPh_3 Lewis acid−base adducts. *Appl. Organomet. Chem.* **2018**, *32*, e4430.
(39) Del Pozo, J.; Gioria, E.; Espinet, P. Olefin Insertion Versus Cross-Coupling in trans-[Pd(Ar)X($AsPh_3$)$_2$] Complexes (X = I, F, CF_3) Treated with a Phosphine-EWOlefin Ligand to Induce Ar−X Coupling. *Organometallics* **2017**, *36*, 2884−2890.
(40) Loza, M. L.; Crabtree, R. H. Synthesis and reactivity of $ReH_7(AsPh_3)_2$. *Inorg. Chim. Acta* **1995**, *236*, 63−66.
(41) Roudesly, F.; Oble, J.; Poli, G. Metal-catalyzed C−H activation/functionalization: The fundamentals. *J. Mol. Catal. A Chem.* **2017**, *426*, 275−296.
(42) Neitzel, A.; Figueroba, A.; Lykhach, Y.; Skála, T.; Vorokhta, M.; Tsud, N.; Mehl, S.; Ševčíková, K.; Prince, K. C.; Neyman, K. M.; Matolin, V.; Libuda, J. Atomically Dispersed Pd, Ni, and Pt Species in Ceria-Based Catalysts: Principal Differences in Stability and Reactivity. *J. Phys. Chem. C* **2016**, *120*, 9852−9862.
(43) Ray, K.; Petrenko, T.; Wieghardt, K.; Neese, F. Joint spectroscopic and theoretical investigations of transition metal complexes involving non-innocent ligands. *Dalton Trans.* **2007**, *2007*, 1552−1566.
(44) Ray, K.; Weyhermüller, T.; Neese, F.; Wieghardt, K. Electronic Structure of Square Planar Bis(benzene-1,2-dithiolato)metal Complexes $[M(L)_2]^z$ (z = 2−, 1−, 0; M = Ni, Pd, Pt, Cu, Au): An

https://doi.org/10.1021/acs.inorgchem.4c05436
Inorg. Chem. 2025, 64, 6561−6574

Experimental, Density Functional, and Correlated ab Initio Study. *Inorg. Chem.* **2005**, *44*, 5345−5360.
(45) Mews, N. M.; Reimann, M.; Hörner, G.; Kaupp, M.; Schubert, H.; Berkefeld, A. A four-parameter system for rationalising the electronic properties of transition metal−radical ligand complexes. *Dalton Trans.* **2020**, *49*, 9735−9742.
(46) Haseloer, A.; Denkler, L. M.; Jordan, R.; Reimer, M.; Olthof, S.; Schmidt, I.; Meerholz, K.; Hörner, G.; Klein, A. Ni, Pd, and Pt complexes of a tetradentate dianionic thiosemicarbazone-based O^N^N^S ligand. *Dalton Trans.* **2021**, *50*, 4311−4322.
(47) Dalmau, D.; Urriolabeitia, E. P. Luminescence and Palladium: The Odd Couple. *Molecules* **2023**, *28*, 2663.
(48) Chow, P. K.; Ma, C.; To, W.-P.; Tong, G. S. M.; Lai, S.-L.; Kui, S. C. F.; Kwok, W.-M.; Che, C.-M. Strongly Phosphorescent Palladium(II) Complexes of Tetradentate Ligands with Mixed Oxygen, Carbon, and Nitrogen Donor Atoms: Photophysics, Photochemistry, and Applications. *Angew. Chem., Int. Ed.* **2013**, *52*, 11775−11779.
(49) Plasser, F. TheoDORE: A toolbox for a detailed and automated analysis of electronic excited state computations. *J. Chem. Phys.* **2020**, *152*, 084108.
(50) To, W.-P.; Wan, Q.; Tong, G. S. M.; Che, C.-M. Recent Advances in Metal Triplet Emitters with d^6, d^8, and d^{10} Electronic Configurations. *Trends. Chem.* **2020**, *2*, 796−812.
(51) Wan, Q.; To, W.-P.; Yang, C.; Che, C.-M. The Metal−Metal-to-Ligand Charge Transfer Excited State and Supramolecular Polymerization of Luminescent Pincer Pd^{II}−Isocyanide Complexes. *Angew. Chem., Int. Ed.* **2018**, *57*, 3089−3093.
(52) Zou, C.; Lin, J.; Suo, S.; Xie, M.; Chang, X.; Lu, W. Palladium(II) N-heterocyclic allenylidene complexes with extended intercationic Pd···Pd interactions and MMLCT phosphorescence. *Chem. Commun.* **2018**, *54*, 5319−5322.
(53) *APEX4—Software Suite for Crystallographic Programs*; Bruker AXS, Inc: Madison, WI, USA, 2021.
(54) Sheldrick, G. M. A short history of SHELX. *Acta Crystallogr. A - Found. Crystallograph.* **2008**, *64*, 112−122.
(55) Sheldrick, G. M. Crystal structure refinement with SHELXL. *Acta Crystallogr. C- Struct. Chem.* **2015**, *71*, 3−8.
(56) Hübschle, C. B.; Sheldrick, G. M.; Dittrich, B. ShelXle: a Qt graphical user interface for SHELXL. *J. Appl. Crystallogr.* **2011**, *44*, 1281−1284.
(57) Neese, F.; Wennmohs, F.; Becker, U.; Riplinger, C. The ORCA quantum chemistry program package. *J. Chem. Phys.* **2020**, *152*, 224108.
(58) Neese, F. Software update: The ORCA program system—Version 5.0. *WIREs Comput. Mol. Sci.* **2022**, *12*, e1606.
(59) Weigend, F.; Ahlrichs, R. Balanced basis sets of split valence, triple zeta valence and quadruple zeta valence quality for H to Rn: Design and assessment of accuracy. *Phys. Chem. Chem. Phys.* **2005**, *7*, 3297.
(60) Becke, A. D. Density-functional exchange-energy approximation with correct asymptotic behavior. *Phys. Rev. A* **1988**, *38*, 3098−3100.
(61) Perdew, J. P.; Yue, W. Accurate and simple density functional for the electronic exchange energy: Generalized gradient approximation. *Phys. Rev. B* **1986**, *33*, 8800−8802.
(62) Grimme, S.; Antony, J.; Ehrlich, S.; Krieg, H. A consistent and accurate ab initio parametrization of density functional dispersion correction (DFT-D) for the 94 elements H-Pu. *J. Chem. Phys.* **2010**, *132*, 154104.
(63) Grimme, S.; Ehrlich, S.; Goerigk, L. Effect of the damping function in dispersion corrected density functional theory. *J. Comput. Chem.* **2011**, *32*, 1456−1465.
(64) Barone, V.; Cossi, M. Quantum Calculation of Molecular Energies and Energy Gradients in Solution by a Conductor Solvent Model. *J. Phys. Chem. A* **1998**, *102*, 1995−2001.
(65) Cossi, M.; Rega, N.; Scalmani, G.; Barone, V. Energies, structures, and electronic properties of molecules in solution with the C-PCM solvation model. *J. Comput. Chem.* **2003**, *24*, 669−681.
(66) Tao, J.; Perdew, J. P.; Stavoverov, V. N.; Scuseria, G. E. Climbing the Density Functional Ladder: Nonempirical Meta−Generalized Gradient Approximation Designed for Molecules and Solids. *Phys. Rev. Lett.* **2003**, *91*, 146401.
(67) Chemcraft − graphical software for visualization of quantum chemistry computations. https://www.chemcraftprog.com (accessed 17/01/2025).
(68) Van Lenthe, E.; Snijders, J. G.; Baerends, E. J. The zero-order regular approximation for relativistic effects: The effect of spin−orbit coupling in closed shell molecules. *J. Chem. Phys.* **1996**, *105*, 6505−6516.
(69) Pantazis, D. A.; Chen, X.-Y.; Landis, C. R.; Neese, F. All-Electron Scalar Relativistic Basis Sets for Third-Row Transition Metal Atoms. *J. Chem. Theory Comput.* **2008**, *4*, 908−919.
(70) Rolfes, J. D.; Neese, F.; Pantazis, D. A. All-electron scalar relativistic basis sets for the elements Rb−Xe. *J. Comput. Chem.* **2020**, *41*, 1842−1849.

https://doi.org/10.1021/acs.inorgchem.4c05436
Inorg. Chem. 2025, 64, 6561−6574

3.3 Preliminary work towards a doubly cyclometalated Ni(II) complex [Ni(C^N^C)(PPh$_3$)]

Investigating the effect of heavy PnPh$_3$ ancillary ligands (Pn = As, Sb) on the Ni(C^N^C) system is precluded by the lack of an operational protocol for the synthesis of these organonickel complexes. Through the work of *Baya et al.* and ourselves, it was established that the Pd(C^N^C) complexes [Pd(dpp)(PnPh$_3$)] (dpp = 2,6-di(phenid-2'-yl)pyridine, Pn = P, As, Sb) can be prepared *via* two subsequent C–H activation steps like their Pt congeners as shown in Figure 3.1.[80,84,109] However, the strategy does not translate to the Ni derivatives. We found that the first C–H activation step using K_2CO_3 and KOAc in *p*-xylene, as established for Ni(C^N^N) and Ni(N^C^N) complexes, is not feasible (experimental details in section 6.3).[1] This is likely due to insufficient or altogether lacking pre-coordination of the monodentate pyridine unit. For the C–H activation in the C^N^N and N^C^N systems, bidentate pre-coordination maintaining proximity of the Ni(II) ion to the respective C–H bond is considered a key step.[110–113]

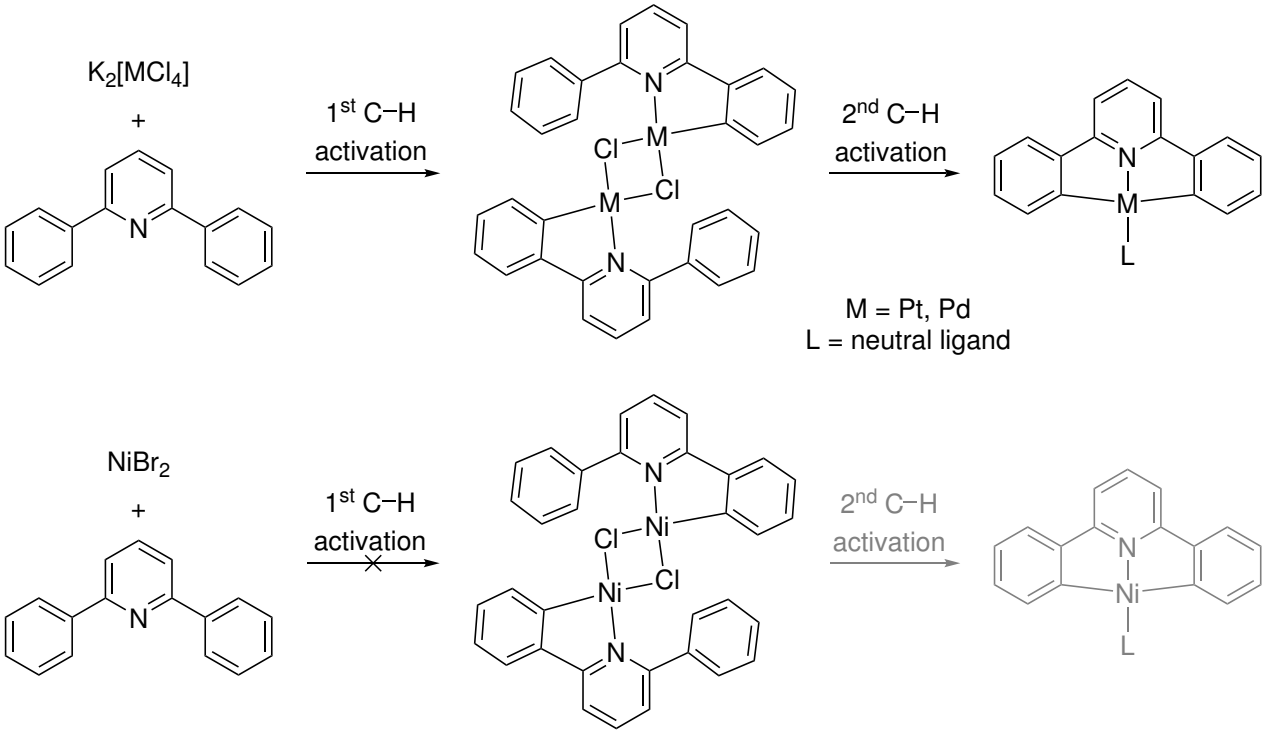

Figure 3.1: Schematic reaction sequences for the synthesis of [M(dpp)(L)] complexes *via* two C–H activation steps.[80,84,109] For M = Ni, the synthesis fails in the first step.

A proven alternative to C–H activation is C–X activation, i.e. oxidative addition starting from a Ni(0) species.[85,113,114] While *Feuerstein* and *Breher* used double C–X activation for the synthesis of [Ni(C^C^N)(py)],[85] we intended to probe whether this is really necessary. If not, the struggle to obtain the double halogenated protoligand as detailed in **Publication 2** might be circumvented. Therefore, we devised a strategy that starts with a single C–X activation step, but converges with the syntheses of the Pd and Pt complexes in that the second Ni–C bond is established *via* C–H activation (Figure 3.2).

1 Experiments performed in collaboration with Dr. Lukas Kletsch.

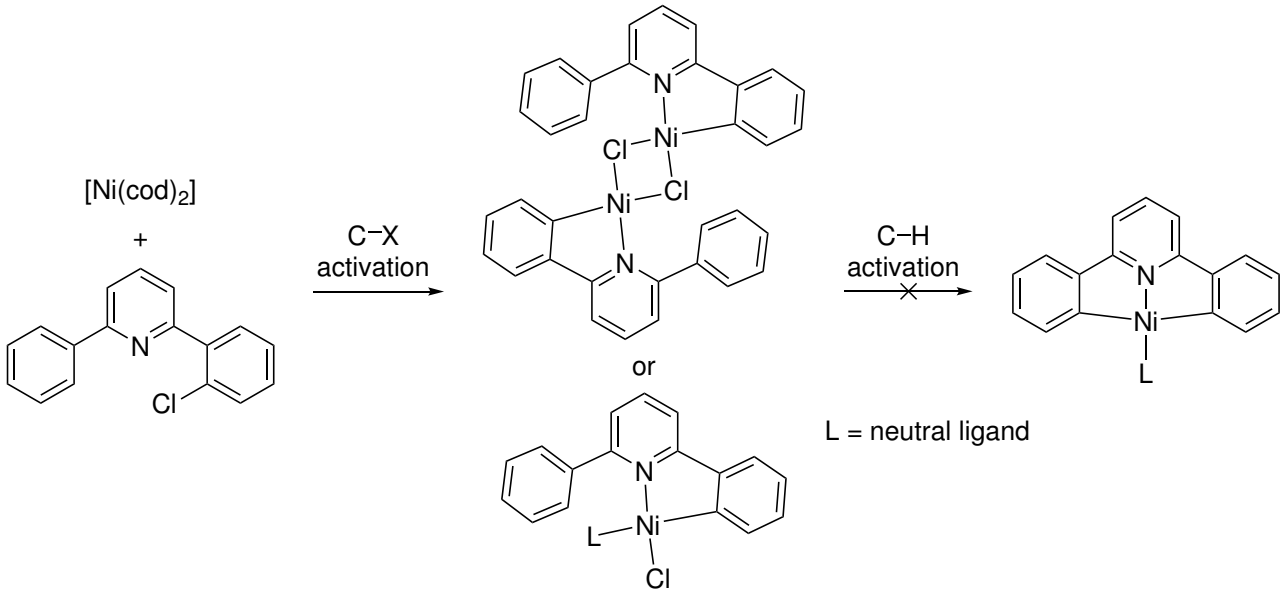

Figure 3.2: Proposed reaction sequence for the synthesis of [Ni(dpp)(L)] *via* a C–X and a C–H activation step. The synthesis fails in the second step.

The mono-halogenated protoligand 2-(2'-chlorophenyl)-6-phenylpyridine can be synthesized in moderate yields following a published procedure.[115] Its reaction with the Ni(0) source [Ni(cod)$_2$] (cod = 1,5-cyclooctadiene) in THF results in a deep red solution, both in the presence and absence of PPh_3 (experimental details in section 6.3). NMR analysis of the reddish brown solid isolated from the reaction indicates the strong presence of paramagnetic, probably tetrahedral Ni(II) species. This is not necessarily an indication of an undesired outcome, as it cannot be ruled out that Ni might be tetrahedrally coordinated in the C^N coordinated species shown in Figure 3.2. However, neither the reaction of the isolated material with KO*t*Bu in THF, nor addition of KO*t*Bu directly to the C–X activation reaction solution leads to an appreciable change in the appearance of either the solution or its ^{1}H NMR spectrum. The target compound [Ni(dpp)(PPh_3)] was not detected or isolated. The conditions of the synthesis attempts that were performed are detailed in the appendix. To get a clearer picture of the reactions at hand in the future, it would probably be helpful to characterize and identify the product of the C–X activation *via* mass spectrometry and, if possible, *sc*-XRD. Potential changes to the reaction conditions include the use of different Ni(0) sources and bases. Meanwhile, we found that organonickel systems with different, but similarly strong carbanionic ligands offer better synthetic accessibility and significant potential for Ni(II)-based triplet emission too, as presented in the next section.

3.4 Assessing the Character of the C_6F_5 Ligand from the Electrochemical and Photophysical Properties of [Ni(C_6F_5)$_2$(N^N)] Complexes (Publication 3)

In response to the synthetic challenges encountered with the doubly cyclometalated Pd(II) and Ni(II) complexes discussed in the preceding sections, we decided to expand our work to an entirely different system. Thereby, we hoped to approach the overarching goal of significant phosphorescence from Ni(II) complexes more directly and from another angle. Following the emitter design principles outlined in section 1.3, the choice fell on complexes of the type [Ni(C_6F_5)$_2$(N^N)] (N^N = α-diimine ligand). Like the not (yet) synthetically accessible [Ni(C^N^C)(L)] complexes, [Ni(C_6F_5)$_2$(N^N)] complexes feature two Ni–C bonds and a multidentate chromophore ligand. Importantly though, their synthesis is well documented in the literature reaching as far back as the 1970s.[89,91,96,97] However, much less is known about their photophysical properties. We therefore sought to investigate whether the system is indeed a good platform for Ni(II)-based triplet emission by studying a range of [Ni(C_6F_5)$_2$(N^N)] derivatives with common α-diimines. In addition to confirming this, we were able to draw conclusions regarding the character and behaviour of the C_6F_5 ligand. These will inform future endeavours both regarding phosphorescent Ni(C_6F_5)$_2$ derivatives and the catalytically relevant stabilization of higher oxidation states in different ligand environments. The results of our study are presented and discussed in **Publication 3**, which is reprinted with permission from Ref.[67]. Copyright © 2024, American Chemical Society.

The author's contributions to the work include the synthesis and characterization of the discussed compounds except for the crystal structures of [Ni(C_6F_5)$_2$(bpy)] · 0.5 CH_2Cl_2 and [Ni(C_6F_5)$_2$(*i*Pr-DAB)]. Furthermore, they include the (TD-)DFT calculations and the autonomous preparation of the manuscript for revision in collaboration with the co-authors. The crystal structures of [Ni(C_6F_5)$_2$(bpy)] · 0.5 CH_2Cl_2 and [Ni(C_6F_5)$_2$(*i*Pr-DAB)] were contributed by Dr. Sascha Schäfer and Jan Koll and by Dr. Claudia Hamacher, respectively. Emission spectroscopy was conducted at the lab of Prof. Dr. Cristian A. Strassert. The individual contributions of all co-authors are described in detail in section "Author information" in the publication. The Supporting Information (spectra and tables) for **Publication 3** is provided in section 6.4.

Inorganic Chemistry

pubs.acs.org/IC

Article

Assessing the Character of the C_6F_5 Ligand from the Electrochemical and Photophysical Properties of $[Ni(C_6F_5)_2(N^\wedge N)]$ Complexes

Rose Jordan,* Sascha A. Schäfer, Noah Sander, Ivan Maisuls, Claudia Hamacher, Joshua Friedel, Cristian A. Strassert,* and Axel Klein*

Cite This: *Inorg. Chem.* 2024, 63, 11079−11091

Read Online

ACCESS | Metrics & More | Article Recommendations | Supporting Information

ABSTRACT: Organonickel complexes containing α-diimine ligands $[Ni(C_6F_5)_2(N^\wedge N)]$ ($N^\wedge N$ = 2,2′-bipyridine (bpy), 2,9-dimethyl-1,10-phenanthroline (dmphen), 3,4,7,8-tetramethyl-1,10-phenanthroline (tmphen), dipyrido[3,2-*a*:2′,3′-*c*]phenazine (dppz), 1,4-bis(isopropyl)-1,4-diazabutadiene (*i*Pr-DAB), and 1,4-bis(2,6-dimethylphenyl)-1,4-diazabutadiene (Xyl-DAB) were prepared and studied structurally, spectroscopically, and electrochemically. Their molecular structures from single-crystal X-ray diffraction show near-perfect square planar Ni(II) coordination except in the case of dmphen. Primary reversible electrochemical reductions in the range from −1 to −2 V vs ferrocene/ferrocenium couple lead to mainly diimine-localized radical anion complexes, while secondary reductions in the range from −2 to −2.5 V lead to dianion complexes, as shown through spectroelectrochemistry. Irreversible metal-centered oxidations at around 0.7 V result in rapid aryl−aryl reductive elimination and formation of decafluorobiphenyl. No photoluminescence was detected for the complexes containing chromophoric α-diimine ligands at room temperature. At 77 K in frozen glassy 2-Me-THF matrices, weak photoluminescence was detected for the dmphen and tmphen derivatives, with broad emission bands peaking around 570 nm. All results are rationalized with the support of (TD-)DFT calculations, highlighting the role of the C_6F_5 ligand in different systems.

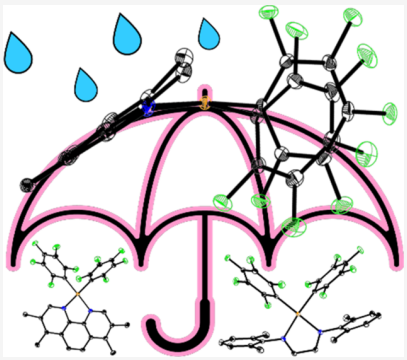

INTRODUCTION

Organometallic nickel complexes with α-diimine ligands such as 2,2′-bipyridine (bpy), 1,10-phenanthroline (phen), or the diazabutadienes (R-DAB) have gained an enormous interest over the last three decades. This is attributed to their success as effective catalysts in olefin polymerization, olefin/CO copolymerization,[1−3] and related olefin functionalizations.[4,5] Moreover, their role in chemically, electrochemically, or photoredox-driven C−C cross-coupling catalysis and related reactions has become prominent.[5−10] In catalysis, the aimed replacement of the expensive Pd by the base-metal Ni has been a driving force for many studies. This development has led to an increasing interest in the fundamental investigation of structures, thus, spectroscopic and electrochemical properties of such organonickel complexes can be stated.[9−15]

In contrast to this, only very recently organonickel complexes have emerged as photoreactive or luminescent materials.[10,16−21] As in catalysis, the replacement of the heavier homolog Pt in luminescent complexes is an important goal. However, Ni(II) presents several challenges compared with Pt(II), such as an intrinsically small ligand-field splitting which leads to low-lying d−d* excited states which are prone to rapid radiation-less decay and/or ligand labilization. Moreover, the far smaller spin−orbit coupling of Ni of 630 cm^{-1}[22] compared with 4253 cm^{-1} for Pt[23] (Pd has 1610 cm^{-1}[24]) leads to less efficient intersystem crossing from the excited singlet to the emissive triplet T_1 state, but most importantly, to a much slower radiative deactivation rate. Furthermore, organometallic Ni−C bonds are by far more reactive toward hydrolysis than the corresponding Pt−C bonds, which is related to the higher difference in electronegativity for Ni or, in other words, its less noble character. These obstacles can be overcome through clever ligand design, but still to this day only a very small number of phosphorescent (emitting from a triplet state) organometallic Ni(II) complexes have been reported.[17,19−21] A recent benchmark in this field was achieved with the complex [Ni(dpb)(carbazolate)] (H_2dpb = 2,6-dipyridyl-benzene), which shows weak triplet emission from a ^{3}IL [$\pi-\pi^*$-($N^\wedge C^\wedge N$)] excited state.[19] In contrast, for the $C^\wedge C^\wedge C$-coordinated complexes [Ni(*$C^\wedge C^\wedge C$*)(MeCN)]X (X = PF_6, BF_4, BPh_4, SO_3CF_3) with *N*-butyl-imidazolydene as pending C* groups, ligand-centered fluorescence was reported.[20] The same is true for the Ni(II) complex with a phenazine-based $O^\wedge N^\wedge N^\wedge O$ ligand that showed fluorescence from a coordination-induced spin-state switch.[18] Efficient thermal quenching

Received: February 14, 2024
Revised: May 16, 2024
Accepted: May 20, 2024
Published: June 6, 2024

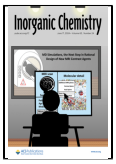

ACS Publications

© 2024 American Chemical Society

https://doi.org/10.1021/acs.inorgchem.4c00649
Inorg. Chem. 2024, 63, 11079−11091

was very recently reported for a Ni(II) complex of an N^N^C^N cyclometalating macrocyclic tripyrrin-phenyldiether ligand, occurring from mixed ligand-centered(^{3}LC)/metal-to-ligand charge transfer (^{3}MLCT) excited states.[16]

C_6F_5 ligands in organometallic Ni(II) complexes have been reported since the late 1970s. They provide chemically rather stable building blocks in complexes like $[Ni(C_6F_5)_2(L)_2]$, $[Ni(C_6F_5)_2(L^L)]$, or $[Ni(C_6F_5)_4]^{2-}$ with neutral ligands L including chelating L^L.[25−38] These complexes include the very versatile olefin polymerization catalysts $[Ni(C_6F_5)_2(\eta^6\text{-arene})]$[36] and $[Ni(C_6F_5)_2(PnPh_3)_2]$ with Pn = P, As, or Sb.[38] Furthermore, $Ni(C_6F_5)$ fragments stood at the cradle of the benchmarking reports by Yamamoto and others on the reductive elimination reactions occurring from Ni(II) complexes $[Ni(R)(R')(L)_2]$ or $[Ni(R)(R')(L^L)]$ (R = aryl, alkyl), which paved the way to the meanwhile established use of organonickel catalysts in C−C coupling reactions.[6,30,34] In their recent studies on Ni-based fluoroarylation catalysis, Espinet and co-workers primarily focused on phosphane electron-withdrawing olefin (PEWO) ligands and demonstrated high efficiency and selectivity for fluoroarylation at their Ni^{II}(PEWO) platforms.[35,36] However, the relative lability of the Ni-olefin coordination compared to, e.g., Pd and the reduced stability of catalytic intermediates were identified as limitations in these experiments.[36]

In this project, we use C_6F_5 ligands as good σ-donors, which provide axial shielding against hydrolysis in square planar organonickel(II) complexes through their hydrophobic F substituents. Furthermore, the presence of *ortho*-F substituents is positively correlated with the strength of the metal-aryl bond.[39,40] Both of these aspects are reflected in the significant number of reported, relatively stable $Ni(C_6F_5)$ complexes,[25−34] especially in contrast to their C_6H_5 congeners, which supports this idea. Anticipating a dual nature as both a strong σ-donor and strong π-acceptor for the C_6F_5 ligand, we furthermore expect comparatively large ligand field splitting and HOMO−LUMO gaps for the $Ni(C_6F_5)_2$ complexes (HOMO = highest occupied molecular orbital; LUMO = lowest unoccupied molecular orbital). Investigating this property of the Ni−C_6F_5 system may be conducive to eventually eliciting significant triplet emission from $Ni(C_6F_5)_n$ complexes through informed emitter design. Reported examples of emissive C_6F_5 complexes of, e.g., Pt(II) and Au(I) confirm that the C_6F_5 ligand does not generally exert a quenching effect on photoemission from transition metal complexes.[41,42] As chromophoric π-accepting ligands, we chose the N^N coordinating diimines bpy (2,2′-bipyridine), tmphen (3,4,7,8-tetramethyl-1,10-phenanthroline), 2,9-dmphen (2,9-dimethyl-1,10-phenanthroline), and dppz (dipyrido-[3,2-*a*:2′,3′-*c*]-phenazine) (Chart 1). To these aromatic diimines, we added also the aliphatic diimines, the so-called diazabutadienes (DABs), Xyl-DAB (*N*,*N*′-di-3,5-xylyl-1,4-diazabutadiene), and *i*Pr-DAB (*N*,*N*′-diisopropyl-1,4-diazabutadien).

The bpy complex[25,27,30] as well as the Tol-DAB (*N*,*N*′-di-2-tolyl-1,4-diazabutadien)[29] derivative have previously been reported but without any electrochemical or photophysical data. In the DAB complexes, the energy of the LUMO, which is of π^* character, lies markedly lower than in the aromatic diimines.[15] This results in interesting (spectro)electrochemical behavior, as the DAB complexes are reduced more easily compared to the aromatic diimine systems. However, these ligands do not contain potent chromophores. To complement the experimental data, we also performed density functional theory (DFT) calculations on all compounds with the aim of shedding light on the specific contributions and character of the C_6F_5 ligand.

Chart 1. Ligands and $Ni(C_6F_5)$ Complexes of this Study

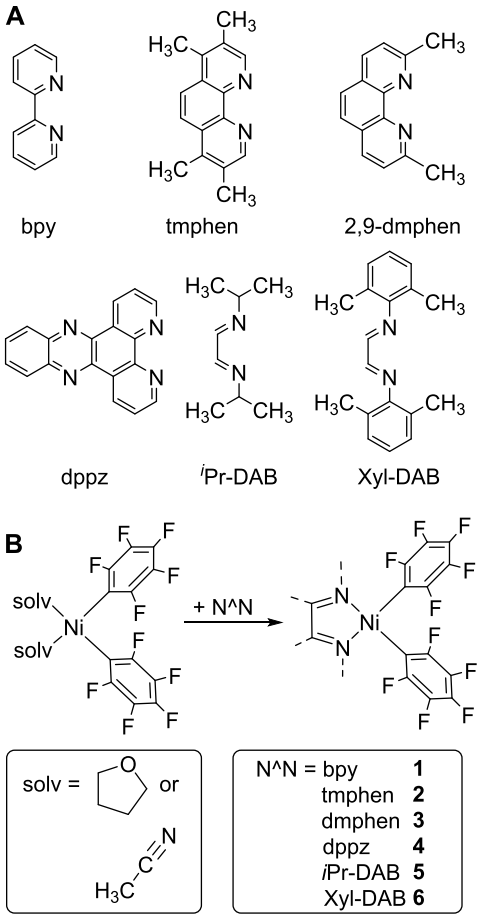

RESULTS AND DISCUSSION

Synthesis and Structural Characterization. The target complexes were prepared through ligand exchange from *cis*-$[Ni(C_6F_5)_2(MeCN)_2]$. Yellow to orange (bpy, tmphen, 2,9-dmphen, dppz), deep red (*i*Pr-DAB), or violet (Xyl-DAB) materials were obtained in good to excellent yields ranging from 68 to 96% (for details, see the Experimental Section).

Analytical data of the literature-reported complex $[Ni(C_6F_5)_2(bpy)]$ (**1**) coincided with reported values.[25,30] The compound was crystallized from CH_2Cl_2/*n*-pentane as $[Ni(C_6F_5)_2(bpy)]\cdot 0.5CH_2Cl_2$, which is isostructural to the Pt(II) derivative $[Pt(C_6F_5)_2(bpy)]\cdot 0.5CH_2Cl_2$[43] but different from the previously reported structure, namely $[Ni(C_6F_5)_2(bpy)]\cdot$acetone.[30] While the cell parameters and volume are similar, the packing is slightly different.[30]

The square planar molecular structure and the purity of the unprecedented diamagnetic complexes $[Ni(C_6F_5)_2(tmphen)]$ (**2**), $[Ni(C_6F_5)_2(2,9\text{-dmphen})]$ (**3**), $[Ni(C_6F_5)_2(dppz)]$ (**4**), $[Ni(C_6F_5)_2(iPr\text{-DAB})]$ (**5**), and $[Ni(C_6F_5)_2(Xyl\text{-DAB})]$ (**6**) were confirmed by ^{1}H and ^{19}F nuclear magnetic resonance (NMR) spectroscopy (spectra in Figures S1−S18, Supporting Information, SI). All new complexes were also structurally characterized by single-crystal X-ray diffraction (sc-XRD). Preparative details on their crystallization are given in the

https://doi.org/10.1021/acs.inorgchem.4c00649
Inorg. Chem. 2024, 63, 11079−11091

Experimental Section, and detailed data on the measurement and refinement of the crystal structures as well as for the starting material $[Ni(C_6F_5)_2(MeCN)_2]$·solv can be found in Tables S1, S3, S5, S7, S9, S11, and S13, SI.

All molecular structures from sc-XRD except **3** $[Ni(C_6F_5)_2(2,9\text{-dmphen})]$ show a near-perfect square-planar coordination environment around Ni (Figure 1). Relevant bond lengths and angles are compiled in Tables S2, S4, S6, S8, S10, S12, and S14, SI.

The structure of **3** shows an umbrella-like distortion of the square planar coordination and a significant tilt of the 2,9-dmphen ligand by about 35° with respect to the coordination plane. This is attributed to the steric demand of the methyl substituents in the ortho position to the *N* coordination sites. A recently reported example of a distorted square planar Ni(II) complex containing a 2,9-dmphen derivative $[Ni(CH_2TMS)_2(N^N)]$ (N^N = 2,9-dimethyl-4,7-dimethoxy-1,10-phenanthroline; TMS = trimethylsilyl) features the same 35° tilt of the sterically hindered ligand and even stronger distortion toward a tetrahedral geometry.[44] Furthermore, numerous reported examples of $[Ni(X)_n(2,9\text{-dmphen})]$ (L = Cl^-, SO_4^{2-}, N_3^-) derivatives actually feature an expanded coordination sphere around nickel, which serves to avoid this geometric strain, i.e., a pentagonal bipyramidal or distorted octahedral geometry.[45−48] We observed significantly lower stability in solution for **3** than for all other compounds, which we attribute to the geometric strain and poor shielding of the Ni center in the compound. A major decomposition product was identified as the hydrolysis product HC_6F_5 by ^1H and ^{19}F NMR spectroscopy (Figures S9 and S10). Spontaneous reductive elimination of $F_5C_6-C_6F_5$ as described by others[30,35,36] was not observed under ambient and anhydrous experimental conditions, including photoirradiation, but was triggered by oxidation (see also later). The remaining complexes with nondistorted square planar geometries and thus full shielding by the C_6F_5 ligands are completely stable under identical conditions.

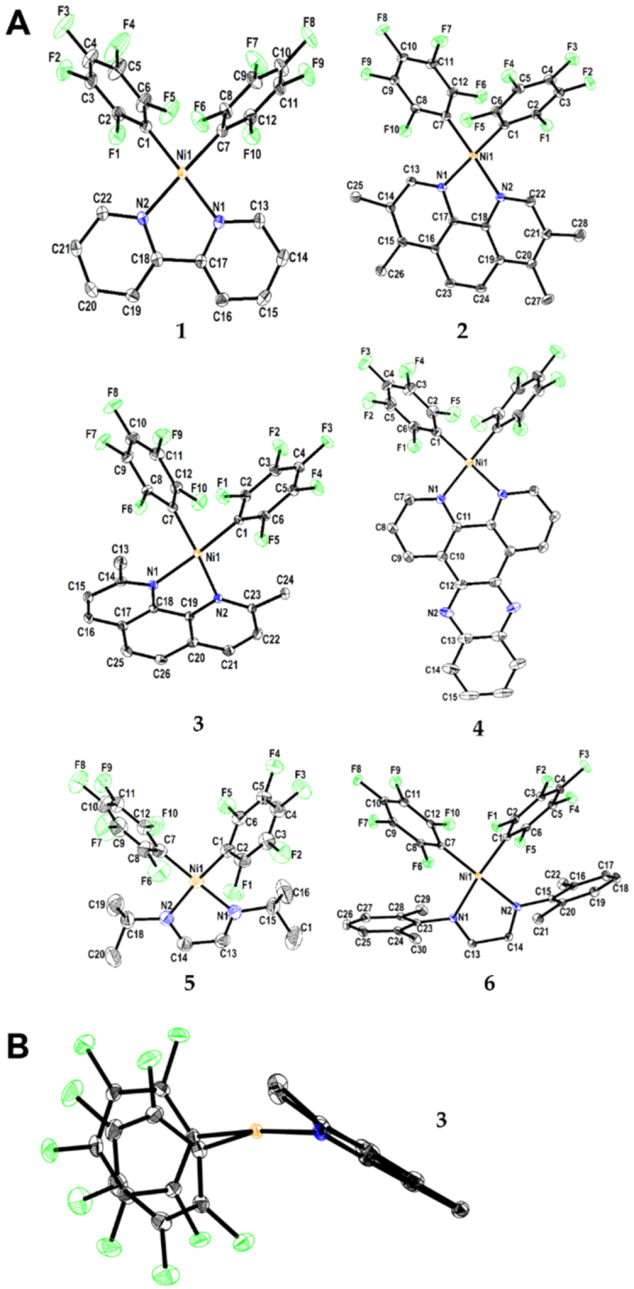

Figure 1. Molecular structures of **1**−**6** (A) and side view of **3** from single-crystal X-ray diffraction (sc-XRD) (B). Displacement ellipsoids drawn at 50% (**1**−**4** and **6**) or 30% (**5**) probability level, with H atoms omitted for clarity.

The complexes **1**−**3** with aromatic diimine ligands tend to crystallize into channel-containing solid-state structures, which are governed by $\pi\cdots\pi$ stacking interactions either between the C_6F_5 or the N^N ligands and contain solvent molecules in these channels (Figures S20−S26, SI). In contrast, the structures of **5** and **6** are nonsolvates, which underlines the role of the aromatic diimine ligands in the formation of the channels. The structures of $[Ni(C_6F_5)_2(MeCN)_2]$ and $[Ni(C_6F_5)_2(dppz)]$ (**4**) exhibit especially large solvent-accessible voids and were crystallized using, among other solvents, *n*-pentane. This resulted in the observation of strongly disordered electron density in these channels, which could not be refined into localized solvent molecules. We chose to omit this electron density in these cases, treating the data sets with Platon SQUEEZE, since the structure of the complexes is not expected to be affected significantly by the solvent molecules in the channels.[49]

The DFT geometry optimization of the structures for **1**−**6** using TPSSh/def2-TZVP/CPCM(THF) gave very good agreement with the experimental data. The resulting *xyz* coordinate files of the optimized structures are enclosed in the Supporting Information.

Electrochemistry and DFT-calculated Frontier Orbitals. Selected electrochemical data for the complexes **1**−**6** from cyclic voltammetry is compiled in Table 1 (full data in Table S15, SI) and the cyclic voltammograms can be found in Figures S27−S32, SI. All complexes exhibit one irreversible oxidative wave at potentials ranging from +0.3 to +1.1 V vs the ferrocene/ferrocenium couple ($FeCp_2/FeCp_2^+$). The potentials are markedly solvent-dependent with higher values in THF compared with MeCN. A very low oxidation potential of +0.30 V was observed for the 2,9-dmphen complex **3** in MeCN, which is probably due to solvent-coordination and/or dimerization forming a penta-coordinated species, e.g., $[Ni(C_6F_5)_2(2,9\text{-dmphen})(MeCN)]$, in MeCN but not in THF. This is supported by multiple literature reports of dimeric 2,9-dmphen containing structures featuring pentacoordinate Ni(II).[45−48]

https://doi.org/10.1021/acs.inorgchem.4c00649
Inorg. Chem. 2024, 63, 11079−11091

Table 1. Selected Electrochemical Data for Complexes 1−6 and for Similar Ni Complexes[a]

compound (N^N =)	$E_{1/2}$ second reduction	$E_{1/2}$ first reduction	E_{pa} first oxidation	ΔEred1 − red2	ΔE_{echem}[b]	solvent	ΔE_{calc}[c]
1 (bpy)	−2.30	−1.62	+0.76	0.68	2.38	MeCN	
	−2.48	−1.84	+0.71	0.64	2.55	THF	2.58
2 (tmphen)	−2.55 irr	−1.96	+0.66	0.59	2.62	MeCN	
	−2.66 irr	−2.02	+0.69	0.64	2.71	THF	2.77
3 (2,9-dmphen)	−2.55 irr	−1.73 irr	+0.30	0.82	2.03	MeCN	
	−2.65 irr	−1.71 irr	+0.87	0.94	2.58	THF	2.64
4 (dppz)	−2.02	−1.43	+0.52	0.59	1.95	MeCN	
	−2.13	−1.51	+0.69	0.62	2.20	THF	2.14
5 (*i*Pr-DAB)	−2.55 irr	−1.29	+0.88	1.26	2.17	MeCN	
	−2.84 irr	−1.51	+1.10	1.33	2.61	THF	2.26
		−1.47	+0.97		2.44	CH_2Cl_2	
6 (Xyl-DAB)	−2.12 irr	−1.00	+1.06	1.12	2.06	MeCN	
	−2.24 irr	−1.09	+1.04	1.15	2.13	THF	2.11
		−1.16	+1.10		2.26	CH_2Cl_2	
other complexes							
$[Ni(Mes)_2(bpy)]$[d]	−2.97	−2.19	−0.14	0.78	2.05	THF	
$[Ni(C_6F_5)_2(Tp)]^-$[e]			+0.55			MeCN	
$(nBu_4N)_2[Ni(C_6F_5)_4]$[f]			+0.54			CH_2Cl_2	

[a]From cyclic voltammetry in 0.1 M nBu_4NPF_6/solvent solutions at a 100 mV/s scan rate. Potentials E in V vs ferrocene/ferrocenium, accuracy: ±0.003 V. Half-wave potentials $E_{1/2}$ for reversible waves; peak potentials E_p for irreversible waves (irr). [b]Electrochemical HOMO−LUMO gap $\Delta E_{echem} = E_{Ox1} - E_{Red1}$ in V. [c]ΔE_{calc} = DFT-calculated HOMO−LUMO gap; TPSSh/def2-TZVP/CPCM(THF). [d]From ref 50. [e]From ref 34, Tp = tripyrazolylborate; no reduction potentials reported. [f]From ref 33, reversible oxidation, no reduction potentials reported.

Based on similar results for $[Ni(Mes)_2(N^N)]$-type complexes (Mes = mesityl = 2,4,6,-trimethylphenyl),[15,50,51] we assign them to metal-centered Ni(II)/Ni(III) oxidation processes. However, the first oxidation of analogous Mes complexes occurs at severely negatively shifted potentials (−0.14 V vs $FeCp_2/FeCp_2^+$ for $[Ni(Mes)_2(bpy)]$ in THF) compared to the herein studied C_6F_5 derivatives due to the strongly σ- and π-donating character of the electron-rich Mes ligand.[50,51] Values around +0.5 V were reported for the tris(pyrazoyl)borate (Tp) complex $[Ni(C_6F_5)_2(Tp)]^-$[34] and the homoleptic $[Ni(C_6F_5)_4]^{2-}$,[33] underpinning the strongly σ-donating character of the C_6F_5 ligand, which is frequently overlooked in favor of its π-accepting properties. The same publication also notes the higher stability for $[Ni^{III}(C_6F_5)_4]^-$ compared to $[Ni^{III}(C_6Cl_5)_4]^-$,[33] as a result of the σ-donating properties, also evoking the similar and somewhat paradoxically strong σ-donating properties of the simplest perfluoroalkyl ligand CF_3.[52] The highest oxidation potentials in our series are recorded for the DAB derivatives **5** and **6** in line with a rather poor σ-donating character of these ligands.[15,51]

Furthermore, all complexes except **3** display a reversible first reduction within a range of −1.0 to −2.0 V, which can be assigned to a reduction of the N^N ligand. The first reduction of **3** is irreversible, which aligns with the observed lower stability of the geometrically strained 2,9-dmphen-containing complex in solution. The cathodic half-wave potentials shift positively along the series tmphen (**2**) > 2,9-dmphen (**3**) > bpy (**1**) > dppz (**4**) > *i*Pr-DAB (**5**) > Xyl-DAB (**6**), which aligns with the increasing π-accepting ability from tmphen to Xyl-DAB.[47] Compared to the $[Ni(Mes)_2(N^N)]$ analogues, the reductions occur more positively shifted, which underlines the electron-withdrawing character of the C_6F_5 ligand.

All compounds show second reduction processes at potentials between −2.0 and −2.6 V. The difference between the first and the second reduction waves ($\Delta E_{red1-red2}$) of 0.59 to 0.68 mV is characteristic for aromatic α-diimine ligands,[15,51,53] while for the DAB ligands far larger values of around 1 V and more were found. At least for the complexes of the aromatic diimine ligands, we can assign the second reduction to be ligand-centered as well.

A DFT-calculated frontier molecular orbital scheme for the aromatic diimine containing ligands **1**−**4** is shown in Figure 2.

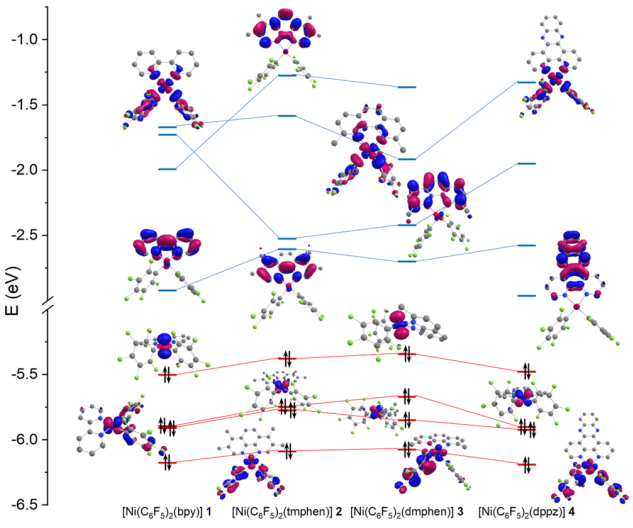

Figure 2. DFT-calculated frontier molecular orbital landscape of **1**−**4** using TPSSh/def2-TZVP/CPCM(THF). Red lines connect occupied molecular orbitals of similar character, as eye guides. Blue lines connect unoccupied molecular orbitals of similar character.

An analogous scheme for **5** and **6** can be found in Figure S33, SI. In all cases, the HOMOs exhibit strong metal d-orbital character in the energetic order $d_{z2} > d_{xz} \approx d_{yz} > d_{xy}$, supporting our assignments of the oxidative waves in the CVs. The energy differences between these orbitals are largely invariant in all complexes except for **3**, where the d_{xz} and d_{yz} (HOMO−1 and HOMO−2) levels are split significantly by about 0.2 eV, whereas the differences are below 0.05 eV in all other cases.

https://doi.org/10.1021/acs.inorgchem.4c00649
Inorg. Chem. 2024, 63, 11079−11091

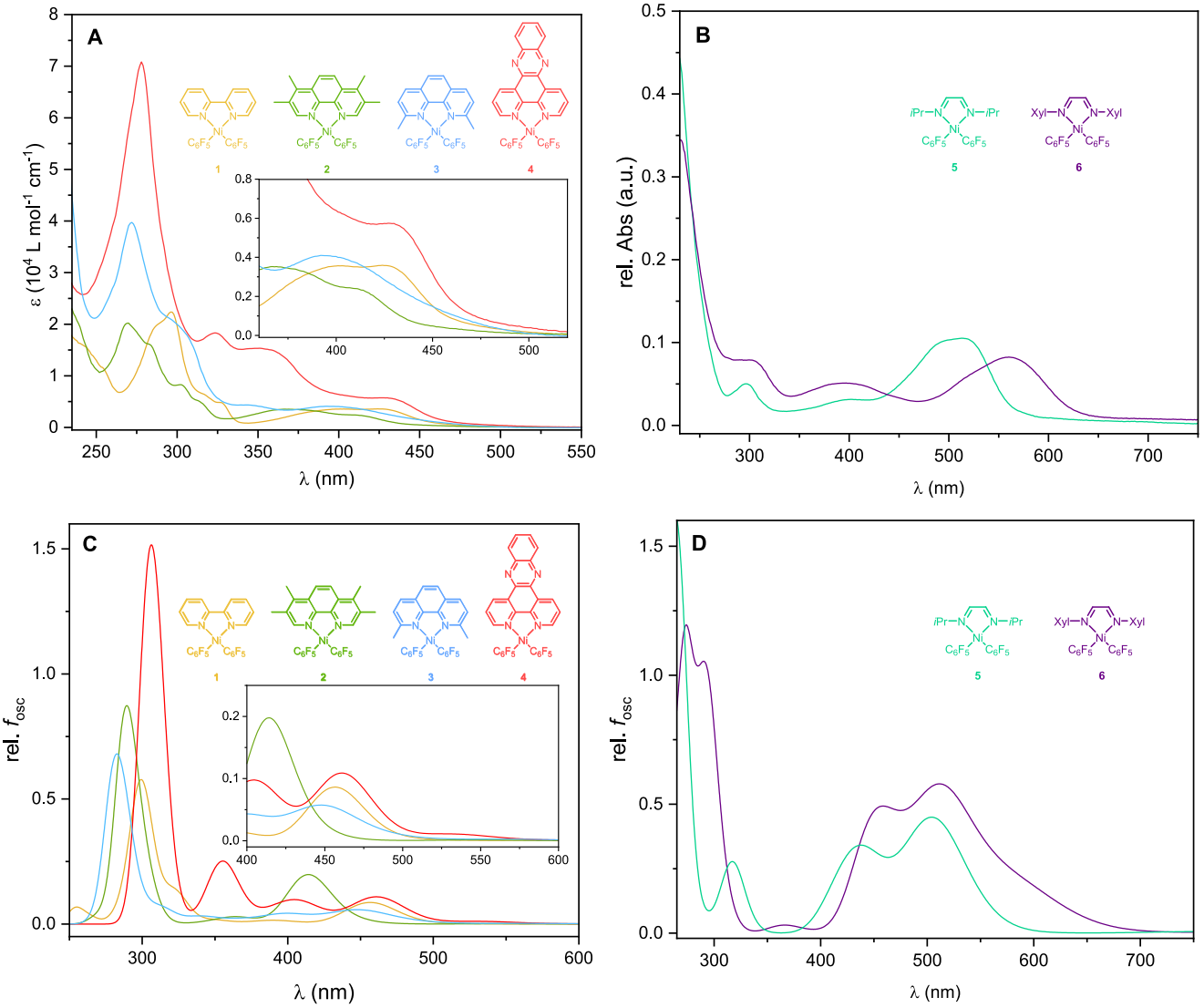

Figure 3. Experimental UV−vis absorption spectra of **1**−**4** in THF (A) and of **5** and **6** in CH_2Cl_2 (B) at 298 K. TD-DFT calculated UV−vis absorption spectra of **1**−**4** (C) and of **5** and **6** (D) using TPSSh/def2-TZVP/CPCM(THF).

Table 2. Selected UV−vis Absorption Data of Complexes 1−6[a]

compound (N^N =)	solvent	λ_1 (ε)	λ_2 (ε)	λ_3 (ε)	λ_4 (ε)	λ_5 (ε)	λ_6 (ε)	ΔE_{opt}[b]
1 (bpy)	THF	286sh (1.94)	296 (2.23)	316sh (0.64)	327 (0.49)	402 (0.36)	423 (0.35)	2.65
2 (tmphen)	THF	269 (2.03)	283 (1.61)	302 (0.83)	315sh (0.50)	368 (0.35)	411 (0.23)	2.74
3 (2,9-dmphen)	THF	272 (3.97)		298sh (2.06)	343 (0.44)	394 (0.40)		2.60
4 (dppz)	THF	278 (7.09)		324 (1.82)	350 (1.53)	427 (0.58)		2.63
5 (*i*Pr-DAB)	CH_2Cl_2	229		297	401	488sh	514	2.17
6 (Xyl-DAB)	CH_2Cl_2	230		303	396	513	560	1.94

[a]Absorption maxima λ in nm; absorption coefficient ε in 10^4 L mol^{-1} cm^{-1}. sh = shoulder. [b]Optical HOMO−LUMO gap extrapolated from the lowest energy absorption band in eV.

This reflects the comparatively low symmetry of **3**. The HOMOs are overall stabilized along the series **3** > **2** > **4** > **1** > **5** > **6**.

A larger variance between the complexes is found among the LUMOs. The energy of the LUMO decreases along **2** > **3** > **1** > **4** > **5** > **6**. The predicted HOMO−LUMO gaps ΔE_{calc} range from 2.77 eV for **2** [$Ni(C_6F_5)_2$(tmphen)] to 2.11 eV for **6** [$Ni(C_6F_5)_2$(Xyl-DAB)], decreasing along **2** > **3** > **1** > **5** > **4** > **6**. This mostly parallels the experimental electrochemical results (Table 1) except for the reversed order for **5** and **4**. However, the deviation between the two is within the approximate uncertainty margins.

According to the DFT calculations, the LUMO has π_{bpy}* character in **1**. For **4**, the LUMO shows a marked $\pi_{phenazine}$* character, while the LUMO+1 is of π_{bpy}* character in agreement with studies on similar dppz complexes.[21,54−57] A molecular orbital of significant $d_{x_2-y_2}$ character can be identified as the LUMO+3 in **1** and **4** and the LUMO+2 in **2** and **3**;

https://doi.org/10.1021/acs.inorgchem.4c00649
Inorg. Chem. 2024, 63, 11079−11091

however, the energy of this $d_{x_2-y_2}$ orbital decreases along **4** > **2** > **1** > **3**, indicating the strongest splitting of the d levels for **4** and the smallest for **3**. The latter is probably due to comparatively poor orbital overlap between the metal d orbitals and the orbitals of the distorted/tilted 2,9-dmphen ligand. In **5** and **6**, the LUMO has π_{DAB}* character and the $d_{x_2-y_2}$ orbital is the LUMO+1, indicating even smaller ligand field splitting for the DAB complexes.

UV−vis Absorption Spectroscopy. Complexes **1**−**6** were studied by UV−vis−NIR absorption spectroscopy. The analysis of the spectra (Figure 3 (top), maxima compiled in Table 2) and assignment of transition character to the observed absorption bands were supported by TD-DFT calculations for all complexes and UV−vis−NIR spectroelectrochemistry for **1** (see later). The TD-DFT (TPSSh/def2-TZVP/CPCM(THF)) calculated the UV−vis absorption spectra (Figure 3, bottom) provide a good qualitative match with the experimental data. Overlay comparison of experimental and calculated spectra for the individual compounds can be found in Figures S34−S39, SI.

Complex **1** [$Ni(C_6F_5)_2$(bpy)] shows an intense absorption band around 300 nm, which can be assigned to a ligand-centered transition into a $\pi-\pi$* state. In **2** [$Ni(C_6F_5)_2$(tmphen)], **3** [$Ni(C_6F_5)_2$(2,9-dmphen)], and **4** [$Ni(C_6F_5)_2$(dppz)], similar bands are hypsochromically shifted to around 270−280 nm. Weaker, relatively narrow absorption bands or shoulders, observed around 325 nm for **1** and around 310 nm for **2** and **3**, are likely attributable to transitions into states with mixed $\pi-\pi$*/metal-to-ligand charge transfer (MLCT)/ligand'-to-ligand charge transfer (L'LCT) character, based on our TD-DFT calculations. In the case of **3**, significant contributions from transitions into configurations involving the LUMO+2, which represents essentially the antibonding $d_{x_2-y_2}$ orbital, are also predicted in this spectral region, likely promoted by the low energy of the $d_{x_2-y_2}$ orbital as well as the distorted geometry of the complex. Broad, low-intensity absorption bands into states of almost exclusively MLCT character (with particularly strong $d_{xz/yz}-\pi$* contributions, according to our TD-DFT calculations and with maxima around 370−430 nm) are observed for **1**−**3**. These bands shift bathochromically along the series **2** > **3** > **1**, paralleling the experimentally estimated and DFT-calculated HOMO−LUMO gaps. For the dimesityl analogues of **1** and **2** [$Ni(Mes)_2$(N^N)], the corresponding MLCT-related absorption bands in the range from 500 to 580 nm and a similar hypsochromic shift from bpy to tmphen are reported.[47] The marked hypsochromic shift from the electron-rich Mes to the electron-poor C_6F_5 ligand underlines the stabilizing effect of the electron-deficient C_6F_5 ligand on the d_π levels. The dimesityl complexes additionally show comparatively strong L'LCT ($\pi_{Mes}-\pi_{N^N}$*) absorption bands above 550−600 nm, which are not present in this spectral region in the C_6F_5 derivatives due to the significantly lower energy of the π_{C6F5} levels.

In addition to the extremely intense band at 278 nm, which according to the DFT calculations corresponds to a transition into a state with mixed $\pi-\pi$*/LMCT character, **4** shows three more absorption maxima at 324, 350, and 427 nm. The former can be assigned to transitions into $\pi-\pi$* states involving a phenazine-centered π* orbital, while the latter two correspond to different MLCT states. The optical HOMO−LUMO gaps ΔE_{opt} extrapolated from the lowest energy absorption bands for **1**−**4** range from 2.60 eV for **3** to 2.74 eV for **2**. ΔE_{opt} for **4** is remarkably large (2.63 eV) compared to the electrochemical and calculated HOMO−LUMO gaps ΔE_{echem} (1.95 V in MeCN, 2.20 V in THF) and ΔE_{calc} (2.13 eV with CPCM(THF)), which is probably related to the rigidity of the extended diimine ligand. Contrarily, ΔE_{opt}, ΔE_{echem}, and ΔE_{calc} for **3** are very similar at around 2.6 eV for all values. This might indicate exceptionally little reorganization between the ground state and the excited state due to the already distorted geometry of the ground state.

The red and purple complexes **5** [$Ni(C_6F_5)_2$(*i*Pr-DAB)] and **6** [$Ni(C_6F_5)_2$(Xyl-DAB)] both show an intense absorption band a into a $\pi-\pi$* state with a maximum at ca. 230 nm near the solvent UV cutoff as well as two weak absorption bands at about 300 and 400 nm. The latter include large contributions from transitions into excited configurations involving the LUMO+1 ($d_{x_2-y_2}$), attributed to both the apparent small ligand field splitting and the low rigidity of the DAB backbone. Around 500 nm for **5** and 550 nm for **6**, an intense absorption band into a state of mixed MLCT, consequently: $d-d$* character is observed. The bathochromic shift from **5** to **6** is consistent with the lower LUMO energy of **6** in line with electrochemistry and DFT. ΔE_{opt} is consistently about 0.3 eV larger than ΔE_{echem} for both complexes.

Photoluminescence Spectroscopy Experiments. We tested complexes **1**−**4** for photoluminescence in liquid THF and CH_2Cl_2 solutions at 298 K as well as in poly(methyl methacrylate) (PMMA) films but found them to be practically nonemissive in both conditions. At 77 K in frozen glassy 2-MeTHF matrices, we found very weak but significant emission only for **2** [$Ni(C_6F_5)_2$(tmphen)] and **3** [$Ni(C_6F_5)_2$(2,9-dmphen)] (spectra in Figure S40, SI). Both **2** and **3** show an unstructured emission band with maxima at 568 and 584 nm, respectively. This redshift from **2** to **3** is consistent with our observations from UV−vis absorption spectroscopy and (TD-)DFT calculations. The emission lifetimes τ are in the nanosecond range, with 12.8 ± 0.2 ns for **2** and 15.9 ± 0.5 ns for **3** (Figures S41 and S42). The photoluminescence quantum yields Φ_L are below 0.02 in both cases. For comparison, we also studied the photoluminescence of the uncoordinated ligands and thus can rule out that the observed emission for **2** and **3** stems from traces of the ligands in the studied samples.

For **3**, we had initially postulated enhanced photoluminescence properties due to the added geometric strain, minimizing structural reorganization between the ground state and the excited state, which would otherwise promote thermal deactivation through vibronic coupling. As indicated by the minimal difference between ΔE_{opt} and ΔE_{echem} (as discussed earlier), this effect is probably operative in **3** in principle; however, the positive effect on the photoluminescence is probably largely lost to the remarkably stabilized $d_{x_2-y_2}$ orbital, thus significantly increasing the accessibility of dissociative and dark metal-centered (MC) states. In **2**, however, the $d_{x_2-y_2}$ orbital is destabilized by 0.33 eV compared to **3**, according to our calculations.

Despite its even larger ligand field splitting (according to DFT) and its very rigid extended π system, **4** [$Ni(C_6F_5)_2$(dppz)] is practically nonemissive even at low temperature. This observation led us to conclude that the $Ni(C_6F_5)_2$ platform is likely unsuited to enhance dppz-centered triplet emission, potentially due to photoinduced electron transfer, as observed in other dppz-related com-

https://doi.org/10.1021/acs.inorgchem.4c00649
Inorg. Chem. 2024, 63, 11079−11091

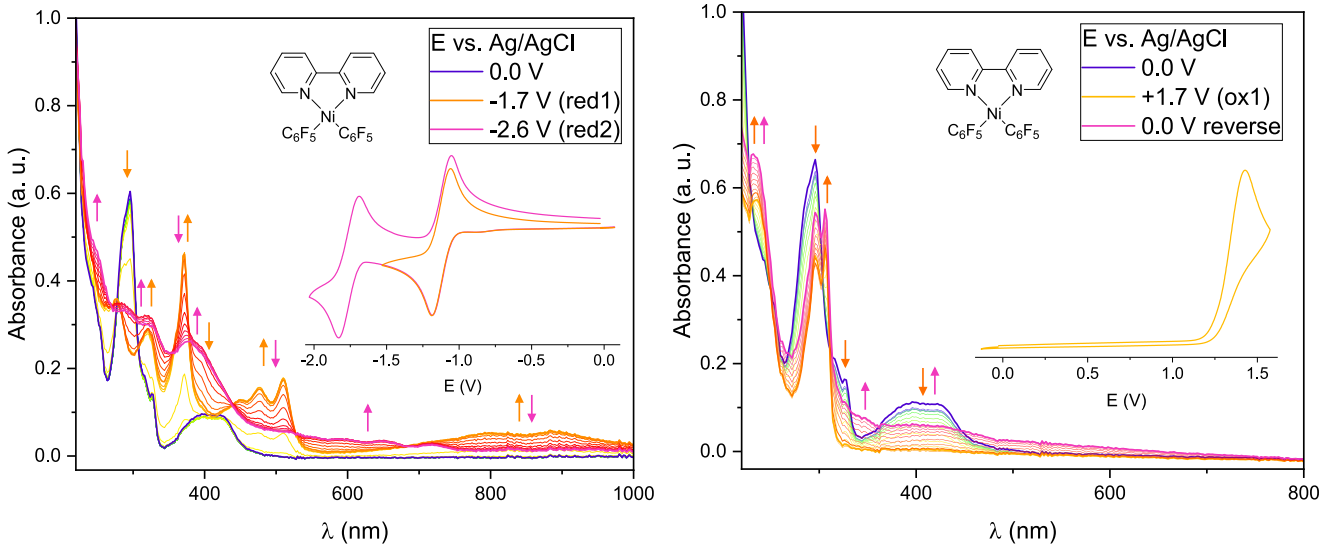

Figure 4. UV−vis-NIR absorption spectra of **1** during cathodic reduction (left) and anodic oxidation (right) in 0.1 M *n*-Bu_4NPF_6/THF solution; inset: noninternally referenced cyclic voltammograms of **1** in THF.

plexes.[21,54−57] The uncoordinated dppz ligand is reported to exhibit a structured photoluminescence, which is concentration-dependent and also relatively weak photoluminescence around 470 nm (quantum yield $\Phi_L \leq 0.02$ depending on solvent and λ_{ex}) from excited $^3\pi-\pi^*$ states that can be easily quenched via photoinduced electron transfer and the presence of water or any other protic solvent.[58] Using transient UV−vis absorption spectroscopy, a quenching process between the excited state and a ground state dppz molecule was identified as the reason for the concentration dependency.[58] For [Ni(Mes)Br(dppz)], very weak photoluminescence was reported and explained in terms of photoluminescence quenching related to stacking of the dppz unit.[21] Compared to the molecular structure in the crystal of [Ni(Mes)Br(dppz)], complex **4** features a larger overlap between the head-to-tail-stacked dppz moieties, likely due to its higher symmetry, at a similar interplanar distance of 3.47 Å ([Ni(Mes)Br(dppz)]: 3.39 Å).[21] In both cases, the atoms of the dppz ligand are staggered with respect to the vertical direction between the stacked molecules. In contrast, they are eclipsed in the crystal structure of dppz·MeCN at an interplanar distance of 3.56 Å.[59] Obviously, coordination to nickel significantly alters the $\pi-\pi$ interaction between the dppz fragments beyond the obvious added geometric constraints. The diminished photoluminescence intensity from $[Ni(X)_2(dppz)]$ complexes may thus be partially attributed to stronger intermolecular interactions between the dppz-centered orbitals. The effect of different organometallic coligands, i.e., Mes versus C_6F_5, is probably small, as the frontier MOs calculated for **4** reveal little coupling between dppz and C_6F_5 orbitals. An indirect effect may involve variations in d orbital levels with electron-rich or electron-poor aryl ligands, affecting both molecular orbital contributions and the HOMO−LUMO gap. Considering the practical absence of photoluminescence from **4** and the weak photoluminescence of [Ni(Mes)Br(dppz)], even a qualitative comparison of quantum yields is not reasonable with respect to experimental uncertainty margins, preventing detailed comparative conclusions on Ni-aryl bonding in the two systems from photoluminescence studies.

UV−vis−NIR and EPR/NMR Spectroelectrochemistry. Of the aromatic diimine-containing complexes, the bpy derivative **1** was studied representatively via UV−vis−NIR and electron paramagnetic resonance (EPR) spectroelectrochemistry[60] as the structurally most simple example. During the first cathodic reduction wave, a very intense band at 300 nm, a pronounced structured band system centered at around 500 nm and a broad long-wavelength band appear in the UV−vis−NIR absorption spectrum (Figure 4), which are very similar to those reported for the organo Ni(II) complexes [Ni(Mes)Br(bpy)] and $[Ni(Mes)_2(bpy)]$[15,50] and for other transition metal-bpy complexes[61−63] but have also been reported for reduced $[Ni(terpy)Ni(Mes)]^n$ species (terpy = 2,2′;6′,2″-terpyridine, $n = 0$ and -1).[64] These bands clearly indicate $\pi^*-\pi^*$ transitions in mono- and doubly reduced bpy. EPR spectroscopy of an electrochemically reduced *n*Bu_4N/THF solution of **1** gave a narrow isotropic signal at $g = 2.0015$ at 293 K (Figure S43, SI). The intrinsically high line width of about 40 G precluded the observation of hyperfine structuring, which has been observed for the $[Ni(Mes)(bpy^-)]^{\bullet-}$ derivative.[15,50] Besides this, all parameters are very similar. Further reduction goes into the bpy π^* singly occupied molecular orbital (SOMO), producing the diamagnetic $[Ni(C_6F_5)(bpy^{2-})]^{2-}$ with the typical UV−vis absorption bands at 230, 400, and 620 nm yet no EPR signal.[15,50] This is completely in line with our assumptions on the cyclic voltammetry (vide supra). Upon oxidation, the long-wavelength absorption vanishes, leaving a broad absorption ranging from 320 to 600 nm. Furthermore, the band at 300 nm corresponding to the transition into the $\pi-\pi^*$ state is shifted to lower energy, becoming more structured (Figure 4 right). The latter strongly supports the formation of uncoordinated bpy.

Furthermore, a sample of compound **1** was chemically oxidized using tris(4-bromophenyl)ammoniumyl hexachloridoantimonate ("magic blue") and the reaction solution was analyzed by ^{19}F NMR spectroscopy. As reported in recent literature for the chemical oxidation of $[Ni(C_6F_5)_2(Tp)]^-$,[34] we found no evidence for a paramagnetic Ni^{III} species, but the C−C coupling product $C_{12}F_{10}$, resulting from oxidatively

https://doi.org/10.1021/acs.inorgchem.4c00649
Inorg. Chem. 2024, 63, 11079−11091

triggered reductive elimination, was quantitatively detected using ^{19}F NMR spectroscopy (Figure S44, SI). This is consistent with the irreversible first oxidation waves observed for all derivatives in CV. After evaporation of the sample from the oxidation experiment, we were able to isolate blue crystals of the composition $[Ni(bpy)_2Cl_2]\cdot SbCl_3\cdot MeCN$ (Figure S45, SI; CCDC 2327966), which is consistent with oxidatively triggered reductive elimination of $F_5C_6-C_6F_5$ from $[Ni^{III}(C_6F_5)_2(bpy)]^{\bullet+}$ producing $[Ni^{I}(bpy)(solv)_2]^+$ followed by disproportionation into Ni(0) and $[Ni(bpy)_2Cl_2]$ (Cl stems from magic blue). $SbCl_3$ probably stems from the reduction of $SbCl_6^-$ by low-valent nickel species. Furthermore, we identified crystals of tris(4-bromophenyl)amine and $C_{12}F_{10}$.

The instantaneous reductive elimination of $C_{12}F_{10}$ from both $[Ni(C_6F_5)_2(bpy)]$ and $[Ni(C_6F_5)_2(Tp)]^-$[34] upon oxidation is interesting when considering the reported relative stability of $[Ni^{III}(C_6F_5)_4]^{\bullet-}$.[33,34] $[Ni^{III}(C_6F_5)_4]^{\bullet-}$ is "reasonably stable" at room temperature allowing for structural and spectroscopic characterization of the complex.[33] While $[Ni^{II}(C_6F_5)_4]^{2-}$ clearly features superior shielding of the Ni−C bonds against hydrolysis, the higher stability of the oxidized species $[Ni^{III}(C_6F_5)_4]^-$ compared with $[Ni^{III}(C_6F_5)_2(N^\wedge N)]^+$ also suggests a promoting effect of the bidentate N^N ligand on reductive elimination from $[Ni^{III}(C_6F_5)_2(N^\wedge N)]^+$. The purely thermally induced Ni^{II}/Ni^0 reductive elimination of $C_{12}F_{10}$ from $Ni(C_6F_5)_2$ complexes can be accelerated significantly through variations of the bidentate ligand,[30,35] which affect the activation energy for the reductive elimination.[31] Conversely, this suggests that the activation barrier for $C_{12}F_{10}$ elimination from $[Ni^{III}(C_6F_5)_4]^-$ is higher than that from $[Ni^{III}(C_6F_5)_2(N^\wedge N)]^+$. Furthermore, regarding the (de)-stabilization of high oxidation states by C_6F_5, the better stabilization of Ni^{III} in $[Ni^{III}(C_6F_5)_4]^-$ than in $[Ni^{III}(C_6F_5)_2(N^\wedge N)]^+$ suggests a higher electron density at the formal Ni^{III} center in the former. This assumption is supported by the crystal structure of $(NBu_4)[Ni^{III}(C_6F_5)_4]$, which features an only slightly distorted square planar coordination environment around nickel and near-identical Ni−C bond lengths compared to $[Ni(C_6F_5)_4]^{2-}$.[33] On the other hand, Menjón et al. nonetheless conclude, based on its magnetic properties, that $[Ni^{III}(C_6F_5)_4]^-$ is an authentic d^7 system with the unpaired electron strongly localized to the metal center.

These ambiguous observations have evoked in recent years an increasingly lively debate in the organometal chemistry community about the interpretation of oxidation states in $M(CF_3)_n$ complexes.[52,65,66] For the C_6F_5 ligand with its dual donor and acceptor character, we interpret our results in terms of a context-dependent donor/acceptor behavior of C_6F_5, meaning that in $[Ni^{II}(C_6F_5)_4]^{2-}$ and $[Ni^{III}(C_6F_5)_4]^-$, the C_6F_5 ligand predominantly shows its strongly σ-donating character, while in the $[Ni(C_6F_5)_2(N^\wedge N)]$ complexes, the π-accepting character is more evident. This observation would also have interesting implications for the design of potential $Ni(C_6F_5)_n$-based triplet emitters in the future in terms of tuning excited state character and ligand field engineering.

CONCLUSIONS

The structural, electrochemical, and optical properties of six $[Ni(C_6F_5)_2(N^\wedge N)]$ (N^N = bpy, tmphen, 2,9-dmphen, dppz, *i*Pr-DAB, Xyl-DAB) derivatives were studied to probe the character of the C_6F_5 ligand. $[Ni(C_6F_5)_2(2,9\text{-dmphen})]$ shows significant deviations from an ideal square-planar geometry in contrast to the planar geometries found for the other complexes. Its umbrella-like distortion correlates with lower stability against hydrolysis of the complex in solution. Decomposition by reductive elimination was exemplarily shown to proceed rapidly in the case of $[Ni(C_6F_5)_2(bpy)]$ upon chemical oxidation, which is consistent with the irreversible oxidation processes observed for all complexes via cyclic voltammetry. In agreement with results reported for $[Ni(C_6F_5)_2(tris(pyrazolyl)borate)]$, we conclude that the $Ni(C_6F_5)_2$ platform is less suited for stabilizing Ni^{III} compared with the homoleptic species $[Ni^{III}(C_6F_5)_4]^-$, which is reported to be fairly stable. However, we are optimistic that specific chelate ligands might facilitate the isolation of relatively stable $[Ni^{III}(C_6F_5)_2(L)]^n$ or even $[Ni^{III}(C_6F_5)_3(L)]$ (L = neutral or anionic ligands) complexes in the future, as the dominant characteristics of the C_6F_5 ligand seem to be strongly depending on the context, which is the combination of the number of C_6F_5 ligands and number and character of the ligands, as suggested by our study. Furthermore, designing suitable combinations of C_6F_5 and new electron-accepting ligands may contribute to the further optimization of nickel-based perfluoroarylation catalysis. Our $Ni(C_6F_5)_2$ complexes were able to store up to 2 electrons in the N^N ligands in quite stable complex species $[Ni(C_6F_5)_2(N^\wedge N)]^{2-}$.

In this study, significant photoluminescence was only observed for $[Ni(C_6F_5)_2(tmphen)]$ and $[Ni(C_6F_5)_2(2,9\text{-dmphen})]$ at 77 K among the chromophore-containing complexes, with photoluminescence quantum yields Φ_L below 0.02. We attribute the overall rather poor performance to efficient quenching related to intermolecular $\pi_L-\pi_L^*$ interactions, especially in the dppz derivative as well as to the low rigidity of the coordination environment. Additionally, we found that the distorted geometry of the 2,9-dmphen derivative significantly reduces the ligand field splitting compared to the nondistorted complexes, likely counteracting the potentially beneficial effect of increased rigidity through steric hindrance on the photoluminescence. These insights suggest that with a thoughtful combination of C_6F_5 ligands and bulky and/or rigid L or N^N ligands, $Ni(C_6F_5)_n$ could serve as a promising platform for developing future triplet-emitting systems.

EXPERIMENTAL SECTION

Materials and General Information. C_6F_5Br, tmphen, and TMS-C_6F_5 were purchased from Aldrich and used without further purification. AgF was purchased from Acros or TCI. $NiBr_2$ was purchased from BLDpharm and used for the preparation of $[NiBr_2(dme)]$ following a reported procedure.[67] Xyl-DAB,[68] *i*Pr-DAB,[69] and dppz[70] were prepared following reported procedures. Solvents were degassed over three freeze−pump−thaw cycles and dried over activated molecular sieves. All reactions involving metal complexes were conducted under argon using standard Schlenk techniques.

Preparation of *cis*-$[Ni(C_6F_5)_2(MeCN)_2]$. *cis*-$[Ni(C_6F_5)_2(MeCN)_2]$ was prepared using a modified procedure from recent literature,[35] which we adapted as follows to avoid the explosive LiC_6F_5:[71] AgF (1.9 equiv) at ambient temperature and TMS-C_6F_5 (2.0 equiv) were reacted in MeCN under exclusion of light for 2 h at room temperature. To the thus-prepared AgC_6F_5 solution, a solution of $[NiBr_2(dme)]$ (1.0 equiv) in MeCN was added and the reaction mixture was stirred in the dark for 24 h. The yellowish-gray suspension was filtered through Celite and concentrated until $[Ni(C_6F_5)_2(MeCN)_2]$ precipitated as a yellow solid, which was washed with *n*-pentane and dried. More $[Ni(C_6F_5)_2(MeCN)_2]$ crystallized from the remaining solution at −20 °C. Isolated yields

https://doi.org/10.1021/acs.inorgchem.4c00649
Inorg. Chem. 2024, 63, 11079−11091

ranged from 24 to 31% in different batches; more material can in principle be extracted from the mother liquor. The success of the synthesis depends strongly on the quality of the used AgF. ^{1}H NMR (300 MHz, MeCN-d_3): δ (ppm) = 1.96 (s, 6H, CH_3). ^{19}F NMR (282 MHz, MeCN-d_3): δ (ppm) = −120.0 (m, 4F, *o*-F,), −164.3 (t, 2F, J = 19.1 Hz, *p*-F), −167.2 (m, 4F, *m*-F). Structural data of [Ni(C_6F_5)$_2$(MeCN)$_2$] from *sc*-XRD can be found in the SI.

Synthesis of the Complexes 1−6. 1.0 equiv *cis*-[Ni(C_6F_5)$_2$(MeCN)$_2$] was dissolved in MeCN and added to a solution of 1.0 equiv of the α-diimine ligand in CH_2Cl_2. After stirring at room temperature until full consumption of [Ni(C_6F_5)$_2$(MeCN)$_2$] is observed via ^{19}F NMR (generally within 2 h), the volume of the reaction solution is reduced to 5−10 mL. In case precipitates are formed, these are removed before cooling the product-containing solutions to −20 °C to crystallize the target complexes. The complexes were washed twice with *n*-pentane and dried under high vacuum.

1 [Ni(C_6F_5)$_2$(bpy)]. From 27.1 mg (0.057 mmol) [Ni(C_6F_5)$_2$(MeCN)$_2$] and 8.9 mg (0.057 mmol) bpy. Yield: 27.2 mg (0.050 mmol, 87%) dark yellow solid. Elemental analysis ($C_{22}H_8F_{10}N_2Ni$, 549.00 g/mol), found (calculated): C, 48.08 (48.13); H, 1.47 (1.47); N, 5.07 (5.10)%. ^{1}H NMR (300 MHz, CD_2Cl_2): δ (ppm) = 8.05 (m, 4H, H-2 and H-4), 7.54 (d, 2H, J = 5.48 Hz, H-1), 7.36 (m, 2H, H-3). ^{19}F NMR (282 MHz, CD_2Cl_2): δ (ppm) = −118.3 (m, 4F, *o*-F,), −162.2 (t, 2F, J = 19.1 Hz, *p*-F), −165.0 (m, 4F, *m*-F).

2 [Ni(C_6F_5)$_2$(tmphen)]. From 62.7 mg (0.132 mmol) [Ni(C_6F_5)$_2$(MeCN)$_2$] and 31.2 mg (0.132 mmol) tmphen. Yield: 71.1 mg (0.113 mmol, 86%) light yellow solid. Single crystals for sc-XRD were grown through slow diffusion of *n*-pentane into a concentrated solution in $CHCl_3$. Elemental analysis ($C_{28}H_{16}F_{10}N_2Ni$, 629.13 g/mol), found (calculated): C, 53.48 (53.46); H, 2.54 (2.56); N, 4.45 (4.45)%. ^{1}H NMR (300 MHz, CD_2Cl_2): δ (ppm) = 8.12 (s, 2H, H-1), 7.49 (s, 2H, H-2), 2.70 (s, 6H, H-3), 2.38 (s, 6H, H-4). ^{19}F NMR (282 MHz, CD_2Cl_2): δ (ppm) = −118.1 (m, 4F, *o*-F,), −162.5 (t, 2F, J = 19.7 Hz, *p*-F), −165.2 (m, 4F, *m*-F).

3 [Ni(C_6F_5)$_2$(2,9-dmphen)]. From 64.5 mg (0.136 mmol) [Ni(C_6F_5)$_2$(MeCN)$_2$] and 28.3 mg (0.136 mmol) 2,9-dmphen. Yield: 71.8 mg (0.119 mmol, 88%) yellow solid. Single crystals for sc-XRD were obtained from a concentrated MeCN solution at −20 °C. Elemental analysis ($C_{26}H_{12}F_{10}N_2Ni$, 601.07 g/mol) found (calculated): C, 51.95 (51.95); H, 1.99 (2.01); N, 4.61 (4.66)%. ^{1}H NMR (300 MHz, CD_2Cl_2): δ (ppm) = 8.34 (d, J = 8.6 Hz, 2H, H-1), 7.92 (s, 2H, H-3), 7.41 (d, J = 8.6 Hz, 2H, H-2), 2.19 (s, 6H, H-4). ^{19}F NMR (282 MHz, CD_2Cl_2): δ (ppm) = −118.5 (m, 4F, *o*-F,), −163.2 (t, 2F, J = 19.8 Hz, *p*-F), −165.9 (m, 4F, *m*-F).

4 [Ni(C_6F_5)$_2$(dppz)]. 78.0 mg (0.164 mmol) [Ni(C_6F_5)$_2$(MeCN)$_2$], 46.3 mg (0.164 mmol) dppz; yield: 75.0 mg (0.111 mmol, 68%) orange solid. Single crystals for sc-XRD were grown through slow diffusion of *n*-pentane into a concentrated solution in $CHCl_3$. Elemental analysis ($C_{30}H_{10}F_{10}N_2Ni$, 675.12 g/mol), found (calculated): C, 53.33 (53.37); H, 1.48 (1.49); N, 8.29 (8.30)%. ^{1}H NMR (300 MHz, CD_2Cl_2) δ (ppm) = 9.51 (d, J = 7.9 Hz, 2H, H-1), 9.10 (m, 2H, H-4), 8.25 (dd, J = 6.3, 3.7 Hz, 2H, H-5), 7.85 (dd, J = 6.4, 3.4 Hz, 2H, H-2), 7.69 (dd, J = 7.9, 3.2 Hz, 2H, H-3). ^{19}F NMR (282 MHz, CD_2Cl_2): δ (ppm) = −118.2 (m, 4F, *o*-F,), −161.9 (t, 2F, J = 19.4 Hz, *p*-F), −164.8 (m, 4F, *m*-F). ^{1}H NMR (300 MHz, acetone-d_6): δ (ppm) = 9.83 (dd, J = 8.1, 1.5 Hz, 2H, H-1), 8.50 (dd, J = 6.5, 3.4 Hz, 2H, H-4), 8.19 (dd, J = 6.6, 3.4 Hz, 2H, H-5), 8.15 (dd, J = 5.3, 1.5 Hz, 2H, H-2), 8.11 (dd, J = 8.1, 5.3 Hz, 2H, H-3). ^{19}F NMR (282 MHz, acetone-d_6): δ (ppm) = −117.8 (m, 4F, *o*-F,), −163.3 (t, 2F, J = 19.4 Hz, *p*-F), −165.9 (m, 4F, *m*-F).

5 [Ni(C_6F_5)$_2$(*i*Pr-DAB)]. From 40.0 mg (0.084 mmol) [Ni(C_6F_5)$_2$(MeCN)$_2$] and 11.8 mg (0.084 mmol) *i*Pr-DAB. Yield: 33.2 mg (0.062 mmol, 74%) dark red solid. Single crystals for sc-XRD were obtained from concentrated acetone or MeCN solutions. Elemental analysis ($C_{20}H_{16}F_{10}N_2Ni$, 533.04 g/mol), found (calculated): C, 45.08 (45.07); H, 3.07 (3.03); N, 5.27 (5.26)%. ^{1}H NMR (300 MHz, CD_2Cl_2): δ (ppm) = 7.99 (s, 2H, H_{imine}), 3.27 (hept, 2H, J = 6.5 Hz, CH_{iPr}), 1.18 (d, 12H, J = 6.5 Hz, CH_{3iPr}). ^{19}F NMR (300 MHz, CD_2Cl_2): δ (ppm) = −118.5 (m, 4F, *o*-F,), −162.1 (t, 2F, J = 19.7 Hz, *p*-F), −165.0 (m, 4F, *m*-F).

6 [Ni(C_6F_5)$_2$(Xyl-DAB)]. From 36.0 mg (0.076 mmol) [Ni(C_6F_5)$_2$(MeCN)$_2$] and 20.1 mg (0.076 mmol) Xyl-DAB. Yield: 45.2 mg (0.076 mmol, 90%) purple solid. Single crystals for sc-XRD were grown through slow evaporation of a solution in EtOAc/*n*-heptane. Elemental analysis ($C_{30}H_{20}F_{10}N_2Ni$, 657.18 g/mol), found (calculated): C, 54.88 (54.83); H, 3.17 (3.07); N, 4.23 (4.26)%. ^{1}H NMR (300 MHz, CD_2Cl_2): δ (ppm) = 8.23 (s, 2H, H_{imine}), 7.05−6.94 (m, 6H, H_{Xyl}), 2.44 (s, 12H, CH_{3Xyl}). ^{19}F NMR (376.50 MHz, CD_2Cl_2): δ (ppm) = −117.2 (m, 4F, *o*-F), −162.6 (t, 2F, J = 19.7 Hz, *p*-F), −165.9 (m, 4F, *m*-F).

Chemical Oxidation of Complex 1. 55 mg (0.1 mmol, 1 equiv) **1** and 82 mg (0.1 mmol, 1 equiv) tris(4-bromophenyl)ammoniumyl hexachloridoantimonate ("magic blue") were reacted in a mixture of 4.9 mL MeCN-d_3 and 0.1 mL of a $PhCF_3$/MeCN stock solution (c($PhCF_3$) = 0.8 M). The reaction solution was analyzed via ^{19}F NMR immediately upon mixing of the reagents and once more after 9 h.

Instrumentation and Software. Elemental analysis was obtained using a HEKAtech CHNS EuroEA 3000 analyzer. The NMR spectra were recorded on a Bruker Avance II 300 (^{1}H: 300, ^{13}C: 75, ^{19}F: 282 MHz), Bruker Avance 400 (^{1}H: 400.13, ^{13}C: 100.61, ^{19}F: 376.50 MHz), Bruker Avance III 499 (^{1}H: 500, ^{13}C: 125, ^{19}F: 470 MHz), or Bruker Avance III 500 (^{1}H: 500, ^{13}C: 125, ^{19}F: 470 MHz) spectrometer. Chemical shifts were referenced to $SiMe_4$ (^{1}H, 0 ppm) and $PhCF_3$ (^{19}F, −63.7 ppm) as internal standards unless otherwise specified. Numbering schemes for the assignments of ^{1}H NMR signals of the complexes are shown in Figure S19, SI.

X-ray diffraction measurements on single crystals were performed on a Bruker D8 Venture diffractometer including a Bruker Photon 100 CMOS detector using Ag K_α (λ = 0.56086 Å) or Mo Kα (λ = 0.71073 Å) radiation. The crystal data was collected using APEX4 v2021.10-0.[72] The structures were solved by dual space methods using SHELXT, and the refinement was carried out with SHELXL employing the full-matrix least-squares methods on $F_O^2 < 2\sigma(F_O^2)$, as implemented in ShelXle.[73−75] The non-hydrogen atoms were refined with anisotropic displacement parameters without any constraints. The hydrogen atoms were included by using appropriate riding models.

The UV−vis−NIR absorption spectra were recorded on Varian Cary 05E, Cary50 Scan, or Cary60 spectrophotometers. Cyclic voltammetry was carried out at a 100 mV/s scan rate in 0.1 M nBu$_4$NPF$_6$ solutions using a three-electrode configuration (glassy carbon working electrode, Pt counter electrode, Ag/AgCl reference) and a Metrohm Autolab PG STAT 30 potentiostat with ferrocene/ferrocenium as internal reference. Spectroelectrochemical measurements (in 0.1 M n-Bu$_4$NPF$_6$ solutions) were performed using an optically transparent thin-layer electrode (OTTLE) cell at ambient temperature[76] for the UV−vis−NIR absorption spectra and a two-electrode capillary for EPR studies. The EPR spectra were recorded in the X band on a Bruker System ELEXSYS 500E, with a Bruker Variable Temperature Unit ER 4131VT (500−100 K). g values were calibrated using a dpph sample.

The photoluminescence spectra were recorded with a Spex FluoroMax-3 spectrometer. A PicoQuant Fluo-Time 300 spectrometer was used for obtaining the emission spectra and for lifetime measurements at low temperature (for the complete description, see ref 77). Lifetime analysis was performed using the commercial FluoFit software. The quality of the fit was assessed by minimizing the reduced χ^2 function. Photoluminescence quantum yields were determined with a Hamamatsu Photonics absolute photoluminescence quantum yield measurement system (C9920-02), equipped with a L9799-01 CW Xenon light source, monochromator, photonic multichannel analyzer, and integrating sphere. An uncertainty of ±5% for the photoluminescence quantum yield Φ_L is estimated. Degassed spectroscopic grade solvents were used.

Computational Details. All DFT calculations were performed using ORCA 5.0.2.[78,79] For all atoms, def2-TZVP basis sets were used.[80] The geometry of all compounds was optimized at the BP86

https://doi.org/10.1021/acs.inorgchem.4c00649
Inorg. Chem. 2024, 63, 11079−11091

level of theory, using Grimme's D3 dispersion correction and the conductor-like polarizable continuum model (CPCM) parametrized for THF as an approximate solvation model.[81−86] The geometry optimization results were followed up with numerical frequency calculations in order to confirm the energetic minimum nature of the optimized structure, as indicated by the absence of imaginary modes. On the optimized geometries, single-point and TD-DFT calculations were performed using the TPSSh functional, Grimme's D3 dispersion correction, and CPCM parametrized for THF.[87] Orbital isosurfaces were extracted from the single-point calculations using the ORCA module orca_plot and plotted with the visualization software CHEMCRAFT at a contour value of 0.04.[88] For the TD-DFT calculations of the absorption spectra, 40 roots (transitions) for singlets and triplets each were included for each complex. The broadened spectra were obtained using the orca_mapspc module with 2000 cm^{-1} full width at half-maximum band broadening.

■ ASSOCIATED CONTENT

Supporting Information

The Supporting Information is available free of charge at https://pubs.acs.org/doi/10.1021/acs.inorgchem.4c00649.

^{1}H and ^{19}F NMR spectra, additional structural information, electrochemical plots and data, experimental and TD-DFT-calculated UV−vis absorption spectra of complexes **1** to **6**, along with DFT-calculated MO landscapes of **5** and **6**, photoluminescence spectra of **2** and **3**, the EPR spectrum of $\mathbf{1}^{\bullet-}$, and the crystal structure of $[Ni(bpy)_2Cl_2]\cdot SbCl_3\cdot MeCN$ are provided (PDF)

DFT calculated structures of complexes **1**−**6** (ZIP)

Ni C_6F_5 dppz squeeze_checkcif_new (PDF)

Accession Codes

CCDC 2262015 (for $[Ni(C_6F_5)_2(MeCN)_2]\cdot$solv), 2171187 (**1**), 2253625 (**2**), 2327972 (**3**), 2259509 (**4**), 2259505 (**5**), 2279587 (**6**), and 2327966 ($[Ni(bpy)_2Cl_2]\cdot SbCl_3\cdot MeCN$) contain the supplementary crystallographic data for this paper. These data can be obtained free of charge via www.ccdc.cam.ac.uk/data_request/cif, or by emailing data_request@ccdc.cam.ac.uk, or by contacting The Cambridge Crystallographic Data Centre, 12 Union Road, Cambridge CB2 1EZ, UK; fax: + 44 1223 336033.

■ AUTHOR INFORMATION

Corresponding Authors

Rose Jordan − *Department of Chemistry and Biochemistry, Institute for Inorganic Chemistry, University of Cologne, Faculty for Mathematics and Natural Sciences, D-50939 Köln, Germany*; Email: rose.jordan@uni-koeln.de

Cristian A. Strassert − *Institut für Anorganische und Analytische Chemie, Universität Münster, 48149 Münster, Germany; CeNTech, CiMIC, SoN, 48149 Münster, Germany*; Email: cstra_01@uni-muenster.de

Axel Klein − *Department of Chemistry and Biochemistry, Institute for Inorganic Chemistry, University of Cologne, Faculty for Mathematics and Natural Sciences, D-50939 Köln, Germany*; orcid.org/0000-0003-0093-9619; Email: axel.klein@uni-koeln.de

Authors

Sascha A. Schäfer − *Department of Chemistry and Biochemistry, Institute for Inorganic Chemistry, University of Cologne, Faculty for Mathematics and Natural Sciences, D-50939 Köln, Germany*

Noah Sander − *Department of Chemistry and Biochemistry, Institute for Inorganic Chemistry, University of Cologne, Faculty for Mathematics and Natural Sciences, D-50939 Köln, Germany*

Ivan Maisuls − *Institut für Anorganische und Analytische Chemie, Universität Münster, 48149 Münster, Germany; CeNTech, CiMIC, SoN, 48149 Münster, Germany*

Claudia Hamacher − *Department of Chemistry and Biochemistry, Institute for Inorganic Chemistry, University of Cologne, Faculty for Mathematics and Natural Sciences, D-50939 Köln, Germany*

Joshua Friedel − *Department of Chemistry and Biochemistry, Institute for Inorganic Chemistry, University of Cologne, Faculty for Mathematics and Natural Sciences, D-50939 Köln, Germany*; orcid.org/0000-0001-6215-7271

Complete contact information is available at: https://pubs.acs.org/10.1021/acs.inorgchem.4c00649

Author Contributions

R.J. prepared and characterized *cis*-$[Ni(C_6F_5)_2(MeCN)_2]$ and the complexes **1**−**6**, solved and refined the crystal structures of *cis*-$[Ni(C_6F_5)_2(MeCN)_2]\cdot$solv, $[Ni(C_6F_5)_2(tmphen)]$, $[Ni(C_6F_5)_2(2,9\text{-dmphen})]$, $[Ni(C_6F_5)_2(dppz)]\cdot$solv, and $[Ni(C_6F_5)_2(Xyl\text{-}DAB)]$, performed the DFT calculations, and provided all figures. S.A.S. solved and refined the crystal structure of $[Ni(C_6F_5)_2(bpy)].0.5CH_2Cl_2$. N.S. reproduced selected compounds and experiments. I.M. and J.F. performed photoluminescence spectroscopy. C.H. carried out initial preparative work and contributed to the crystal structure of $[Ni(C_6F_5)_2(i\text{Pr-}DAB)]$. R.J. and A.K. wrote the original draft, and R.J., I.M., C.A.S., and A.K. revised the manuscript. All authors agreed with the final version.

Notes

The authors declare no competing financial interest.

■ ACKNOWLEDGMENTS

We thank the Deutsche Forschungsgemeinschaft [DFG Priority Programme 2102 "Light-controlled Reactivity of Metal Complexes", STR 1186/6-1 and 6-2 (C.A.S.) and KL1194/16-1 and 16-2 (A.K.)] and the Studienstiftung des Deutschen Volkes (R.J.) for funding. C.A.S. gratefully acknowledges the generous financial support for the acquisition of an "Integrated Confocal Luminescence Spectrometer with Spatiotemporal Resolution and Multiphoton Excitation" (DFG/Land NRW: INST 211/915-1 FUGG; DFG EXC1003: "Berufungsmittel"). We thank the late André Uthe for assistance with EPR measurements, Christopher Wallerius and Elisabeth Pankert for attempting photoluminescence spectroscopy in PMMA films as well as our students Vladimir Stojadinovic, Jan Koll, and Rebecca Maier (all University of Cologne, Department of Chemistry and Biochemistry) for assistance in the lab. Jaime Ponce-de-León and Pablo Espinet, Universidad de Valladolid, are acknowledged for a fruitful discussion on $[Ni(C_6F_5)_2(solv)_2]$ precursor complexes.

■ REFERENCES

(1) Goldfogel, M. J.; Huang, L.; Weix, D. J. Cross-Electrophile Coupling: Principles and New Reactions. In *Nickel Catalysis in Organic Synthesis − Methods and Reactions*; Ogishi, S., Ed.; Wiley/VCH: Weinheim, 2019; pp 183−222.

(2) Pawlak, M.; Drzezdzon, J.; Jacewicz, D. The greener side of polymers in the light of d-block metal complexes as Precatalysts. *Coord. Chem. Rev.* **2023**, *484*, No. 215122.

(3) Zhang, R.; Gao, R.; Gou, Q.; Lai, J.; Li, X. Recent Advances in the Copolymerization of Ethylene with Polar Comonomers by Nickel Catalysts. *Polymers* **2022**, *14*, 3809.
(4) Lee, B. C.; Liu, C.-F.; Lin, L. Q. H.; Yap, K. Z.; Song, N. X.; Ko, C. H. M.; Chan, P. H.; Koh, M. J. N-Heterocyclic carbenes as privileged ligands for nickel-catalysed alkene functionalization. *Chem. Soc. Rev.* **2023**, *52*, 2946−2991.
(5) Diccianni, J.; Lin, Q.; Diao, T. Mechanisms of Nickel-Catalyzed Coupling Reactions and Applications in Alkene Functionalization. *Acc. Chem. Res.* **2020**, *53*, 906−919.
(6) Kranthikumar, R. Recent Advances in $C(sp^3)-C(sp^3)$ Cross-Coupling Chemistry: A Dominant Performance of Nickel Catalysts. *Organometallics* **2022**, *41*, 667−679.
(7) Yi, L.; Ji, T.; Chen, K.-Q.; Chen, X.-Y.; Rueping, M. Nickel-Catalyzed Reductive Cross-Couplings: New Opportunities for Carbon−Carbon Bond Formations through Photochemistry and Electrochemistry. *CCS Chem.* **2022**, *4*, 9−30.
(8) Zhu, C.; Yue, H.; Jia, J.; Rueping, M. Nickel-Catalyzed C-Heteroatom Cross-Coupling Reactions under Mild Conditions via Facilitated Reductive Elimination. *Angew. Chem., Int. Ed.* **2021**, *60*, 17810−17831.
(9) Gafurov, Z. N.; Kagilev, A. A.; Kantyukov, A. O.; Sinyashin, O. G.; Yakhvarov, D. G. The role of organonickel reagents in organophosphorus chemistry. *Coord. Chem. Rev.* **2021**, *438*, No. 213889.
(10) Wenger, O. S. Photoactive Nickel Complexes in Cross-Coupling Catalysis. *Chem. − Eur. J.* **2021**, *27*, 2270−2278.
(11) Sondermann, C.; Pižl, M.; Paretzki, A.; Feil, C.; Ringenberg, M. R.; Záliš, S.; Kaim, W. Analysis of a Diimine-Organonickel Redox Series. *Eur. J. Inorg. Chem.* **2020**, *2020*, 3010−3015.
(12) Dudkina, Yu. B.; Fayzullin, R. R.; Lyssenko, K. A.; Gubaidullin, A. T.; Kholin, K. V.; Levitskaya, A. I.; Balakina, M. Yu.; Budnikova, Yu. H. Cyclometalated Nickel Complexes as Key Intermediates in $C(sp^2)-H$ Bond Functionalization: Synthesis, Catalysis, Electrochemical Properties, and DFT Calculations. *Organometallics* **2019**, *38*, 1254−1263.
(13) Yakhvarov, D. G.; Khusnuriyalova, A. F.; Sinyashin, O. G. Electrochemical Synthesis and Properties of Organonickel σ-Complexes. *Organometallics* **2014**, *33*, 4574−4589.
(14) Klein, A.; Budnikova, Y. H.; Sinyashin, O. G. Electron transfer in organonickel complexes of a-diimines: Versatile redox catalysts for C−C or C−P coupling reactions − A review. *J. Organomet. Chem.* **2007**, *692*, 3156−3167.
(15) Klein, A.; Kaiser, A.; Sarkar, B.; Wanner, M.; Fiedler, J. The Electrochemical Behaviour of Organonickel Complexes: Mono-, Di- and Trivalent Nickel. *Eur. J. Inorg. Chem.* **2007**, *2007*, 965−976.
(16) Yao, Y.; Ran, G.; Hou, C.-L.; Zhang, R.; Mangel, D. N.; Yang, Z.-S.; Zhu, M.; Zhang, W.; Zhang, J.; Sessler, J. L.; Gao, S.; Zhang, J.-L. Nonaromatic Organonickel(II) Phototheranostics. *J. Am. Chem. Soc.* **2022**, *144*, 7346−7356.
(17) Wegeberg, C.; Wenger, O. S. Luminescent First-Row Transition Metal Complexes. *JACS Au* **2021**, *1*, 1860−1876.
(18) Kurz, H.; Schötz, K.; Papadopoulos, I.; Heinemann, F. W.; Maid, H.; Guldi, D. M.; Köhler, A.; Hörner, G.; Weber, B. A Fluorescence-Detected Coordination-Induced Spin State Switch. *J. Am. Chem. Soc.* **2021**, *143*, 3466−3480.
(19) Wong, Y.-S.; Tang, M.-C.; Ng, M.; Yam, V. W.-W. Toward the Design of Phosphorescent Emitters of Cyclometalated Earth-Abundant Nickel(II) and Their Supramolecular Study. *J. Am. Chem. Soc.* **2020**, *142*, 7638−7646.
(20) Cope, J. D.; Denny, J. A.; Lamb, R. W.; McNamara, L. E.; Hammer, N. I.; Webster, C. E.; Hollis, T. K. Synthesis, Characterization, Photophysics, and a Ligand Rearrangement of CCC-NHC Pincer Nickel Complexes: Colors, Polymorphs, Emission, and Raman Spectra. *J. Organomet. Chem.* **2017**, *845*, 258−265.
(21) Klein, A.; Hurkes, N.; Kaiser, A.; Wielandt, W. π-Stacking Modulates the Luminescence of [(dppz)Ni(Mes)Br] (dppz = dipyrido[3,2-*a*:2′,3′-*c*]phenazine, Mes = 2,4,6-trimethylphenyl). *Z. Anorg. Allg. Chem.* **2007**, *633*, 1659−1665.
(22) Goodman, B. A.; Raynor, J. B. Electron Spin Resonance of Transition Metal Complexes. *Adv. Inorg. Chem. Radiochem.* **1970**, *13*, 135−361.
(23) Dunn, T. M. Spin-orbit coupling in the first and second transition series. *Trans. Faraday Soc.* **1961**, *57*, 1441−1444.
(24) Herberger, J.; Winter, R. F. Platinum emitters with dye-based σ-aryl ligands. *Coord. Chem. Rev.* **2019**, *400*, No. 213048.
(25) Cookson, P. G.; Deacon, G. B. Preparations of organonickel compounds by thermal decomposition of nickel carboxylates. *Aust. J. Chem.* **1972**, *25*, 2095−2105.
(26) Arcas, A.; Royo, P. Bispentafluorophenyl nickel(II) complexes. *Inorg. Chim. Acta* **1978**, *30*, 205−207.
(27) Arcas, A.; Royo, P. New bispentafluorophenyl nickel(II) complexes. *Inorg. Chim. Acta* **1978**, *31*, 97−99.
(28) Sánchez, G.; Ruiz, F.; Garcia, J.; Ramírez de Arellano, M. C.; López, G. Organonickel(II) Complexes with Anionic N-Donor Ligands. Hydration of coordinated nitriles at a nickel(II) site. *Helv. Chim. Acta* **1997**, *80*, 2477−2485.
(29) Sánchez, G.; Serrano, J. L.; Ruiz, F.; López, G. Bis-(pentafluorophenyl) nickel(II) complexes with α-diimines and iminophosphines. *J. Fluorine Chem.* **1998**, *91*, 165−169.
(30) (a) Yamamoto, T.; Abla, M. Reductive elimination of Et−Et from $NiEt_2$(bpy) promoted by electron-accepting aromatic compounds. *J. Organomet. Chem.* **1997**, *535*, 209−211. (b) Yamamoto, T.; Abla, M.; Murakami, Y. Promotion of Reductive Elimination Reaction of Diorgano(2,2′-bipyridyl)nickel(II) Complexes by Electron-Accepting Aromatic Compounds, Lewis Acids, and Brønsted Acids. *Bull. Chem. Soc. Jpn.* **2002**, *75*, 1997−2009.
(31) Forniés, J.; Martín, A.; Martín, L. F.; Menjón, B.; Kalamarides, H. A.; Rhodes, L. F.; Day, C. S.; Day, V. W. Synthesis and Characterization of a New Family of Square-Planar Nickel(II) Carbonyl Derivatives. *Chem. − Eur. J.* **2002**, *8*, 4925−4934.
(32) Sánchez, G.; García, J.; Meseguer, D.; Serrano, J. L.; García, L.; Pérez, J.; López, G. New pentafluorophenyl complexes with phosphine-amide ligands. *Inorg. Chim. Acta* **2006**, *359*, 1650−1658.
(33) Alonso, P. J.; Arauzo, A. B.; García-Monforte, M. A.; Martín, A.; Menjón, B.; Conrado Rillo, C.; Tomás, M. Homoleptic Organo-derivatives of High-Valent Nickel(III). *Chem. − Eur. J.* **2009**, *15*, 11020−11030.
(34) Bour, J. R.; Camasso, N. M.; Meucci, E. A.; Kampf, J. W.; Canty, A. J.; Sanford, M. S. Carbon−Carbon Bond-Forming Reductive Elimination from Isolated Nickel(III) Complexes. *J. Am. Chem. Soc.* **2016**, *138*, 16105−16111.
(35) Ponce-de-León, J.; Gioria, E.; Martínez-Ilarduya, J. M.; Espinet, P. Ranking Ligands by Their Ability to Ease $(C_6F_5)_2Ni^{II}L \rightarrow Ni^0L + (C_6F_5)_2$ Coupling versus Hydrolysis: Outstanding Activity of PEWO Ligands. *Inorg. Chem.* **2020**, *59*, 18287−18294.
(36) Ponce-de-León, J.; Espinet, P. Selective synthesis of fluorinated biaryls by [MCl_2(PhPEWO-F)] (M = Ni, Pd) catalysed Negishi cross-coupling. *Chem. Commun.* **2021**, *57*, 10875−10878.
(37) Burgoon, H.; Cyrus, C.; Skilskyj, D.; Thoresen, J.; Ebner, C.; Meyer, G. A.; Filson, P.; Rhodes, L. F.; Backlund, T.; Meneau, A.; Cull, T.; Afonina, I. Photopatterning of Low Dielectric Constant Cycloolefin Polymers Using Azides and Diazirines. *ACS Appl. Polym. Mater.* **2020**, *2*, 1819−1826.
(38) Pérez-Ortega, I.; Albéniz, A. C. A different polynorbornene backbone by combination of two polymer growth pathways: vinylic addition and ring opening via β-C elimination. *Chem. Sci.* **2022**, *13*, 1823−1828.
(39) Clot, E.; Mégret, C.; Eisenstein, O.; Perutz, R. N. Exceptional Sensitivity of Metal−Aryl Bond Energies to ortho-Fluorine Substituents: Influence of the Metal, the Coordination Sphere, and the Spectator Ligands on M−C/H−C Bond Energy Correlations. *J. Am. Chem. Soc.* **2009**, *131*, 7817−7827.
(40) Tanabe, T.; Brennessel, W. W.; Clot, E.; Eisenstein, O.; Jones, W. D. Synthesis, structure, and reductive elimination in the series $Tp'Rh(PR_3)(Ar^F)H$; Determination of rhodium−carbon bond energies of fluoroaryl substituents. *Dalton Trans.* **2010**, *39*, 10495−10509.

https://doi.org/10.1021/acs.inorgchem.4c00649
Inorg. Chem. 2024, 63, 11079−11091

(41) Casas, J. M.; Forniés, J.; Martín, A.; Orera, V. M.; Orpen, A. G.; Rueda, A. J. Synthesis, Structural Characterization, and Spectroscopic Studies of Heterodimetallic $[NBu_4][(C_6F_5)_3Pt(\mu\text{-}Pb)(\mu\text{-}X)Pt(C_6F_5)_3]$ (X = Cl, OH) Complexes. *Inorg. Chem.* **1995**, *34*, 6514−6519.
(42) López-de-Luzuriaga, J. M.; Monge, M.; Olmos, M. E.; Rodríguez-Castillo, M.; Soldevilla, I.; Sundholm, D.; Valiev, R. R. Perhalophenyl Three-Coordinate Gold(I) Complexes as TADF Emitters: A Photophysical Study from Experimental and Computational Viewpoints. *Inorg. Chem.* **2020**, *59*, 14236−14244.
(43) Casas, J. M.; Diosdado, B. E.; Falvello, L. R.; Forniés, J.; Martín, A.; Rueda, A. J. Hydrogen-bond mediation of supramolecular aggregation in neutral bis-(C_6F_5)Pt complexes with aromatic H-bond donating ligands. A synthetic and structural study. *Dalton Trans.* **2004**, 2733−2740.
(44) Day, C. S.; Ton, S. J.; McGuire, R. T.; Foroutan-Nejad, C.; Martin, R. Reductive Elimination from Sterically Encumbered Ni−Polypyridine Complexes. *Organometallics* **2022**, *41*, 2662−2667.
(45) Barakat, A.; Al-Noaimi, M.; Suleiman, M.; Aldwayyan, A. S.; Hammouti, B.; Hadda, T. B.; Haddad, S. F.; Boshaala, A.; Warad, I. One Step Synthesis of NiO Nanoparticles via Solid-State Thermal Decomposition at Low-Temperature of Novel Aqua(2,9-dimethyl-1,10-phenanthroline)$NiCl_2$ Complex. *Int. J. Mol. Sci.* **2013**, *14* (12), 23941−23954.
(46) Warad, I.; Hammouti, B.; Hadda, T. B.; Boshaala, A.; Haddad, S. F. X-ray single-crystal structure of a novel di-l-chloro-bis[chloro-(2,9-dimethyl-1,10-phenanthroline)nickel(II)] complex: synthesis, and spectral and thermal studies. *Res. Chem. Intermed.* **2013**, *39*, 4011−4020.
(47) Harvey, M. A.; Díaz de Vivar, M. E.; Garland, M. T.; Baggio, S. Single Crystal XRD Structure Determination and Analysis of Bis(2,9-Dimethyl-1,10-Phenanthroline-κ^2-*N,N′*)(Sulfato-κ^2-*O,O′*)Nickel(II) Hydrate ($NiNeo_2SO_4\bullet H_2O$; Neo: 2,9-Dimethyl-1,10-Phenanthroline). *J. Chem. Crystallogr.* **2011**, *41*, 155−158.
(48) Yuan, J.; Shi, W.-B.; Kou, H.-Z. Syntheses, crystal structures and magnetism of azide-bridged five-coordinate binuclear nickel(II) and cobalt(II) complexes. *Transition Met. Chem.* **2015**, *40*, 807−811.
(49) Spek, A. L. PLATON SQUEEZE: a tool for the calculation of the disordered solvent contribution to the calculated structure factors. *Acta Crystallogr., Sect. C: Struct. Chem.* **2015**, *71*, 9−18.
(50) Klein, A. Synthesis, Spectroscopic Properties, and Crystal Structure of 2,2′-Bipyridyldimesitylnickel(II). *Z. Anorg. Allg. Chem.* **2001**, *627*, 645−650.
(51) Klein, A.; Feth, M. P.; Bertagnolli, H.; Zális, S. On the Electronic Structure of Mesitylnickel Complexes of α-Diimines—Combining Structural Data, Spectroscopy and Calculations. *Eur. J. Inorg. Chem.* **2004**, *2004*, 2784−2796.
(52) Hoffmann, R.; Alvarez, S.; Mealli, C.; Falceto, A.; Cahill, T. J.; Zeng, T.; Manca, G. From Widely Accepted Concepts in Coordination Chemistry to Inverted Ligand Fields. *Chem. Rev.* **2016**, *116*, 8173−8192.
(53) Ernst, S. D.; Kaim, W. Energy level tailoring in ruthenium(II) polyazine complexes based on calculated and experimental ligand properties. *Inorg. Chem.* **1989**, *28*, 1520−1528.
(54) Smith, J. A.; George, M. W.; Kelly, J. M. Transient spectroscopy of dipyridophenazine metal complexes which undergo photo-induced electron transfer with DNA. *Coord. Chem. Rev.* **2011**, *255*, 2666−2675.
(55) McKinley, A. W.; Lincoln, P.; Tuite, E. M. Environmental effects on the photophysics of transition metal complexes with dipyrido[2,3-a:3′,2′-c]phenazine (dppz) and related ligands. *Coord. Chem. Rev.* **2011**, *255*, 2676−2692.
(56) Lazzaro, D. P.; McGuire, R., Jr.; McMillin, D. R. Regiospecific Quenching of a Photoexcited Platinum(II) Complex at Acidic and Basic Sites. *Inorg. Chem.* **2011**, *50*, 4437−4444.
(57) Butsch, K.; Gust, R.; Klein, A.; Ott, I.; Romanski, M. Tuning the Electronic Properties of dppz-Ligands and their Palladium(II) Complexes. *Dalton Trans.* **2010**, *39*, 4331−4340.
(58) Ruiz, G. T.; Juliarena, M. P.; Lezna, R. O.; Feliz, M. R.; Ferraudi, G. On the parallel formation of long-lived excited states of dipyridil[3,2-a:2′3′-c]phenazine, dppz. A contrast between the electrochemically and photochemically induced reduction of dppz. *J. Photochem. Photobiol., A* **2006**, *179*, 289−297.
(59) Phillips, T.; Haq, I.; Meijer, A. J. H. M.; Adams, H.; Soutar, I.; Swanson, L.; Sykes, M. J.; Thomas, J. A. DNA Binding of an Organic dppz-Based Intercalator. *Biochemistry* **2004**, *43*, 13657−13665.
(60) *Spectroelectrochemistry*; Kaim, W.; Klein, A., Eds.; The Royal Society of Chemistry: Cambridge, UK, 2008 978−0-85404−550−1.
(61) Lang, P.; Giereth, R.; Tschierlei, S.; Schwalbe, M. Unexpected wavelength dependency of the photocatalytic CO_2 reduction performance of the well-known $(bpy)Re(CO)_3Cl$ complex. *Chem. Commun.* **2019**, *55*, 600−603.
(62) Kokatam, S.-L.; Chaudhuri, P.; Weyhermüller, T.; Wieghardt, K. Molecular and electronic structure of square planar complexes $[Pd^{II}(^tbpy)(L_{N,O}{}^{IP})]^0$, $[Pd^{II}(^tbpy)(L_{N,O}{}^{ISQ})](PF_6)$, and $[Pd^{II}(^tbpy)(L_{N,O}{}^{IBQ})](PF_6)(BF_4)\cdot 2CH_2Cl_2$: an *o*-iminophenolato based ligand centered, three-membered redox series. *Dalton Trans.* **2007**, *2007*, 373−378.
(63) Klein, A.; Kaim, W. Axial Shielding of $5d^8$ and $5d^7$ Metal Centers in Dimesitylplatinum Complexes with Unsaturated Chelate Ligands: Spectroscopic and Spectroelectrochemical Studies of Four Different Oxidation States. *Organometallics* **1995**, *14*, 1176−1186.
(64) Hamacher, C.; Hurkes, N.; Kaiser, A.; Klein, A.; Schüren, A. Electrochemistry and Spectroscopy of Organometallic Terpyridine Nickel Complexes. *Inorg. Chem.* **2009**, *48*, 9947−9951.
(65) DiMucci, I. M.; Titus, C. J.; Nordlund, D.; Bour, J. R.; Chong, E.; Grigas, D. P.; Hu, C.-H.; Kosobokov, M. D.; Martin, C. D.; Mirica, L. M.; Nebra, N.; Vicic, D. A.; Yorks, L. L.; Yruegas, S.; MacMillan, S. N.; Shearer, J.; Lancaster, K. M. Scrutinizing formally Ni^{IV} centers through the lenses of core spectroscopy, molecular orbital theory, and valence bond theory. *Chem. Sci.* **2023**, *14*, 6915−6929.
(66) Steen, J. S.; Knizia, G.; Klein, J. E. M. N. σ-Noninnocence: Masked Phenyl-Cation Transfer at Formal Ni^{IV}. *Angew. Chem., Int. Ed.* **2019**, *58*, 13133−13139.
(67) Gomes, C. S. B.; Costa, S. I.; Silva, L. C.; Jiménez-Tenorio, M.; Valerga, P.; Puerta, M. C.; Gomes, P. T. Cationic R-Substituted-Indenyl Nickel(II) Complexes of Arsine and Stibine Ligands: Synthesis, Characterization, and Catalytic Behavior in the Oligomerization of Styrene. *Eur. J. Inorg. Chem.* **2018**, *2018*, 597−607.
(68) Kliegman, J. M.; Barnes, R. K. Glyoxal derivatives—I: Conjugated aliphatic diimines from glyoxal and aliphatic primary amines. *Tetrahedron* **1970**, *26*, 2555−2560.
(69) Tom Dieck, H.; Svoboda, M.; Greiser, T. Bis(diazadien)-metall(0)-Komplexe, IV [1] Nickel(0)-bis(chelate) mit aromatischen N-Substituenten. *Naturforsch* **1981**, *36*, 823−832.
(70) Dupureur, C. M.; Barton, J. K. Structural Studies of Λ- and Δ-$[Ru(phen)_2dppz]^{2+}$ Bound to $d(GTCGAC)_2$: Characterization of Enantioselective Intercalation. *Inorg. Chem.* **1997**, *36*, 33−43.
(71) Piers, W. E.; Chivers, T. Pentafluorophenylboranes: from obscurity to applications. *Chem. Soc. Rev.* **1997**, *26*, 345−354.
(72) *APEX4 - Software Suite for Crystallographic Programs*; Bruker AXS, Inc.: Madison, WI, USA, 2021.
(73) Sheldrick, G. M. A short history of SHELX. *Acta Crystallogr., Sect. A: Found. Crystallogr.* **2008**, *64*, 112−122.
(74) Sheldrick, G. M. Crystal structure refinement with SHELXL. *Acta Crystallogr., Sect. C: Struct. Chem.* **2015**, *71*, 3−8.
(75) Hübschle, C. B.; Sheldrick, G. M.; Dittrich, B. ShelXle: a Qt graphical user interface for SHELXL. *J. Appl. Crystallogr.* **2011**, *44*, 1281−1284.
(76) Krejčik, M.; Daněk, M.; Hartl, F. Simple construction of an infrared optically transparent thin-layer electrochemical cell: Applications to the redox reactions of ferrocene, $Mn_2(CO)_{10}$ and $Mn(CO)_3$(3,5-di-t-butyl-catecholate)$^-$. *J. Electroanal. Chem.* **1991**, *317*, 179−187.
(77) Kirse, T. M.; Maisuls, I.; Cappellari, M. V.; Niehaves, E.; Kösters, J.; Hepp, A.; Karst, U.; Wolcan, E.; Strassert, C. A. Neutral and Cationic Re(I) Complexes with Pnictogen-Based Coligands and

https://doi.org/10.1021/acs.inorgchem.4c00649
Inorg. Chem. 2024, 63, 11079−11091

Tunable Functionality: From Phosphorescence to Photoinduced CO Release. *Inorg. Chem.* **2024**, *63*, 4132−4151.
(78) Neese, F.; Wennmohs, F.; Becker, U.; Riplinger, C. The ORCA quantum chemistry program package. *J. Chem. Phys.* **2020**, *152*, No. 224108.
(79) Neese, F. Software update: The ORCA program system—Version 5.0. *Wiley Interdiscip. Rev.: Comput. Mol. Sci.* **2022**, *12*, No. e1606, DOI: 10.1002/wcms.1606.
(80) Weigend, F.; Ahlrichs, R. Balanced basis sets of split valence, triple zeta valence and quadruple zeta valence quality for H to Rn: Design and assessment of accuracy. *Phys. Chem. Chem. Phys.* **2005**, *7*, 3297.
(81) Becke, A. D. Density-functional exchange-energy approximation with correct asymptotic behavior. *Phys. Rev. A* **1988**, *38*, 3098−3100.
(82) Perdew, J. P.; Yue, W. Accurate and simple density functional for the electronic exchange energy: Generalized gradient approximation. *Phys. Rev. B* **1986**, *33*, 8800−8802.
(83) Grimme, S.; Antony, J.; Ehrlich, S.; Krieg, H. A consistent and accurate ab initio parametrization of density functional dispersion correction (DFT-D) for the 94 elements H-Pu. *J. Chem. Phys.* **2010**, *132*, No. 154104.
(84) Grimme, S.; Ehrlich, S.; Goerigk, L. Effect of the damping function in dispersion corrected density functional theory. *J. Comput. Chem.* **2011**, *32*, 1456−1465.
(85) Barone, V.; Cossi, M. Quantum Calculation of Molecular Energies and Energy Gradients in Solution by a Conductor Solvent Model. *J. Phys. Chem. A* **1998**, *102*, 1995−2001.
(86) Cossi, M.; Rega, N.; Scalmani, G.; Barone, V. Energies, structures, and electronic properties of molecules in solution with the C-PCM solvation model. *J. Comput. Chem.* **2003**, *24*, 669−681.
(87) Tao, J.; Perdew, J. P.; Stavoverov, V. N.; Scuseria, G. E. Climbing the Density Functional Ladder: Nonempirical Meta−Generalized Gradient Approximation Designed for Molecules and Solids. *Phys. Rev. Lett.* **2003**, *91*, No. 146401.
(88) Chemcraft—Graphical Software for Visualization of Quantum Chemistry Computations. https://www.chemcraftprog.com.

https://doi.org/10.1021/acs.inorgchem.4c00649
Inorg. Chem. 2024, 63, 11079−11091

4 Conclusions and Outlook

In the frame of this project, efforts were made to explore two major research questions: 1) Are heavy $PnPh_3$ (Pn = As, Sb) ancillary ligands able to significantly and predictably enhance the triplet emission of cyclometalated complexes compared to the lighter PPh_3 ligand, and 2) does the combination of the *cis*-Ni$(C_6F_5)_2$ platform with chromophoric α-diimine ligands facilitate Ni-based triplet emission, and which ligands are most suitable? In the process of tackling these research objectives, additional questions and challenges arose, for example optimizing the challenging syntheses of sensitive organonickel and organopalladium compounds.

The first research question was addressed through extensive photophysical studies on the doubly cyclometalated complex series [Pt(dpp)($PnPh_3$)], [Pt(dba)($PnPh_3$)] and [Pd(dpp)($PnPh_3$)] (Pn = P, As, Sb; dpp = 2,6-diphenid-2'-ylpyridine, dba = dibenzo[*c*,*h*]acridine). Therein, the comparison between the Pd(II) and Pt(II) systems in **Publication 2**, as well as between the dpp and dba ligands for Pt(II) in **Publication 1**, was helpful for the assessment of cause-effect relationships. Essentially, we found that the appreciable differences in the photophysical properties of the complexes with Pn = P, As or Sb were not mainly related to differences in spin-orbit coupling (SOC), contrary to what might be assumed at a first glance. Instead, our findings additionally highlighted the effects of the metal–pnictogen bond on the ligand field, on the character of the (potentially) emissive triplet state, and on the vibronic coupling as governed by the shapes of the potential energy surfaces of the involved electronic states, all of which influence the photophysical properties significantly.

This is not surprising when the research question is interpreted beyond a very simplified view of the issue at hand. The property that sets Ni and to a lesser extent also Pd apart from Pt the most in the context of photoluminescence, and makes it so challenging to achieve efficient triplet emission from their complexes, is not SOC, but ligand field splitting. While the SOC constants of Ni and Pd are much lower than that of Pt, the reason for the failure of most Ni(II) complexes to exhibit detectable phosphorescence is not inaccessibility of the triplet manifold, but non-radiative deactivation through metal-centered ^{3}MC states. This means that, while simply increasing the SOC in a given Ni(II) system by any means will not fix its emission behaviour, strategies like replacing PPh_3 with its heavier analogues can be effective and useful tools precisely because their mode of effect is manifold. Therefore, our experiments provided us with quite helpful and promising insights after all.

Our findings confirm the notion that an important prerequisite for triplet emission from Pd(II) and Ni(II) complexes is a mostly ligand-centered, only weakly metal-perturbed (^{3}MP-LC) T_1 state. A ^{3}MP-LC state tends to be geometrically more similar to the ground state than a state with stronger MLCT contributions, decreasing the probability of populating ^{3}MC states, while the weak metal contribution still facilitates access to the triplet manifold. The effects of increased LC character and increased SOC on radiative and non-radiative rates are essentially opposite, so a key consideration for

emitter design must be the delicate balance between the two. Our study of the [Pt(dpp)($PnPh_3$)], [Pt(dba)($PnPh_3$)] and [Pd(dpp)($PnPh_3$)] complex series indicated that the LC character of the T_1 state is consistently slightly decreased along the series P > As > Sb, while the MLCT character is slightly increased. Furthermore, the LC character was increased both in the Pt(dba) and in the Pd(dpp) derivatives compared to the Pt(dpp) parent system. Taken together, this suggests that the use of $AsPh_3$ or $SbPh_3$ as ancillary ligands is probably favourable in Pd(II) or Ni(II) complexes with rigid, π-extended ligand platforms similar to dba, providing a tool to fine-tune the degree of metal perturbation to the emissive ^{3}LC state.

As reinforced by the observation that neither [Pd(dpp)($PnPh_3$)] nor [Pt(dpp)($PnPh_3$)] is emissive at room temperature in fluid solution, the rigidity of the pincer ligand is also essential. Therefore, future efforts to improve the phosphorescence of the Pd(C^N^C) system through modification of the tridentate ligand must be focused on rigidification, ideally through extension of the π system, to concurrently support the ^{3}MP-LC character of the T_1 state. While our studies in **Publication 2** on the synthesis of doubly cyclometalated Pd(C^N^C) complexes, exploring both C–H and C–X activation pathways, have laid important groundwork towards wider accessibility of the platform, success is not guaranteed for any ligand. A possible alternative in cases where the first C–H activation step is problematic can be a C–X-activation/C–H-activation sequence, as was also considered for the Ni(II) system. However, as halogenated ligand precursors tend to be less accessible due to higher prices for building blocks and incompatibility issues of substrates with the required reaction conditions, attempting the sequential double C–H activation should remain the first line of action when trying new systems.

For example, an obvious candidate to be adapted from Pt to Pd is the dba ligand, since extrapolation of the properties of the hypothetical complexes [Pd(dba)($PnPh_3$)] (Pn = P, As, Sb) from the results in **Publication 1** and **Publication 2** is promising. However, an issue that needs to be overcome is metalation in the wrong position in the synthesis of the intermediate {[Pd(Hdba)Cl]}$_2$, as the target C–H bond is not the most acidic one in H_2dba. The sequence shown in Figure 4.1 is probably a viable alternative for the synthesis of the [Pd(dba)($PnPh_3$)] complexes, but obtaining the protoligand HdbaCl might already be challenging. The synthesis of HdbaCl paralleling the route to H_2dba is expected to be rather inefficient, as the yield is already moderate at best for H_2dba, and is furthermore limited to a maximum of 50% of the converted material if the combination of the two different building blocks is statistic.

Another ligand type that can hardly be overlooked in the context of emitter design are carbene ligands and specifically NHCs due to their high ligand strength. NHC pincer ligands are nowadays commonly seen in place of or in combination with cyclometalation for emissive transition metal complexes. While both feature C–coordinating ligands, the comparability and interchangeability between cyclometalation *vs.* carbene pincer is limited due to their differing charge. On the other hand, N donors like pyridine can be replaced by carbene moieties without completely transforming the structure and properties. Therefore, the next frontier for doubly cyclometalated Pd complexes might be the replacement of the central pyridine unit of C^N^C ligands with an NHC. However,

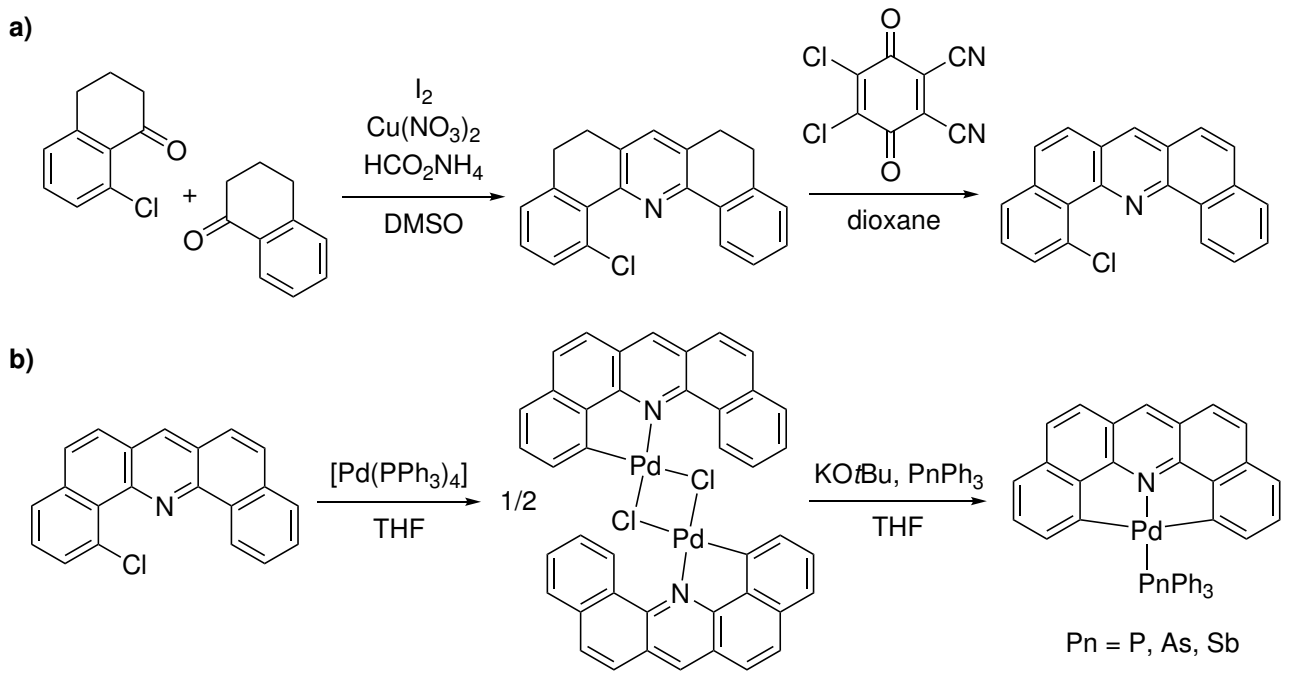

Figure 4.1: Proposed synthesis routes to the chlorinated ligand precursor HdbaCl (a) and to the complexes [Pd(dba)($PnPh_3$)] (b), which we expect to perform well as triplet emitters.

at the present time we have not even started varying the C^N^C platform for Pd as it is. The possibility to use monodentate carbene ligands as ancillary ligands for the C^N^C system has already been demonstrated for Pt and can probably be translated to the Pd(C^N^C) system. This would mean dropping the $PnPh_3$ ancillary ligands completely, leading further away from the core of the project.

Regarding the Ni(C^N^C) case, we did not obtain the target compound [Ni(dpp)(PPh_3)] within the frame of this project, but took preliminary steps towards its possible isolation in the future. It is entirely possible that dedicated work to establish a synthetic route based on our considerations and initial experiments will be successful in the future. However, while it would certainly be an appreciable advance in the field of organonickel chemistry to obtain doubly cyclometalated Ni(C^N^C) complexes, their potential as triplet emitters must be regarded realistically and weighed against the required time and effort. Specifically [Ni(dpp)(PPh_3)] as well as its $AsPh_3$ ans $SbPh_3$ congeners are most likely non-emissive, extrapolating from the already weak emission of the Pd derivatives. Like for the Pd complexes, the task of establishing the synthesis of [Ni(dpp)(PPh_3)] will be followed by the even bigger task of adapting the conditions to a range of other, more structurally embellished C^N^C ligands. Unfortunately, the dba ligand is probably not an exception in that ligands with desirable properties like high rigidity and an extended π system tend to make the complex synthesis more challenging. Due to these persisting limitations, it is advisable to remain open to different ligand classes and coordination motifs in view of the practical goal of finding Ni(II)-based replacements for Pt(II) complexes for optoelectronic applications.

In this sense, we were led to our second research question, which was addressed by studying a number of [Ni(C_6F_5)$_2$(N^N)] (N^N = α-diimine ligand) derivatives photophysically as well as electrochemically in **Publication 3**. We observed weak photoluminescence at 77 K from two Ni(C_6F_5)$_2$ complexes containing the phenanthroline derivatives 3,4,7,8-tetramethylphenanthroline (tmphen) and 2,9-dimethylphenanthroline (dmphen), but not from [Ni(C_6F_5)$_2$(bpy)] or [Ni(C_6F_5)$_2$(dppz)] (bpy = 2,2'-bipyridine, dppz = dipyrido[3,2-*a*:2',3'-*c*]phenazine). Based on the large stokes shifts and lower ns range lifetimes consistent with previous reports on phosphorescent Ni(II) complexes, the observed emission is tentatively interpreted to be phosphorescent in nature. The results confirm that the Ni(C_6F_5)$_2$ platform is generally appropriate for building up emissive Ni(II) complexes if combined with suitable chromophores. Judging from our findings, a suitable chromophore ligand in this context needs to be not only sufficiently rigid, i.e. more rigid than bpy, but also unaffected by intermolecular quenching processes, unlike dppz. Intermolecular quenching due to stacking interactions was identified as the most likely reason for the non-emissive behaviour of [Ni(C_6F_5)$_2$(dppz)], but also a factor for the tmphen and dmphen complexes.

We therefore initially concluded that Ni(C_6F_5)$_2$ might be unsuited to enhance dppz-centered luminescence, however, as the underlying reason is traced to the dppz ligand itself, the challenge can probably be overcome by modifying the dppz ligand. While the *cis*-Ni(C_6F_5)$_2$ fragment appears to exacerbate the stacking-related photoluminescence quenching issues in [Ni(C_6F_5)$_2$(dppz)] compared to free dppz, this probably becomes irrelevant if the stacking is suppressed altogether. As dppz and its derivatives are typically synthesized *via* a double condensation reaction between phenathroline-5,6-dione and 1,2-diaminobenzene, modifications on the terminal benzene moiety can be introduced conveniently with the diamino building block. The introduction of e.g. a *tert*-butyl group (Figure 4.2 a) might already be sufficient to inhibit stacking of the phenazine moiety. At the same time, such ligand modifications can help address another potential quenching issue, which is related to hydrogen bonding of the phenazine N atoms of dppz with protic solvents. Alkylation is a promising strategy to increase the solubility of the complexes in organic, including aprotic, solvents, thus circumventing the problem. Furthermore, the hydrogen bonding interactions may also be suppressed by steric protection offered by nearby substituents.

Furthermore, by functionalizing the dppz ligand with a suitable anchor group which can undergo facile reactions with different building blocks, the scope of accessible ligands can be vastly enlarged while retaining the modular character of the synthesis (Figure 4.2 b). Introducing an amino group, which can react with a variety of substrates bearing an acyl chloride functionality, would give access to amide-conjugated structures. Converting the amino group to an azido group first would provide access to triazole conjugates *via* click reactions with alkynes. A possible application for these strategies is the introduction of light-harvesting groups, i.e. structural motifs which strongly absorb visible light and are able to subsequently transfer the absorbed energy to the emissive triplet state of the Ni(C_6F_5)$_2$(dppz)-fragment. A limitation to be kept in mind here is that the conjugate group should not be a good electron acceptor, because electron transfer is another common quenching mechanism of MLCT states involving the dppz moiety. The same conjugation strategies

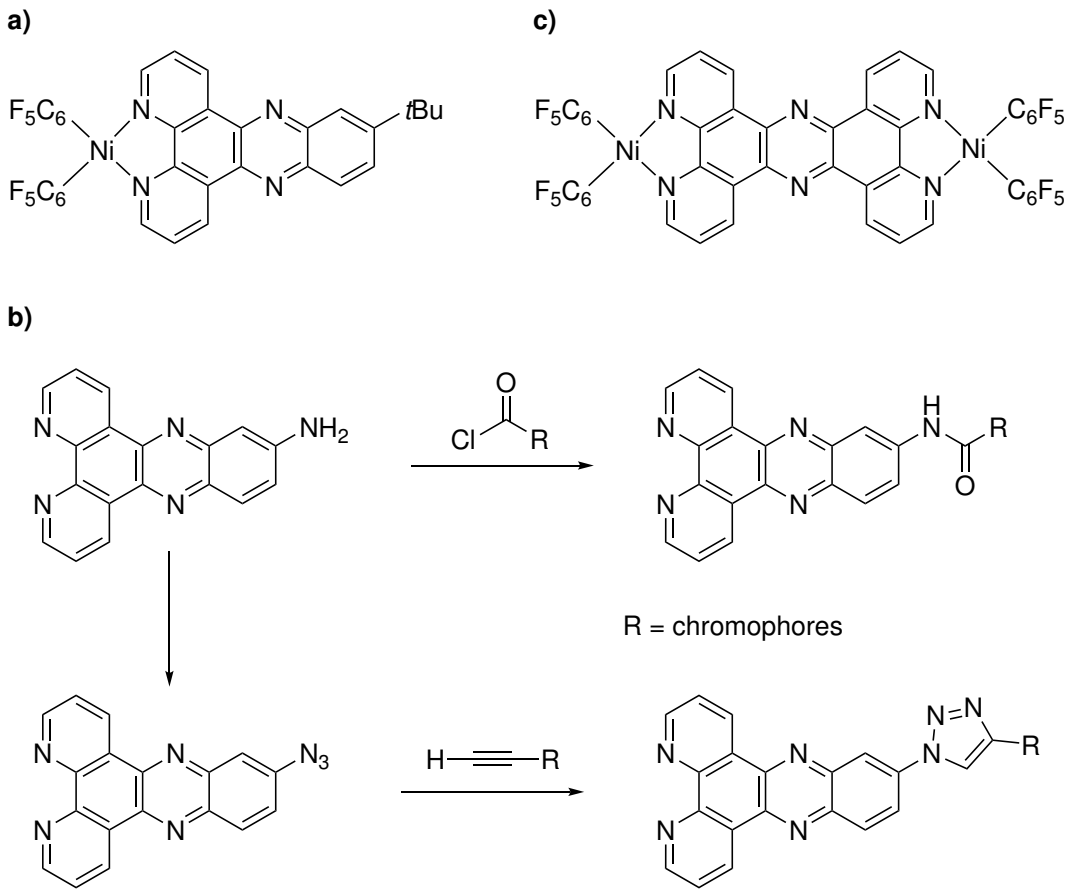

Figure 4.2: Proposed modifications to the dppz ligand and its $Ni(C_6F_5)_2$ complexes to improve triplet emission by suppressing stacking interactions (a, c) and introducing additional chromophore moieties (b).

using such anchor groups can probably also be applied to phen, with increased potential for direct electronic interaction between the conjugate group and the Ni(II) center due to their decreased spatial distance. Finally, it might be interesting to study the dinuclear complex $[Ni_2(C_6F_5)_4(tppz)]$ (tppz = tetrapyrido[3,2-*a*:2',3'-*c*:3'',2''-*h*:2''',3'''-*j*]phenazine, Figure 4.2 c), containing a derivative of the dppz ligand with a mirror plane through the phenazine N atoms. Paralleling the synthesis of all dppz derivatives, the tppz ligand can be synthesized from phenathroline-5,6-dione and phenanthroline-5,6-diamine. All future studies on the $[Ni(C_6F_5)_2(N^\wedge N)]$ system may be complemented and enhanced by additional and more specific theoretical studies, for example of the T_1 state of the complexes.

Summarizing and comparing the two sub-projects $[M(C^\wedge N^\wedge C)(PnPh_3)]$ *vs.* $[Ni(C_6F_5)_2(N^\wedge N)]$, we find that both have provided us with valuable takeaways regarding our research questions, and contributed to the wider field of research in meaningful ways. Our work on the $[M(C^\wedge N^\wedge C)(PnPh_3)]$ project has essentially established the pnictogen variation in $PnPh_3$ ancillary ligands as a fine-tuning tool for the character of excited states, the ligand field and SOC. This represents a specific case of the general concept of using tridentate pincers as strong platforms and monodentate ligands as fine-tuning turnscrews. Perhaps a more ground-breaking result of our research on the $[M(C^\wedge N^\wedge C)(PnPh_3)]$ system is the optimized synthesis and first comprehensive photophysical and electrochemical characterization of a doubly cyclometalated $Pd(C^\wedge N^\wedge C)$ complex. This milestone represents the basis for all future work on $Pd(C^\wedge N^\wedge C)$ triplet emitters with the dpp parent system

as as starting point and point of reference. In this way, the [M(C^N^C)($PnPh_3$)] project has significantly advanced the field of organometallic group ten triplet emitters. Similarly, our contributions to the study of [Ni(C_6F_5)$_2$(N^N)] complexes represent the first detailed look into their photophysical properties and potential as emitter materials, whereas previous reports were focused on their potential for catalytic applications.

The key differences between the two sub-projects lie in their proximity to the overarching goal of obtaining phosphorescent Ni(II) complexes as substitutes for Pt(II) emitters, as well as in the effort required to produce new derivatives. With two emissive derivatives already identified among the group of [Ni(C_6F_5)$_2$(N^N)] complexes studied by us for **Publication 3**, this sub-project is evidently far more directly in touch with the ultimate goal. The [Ni(C_6F_5)$_2$(N^N)] system also has the advantage of much higher accessibility of a wide scope of complex derivatives, as variations of the chromophoric ligand are synthetically independent of the critical Ni–C bonds. Therefore, the potential for short- to mid-term success at identifying Ni(II)-based triplet emitters appears to be significantly greater for the [Ni(C_6F_5)$_2$(N^N)] than the [M(C^N^C)($PnPh_3$)] system, following for example the proposals for variation of the dppz ligand described above. Obtaining emissive [Ni(C^N^C)(L)] derivatives will be a much longer road with more synthetic obstacles and must therefore be acknowledged as a rather long-term goal. Nonetheless, we maintain both approaches as worthwhile for the growing research community of our field, not only because of their ultimate objectives, but also for the fundamental knowledge that is gained in the process.

5 References

[1] *Highly Efficient OLEDs with Phosphorescent Materials*, (Ed.: H. Yersin), Wiley, **2007**, DOI 10.1002/9783527621309.

[2] C. Bizzarri, E. Spuling, D. M. Knoll, D. Volz, S. Bräse, *Coord. Chem. Rev.* **2018**, *373*, 49–82, DOI 10.1016/j.ccr.2017.09.011.

[3] Y. Chen, R. Guan, C. Zhang, J. Huang, L. Ji, H. Chao, *Coord. Chem. Rev.* **2016**, *310*, 16–40, DOI 10.1016/j.ccr.2015.09.010.

[4] Q. Zhao, F. Li, C. Huang, *Chem. Soc. Rev.* **2010**, *39*, 3007, DOI 10.1039/b915340c.

[5] D.-L. Ma, H.-Z. He, K.-H. Leung, D. S.-H. Chan, C.-H. Leung, *Angew. Chem. Int. Ed.* **2013**, *52*, 7666–7682, DOI 10.1002/anie.201208414.

[6] C.-N. Ko, G. Li, C.-H. Leung, D.-L. Ma, *Coord. Chem. Rev.* **2019**, *381*, 79–103, DOI 10.1016/j.ccr.2018.11.013.

[7] K. N. Shinde, S. J. Dhoble, H. C. Swart, K. Park in *Phosphate Phosphors for Solid-State Lighting*, Springer Berlin Heidelberg, **2012**, pp. 41–59, DOI 10.1007/978-3-642-34312-4_2.

[8] A. W. Adamson, J. N. Demas, *J. Phys. Chem.* **1971**, *75*, 2463–2466, DOI 10.1021/j100685a009.

[9] G. A. Crosby, J. N. Demas, *J. Phys. Chem.* **1971**, *75*, 991–1024, DOI 10.1021/j100678a001.

[10] H. Yersin, A. F. Rausch, R. Czerwieniec, T. Hofbeck, T. Fischer, *Coord. Chem. Rev.* **2011**, *255*, 2622–2652, DOI 10.1016/j.ccr.2011.01.042.

[11] H. Fang, Y. Chen, Z. Jiang, W. He, Z. Guo, *Acc. Chem. Res.* **2023**, *56*, 258–269, DOI 10.1021/acs.accounts.2c00643.

[12] J. Zhou, P. Jangili, S. Son, M. S. Ji, M. Won, J. S. Kim, *Adv. Mater.* **2020**, *32*, DOI 10.1002/adma.202001945.

[13] N. Aizawa, Y.-J. Pu, Y. Harabuchi, A. Nihonyanagi, R. Ibuka, H. Inuzuka, B. Dhara, Y. Koyama, K.-i. Nakayama, S. Maeda, F. Araoka, D. Miyajima, *Nature* **2022**, *609*, 502–506, DOI 10.1038/s41586-022-05132-y.

[14] A. Szabo, N. S. Ostlund, *Modern quantum chemistry: Introduction to advanced electronic structure theory*, Courier Corporation, **2012**.

[15] F. B. Dias, T. J. Penfold, A. P. Monkman, *Methods Appl. Fluoresc.* **2017**, *5*, 012001, DOI 10.1088/2050-6120/aa537e.

[16] Z. Yang, Z. Mao, Z. Xie, Y. Zhang, S. Liu, J. Zhao, J. Xu, Z. Chi, M. P. Aldred, *Chem. Soc. Rev.* **2017**, *46*, 915–1016, DOI 10.1039/c6cs00368k.

[17] H. Uoyama, K. Goushi, K. Shizu, H. Nomura, C. Adachi, *Nature* **2012**, *492*, 234–238, DOI 10.1038/nature11687.

[18] M. Zheng, Y. Li, Y. Wei, L. Chen, X. Zhou, S. Liu, *J. Phys. Chem. Lett.* **2022**, *13*, 2507–2515, DOI 10.1021/acs.jpclett.2c00428.

[19] C. M. Marian in *Reviews in Computational Chemistry, Volume 17*, Wiley, **2001**, pp. 99–204, DOI 10.1002/0471224413.ch3.

[20] T. M. Dunn, *Trans. Faraday Soc.* **1961**, *57*, 1441, DOI 10.1039/tf9615701441.

[21] B. Goodman, J. Raynor in *Adv. Inorg. Chem. Radiochem.* Elsevier, **1970**, pp. 135–362, DOI 10.1016/s0065-2792(08)60336-2.

[22] D. D. Sarma, *Proc. Indian Acad. Sci. (Chem. Sci.)* **1981**, *90*, 19–26, DOI 10.1007/bf02841324.

[23] W.-P. To, Q. Wan, G. S. M. Tong, C.-M. Che, *Trends Chem.* **2020**, *2*, 796–812, DOI 10.1016/j.trechm.2020.06.004.

[24] I. O. Koshevoy, M. Krause, A. Klein, *Coord. Chem. Rev.* **2020**, *405*, 213094, DOI 10.1016/j.ccr.2019.213094.

[25] J. A. G. Williams in *Photochemistry and Photophysics of Coordination Compounds II*, Springer Berlin Heidelberg, **2007**, pp. 205–268, DOI 10.1007/128_2007_134.

[26] K. L. Garner, L. F. Parkes, J. D. Piper, J. A. G. Williams, *Inorg. Chem.* **2009**, *49*, 476–487, DOI 10.1021/ic9016323.

[27] M. Niazi, I. Maisuls, C. A. Strassert, A. Klein, *Organometallics* **2024**, *43*, 1547–1556, DOI 10.1021/acs.organomet.4c00121.

[28] S. Garbe, M. Krause, A. Klimpel, I. Neundorf, P. Lippmann, I. Ott, D. Brünink, C. A. Strassert, N. L. Doltsinis, A. Klein, *Organometallics* **2020**, *39*, 746–756, DOI 10.1021/acs.organomet.0c00015.

[29] M. Krause, I. Maisuls, S. Buss, C. A. Strassert, A. Winter, U. S. Schubert, S. S. Nair, B. Dietzek-Ivanšić, A. Klein, *Molecules* **2022**, *27*, 7022, DOI 10.3390/molecules27207022.

[30] J. Soellner, P. Pinter, S. Stipurin, T. Strassner, *Angew. Chem. Int. Ed.* **2020**, *60*, 3556–3560, DOI 10.1002/anie.202011927.

[31] S.-N. Liu, K.-N. Tong, Y. Zhao, J.-F. Cheng, M.-K. Fung, J. Fan, *J. Mater. Chem. C* **2020**, *8*, 6168–6175, DOI 10.1039/c9tc06940b.

[32] A. F. Rausch, L. Murphy, J. A. G. Williams, H. Yersin, *Inorg. Chem.* **2011**, *51*, 312–319, DOI 10.1021/ic201664v.

[33] M. Atanasov, C. Rauzy, P. Baettig, C. Daul, *Int. J. Quantum Chem.* **2005**, *102*, 119–131, DOI 10.1002/qua.20376.

[34] R. J. Deeth, *Dalton Trans.* **2020**, *49*, 9641–9650, DOI 10.1039/d0dt02022b.

[35] L. E. Orgel, *An Introduction to Transition-Metal Chemistry: Ligand-Field Theory*, Taylor & Francis, **1966**.

[36] V. W.-W. Yam, A. S.-Y. Law, *Coord. Chem. Rev.* **2020**, *414*, 213298, DOI 10.1016/j.ccr.2020.213298.

[37] J. Herberger, R. F. Winter, *Coord. Chem. Rev.* **2019**, *400*, 213048, DOI 10.1016/j.ccr.2019.213048.

[38] J. Kalinowski, V. Fattori, M. Cocchi, J. G. Williams, *Coord. Chem. Rev.* **2011**, *255*, 2401–2425, DOI 10.1016/j.ccr.2011.01.049.

[39] T. Fleetham, G. Li, J. Li, *Adv. Mater.* **2016**, *29*, DOI 10.1002/adma.201601861.

[40] J. Friedel, M. Krause, R. Jordan, I. Maisuls, D. Brünink, D. Schwab, N. L. Doltsinis, C. A. Strassert, A. Klein, *Molecules* **2022**, *27*, 8054, DOI 10.3390/molecules27228054.

[41] R. Alrefai, G. Hörner, H. Schubert, A. Berkefeld, *Organometallics* **2021**, *40*, 1163–1177, DOI 10.1021/acs.organomet.1c00121.

[42] K. WONG, V. YAM, *Coord. Chem. Rev.* **2007**, *251*, 2477–2488, DOI 10.1016/j.ccr.2007.02.003.

[43] E. V. Puttock, M. T. Walden, J. G. Williams, *Coord. Chem. Rev.* **2018**, *367*, 127–162, DOI 10.1016/j.ccr.2018.04.003.

[44] C.-W. Chan, L.-K. Cheng, C.-M. Che, *Coord. Chem. Rev.* **1994**, *132*, 87–97, DOI 10.1016/0010-8545(94)80027-8.

[45] H.-K. Yip, L.-K. Cheng, K.-K. Cheung, C.-M. Che, *Dalton Trans.* **1993**, 2933–2938, DOI 10.1039/dt9930002933.

[46] J. A. Gareth Williams, S. Develay, D. Rochester, L. Murphy, *Coord. Chem. Rev.* **2008**, *252*, 2596–2611, DOI 10.1016/j.ccr.2008.03.014.

[47] S.-W. Lai, H.-W. Lam, W. Lu, K.-K. Cheung, C.-M. Che, *Organometallics* **2001**, *21*, 226–234, DOI 10.1021/om0106276.

[48] S. Roy, A. A. Lopez, J. E. Yarnell, F. N. Castellano, *Inorg. Chem.* **2021**, *61*, 121–130, DOI 10.1021/acs.inorgchem.1c02469.

[49] W. Lu, M. C. W. Chan, N. Zhu, C.-M. Che, C. Li, Z. Hui, *J. Am. Chem. Soc.* **2004**, *126*, 7639–7651, DOI 10.1021/ja039727o.

[50] S. C. F. Kui, P. K. Chow, G. S. M. Tong, S.-L. Lai, G. Cheng, C.-C. Kwok, K.-H. Low, M. Y. Ko, C.-M. Che, *Chem. Eur. J.* **2012**, *19*, 69–73, DOI 10.1002/chem.201203687.

[51] Y.-C. Wei, K.-H. Kuo, Y. Chi, P.-T. Chou, *Acc. Chem. Res.* **2023**, *56*, 689–699, DOI 10.1021/acs.accounts.2c00827.

[52] C.-Y. Sun, W.-P. To, F.-F. Hung, X.-L. Wang, Z.-M. Su, C.-M. Che, *Chem. Sci.* **2018**, *9*, 2357–2364, DOI 10.1039/c7sc04528j.

[53] K.-C. Wong, V.-M. Au, V.-W. Yam in *Comprehensive Inorganic Chemistry II*, Elsevier, **2013**, pp. 59–130, DOI 10.1016/b978-0-08-097774-4.00813-5.

[54] P. Pander, A. Sil, R. J. Salthouse, C. W. Harris, M. T. Walden, D. S. Yufit, J. A. G. Williams, F. B. Dias, *J. Mater. Chem. C* **2022**, *10*, 15084–15095, DOI 10.1039/d2tc01511k.

[55] P.-K. Chow, G. Cheng, G. S. M. Tong, C. Ma, W.-M. Kwok, W.-H. Ang, C. Y.-S. Chung, C. Yang, F. Wang, C.-M. Che, *Chem. Sci.* **2016**, *7*, 6083–6098, DOI 10.1039/c6sc00462h.

[56] F. Neve, A. Crispini, C. Di Pietro, S. Campagna, *Organometallics* **2002**, *21*, 3511–3518, DOI 10.1021/om020204j.

[57] M. Ghedini, T. Pugliese, M. La Deda, N. Godbert, I. Aiello, M. Amati, S. Belviso, F. Lelj, G. Accorsi, F. Barigelletti, *Dalton Trans.* **2008**, 4303, DOI 10.1039/b804478c.

[58] S.-W. Lai, T.-C. Cheung, M. C. W. Chan, K.-K. Cheung, S.-M. Peng, C.-M. Che, *Inorg. Chem.* **2000**, *39*, 255–262, DOI 10.1021/ic991089g.

[59] D. Dalmau, E. P. Urriolabeitia, *Molecules* **2023**, *28*, 2663, DOI 10.3390/molecules28062663.

[60] P. K. Chow, C. Ma, W.-P. To, G. S. M. Tong, S.-L. Lai, S. C. F. Kui, W.-M. Kwok, C.-M. Che, *Angew. Chem. Int. Ed.* **2013**, *52*, 11775–11779, DOI 10.1002/anie.201305590.

[61] M. D. Santana, R. García-Bueno, G. García, J. Pérez, L. García, M. Monge, A. Laguna, *Dalton Trans.* **2010**, *39*, 1797–1806, DOI 10.1039/b917994a.

[62] J. D. Cope, J. A. Denny, R. W. Lamb, L. E. McNamara, N. I. Hammer, C. E. Webster, T. K. Hollis, *J. Organomet. Chem.* **2017**, *845*, 258–265, DOI 10.1016/j.jorganchem.2017.05.046.

[63] Y.-S. Wong, M.-C. Tang, M. Ng, V. W.-W. Yam, *J. Am. Chem. Soc.* **2020**, *142*, 7638–7646, DOI 10.1021/jacs.0c02172.

[64] H. Kurz, K. Schötz, I. Papadopoulos, F. W. Heinemann, H. Maid, D. M. Guldi, A. Köhler, G. Hörner, B. Weber, *J. Am. Chem. Soc.* **2021**, *143*, 3466–3480, DOI 10.1021/jacs.0c12568.

[65] C. Wegeberg, O. S. Wenger, *JACS Au* **2021**, *1*, 1860–1876, DOI 10.1021/jacsau.1c00353.

[66] C.-L. Hou, J.-X. Song, X. Chang, Y. Chen, *Chin. Chem. Lett.* **2024**, *35*, 108333, DOI 10.1016/j.cclet.2023.108333.

[67] R. Jordan, S. A. Schäfer, N. Sander, I. Maisuls, C. Hamacher, J. Friedel, C. A. Strassert, A. Klein, *Inorg. Chem.* **2024**, *63*, 11079–11091, DOI 10.1021/acs.inorgchem.4c00649.

[68] D. Moreth, M. V. Cappellari, A. Müller, A. Oster, D. Schwab, N. L. Doltsinis, C. A. Strassert, U. Schatzschneider, *Inorg. Chem.* **2025**, *64*, 4223–4235, DOI 10.1021/acs.inorgchem.4c03773.

[69] M. Niazi, I. Maisuls, L. A. Mai, S. A. Schäfer, A. Oster, L. S. Diaz, D. M. Guldi, N. L. Doltsinis, C. A. Strassert, A. Klein, *Molecules* **2025**, *30*, 1901, DOI 10.3390/molecules30091901.

[70] T. Ogawa, N. Sinha, B. Pfund, A. Prescimone, O. S. Wenger, *J. Am. Chem. Soc.* **2022**, *144*, 21948–21960, DOI 10.1021/jacs.2c08838.

[71] T. Ogawa, O. S. Wenger, *Angew. Chem. Int. Ed.* **2023**, *62*, DOI 10.1002/anie.202312851.

[72] Y. Gu, K. Wang, Y. Dai, G. Xiao, Y. Ma, Y. Qiao, B. Zou, *J. Phys. Chem. Lett.* **2017**, *8*, 4191–4196, DOI 10.1021/acs.jpclett.7b01796.

[73] S. C. Gangadharappa, I. Maisuls, D. A. Schwab, J. Kösters, N. L. Doltsinis, C. A. Strassert, *J. Am. Chem. Soc.* **2020**, *142*, 21353–21367, DOI 10.1021/jacs.0c09467.

[74] S. Buss, L. Ketter, D. Brünink, D. Schwab, S. Klenner, A. Hepp, J. Kösters, T. J. Schmidt, R. Pöttgen, N. L. Doltsinis, C. A. Strassert, *Inorg. Chem.* **2024**, *63*, 10114–10126, DOI 10.1021/acs.inorgchem.3c02727.

[75] J. Ramler, C. Lichtenberg, *Dalton Transac.* **2021**, *50*, 7120–7138, DOI 10.1039/d1dt01300a.

[76] J. M. de Rezende, D. W. Franco, *Transit. Met. Chem.* **1987**, *12*, 267–270, DOI 10.1007/bf01023546.

[77] R. Asano, I. Moritani, Y. Fujiwara, S. Teranishi, *Bull. Chem. Soc. Jpn.* **1973**, *46*, 2910–2911, DOI 10.1246/bcsj.46.2910.

[78] W. Lu, M. C. W. Chan, K.-K. Cheung, C.-M. Che, *Organometallics* **2001**, *20*, 2477–2486, DOI 10.1021/om0009839.

[79] A. Kergreis, R. M. Lord, S. J. Pike, *Chem. Eur. J.* **2020**, *26*, 14938–14946, DOI 10.1002/chem.202002517.

[80] G. W. V. Cave, F. P. Fanizzi, R. J. Deeth, W. Errington, J. P. Rourke, *Organometallics* **2000**, *19*, 1355–1364, DOI 10.1021/om9910423.

[81] G. W. V. Cave, N. W. Alcock, J. P. Rourke, *Organometallics* **1999**, *18*, 1801–1803, DOI 10.1021/om981006o.

[82] M. V. Kulikova, K. P. Balashev, K. Erzin, *Russ. J. Gen. Chem.* **2003**, *73*, 1839–1845, DOI 10.1023/b:rugc.0000025140.64970.10.

[83] C. Cornioley-Deuschel, T. Ward, A. V. Zelewsky, *Helv. Chim. Acta* **1988**, *71*, 130–133, DOI 10.1002/hlca.19880710116.

[84] D. Campillo, D. Escudero, M. Baya, A. Martín, *Chem. Eur. J.* **2022**, *28*, DOI 10.1002/chem.202104538.

[85] W. Feuerstein, F. Breher, *Chem. Commun.* **2020**, *56*, 12589–12592, DOI 10.1039/d0cc04065g.

[86] B. Pinter, V. Van Speybroeck, M. Waroquier, P. Geerlings, F. De Proft, *Phys. Chem. Chem. Phys.* **2013**, *15*, 17354, DOI 10.1039/c3cp52383g.

[87] R. C. Evans, P. Douglas, C. J. Winscom, *Coord. Chem. Rev.* **2006**, *250*, 2093–2126, DOI 10.1016/j.ccr.2006.02.007.

[88] D. C. Ashley, E. Jakubikova, *Inorg. Chem.* **2018**, *57*, 9907–9917, DOI 10.1021/acs.inorgchem.8b01002.

[89] T. Yamamoto, M. Abla, Y. Murakami, *Bull. Chem. Soc. Jpn.* **2002**, *75*, 1997–2009, DOI 10.1246/bcsj.75.1997.

[90] J. A. Casares, P. Espinet, J. M. Martín-Alvarez, J. M. Martínez-Ilarduya, G. Salas, *Eur. J. Inorg. Chem.* **2005**, *2005*, 3825–3831, DOI 10.1002/ejic.200500121.

[91] J. Ponce-de-León, E. Gioria, J. M. Martínez-Ilarduya, P. Espinet, *Inorg. Chem.* **2020**, *59*, 18287–18294, DOI 10.1021/acs.inorgchem.0c02831.

[92] J. Forniés, A. Martín, L. F. Martín, B. Menjón, H. A. Kalamarides, L. F. Rhodes, C. S. Day, V. W. Day, *Chem. Eur. J.* **2002**, *8*, 4925–4934, DOI 10.1002/1521-3765(20021104)8:21<4925::aid-chem4925>3.0.co;2-4.

[93] G. Sánchez, J. Serrano, F. Ruiz, G. López, *J. Fluor. Chem.* **1998**, *91*, 165–169, DOI 10.1016/s0022-1139(98)00221-8.

[94] G. Sánchez, J. García, D. Meseguer, J. L. Serrano, L. García, J. Pérez, G. López, *Inorganica Chim. Acta* **2006**, *359*, 1650–1658, DOI 10.1016/j.ica.2005.11.014.

[95] J. Ponce-de-León, P. Espinet, *Chem. Commun.* **2021**, *57*, 10875–10878, DOI 10.1039/d1cc04915a.

[96] A. Arcas, P. Royo, *Inorganica Chim. Acta* **1978**, *30*, 205–207, DOI 10.1016/s0020-1693(00)89037-4.

[97] A. Arcas, P. Royo, *Inorganica Chim. Acta* **1978**, *31*, 97–99, DOI 10.1016/s0020-1693(00)94984-3.

[98] J. R. Bour, N. M. Camasso, E. A. Meucci, J. W. Kampf, A. J. Canty, M. S. Sanford, *J. Am. Chem. Soc.* **2016**, *138*, 16105–16111, DOI 10.1021/jacs.6b10350.

[99] G. López, G. García, J. Ruiz, G. Sánchez, J. García, C. Vicente, *Chem. Commun.* **1989**, 1045–1046, DOI 10.1039/c39890001045.

[100] G. Lopez, G. Garcia, G. Sanchez, J. Garcia, J. Ruiz, J. A. Hermoso, A. Vegas, M. Martinez-Ripoll, *Inorg. Chem.* **1992**, *31*, 1518–1523, DOI 10.1021/ic00034a038.

[101] R. G. Gastinger, B. B. Anderson, K. J. Klabunde, *J. Am. Chem. Soc.* **1980**, *102*, 4959–4966.

[102] M. M. Brezinski, K. J. Klabunde, *Organometallics* **1983**, *2*, 1116–1123.

[103] E. Clot, C. Mégret, O. Eisenstein, R. N. Perutz, *J. Am. Chem. Soc.* **2009**, *131*, 7817–7827, DOI 10.1021/ja901640m.

[104] A. W. McKinley, P. Lincoln, E. M. Tuite, *Coord. Chem. Rev.* **2011**, *255*, 2676–2692, DOI 10.1016/j.ccr.2011.06.012.

[105] D. P. Rillema, A. J. Cruz, C. Moore, K. Siam, A. Jehan, D. Base, T. Nguyen, W. Huang, *Inorg. Chem.* **2012**, *52*, 596–607, DOI 10.1021/ic301393e.

[106] G. Capano, U. Rothlisberger, I. Tavernelli, T. J. Penfold, *J. Phys. Chem. A* **2015**, *119*, 7026–7037, DOI 10.1021/acs.jpca.5b03842.

[107] D. van der Westhuizen, K. G. von Eschwege, J. Conradie, *Electrochim. Acta* **2019**, *320*, 134540, DOI 10.1016/j.electacta.2019.07.051.

[108] R. Jordan, I. Maisuls, S. S. Nair, B. Dietzek-Ivanšić, C. A. Strassert, A. Klein, *Dalton Trans.* **2023**, *52*, 18220–18232, DOI 10.1039/d3dt03225f.

[109] R. Jordan, S. Kler, I. Maisuls, N. Klosterhalfen, B. Dietzek-Ivanšić, C. A. Strassert, A. Klein, *Inorg. Chem.* **2025**, *64*, 6561–6574, DOI 10.1021/acs.inorgchem.4c05436.

[110] N. Vogt, V. Sivchik, A. Sandleben, G. Hörner, A. Klein, *Molecules* **2020**, *25*, 997, DOI 10.3390/molecules25040997.

[111] N. Vogt, A. Sandleben, L. Kletsch, S. Schäfer, M. T. Chin, D. A. Vicic, G. Hörner, A. Klein, *Organometallics* **2021**, *40*, 1776–1785, DOI 10.1021/acs.organomet.1c00237.

[112] L. Payen, L. Kletsch, T. Lapić, M. Wickleder, A. Klein, *Inorganics* **2023**, *11*, 174, DOI 10.3390/inorganics11040174.

[113] L. Kletsch, R. Jordan, J. Strippel, D. A. Vicic, A. Klein, *Inorganics* **2025**, *13*, 41, DOI 10.3390/inorganics13020041.

[114] A. Sandleben, N. Vogt, G. Hörner, A. Klein, *Organometallics* **2018**, *37*, 3332–3341, DOI 10.1021/acs.organomet.8b00559.

[115] C. Yin, K. Zhong, W. Li, X. Yang, R. Sun, C. Zhang, X. Zheng, M. Yuan, R. Li, Y. Lan, H. Fu, H. Chen, *Adv. Synth. Catal.* **2018**, *360*, 3990–3998, DOI 10.1002/adsc.201800666.

6 Appendix

6.1 Supporting Information for Publication 1

Adapted from Ref.[108] with permission from the Royal Society of Chemistry.

Electronic supplementary information (ESI)
for
Enhanced luminescence properties through heavy ancillary ligands in [Pt(C^N^C)(L)] complexes, L = $AsPh_3$ and $SbPh_3$

Rose Jordan,[a] Iván Maisuls,[b] Shruthi S. Nair[c,d], Benjamin Dietzek-Ivanšić,*[,c,d] Cristian. A. Strassert*[,b] and Axel Klein*[,a]

[a] University of Cologne, Faculty for Mathematics and Natural Sciences, Department of Chemistry, Institute for Inorganic Chemistry, Greinstrasse 6, D-50939 Köln, Germany.
[b] Westfälische Wilhelms-Universität Münster, Institut für Anorganische und Analytische Chemie, CiMIC, CeNTech, Heisenbergstraße 11, D-48149 Münster, Germany.
[c] Friedrich Schiller University Jena, Institute for Physical Chemistry (IPC), Helmholtzweg 4, 07743 Jena, Germany.
[d] Leibniz Institute for Photonic Technologies Jena (IPHT) Albert-Einstein-Str. 9, 07745 Jena, Germany.

Contents

Supporting Tables

Table S6 Electrochemical data for the ligands H_2dpp and H_2dba and the complexes [Pt(C^N^C)($PnPh_3$)] (Pn = P, As, Sb).
Table S7 UV-vis absorption data of the ligand H_2dpp and the complexes [Pt(dpp)($PnPh_3$)] (Pn = P, As, Sb).
Table S8 UV-vis absorption data of the ligand H_2dba and the complexes [Pt(dba)($PnPh_3$)] (Pn = P, As, Sb).

Experimental Section

Materials. All manipulations were carried out using standard *Schlenk* techniques. The reaction solvent CH_2Cl_2 (HPLC grade) was degassed in three freeze-pump-thaw cycles and dried over activated 4 Å molecular sieves. [Pt(dpp)(dmso)], [Pt(dba)(dmso)], [Pt(dpp)(PPh_3)] and [Pt(dba)(PPh_3)] were prepared following reported procedures.[1,2]

Instrumentation – general. NMR spectra were recorded on a 600 MHz *Bruker* Avance II+ spectrometer or a 500 MHz *Bruker* Avance III spectrometer. All measurements were done at room temperature. ^{1}H signals were referenced to TMS. The following abbreviations are used to indicate the multiplicity of signals: s = singlet, d = doublet, t = triplet, q = quartet, quint = quintet, m = multiplet. The assignment of the signals to the protons present in larger molecules was done with the help of 2D NMR experiments. High resolution electrospray ionisation (HR-ESI) mass spectra were measured on a Thermo Scientific LTQ Orbitrap XL spectrometer using an FTMS analyser. Cyclic voltammetry measurements were performed in a baked-out cyclic voltammetry cell with a glassy carbon working electrode, a platinum counter electrode and an Ag/AgCl pseudo reference electrode. Scans were carried out in 0.1 M nBu$_4$NPF$_6$ THF solution at a scan rate of 50 mV/s or 100 mV/s. The potential was regulated using a *Metrohm* μStat400 potentiostat. The measured data was referenced to the $FeCp_2/FeCp_2^+$ redox pair. UV-vis absorption spectra were measured on a *Varian* 50 Scan UV-vis photometer. Quartz glass cuvettes with a length of 1 cm were used and all spectra were baseline corrected.

Photoluminescence experiments. Photoluminescence spectra at were recorded with a *Spex FluoroMax-3* spectrometer. Luminescence quantum yields were determined with a *Hamamatsu Photonic*s absolute PL quantum yield measurement system (C9920–02), equipped with a L9799-01 CW Xenon light source, monochromator, photonic multichannel analyser and integrating sphere. An error ± 2% for the photoluminescence quantum yield Φ is estimated. Degassed spectroscopic grade solvents were used. Photoluminescence quantum yields were measured with a Hamamatsu Photonics absolute PL quantum yield measurement system (C9920-02) equipped with a L9799-01 CW Xe light source (150 W), a monochromator, a C7473 photonic multi-channel analyser, an integrating sphere and employing U6039-05 software (Hamamatsu Photonics, Ltd., Shizuoka, Japan). Steady-state excitation and emission spectra were recorded on a FluoTime 300 spectrometer from PicoQuant equipped with: a 300 W ozone-free Xe lamp (250-900 nm), a 10 W Xe flash-lamp (250-900 nm, pulse width ca. 1 μs) with repetition rates of 0.1 – 300 Hz, a double-grating excitation monochromator (Czerny-Turner type, grating with 1200 lines/mm, blaze wavelength: 300 nm), diode lasers (pulse width < 80 ps) operated by a computer-controlled laser driver PDL-828 "Sepia II" (repetition rate up to 80 MHz, burst mode for slow and weak decays), two double-grating emission monochromators (Czerny-Turner, selectable gratings blazed at 500 nm with 2.7 nm/mm dispersion and 1200 lines/mm, or blazed at 1200 nm with 5.4 nm/mm dispersion and 600 lines/mm) with adjustable slit width between 25 μm and 7 mm, Glan-Thompson polarizers for excitation (after the Xe-lamps) and emission (after the sample). Different sample holders (Peltier-cooled mounting unit ranging from –15 to 110 °C or an adjustable front-face sample holder), along with two detectors (namely a PMA Hybrid-07 from PicoQuant with transit time spread FWHM < 50 ps, 200 – 850 nm, or a H10330C-45-C3 NIR detector with transit time spread FWHM 0.4 ns, 950-1700 nm from Hamamatsu) were used. Steady-state spectra and photoluminescence lifetimes were recorded in TCSPC mode by a PicoHarp 300 (minimum base resolution 4 ps) or in MCS mode by a TimeHarp 260 (where up to several ms can be traced). Emission and excitation spectra were corrected for source intensity (lamp and grating) by standard correction curves. For samples with lifetimes in the ns order, an instrument

response function calibration (IRF) was performed using a diluted Ludox® dispersion. Lifetime analysis was performed using the commercial EasyTau 2 software (PicoQuant). The quality of the fit was assessed by minimizing the reduced chi squared function ($\chi 2$) and visual inspection of the weighted residuals and their autocorrelation. Assuming unitary intersystem crossing efficiencies (due to the chelation of a late transition metal), the average radiative and radiationless deactivation rate constants (k_r and k_{nr}, respectively) were calculated according to the following equations and relationships:

$$k_r = \frac{\Phi_L}{\tau_L}, \qquad k_{\mathrm{nr}} = \frac{1-\Phi_L}{\tau_L}, \qquad \text{and } \tau_{\mathrm{L}} = \frac{1}{k_r + k_{nr}}$$

where τ_L is the excited state lifetime (or amplitude-weighted average lifetime, $\tau_{av\_amp,}$ for multiexponential decays).

Transient absorption spectroscopy. The ultrafast transient absorption (TA) experiments were performed using a custom-built setup described in detail elsewhere.[3] We employ a Ti-Sapphire (Astrella, Coherent Inc.) regenerative amplifier, which produces 800 nm, 85-fs pulses (laser power-5W, pulse-to-pulse repetition rate of 1 kHz). A part of the amplifier output at 800 nm is directed to an optical parametric amplifier (TOPAS Prime, Light Conversion) to generate the pump at 340 or 500 nm. The excited state dynamics was studied with white-light supercontinuum pulses (generated by focusing a small portion of the amplifier output onto CaF_2 crystal). The fs-TA data was analysed using the KIMOPACK tool.[4] Prior to global lifetime analysis, the data was arrival-time (chirp) corrected. The temporal resolution of the experiment is limited to 300 fs because of strong contributions of coherent artefact signals to the data interfere with reliable analysis of the pump-probe data at short delay times. The power of pump-pulse used was in the range of 0.4 to 0.8 mW, OD of sample at the excitation wavelength was in the range of 0.3 to 0.5.

Structure solution from single crystal X-ray diffraction. scXRD measurements were performed on a *Bruker D8 Venture* diffractometer including a *Bruker Photon 100 CMOS* detector using Ag K_α (λ = 0.56086 Å) or Mo K_α (λ = 0.71073 Å) radiation. The crystal data was collected using APEX4 v2021.10-0 [5]. The structures were solved by dual space methods using SHELXT, and the refinement was carried out with SHELXL employing the full-matrix least-squares methods on $F_O^2 < 2\sigma(F_O^2)$ as implemented in ShelXle [6–8]. The non-hydrogen atoms were refined with anisotropic displacement parameters without any constraints. The hydrogen atoms were included by using appropriate riding models.

Computational details. All DFT calculations were performed using ORCA 5.0.2.[9,10] For all atoms, def2-TZVP basis sets, as well as the corresponding def2-ECPs for Pt and Sb, were used unless stated otherwise.[11] The S_0 and T_1 geometries of all compounds were optimised at the BP86 level of theory, using *Grimme's* D3 dispersion correction and the conductor-like polarisable continuum model (CPCM) parametrised for CH_2Cl_2 as an approximate solvation model.[12–17] The geometry optimisations were followed up with numerical frequency calculations in order to confirm the energetic minimum nature of the optimised structure as indicated by the absence of imaginary modes. On the optimised geometries, single point and TD-DFT calculations were performed using the TPSSh functional, *Grimme's* D3 dispersion correction and CPCM parametrised for CH_2Cl_2.[18] Orbital isosurfaces were extracted from the S_0 single point calculations using the ORCA module orca_plot and plotted with the visualisation software CHEMCRAFT at an isovalue of 0.04.[19] For the TD-DFT calculations of absorption spectra for the S_0 states, 40 roots (transitions) for singlets and triplets each were included for each complex. Broadened spectra were obtained using the orca_mapspc module with 2000 cm^{-1} full width at half maximum band broadening. The TD-DFT calculation output was further evaluated using the software package TheoDORE to analyse relative MLCT, L'MCT, LC, LL'CT, and MC contributions to the emissive T_1 states, using the implemented standard algorithm for molecular partitioning of transition metal complexes employing Openbabel.[20] At the T_1 geometries, spin-orbit (SO) calculations were performed using the Zeroth-Order Regular Approximation (ZORA), the TPSSh functional, SARC-ZORA-TZVP basis sets for Pt and Sb, and the CPCM parametrised for CH_2Cl_2.[21–23]

Syntheses

[Pt(dpp)(AsPh$_3$)] 50.0 mg (0.100 mmol, 1.00 eq.) [Pt(dpp)(dmso)] were dissolved in 3 mL CH_2Cl_2 and 30.6 mg (0.100 mmol, 1.00 eq.) $AsPh_3$ were added. After 10 min, the solvent was removed and the crude product was purified via silica gel column chromatography (eluent: CH_2Cl_2). Yield: 54.1 mg (0.074 mmol, 74%) orange solid. ^{1}H NMR (600 MHz, CD_2Cl_2): δ [ppm] = 7.81–7.75 (m, 6H, H13), 7.66 (t, $^3J_{H,H}$ = 8.0 Hz, 1H, H4), 7.46 (t, $^3J_{H,H}$ = 7.4 Hz, 3H, H14), 7.44–7.38 (m, 8H, H10 and H12), 7.34 (d, $^3J_{H,H}$ = 8.0 Hz, 2H, H3), 6.90 (td, $J_{H,H}$ = 7.4 Hz, 1.3 Hz, 2H, H9), 6.62 (td, $J_{H,H}$ = 7.3 Hz, 1.4 Hz, 2H, H8), 6.48 (dd, $J_{H,H}$ = 7.4 Hz, 0.7 Hz, $^3J_{Pt,H}$ = 25.5 Hz, 2H, H7). ^{13}C NMR (125 MHz, CD_2Cl_2): δ [ppm] = 166.7 (C2), 164.9 (C5), 150.8 (C6), 140.4 (C4), 139.2 (C7), 134.5 (C13), 133.2 (C11), 130.4 (C14), 129.8 (C8), 128.6 (C12), 123.8 (C10), 123.5 (C9), 114.8 (C3). HR-ESI-MS(+): m/z = 730.09913 ([M]$^+$, calc.: m/z = 730.09806).

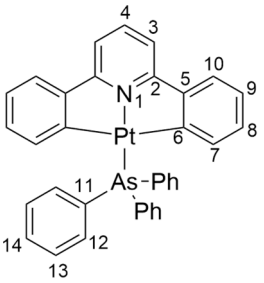

[Pt(dpp)(SbPh$_3$)] 50.0 mg (0.100 mmol, 1.00 eq.) [Pt(dpp)(dmso)] were dissolved in 3 mL CH_2Cl_2 and 38.8 mg (0.110 mmol, 1.10 eq.) SbPh3 were added. After 10 min, the solvent was removed and the crude product was purified via silica gel column chromatography (eluent: CH_2Cl_2). Yield: 50.0 mg (0.064 mmol, 64%) orange solid. ^{1}H NMR (600 MHz, CD_2Cl_2): δ [ppm] = 7.76–7.72 (m, 6H, H13), 7.67 (t, $^3J_{H,H}$ = 8.0 Hz, 1H, H4), 7.50 (m, 3H, H14), 7.45–7.40 (m, 8H, H10 and H12), 7.34 (d, $^3J_{H,H}$ = 8.0 Hz, 2H, H3), 7.03 (dd, $J_{H,H}$ = 7.3 Hz, 1.3 Hz, $^3J_{Pt,H}$ = 32.6 Hz, 2H, H7) 6.93 (td, $J_{H,H}$ = 7.5 Hz, 1.3 Hz, 2H, H9), 6.67 (td, $J_{H,H}$ = 7.3 Hz, 1.3 Hz, 2H, H8). ^{13}C NMR (125 MHz, CD_2Cl_2): δ [ppm] = 166.6 (C2), 164.0 (C5), 150.9 (C6), 141.7 (C7), 140.6 (C4), 136.5 (C13), 130.7 (C8), 130.4 (C14), 129.9 (C11), 129.0 (C12), 124.0 (C10), 123.6 (C9), 115.0 (C3). HR-ESI-MS(+): m/z = 776.08145 ([M]$^+$, calc.: m/z = 776.08028).

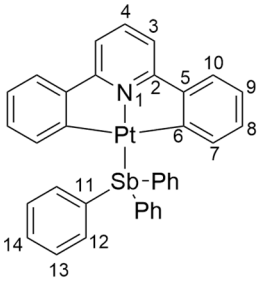

[Pt(dba)(AsPh$_3$)] 35.0 mg (0.068 mmol, 1.00 eq.) [Pt(dba)(dmso)] were dissolved in 3 mL CH_2Cl_2 and 20.7 mg (0.068 mmol, 1.00 eq.) $AsPh_3$ were added. After 40 min, the solvent was removed and the crude product was purified via silica gel column chromatography (eluent: CH_2Cl_2). Yield: 34.3 mg (0.044 mmol, 65%) red solid. ^{1}H NMR (600 MHz, CD_2Cl_2): δ [ppm] = 8.49 (s, 1H, H4), 7.92–7.84 (m, 6H, H15), 7.61 (d, $^3J_{H,H}$ = 8.9 Hz, 2H, H5), 7.56 (d, $^3J_{H,H}$ = 9.1 Hz, 2H, H6), 7.53–7.47 (m, 3H, H16), 7.47–7.42 (m, 6H, H14), 7.37 (dd, $J_{H,H}$ = 7.9 Hz, 0.9 Hz, 2H, H12), 7.06–7.00 (m, 2H, H11), 6.53 (dd, $J_{H,H}$ = 7.1 Hz, 0.7 Hz, $^3J_{Pt,H}$ = 12.7 Hz, 2H, H10). ^{13}C NMR (125 MHz, CD_2Cl_2): δ [ppm] = 162.5 (C8), 155.6 (C2), 147.4 (C9), 135.7 (C10), 135.2 (C15), 134.6 (C4), 134.4 (C7), 133.2 (C11), 130.6 (C16), 130.5 (C13), 129.0 (C14), 128.7 (C5), 124.4 (C3), 122.9 (C6), 121.4 (C12). HR-ESI-MS(+): m/z = 778.09874 ([M]$^+$, calc.: m/z = 778.09806).

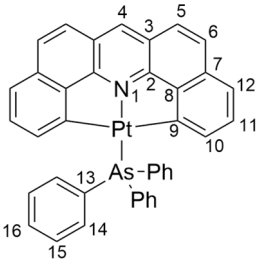

[Pt(dba)(SbPh$_3$)] 31.0 mg (0.060 mmol, 1.00 eq.) [Pt(dba)(dmso)] were dissolved in 3 mL CH_2Cl_2 and 21.1 mg (0.060 mmol, 1.00 eq.) $SbPh_3$ were added. After 45 min, the solvent was removed and the crude product was purified via silica gel column chromatography (eluent: CH_2Cl_2). Yield: 41.7 mg (0.051 mmol, 84%) red solid. ^{1}H NMR (600 MHz, CD_2Cl_2): δ [ppm] = 8.51 (s, 1H, H4), 7.86–7.80 (m, 6H, H15), 7.63 (d, $^3J_{H,H}$ = 8.9 Hz, 2H, H5), 7.58 (d, $^3J_{H,H}$ = 8.9 Hz, 2H, H6), 7.54–7.49 (m, 3H, H16), 7.48–7.43 (m, 6H, H14), 7.40 (dd, $J_{H,H}$ = 6.2 Hz, 4.2 Hz, $^5J_{Pt,H}$ = 15.4 Hz, 2H, H12), 7.12–7.05 (m, 4H, H10 and H11). ^{13}C NMR (125 MHz, CD_2Cl_2): δ [ppm] = 161.3 (C8), 155.5 (C2), 147.5 (C9), 137.9 (C10), 136.5 (C15), 135.4 (C4), 134.8 (C7), 131.3 (C11), 130.5 (C16), 129.8 (C13), 129.2 (C14), 129.0 (C5), 124.6 (C3), 123.0 (C6), 121.6 (C12). HR-ESI-MS(+): m/z = 824.08130 ([M]+, calc.: m/z = 824.08028).

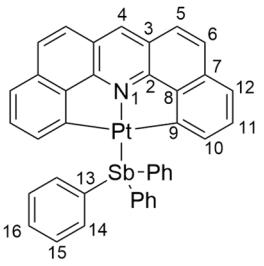

Attempted synthesis of [Pt(dpp)(BiPh$_3$)]

Time resolved NMR study. For *in situ* observation of the reaction of [Pt(dpp)(dmso)] with $BiPh_3$, the latter (0.75 eq.) was added to a solution of the Pt complex in CD_2Cl_2, and the sample was quickly transferred into a 600 MHz NMR spectrometer (see above for details on instrumentation). During the

first few minutes, ^{1}H NMR spectra were recorded in quick succession, but no change was detected between them. ^{1}H NMR (600 MHz, CD_2Cl_2): δ [ppm] = 7.68 (d, $H_{complex}$), 7.65 (d, H_{BiPh3}), 7.53 (t, $H_{complex}$), 7.38 (dd, $H_{complex}$), 7.29 (t, H_{BiPh3}), 7.23 (m, H_{BiPh3}), 7.16 (td, $H_{complex}$), 7.01 (td, $H_{complex}$). For the following 12 h, spectra were recorded every 10 min. The integrals of the observed signals were normalised to a value of 2.00 for the signal at 7.38 ppm which belongs to [Pt(dpp)(dmso)]. The integral of the well-isolated multiplet at 7.29 ppm belonging to $BiPh_3$ decreased significantly over the timescale of the experiment from ca. 4.5 to ca. 3.8 (Fig. S21). The less well-isolated $BiPh_3$ signals decreased in an approximately proportional manner.

MS analysis. A mixture of [Pt(dpp)(dmso)] (68.6 mg, 0.137 mmol, 1.0 eq.) and $BiPh_3$ (120.2 mg, 0.273 mmol, 2.0 eq.) in 4 mL CH_2Cl_2 was stirred at room temperature for 6 d. Precipitation of black solids was observed. The solids were removed by filtration and the filtrate was evaporated to dryness. EI-MS analysis of the residue detected a variety of fragments and coupling products, i.e. phenylated H_2dpp derivatives, derived from the starting materials. m/z = 154.07748 ($[PhPy]^+$, calc.: 154.065674), 208.97958 ($[Bi]^+$, calc.: 208.980399), 230.09628 ($[Hdpp]^+$, calc.: 230.096974), 286.01876 ($[PhBi]^+$, calc.: 286.019524), 306.12744 ($[Hdpp–Ph]^+$, calc.: 306.128275), 382.15869 ($[Ph\text{-}dpp\text{-}Ph]^+$, calc.: 382.159575), 458.19002 ($[Ph_2–dpp–Ph]^+$, calc.: 458.190875), 535.21646 ($[Ph_2–dpp–Ph_2]^+$, calc.: 535.230000).

Supporting Figures

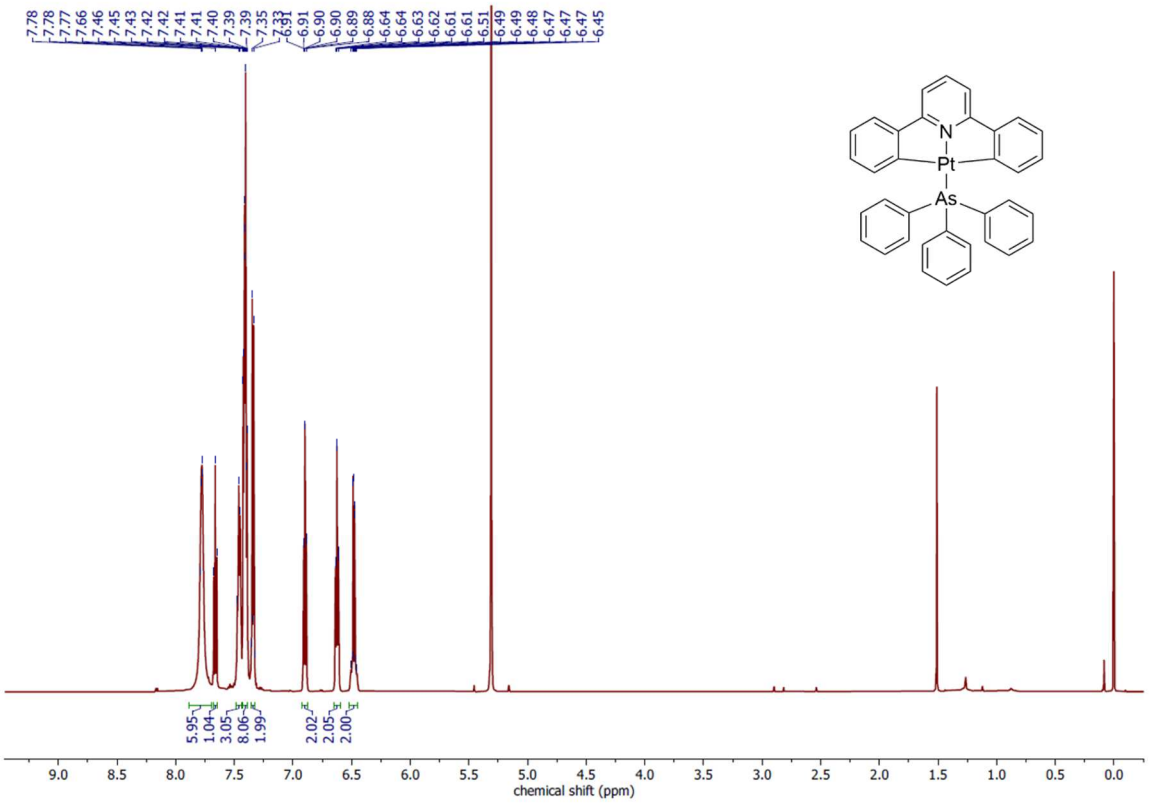

Fig. S1 600 MHz ^{1}H NMR of [Pt(dpp)($AsPh_3$)] in CD_2Cl_2.

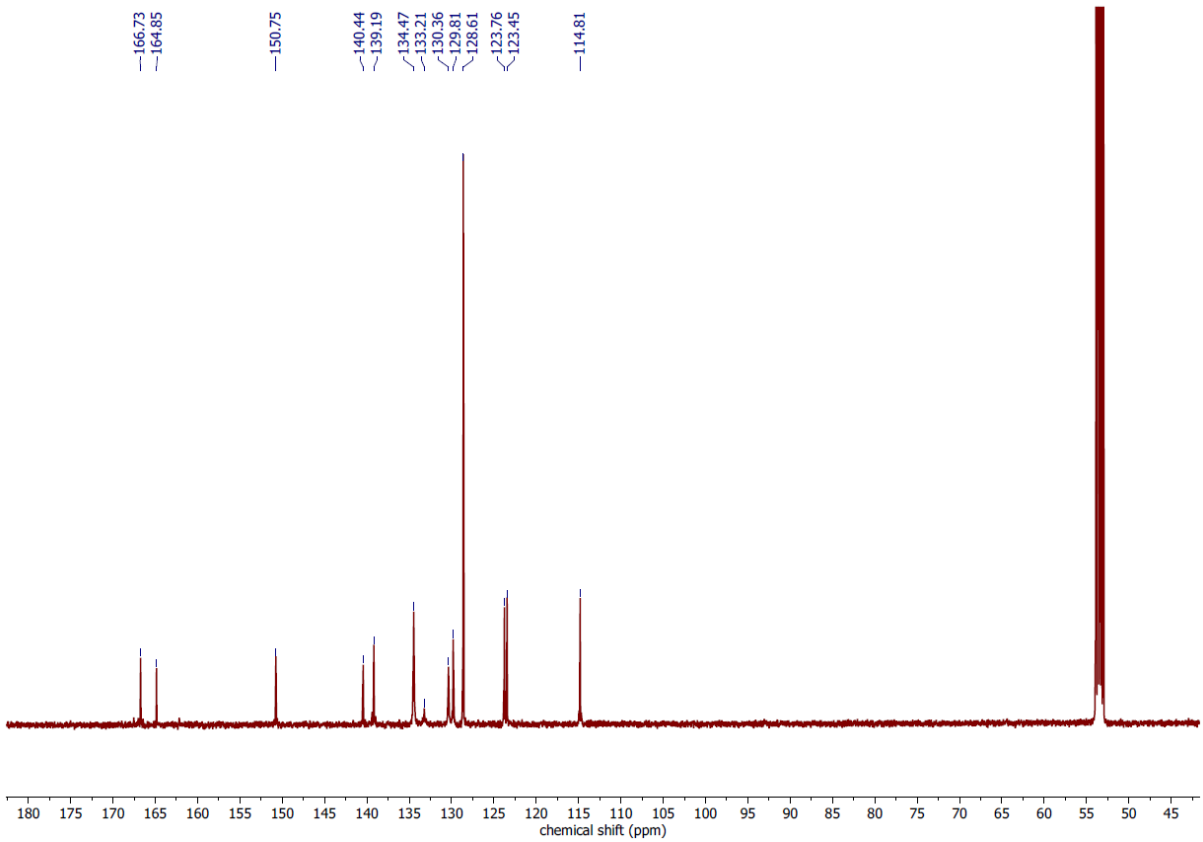

Fig. S2 125 MHz ^{13}C NMR of [Pt(dpp)($AsPh_3$)] in CD_2Cl_2.

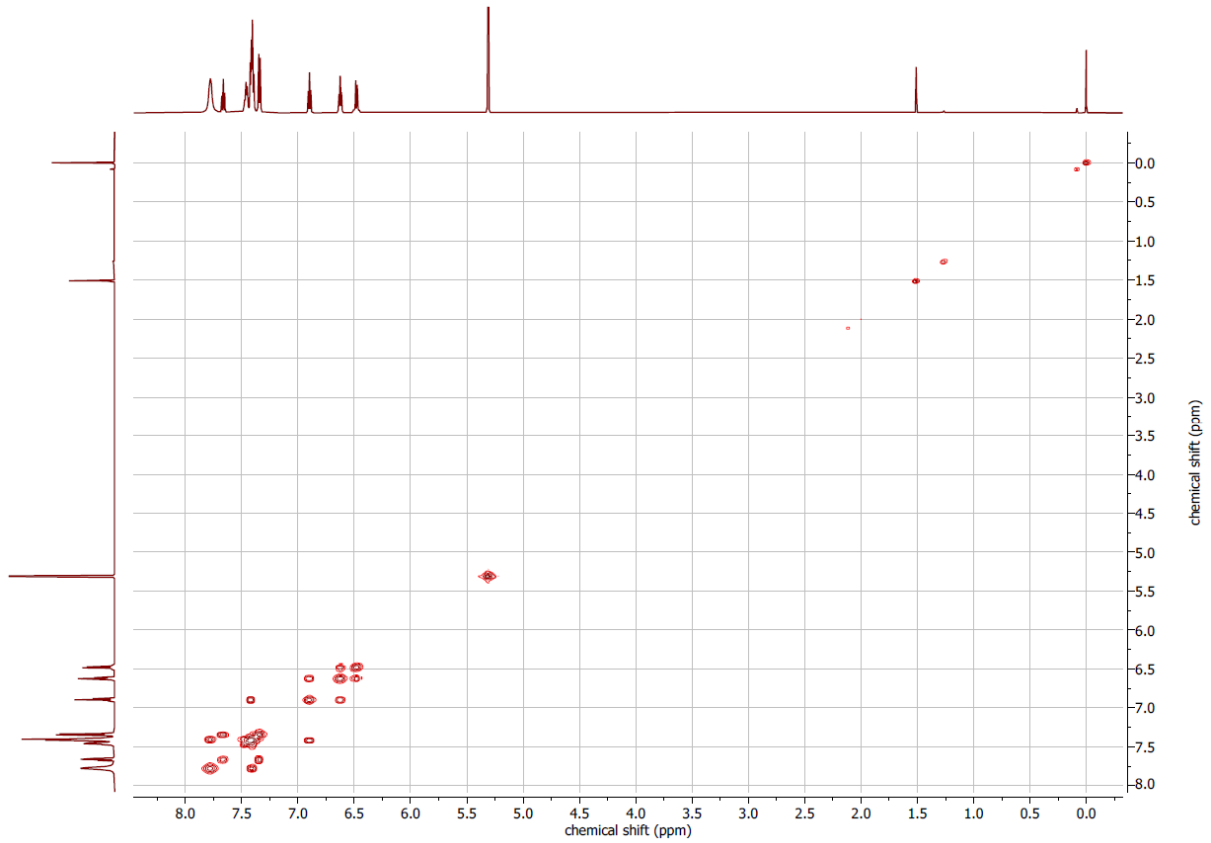

Fig. S3 500 MHz $^{1}H,^{1}H$ COSY of [Pt(dpp)($AsPh_3$)] in CD_2Cl_2.

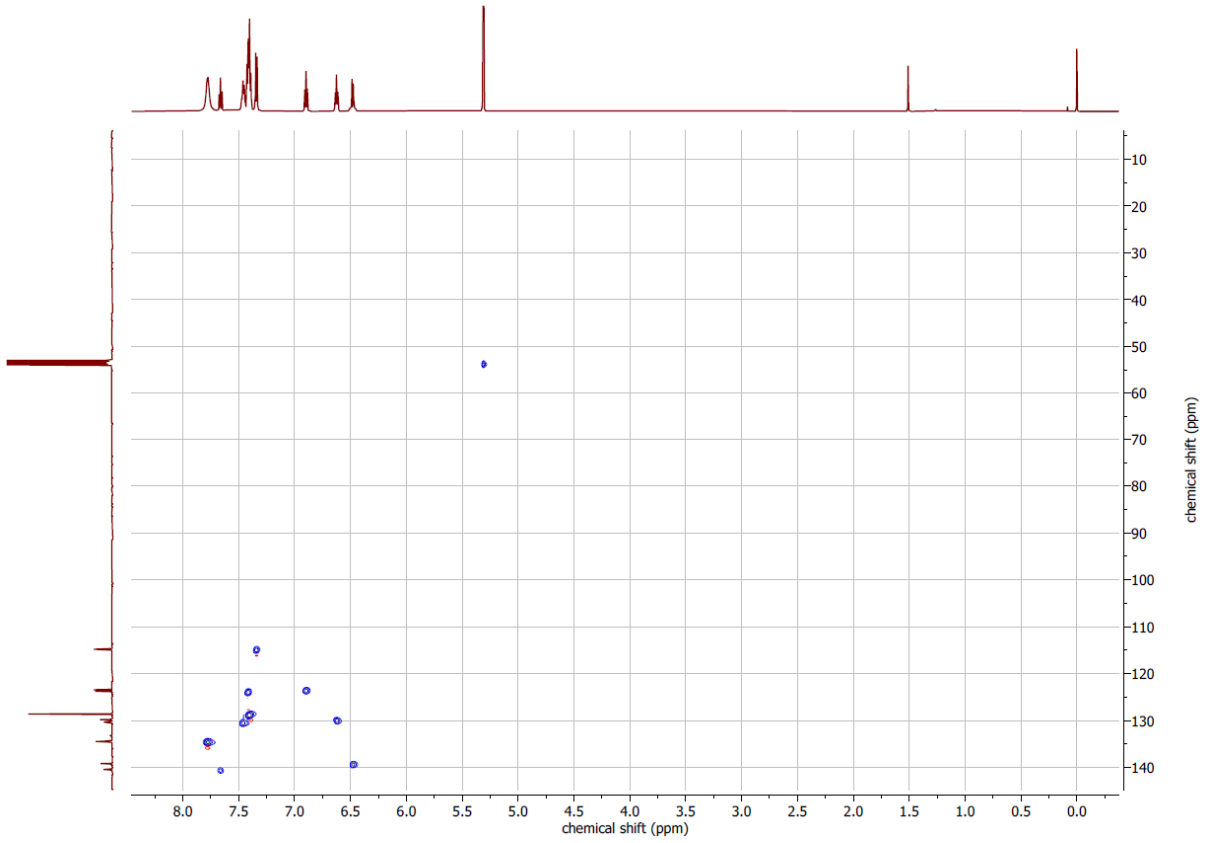

Fig. S4 500 MHz $^{1}H,^{13}C$ HSQC of [Pt(dpp)($AsPh_3$)] in CD_2Cl_2.

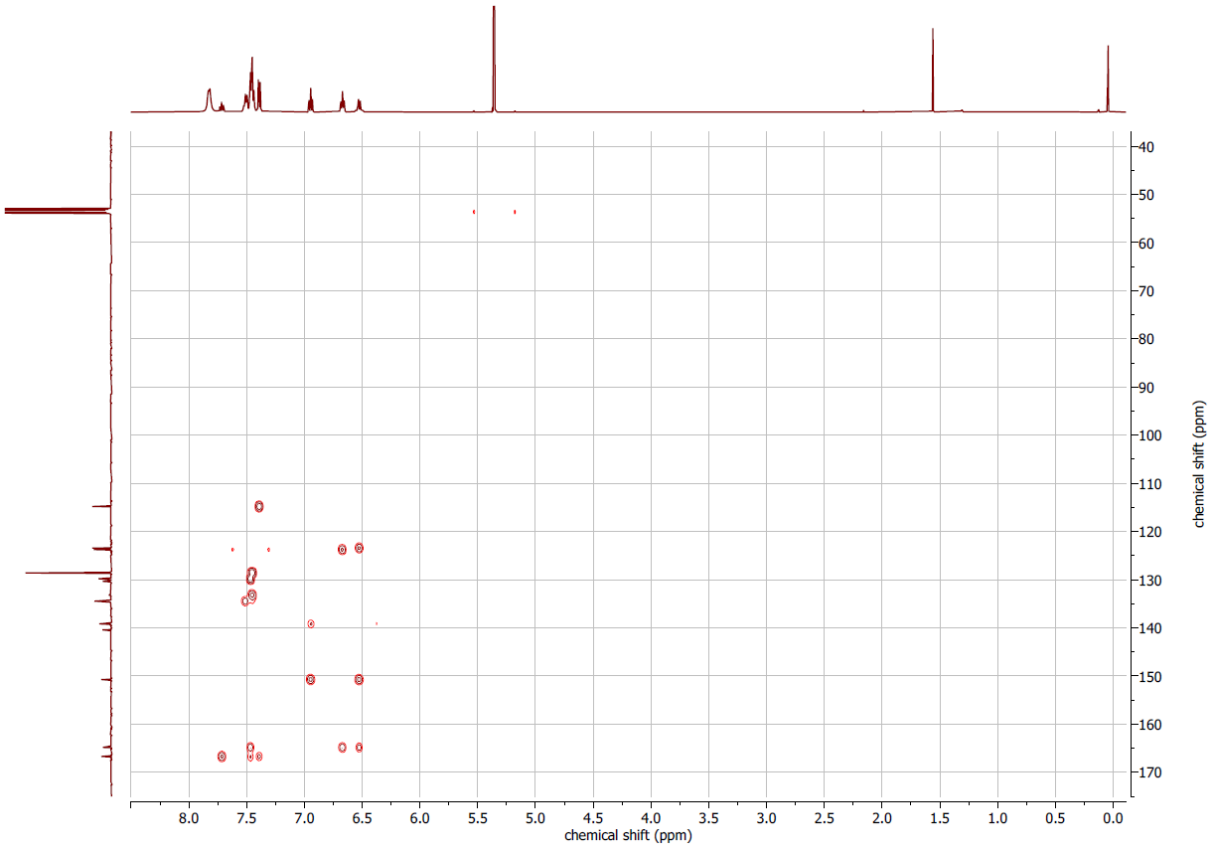

Fig. S5 500 MHz $^{1}H,^{13}C$ HMBC of [Pt(dpp)($AsPh_3$)] in CD_2Cl_2.

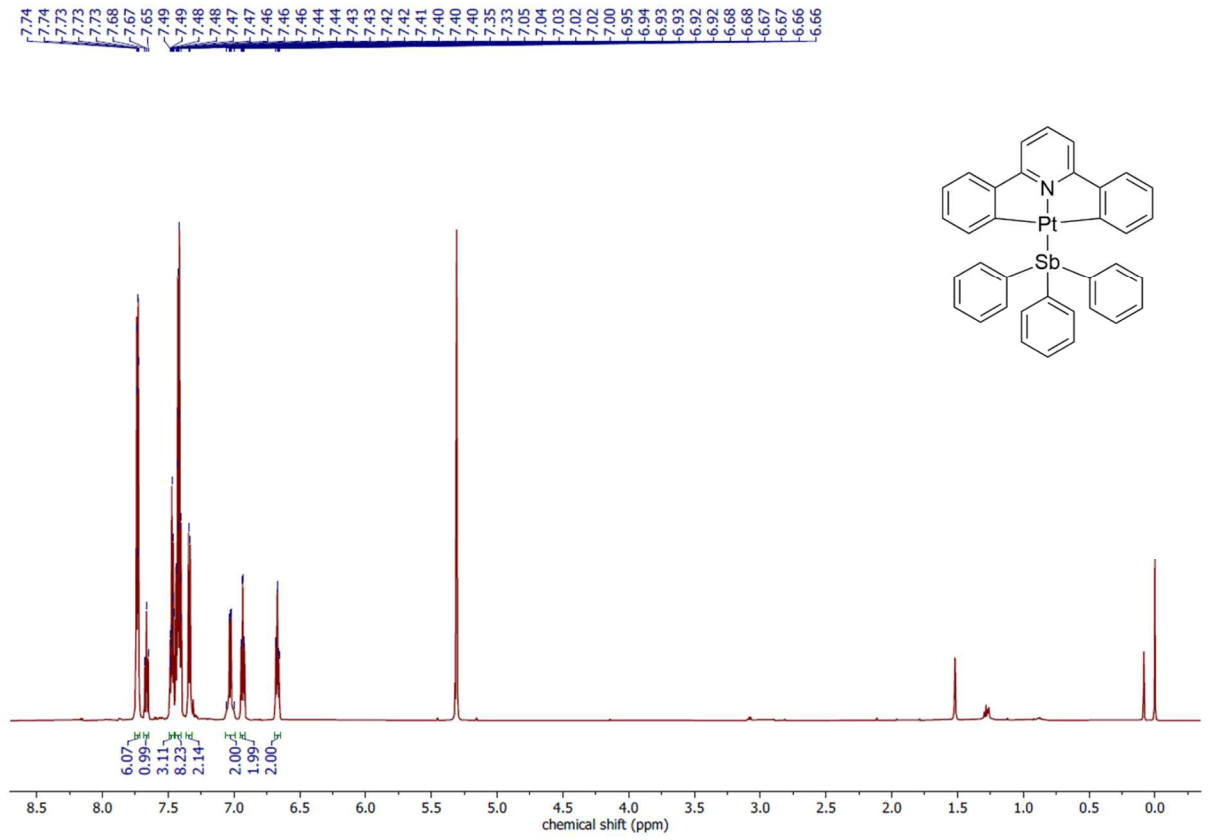

Fig. S6 600 MHz ^{1}H NMR of [Pt(dpp)($SbPh_3$)] in CD_2Cl_2.

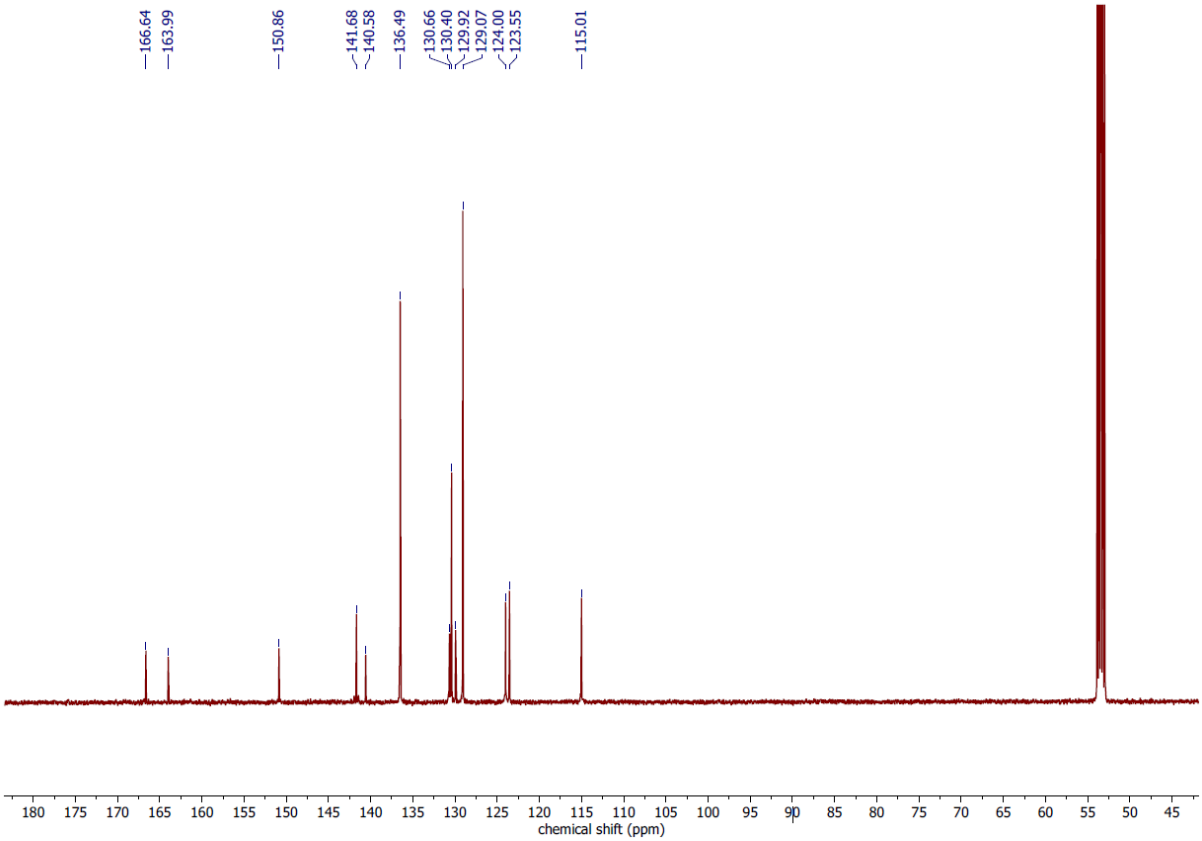

Fig. S7 125 MHz ^{13}C NMR of [Pt(dpp)($SbPh_3$)] in CD_2Cl_2.

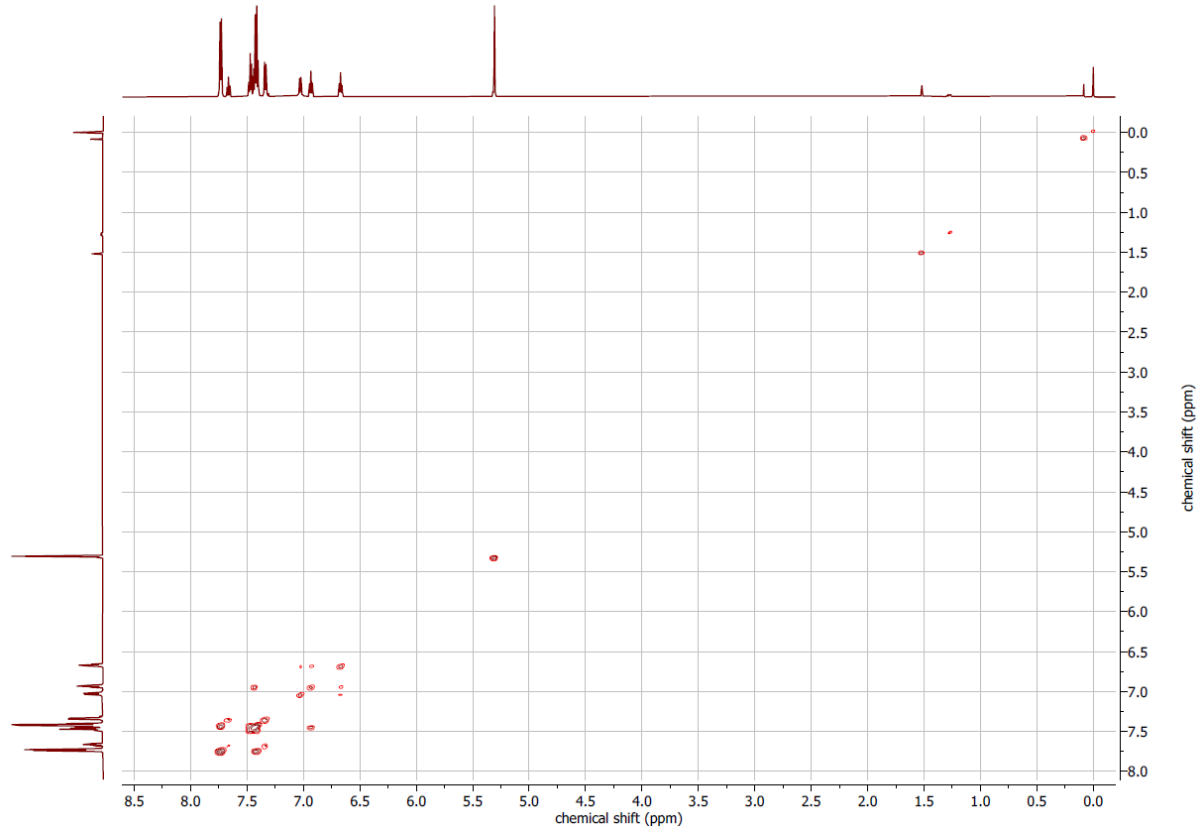

Fig. S8 500 MHz $^{1}H,^{1}H$ COSY of [Pt(dpp)($SbPh_3$)] in CD_2Cl_2.

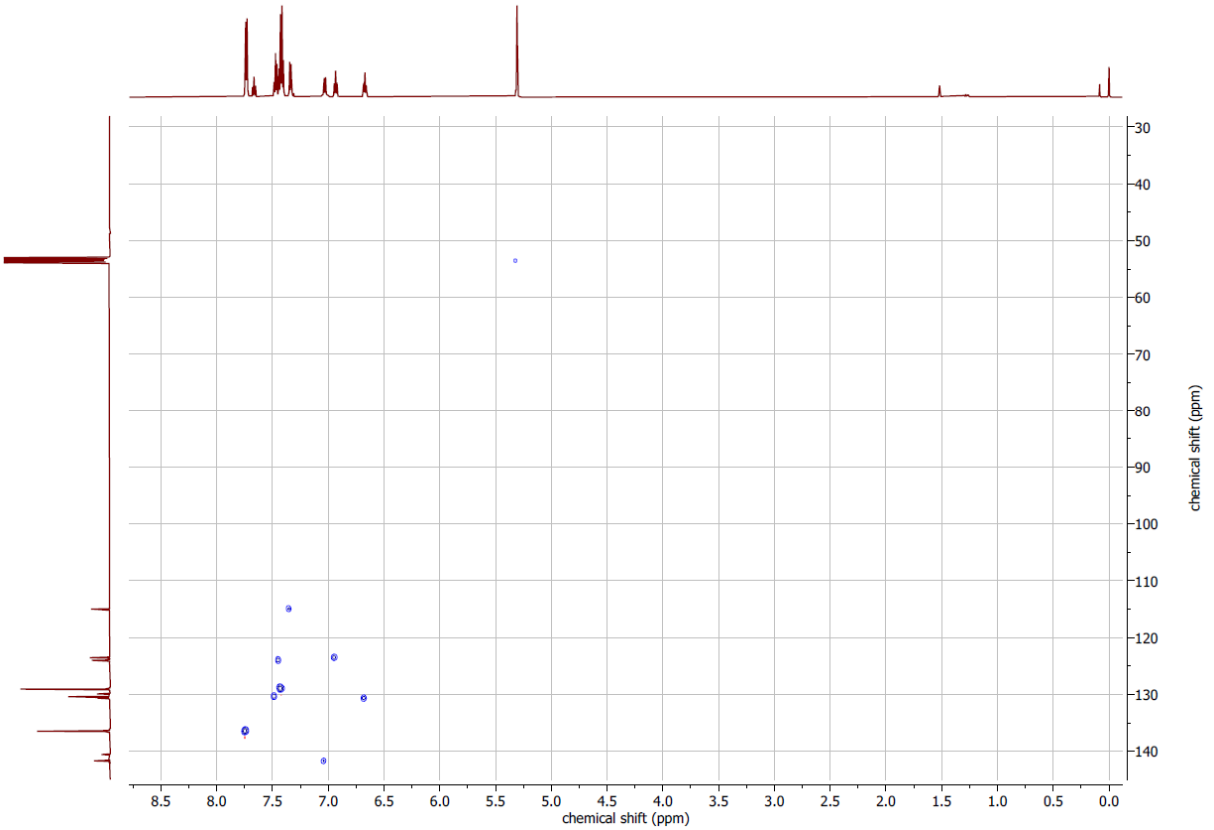

Fig. S9 500 MHz $^{1}H,^{13}C$ HSQC of [Pt(dpp)($SbPh_3$)] in CD_2Cl_2.

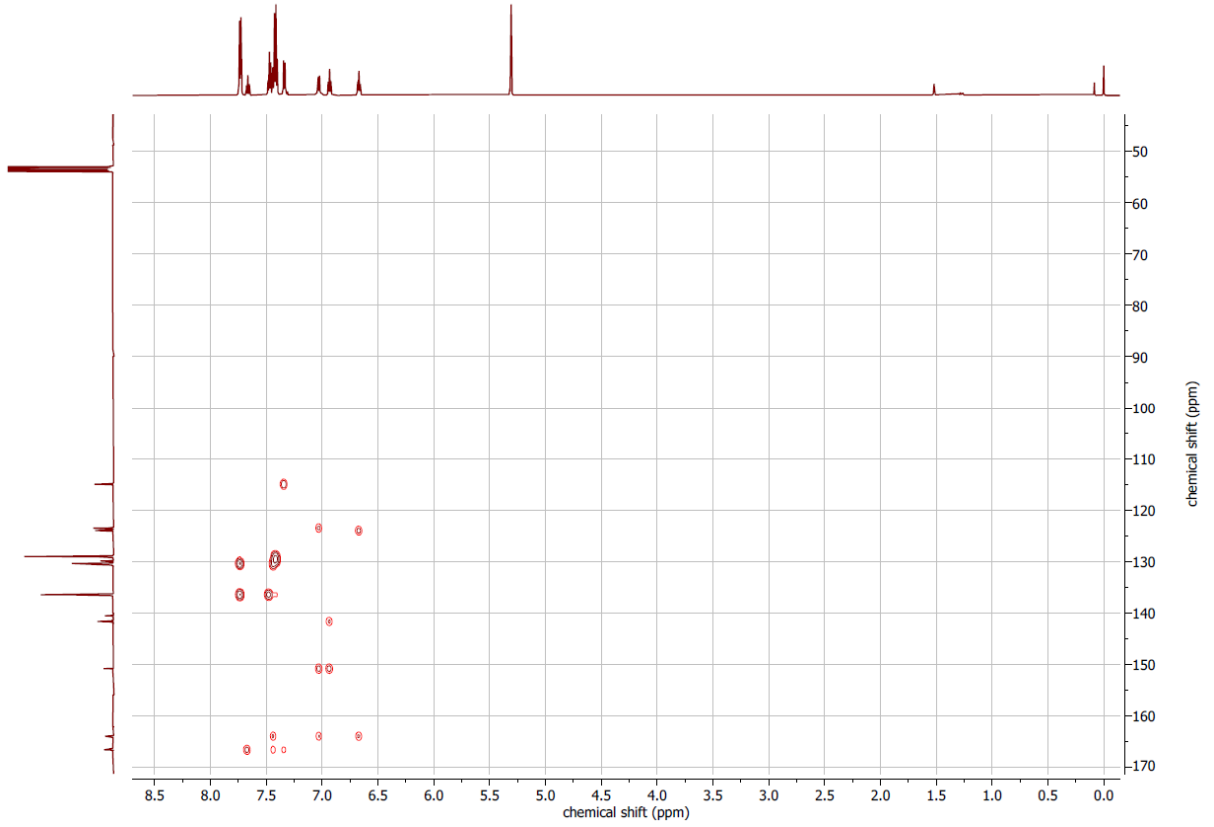

Fig. S10 500 MHz $^{1}H,^{13}C$ HMBC of [Pt(dpp)($SbPh_3$)] in CD_2Cl_2.

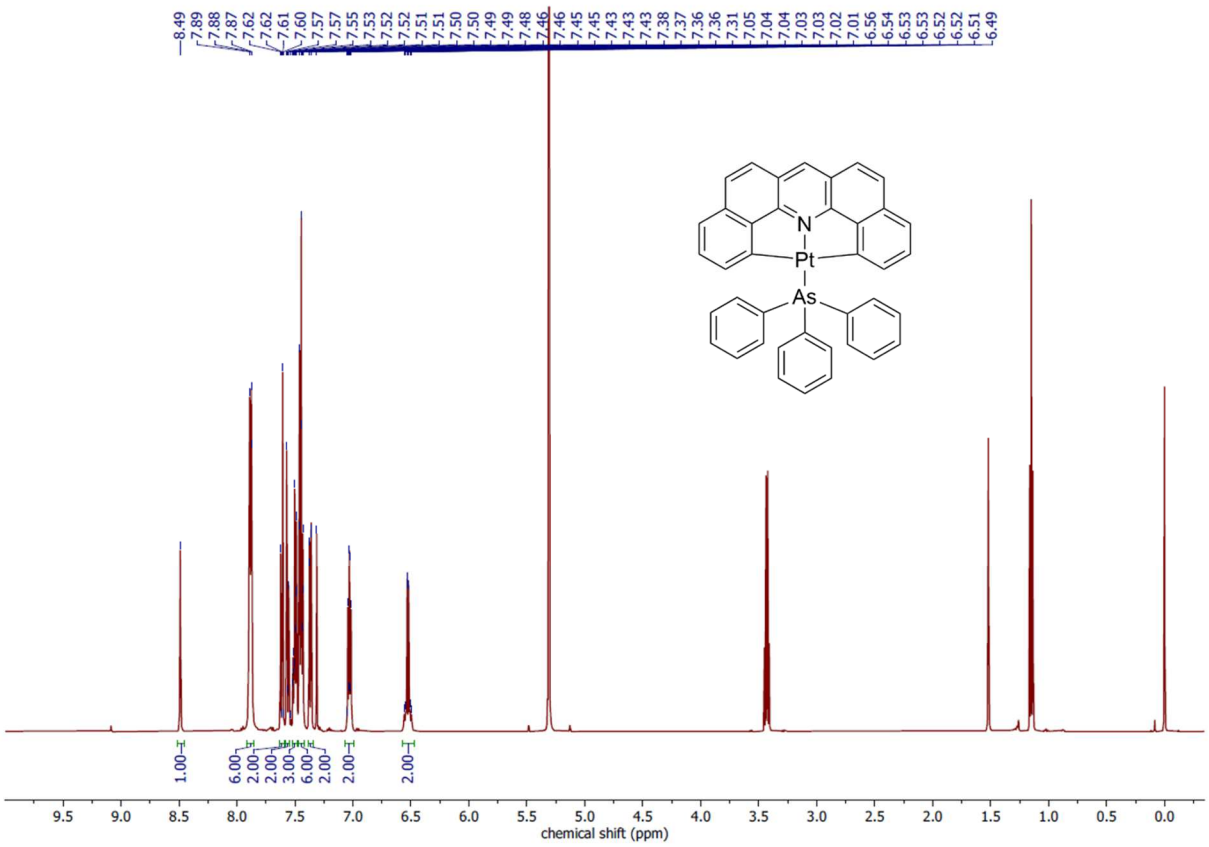

Fig. S11 500 MHz ^{1}H NMR of [Pt(dba)(AsPh$_3$)] in CD_2Cl_2.

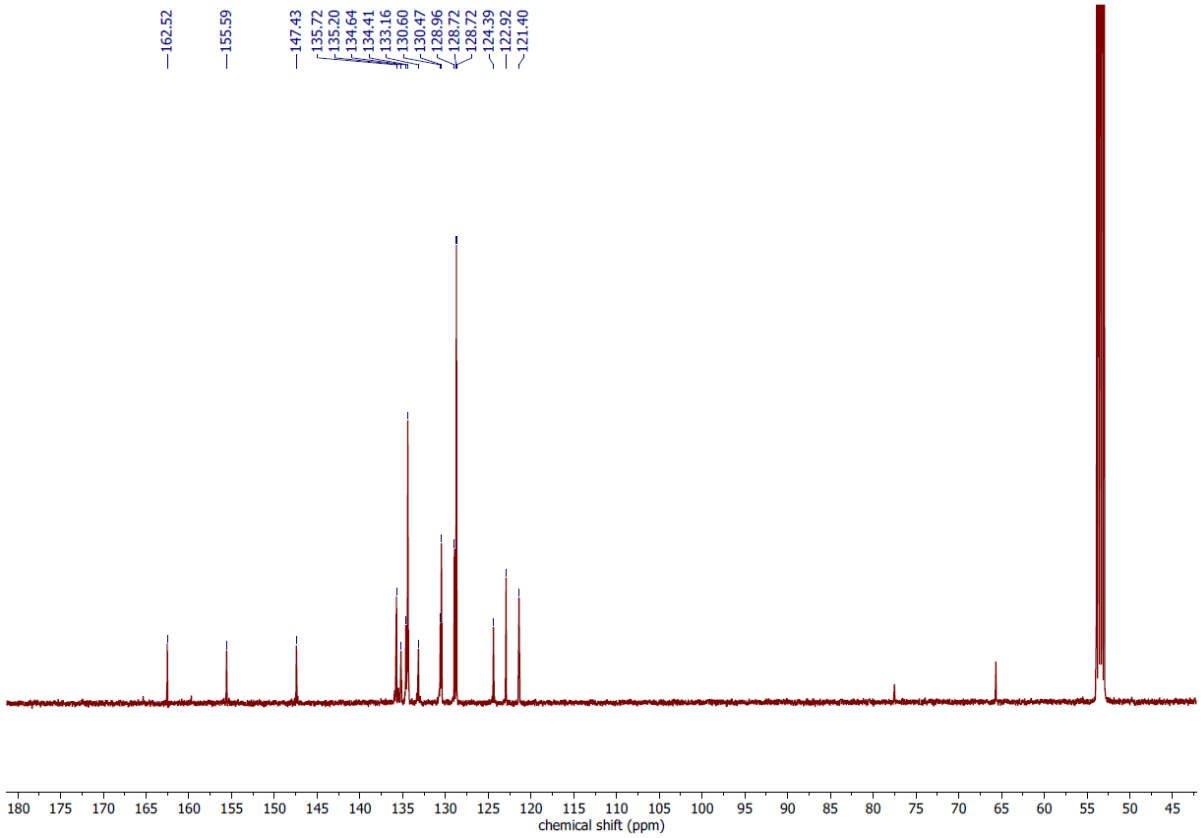

Fig. S12 125 MHz ^{13}C NMR of [Pt(dba)(AsPh$_3$)] in CD_2Cl_2.

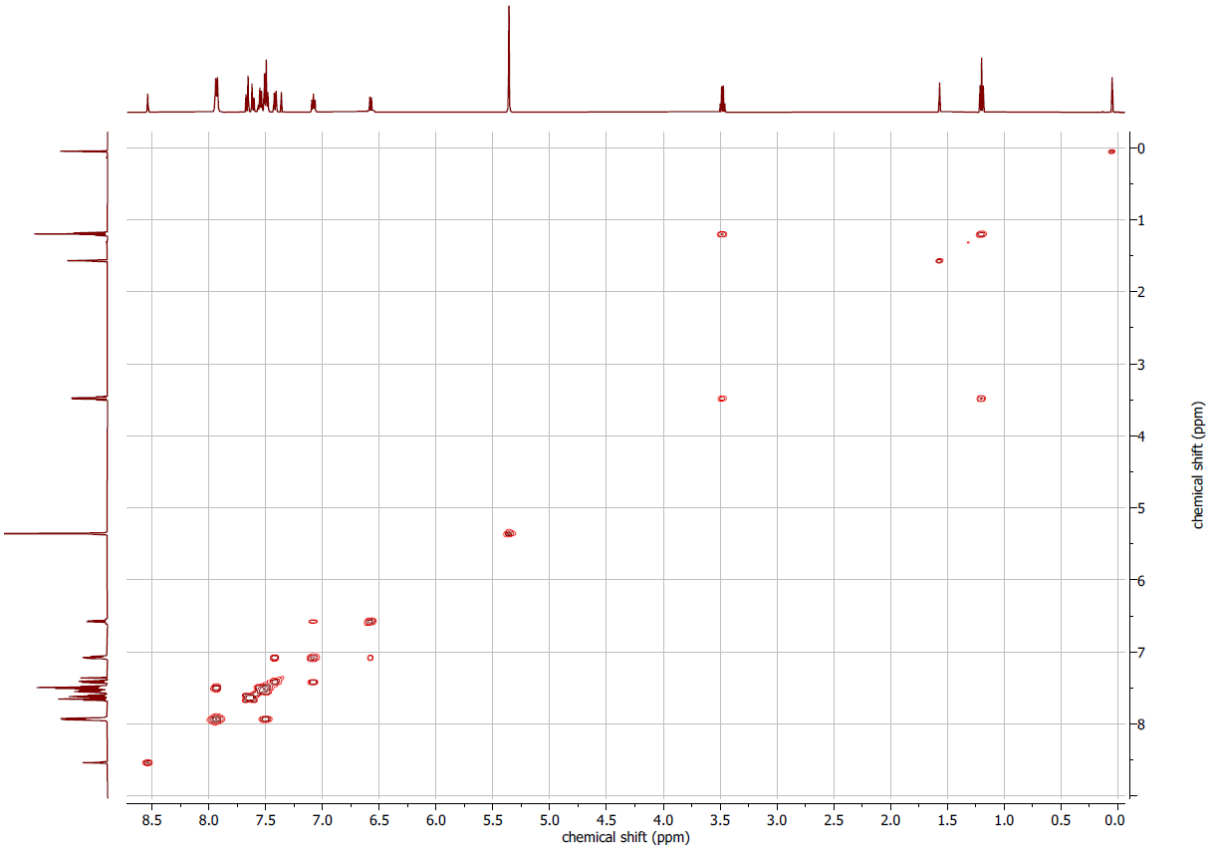

Fig. S13 500 MHz $^{1}H,^{1}H$ COSY of [Pt(dba)($AsPh_3$)] in CD_2Cl_2.

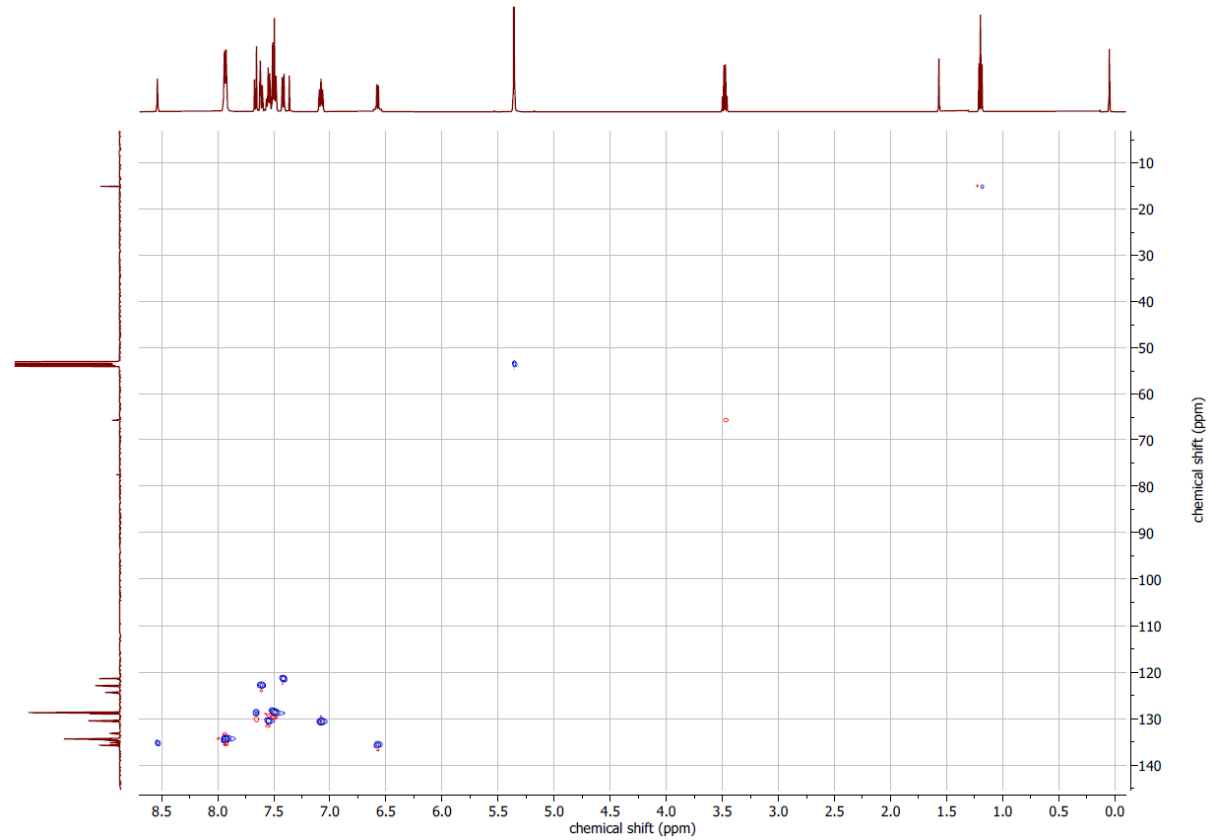

Fig. S14 500 MHz $^{1}H,^{13}C$ HSQC of [Pt(dba)($AsPh_3$)] in CD_2Cl_2.

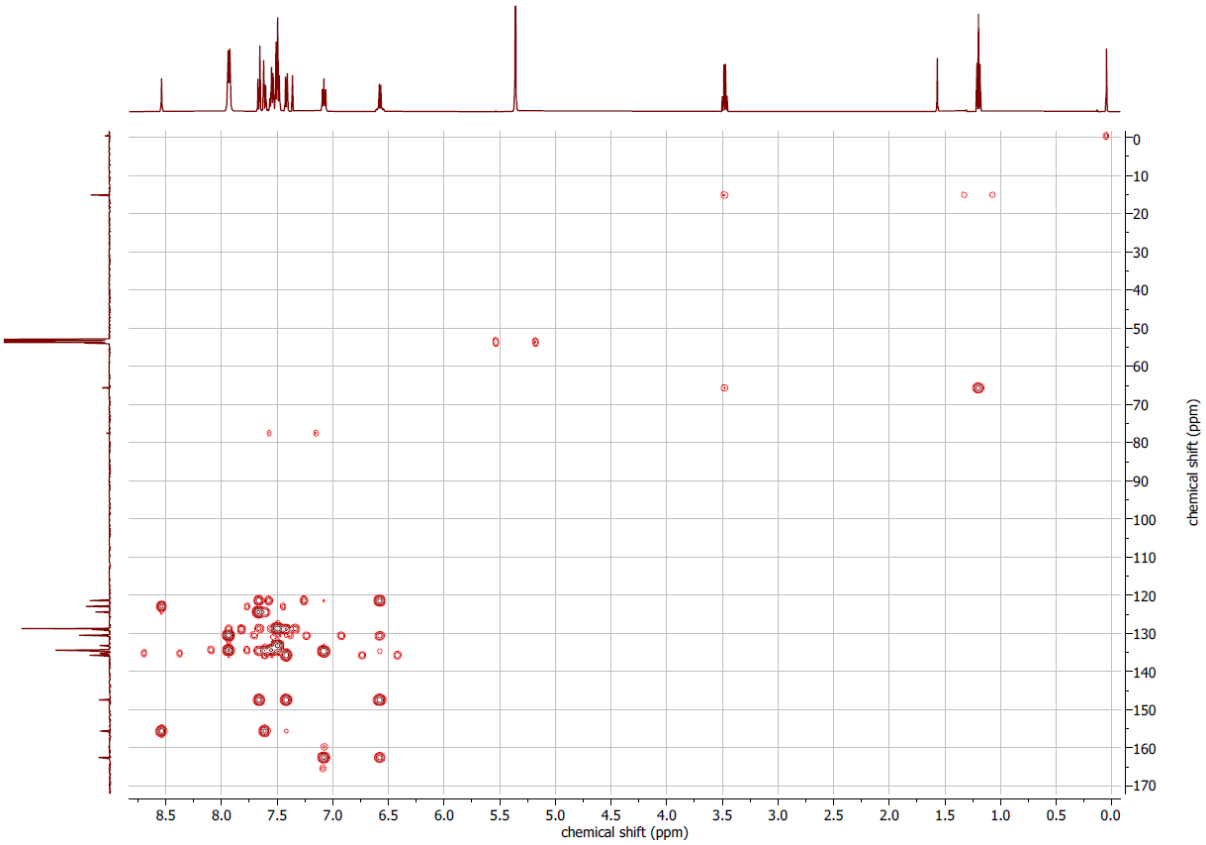

Fig. S15 500 MHz $^{1}H,^{13}C$ HMBC of [Pt(dba)($AsPh_3$)] in CD_2Cl_2.

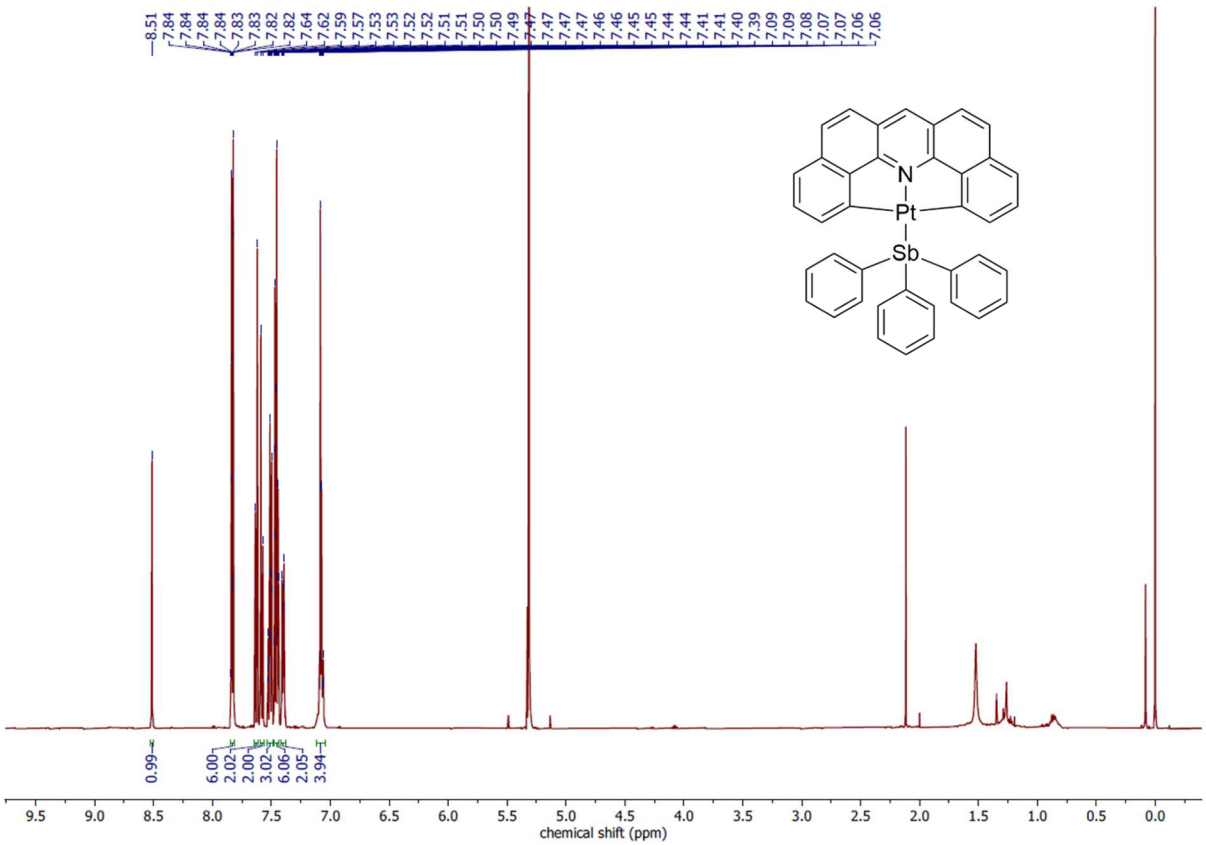

Fig. S16 500 MHz ^{1}H NMR of [Pt(dba)($SbPh_3$)] in CD_2Cl_2.

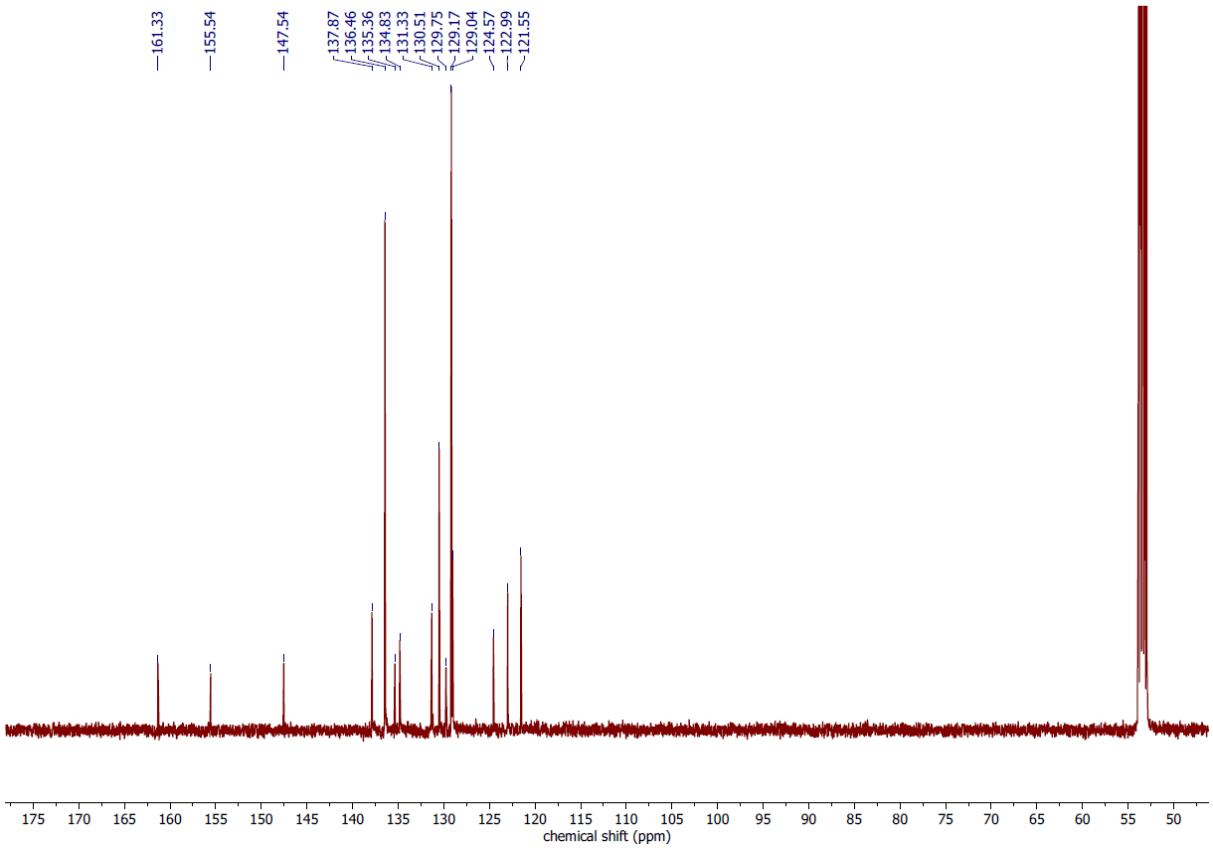

Fig. S17 125 MHz ^{13}C NMR of [Pt(dba)($SbPh_3$)] in CD_2Cl_2.

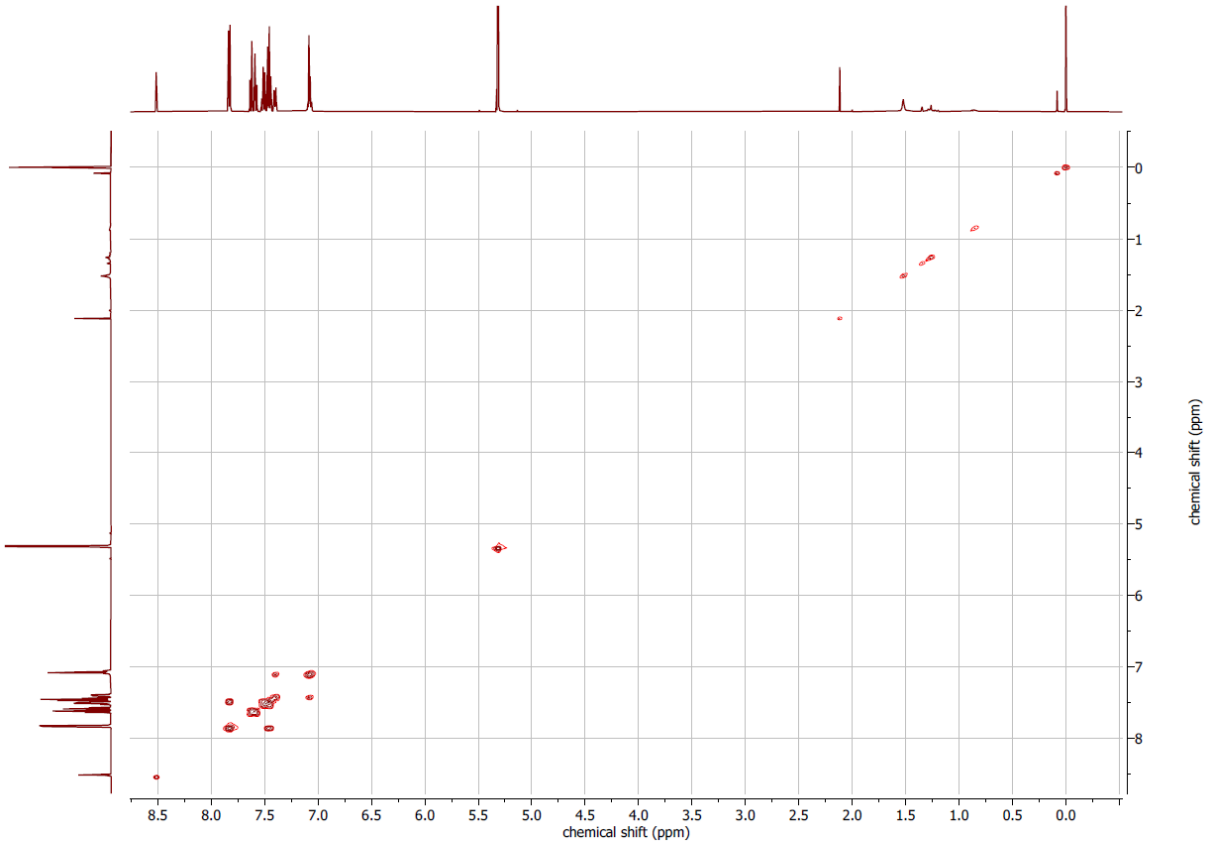

Fig. S18 500 MHz $^{1}H,^{1}H$ COSY of [Pt(dba)($SbPh_3$)] in CD_2Cl_2.

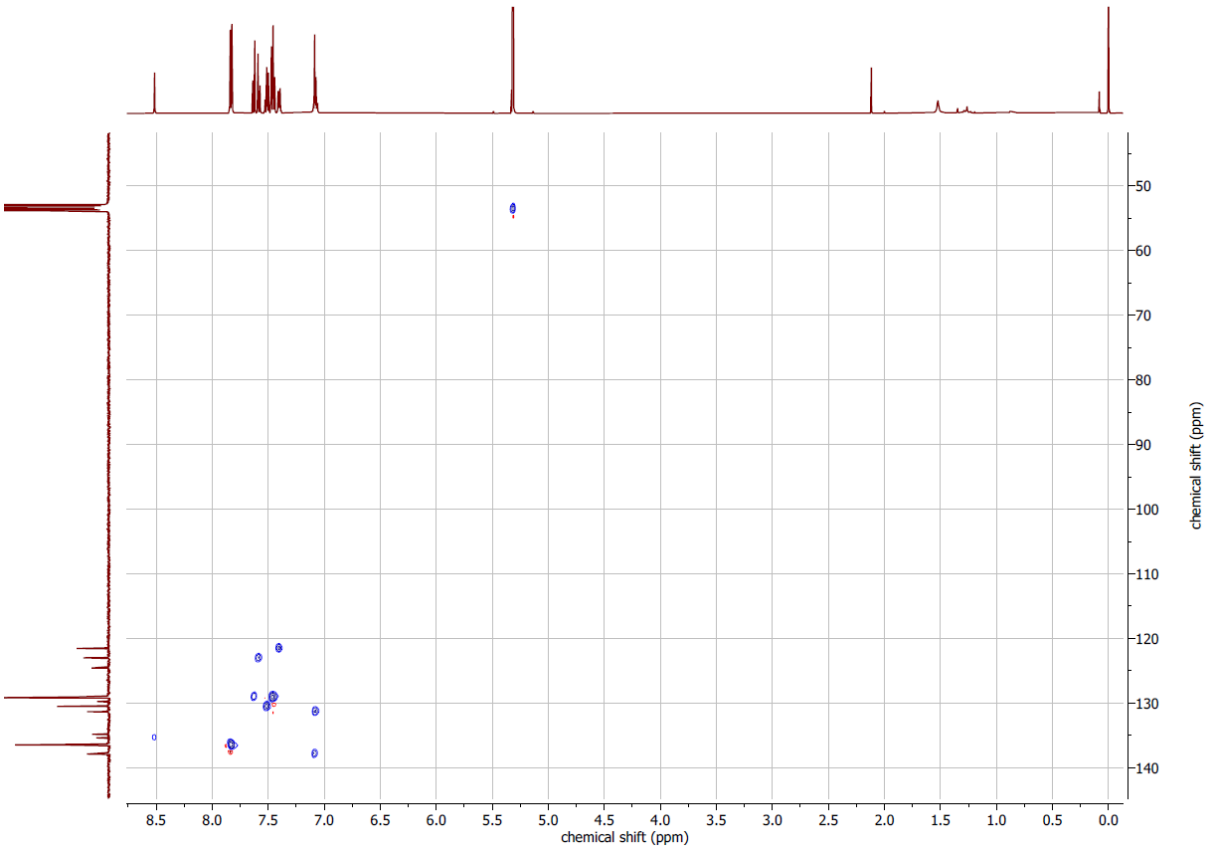

Fig. S19 500 MHz $^{1}H,^{13}C$ HSQC of [Pt(dba)($SbPh_3$)] in CD_2Cl_2.

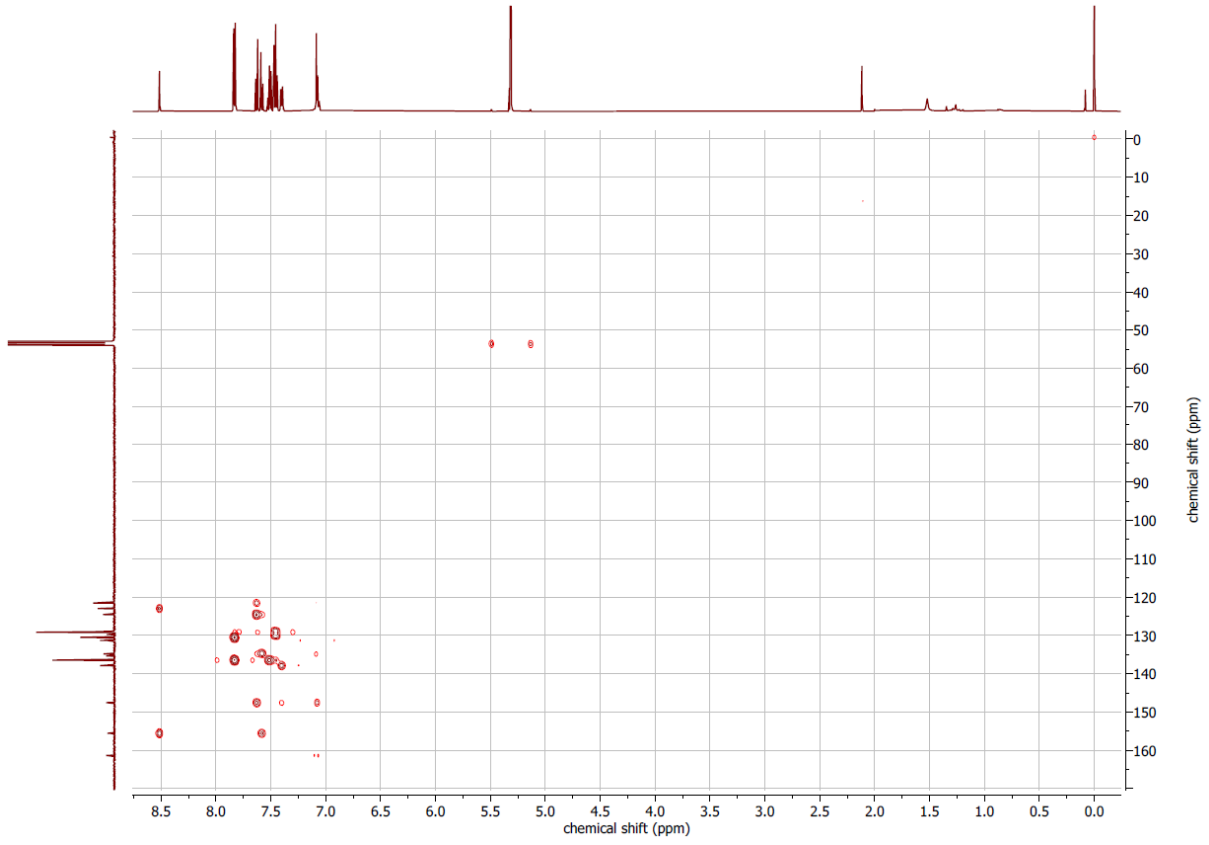

Fig. S20 500 MHz $^{1}H,^{13}C$ HMBC of [Pt(dba)($SbPh_3$)] in CD_2Cl_2.

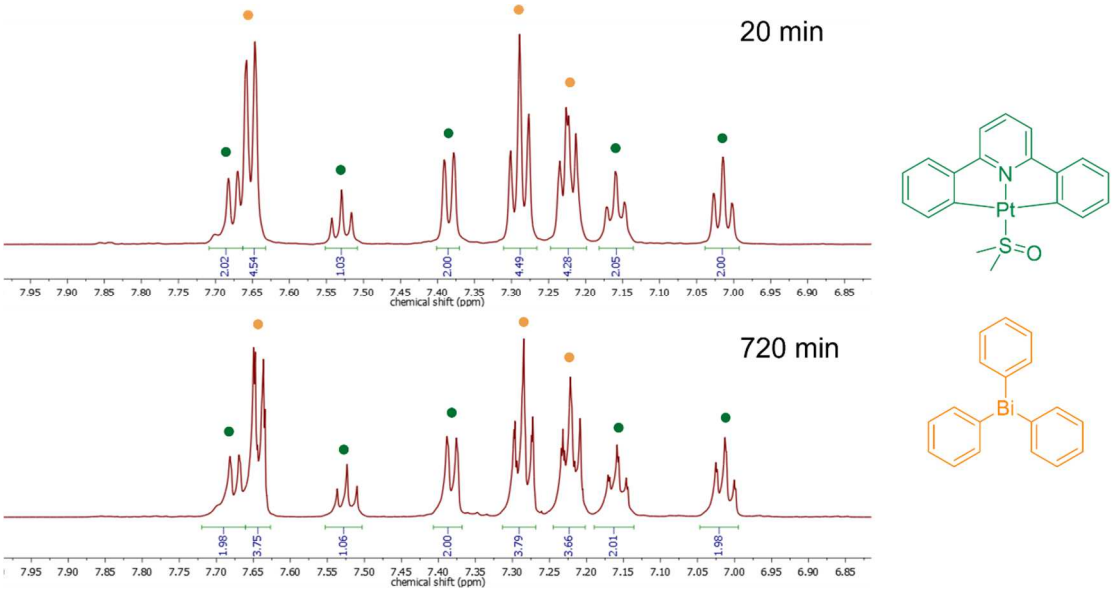

Fig. S21 600 MHz ^{1}H NMR spectra from *in situ* NMR observation of a mixture of [Pt(dpp)(dmso)] and $BiPh_3$ in CD_2Cl_2.

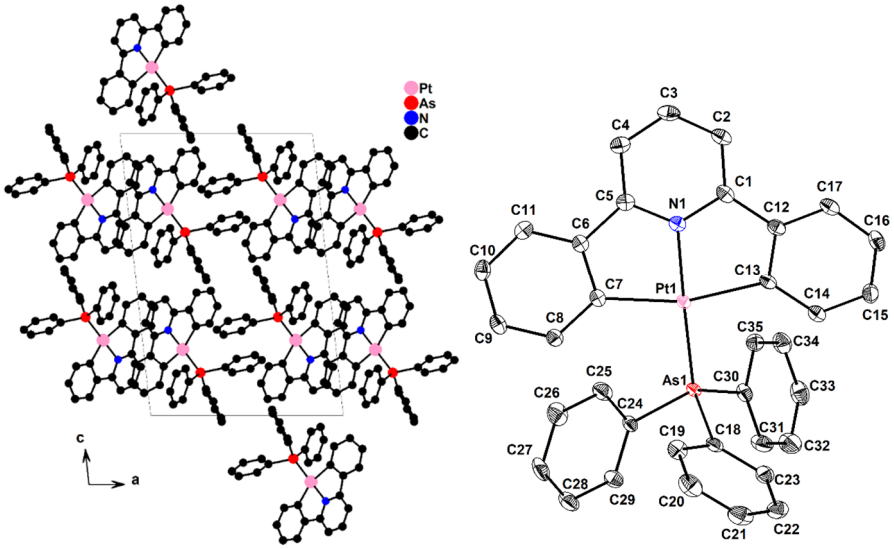

Fig. S22 Crystal structure (left) of [Pt(dpp)($AsPh_3$)] viewed along the *b* axis and molecular structure (right) with 50% ellipsoids, H atoms omitted for clarity.

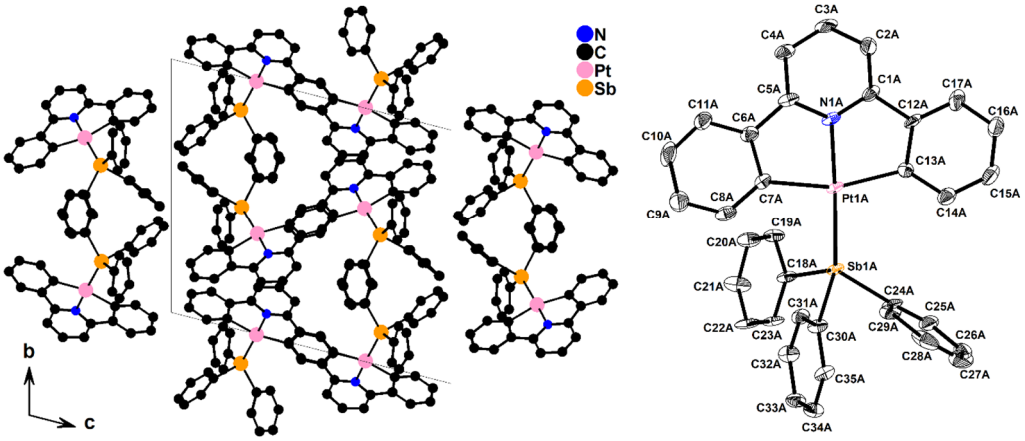

Fig. S23 Crystal structure (left) of [Pt(dpp)($SbPh_3$)] viewed along the *a* axis and molecular structure (right) with 50% ellipsoids, H atoms omitted for clarity.

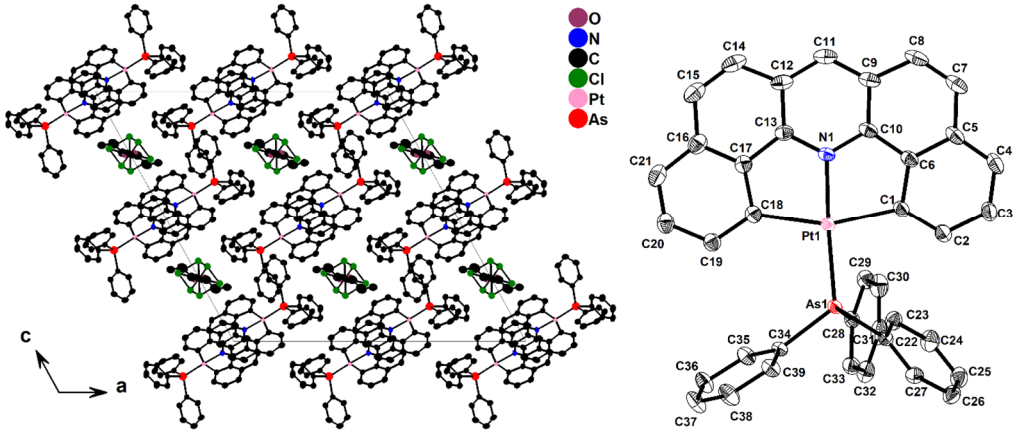

Fig. S24 Crystal structure (left) of [Pt(dba)(AsPh$_3$)]·Et$_2$O·CHCl$_3$ viewed along the *b* axis and molecular structure of [Pt(dbaAsPh$_3$] (right) with 50% ellipsoids, H atoms and co-crystallised solvent molecules omitted for clarity.

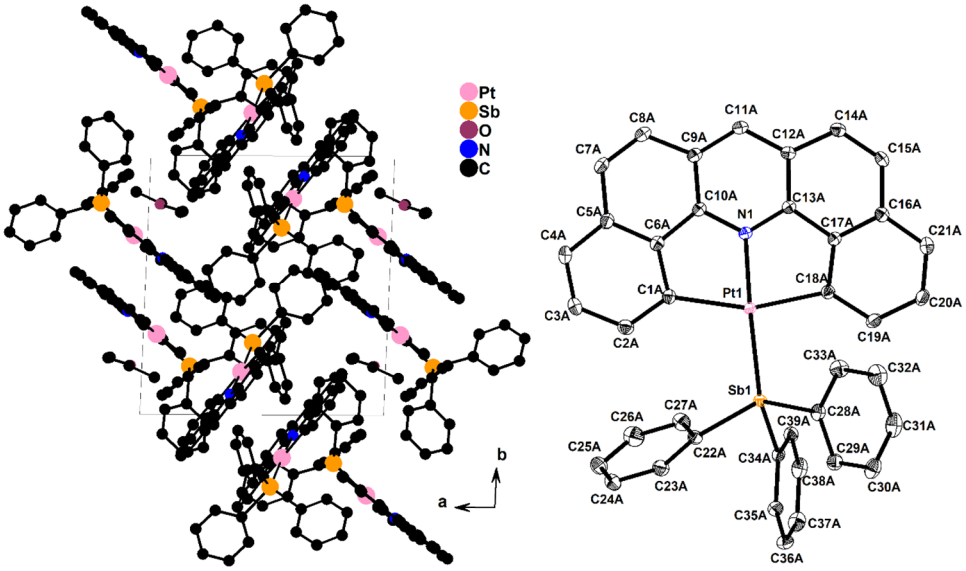

Fig. S25 Crystal structure (left) of [Pt(dba)(SbPh$_3$)]·0.5Et$_2$O viewed along the *c* axis and molecular structure of [Pt(dba)(SbPh$_3$)] (right) with 50% ellipsoids, H atoms and co-crystallised solvent molecules omitted for clarity.

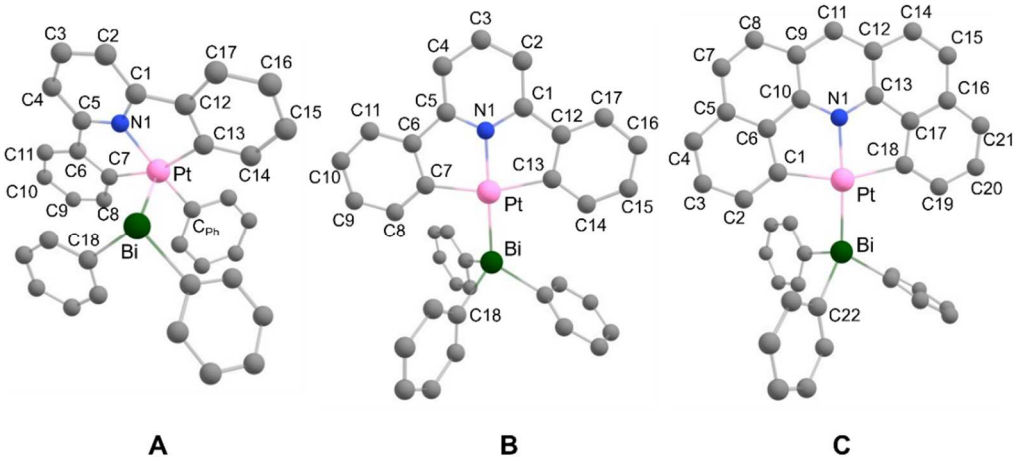

Fig. S26 Structures of [Pt(dpp)(BiPh$_3$)] and [Pt(dba)(BiPh$_3$)] from free (left) and constrained (middle and right) DFT geometry optimisations.

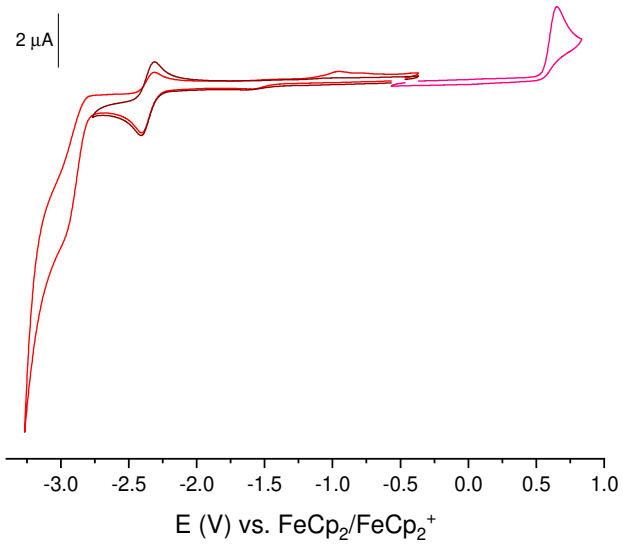

Fig. S27 Cyclic voltammograms of [Pt(dpp)(PPh_3)] in 0.1 M *n*-Bu_4NPF_6/THF.

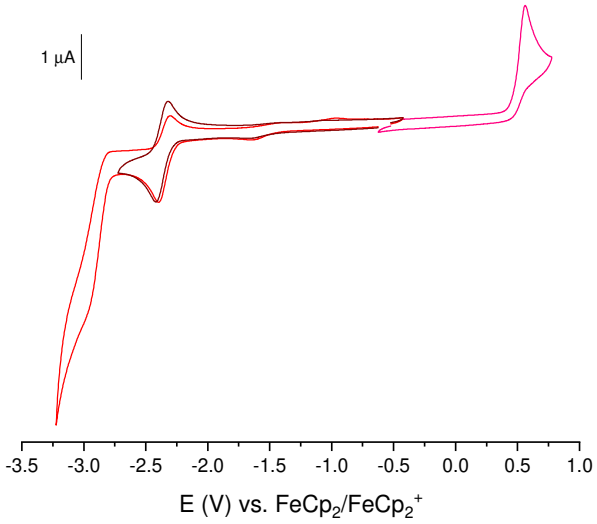

Fig. S28 Cyclic voltammograms of [Pt(dpp)($AsPh_3$)] in 0.1 M *n*-Bu_4NPF_6/THF.

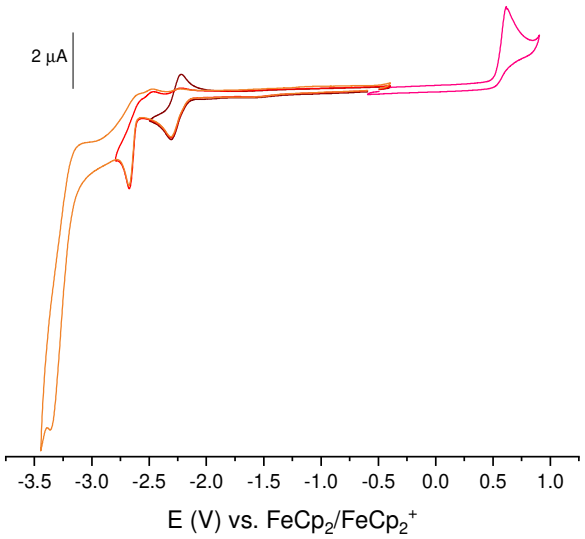

Fig. S29 Cyclic voltammograms of [Pt(dpp)($SbPh_3$)] in 0.1 M *n*-Bu_4NPF_6/THF.

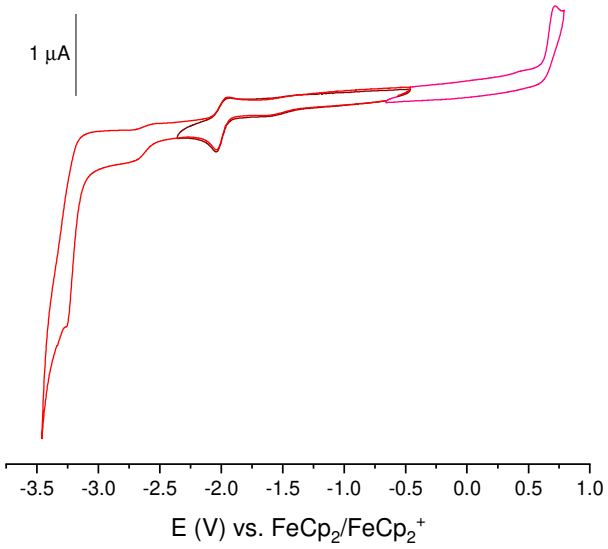

Fig. S30 Cyclic voltammograms of [Pt(dba)(PPh_3)] in 0.1 M *n*-Bu_4NPF_6/THF.

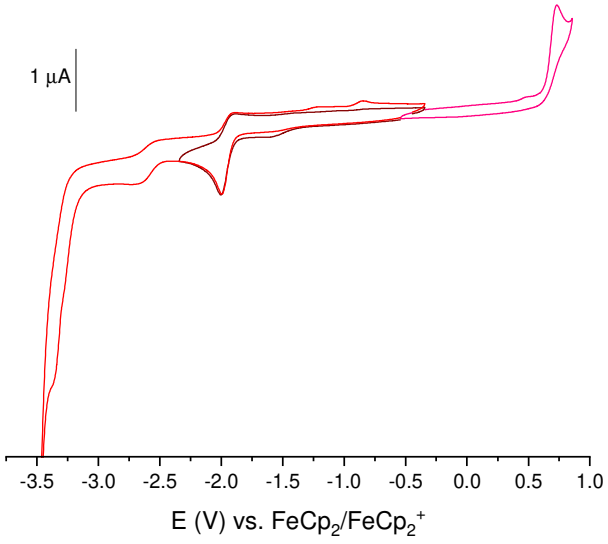

Fig. S31 Cyclic voltammograms of [Pt(dba)($AsPh_3$)] in 0.1 M *n*-Bu_4NPF_6/THF.

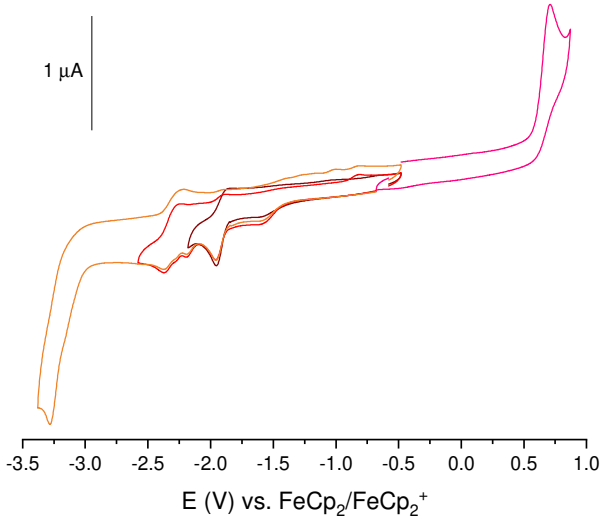

Fig. S32 Cyclic voltammograms of [Pt(dba)($SbPh_3$)] in 0.1 M *n*-Bu_4NPF_6/THF.

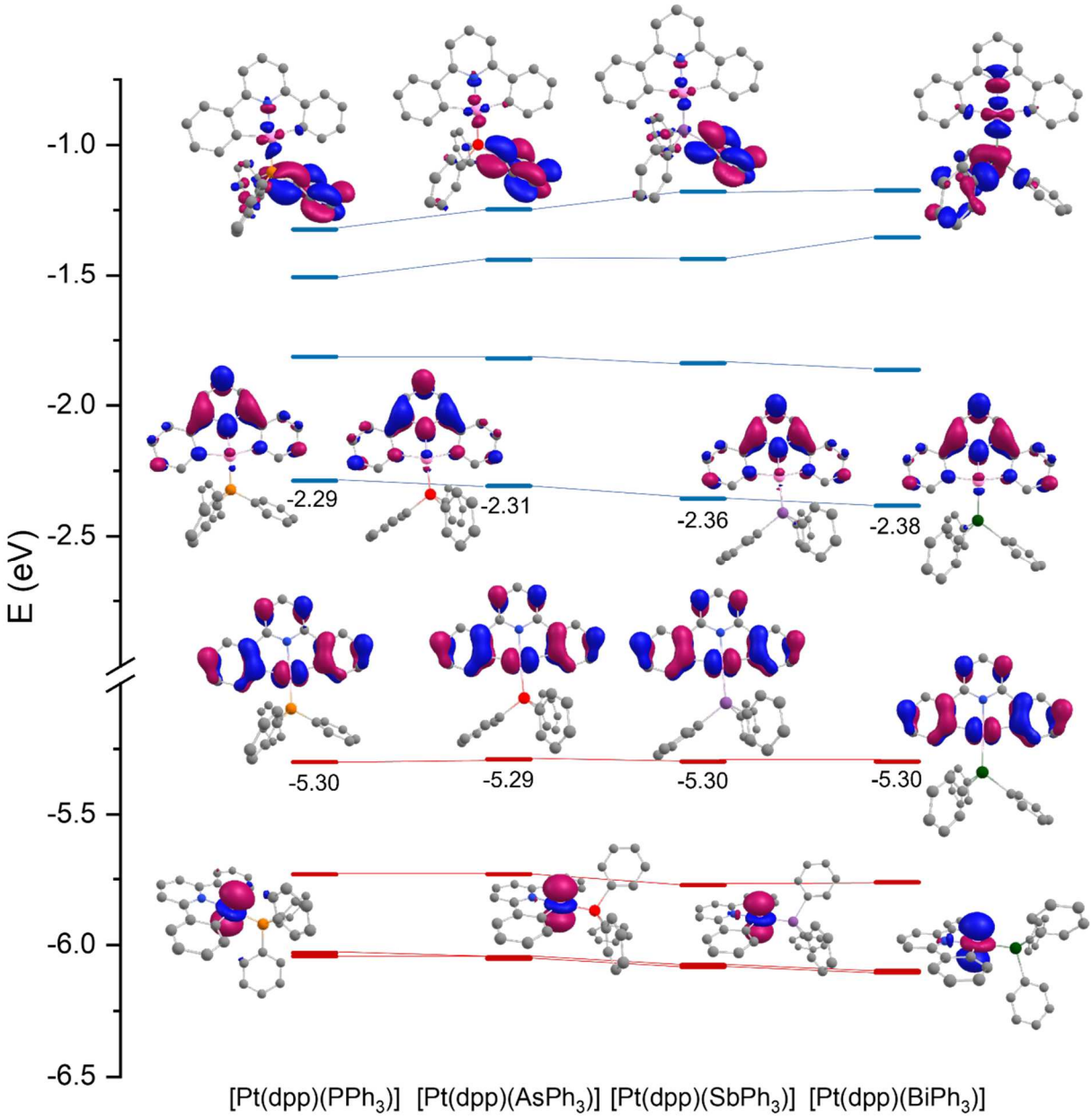

Fig. S33 Selected DFT-calculated frontier orbitals and energies for [Pt(dpp)(PnPh3)] (Pn = P, As, Sb, Bi).

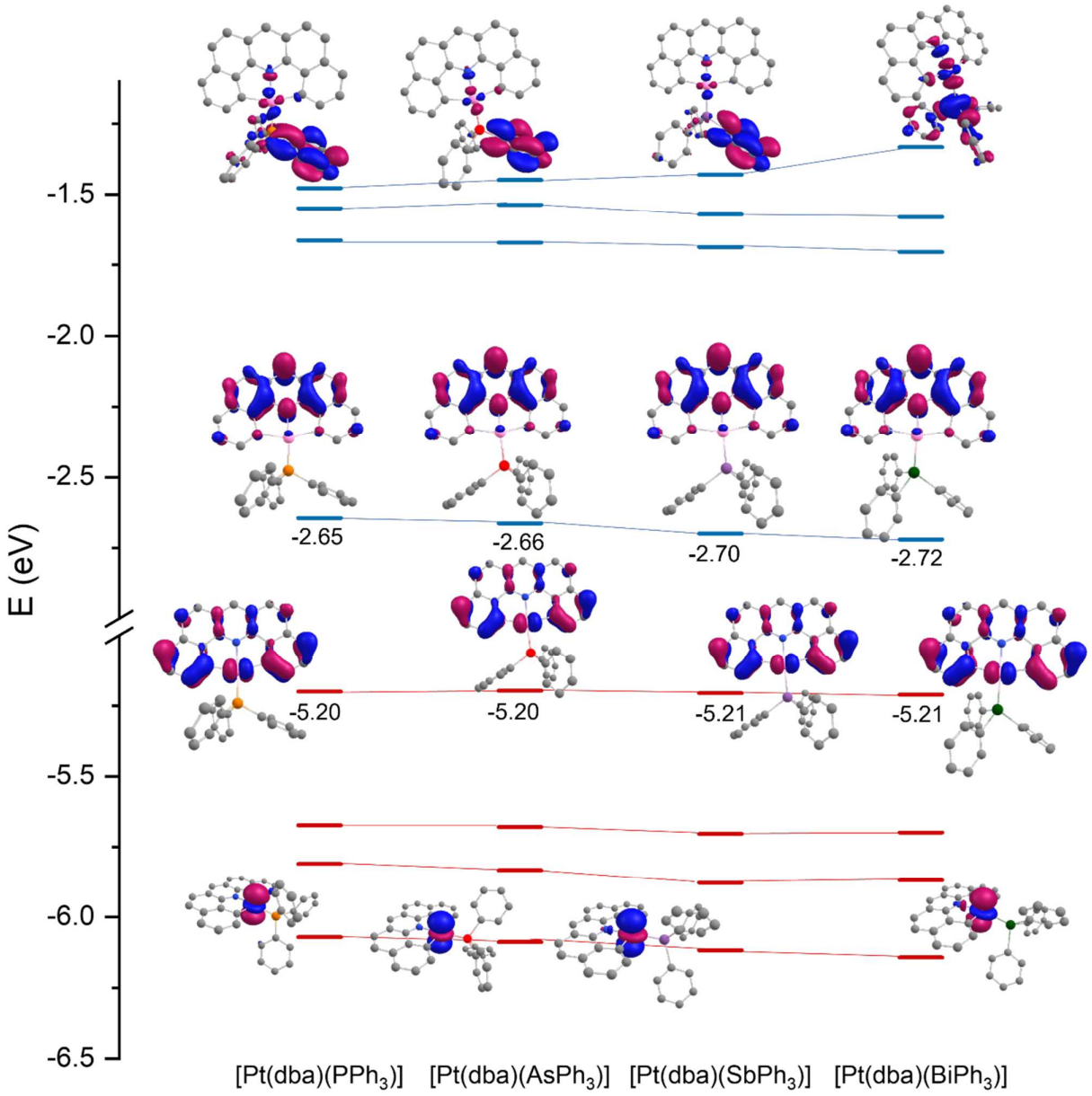

Fig. S34 Selected DFT-calculated frontier orbitals and energies for [Pt(dba)($PnPh_3$)] (Pn = P, As, Sb, Bi).

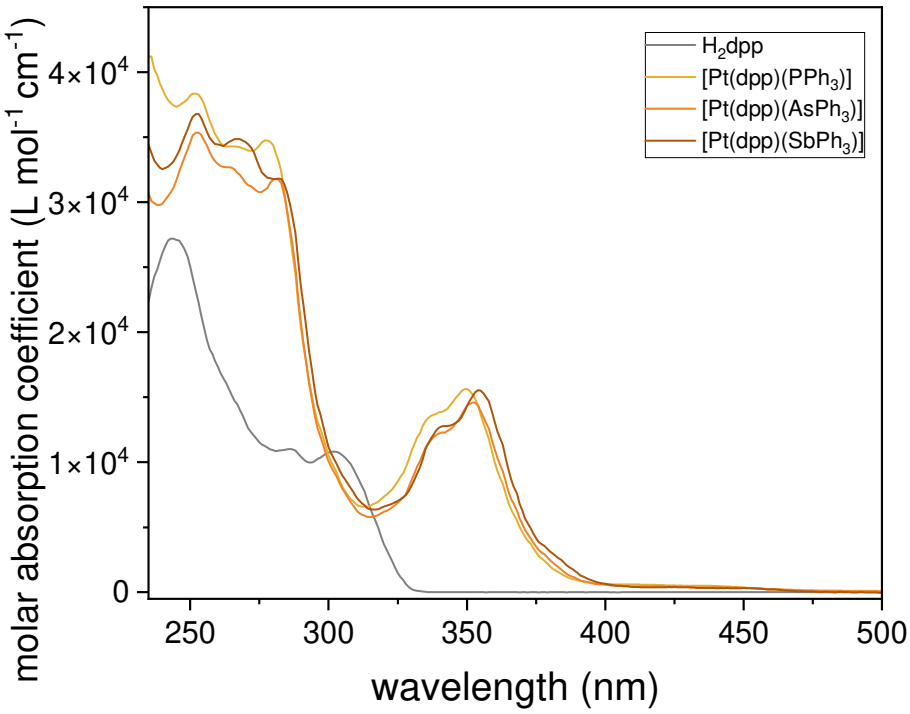

Fig. S35 Experimental UV-vis absorption spectra of H_2dpp, and the complexes [Pt(dpp)(PnPh$_3$)] (Pn = P, As, and Sb) in CH_2Cl_2 solution at 298 K.

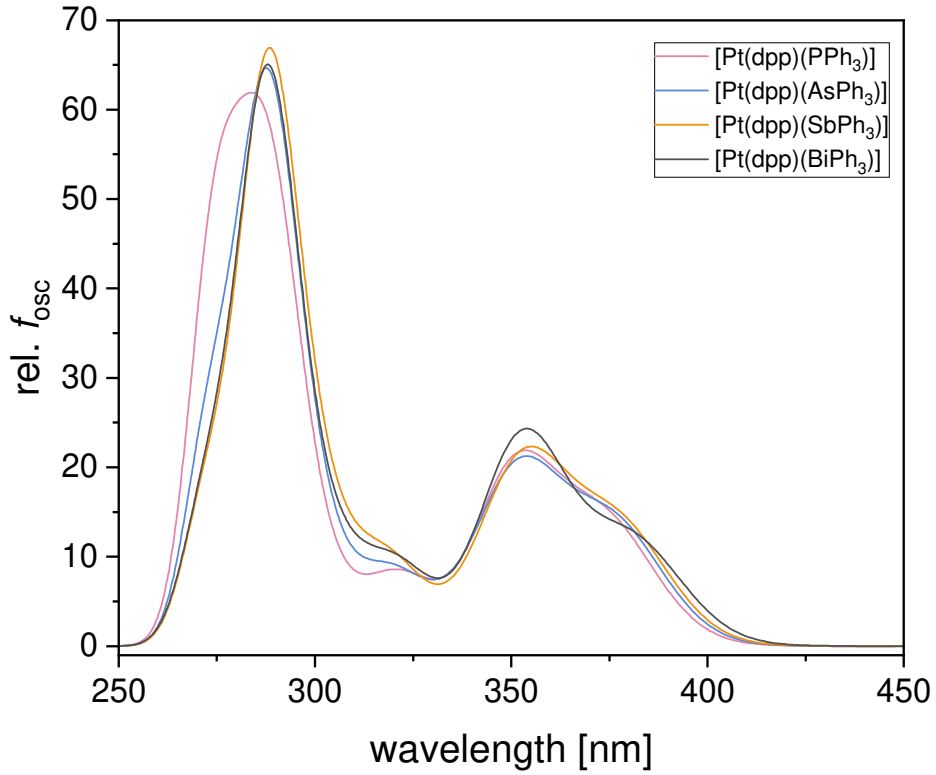

Fig. S36 TD-DFT calculated (TPSSh/def2-TZVP/CPCM(CH_2Cl_2)) UV-vis absorption spectra of the complexes [Pt(dpp)(PnPh$_3$)] (Pn = P, As, Sb, Bi).

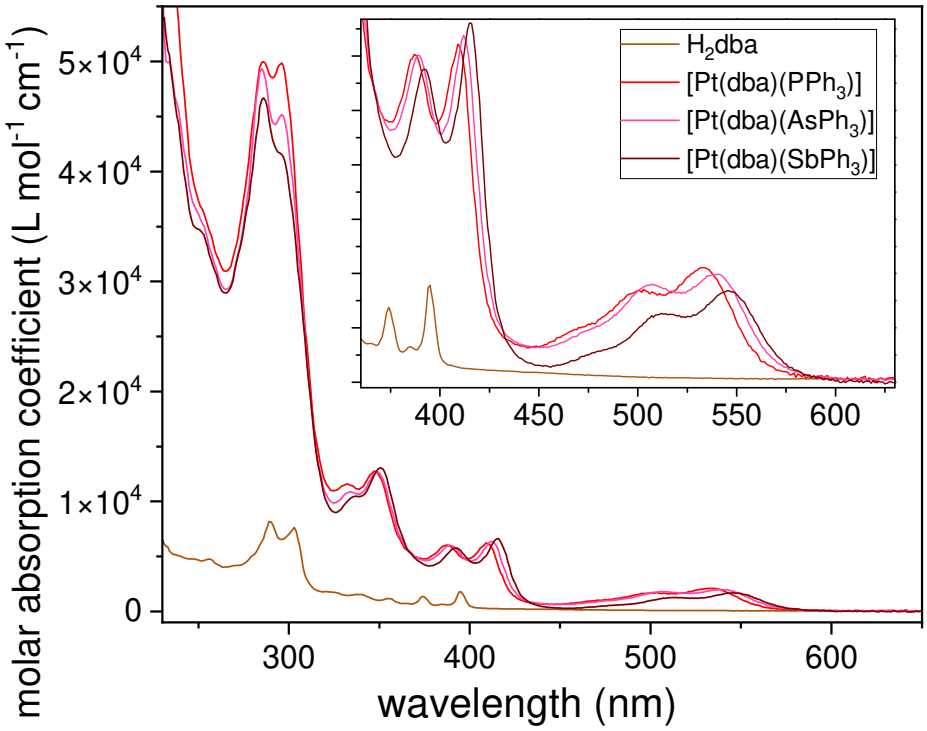

Fig. S37 Experimental UV-vis absorption spectra of H_2dba, and the complexes [Pt(dba)($PnPh_3$)] (Pn = P, As, and Sb) in CH_2Cl_2 solution at 298 K.

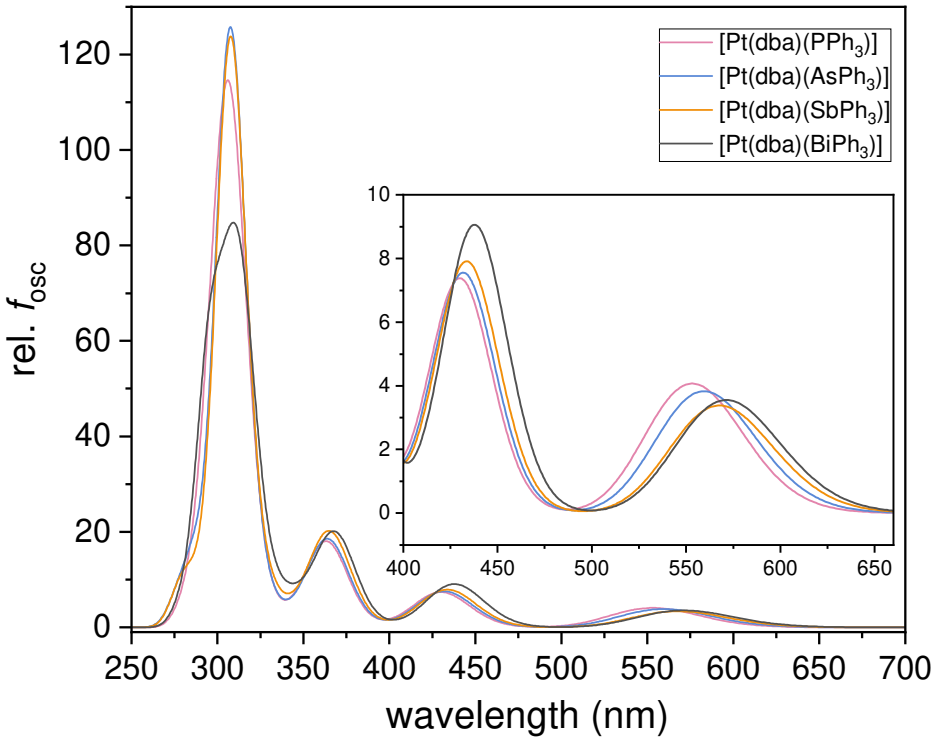

Fig. S38 TD-DFT-calculated (TPSSh/def2-TZVP/CPCM(CH_2Cl_2)) UV-vis absorption spectra of [Pt(dba)($PnPh_3$)] (Pn = P, As, Sb, Bi).

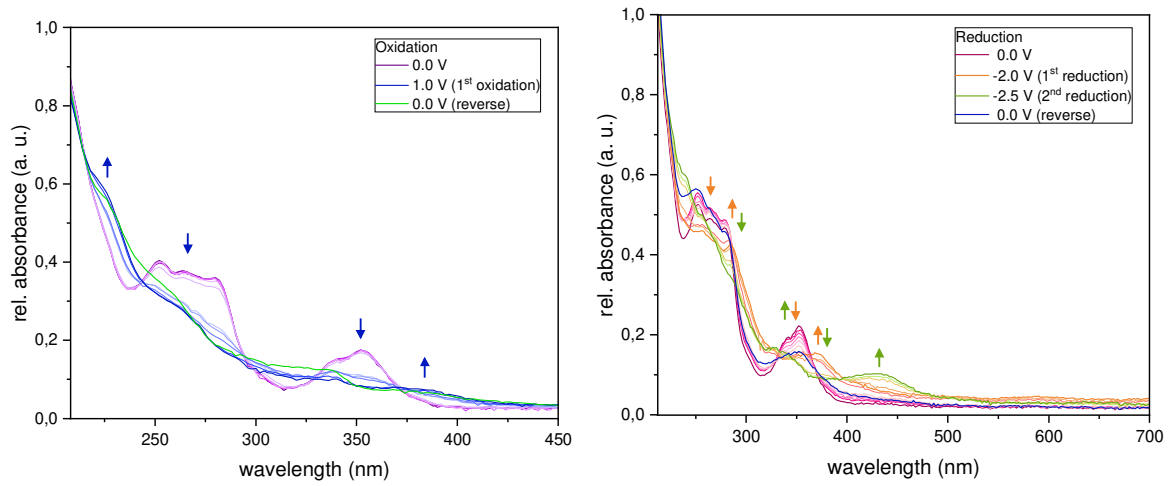

Fig. S39 UV-vis absorption spectra of [Pt(dpp)($AsPh_3$)] during anodic (left) and cathodic (right) electrolysis (spectroelectrochemistry) in 0.1 M *n*-Bu_4NPF_6 THF solution.

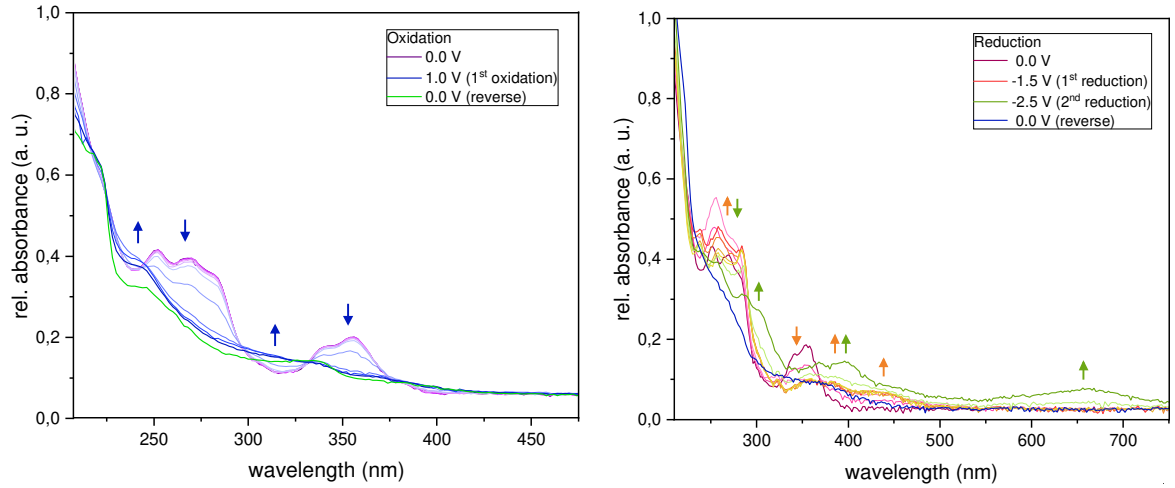

Fig. S40 UV-vis absorption spectra of [Pt(dpp)($SbPh_3$)] during anodic (left) and cathodic (right) electrolysis (spectroelectrochemistry) in 0.1 M *n*-Bu_4NPF_6 THF solution.

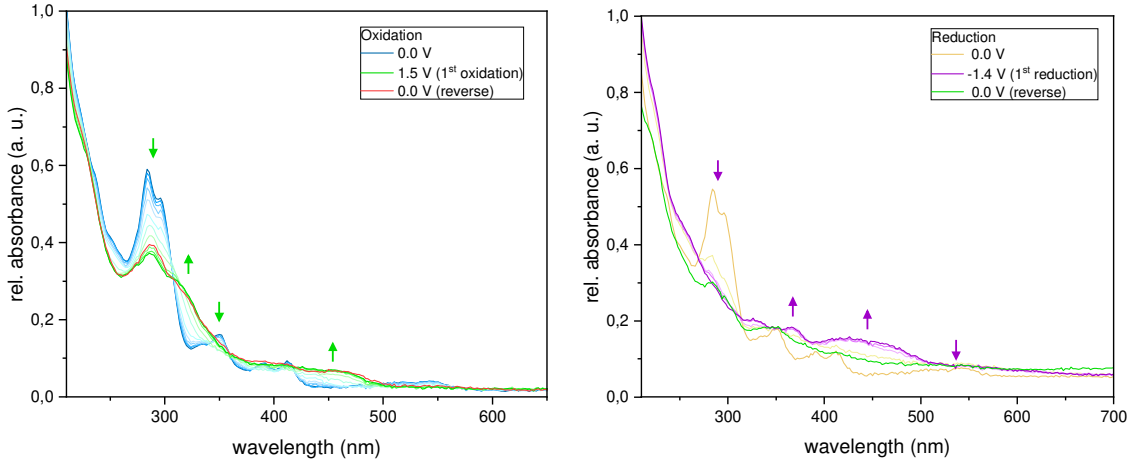

Fig. S41 UV-vis absorption spectra of [Pt(dba)($AsPh_3$)] during anodic (left) and cathodic (right) electrolysis (spectroelectrochemistry) in 0.1 M *n*-Bu_4NPF_6 THF solution.

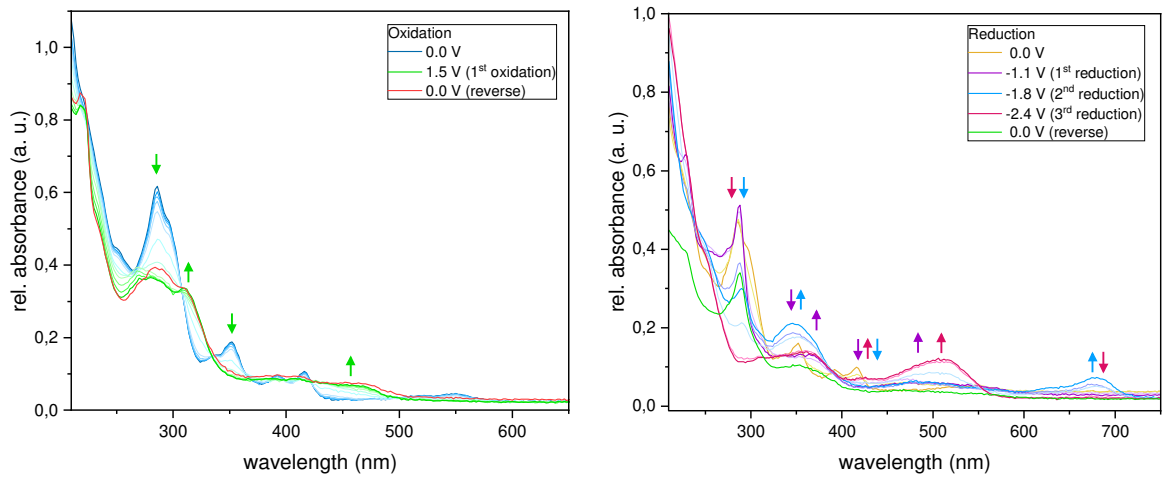

Fig. S42 UV-vis absorption spectra of [Pt(dba)($SbPh_3$)] during anodic (left) and cathodic (right) electrolysis (spectroelectrochemistry) in 0.1 M *n*-Bu_4NPF_6 THF solution.

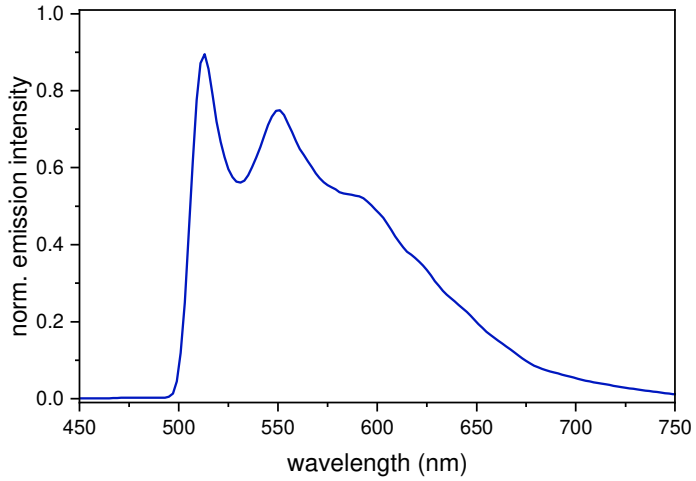

Fig. S43 Photoluminescence spectrum of [Pt(dpp)(PPh_3)] at 77 K in a frozen glassy MeOH/CH_2Cl_2 1:1 matrix, λ_{exc} = 350 nm.

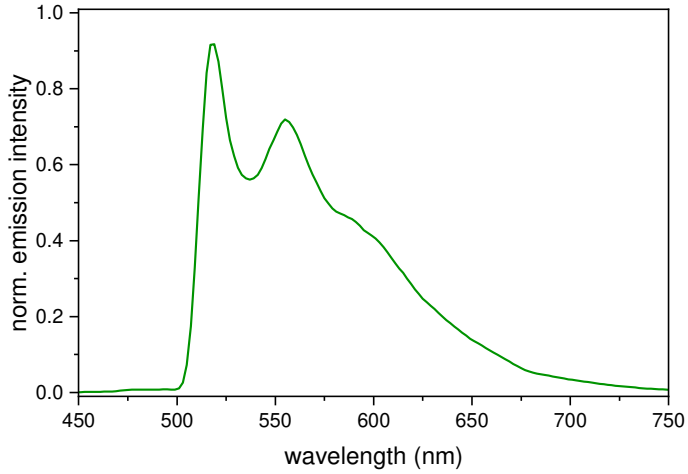

Fig. S44 Photoluminescence spectrum of [Pt(dpp)($AsPh_3$)] at 77 K in a frozen glassy MeOH/CH_2Cl_2 1:1 matrix, λ_{exc} = 350 nm.

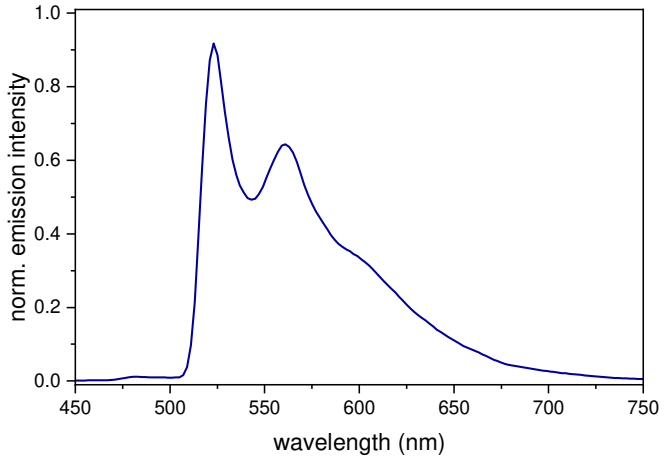

Fig. S45 Photoluminescence spectrum of [Pt(dpp)($SbPh_3$)] at 77 K in a frozen glassy MeOH/CH_2Cl_2 1:1 matrix, λ_{exc} = 350 nm.

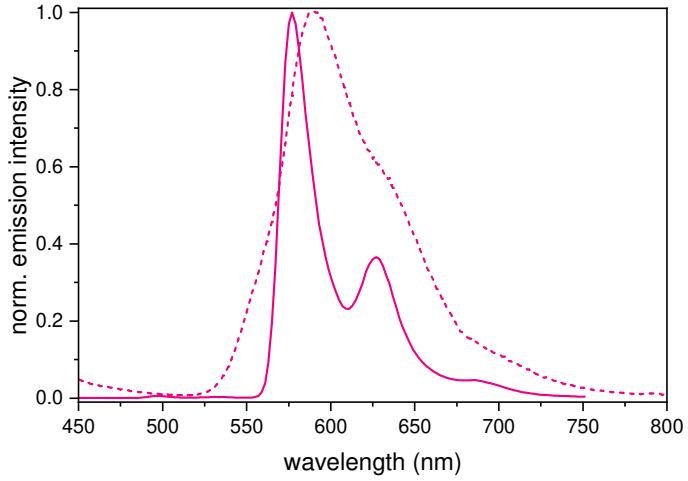

Fig. S46 Photoluminescence spectra of [Pt(dba)(PPh_3)] at 77 K in a frozen glassy MeOH/CH_2Cl_2 1:1 matrix (solid line) and in fluid CH_2Cl_2 solution at 298 K (dashed line) λ_{exc} = 350 nm.

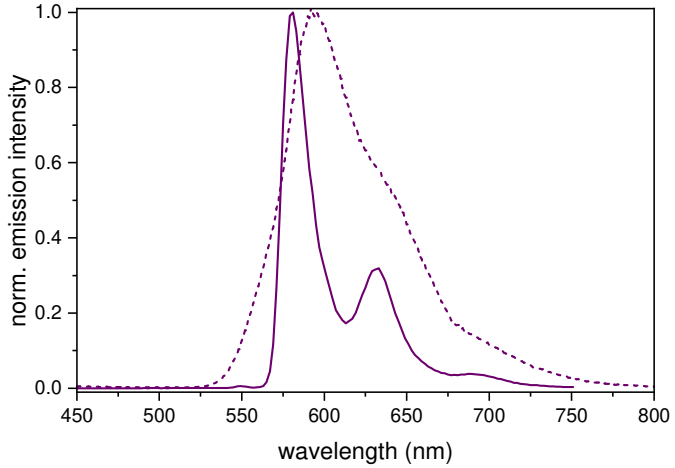

Fig. S47 Photoluminescence spectra of [Pt(dba)($AsPh_3$)] at 77 K in a frozen glassy MeOH/CH_2Cl_2 1:1 matrix (solid line) and in fluid CH_2Cl_2 solution at 298 K (dashed line), λ_{exc} = 350 nm.

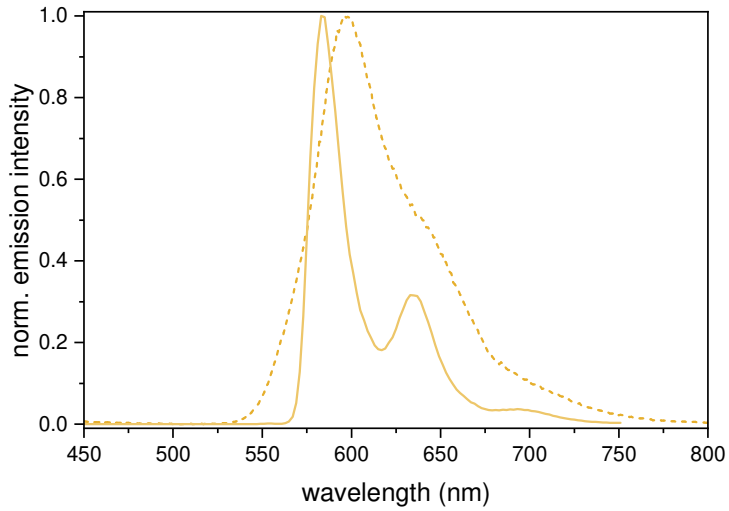

Fig. S48 Photoluminescence spectra of [Pt(dba)($SbPh_3$)] at 77 K in a frozen glassy MeOH/CH_2Cl_2 1:1 matrix (solid line) and in fluid CH_2Cl_2 solution at 298 K (dashed line), λ_{exc} = 350 nm.

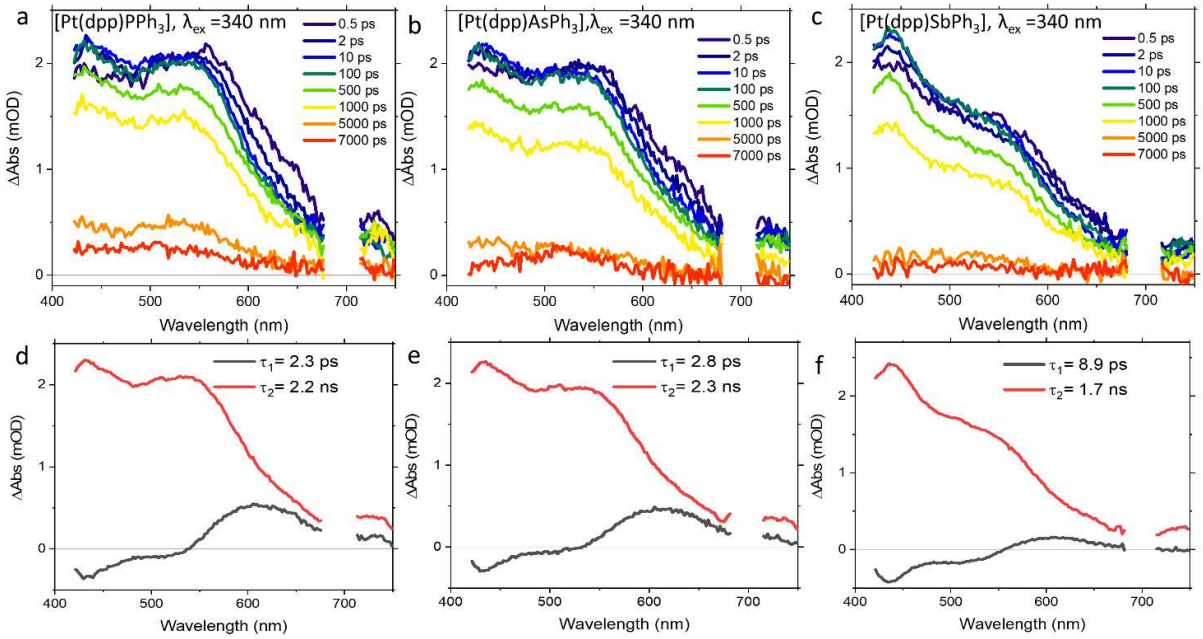

Fig. S49 Transient absorption spectra (TAS) at selected delay times (a-c) and decay associated spectra (d-f) for [Pt(dpp)(PPh_3)] (a and d), [Pt(dpp)($AsPh_3$)] (b and e) and [Pt(dpp)($SbPh_3$)] (c and f) upon excitation at 340 nm in THF.

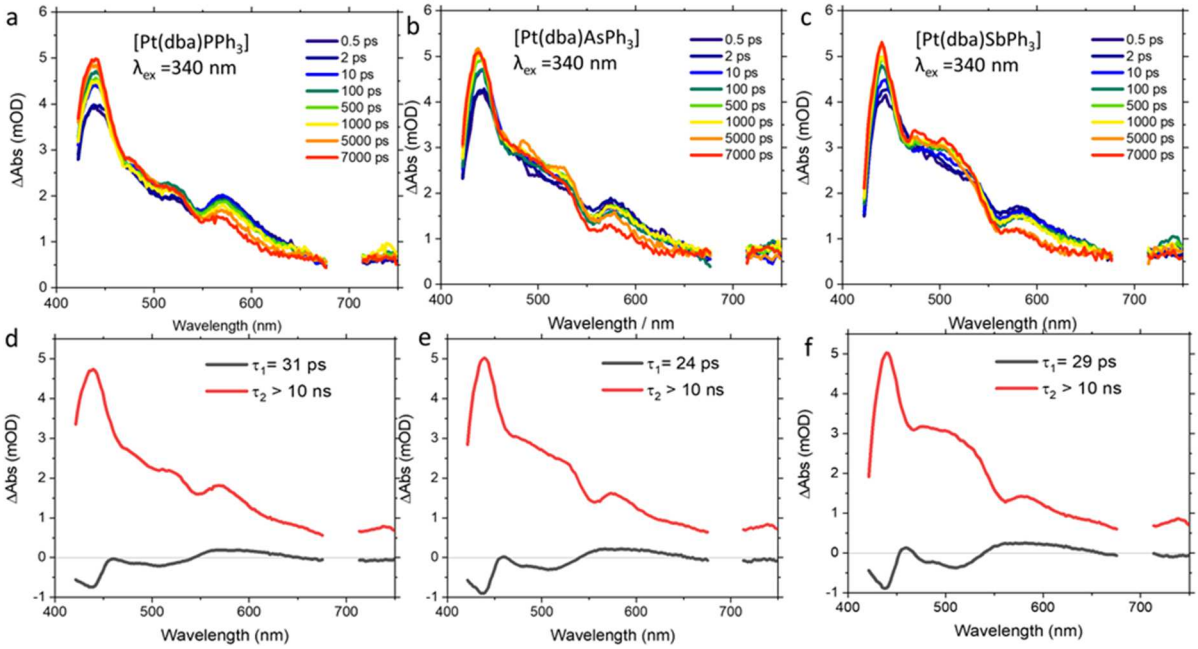

Fig. S50 TAS at selected delay times (a-c) and decay associated spectra (d-f) for [Pt(dba)(PPh3)] (a and d), [Pt(dba)(AsPh3)] (b and e) and [Pt(dba)(SbPh3)] (c and f) upon excitation at 340 nm in THF.

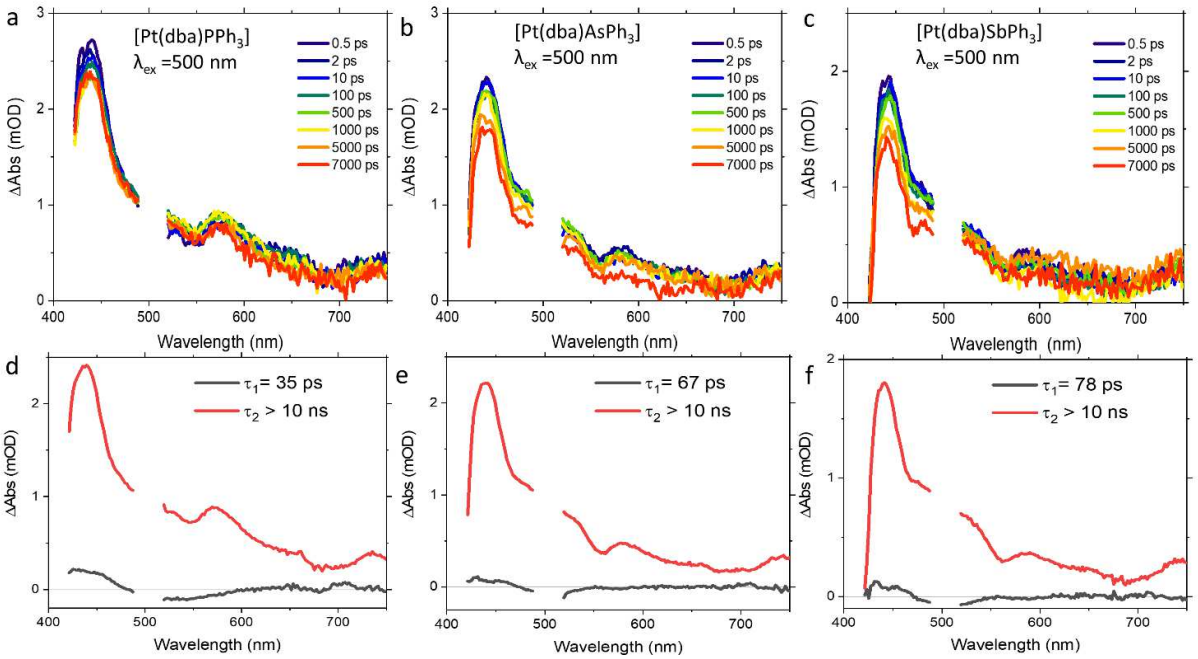

Fig. S51 TAS at selected delay times (a-c) and decay associated spectra (d-f) for [Pt(dba)(PPh3)] (a and d), [Pt(dba)(AsPh3)] (b and e) and [Pt(dba)(SbPh3)] (c and f) upon excitation at 500 nm in THF.

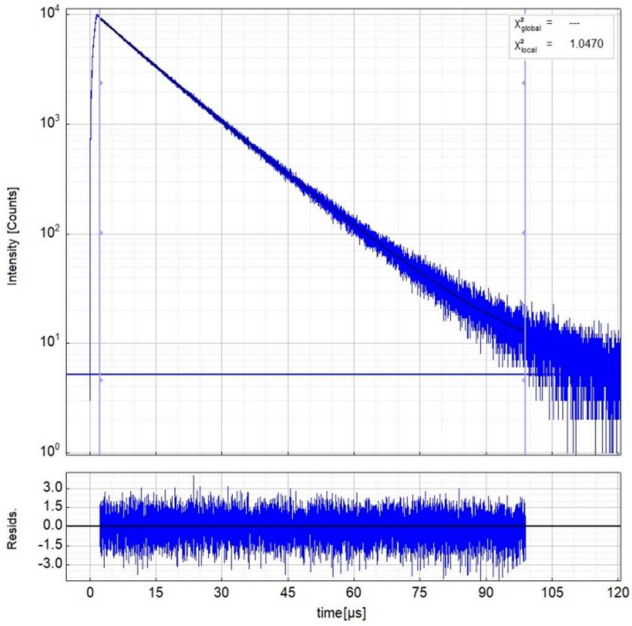

Parameter	Value	Δ	δ
A_1[kCnts/Chnl]	5.69	±0.54	9.4%
τ_1[ns]	14 490	±220	1.5%
I_1[kCnts]	10 310	±810	7.8%
A_{Rel1}[%]	61.7	±5.8	9.3%
I_{Rel1}[%]	70.3	±5.5	7.8%
A_2[kCnts/Chnl]	3.55	±0.53	15%
τ_2[ns]	9 860	±420	4.2%
I_2[kCnts]	4 370	±810	19%
A_{Rel2}[%]	38.4	±5.8	15%
I_{Rel2}[%]	29.8	±5.5	18%
$Bkgr_{Dec}$[kCnts]	0.0052	±0.0003	5.1%
τ_{AvInt}[ns]	13 107	±13	0.1%
τ_{AvAmp}[ns]	12 709	±13	0.1%

Fig. S52 Left: Raw (experimental) time-resolved photoluminescence decay of [Pt(dpp)(PPh_3)] in a frozen MeOH/CH_2Cl_2 1:1 glassy matrix at 77K including the residuals (λ_{ex} = 376 nm, λ_{em} = 510 nm). Right: Fitting parameters including pre-exponential factors and confidence limits.

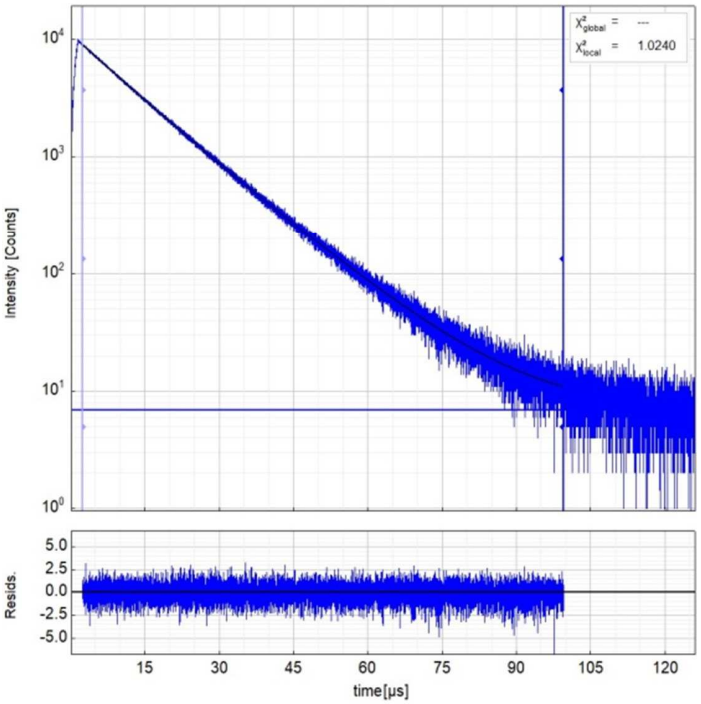

Parameter	Value	Δ	δ
A_1[kCnts/Chnl]	4.99	±0.69	14%
τ_1[ns]	13 570	±280	2.0%
I_1[kCnts]	8 460	±970	11%
A_{Rel1}[%]	55.9	±7.7	14%
I_{Rel1}[%]	64.3	±7.4	11%
A_2[kCnts/Chnl]	3.94	±0.69	17%
τ_2[ns]	9 570	±390	4.0%
I_2[kCnts]	4 700	±980	21%
A_{Rel2}[%]	44.2	±7.7	17%
I_{Rel2}[%]	35.8	±7.4	21%
$Bkgr_{Dec}$[kCnts]	0.0070	±0.0002	2.5%
τ_{AvInt}[ns]	12 133	±11	0.1%
τ_{AvAmp}[ns]	11 797.7	±8.3	0.1%

Fig. S53 Left: Raw (experimental) time-resolved photoluminescence decay of [Pt(dpp)($AsPh_3$)] in a frozen MeOH/CH_2Cl_2 1:1 glassy matrix at 77K including the residuals (λ_{ex} = 376 nm, λ_{em} = 515 nm). Right: Fitting parameters including pre-exponential factors and confidence limits.

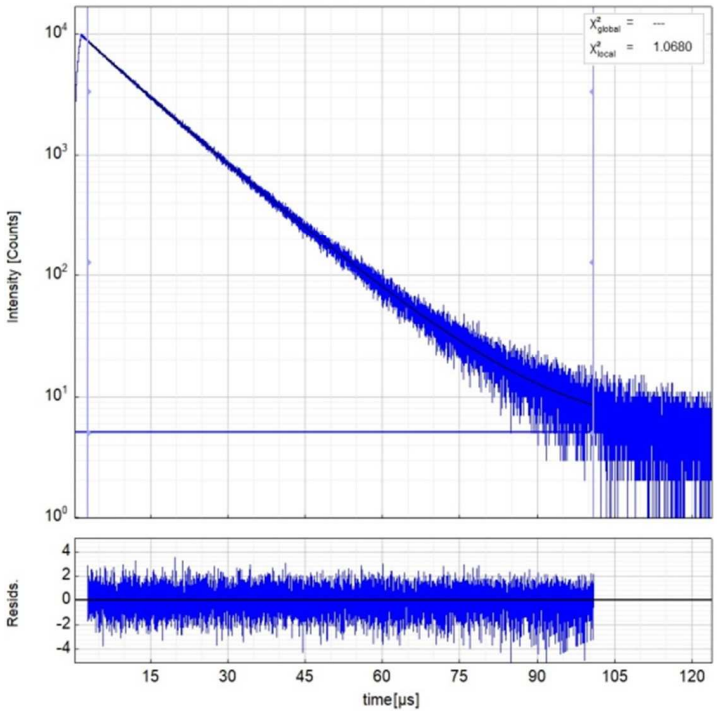

Parameter	Value	Δ	δ
A_1[kCnts/Chnl]	3.13	±0.31	9.7%
τ_1[ns]	14 210	±240	1.7%
I_1[kCnts]	5 550	±460	8.2%
A_{Rel1}[%]	35.9	±3.5	9.7%
I_{Rel1}[%]	44.0	±3.7	8.2%
A_2[kCnts/Chnl]	5.60	±0.30	5.3%
τ_2[ns]	10 130	±110	1.1%
I_2[kCnts]	7 080	±460	6.5%
A_{Rel2}[%]	64.2	±3.5	5.4%
I_{Rel2}[%]	56.1	±3.7	6.4%
$Bkgr_{Dec}$[kCnts]	0.0051	±0.0002	3.3%
τ_{AvInt}[ns]	11 916	±13	0.1%
τ_{AvAmp}[ns]	11 584.9	±7.0	0.1%

Fig. S54 Left: Raw (experimental) time-resolved photoluminescence decay of [Pt(dpp)($SbPh_3$)] in a frozen MeOH/CH_2Cl_2 1:1 glassy matrix at 77K including the residuals (λ_{ex} = 376 nm, λ_{em} = 515 nm). Right: Fitting parameters including pre-exponential factors and confidence limits.

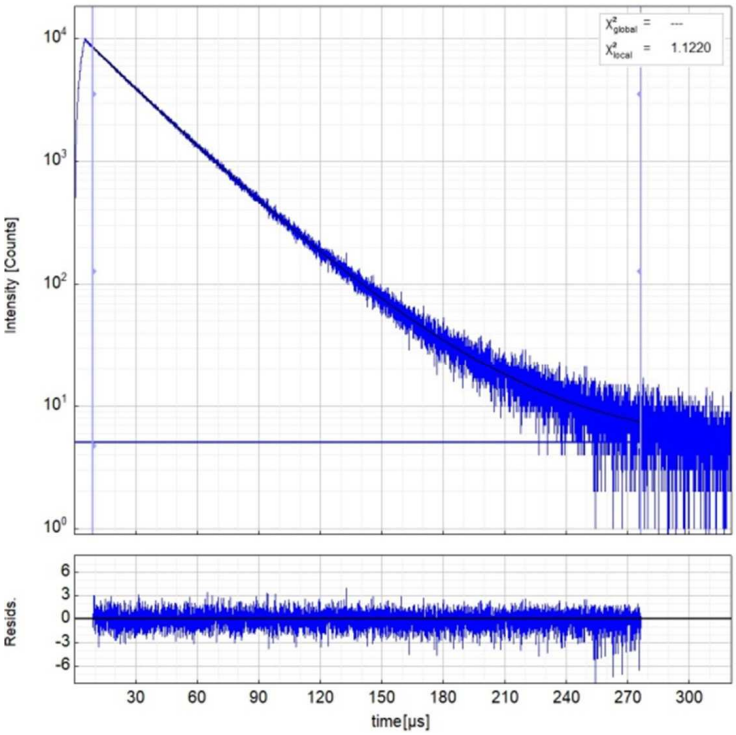

Parameter	Value	Δ	δ
A_1[kCnts/Chnl]	7.33	±0.40	5.3%
τ_1[ns]	25 620	±520	2.0%
I_1[kCnts]	5 870	±430	7.3%
A_{Rel1}[%]	86.8	±4.8	5.4%
I_{Rel1}[%]	79.7	±5.7	7.1%
A_2[kCnts/Chnl]	1.13	±0.41	36%
τ_2[ns]	42 900	±3 200	7.4%
I_2[kCnts]	1 510	±420	28%
A_{Rel2}[%]	13.3	±4.8	36%
I_{Rel2}[%]	20.4	±5.7	28%
$Bkgr_{Dec}$[kCnts]	0.0051	±0.0006	11%
τ_{AvInt}[ns]	29 128	±65	0.2%
τ_{AvAmp}[ns]	27 905	±64	0.2%

Fig. S55 Left: Raw (experimental) time-resolved photoluminescence decay of [Pt(dba)(PPh_3)] in a frozen MeOH/CH_2Cl_2 1:1 glassy matrix at 77K including the residuals (λ_{ex} = 376 nm, λ_{em} = 575 nm). Right: Fitting parameters including pre-exponential factors and confidence limits.

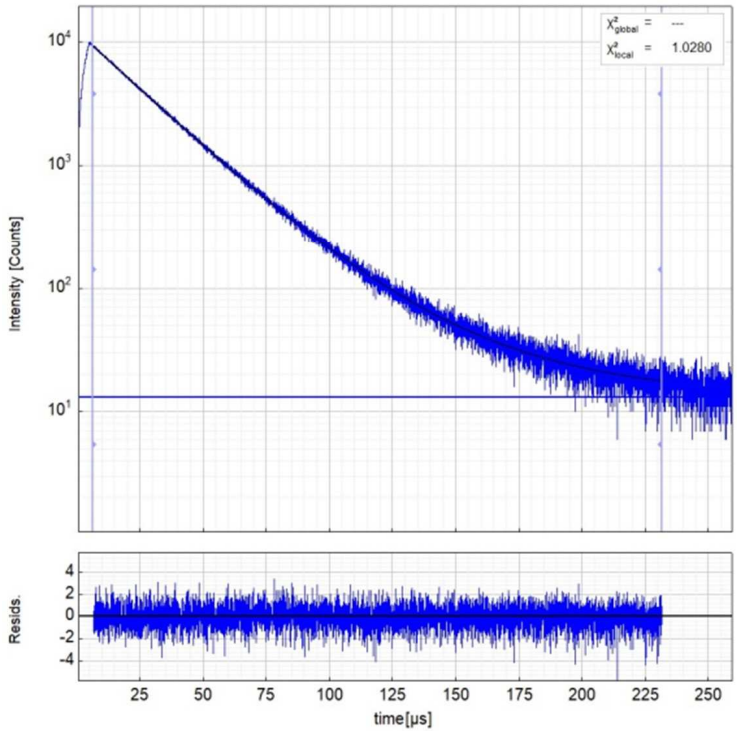

Parameter	Value	Δ	δ
A_1[kCnts/Chnl]	8.868	±0.090	1.0%
τ_1[ns]	22 590	±160	0.7%
I_1[kCnts]	6 260	±110	1.7%
A_{Rel1}[%]	95.9	±1.1	1.1%
I_{Rel1}[%]	91.3	±1.5	1.6%
A_2[kCnts/Chnl]	0.382	±0.099	26%
τ_2[ns]	50 400	±6 500	13%
I_2[kCnts]	600	±98	16%
A_{Rel2}[%]	4.2	±1.1	26%
I_{Rel2}[%]	8.8	±1.5	16%
$Bkgr_{Dec}$[kCnts]	0.0131	±0.0013	9.7%
τ_{AvInt}[ns]	25 010	±220	0.9%
τ_{AvAmp}[ns]	23 725	±65	0.3%

Fig. S56 Left: Raw (experimental) time-resolved photoluminescence decay of [Pt(dba)($AsPh_3$)] in a frozen MeOH/CH_2Cl_2 1:1 glassy matrix at 77K including the residuals (λ_{ex} = 376 nm, λ_{em} = 575 nm). Right: Fitting parameters including pre-exponential factors and confidence limits.

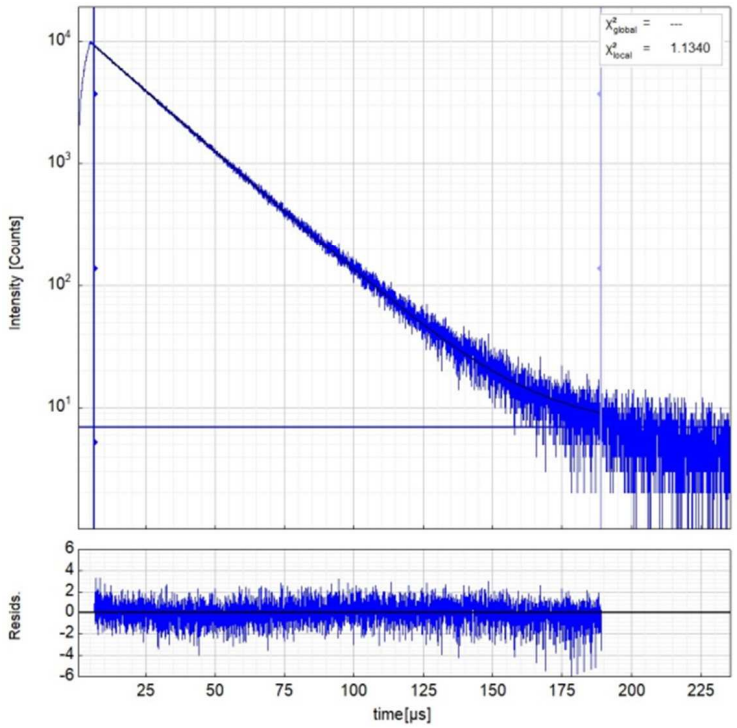

Parameter	Value	Δ	δ
A_1[kCnts/Chnl]	9.1815	±0.0100	0.1%
τ_1[ns]	21 912	±15	0.1%
I_1[kCnts]	6 286.9	±3.4	0.1%
A_{Rel1}[%]	100.0	---	---
I_{Rel1}[%]	100.0	---	---
$Bkgr_{Dec}$[kCnts]	0.0069	±0.0002	2.6%
τ_{AvInt}[ns]	21 912	±15	0.1%
τ_{AvAmp}[ns]	21 912	±15	0.1%

Fig. S57 Left: Raw (experimental) time-resolved photoluminescence decay of [Pt(dba)($SbPh_3$)] in a frozen MeOH/CH_2Cl_2 1:1 glassy matrix at 77K including the residuals (λ_{ex} = 376 nm, λ_{em} = 575 nm). Right: Fitting parameters including pre-exponential factors and confidence limits.

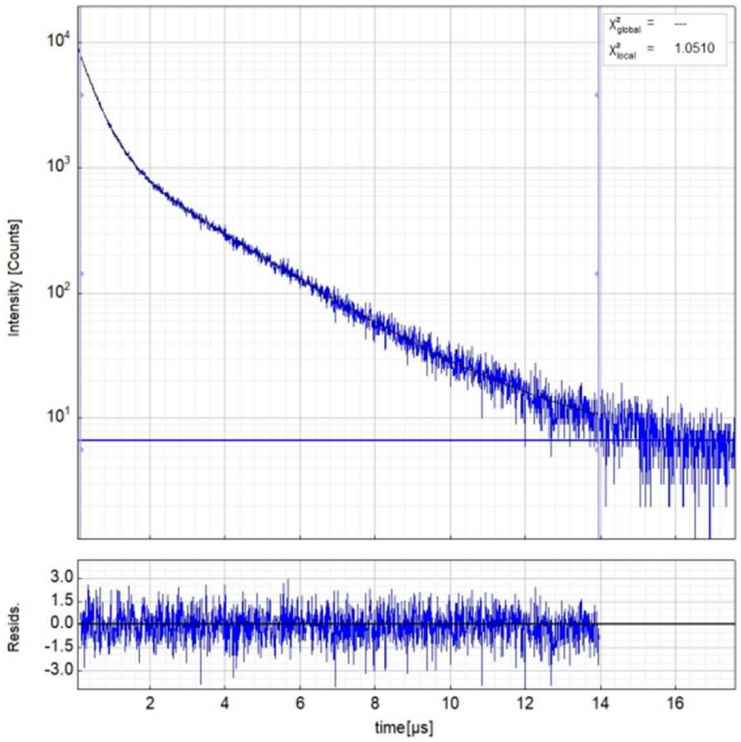

Parameter	Value	Δ	δ
A_1[kCnts/Chnl]	1.492	±0.015	0.9%
τ_1[ns]	2 352	±19	0.8%
I_1[kCnts]	438.4	±1.7	0.4%
A_{Rel1}[%]	19.1	±0.3	1.3%
I_{Rel1}[%]	55.2	±0.4	0.6%
A_2[kCnts/Chnl]	6.346	±0.040	0.6%
τ_2[ns]	449.2	±2.8	0.6%
I_2[kCnts]	356.3	±3.8	1.1%
A_{Rel2}[%]	81.0	±0.3	0.3%
I_{Rel2}[%]	44.9	±0.4	0.8%
$Bkgr_{Dec}$[kCnts]	0.0067	±0.0006	8.3%
τ_{AvInt}[ns]	1 498.6	±9.2	0.6%
τ_{AvAmp}[ns]	811.2	±4.3	0.5%

Fig. S58 Left: Raw (experimental) time-resolved photoluminescence decay of [Pt(dba)(PPh_3)] in fluid CH_2Cl_2 at 298 K including the residuals (λ_{ex} = 376 nm, λ_{em} = 600 nm). Right: Fitting parameters including pre-exponential factors and confidence limits.

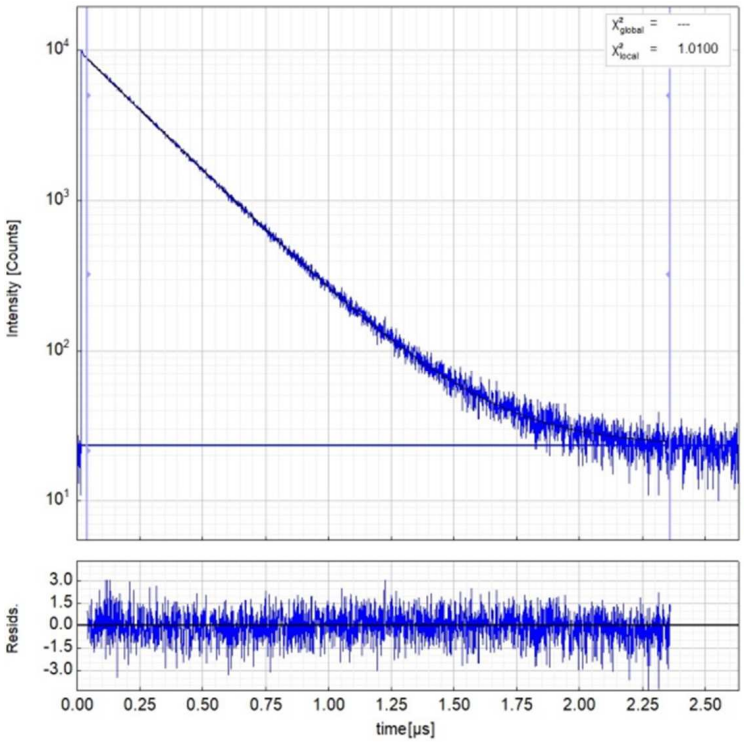

Parameter	Value	Δ	δ
A_1[kCnts/Chnl]	8.739	±0.013	0.1%
τ_1[ns]	268.40	±0.44	0.2%
I_1[kCnts]	2 345.5	±3.9	0.2%
A_{Rel1}[%]	100.0	---	---
I_{Rel1}[%]	100.0	---	---
$Bkgr_{Dec}$[kCnts]	0.0233	±0.0006	2.3%
τ_{AvInt}[ns]	268.40	±0.44	0.2%
τ_{AvAmp}[ns]	268.40	±0.44	0.2%

Fig. S59 Left: Raw (experimental) time-resolved photoluminescence decay of [Pt(dba)($AsPh_3$)] in fluid CH_2Cl_2 at 298 K including the residuals (λ_{ex} = 376 nm, λ_{em} = 600 nm). Right: Fitting parameters including pre-exponential factors and confidence limits.

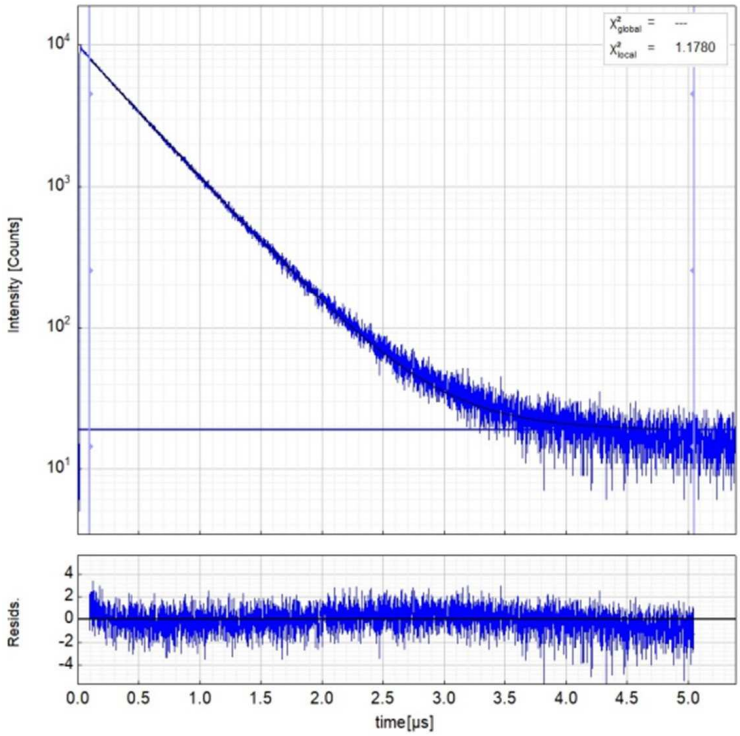

Parameter	Value	Δ	δ
A_1[kCnts/Chnl]	7.9869	±0.0097	0.1%
τ_1[ns]	469.23	±0.45	0.1%
I_1[kCnts]	3 747.7	±5.9	0.2%
A_{Rel1}[%]	100.0	---	---
I_{Rel1}[%]	100.0	---	---
$Bkgr_{Dec}$[kCnts]	0.0190	±0.0002	1.0%
τ_{AvInt}[ns]	469.23	±0.45	0.1%
τ_{AvAmp}[ns]	469.23	±0.45	0.1%

Fig. S60 Left: Raw (experimental) time-resolved photoluminescence decay of [Pt(dba)($SbPh_3$)] in fluid CH_2Cl_2 at 298 K including the residuals (λ_{ex} = 376 nm, λ_{em} = 600 nm). Right: Fitting parameters including pre-exponential factors and confidence limits.

Supporting Tables

Table S1 Selected structure solution and refinement data for crystal structures containing [Pt(C^N^C)($PnPh_3$)] (C^N^C = dpp, dba; Pn = As, Sb).

compound	[Pt(dpp)($AsPh_3$)]	[Pt(dba)($AsPh_3$)] ·Et_2O·$CHCl_3$ [a]	[Pt(dpp)($SbPh_3$)]	[Pt(dba)($SbPh_3$)]·0.5Et_2O
empirical formula	$C_{35}H_{26}AsNPt$	$C_{44}H_{37}AsCl_3NOPt$	$C_{35}H_{26}SbNPt$	$C_{82}H_{62}N_2OSb_2Pt_2$
formula weight (g/mol)	730.58	972.14	777.41	1725.10
temperature (K)	100(2)	109(2)	100(2)	100(2)
wavelength	Ag K_α	Mo K_α	Mo K_α	Mo K_α
crystal system	monoclinic	monoclinic	triclinic	triclinic
space group	$P2_1/c$	$C2/c$	$P\bar{1}$	$P\bar{1}$
cell parameters				
a (Å)	4.0056(6)	27.2312(16)	10.1552(6)	12.559(2)
b (Å)	9.5784(4)	10.5042(5)	15.5531(9)	13.453(2)
c (Å)	20.6896(9)	26.597(2)	17.832(1)	19.012(2)
α (°)	90	90	104.044(3)	99.710(4)
β (°)	96.219(2)	118.864(2)	97.175(3)	97.164(4)
γ (°)	90	90	90.067(2)	90.961(5)
V (Å^3)	2759.2(2)	6662.6(8)	2709.4(3)	3139.3(7)
Z	4	8	4	2
μ (mm^{-1})	3.41	5.35	6.18	5.35
crystal size (mm^3)	0.06 × 0.03 × 0.03	0.1 × 0.1 × 0.1	0.15 × 0.08 × 0.02	0.3 × 0.3 × 0.2
crystal colour/shape	yellow prism	red prism	orange prism	red prism
F(000)	1416	3412	1488	1668
2θ range (°)	1.9 – 22.0	3.0 – 30.5	2.0 – 30.2	2.0 – 28.3
index ranges				

$h_{min/max}$	–18 / 18	–38 / 38	–14 / 14	–16 / 16
$k_{min/max}$	–12 / 12	–14 / 14	–21 / 21	–17 / 17
$l_{min/max}$	–27 / 27	–37 / 37	–25 / 25	–25 / 25
reflections				
total	52922	85756	153953	146817
independent	6871	10116	15935	15332
completeness	99.9%	99.9%	99.9%	99.9%
data / restraints / parameters	6871 / 0 / 343	10116 / 0 / 457	15935 / 0 / 667	15332 / 0 / 804
GooF on F^2	1.06	1.02	1.10	1.08
final R values				
R_1 (I≥2σ(I)/all data)	0.021/0.023	0.020/0.022	0.075/0.090	0.021/0.022
wR_2	0.050	0.046	0.161	0.051
R_{int}	0.059	0.046	0.083	0.043
R_σ	0.031	0.026	0.050	0.024
largest peak / hole (e/Å^3)	1.07 / –0.80	0.63 / –0.66	3.75 / –6.41	4.48[a] / –1.17
CCDC	2149899	2194357	2257280	2208288

[a] Due to the disordered solvent molecules Et_2O and $CHCl_3$ occupying special positions with respect to the cell symmetry, the refinement of these molecules was impaired and the corresponding H atoms could not be added to the model using AFIX in all cases. The H atoms missing in the structure solution were nonetheless included in the calculation of the empirical formula and formula weight. [b] This residual electron density is localised in direct proximity to the Et_2O molecule found in the structure and is attributed to its disorder which could not be explicitly refined.

Table S2 Selected structural data for [Pt(dpp)($PnPh_3$)] (Pn = P, As, Sb) from scXRD and DFT geometry optimisations of the S_0 states.[a]

	[Pt(dpp)(PPh_3)]		[Pt(dpp)($AsPh_3$)]		[Pt(dpp)($SbPh_3$)]	
	scXRD [a]	DFT	scXRD	DFT	scXRD [b]	DFT
distances (Å)						
Pt–N1	2.026(6)	2.042	2.008(2)	2.025	2.01(1)/2.03(1)	2.022
Pt–C7	2.065(6)	2.090	2.067(2)	2.083	2.08(1)/2.08(1)	2.081
Pt–C13	2.080(6)	2.090	2.066(2)	2.086	2.07(1)/2.06(1)	2.076
Pt–Pn	2.209(2)	2.234	2.321(1)	2.351	2.504(1)/2.491(1)	2.507
N1–C5	1.347(8)	1.358	1.347(3)	1.359	1.35(1)/1.36(1)	1.359
N1–C1	1.355(8)	1.357	1.353(3)	1.360	1.34(1)/1.35(2)	1.359
C5–C6	1.466(9)	1.468	1.471(4)	1.468	1.48(2)/1.47(2)	1.469
C1–C12	1.479(8)	1.468	1.474(4)	1.468	1.48(1)/1.48(2)	1.469
C6–C7	1.427(9)	1.434	1.431(4)	1.436	1.43(2)/1.44(1)	1.436
C12–C13	1.409(9)	1.436	1.423(4)	1.434	1.42(2)/1.42(2)	1.436
angles (°)						
C7–Pt–C13	159.8(2)	159.5	161.0(1)	160.5	160.6(4)/161.5(5)	161.0
Pn–Pt–N1	175.9(2)	174.9	175.8(1)	176.3	172.9(2)/170.2(2)	177.5
N1–Pt–C7	80.3(2)	79.9	80.7(1)	80.2	80.4(4)/81.0(4)	80.5
N1–Pt–C13	80.2(2)	79.7	80.9(1)	80.3	80.2(4)/80.5(4)	80.5
C7–Pt–Pn	97.6(2)	95.7	101.4(7)	103.3	97.4(3)/95.7(3)	97.0
C13–Pt–Pn	102.2(2)	104.8	97.3(1)	96.1	101.9(3)/102.6(3)	102.0
C–Pn–C averaged	104.1(2)	103.7	103.7(1)	102.7	98.3(2)/99.7(2)	101.2
C–Pn–Pt averaged	114.6(2)	114.8	114.9(1)	115.6	118.8(1)/118.1(1)	116.9
Sum of ∧ around Pt	360.3	360.1	360.3	359.9	359.9/360.2	360.0
dihedral angles (°)						
C7–Pt–Pn–C18	78.4(3)	56.6	97.3(1)	62.4	51.1(4)/66.8(5)	60.6
C13–Pt–Pn–C18	97.8(3)	121.6	79.4(1)	122.7	127.4(4)/115.6(6)	122.2
N1–Pt–Pn–C18	136.7(23)	85.6	143.2(8)	68.9	20(2)/136(2)	67.0
N1–C1–C12–C17	2.9(6)	2.7	11.1(2)	0.9	7(1)/4(1)	0.2

N1–C5–C6–C11	12.1(6)	2.6	2.3(2)	1.2	3(1)/0.51(1)	179.7

[a] scXRD data for [Pt(dpp)(PPh_3)] from ref.[1] [b] Data for two molecules in the unit cell.

Table S3 Selected structural data for [Pt(dba)($PnPh_3$)] (Pn = P, As, Sb) from scXRD and DFT geometry optimisations of the S_0 states.[a]

	[Pt(dba)(PPh_3)]		[Pt(dba)($AsPh_3$)]		[Pt(dba)($SbPh_3$)]	
	scXRD [a]	DFT	scXRD	DFT	scXRD [b]	DFT
distances (Å)						
Pt–N1	2.003(4)	2.030	1.996(2)	2.014	1.996(2)/1.994(2)	2.010
Pt–C1	2.099(5)	2.117	2.086(2)	2.115	2.110(3)/2.100(3)	2.107
Pt–C18	2.106(5)	2.122	2.101(2)	2.114	2.092(3)/2.098(3)	2.110
Pt–Pn	2.230(2)	2.232	2.335(1)	2.349	2.487(1)/2.493(1)	2.505
N1–C13	1.333(5)	1.340	1.334(3)	1.341	1.337(3)/1.332(3)	1.340
N1–C10	1.338(7)	1.339	1.335(3)	1.341	1.339(3)/1.340(3)	1.340
C13–C17	1.420(8)	1.426	1.428(4)	1.425	1.429(4)/1.425(3)	1.426
C10–C6	1.440(6)	1.426	1.421(3)	1.426	1.423(3)/1.425(4)	1.425
C17–C18	1.439(6)	1.440	1.448(3)	1.440	1.434(3)/1.432(3)	1.440
C6–C1	1.431(7)	1.438	1.432(3)	1.438	1.440(3)/1.435(4)	1.440
C7–C8	1.363(7)	1.373	1.356(3)	1.373	1.357(4)/1.365(4)	1.373
C14–C15	1.354(8)	1.373	1.361(4)	1.373	1.361(4)/1.359(4)	1.373
angles (°)						
C1–Pt–C18	158.6(2)	158.1	159.6(1)	158.1	159.5(1)/159.3(1)	159.4
Pn–Pt–N1	176.2(1)	175.8	176.5(1)	177.1	174.0(1)/177.3(1)	178.1
N1–Pt–C1	79.5(2)	79.2	80.1(1)	79.5	79.6(1)/79.8(1)	79.7
N1–Pt–C18	79.2(2)	79.0	79.6(1)	79.4	80.0(1)/79.5(1)	79.7
C1–Pt–Pn	96.8(1)	96.7	96.5(1)	97.7	102.9(1)/99.6(1)	102.2
C18–Pt–Pn	104.5(1)	105.1	103.8(1)	103.4	97.6(1)/101.1(1)	98.4
C–Pn–C averaged	104.3(1)	104.0	103.5(1)	103.0	102.5(1)/99.8(1)	101.5
C–Pn–Pt averaged	114.4(1)	114.5	114.9(1)	115.4	115.8(1)/118.2(1)	116.6
Sum of ∧ around Pt	360.0	360.0	360.0	360.0	360.1/360.0	360.0
dihedral angles (°)						
C1–Pt–Pn–C28	169.7(2)	174.0	69.9(1)	62.9	128.9(1)/170.0(1)	119.1
C18–Pt–Pn–C28	12.1(2)	4.4	108.6(1)	117.7	49.4(1)/10.9(1)	60.8
N1–Pt–Pn–C28	5.6(17)	8.9	73.5(9)	49.8	15.5(6)/112.0(1)	47.1
N1–C10–C6–C5	1.0(4)	1.1	1.7(2)	0.6	0.6(3)/1.2(2)	0.0
N1–C13–C17–C16	2.5(4)	1.3	0.2(2)	0.5	1.8(2)/0.8(2)	0.2
N1–C10–C9–C8	1.3(4)	0.5	0.5(2)	0.2	0.4(2)/0.4(2)	0.0
N1–C13–C12–C14	0.1(4)	0.6	0.3(2)	0.2	0.4(2)/1.5(2)	0.0
C14–C12–C11–C9	0.5(5)	0.9	0.1(2)	0.4	0.5(2)/0.9(3)	0.0

[a] Data for [Pt(dba)(PPh_3)] from ref.2. [b] Data for two molecules in the unit cell.

Table S4 Selected structural data for [Pt(C^N^C)($PnPh_3$)] (C^N^C = dpp, dba; Pn = P, As, Sb) from DFT geometry optimizations of the T_1 states.

	dpp				dba		
	P	As	Sb		P	As	Sb
distances (Å)				distances (Å)			
Pt–N1	2.033	2.021	2.025	Pt–N1	2.020	2.009	2.005
Pt–C7	2.060	2.054	2.051	Pt–C1	2.084	2.081	2.081
Pt–C13	2.054	2.050	2.049	Pt–C18	2.093	2.086	2.080
Pt–Pn	2.259	2.373	2.531	Pt–Pn	2.255	2.368	2.524
N1–C5	1.378	1.380	1.379	N1–C10	1.357	1.358	1.357
N1–C1	1.379	1.381	1.380	N1–C13	1.357	1.357	1.357
C5–C6	1.448	1.448	1.449	C13–C17	1.402	1.402	1.403
C1–C12	1.448	1.448	1.449	C10–C6	1.403	1.403	1.403
C6–C7	1.440	1.440	1.440	C17–C18	1.449	1.449	1.450

C12–C13	1.439	1.440	1.440	C6–C1	1.447	1.447	1.450
angles (°)				C7–C8	1.385	1.386	1.386
C7–Pt–C13	145.4	146.5	147.4	C14–C15	1.386	1.386	1.386
Pn–Pt–N1	174.2	174.5	174.4	angles (°)			
N1–Pt–C7	79.1	79.5	79.7	C1–Pt–C18	152.3	153.2	154.9
N1–Pt–C13	79.3	79.7	79.8	Pn–Pt–N1	176.6	177.1	178.1
C7–Pt–Pn	103.9	103.3	103.1	N1–Pt–C1	78.9	79.2	79.4
C13–Pt–Pn	100.3	99.8	99.7	N1–Pt–C18	78.6	79.0	79.3
C–Pn–C averaged	104.1	103.0	101.3	C1–Pt–Pn	98.3	98.2	98.7
C–Pn–Pt averaged	114.5	115.3	116.7	C18–Pt–Pn	104.6	103.8	102.6
Sum of ∧ around Pt	362.6	362.3	362.3	C–Pn–C averaged	104.1	103.1	101.4
dihedral angles (°)				C–Pn–Pt averaged	114.4	115.3	116.6
C8–C7–Pt–C13	121.3	122.2	124.3	Sum of ∧ around Pt	360.4	360.2	360.0
C7-Pt-C13-C14	123.0	123.1	124.4	dihedral angles (°)			
N1–C1–C12–C17	173.5	173.1	172.2	N1–C10–C6–C5	180.0	179.8	179.5
N1–C5–C6–C11	173.8	173.3	172.2	N1–C13–C17–C16	179.5	179.9	179.6
				N1–C10–C9–C8	178.7	178.6	178.6
				N1–C13–C12–C14	179.0	178.8	178.7
				C14–C12–C11–C9	175.6	174.7	175.5

Table S5 Selected structural data for [Pt(C^N^C)($BiPh_3$)] (C^N^C = dpp, dba) from DFT geometry optimisations of the S_0 state.

	[Pt(dpp)($BiPh_3$)]			[Pt(dba)($BiPh_3$)]
	free	constrained		constrained
distances (Å)			distances (Å)	
Pt–N1	2.065	2.004	Pt–N1	1.997
Pt–C7	2.080	2.076	Pt–C1	2.101
Pt–C13	2.102	2.065	Pt–C18	2.103
Pt–Bi	2.722	2.602	Pt–Bi	2.599
Pt–C_{Ph}	2.016	–		
N1–C5	1.356	1.360	N1–C13	1.342
N1–C1	1.354	1.362	N1–C10	1.343
C5–C6	1.471	1.469	C13–C17	1.425
C1–C12	1.474	1.467	C10–C6	1.424
C6–C7	1.434	1.435	C17–C18	1.439
C12–C13	1.435	1.436	C6–C1	1.438
			C7–C8	1.374
			C14–C15	1.373
angles (°)			angles (°)	
C7–Pt–C13	159.6	161.9	C1–Pt–C18	160.26
Bi–Pt–N1	87.6	175.8	Bi–Pt–N1	169.1
N1–Pt–C7	80.1	81.0	N1–Pt–C1	80.2
N1–Pt–C13	79.6	80.9	N1–Pt–C18	80.1
C7–Pt–Bi	101.1	98.3	C1–Pt–Bi	96.6
C13–Pt–Bi	79.7	99.8	C18–Pt–Bi	102.4
N1–Pt–C_{Ph}	175.7	–	C–Bi–C averaged	100.1
C7–Pt–C_{Ph}	98.5	–	C–Bi–Pt averaged	117.7
C18–Pt–C_{Ph}	101.6	–		–
Bi–Pt–C_{Ph}	96.7	–		–
C–Bi–C averaged	–	99.9		
C–Bi–Pt averaged	–	117.9		
Sum of ∧ around Pt	–	360.0	Sum of ∧ around Pt	359.3
dihedral angles (°)			dihedral angles (°)	
C7–Pt–Bi–C18	21.3	56.0	C1–Pt–Bi–C22	65.0

C13–Pt–Bi–C18	0.6	125.2	C18–Pt–Bi–C22	120.3
N1–Pt–Bi–C18	100.7	44.4	N1–Pt–Bi–C22	42.4
N1–C1–C12–C17	1.9	3.3	N1–C10–C6–C5	5.5
N1–C5–C6–C11	1.7	0.8	N1–C13–C17–C16	0.4
			N1–C10–C9–C8	5.5
			N1–C13–C12–C14	0.9
			C14–C12–C11–C9	3.1

Table S6 Electrochemical data for the ligands H_2dpp and H_2dba and the complexes [Pt(C^N^C)(PnPh$_3$)] (Pn = P, As, Sb).[a]

	Red3 E_p (V)	Red2 E_p (V)	Red1 $E_{1/2}$ (V)	Ox1 E_p (V)	ΔRed1-Red2	ΔRed1–Ox1
H_2dpp	–		–2.85	–		–
[Pt(dpp)(PPh$_3$)]	–	–2.96	–2.36	0.65	0.60	3.01
[Pt(dpp)(AsPh$_3$)]	–	–2.97	–2.36	0.56	0.61	2.92
[Pt(dpp)(SbPh$_3$)]	–3.36	–2.67	–2.26	0.61	0.41	2.87
H_2dba	–	–2.96	–2.31	–	0.65	–
[Pt(dba)(PPh$_3$)]	–3.26	–2.70	–2.00	0.72	0.70	2.72
[Pt(dba)(AsPh$_3$)]	–3.37	–2.68	–1.95	0.73	0.73	2.68
[Pt(dba)(SbPh$_3$)]	–3.28	–2.31[b]	–1.91	0.71	0.40	2.62

[a] Measured in 0.1 M nBu$_4$NPF$_6$ THF solution at a scan rate of 50 mV/s. Potentials E (V) referenced against the $FeCp_2/FeCp_2^+$ redox pair, accuracy of potentials: ± 0.003 V. $E_{1/2}$: half-wave potential for reversible processes, E_p: peak potential for irreversible processes. [b] Reversible, $E_{1/2}$ given.

Table S7 UV-vis absorption data of the ligand H_2dpp and the complexes [Pt(dpp)(PnPh$_3$)] (Pn = P, As, Sb).[a]

	λ_1 (ε)	λ_2 (ε)	λ_3 (ε)	λ_4 (ε)	λ_5 (ε)
H_2dpp	244 (27.2)	286 (11.1)	302 (10.8)	–	–
[Pt(dpp)(PPh$_3$)]	252 (38.4)	267 (34.3)	278 (34.8)	336 (13.8)	349 (15.7)
[Pt(dpp)(AsPh$_3$)]	252 (35.4)	265 (32.7)	281 (31.9)	339 (12.2)	352 (14.7)
[Pt(dpp)(SbPh$_3$)]	253 (36.7)	267 (34.9)	282 (31.7)	340 (12.9)	354 (15.5)

[a] Absorption maxima λ_n in nm in CH_2Cl_2, molar absorption coefficient in 10^3 M^{-1} cm^{-1}.

Table S8 UV-vis absorption data of the ligand H_2dba and the complexes [Pt(dba)(PnPh$_3$)] (Pn = P, As, Sb).[a]

	λ_1 (ε)	λ_2 (ε)	λ_3 (ε)	λ_4 (ε)	λ_5 (ε)	λ_6 (ε)	λ_7 (ε)	λ_8 (ε)
H_2dba	289 (8.2)	303 (7.6)	339 (1.6)	355 (1.1)	374 (1.3)	394 (1.8)	–	–
[Pt(dba)(PPh$_3$)]	286 (50.0)	296 (50.0)	333 (11.6)	348 (12.8)	387 (6.0)	409 (6.2)	499 (1.7)	533 (2.2)
[Pt(dba)(AsPh$_3$)]	285 (48.4)	296 (45.1)	333 (10.8)	354 (12.7)	390 (6.1)	412 (6.4)	505 (1.8)	539 (1.9)
[Pt(dba)(SbPh$_3$)]	286 (46.7)	296 (41.6)	335 (10.5)	351 (13.1)	392 (5.7)	416 (6.6)	511 (1.2)	546 (1.7)

[a] Absorption maxima λ_n in nm in CH_2Cl_2, molar absorption coefficient in 10^3 M^{-1} cm^{-1}.

References

1. A. Kergreis, R. M. Lord and S. J. Pike, Influence of ligand and nuclearity on the cytotoxicity of cyclometallated C^N^C platinum(II) complexes, *Chem.–Eur. J.*, 2020, **26**, 14938–14946. DOI: 10.1002/chem.202002517
2. J. N. Friedel, M. Krause, R. Jordan, I. Maisuls, D. Bruenink, D. Schwab, N. L. Doltsinis, C. A. Strassert and A. Klein, Triplet Emitting C^N^C Cyclometalated Dibenzo[c,h]Acridine Pt(II) Complexes, *Molecules*, 2022, **27**, 8054. DOI: 10.3390/molecules27228054
3. R. Siebert, D. Akimov, M. Schmitt, A. Winter, U.S. Schubert, B. Dietzek, J. Popp, Spectroscopic Investigation of the Ultrafast Photoinduced Dynamics in π-Conjugated Terpyridines, *ChemPhysChem.*, 2009, **10**, 910-919, DOI: 10.1002/cphc.200800847
4. C. Müller, T. Pascher, A. Eriksson, P. Chabera, J. Uhlig, KiMoPack: A python Package for Kinetic Modeling of the Chemical Mechanism, *J. Phys. Chem. A*, 2022, **126**, 4087–4099, DOI: 10.1021/acs.jpca.2c00907
5. *APEX4—Software Suite for Crystallographic Programs*; Bruker AXS, Inc.: Madison, WI, USA, 2021.
6. G. M. Sheldrick, A short history of SHELX, *Acta Crystallogr. A - Found. Crystallograph.*, 2008, **64**, 112–122. DOI: 10.1107/S0108767307043930
7. G. M. Sheldrick, Crystal structure refinement with SHELXL, *Acta Crystallogr. C- Struct. Chem.*, 2015, **71**, 3–8. DOI: 10.1107/S2053229614024218
8. C. B. Hübschle, G. M. Sheldrick, B. Dittrich, ShelXle: a Qt graphical user interface for SHELXL, *J. Appl. Crystallogr.*, 2011, **44**, 1281–1284. DOI: 10.1107/S0021889811043202
9. F. Neese, F. Wennmohs, U. Becker und C. Riplinger, *J. Chem. Phys.*, 2020, **152**, 224108. DOI: 10.1063/5.0004608.
10. F. Neese, The ORCA quantum chemistry program package, *WIREs Comput Mol Sci.*, 2022, **12**, e1606. DOI: 10.1002/wcms.1606
11. F. Weigend and R. Ahlrichs, Balanced basis sets of split valence, triple zeta valence and quadruple zeta valence quality for H to Rn: Design and assessment of accuracy, *Phys. Chem. Chem. Phys.*, 2005, **7**, 3297. DOI: 10.1039/b508541a
12. A. D. Becke, Density-functional exchange-energy approximation with correct asymptotic behavior, *Phys. Rev. A*, 1988, **38**, 3098–3100. DOI: 10.1103/PhysRevA.38.3098
13. J. P. Perdew and W. Yue, Accurate and simple density functional for the electronic exchange energy: Generalized gradient approximation, *Phys. Rev. B*, 1986, **33**, 8800–8802. DOI: 10.1103/PhysRevB.33.8800
14. S. Grimme, J. Antony, S. Ehrlich and H. Krieg, A consistent and accurate ab initio parametrization of density functional dispersion correction (DFT-D) for the 94 elements H-Pu, *J. Chem. Phys.* 2010, **132**, 154104. DOI: 10.1063/1.3382344
15. S. Grimme, S. Ehrlich and L. Goerigk, Effect of the damping function in dispersion corrected density functional theory, *J. Comput. Chem.*, 2011, **2011**, 1456–1465. DOI: 10.1002/jcc.21759
16. V. Barone and M. Cossi, Effect of the damping function in dispersion corrected density functional theory, *J. Phys. Chem. A*, 1998, **102**, 1995–2001. DOI: 10.1021/jp9716997
17. M. Cossi, N. Rega, G. Scalmani and V. Barone, Energies, structures, and electronic properties of molecules in solution with the C-PCM solvation model, *J. Comput. Chem.*, 2003, **24**, 669–681. DOI: 10.1002/jcc.10189
18. J. Tao, J. P. Perdew, V. N. Stavoverov and G. E. Scuseria, Climbing the density functional ladder: Nonempirical meta–generalized gradient approximation designed for molecules and solids, *Phys. Rev. Lett.*, 2003, **91**, 146401. DOI: 10.1103/PhysRevLett.91.146401
19. Chemcraft – graphical software for visualization of quantum chemistry computations. https://www.chemcraftprog.com.
20. F. Plasser, TheoDORE: A toolbox for a detailed and automated analysis of electronic excited state computations, *J. Chem. Phys.*, 2020, **152**, 084108. DOI: 10.1063/1.5143076
21. E. van Lenthe, J. G. Snijders and E. J. Baerends, The zero-order regular approximation for relativistic effects: The effect of spin–orbit coupling in closed shell molecules, *J. Chem. Phys.*, 1996, **105**, 6505–6516. DOI: 10.1063/1.472460

22. D. A. Pantazis, X.-Y. Chen, C. R. Landis and F. Neese, All-Electron Scalar Relativistic Basis Sets for Third-Row Transition Metal Atoms, *J. Chem. Theory Comput.*, 2008, **4**, 908–919. DOI: 10.1021/ct800047t
23. J. D. Rolfes, F. Neese and D. A. Pantazis, All-electron scalar relativistic basis sets for the elements Rb–Xe, *J. Comput. Chem.*, 2020, **41**, 1842–1849. DOI: 10.1002/jcc.26355

6.2 Supporting Information for Publication 2

Reprinted with permission from Ref.[109]. Copyright © 2025, American Chemical Society.

Supporting Information for

Synthesis and photophysics of the doubly cyclometalated Pd(II) complexes [Pd(C^N^C)(L)], L = PPh_3, $AsPh_3$ and $SbPh_3$

Rose Jordan,[a] Sam Kler,[a] Iván Maisuls,[b] Niklas Klosterhalfen,[c,d] Benjamin Dietzek-Ivanšić,*[,c,d] Cristian A. Strassert*[,b] and Axel Klein*[,a]

[a] University of Cologne, Faculty for Mathematics and Natural Sciences, Department of Chemistry, Institute for Inorganic Chemistry, Greinstrasse 6, D-50939 Köln, Germany. Rose Jordan, email: rjordan1@uni-koeln.de, ORCID: 0000-0003-0764-1639 (R.J.); Axel Klein, Email: axel.klein@uni-koeln.de, ORCID: 0000-0003-0093-9619 (A.K.)

[b] Universität Münster, Institut für Anorganische und Analytische Chemie, CiMIC, CeNTech, Heisenbergstraße 11, D-48149 Münster, Germany. Iván Maisuls, email: maisuls@uni-muenster.de, ORCID: 0000-0002-6494-1446 (I.M.); Cristian A. Strassert, Email: cstra_01@uni-muenster.de, ORCID: 0000-0002-1964-0169 (C.A.S.)

[c] Friedrich Schiller University Jena, Institute for Physical Chemistry (IPC), Helmholtzweg 4, 07743 Jena, Germany. Niklas Klosterhalfen, Email: niklas.klosterhalfen@uni-jena.de, ORCID: 0009-0005-4307-0644 (N.K.); Benjamin Dietzek-Ivanšić, Email: benjamin.dietzek@uni-jena.de; ORCID: 0000-0002-2842-3537 (B.D.I)

[d] Leibniz Institute for Photonic Technologies Jena (IPHT), Research Department Functional Interfaces, Albert-Einstein-Str. 9, 07745 Jena, Germany. Niklas Klosterhalfen, Email: niklas.klosterhalfen@leibniz-ipht.de, ORCID: 0009-0005-4307-0644 (N.K.); Benjamin Dietzek-Ivanšić, Email: benjamin.dietzek@leibniz-ipht.de; ORCID: 0000-0002-2842-3537 (B.D.I.)

* Corresponding authors: Rose Jordan, Prof. Dr. Benjamin Dietzek-Ivanšić, Prof. Dr. Cristian A. Strassert, and Prof. Dr. Axel Klein

Table of Contents

Supporting Figures

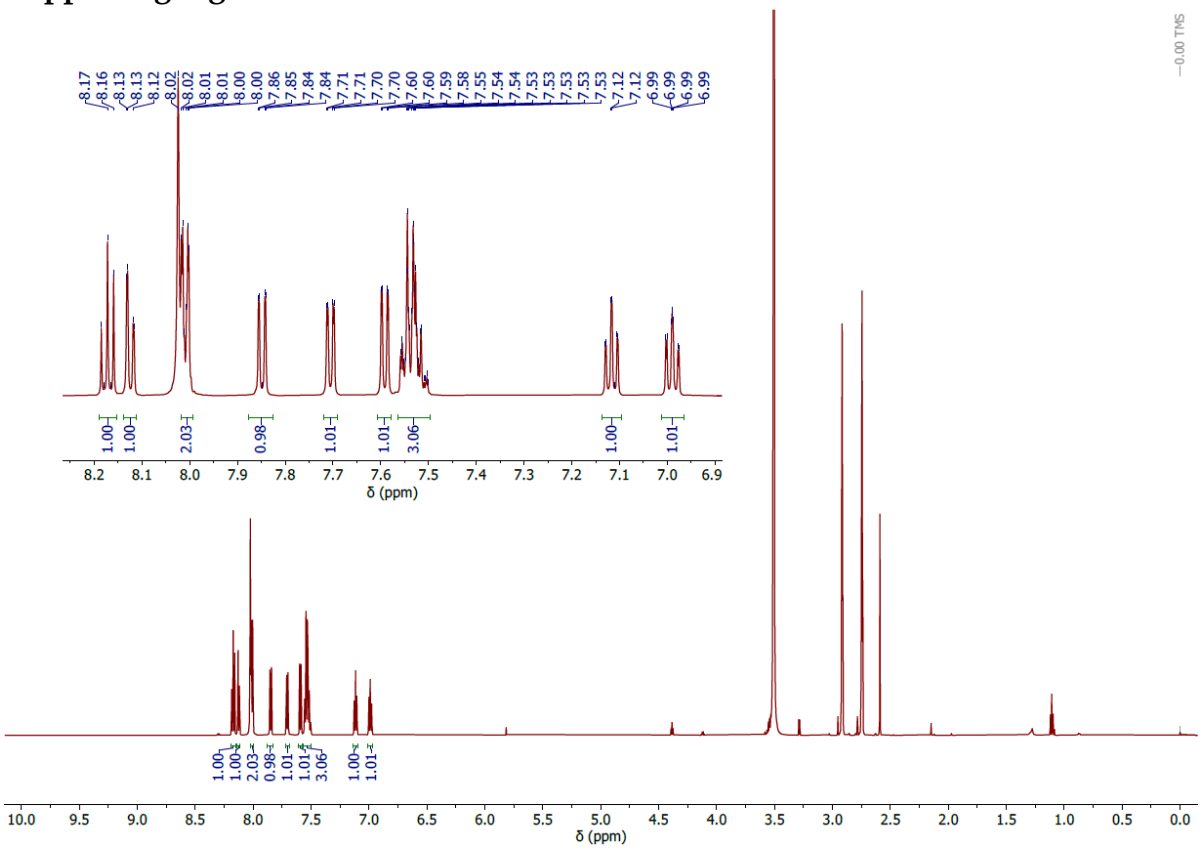

Figure S1. ^{1}H NMR spectrum (600 MHz, DMF-d_7) of {[Pd(dppH)Cl]}$_2$ (**1**).

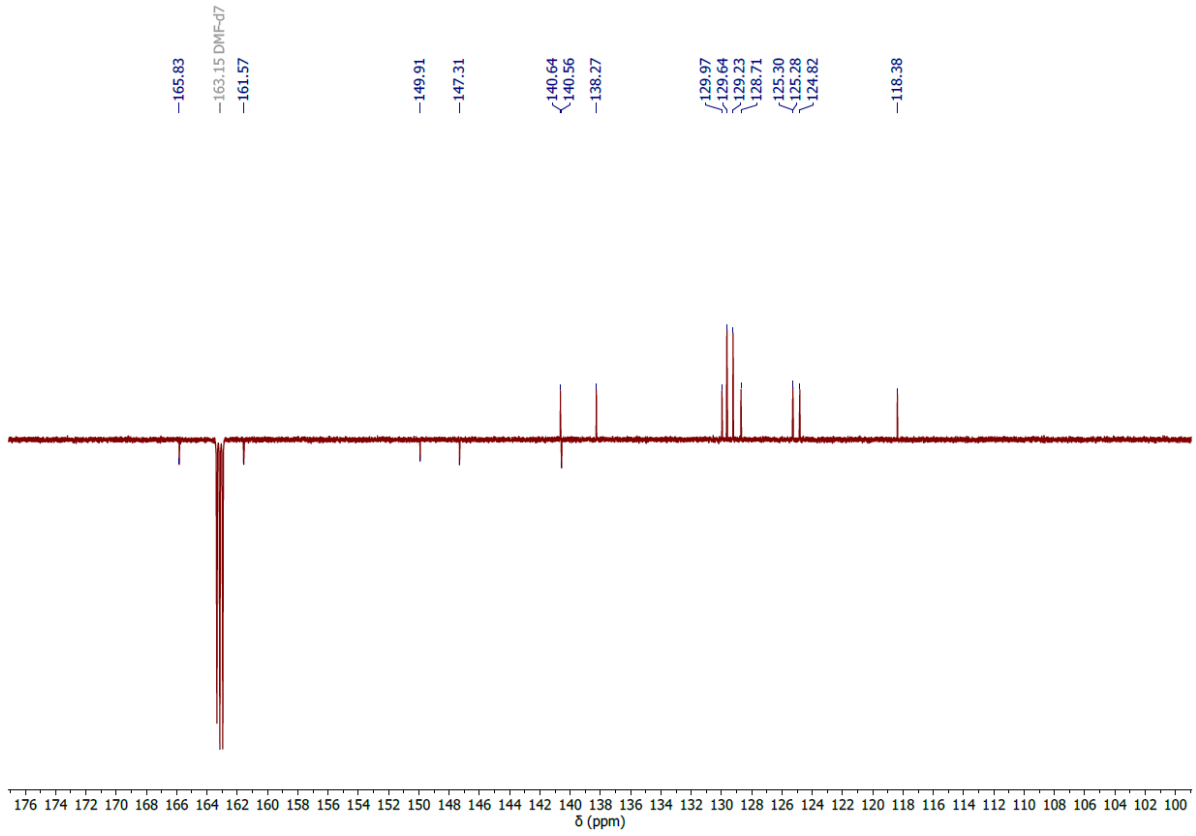

Figure S2. ^{13}C NMR spectrum (151 MHz, DMF-d_7) of {[Pd(dppH)Cl]}$_2$ (**1**).

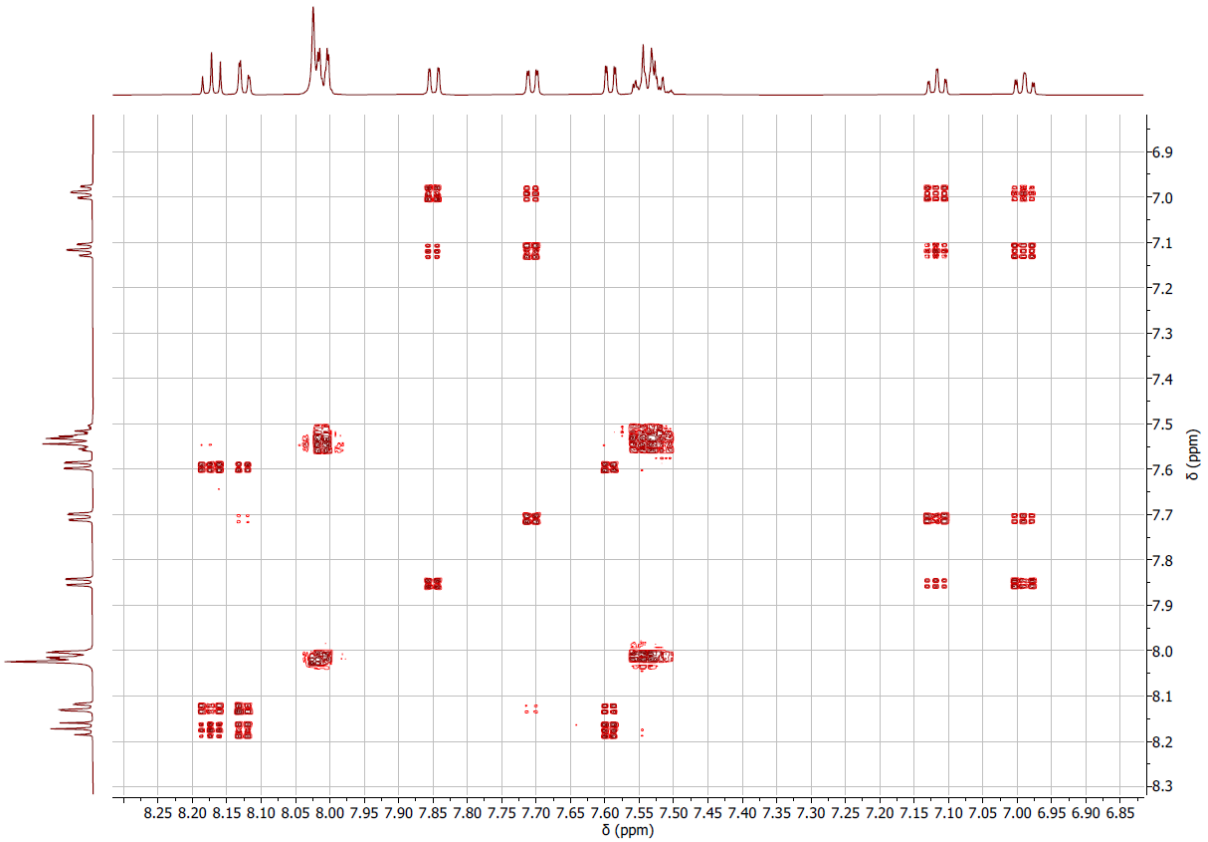

Figure S3. ^{1}H,^{1}H COSY spectrum (600 MHz, DMF-d_7) of {[Pd(dppH)Cl]}$_2$ (**1**).

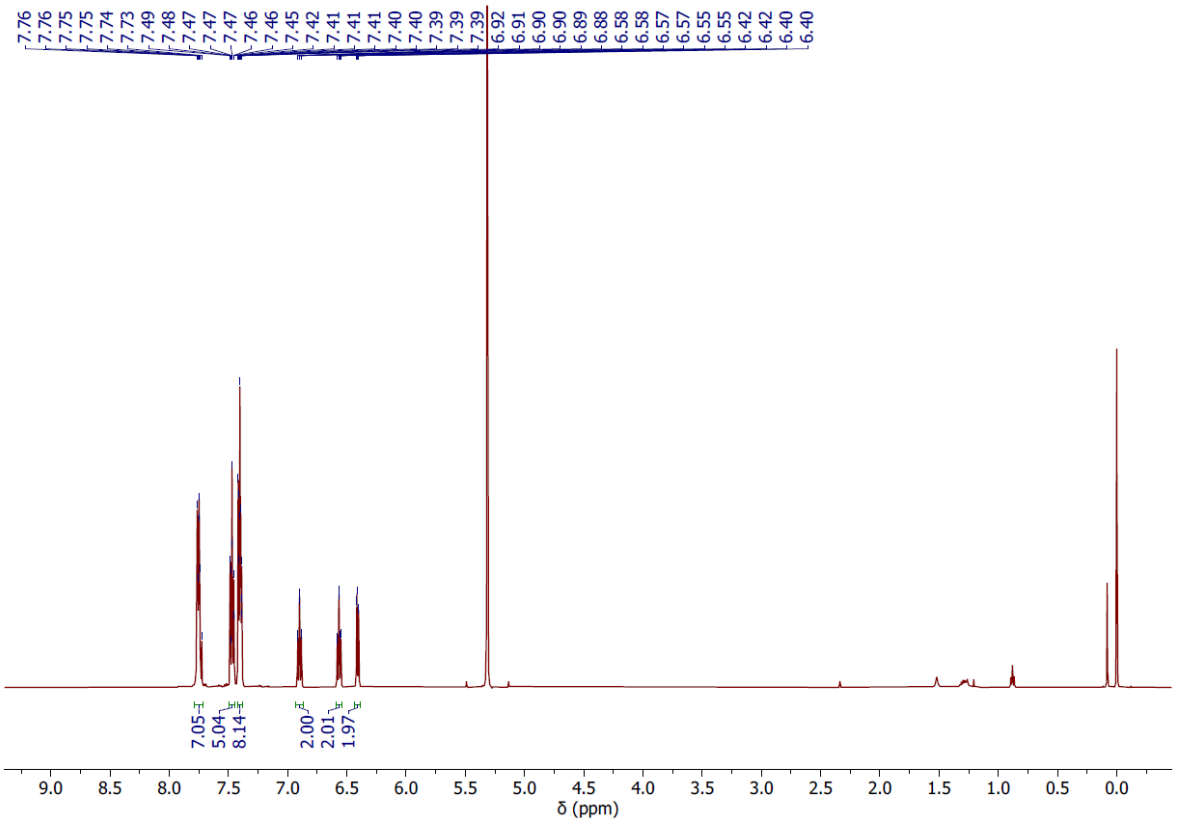

Figure S4. ^{1}H NMR spectrum (500 MHz, CD_2Cl_2) of [Pd(dpp)($AsPh_3$)] (**3b**).

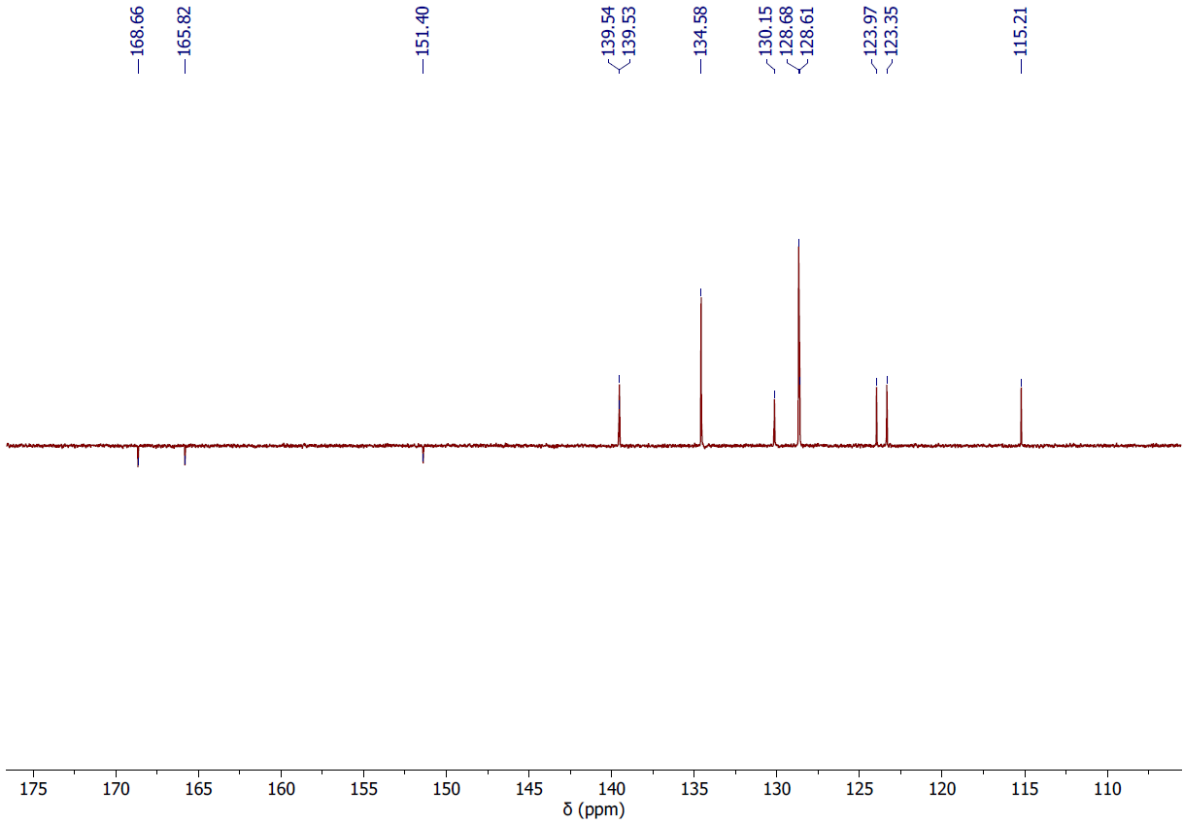

Figure S5. ^{13}C NMR spectrum (126 MHz, CD_2Cl_2) of [Pd(dpp)($AsPh_3$)] (**3b**).

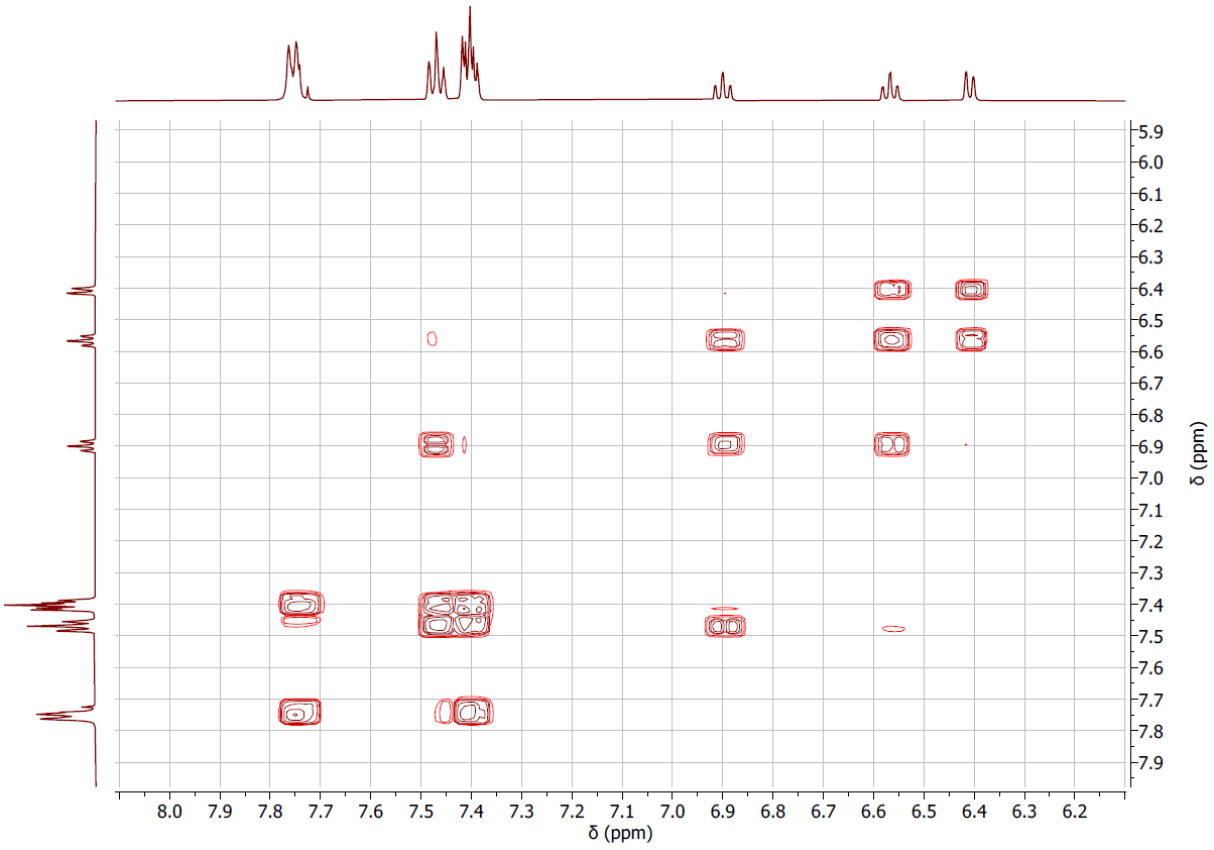

Figure S6. $^{1}H,^{1}H$ COSY spectrum (500 MHz, CD_2Cl_2) of [Pd(dpp)($AsPh_3$)] (**3b**).

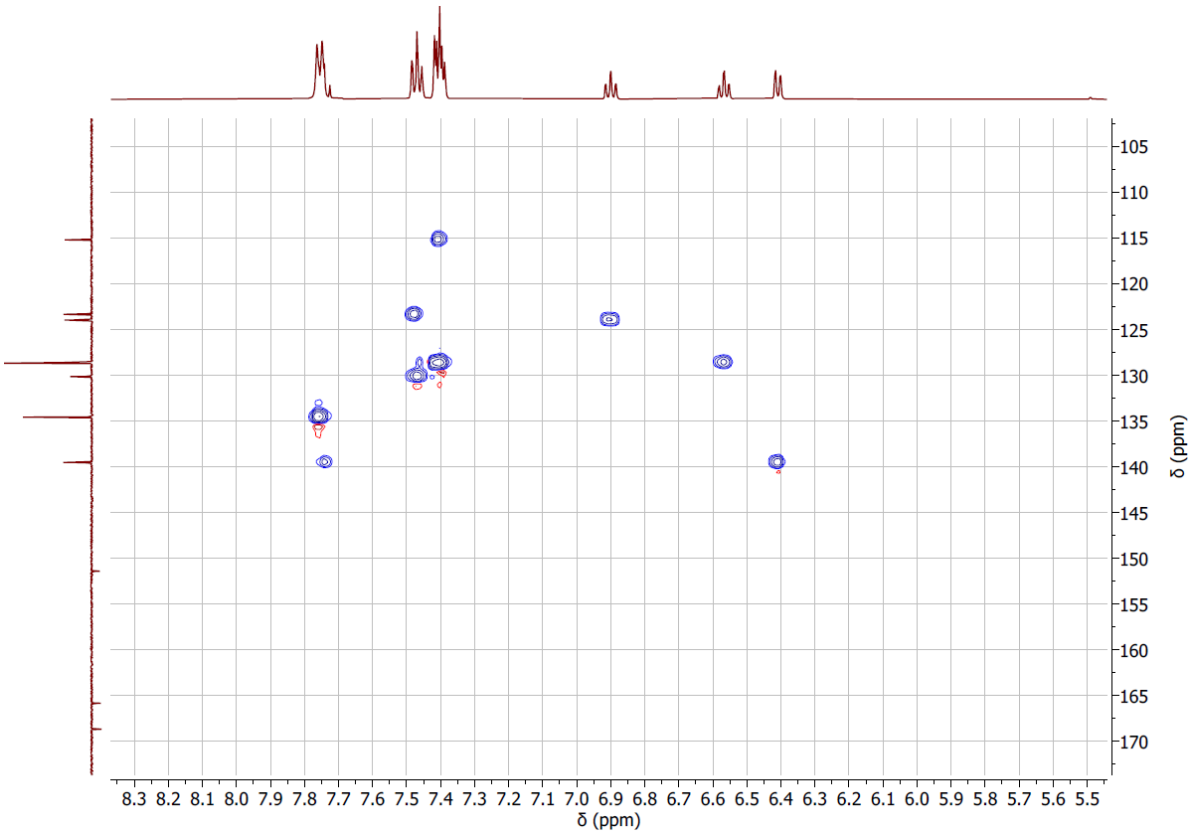

Figure S7. $^{13}C,^{1}H$ HSQC spectrum (500 MHz, CD_2Cl_2) of [Pd(dpp)($AsPh_3$)] (**3b**).

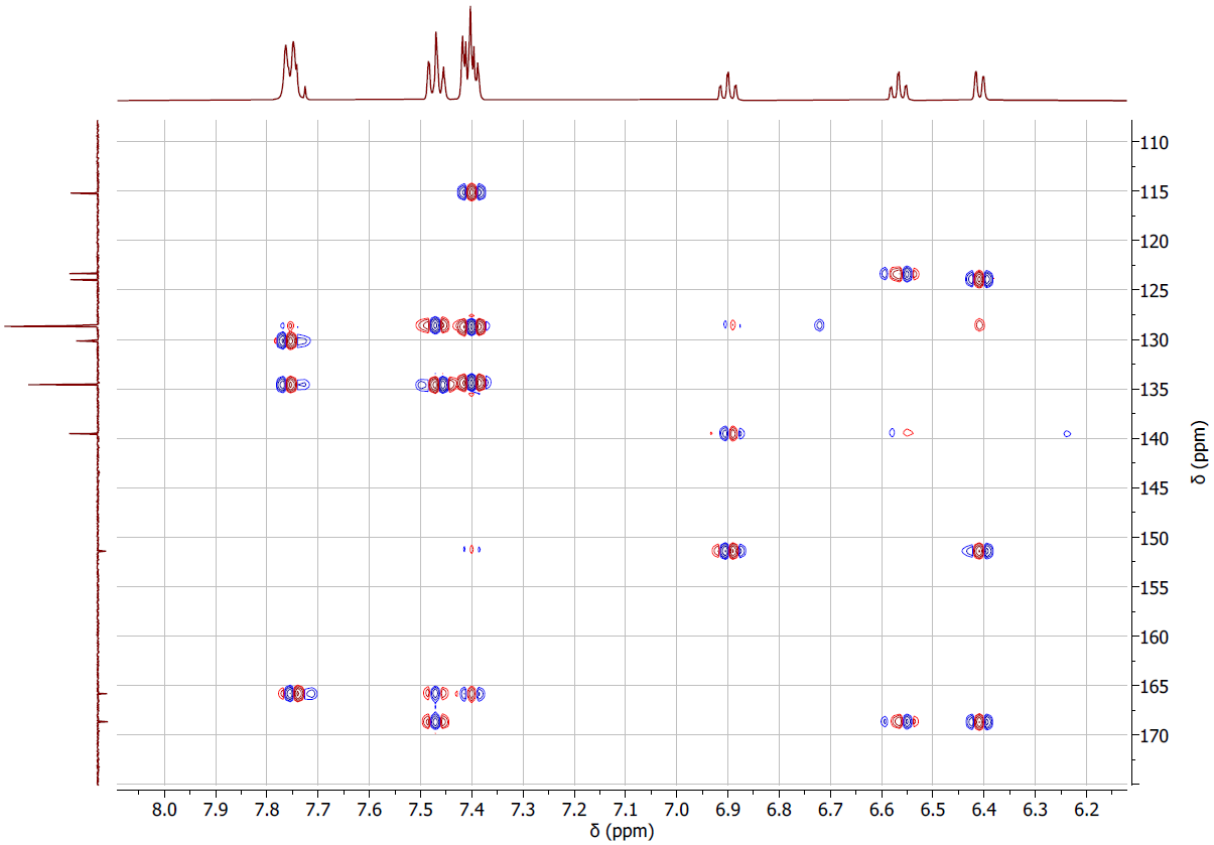

Figure S8. $^{13}C,^{1}H$ HMBC spectrum (500 MHz, CD_2Cl_2) of [Pd(dpp)($AsPh_3$)] (**3b**).

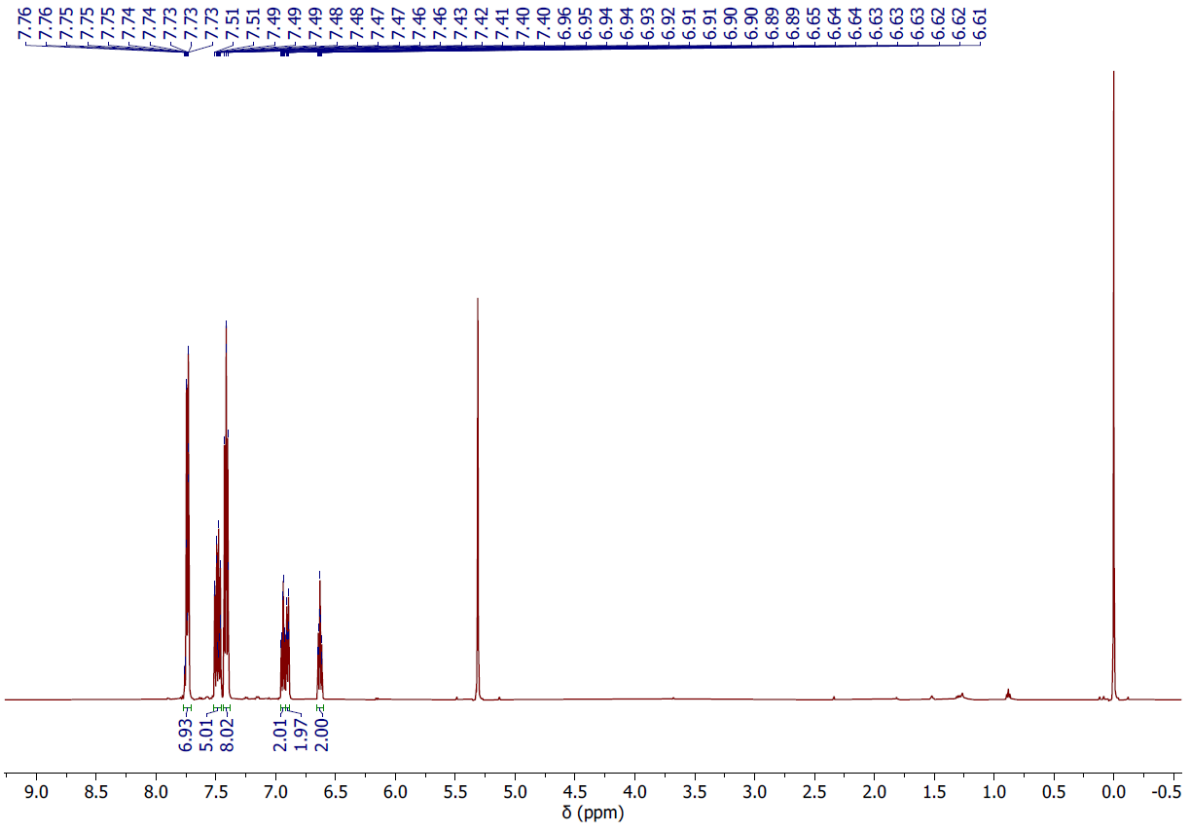

Figure S9. ^{1}H NMR spectrum (300 MHz, CD_2Cl_2) of [Pd(dpp)($SbPh_3$)] (**3c**).

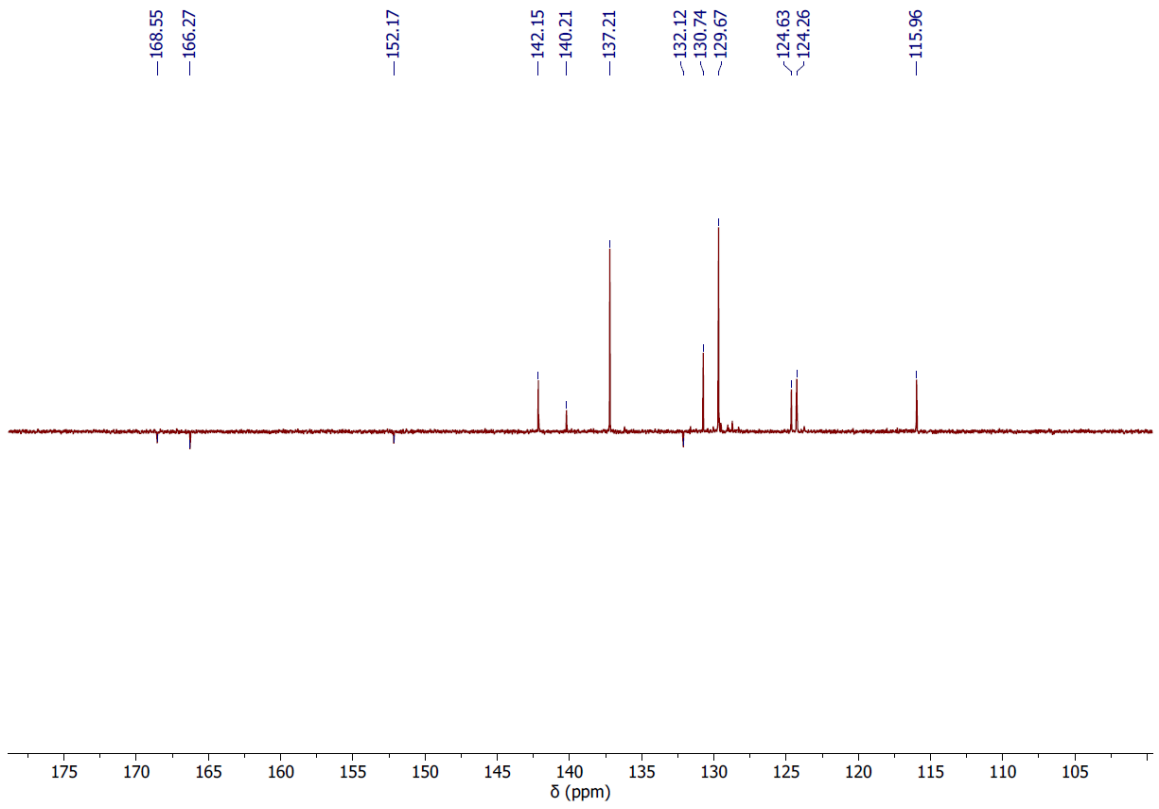

Figure S10. ^{13}C NMR spectrum (126 MHz, CD_2Cl_2) of [Pd(dpp)($SbPh_3$)] (**3c**).

Figure S11. $^{1}H,^{1}H$ COSY spectrum (500 MHz, CD_2Cl_2) of [Pd(dpp)($SbPh_3$)] (**3c**).

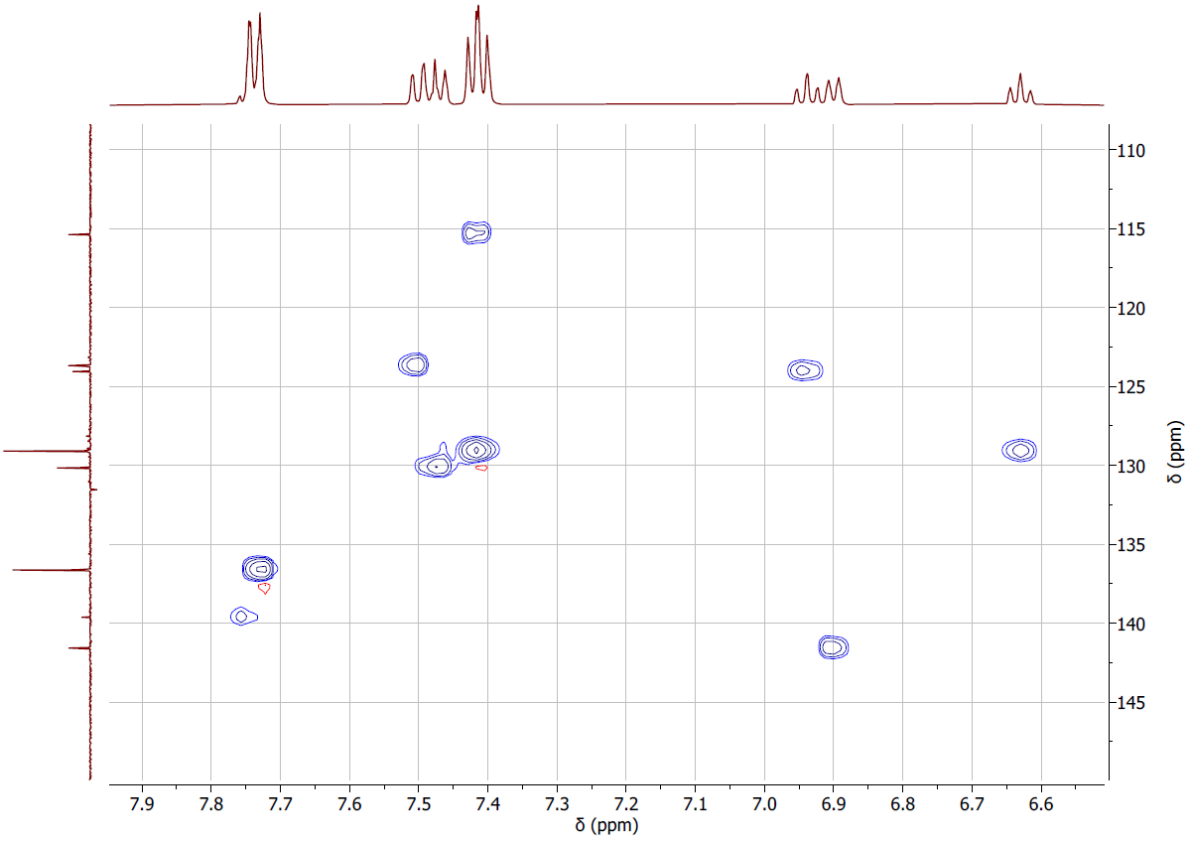

Figure S12. $^{13}C,^{1}H$ HSQC spectrum (500 MHz, CD_2Cl_2) of [Pd(dpp)($SbPh_3$)] (**3c**).

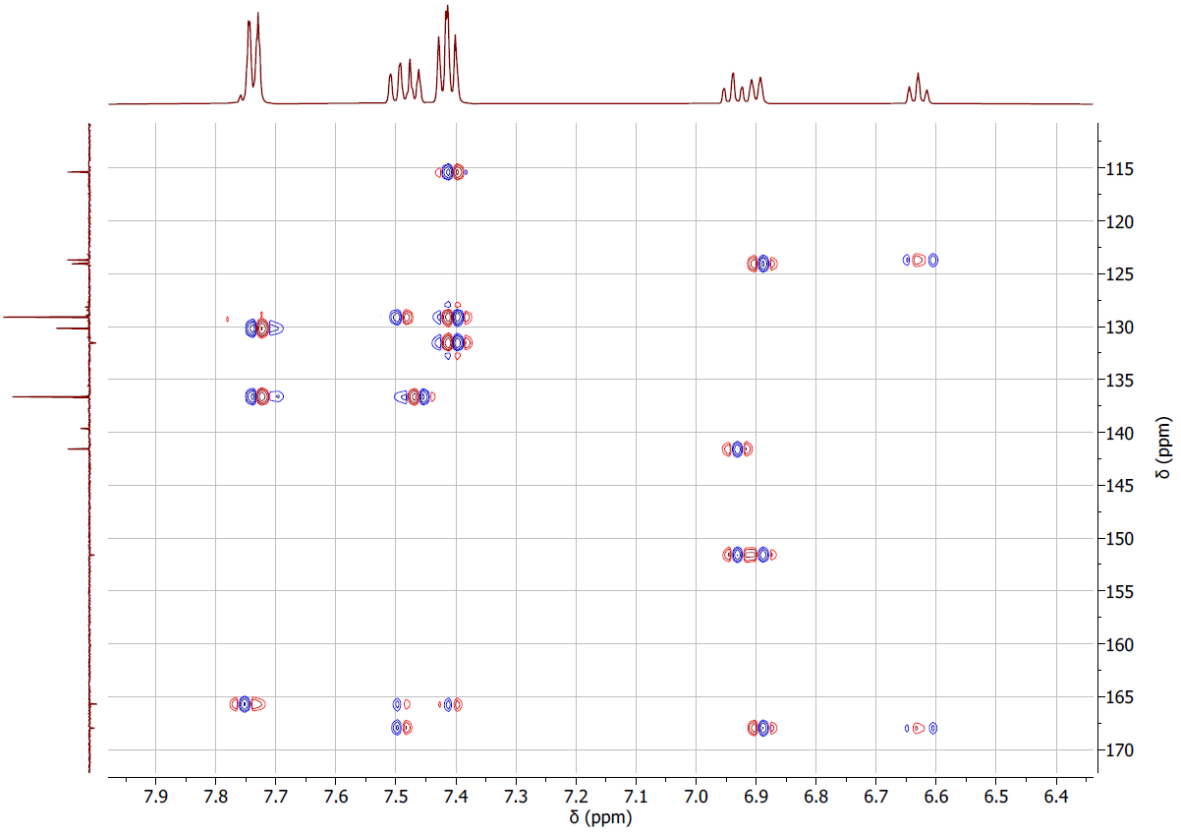

Figure S13. $^{13}C,^{1}H$ HMBC spectrum (500 MHz, CD_2Cl_2) of [Pd(dpp)($SbPh_3$)] (**3c**).

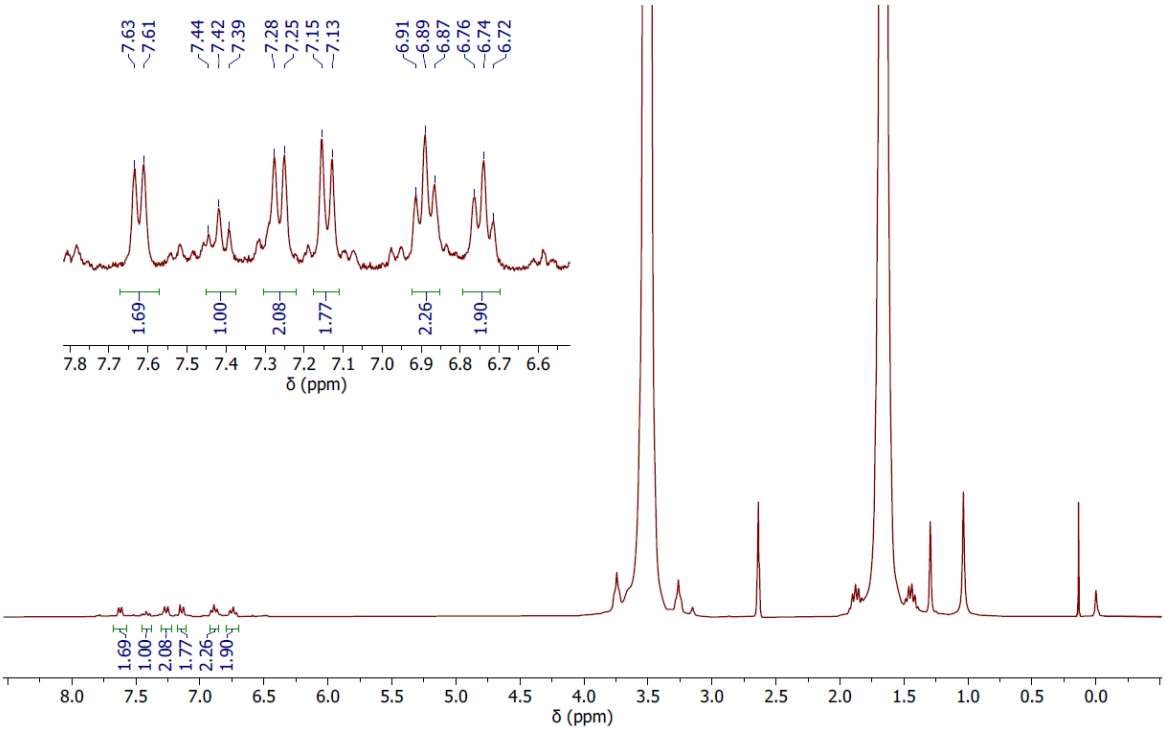

Figure S14. ^{1}H NMR spectrum (300 MHz, THF/DMSO-d_6) of a THF solution in which {[Pd(dppH)(μ-Cl)]}$_2$ (**1**) was reacted with KO*t*Bu (2.2 eq.) for 30 min. A sealed glass ampoule containing DMSO-d_6 was used as an internal standard and for shimming.

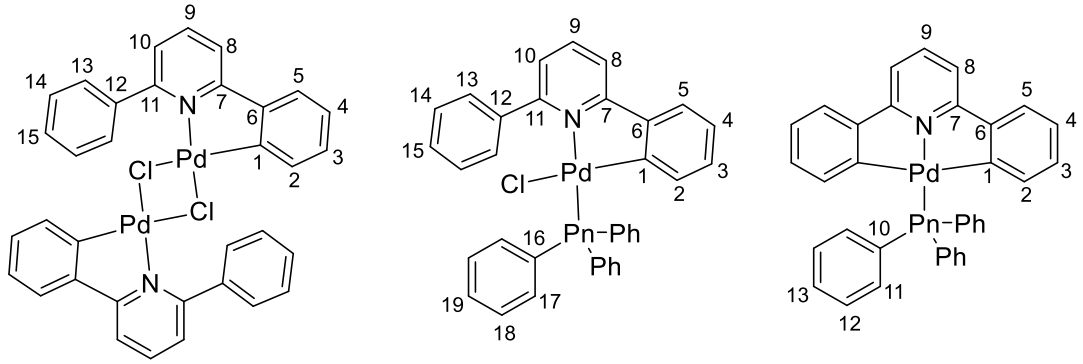

Figure S15. Numbering scheme for NMR assignment of nuclei.

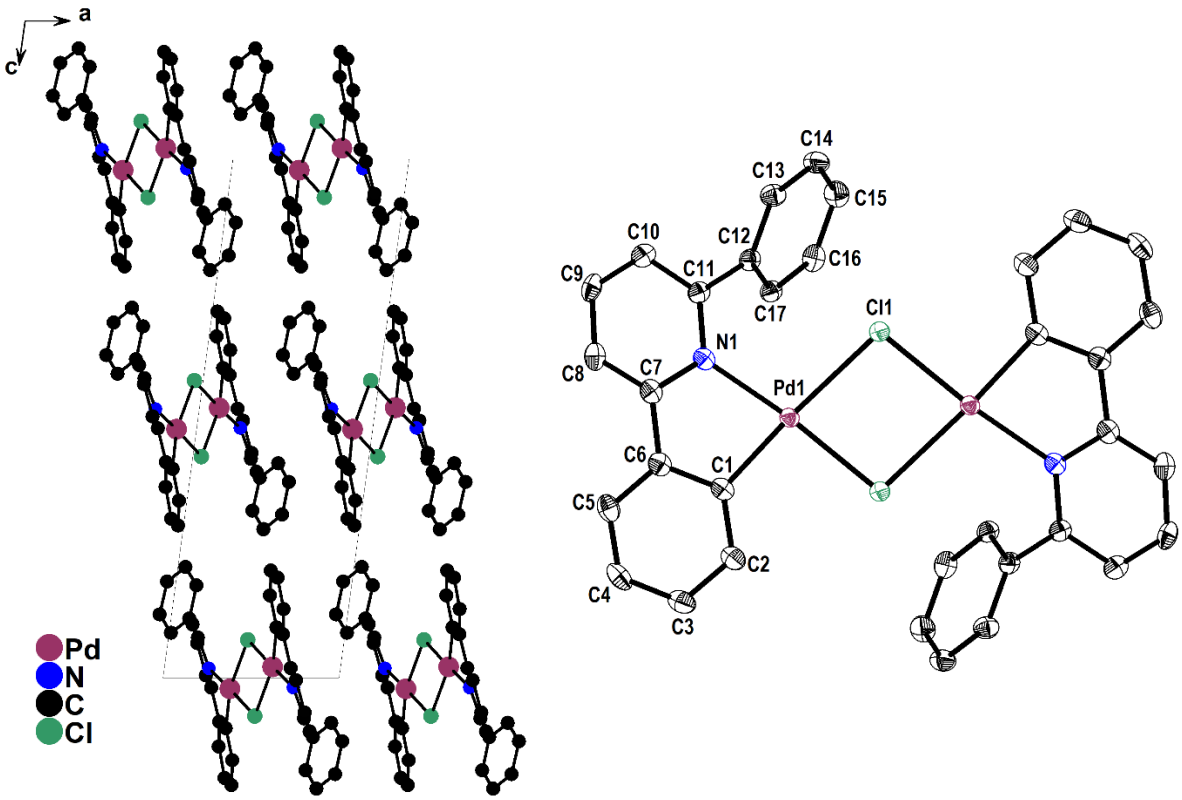

Figure S16. Crystal structure of {[Pd(dppH)(μ-Cl)]}$_2$ (**1**) viewed along the *c* axis (left) and molecular structure of **1** from *sc*-XRD (right). Displacement elipsoids shown at 50% probability level, H atoms omitted for clarity.

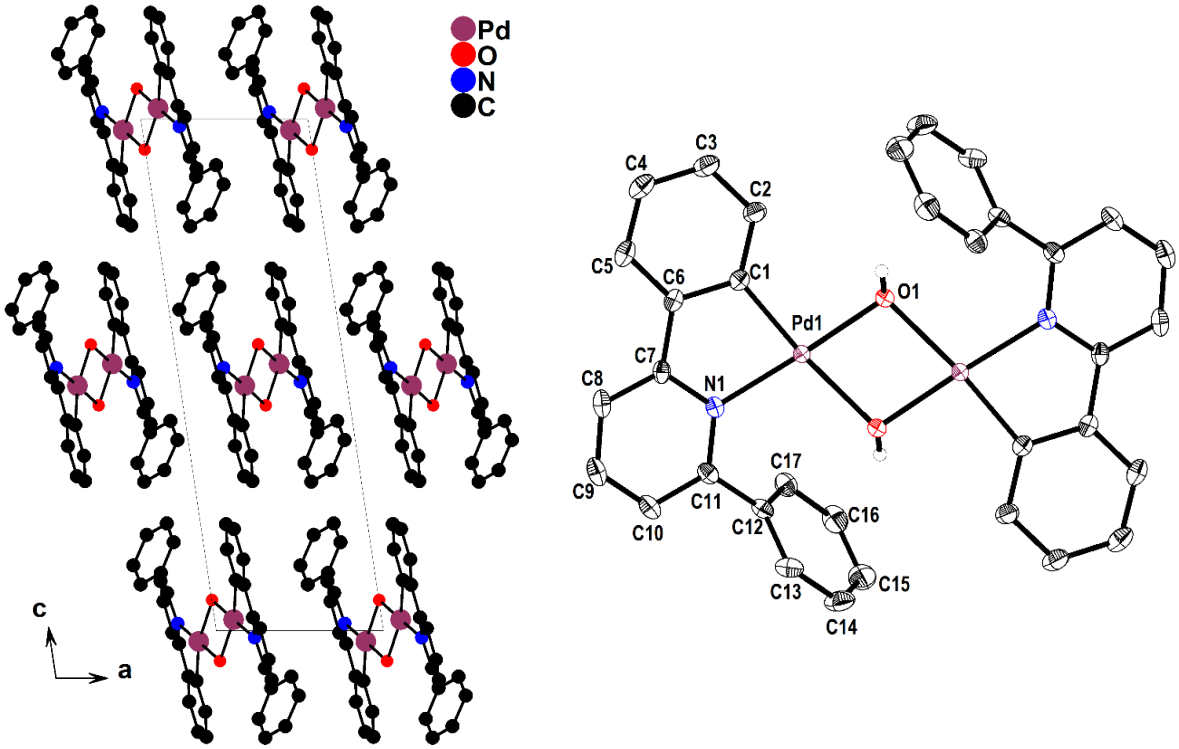

Figure S17. Crystal structure of {[Pd(dppH)((μ-OH)]}$_2$ (**4**) viewed along the *c* axis (left) and molecular structure of **4** from *sc*-XRD (right). Displacement ellipsoids shown at 50% probability level, H atoms except H_{OH} omitted for clarity.

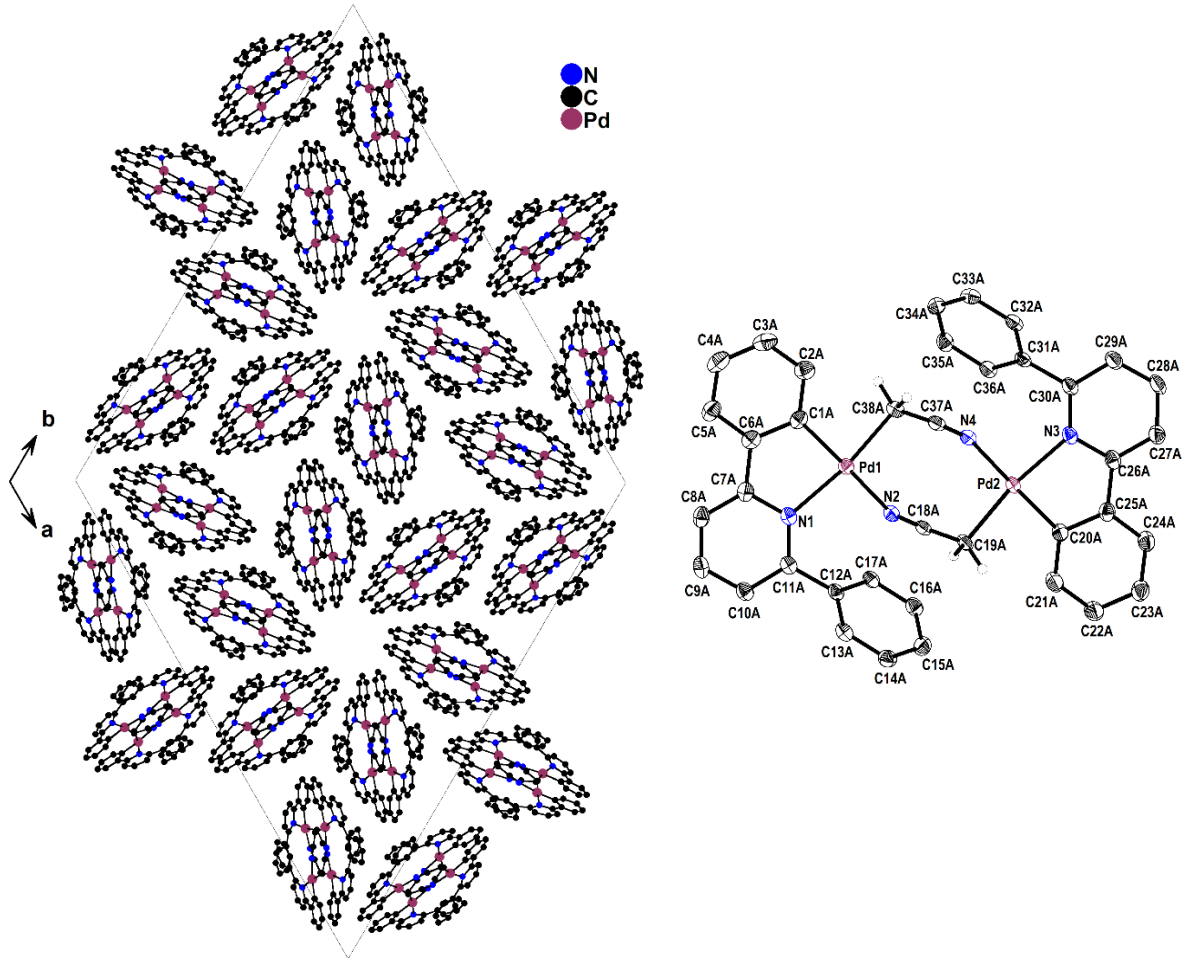

Figure S18. Crystal structure of {[Pd(dppH)(μ-κ$_2$-NCCH$_2$)]}$_2$ (**5**) viewed along the *c* axis (left) and molecular structure of **5** from *sc*-XRD (right). Displacement ellipsoids shown at 40% probability level, H atoms except H$_{CH2}$ omitted for clarity.

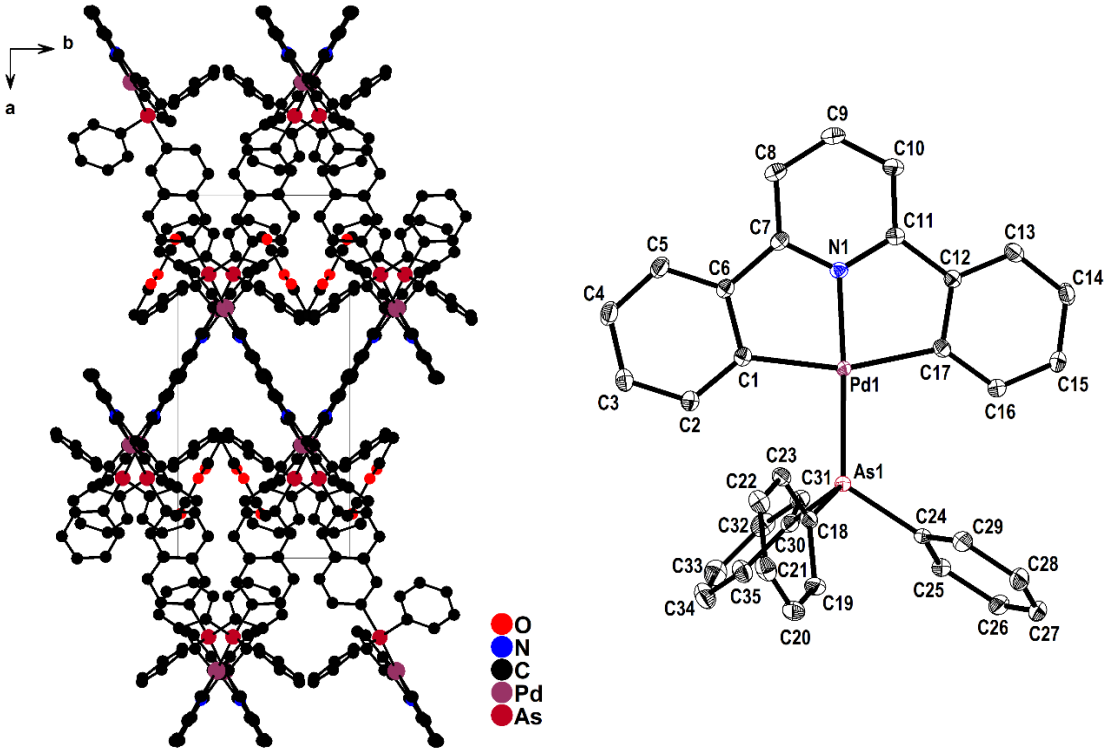

Figure S19. Crystal structure of [Pd(dpp)(AsPh$_3$)] · EtOAc viewed along the *c* axis (left) and molecular structure of [Pd(dpp)(AsPh$_3$)] (**3b**) from *sc*-XRD (right). Displacement ellipsoids shown at 50% probability level, H atoms omitted for clarity.

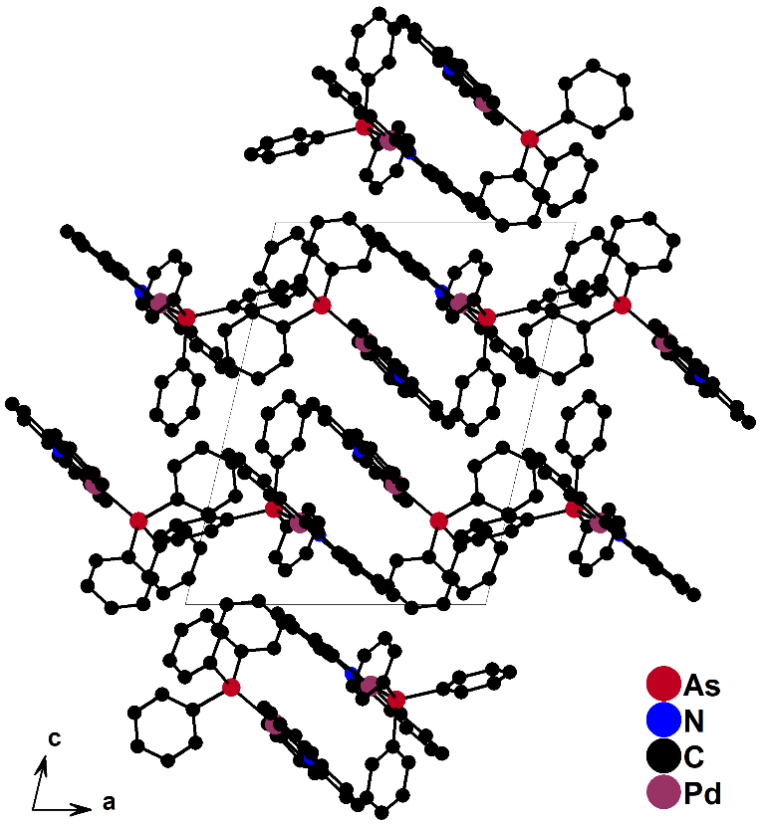

Figure S20. Crystal structure of [Pd(dpp)(AsPh$_3$)] viewed along the *c* axis, H atoms omitted for clarity.

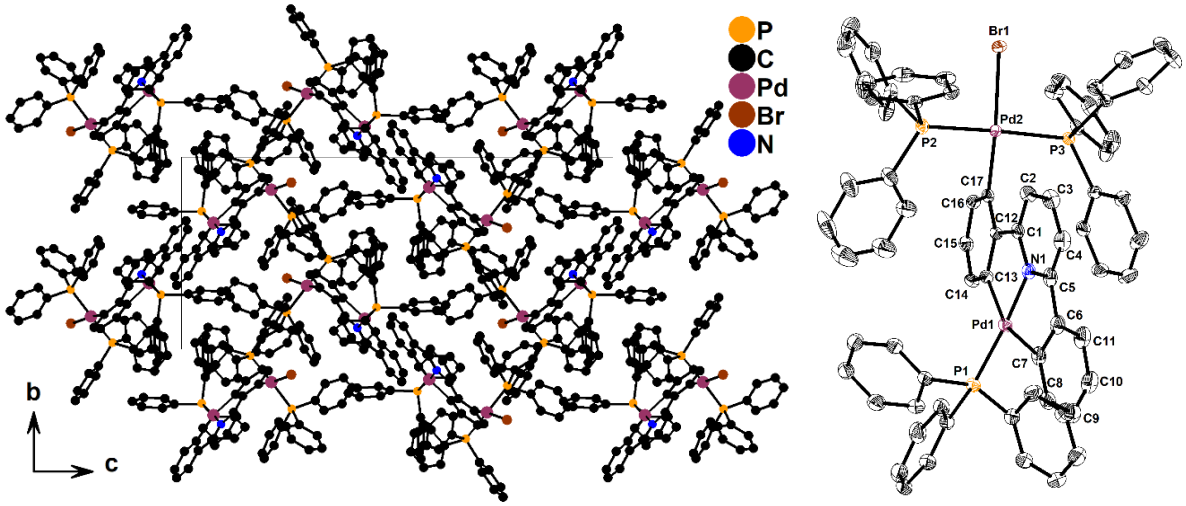

Figure S21. Crystal structure of [(PPh3)Pd(dpp)Pd(PPh3)2Br] (**8**) viewed along the *c* axis (left) and molecular structure of **8** from *sc*-XRD (right). Displacement ellipsoids shown at 50% probability level, H atoms omitted for clarity.

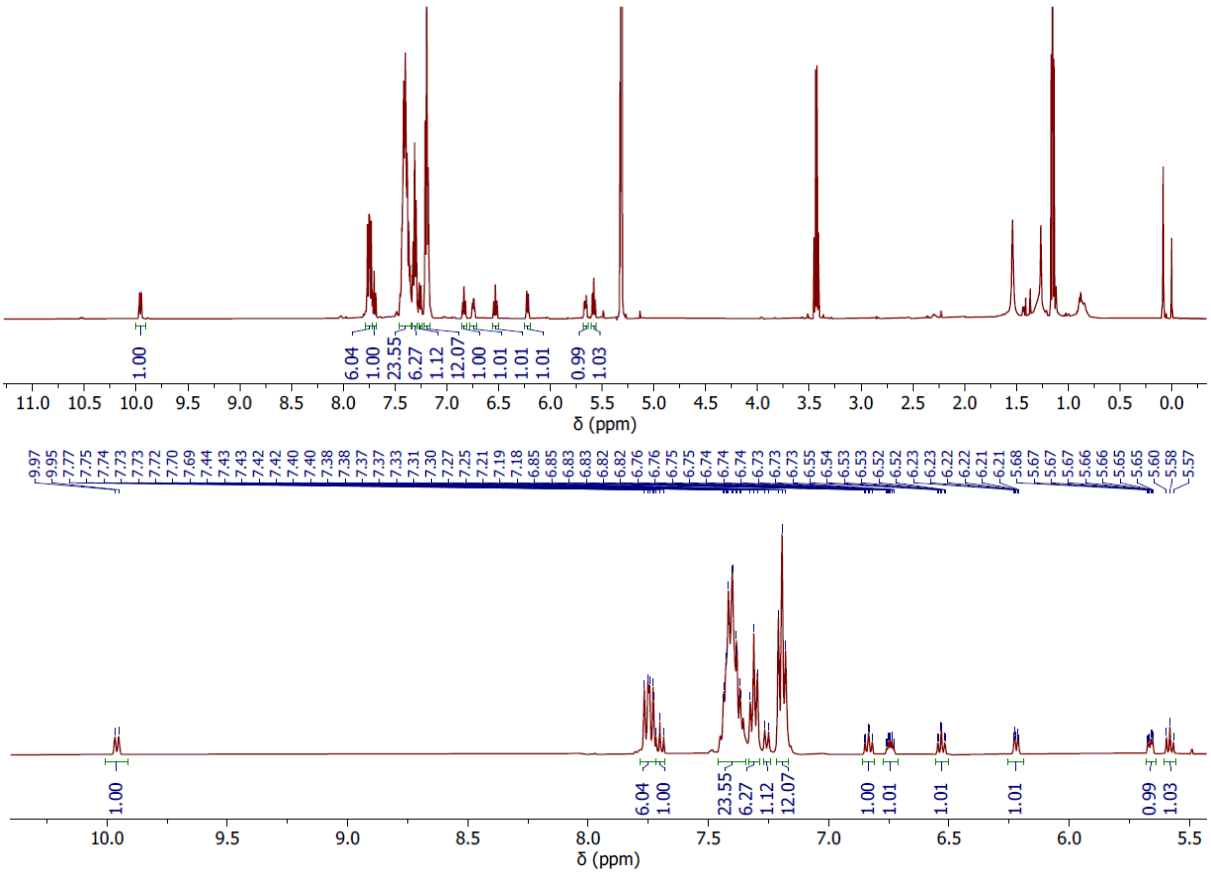

Figure S22. ^{1}H NMR spectrum (500 MHz, CD_2Cl_2) of [(PPh3)Pd(dpp)Pd(PPh3)2Br] (**8**). Top: full spectrum. Bottom: detail of the aromatic range.

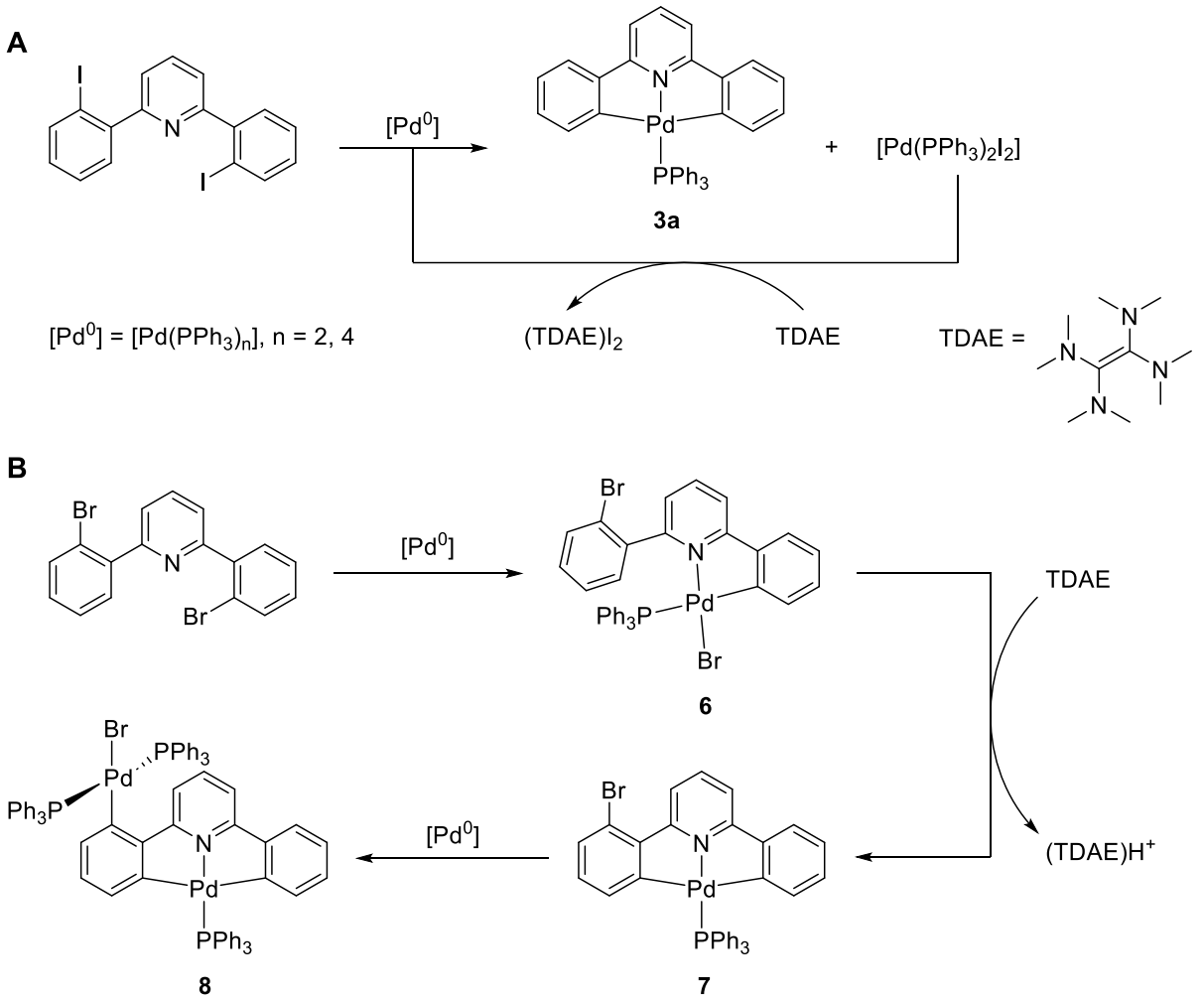

Figure S23. Expected mechanism for the formation of [Pd(dpp)(PPh_3)] (**3a**) from I_2dpp and [Pd(PPh_3)$_4$] adapted from *Feuerstein* and *Breher*[2] (**A**) and hypothesized mechanism for the formation of [(PPh_3)Pd(dpp)Pd(PPh_3)$_2$Br] (**8**) in the presence of Br_2dpp instead of I_2dpp (**B**).

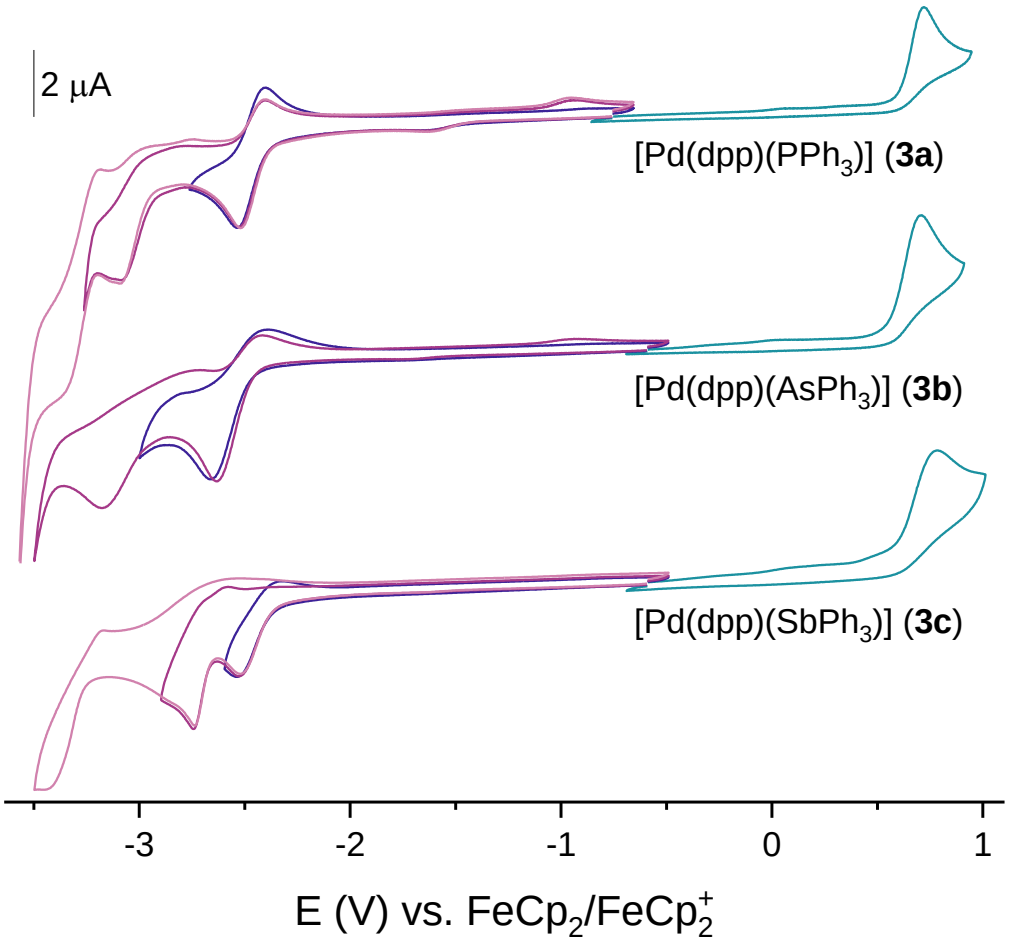

Figure S24. Cyclic voltammograms of [Pd(dpp)(PnPh3)] (**3a-c**, Pn = P, As, Sb) in 0.1 M *n*BuN4PF6/THF solution at 298 K, scan rate 100 mV/s.

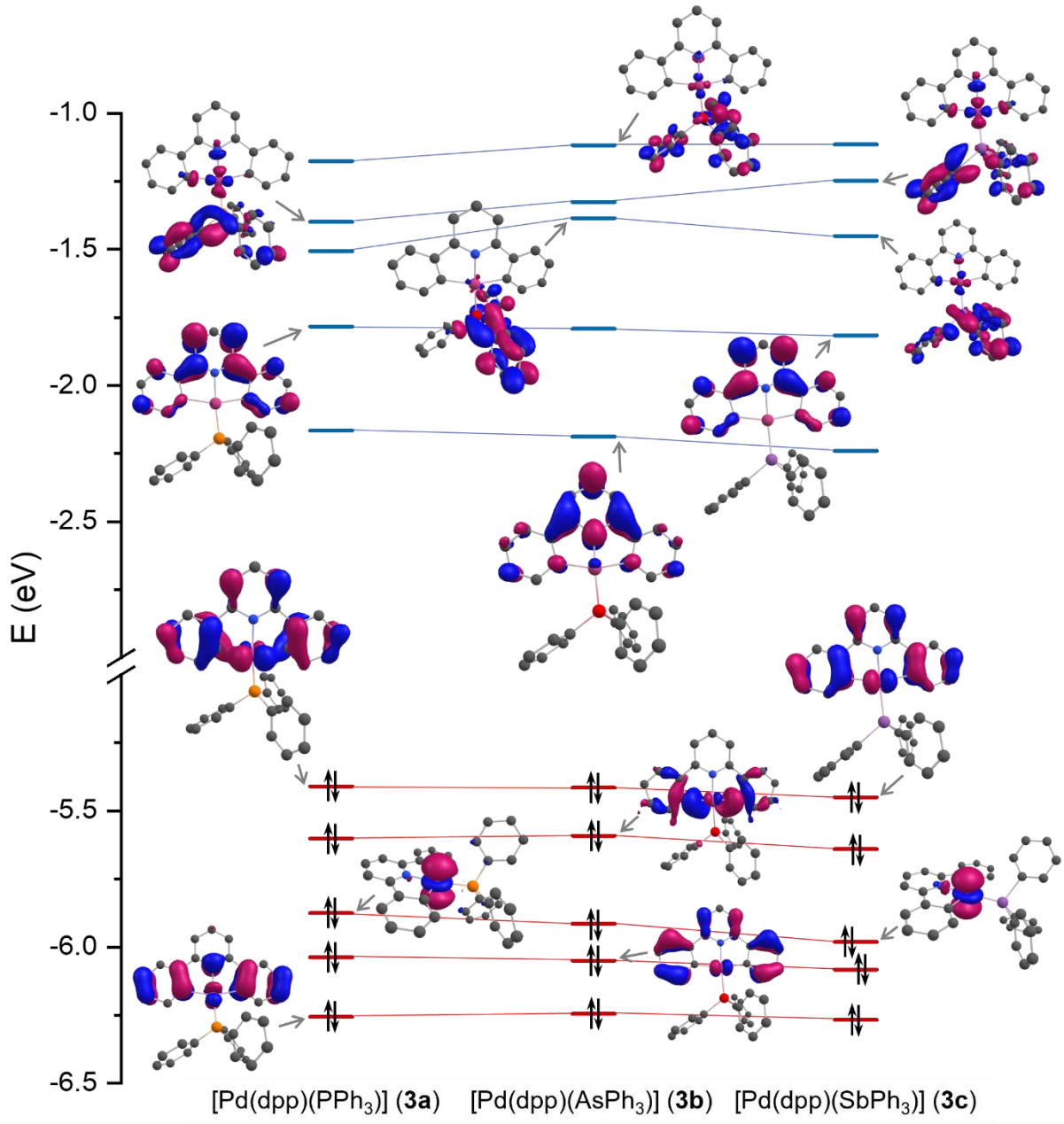

Figure S25. DFT calculated frontier molecular orbital (FMO) scheme for [Pd(dpp)(PnPh$_3$)] (**3a-c**, Pn = P, As, Sb). Lines connect MOs of equivalent character, *i.e.*, the isosurface plots of these orbitals for **3a-c** resemble each other.

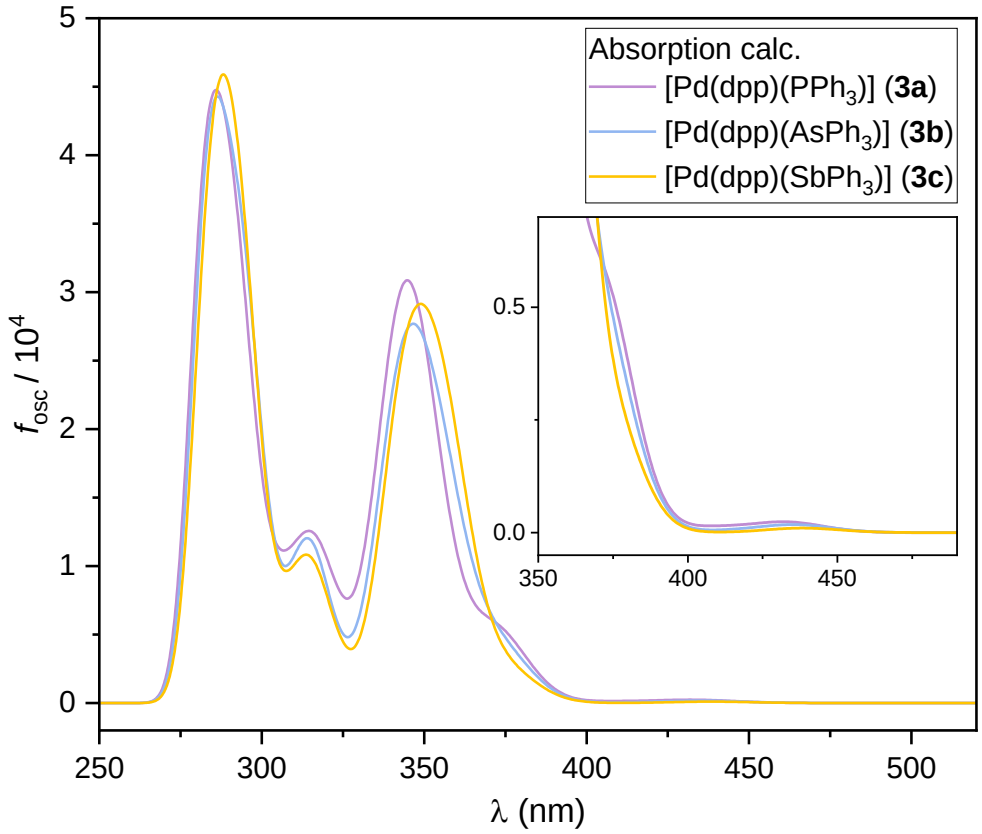

Figure S26. TD-DFT calculated UV-vis absorption spectra for [Pd(dpp)(PnPh$_3$)] (**3a-c**, Pn = P, As, Sb).

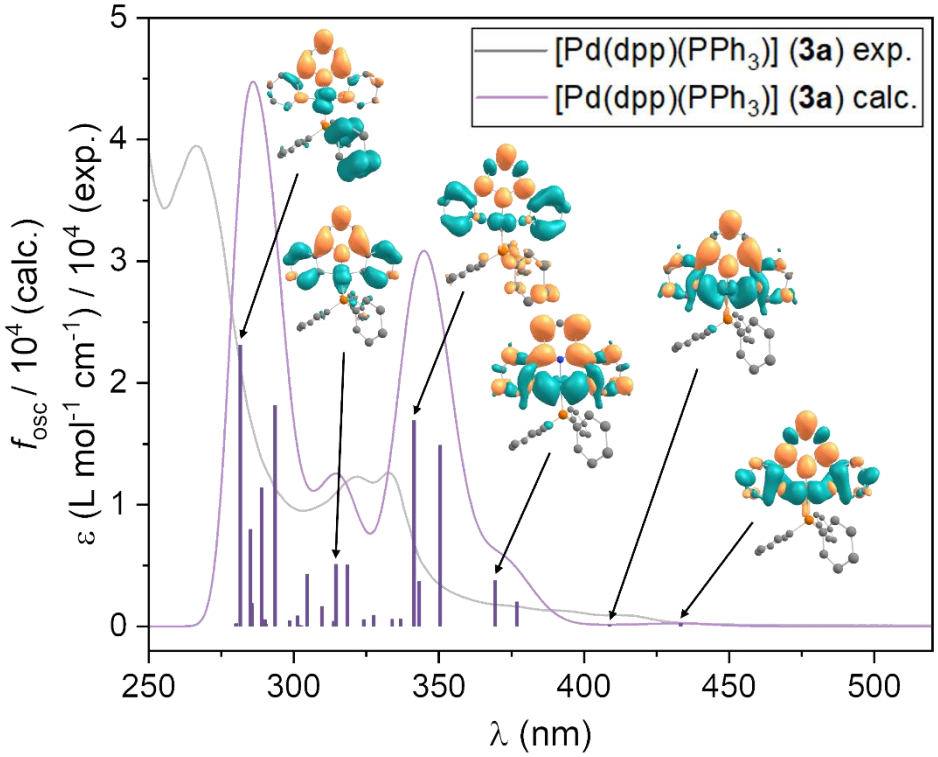

Figure S27. Experimental and TD-DFT calculated UV-vis absorption spectra for [Pd(dpp)(PPh$_3$)] (**3a**) with transition difference densities densities (blue = negative, orange = positive) for selected transitions.

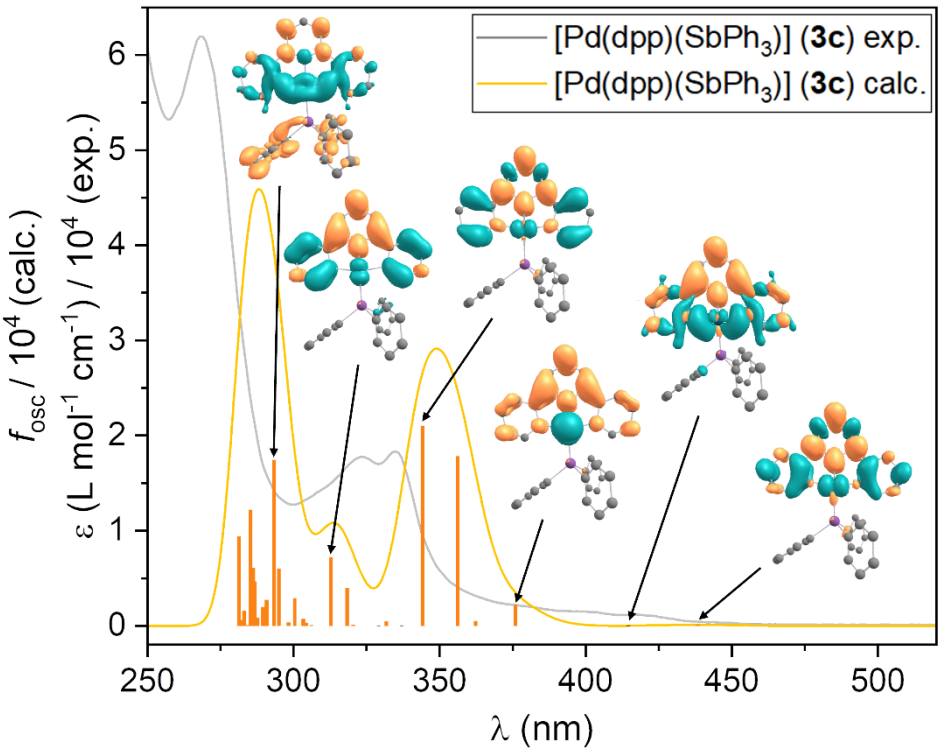

Figure S28. Experimental and TD-DFT calculated UV-vis absorption spectra for [Pd(dpp)(SbPh3)] (**3c**) with transition difference densitiesdensities (blue = negative, orange = positive) for selected transitions.

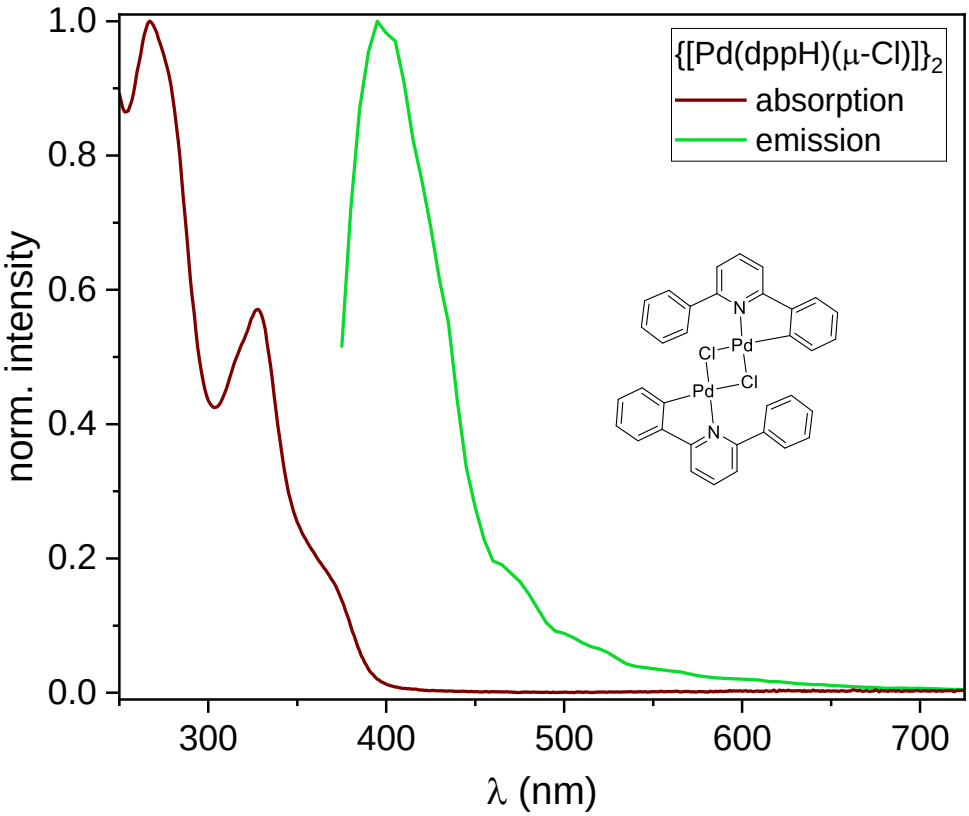

Figure S29. Normalized UV/vis absorption (THF, 298 K) and photoluminescence (77 K, frozen glassy 2-MeTHF matrix, λ_{ex} = 350 nm) spectra of {[Pd(dppH)(μ-Cl)]}2 (**1**).

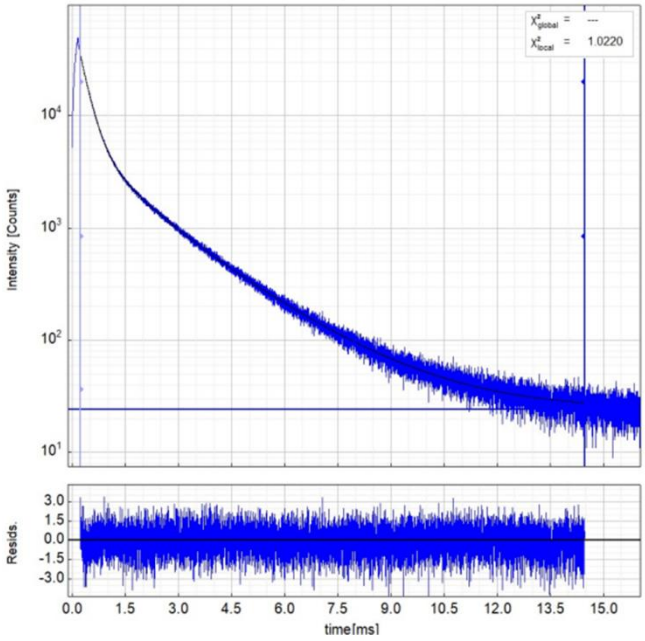

Parameter	Value	Δ	δ
A_1[kCnts/Chnl]	2.59	±0.30	12%
τ_1[ns]	2 149 000	±69 000	3.2%
I_1[kCnts]	5 430	±470	8.6%
A_{Rel1}[%]	7.5	±0.9	11%
I_{Rel1}[%]	33.8	±3.0	8.6%
A_2[kCnts/Chnl]	3.39	±0.17	4.8%
τ_2[ns]	1 038 000	±73 000	7.0%
I_2[kCnts]	3 430	±410	12%
A_{Rel2}[%]	9.8	±0.5	4.9%
I_{Rel2}[%]	21.4	±2.5	12%
A_3[kCnts/Chnl]	28.80	±0.13	0.4%
τ_3[ns]	256 700	±1 500	0.6%
I_3[kCnts]	7 217	±71	1.0%
A_{Rel3}[%]	82.9	±0.5	0.5%
I_{Rel3}[%]	45.0	±0.5	0.9%
$Bkgr_{Dec}$[kCnts]	0.0242	±0.0007	2.7%
τ_{AvInt}[ns]	1 062 100	±4 300	0.4%
τ_{AvAmp}[ns]	473 350	±830	0.2%

Figure S30. Left: Raw (experimental) time-resolved photoluminescence decay of [Pd(dpp)(PPh_3)] (**3a**) in a frozen glassy matrix of 2Me-THF at 77 K, including the residuals (λ_{exc} = 376.7 nm, λ_{em} = 480 nm). Right: Fitting parameters including pre-exponential factors and confidence limits.

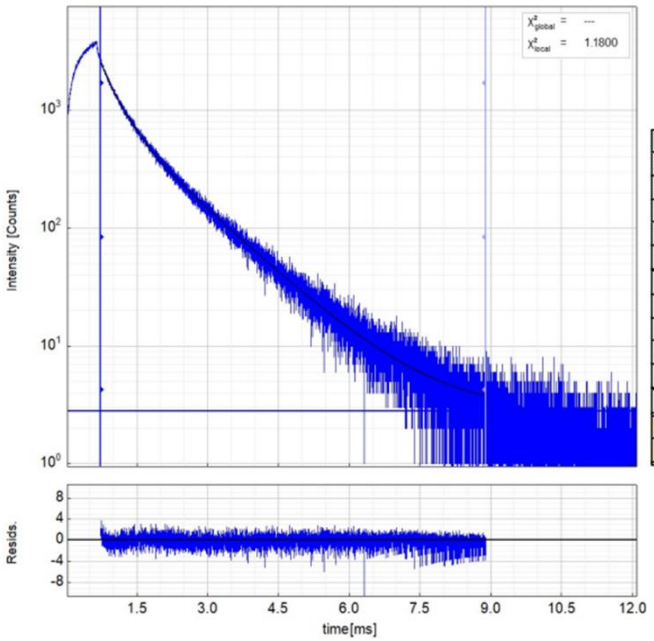

Parameter	Value	Δ	δ
A_1[kCnts/Chnl]	0.951	±0.027	2.8%
τ_1[ns]	1 191 000	±11 000	0.9%
I_1[kCnts]	1 106	±22	1.9%
A_{Rel1}[%]	37.7	±0.9	2.3%
I_{Rel1}[%]	67.4	±0.9	1.3%
A_2[kCnts/Chnl]	1.575	±0.053	3.3%
τ_2[ns]	348 100	±7 200	2.1%
I_2[kCnts]	536	±22	4.0%
A_{Rel2}[%]	62.4	±0.9	1.4%
I_{Rel2}[%]	32.7	±0.9	2.7%
$Bkgr_{Dec}$[kCnts]	0.0028	±0.0002	5.4%
τ_{AvInt}[ns]	915 500	±6 200	0.7%
τ_{AvAmp}[ns]	665 200	±7 500	1.1%

Figure S31. Left: Raw (experimental) time-resolved photoluminescence decay of [Pd(dpp)($AsPh_3$)] (**3b**) in a frozen glassy matrix of 2Me-THF at 77 K, including the residuals (λ_{exc} = 376.7 nm, λ_{em} = 480 nm). Right: Fitting parameters including pre-exponential factors and confidence limits.

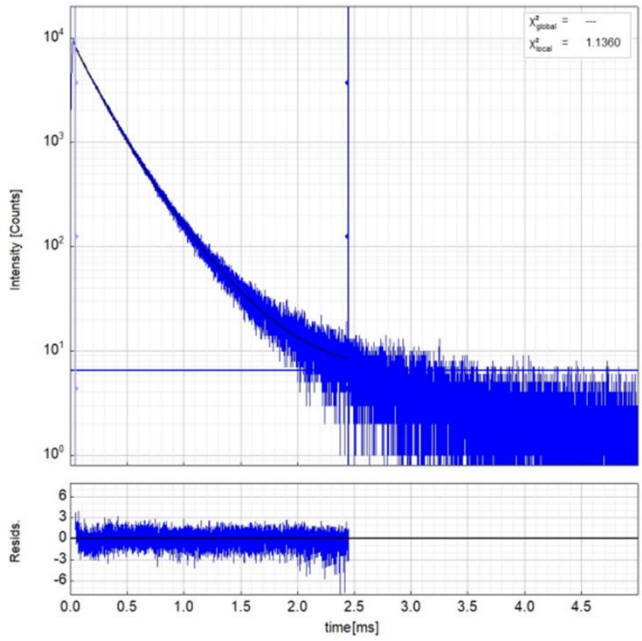

Parameter	Value	Δ	δ
A_1[kCnts/Chnl]	1.75	±0.21	12%
τ_1[ns]	353 000	±11 000	3.1%
I_1[kCnts]	2 400	±220	8.8%
A_{Rel1}[%]	21.9	±2.6	12%
I_{Rel1}[%]	34.6	±3.1	8.8%
A_2[kCnts/Chnl]	6.23	±0.20	3.1%
τ_2[ns]	187 000	±3 100	1.6%
I_2[kCnts]	4 550	±220	4.7%
A_{Rel2}[%]	78.2	±2.6	3.2%
I_{Rel2}[%]	65.5	±3.1	4.6%
$Bkgr_{Dec}$[kCnts]	0.0066	±0.0004	5.9%
τ_{AvInt}[ns]	244 220	±640	0.3%
τ_{AvAmp}[ns]	223 200	±510	0.2%

Figure S32. Left: Raw (experimental) time-resolved photoluminescence decay of [Pd(dpp)($SbPh_3$)] (**3c**) in a frozen glassy matrix of 2Me-THF at 77 K, including the residuals (λ_{exc} = 376.7 nm, λ_{em} = 480 nm). Right: Fitting parameters including pre-exponential factors and confidence limits.

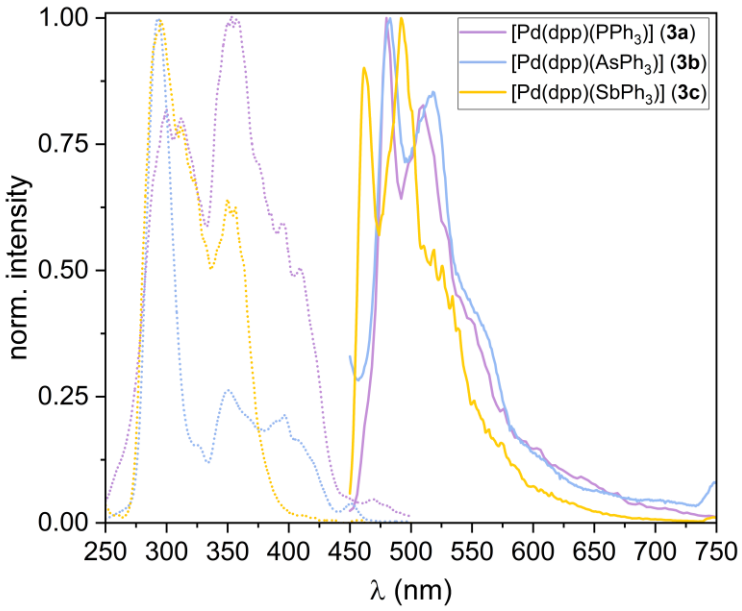

Figure S33. Photoluminescence emission (continuous lines) and excitation (dotted lines) spectra of the complexes [Pd(dpp)($PnPh_3$)] (**3a-c**, Pn = P, As, Sb) at 77 K in a glassy matrix of frozen 2-MeTHF (λ_{ex} = 350 nm, λ_{obs} = 525 nm).

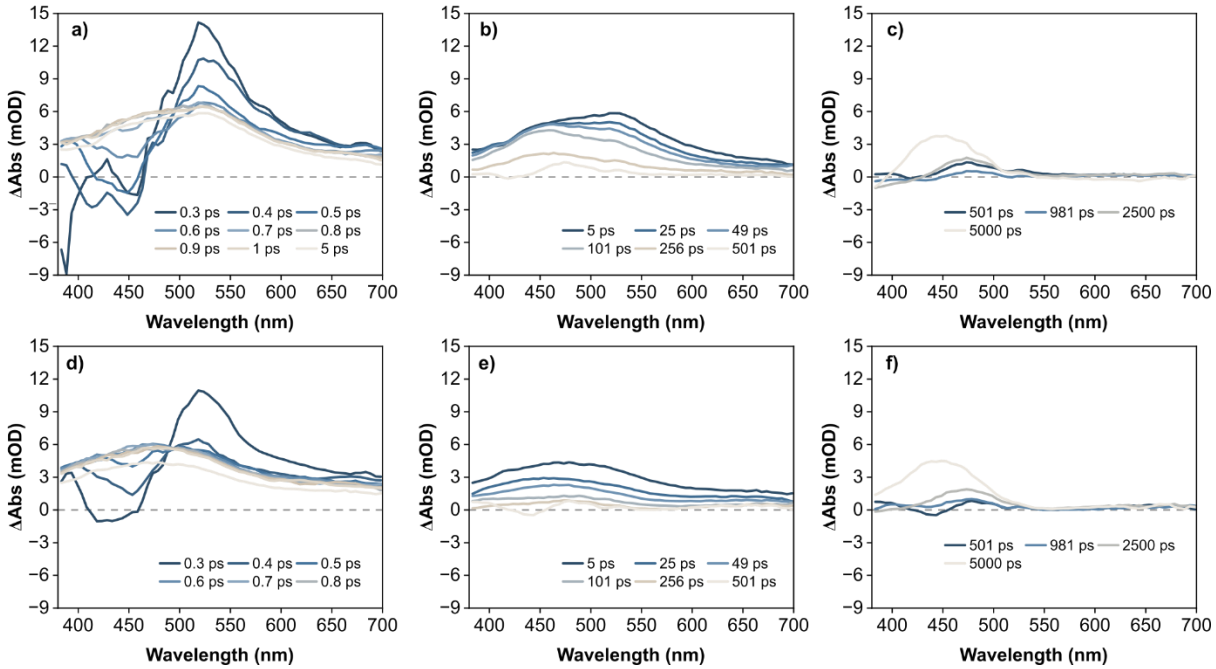

Figure S34. Transient absorption spectra of [Pd(dpp)(PPh_3)] (**3a**, a)-c)) and [Pd(dpp)($SbPh_3$)] (**3c**, d)-f)) measured in dry THF following excitation at 350 nm. Excitation powers were set to 450 µW. Due to the complex kinetics, the spectra are divided into three different panels: a) and d) show the fast kinetics in the region 0.3 – 5 ps, b) and e) the intermediate kinetics in the range 5 – 500 ps and c) and f) the slower one in the range 500 – 5000 ps.

Supporting Tables

Table S1 Selected structure solution and refinement data for crystal structures of {[Pd(dppH)(μ-Cl)]}$_2$ (**1**), {[Pd(dppH)(μ-OH)]}$_2$ (**4**) and Pd(dppH)(μ-κ^2-NCCH$_2$)]}$_2$ (**5**).

compound	{[Pd(dppH)(μ-Cl)]}$_2$ (**1**)	{[Pd(dppH)(μ-OH)]}$_2$ (**4**)	{[Pd(dppH)(μ-κ^2-NCCH$_2$)]}$_2$ (**5**) [a]
empirical formula	$C_{35}H_{24}Cl_2N_2Pd_2$	$C_{17}H_{13}NOPd$	$C_{38}H_{28}N_4Pd_2$
formula weight (g/mol)	744.25	353.68	753.44
temperature (K)	100(2)	100(2)	100(2)
wavelength	Cu K_α	Mo K_α	Cu K_α
crystal system	monoclinic	monoclinic	trigonal
space group (no.)	$P2/c$ (13)	$P2_1/n$ (14)	$R\bar{3}$ (148)
cell parameters			
a (Å)	7.2613(4)	6.9929(4)	53.8129(11)
b (Å)	8.7928(4)	8.9621(5)	53.8129(11)
c (Å)	21.550(1)	21.6159(13)	11.5225(3)
α (°)	90.0	90.0	90.0
β (°)	97.658(2)	98.379(2)	90.0
γ (°)	90.0	90.0	120.0
V (Å^3)	1363.63(12)	1340.2(1)	28896.8(14)
Z	2	4	36
μ (mm^{-1})	12.66	1.38	9.29
crystal size (mm^3)	0.05 × 0.05 × 0.02	0.11 × 0.06 × 0.04	0.03 × 0.02 × 0.02
crystal habitus	yellow block	yellow block	yellow prism
F(000)	736	704	13536
2θ range (°)	4.1 – 72.2	2.5 – 35.2	2.8 – 72.2
index ranges			
$h_{min/max}$	–8 / 8	–12 / 12	–66 / 66
$k_{min/max}$	–10 / 10	–15 / 15	–66 / 66
$l_{min/max}$	–26 / 26	–37 / 37	–14 / 13
reflections			
total	33486	162960	176821
independent	2658	7584	12672
completeness (%)	99.9	99.9	99.9
data / restraints / parameters	2658 / 0 / 181	7584 / 0 / 185	12672 / 0 / 793
GooF on F^2	1.09	1.18	1.03
final R values			
R_1 (I≥2σ(I) / all data)	0.027 / 0.028	0.034 / 0.040	0.030 / 0.038
wR_2	0.065	0.070	0.074
R_{int}	0.056	0.075	0.104
R_σ	0.023	0.025	0.038
largest peak / hole (e/Å^3)	0.40 / –0.81	0.84 / – 1.02	0.52 / –0.89
CCDC	2381835	2309500	2364152

[a] Disordered co-crystallized solvent treated with Platon SQUEEZE.[1]

Table S2 Selected refinement and structure solution data for [Pd(dpp)($AsPh_3$)] (**3b**), [Pd(dpp)($AsPh_3$)] (**3b**) · EtOAc and [Pd_2(dpp)(PPh_3)$_3$Br] (**8**).

compound	[Pd(dpp)($AsPh_3$)] (**3b**)	[Pd(dpp)($AsPh_3$)] (**3b**) · EtOAc	[Pd_2(dpp)(PPh_3)$_3$Br] (**8**)
empirical formula	$C_{35}H_{25}AsNPd$	$C_{39}H_{34}AsNO_2Pd$	$C_{71}H_{55}BrNP_3Pd_2$
formula weight (g/mol)	640.88	729.99	1307.78
temperature (K)	100(2)	100(2)	100(2)
wavelength	Mo K_α	Mo K_α	Cu K_α
crystal system	triclinic	monoclinic	monoclinic
space group (no.)	$P\bar{1}$ (2)	$P2_1/c$ (14)	$P2_1/n$ (14)
cell parameters			
a (Å)	12.2339(11)	19.2314(13)	15.847(4)
b (Å)	13.8746(12)	8.3678(6)	12.791(5)
c (Å)	17.0042(14)	21.5805(14)	28.910(6)
α (°)	70.244(3)	90.0	90.0
β (°)	77.005(3)	113.444(2)	96.38(3)
γ (°)	88.569(4)	90.0	90.0
V (Å^3)	2642.7(4)	3186.1(4)	5824(3)
Z	4	4	4
μ (mm^{-1})	1.97	1.65	6.90
crystal size (mm^3)		0.13 × 0.09 × 0.05	0.15 × 0.03 × 0.02
crystal habitus	yellow prism	yellow prism	yellow prism
F(000)	1284	1480	2640
2θ range (°)	2.2 – 28.3	2.7 – 30.5	3.1 – 72.2
index ranges			
$h_{min/max}$	–15 / 15	–27 / 27	–19 / 19
$k_{min/max}$	–18 / 18	–11 / 11	–13 / 15
$l_{min/max}$	–22 / 22	–30 / 30	–35 / 35
reflections			
total	185502	75953	283904
independent	12103	9699	11472
completeness (%)	99.9	99.9	99.9
data / restraints / parameters	12103 / 0 / 685	9699 / 0 / 409	11472 / 0 / 703
GooF on F^2	1.15	1.09	1.05
final R values			
R_1 (I≥2σ(I) / all data)	0.063 / 0.073	0.029 / 0.033	0.027 / 0.027
wR_2	0.169	0.069	0.076
R_{int}	0.089	0.046	0.051
R_σ	0.033	0.027	0.015
largest peak / hole (e/Å^3)	4.66 / –1.20	1.08 / –0.70	0.98 / –1.47
CCDC	-	2331260	2201141

Table S3 Selected structural data for [Pd(dpp)(PnPh$_3$)] (**3a-c**, Pn = P, As, Sb) from scXRD and energy minimization by DFT calculations.[a]

	[Pd(dpp)(PPh$_3$)] (**3a**)		[Pd(dpp)(AsPh$_3$)] (**3b**)		[Pd(dpp)(SbPh$_3$)] (**3c**)
	scXRD [b]	DFT	scXRD [c]	DFT	DFT
distances (Å)					
Pd–N1	2.011(1)	2.027	2.001(2)	2.012	2.010
Pd–C1	2.079(1)	2.089	2.080(2)	2.083	2.079
Pd–C17	2.079(1)	2.087	2.079(2)	2.077	2.071
Pd–Pn	2.225(1)	2.239	2.346(1)	2.349	2.499
N1–C7	1.348(2)	1.355	1.352(2)	1.356	1.355
N1–C11	1.349(2)	1.355	1.352(3)	1.356	1.356
C1–C6	1.424(2)	1.431	1.426(3)	1.432	1.433
C17–C12	1.426(2)	1.433	1.428(3)	1.433	1.433
C6–C7	1.477(2)	1.469	1.472(3)	1.469	1.470
C12–C11	1.474(2)	1.469	1.468(2)	1.469	1.470
angles (°)					
C1–Pd–C17	160.7(1)	160.3	160.9(1)	161.3	161.9
Pn–Pd–N1	175.6(1)	174.0	176.4(1)	175.2	177.4
N1–Pd–C1	80.7(1)	80.3	80.7(1)	80.7	81.0
N1–Pd–C17	80.6(1)	80.2	80.6(1)	80.6	80.9
C1–Pd–Pn	97.1(1)	95.4	95.8(1)	95.6	96.5
C17–Pd–Pn	101.9(1)	104.2	102.9(1)	103.2	101.6
C–Pn–C averaged	104.3	103.8	101.8	102.5	100.9
C–Pn–Pd averaged	114.4	114.8	116.4	115.8	117.1
Sum of ∧ around Pd	360.3	360.1	360.0	360.1	360.0
dihedral angles (°)					
C1–Pd–Pn–C18	46.8(1)	58.2	60.2(1)	56.5	58.5
C17–Pd–Pn–C18	136.6(1)	119.9	123.5(1)	122.3	121.4
N1–C7–C6–C1	9.9(2)	2.7	5.0(2)	1.8	0.3
N1–C11–C12–C17	3.1(2)	2.0	4.7(2)	1.5	0.5

[a] Using BP86/def2-TZVP/CPCM(THF). [b] From ref.[3] [c] From scXRD of [Pd(dpp)(AsPh$_3$)] · EtOAc.

References

(1) Spek, A. L. PLATON SQUEEZE: a tool for the calculation of the disordered solvent contribution to the calculated structure factors, *Acta Cryst. C – Struct. Chem.* **2015**, *C71*, 9–18. https://doi.org/10.1107/S2053229614024929

(2) Feuerstein, W.; Breher, F. Synthetic access to a phosphorescent non-palindromic pincer complex of palladium by a double oxidative addition – comproportionation sequence. *Chem. Commun.* **2020**, *56*, 12589. https://doi.org/10.1039/D0CC04065G

(3) Campillo, D.; Escudero, D.; Baya, M.; Martín, A. Heteropolymetallic Architectures as Snapshots of Transmetallation Processes at Different Degrees of Transfer. *Chem.–Eur. J.* **2022**, *28*, e202104538. https://doi.org/10.1002/chem.202104538

6.3 Experimental details for the work towards [Ni(C^N^C)(PPh$_3$)]

General conditions

All reactions were performed under inert conditions using Ar inert gas and standard *Schlenk* techniques. *p*-Xylene was dried by distillation over Na prior to use. THF was deoxygenated in three freeze-pump-thaw cycles and stored over activated molecular sieves. Solid reagents were dried *in vacuo* prior to use. 2,6-Diphenylpyridine (H_2dpp) was synthesized under typical *Suzuki* or *Kröhnke* conditions. 2-(2'-Chlorophenyl)-6-phenylpyridine (HdppCl) and [Ni(cod)$_2$] (cod = 1,5-cyclooctadiene) were prepared following published procedures.[114,115]

Attempted synthesis of {[Ni(Hdpp)(μ-Br)]}$_2$

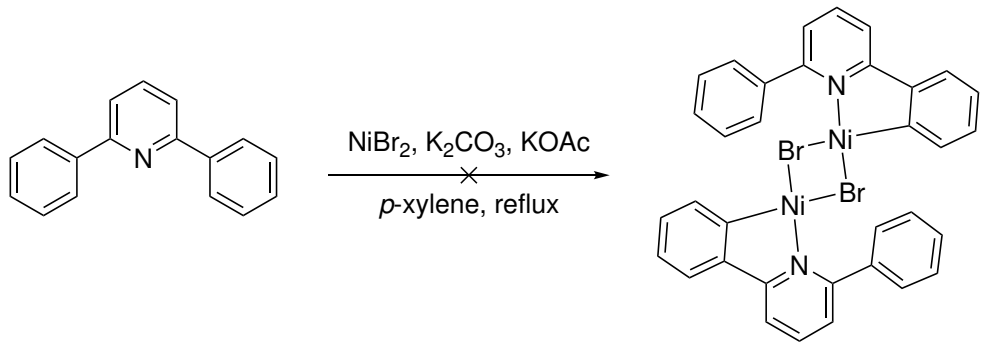

The experiment was performed in collaboration with Dr. Lukas Kletsch. A *Dean-Stark* apparatus was charged with 232 mg (1.0 mmol, 1.1 eq.) H_2dpp and 200 mg (0.9 mmol, 1.0 eq.) $NiBr_2$, 200 mg (2.0 mmol, 2.2 eq) KOAc and 250 mg (2.0 mmol, 2.2 eq.) K_2CO_3. The water trap of the apparatus was filled with activated molecular sieves. 200 mL *p*-xylene were added to the reactants and the mixture was heated to reflux vigorously. Within 72 h, no conversion of the starting materials was observed, and H_2dpp was reisolated quantitatively.

Attempted synthesis of [Ni(Hdpp)(PPh$_3$)Br]

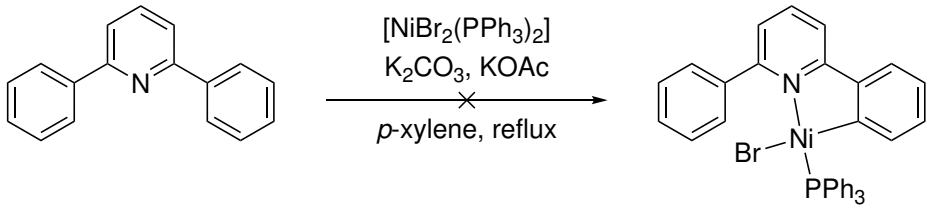

The experiment was performed in collaboration with Dr. Lukas Kletsch. A *Dean-Stark* apparatus was charged with 300 mg (1.3 mmol, 1.3 eq.) H_2dpp and 743 mg (1.0 mmol, 1.0 eq.) [$NiBr_2(PPh_3)_2$, 250 mg (2.5 mmol, 2.5 eq) KOAc and 350 mg (2.5 mmol, 2.5 eq.) K_2CO_3. The water trap of the apparatus was filled with activated molecular sieves. 200 mL *p*-xylene were added to the reactants and the mixture was heated to reflux vigorously. Again, no conversion of the starting materials was observed within 72 h and H_2dpp was reisolated.

Attempted synthesis of [Ni(Hdpp)(PPh_3)Cl]

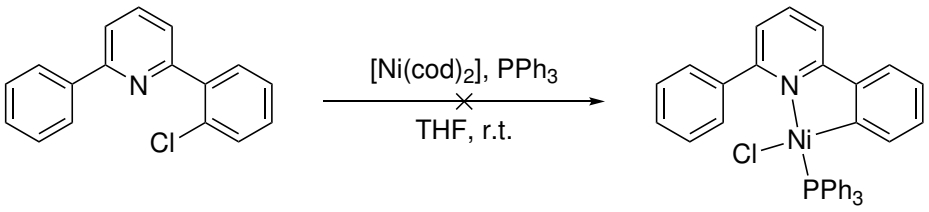

55 mg (0.20 mmol, 1.00 eq.) [Ni(cod)$_2$] were suspended in THF. A solution of 56 mg (0.21 mmol, 1.05 eq.) 2-(2'-chlorophenyl)-6-phenylpyridine and 55 mg (0.21 mmol, 1.05 eq.) PPh_3 in THF was added, resulting in a dark red discoloration. After 30 minutes, the solution was filtered through a syringe filter, and the solvent was removed from the filtrate. The residue was washed twice with *n*-pentane and dried *in vacuo*, affording 51 mg of a raspberry-colored powder. NMR spectroscopy in CD_2Cl_2 showed a paramagnetic sample, as indicated by very broad, poorly resolved signals.

Attempted synthesis of [Ni(dpp)(PPh_3)]

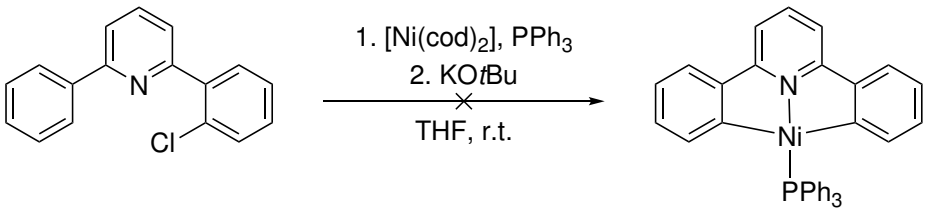

79 mg (0.29 mmol, 1.00 eq.) [Ni(cod)$_2$] were suspended in THF. A solution of 80 mg (0.30 mmol, 1.05 eq.) HdppCl and 80 mg (0.21 mmol, 1.05 eq.) PPh_3 in THF was added, resulting in a dark red discoloration. After 45 minutes, 0.29 mL of a 0.9 M KO*t*Bu/THF solution (0.32 mmol, 1.10 eq.) were added. No significant color change was observed. After 3 h, an aliquot of the reaction solution was analyzed by NMR spectroscopy using a DMSO-d_6 ampoule as internal standard. The results again indicated paramagnetism for the sample solution, and the target compound was not detected.

6.4 Supporting Information for Publication 3

Reprinted with permission from Ref.[67]. Copyright © 2024, American Chemical Society.

Supporting Information
for

Assessing the character of the C_6F_5 ligand from the electrochemical and photophysical properties of $[Ni(C_6F_5)_2(N^N)]$ complexes

Rose Jordan*[‖], Sascha A. Schäfer[‖], Noah Sander[‖], Ivan Maisuls[†], Claudia Hamacher[‖], Joshua Friedel[‖], Cristian A. Strassert*[†] and Axel Klein*[‖]

[‖] University of Cologne, Faculty for Mathematics and Natural Sciences, Department of Chemistry and Biochemistry, Institute for Inorganic Chemistry, Greinstrasse 6, D-50939 Köln, Germany. E-Mail: rose.jordan@uni-koeln.de, axel.klein@uni-koeln.de.
[†] Institut für Anorganische und Analytische Chemie, Universität Münster, Corrensstraße 28/30, 48149 Münster, Germany, and CeNTech, CiMIC, SoN, Heisenbergstraße 11, 48149 Münster, Germany. Email: cstra_01@uni-muenster.de

Table of contents

References

Supporting Tables

Table S1. Crystallographic and Structure Refinement Data for $[Ni(C_6F_5)_2(MeCN)_2]\cdot solv.$[a]

formula / MW	$C_{16}H_6F_{10}N_2Ni$ / 474.94 g·mol^{-1}
temperature / wavelength	100(2) K / 0.71073 Å
crystal system / space group	orthorhombic, *Pnna*
a / *b* / *c*	8.5494(7) Å / 14.6367(14) Å / 14.9657(14) Å
V / Z	1872.7(3) Å^2 / 4
ϱ_{calc} / *F* (000)	1.684 g cm^{-3} / 936
limiting indices	–11 < h < 11; –19 < k < 19; –19 < l < 19
reflections collected/unique	85921 / 2332
R_{int}	0.093
data/restraints/parameters	2332 / 0 / 133
Goodness-of-fit on F^2	1.07
final *R* values [$I > 2\sigma(I)$]	R_1 = 0.040, wR_2 = 0.094
R values (all data)	R_1 = 0.053
largest diff peak and hole	0.52 / –0.43 e·Å^{-3}
CCDC	2262015

[a] Electron density corresponding to strongly disordered solvent inside solvent accessible voids within the structure was removed from the dataset using Platon SQUEEZE.[1]

Table S2. Selected distances (Å) and angles (°) of $[Ni(C_6F_5)_2(MeCN)_2]\cdot solv.$[a]

distances		angles	
Ni–N1	1.904(2)	N1–Ni–C1	177.1(1)
Ni–C1	1.905(2)	C1–Ni–C1′	88.3(1)
		N1–Ni–N1′	88.0(1)
Ni···*o*-F1	3.208(2)	N1–Ni–C1′	92.0(1)
Ni···*o*-F5	3.024(2)		
		C_6F_5(1)/NiNCCN	62.82(3)
		C_6F_5/C_6F_5′	75.25(6)

[a] Electron density corresponding to strongly disordered solvent inside solvent accessible voids within the structure was removed from the dataset using Platon SQUEEZE.[1]

Table S3. Crystallographic and Structure Refinement Data for $[Ni(C_6F_5)_2(bpy)]\cdot 0.5CH_2Cl_2$.

formula / MW	$C_{22.50}H_9ClF_{10}N_2Ni$ / 591.48 g·mol^{-1}
temperature / wavelength	100(2) / 0.71073 Å
crystal system / space group	monoclinic / $P2_1/c$
a (Å) / *b* (Å) / *c* (Å)	13.1728(9) / 7.1383(4) / 24.6258(17)
β (°)	90.670(3)
V (Å^2) / Z	2315.4(3) / Z
ϱ_{calc} (g cm^{-3}) / *F* (000)	1.697 / 1172
limiting indices	–17 < h < 17; –9 < k < 9; –32 < l < 32
reflections collected/unique	74492/5746
R_{int}	0.072
data/restraints/parameters	5746/32/364
Goodness-of-fit on F^2	1.08
final *R* values [$I > 2\sigma(I)$]	R_1 = 0.048, wR_2 = 0.134
R values (all data)	R_1 = 0.060
largest diff peak and hole (e·Å^{-3})	0.63 / –0.59
CCDC	2171187

Table S4. Selected distances (Å) and angles (°) of $[Ni(C_6F_5)_2(bpy)]\cdot 0.5CH_2Cl_2$.

distances		angles	
Ni–N1	1.945(2)	N1–Ni–C1	176.8(1)
Ni–N2	1.941(2)	C1–Ni–C7	86.1(1)
Ni–C1	1.904(3)	C7–Ni–N2	175.9(1)
Ni–C7	1.905(3)	N2–Ni–N1	83.0(1)
		N2–Ni–C1	95.7(1)
Ni···*o*-F1	3.168(2)	N1–Ni–C7	95.5(1)
Ni···*o*-F5	3.067(2)	C_6F_5(1)/NiNCCN	75.4(1)
Ni···*o*-F6	3.053(2)	C_6F_5(2)/NiNCCN	76.4(1)
Ni···*o*-F10	3.179(2)	C_6F_5(1)/C_6F_5(2)	87.3(1)

Table S5. Crystallographic and Structure Refinement Data for $[Ni(C_6F_5)_2(tmphen)]\cdot CHCl_3$.

formula / MW	$C_{29}H_{17}Cl_3F_{10}N_2Ni$ / 748.51 g·mol^{-1}
temperature / wavelength	100(2) K / 0.71073 Å
crystal system / space group	triclinic / $P\bar{1}$
a (Å) / *b* (Å) / *c* (Å)	8.7580(6) / 12.5285(9) / 12.9137(9)
α (°) / β (°) / γ (°)	96.630(3) / 95.411(3) / 90.523(3)
V (Å^2) / Z	1400.92(17) / 2
ϱ_{calc} (g cm^{-3}) / *F* (000)	1.774 / 748
limiting indices	–13 < h < 13; –19 < k < 19; –19 < l < 19
reflections collected/unique (R_{int})	99255 / 10668
R_{int}	0.061
data/restraints/parameters	10668 / 0 / 420
Goodness-of-fit on F^2	1.11
final *R* values [$I > 2\sigma(I)$]	R_1 = 0.038, wR_2 = 0.095
R values (all data)	R_1 = 0.048
largest diff peak and hole (e·Å^{-3})	0.76 / –0.91
CCDC	2253625

Table S6. Selected distances (Å) and angles (°) of $[Ni(C_6F_5)_2(tmphen)]\cdot CHCl_3$.

distances		angles	
Ni–N1	1.939(1)	N1–Ni–C1	178.42(6)
Ni–N2	1.946(1)	C1–Ni–C7	86.70(6)
Ni–C1	1.901(1)	C7–Ni–N2	177.72(6)
Ni–C7	1.894(1)	N2–Ni–N1	83.65(5)
		N2–Ni–C1	95.55(6)
		N1–Ni–C7	94.09(6)
Ni···*o*-F1	3.147(1)		
Ni···*o*-F5	3.102(1)	C_6F_5(1)/NiNCCN	74.45(4)
Ni···*o*-F6	3.129(1)	C_6F_5(2)/NiNCCN	78.92(4)
Ni···*o*-F10	3.098(1)	C_6F_5(1)/C_6F_5(2)	85.79(4)

Table S7. Crystallographic and Structure Refinement Data for $[Ni(C_6F_5)_2(2,9\text{-dmphen})]\cdot MeCN$.

formula / MW	$C_{28}H_{15}F_{10}N_3Ni$ / 642.14 g·mol^{-1}
temperature / wavelength	100(2) K / 0.71073 Å
crystal system / space group	monoclinic / $P2_1/c$
a (Å) / *b* (Å) / *c* (Å)	7.3083(5) / 23.665(2) / 14.6924(13)
β (°)	93.782(3)

V (Å^2) / Z	2535.5(4) / 4
ϱ_{calc} (g cm^{-3}) / *F* (000)	1.682 / 1288
limiting indices	–9 < h < 9; –31 < k < 31; –19 < l < 19
reflections collected/unique	184039/6313
R_{int}	0.080
data/restraints/parameters	6313/0/382
Goodness-of-fit on F^2	1.06
final *R* values [$I > 2\sigma(I)$]	R_1 = 0.052, wR_2 = 0.127
R values (all data)	R_1 = 0.059
largest diff peak and hole (e·Å^{-3})	2.19/–0.63
CCDC	2327972

Table S8. Selected distances (Å) and angles (°) of [Ni(C_6F_5)$_2$(2,9-dmphen)] · MeCN.

distances		angles	
Ni–N1	1.962(2)	N1–Ni–C1	174.7(1)
Ni–N2	1.983(2)	C1–Ni–C7	84.1(1)
Ni–C1	1.906(3)	C7–Ni–N2	164.8(1)
Ni–C7	1.905(3)	N2–Ni–N1	83.7(1)
		N2–Ni–C1	97.8(1)
		N1–Ni–C7	93.1(1)
Ni···*o*-F1	3.122(2)		
Ni···*o*-F5	3.106(2)	C_6F_5(1)/NiNCCN	88.8(1)
Ni···*o*-F6	3.040(2)	C_6F_5(2)/NiNCCN	69.9(1)
Ni···*o*-F10	3.215(2)	C_6F_5(1)/C_6F_5(2)	80.5(1)
		NiNCCN/2,9-dmphen	35.1(2)

Table S9. Crystallographic and structure refinement data for [Ni(C_6F_5)$_2$(dppz)]·solv.[a]

formula / MW	$C_{30}H_{10}F_{10}N_4Ni$ / 675.13 g·mol^{-1}
temperature / wavelength	100(2) K / 1.54178 Å
crystal system / space group	orthorhombic / *Pbcn*
a (Å) / *b* (Å) / *c* (Å)	16.4970(3) / 29.6725(6) / 6.9154(1)
V (Å^2) / Z	3385.14(10) / 4
ϱ_{calc} (g cm^{-3}) / *F* (000)	1.325 / 1344
limiting indices	–17 < h < 20 ; –34 < k < 36 ; –8 < l < 7
reflections collected/unique	19008 / 3273
R_{int}	0.036
data/restraints/parameters	3273 / 0 / 205
Goodness-of-fit on F^2	1.09
final *R* values [$I > 2\sigma(I)$]	R_1 = 0.097, wR_2 = 0.293
R values (all data)	R_1 = 0.098
largest diff peak and hole (e·Å^{-3})	1.33 / –0.86
CCDC	2259509

[a] Electron density corresponding to strongly disordered solvent inside solvent accessible voids within the structure was removed from the dataset using Platon SQUEEZE.[1]

Table S10. Selected distances (Å) and angles (°) of [Ni(C_6F_5)$_2$(dppz)]·solv.[a]

distances		angles	
Ni–N1	1.955(4)	N1–Ni–C1	95.3(2)
Ni–C1	1.901(5)	C1–Ni–C1′	86.0(3)
		N1–Ni–N1′	83.6(2)

		N1–Ni–C1′	176.2(2)
Ni···*o*-F1	3.176(3)	C_6F_5(1)/NiNCCN	71.5(1)
Ni···*o*-F5	3.061(3)	C_6F_5/C_6F_5′	82.1(1)

[a] Electron density corresponding to strongly disordered solvent inside solvent accessible voids within the structure was removed from the dataset using Platon SQUEEZE.[1]

Table S11. Crystallographic and Structure Refinement Data for [Ni(C_6F_5)$_2$(*i*Pr-DAB)].

formula / MW	$C_{20}H_{16}F_{10}N_2Ni$ / 533.04 g mol^{-1}
temperature / wavelength	273 K / 0.71073 Å
crystal system / space group	monoclinic / $P2_1/c$
a (Å) / *b* (Å) / *c* (Å)	9.793(2) / 13.958(2) / 15.823(3)
β (°)	96.55
V (Å^2) / Z	2148.8(6) / 4
ϱ_{calc} (g cm^{-3}) / *F* (000)	1.648 / 1072
limiting indices	–13 < h < 13; –19 < k < 19; –22 < l < 18
reflections collected/unique	31990 / 6043
R_{int}	0.094
data/restraints/parameters	6043 / 0 / 303
GooF on F^2	0.76
final *R* values [$I > 2\sigma(I)$]	R_1 = 0.037, wR_2 = 0.096
R values (all data)	R_1 = 0.115
largest diff peak and hole (e·Å^{-3})	0.45 / –0.76
CCDC	2259505

Table S12. Selected distances (Å) and angles (°) of [Ni(C_6F_5)$_2$(*i*Pr-DAB)].

distances		angles	
Ni–N1	1.961(2)	N1–Ni–C1	93.9(1)
Ni–N2	1.951(2)	C1–Ni–C7	86.6(1)
Ni–C7	1.902(3)	C7–Ni–N2	97.2(1)
Ni–C1	1.897(3)	N2–Ni–N1	82.56(1)
		N2–Ni–C1	172.8(1)
		N1–Ni–C7	177.9(1)
Ni···*o*-F1	3.025(2)		
Ni···*o*-F5	3.185(2)	C_6F_5(1)/NiNCCN	77.4(1)
Ni···*o*-F6	3.155(2)	C_6F_5(2)/NiNCCN	80.1(1)
Ni···*o*-F10	3.085(2)	C_6F_5(1)/C_6F_5(2)	86.7(1)

Table S13. Crystallographic and Structure Refinement Data for [Ni(C_6F_5)$_2$(Xyl-DAB)].

formula / MW	$C_{30}H_{20}F_{10}N_2Ni$ / 657.19 g mol^{-1}
temperature / wavelength	100(2) K / 0.71073 Å
crystal system / space group	monoclinic / $P2_1/c$
a (Å) / *b* (Å) / *c* (Å)	10.9011(12) / 9.4587(13) / 25.367(3)
β (°)	90.09
V (Å^2) / Z	2615.6(6) / 4
ϱ_{calc} (g cm^{-3}) / *F* (000)	1.669 / 1328
limiting indices	–14 < h < 14; –12 < k < 12; –33 < l < 33
reflections collected/unique	154112 / 6557
R_{int}	0.080
data/restraints/parameters	6557 / 0 / 392

GooF on F^2	1.11
final R values [$I > 2\sigma(I)$]	$R_1 = 0.045$, $wR_2 = 0.099$
R values (all data)	$R_1 = 0.054$
largest diff peak and hole (e·Å^{-3})	0.56 / –0.41
CCDC	2279587

Table S14. Selected distances (Å) and angles (°) of [Ni(C$_6$F$_5$)$_2$(Xyl-DAB)].

distances		angles	
Ni–N1	1.958(2)	N1–Ni–C1	171.7(1)
Ni–N2	1.941(2)	C1–Ni–C7	87.4(1)
Ni–C7	1.902(2)	C7–Ni–N2	175.3(1)
Ni–C1	1.893(2)	N2–Ni–N1	81.7(1)
		N2–Ni–C1	92.7(1)
		N1–Ni–C7	97.7(1)
Ni···*o*-F1	3.081(1)		
Ni···*o*-F5	3.126(2)	C$_6$F$_5$(1)/NiNCCN	78.5(1)
Ni···*o*-F6	3.058(2)	C$_6$F$_5$(2)/NiNCCN	64.9(1)
Ni···*o*-F10	3.181(2)	C$_6$F$_5$(1)/C$_6$F$_5$(2)	86.8(1)

Table S15. Electrochemical data for complexes **1** to **6** and for similar Ni complexes.[a]

Compound (N^N =)	E_{1pc} 3rd reduction	$E_{1/2}$ 2nd reduction	$E_{1/2}$ 1st reduction	E_{pa} 1st oxidation	ΔE_{echem}[b]	solvent
1 (bpy)	–2.47	–2.30	–1.62	+0.76	2.38	MeCN
	–2.76	–2.48	–1.84	+0.71	2.55	THF
2 (tmphen)		–2.55 *irr*	–1.96	+0.66	2.62	MeCN
		–2.66 *irr*	–2.02	+0.69	2.71	THF
3 (2,9-dmphen)	–2.78	–2.55 *irr*	–1.73 *irr*	+0.30	2.03	MeCN
		–2.65 *irr*	–1.71 *irr*	+0.87	2.58	THF
4 (dppz)	–2.50	–2.02	–1.43	+0.52	1.95	MeCN
	–3.39	–2.13	–1.51	+0.69	2.20	THF
5 (*i*Pr-DAB)		–2.55 *irr*	–1.29	+0.88	2.17	MeCN
		–2.84 *irr*	–1.51	+1.10	2.61	THF
			–1.47	+0.97	2.44	CH_2Cl_2
6 (Xyl-DAB) [c]		–2.12 *irr*	–1.00	+1.06	2.06	MeCN
		–2.24 *irr*	–1.09	+1.04	2.13	THF
			–1.16	+1.10	2.26	CH_2Cl_2
Other complexes						
[Ni(Mes)$_2$(bpy)] [d]		–2.97	–2.19	–0.14	2.05	THF
[Ni(C$_6$F$_5$)$_2$(Tp)]$^-$ [e]				+0.55		MeCN
(*n*Bu$_4$N)$_2$[Ni(C$_6$F$_5$)$_4$] [f]				+0.54		CH_2Cl_2

[a] From cyclic voltammetry in 0.1 M *n*Bu$_4$NPF$_6$/solvent solutions at 100 mV/s scan rate. Potentials E in V vs. ferrocene/ferrocenium, accuracy: ± 0.003 V. Half-wave potentials $E_{1/2}$ for reversible waves, peak potentials E_p for irreversible waves (*irr*). [b] Electrochemical HOMO-LUMO gap $\Delta E_{echem} = E_{Ox1} - E_{Red1}$ in V. [c] Second oxidation at +1.22 V. [d] From ref. 2, second oxidation at +0.98 *irr*. [e] From ref. 3, Tp = tripyrazolylborate, no reduction potentials reported. [f] From ref. 4, reversible first oxidation, no reduction potentials reported.

Supporting Figures

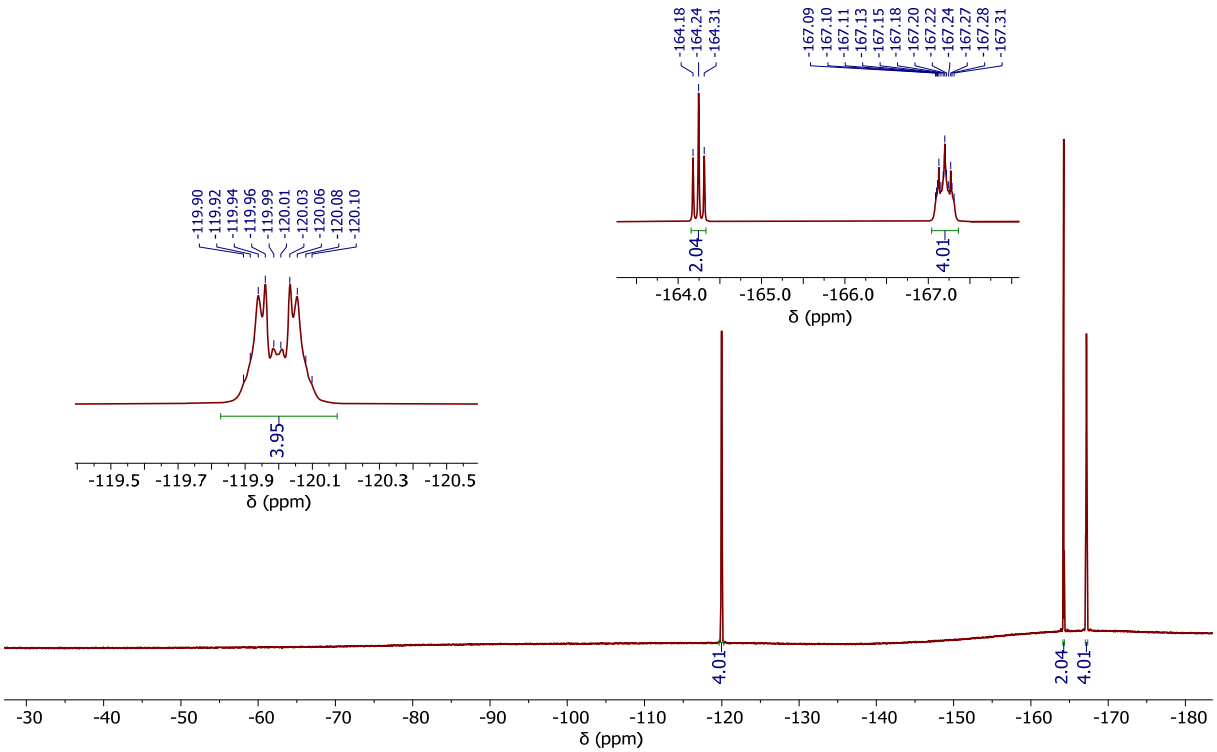

Figure S1. ^{19}F NMR (282 MHz, MeCN-d_3) of $[Ni(C_6F_5)_2(MeCN)_2]$.

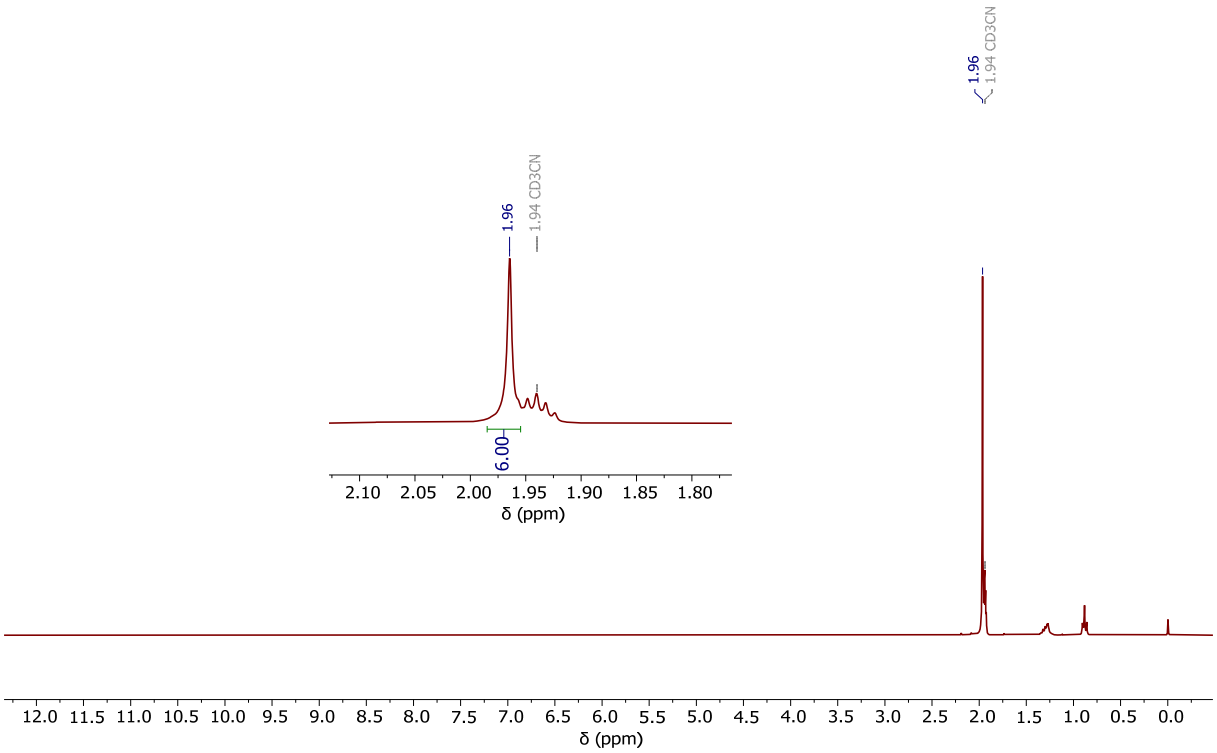

Figure S2. ^{1}H NMR (300 MHz, MeCN-d_3) of $[Ni(C_6F_5)_2(MeCN)_2]$.

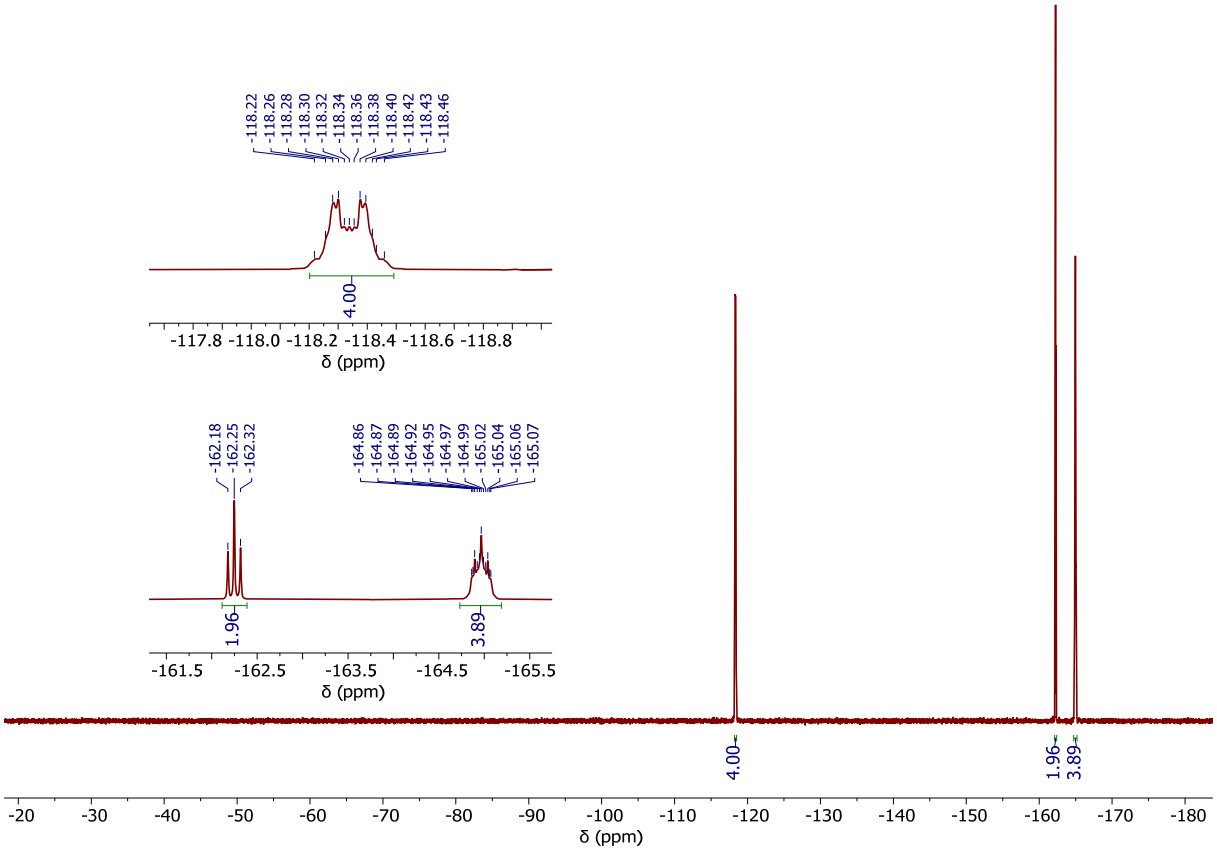

Figure S3. ^{19}F NMR (282 MHz, CD_2Cl_2) of $[Ni(C_6F_5)_2(bpy)]$ (**1**).

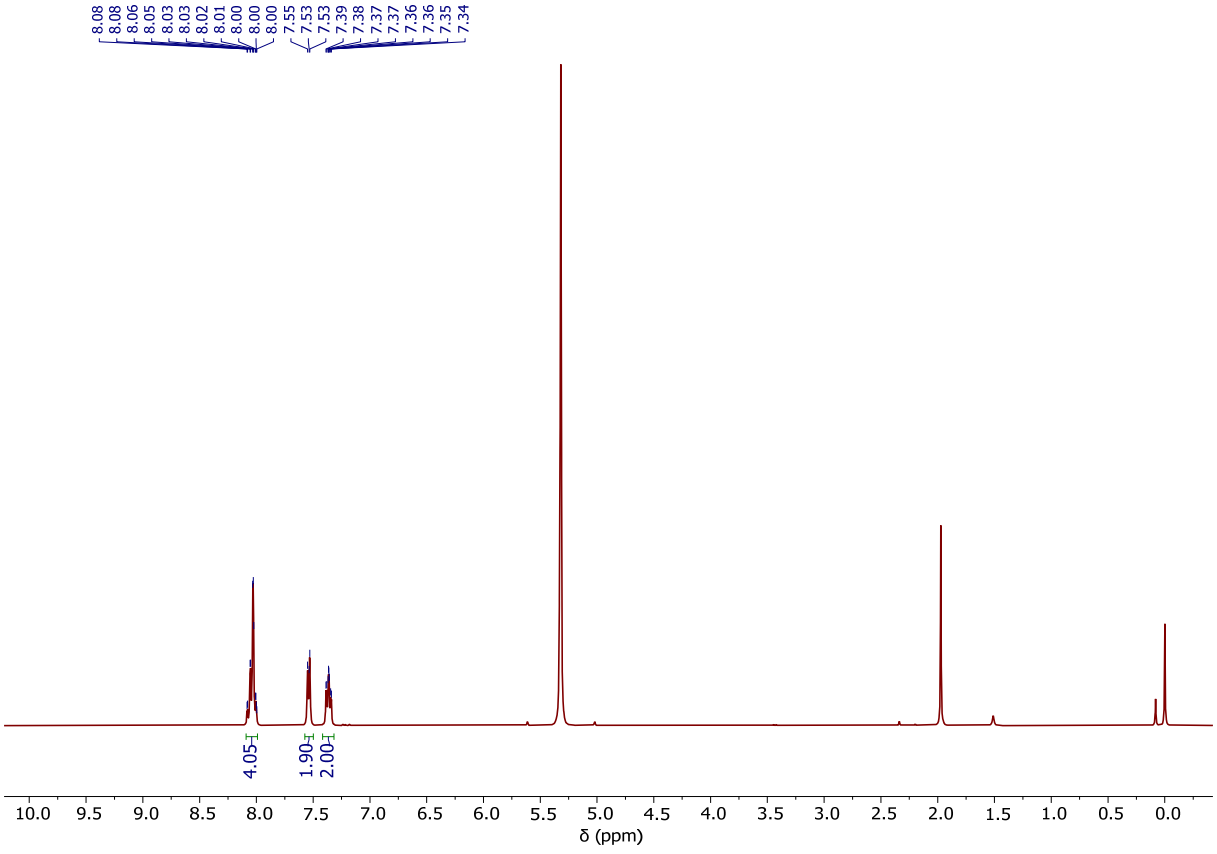

Figure S4. ^{1}H NMR (300 MHz, CD_2Cl_2) of $[Ni(C_6F_5)_2(bpy)]$ (**1**).

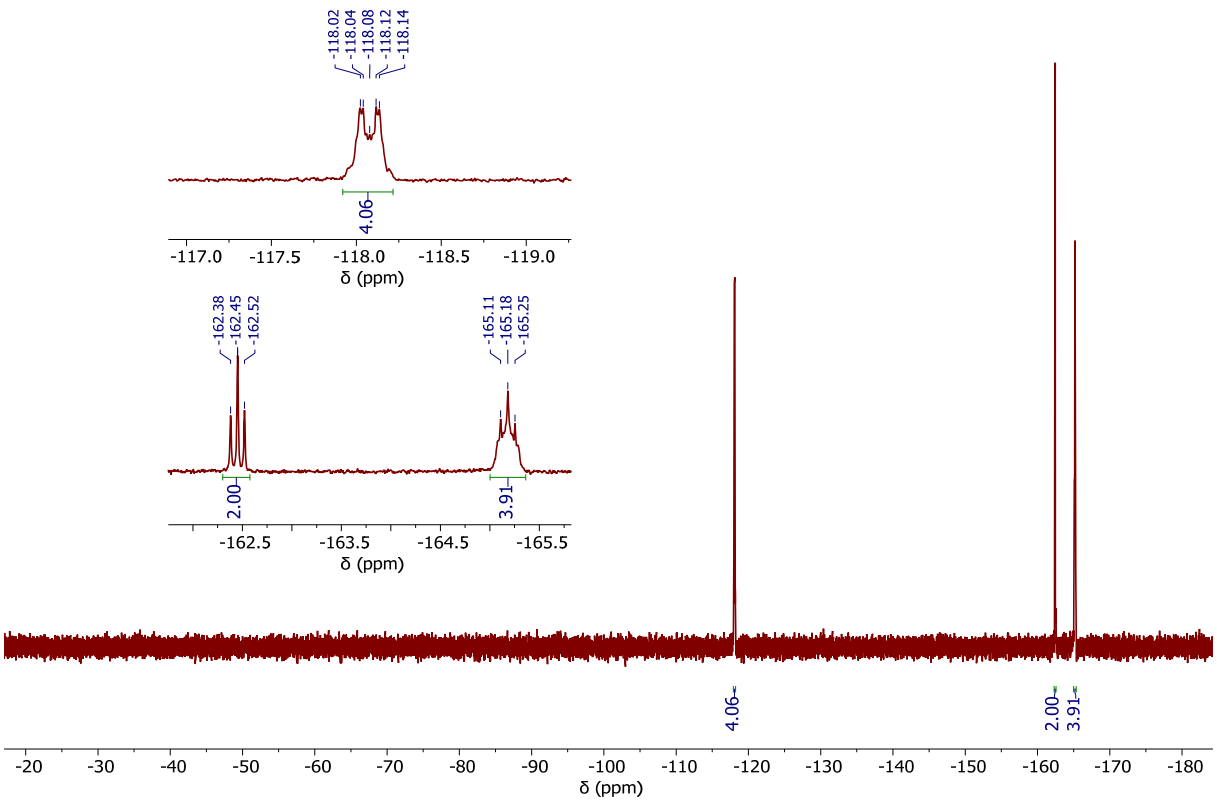

Figure S5. ^{19}F NMR (282 MHz, CD_2Cl_2) of [Ni(C_6F_5)$_2$(tmphen)] (**2**).

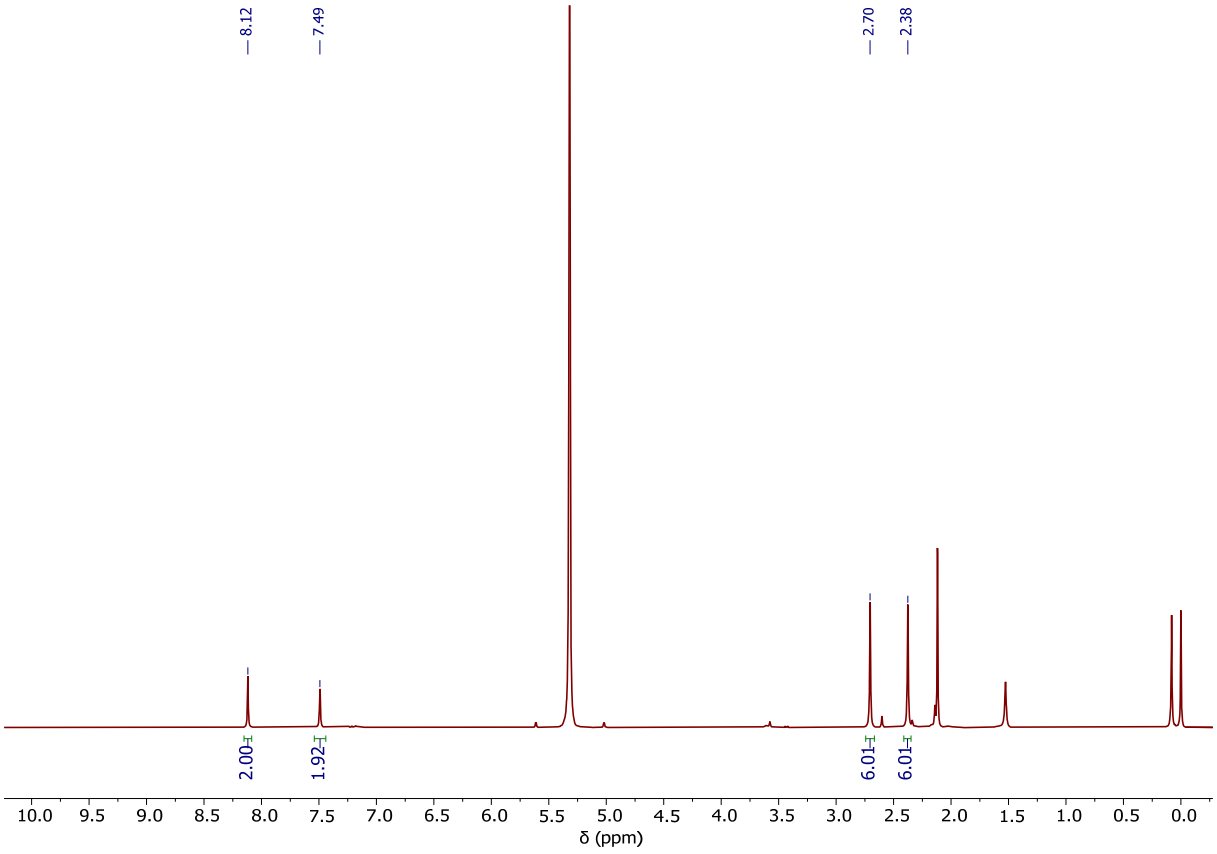

Figure S6. ^{1}H NMR (300 MHz, CD_2Cl_2) of [Ni(C_6F_5)$_2$(tmphen)] (**2**).

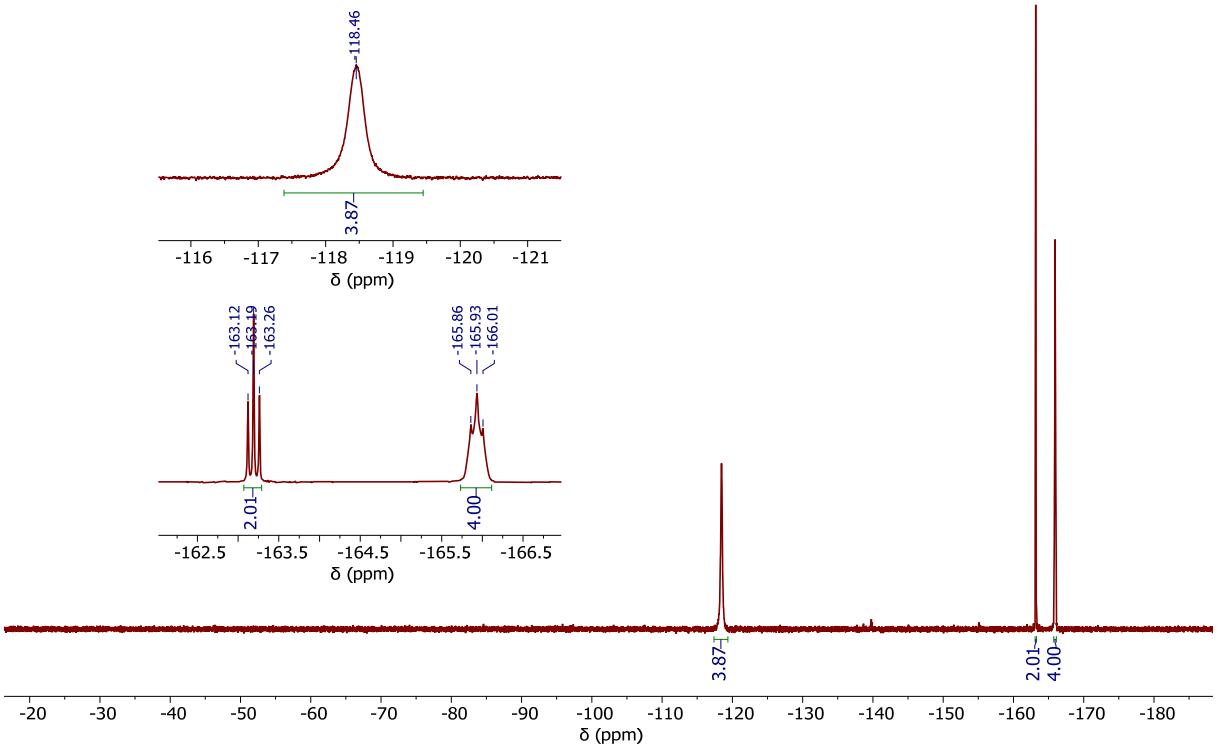

Figure S7. ^{19}F NMR (282 MHz, CD_2Cl_2) of [Ni(C_6F_5)$_2$(2,9-dmphen)] (**3**).

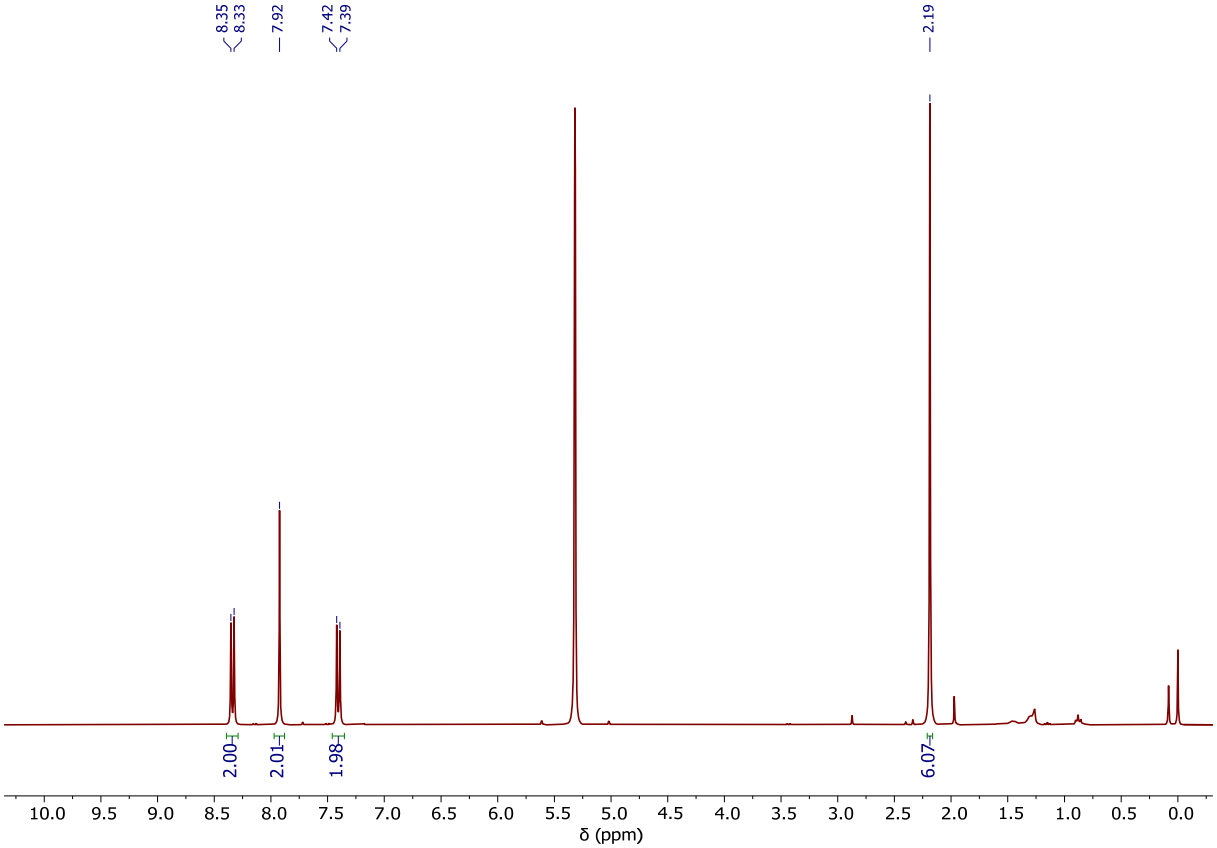

Figure S8. ^{1}H NMR (300 MHz, CD_2Cl_2) of [Ni(C_6F_5)$_2$(2,9-dmphen)] (**3**).

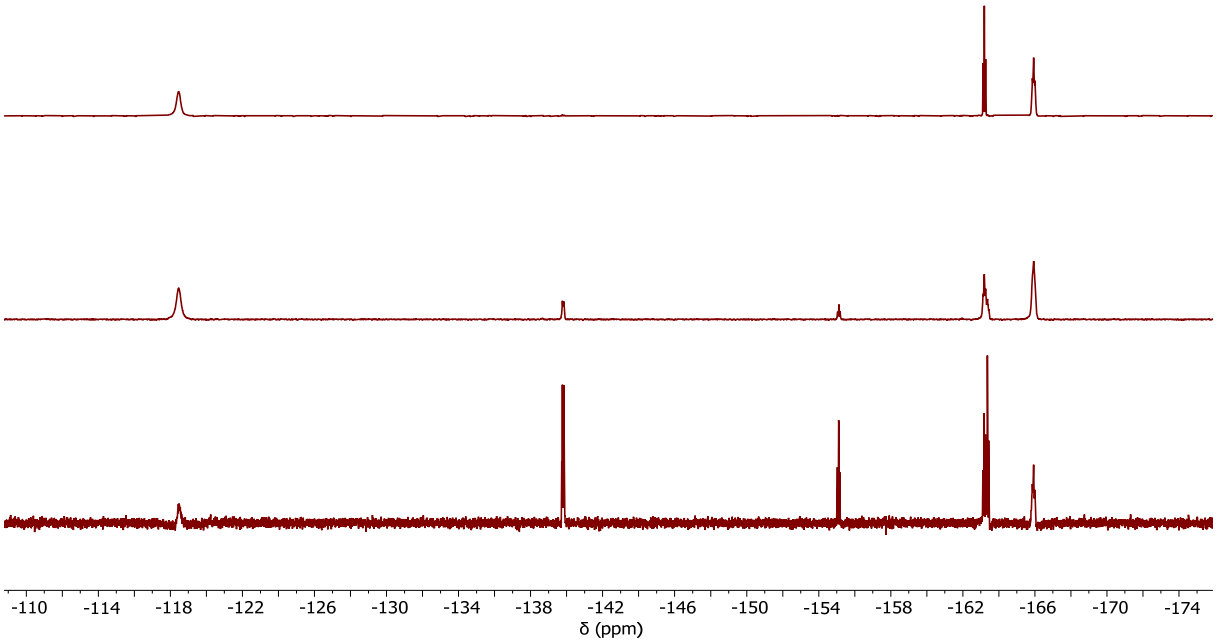

Figure S9. ^{19}F NMR (282 MHz, CD_2Cl_2) of fresh (top) *versus* aged samples of [Ni(C_6F_5)$_2$(2,9-dmphen)] (**3**) after 1 day (middle) and 2 days (bottom).

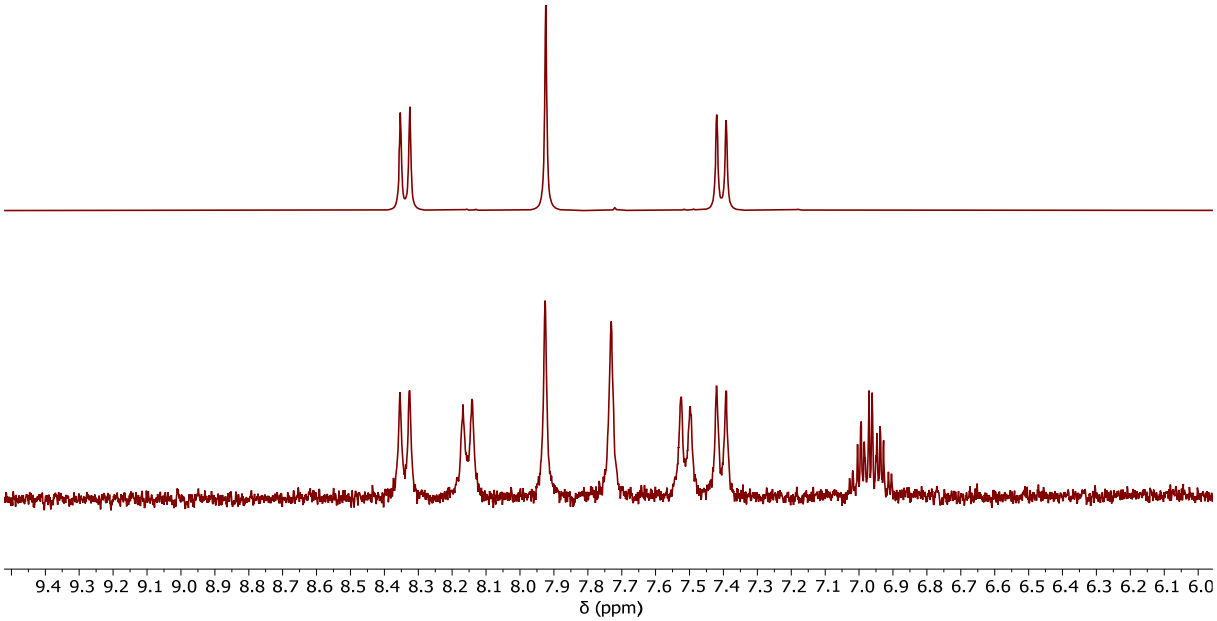

Figure S10. ^{1}H NMR (300 MHz, CD_2Cl_2) of a fresh (top) *versus* aged sample of [Ni(C_6F_5)$_2$(2,9-dmphen)] (**3**) after 2 days (bottom).

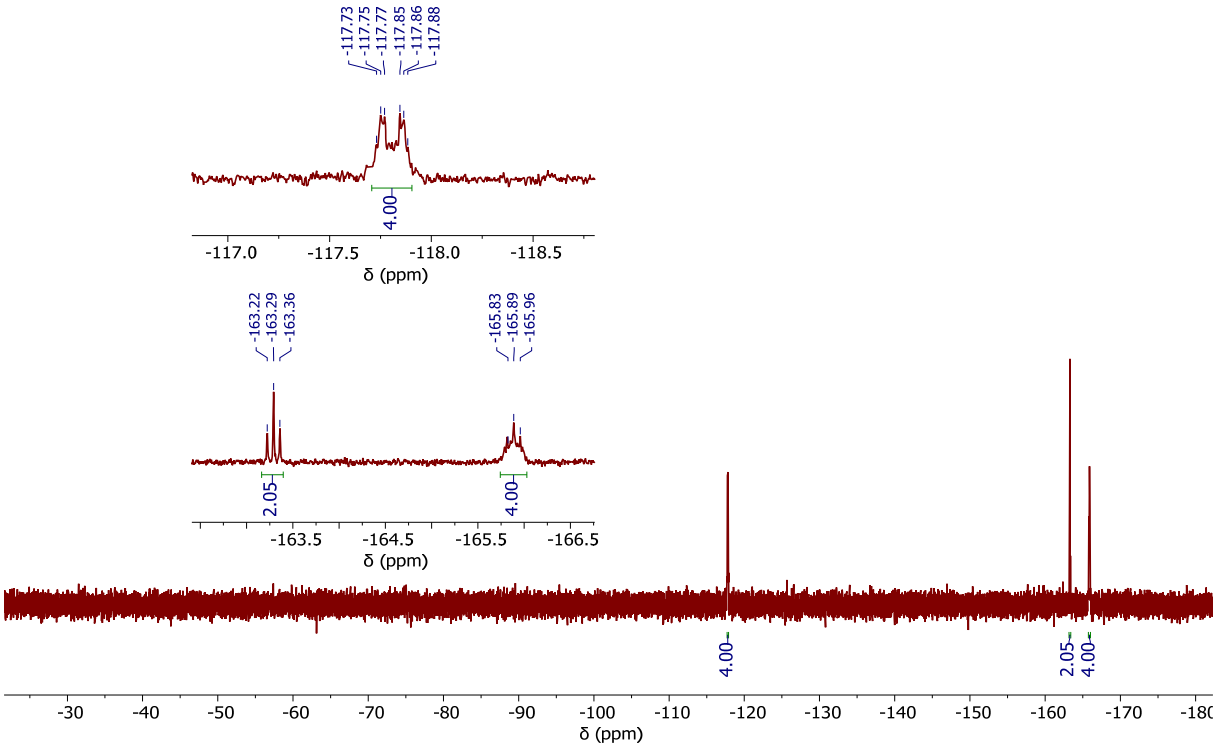

Figure S11. ^{19}F NMR (282 MHz, acetone-d_6) of [Ni(C_6F_5)$_2$(dppz)] (**4**).

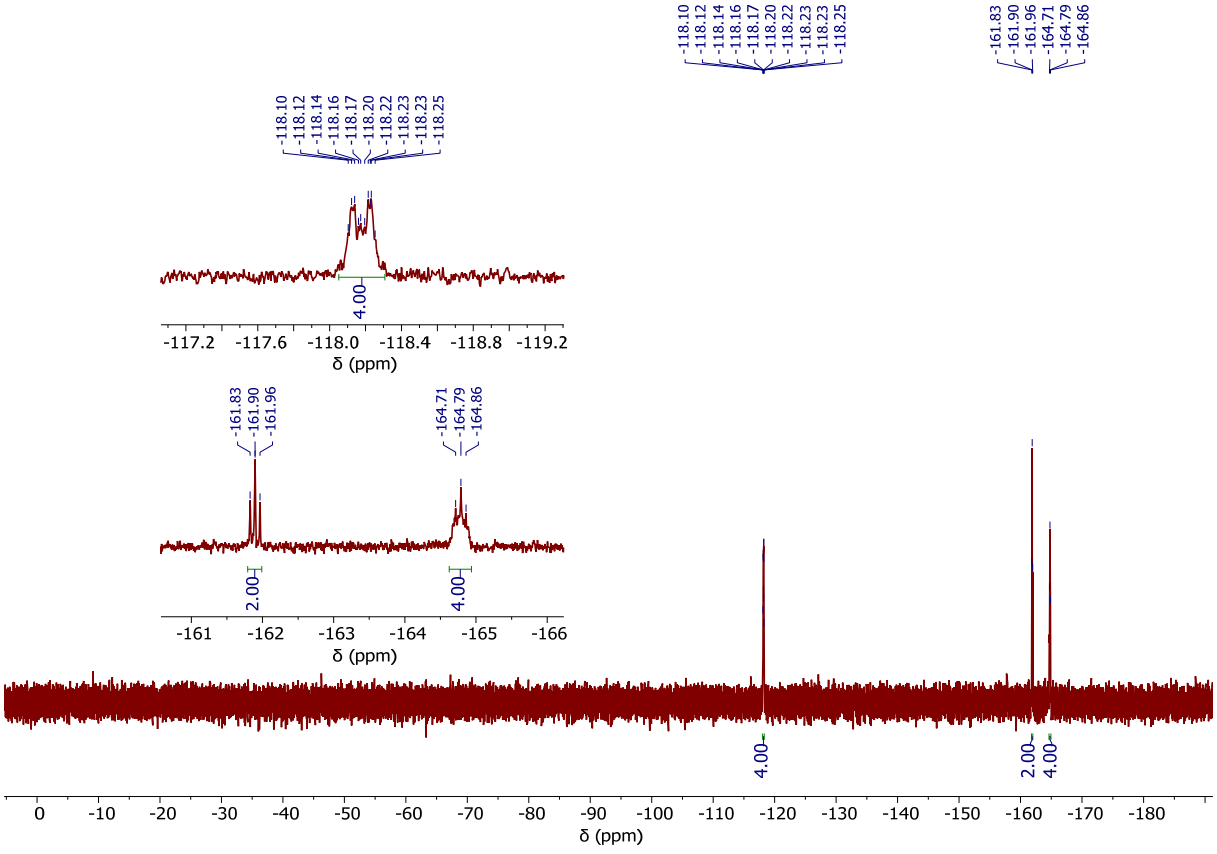

Figure S12. ^{19}F NMR (282 MHz, CD_2Cl_2) of [Ni(C_6F_5)$_2$(dppz)] (**4**).

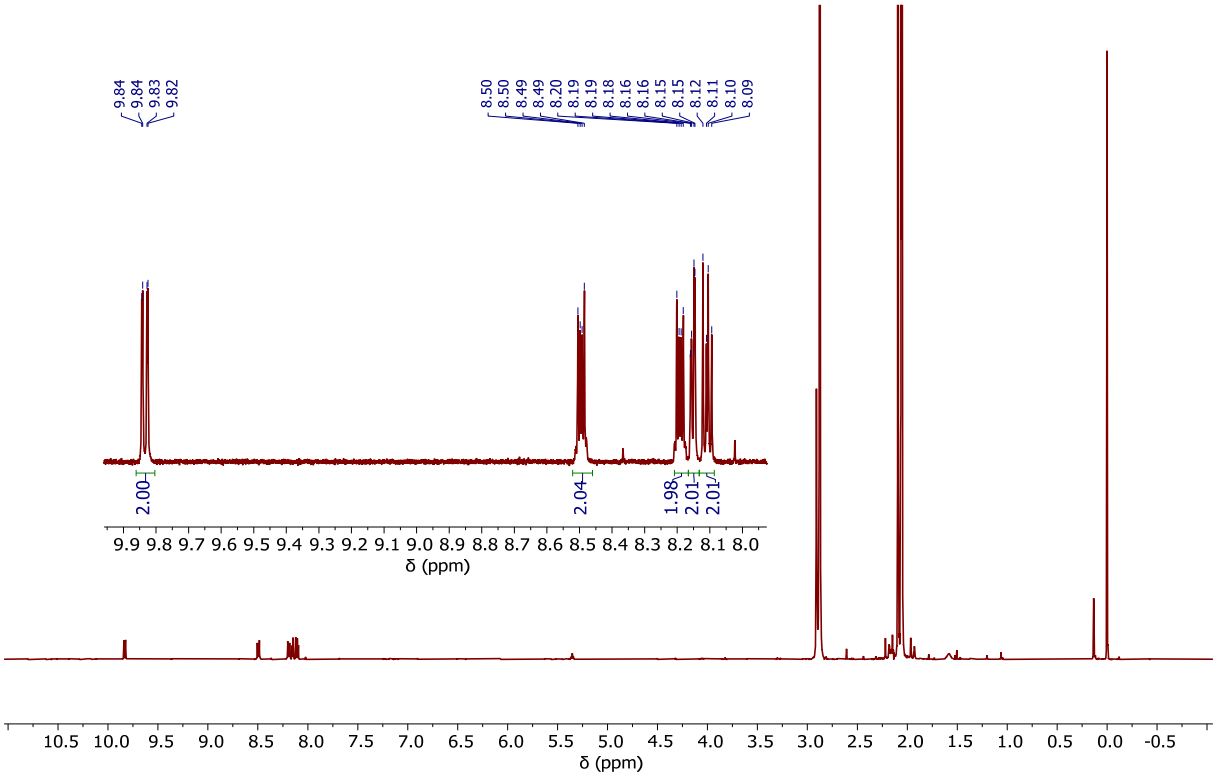

Figure S13. ^{1}H NMR (500 MHz, acetone-d_6) of [Ni(C_6F_5)$_2$(dppz)] (**4**).

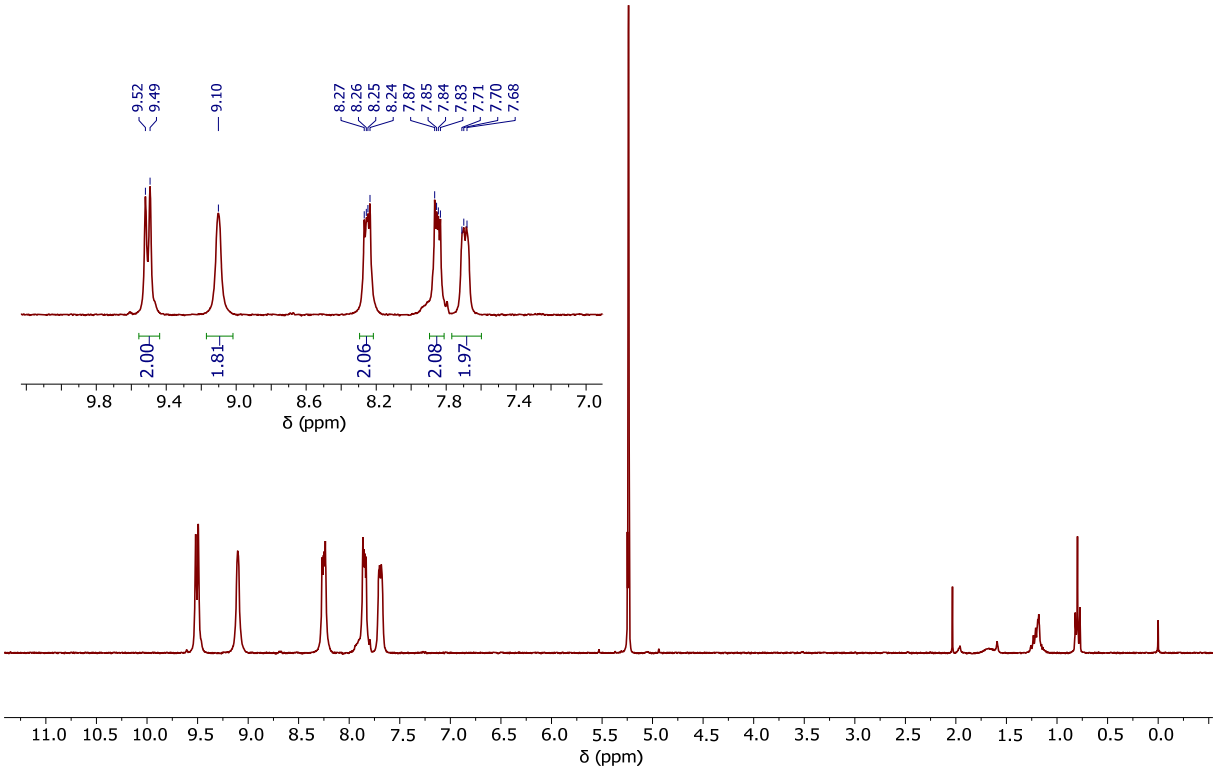

Figure S14. ^{1}H NMR (300 MHz, CD_2Cl_2) of [Ni(C_6F_5)$_2$(dppz)] (**4**).

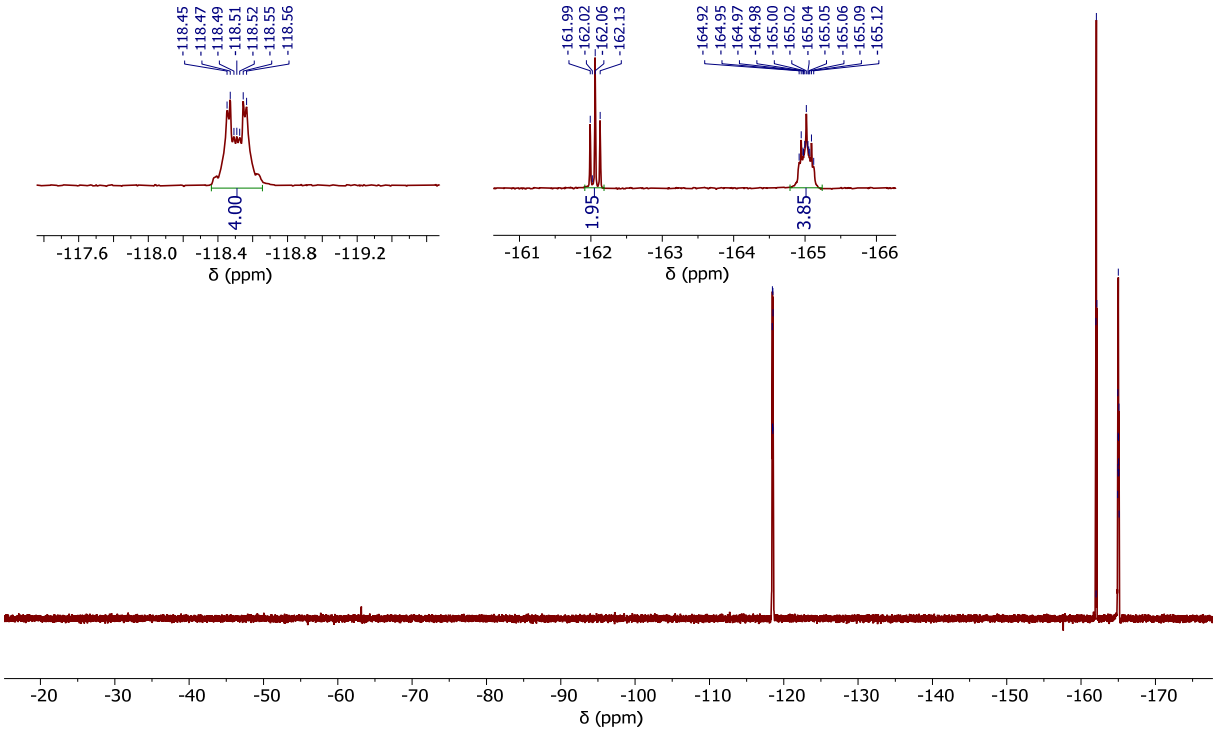

Figure S15. ^{19}F NMR (282 MHz, CD_2Cl_2) of [Ni(C_6F_5)$_2$(*i*Pr-DAB)] (**5**).

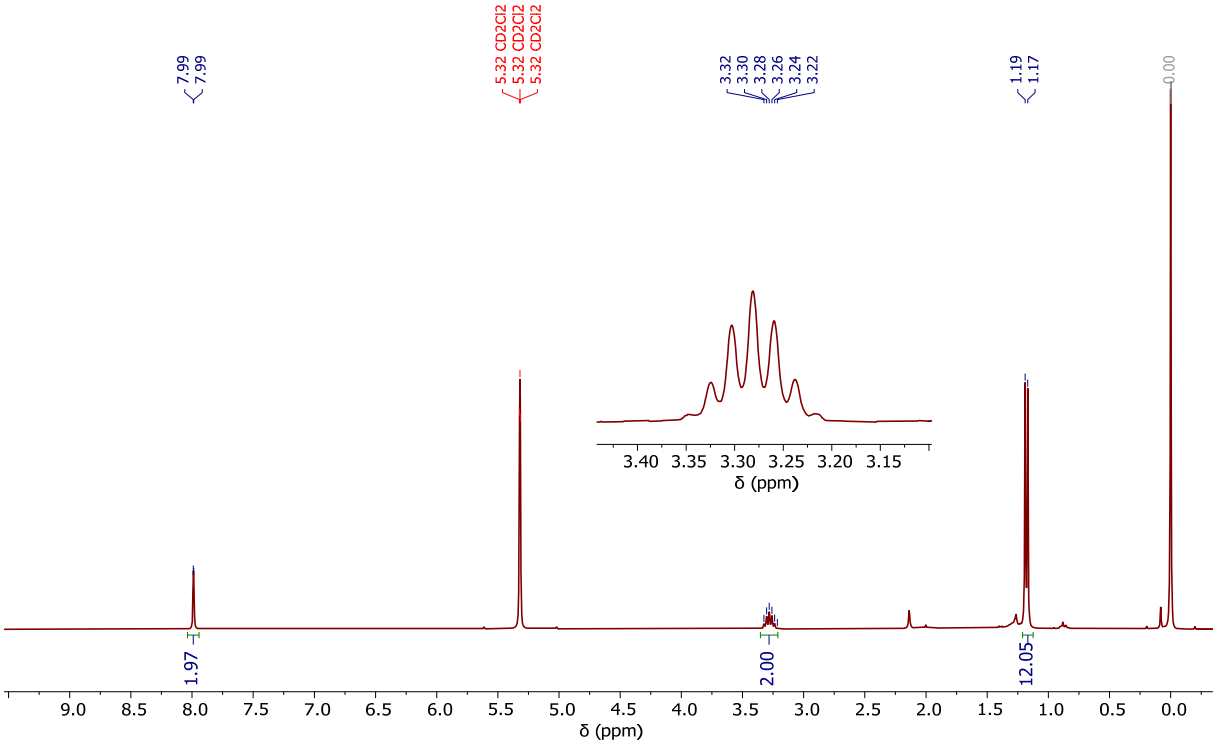

Figure S16. ^{1}H NMR (300 MHz, CD_2Cl_2) of [Ni(C_6F_5)$_2$(*i*Pr-DAB)] (**5**).

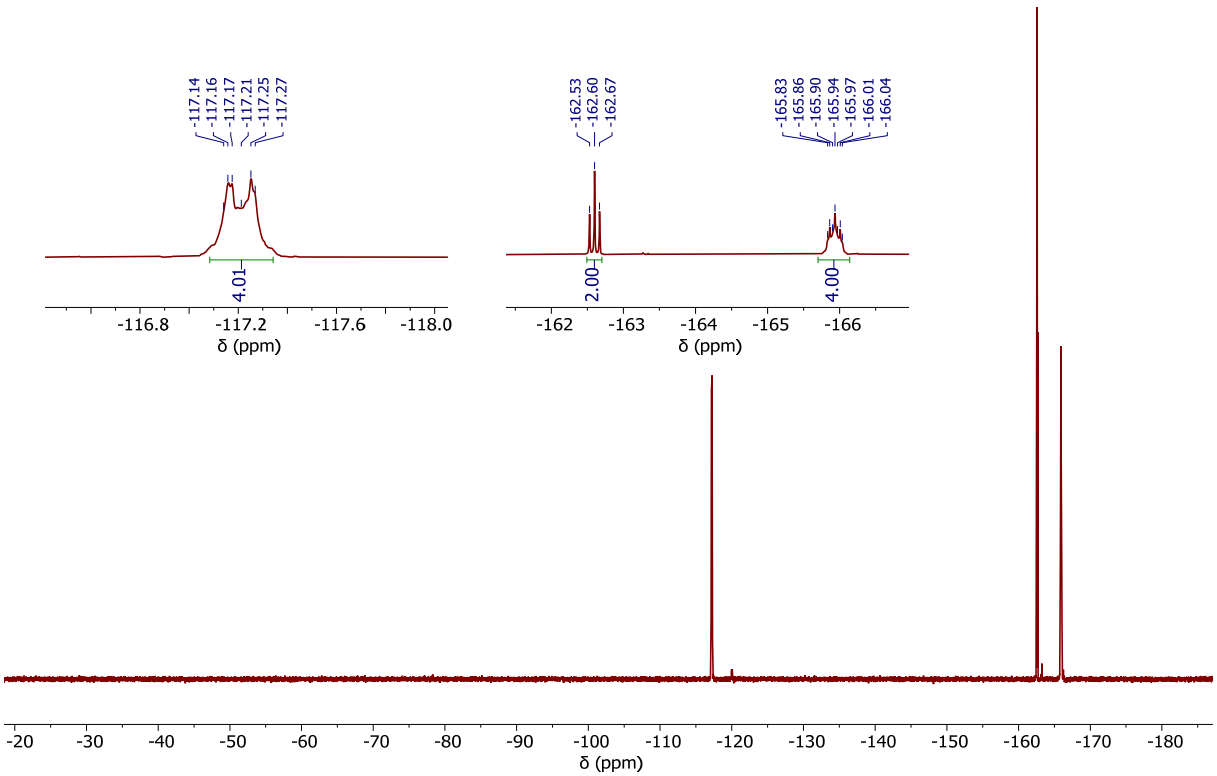

Figure S17. ^{19}F NMR (282 MHz, CD_2Cl_2) of [Ni(C_6F_5)$_2$(Xyl-DAB)] (**6**).

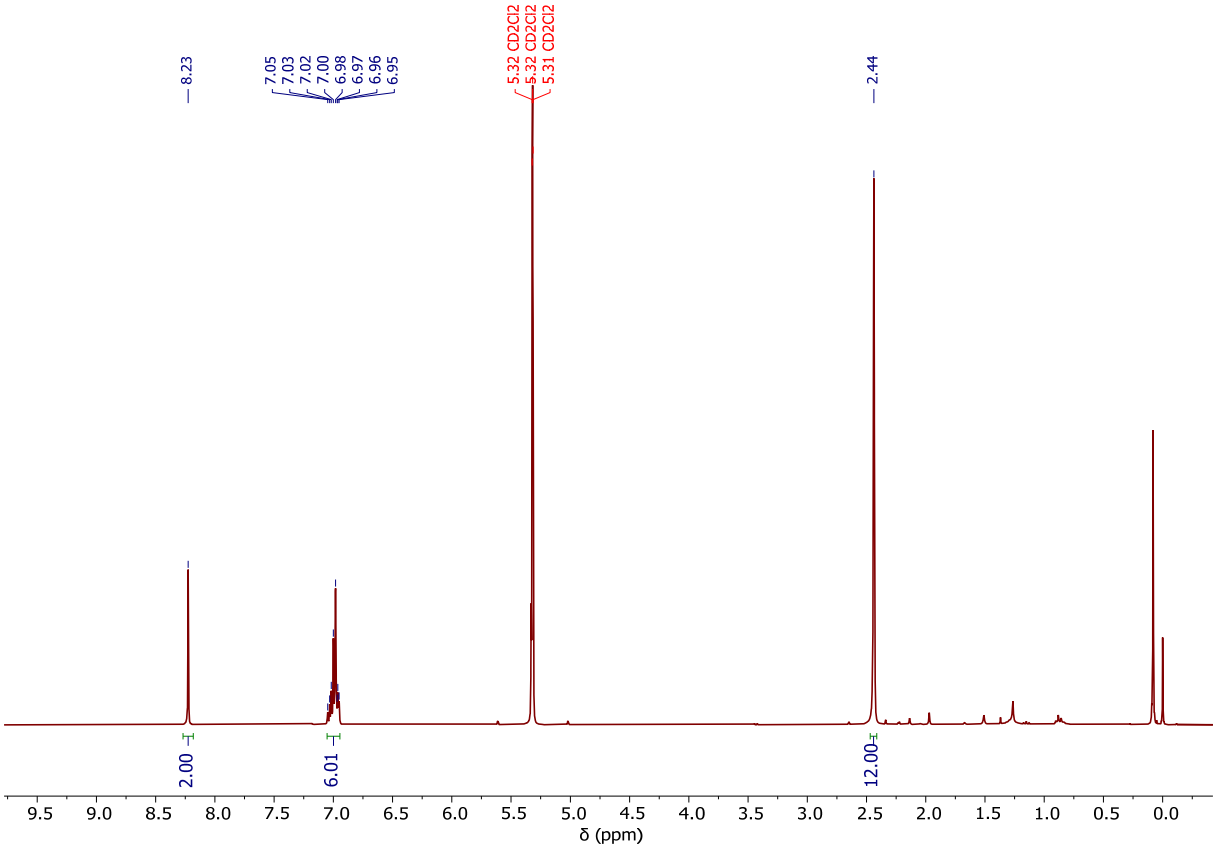

Figure S18. ^{1}H NMR (300 MHz, CD_2Cl_2) of [Ni(C_6F_5)$_2$(Xyl-DAB)] (**6**).

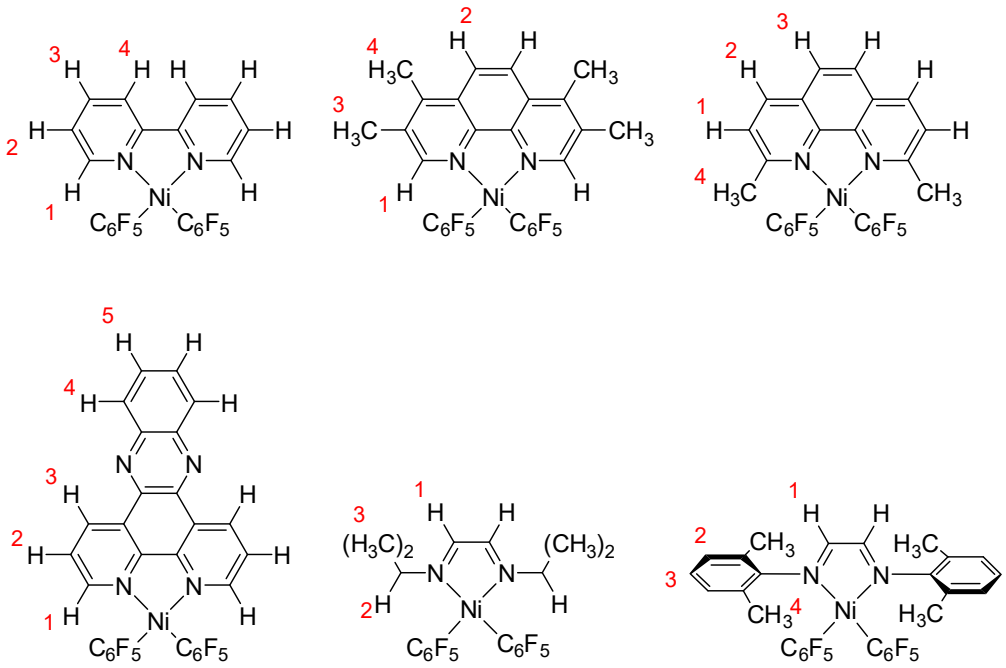

Figure S19. Numbering scheme for ^{1}H NMR signal assignment of target complexes **1** to **6**.

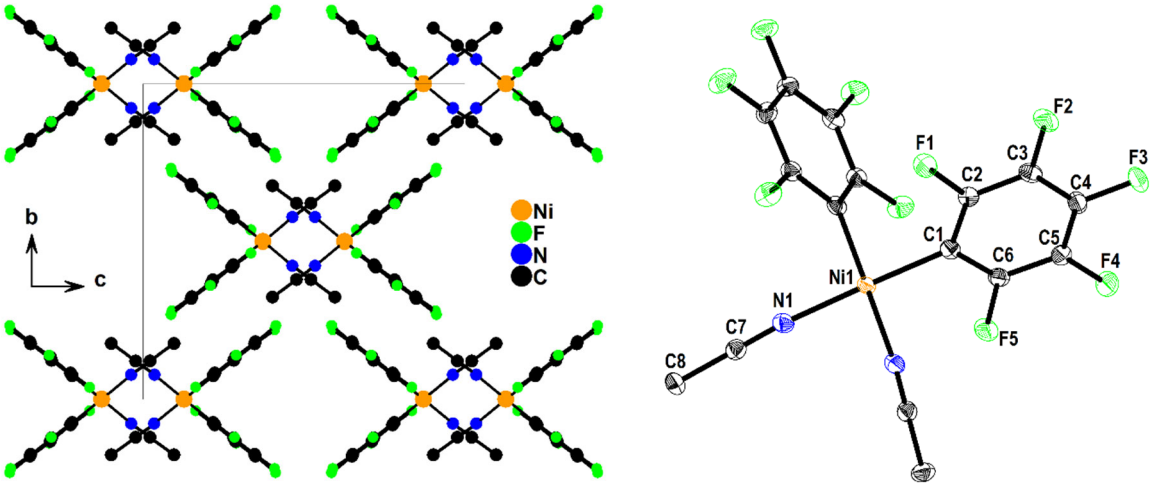

Figure S20. Crystal structure of [Ni(C$_6$F$_5$)$_2$(MeCN)$_2$]·solv viewed along the crystallographic *c* axis (left) and molecular structure of [Ni(C$_6$F$_5$)$_2$(MeCN)$_2$] from *sc*-XRD (right). Ellipsoids shown at 50% probability level, H atoms omitted for clarity. The solvent accessible voids are filled with strongly disordered solvent which was treated with Platon SQUEEZE.[1]

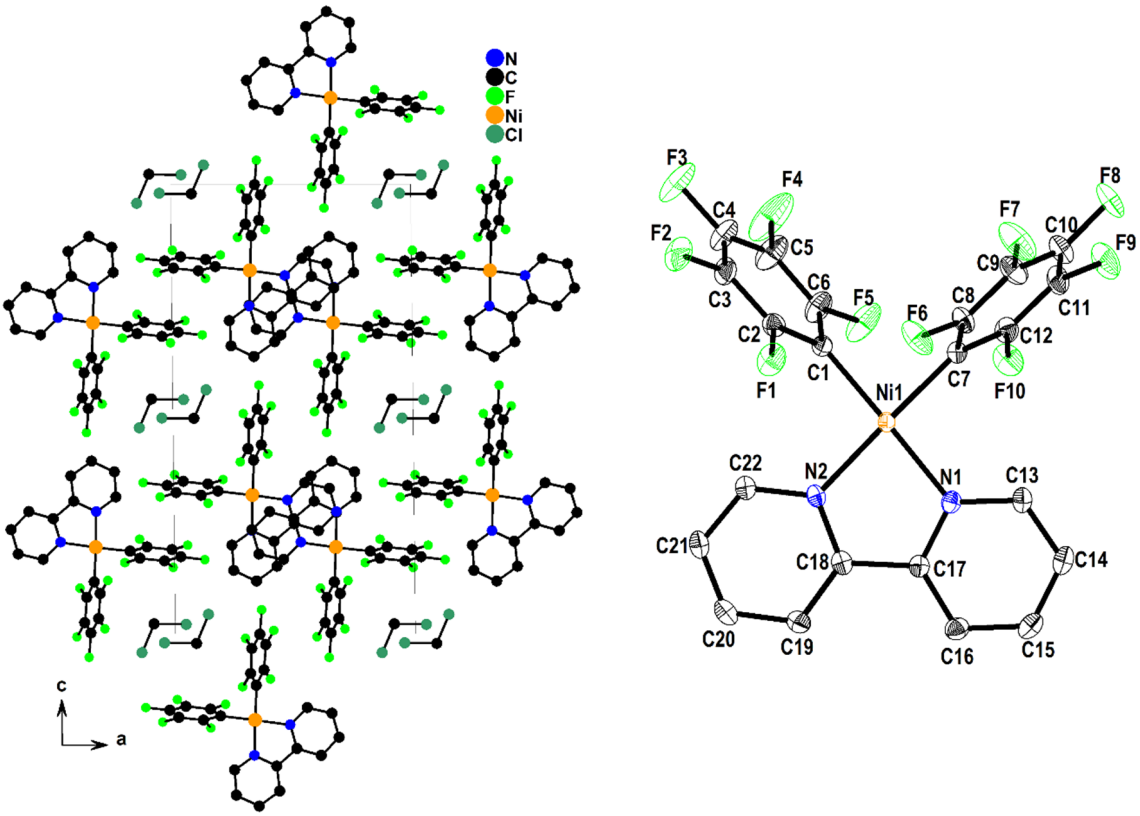

Figure S21. Crystal structure of **1** $[Ni(C_6F_5)_2(bpy)]\cdot 0.5CH_2Cl_2$ viewed along the crystallographic *c* axis (left) and molecular structure of **1** from *sc*-XRD (right). Ellipsoids shown at 50% probability level, H atoms omitted for clarity.

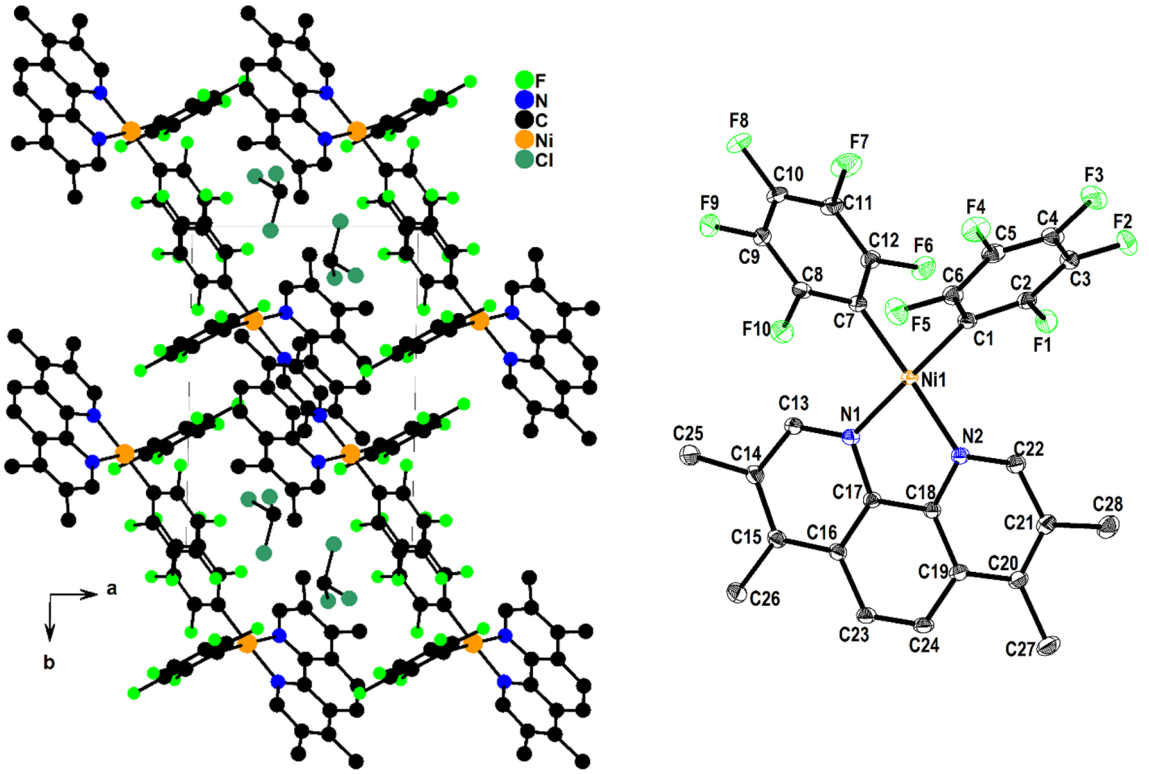

Figure S22. Crystal structure of **2** $[Ni(C_6F_5)_2(tmphen)]\cdot CHCl_3$ viewed along the crystallographic *c* axis (left) and molecular structure of **2** from *sc*-XRD (right). Ellipsoids shown at 50% probability level, H atoms omitted for clarity.

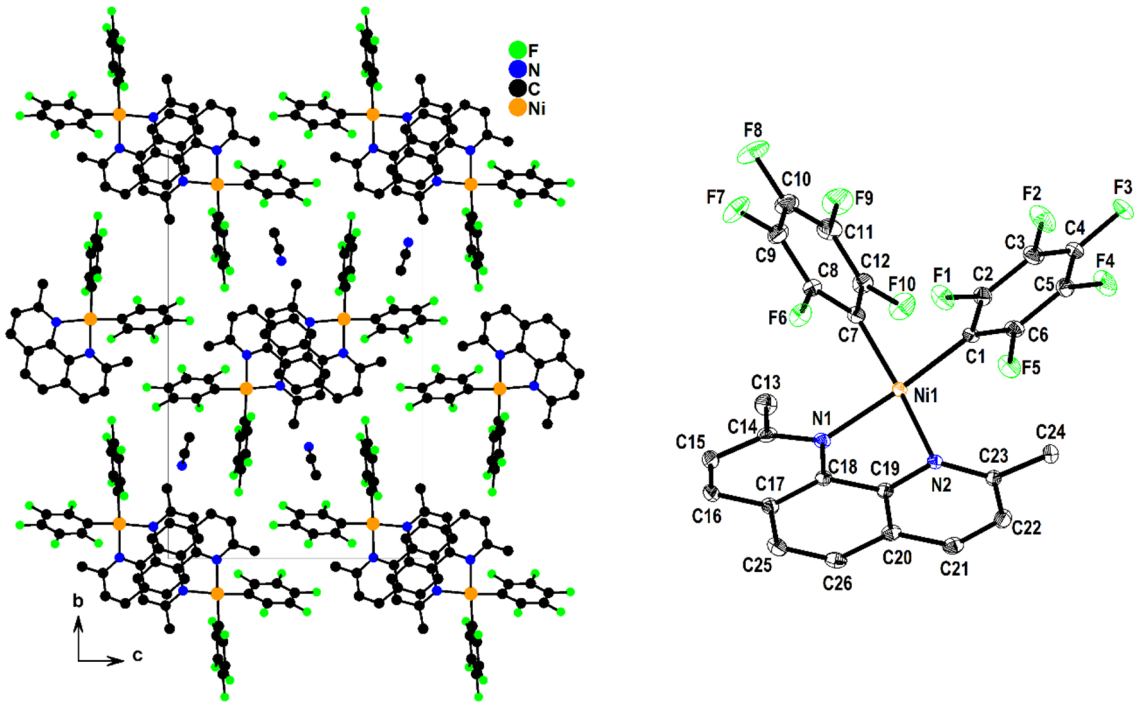

Figure S23. Crystal structure of **3** [Ni(C_6F_5)$_2$(2,9-dmphen)]·MeCN viewed along the crystallographic *a* axis (left) and molecular structure of **3** from *sc*-XRD (right). Ellipsoids shown at 50% probability level, H atoms omitted for clarity.

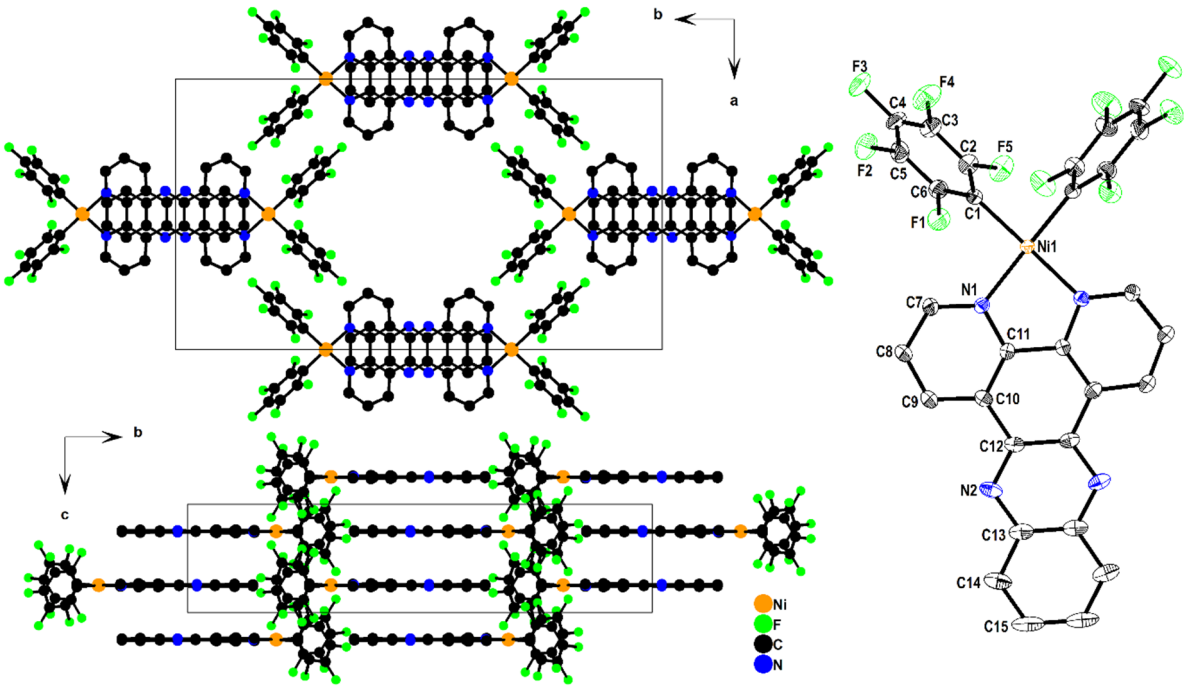

Figure S24. Crystal structure of **4** [Ni(C_6F_5)$_2$(dppz)]·solv viewed along the crystallographic *c* (top left) and *a* (bottom left) axes and molecular structure of **4** from *sc*-XRD (right). Ellipsoids shown at 50% probability level, H atoms omitted for clarity. The solvent accessible voids are filled with strongly disordered solvent which was treated with Platon SQUEEZE.[1]

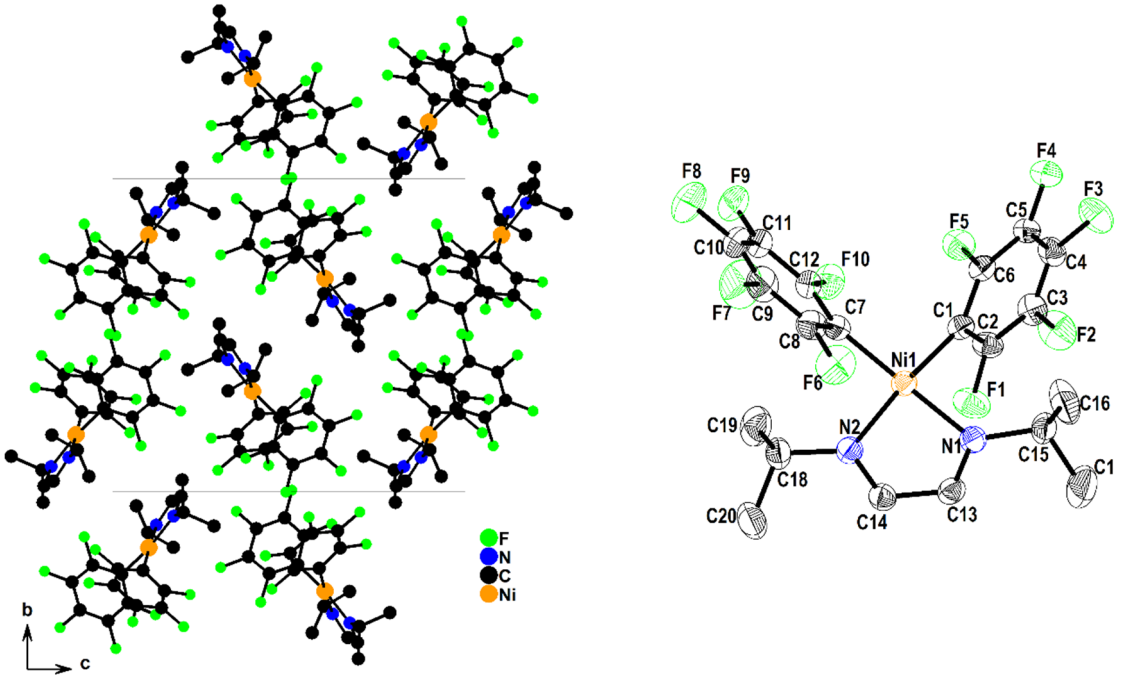

Figure S25. Crystal structure of **5** [Ni(C_6F_5)$_2$(*i*Pr-DAB)] viewed along the crystallographic *a* axis (left) and molecular structure of **4** from *sc*-XRD (right). Ellipsoids shown at 30% probability level, H atoms omitted for clarity.

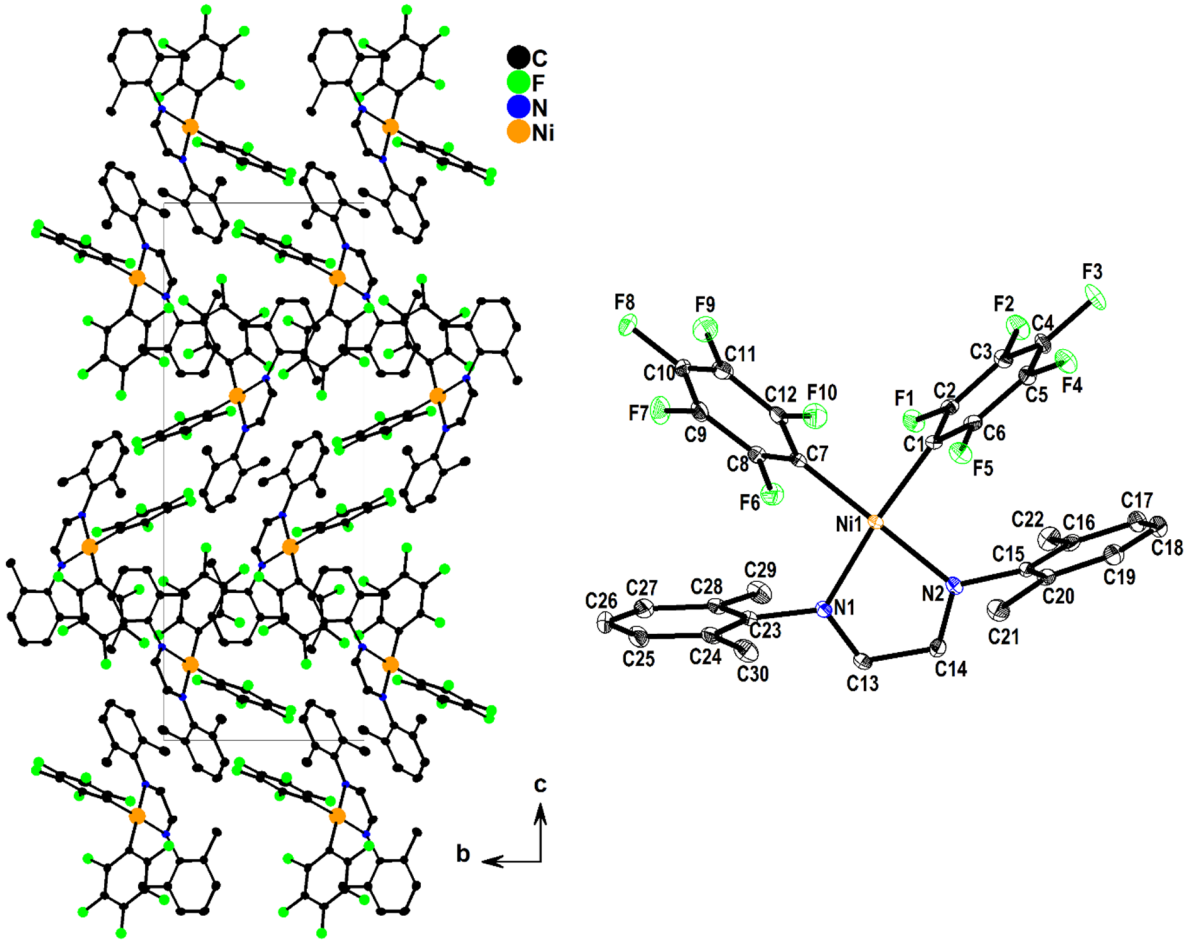

Figure S26. Crystal structure of **6** [Ni(C_6F_5)$_2$(Xyl-DAB)] viewed along the crystallographic *a* axis (left) and molecular structure of **6** from *sc*-XRD (right). Ellipsoids shown at 30% probability level, H atoms omitted for clarity.

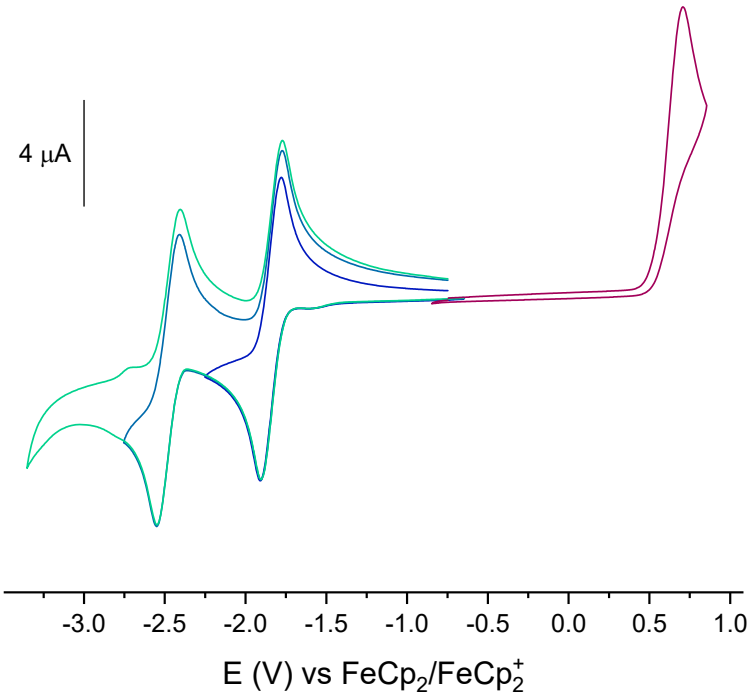

Figure S27. Cyclic voltammograms of **1** in 0.1 M *n*BuN$_4$PF$_6$/THF solution at 298 K, scan rate 100 mV/s.

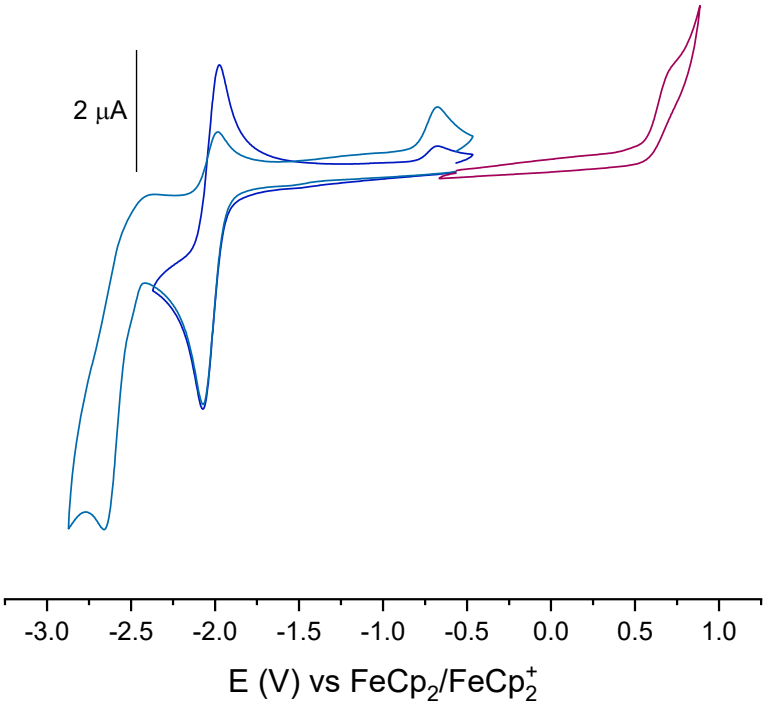

Figure S28. Cyclic voltammograms of **2** in 0.1 M *n*BuN$_4$PF$_6$/THF solution at 298 K, scan rate 100 mV/s.

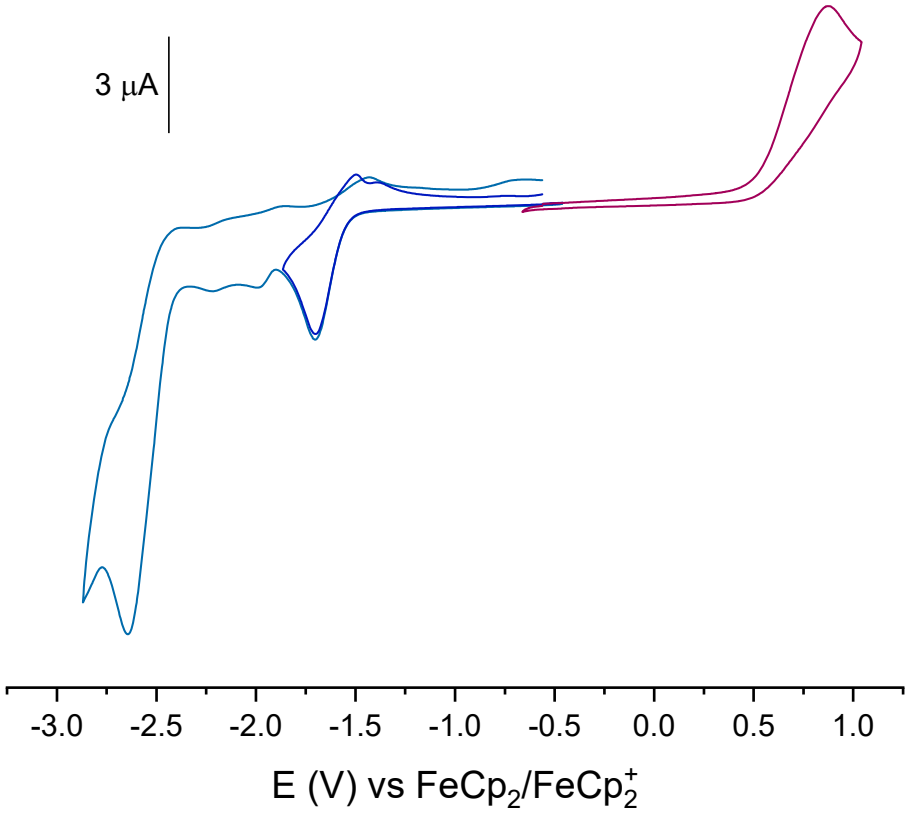

Figure S29. Cyclic voltammograms of **3** in 0.1 M *n*BuN$_4$PF$_6$/THF solution at 298 K, scan rate 100 mV/s.

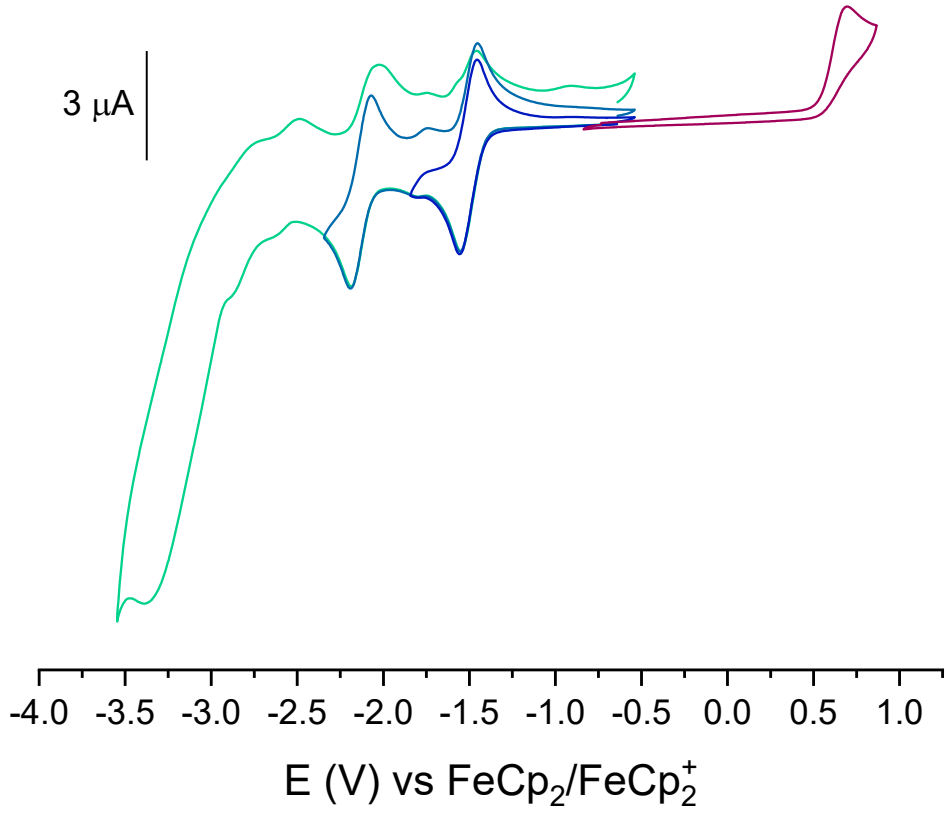

Figure S30. Cyclic voltammograms of **4** in 0.1 M *n*BuN$_4$PF$_6$/THF solution at 298 K, scan rate 100 mV/s.

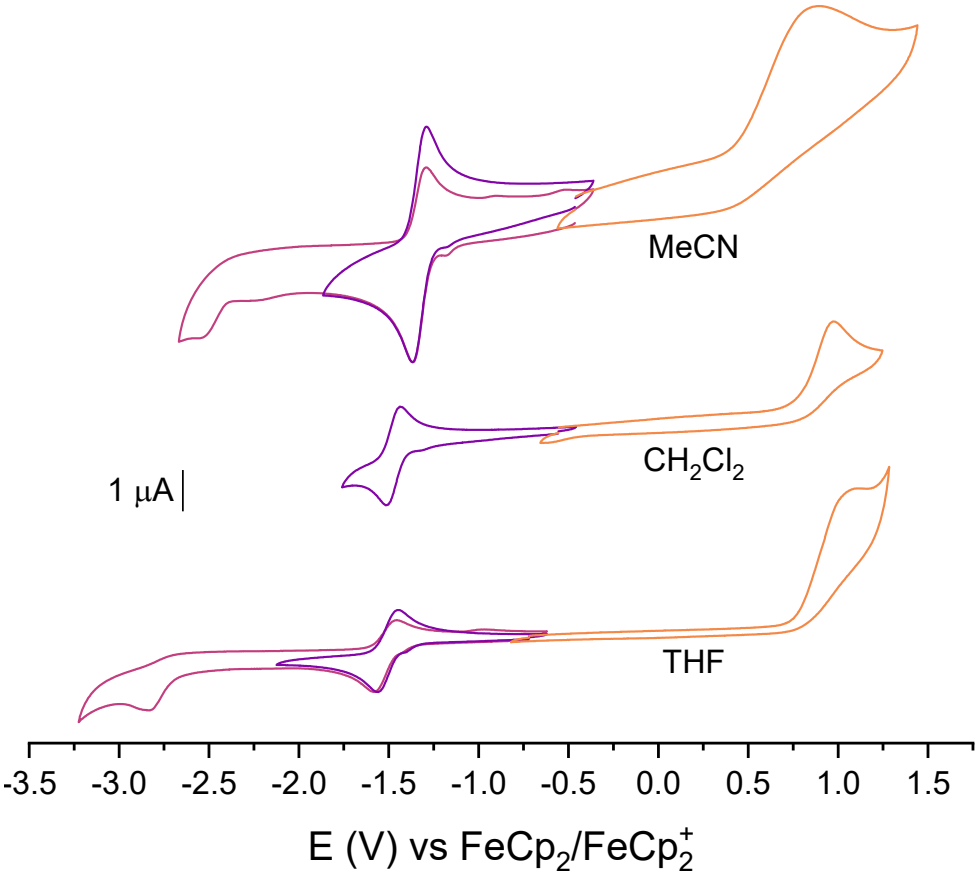

Figure S31. Cyclic voltammograms of **5** in 0.1 M *n*BuN$_4$PF$_6$/solvent (MeCN, CH_2Cl_2, or THF) solution at 298 K, scan rate 100 mV/s.

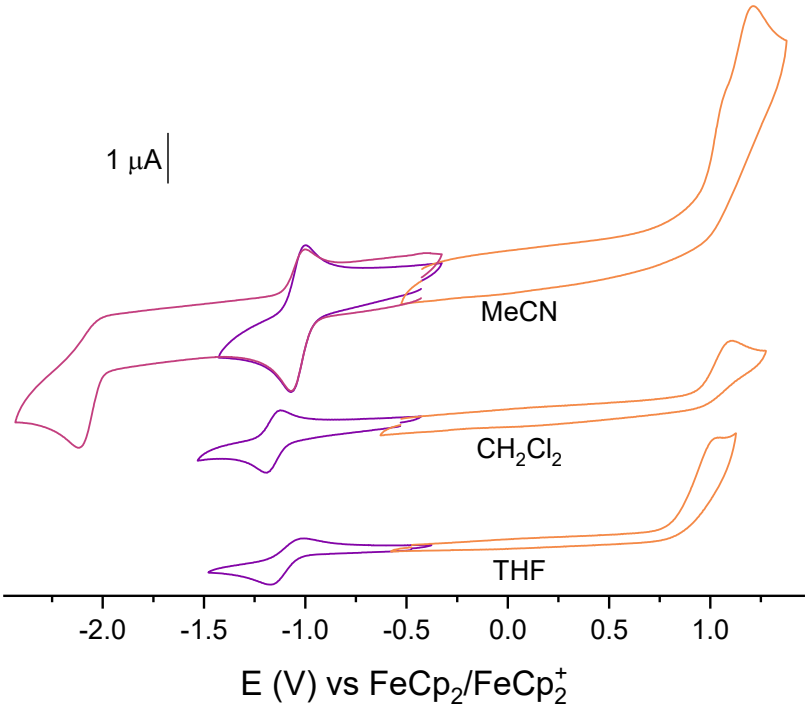

Figure S32. Cyclic voltammograms of **6** in 0.1 M *n*BuN$_4$PF$_6$/solvent (MeCN, CH_2Cl_2, or THF) solution at 298 K, scan rate 100 mV/s.

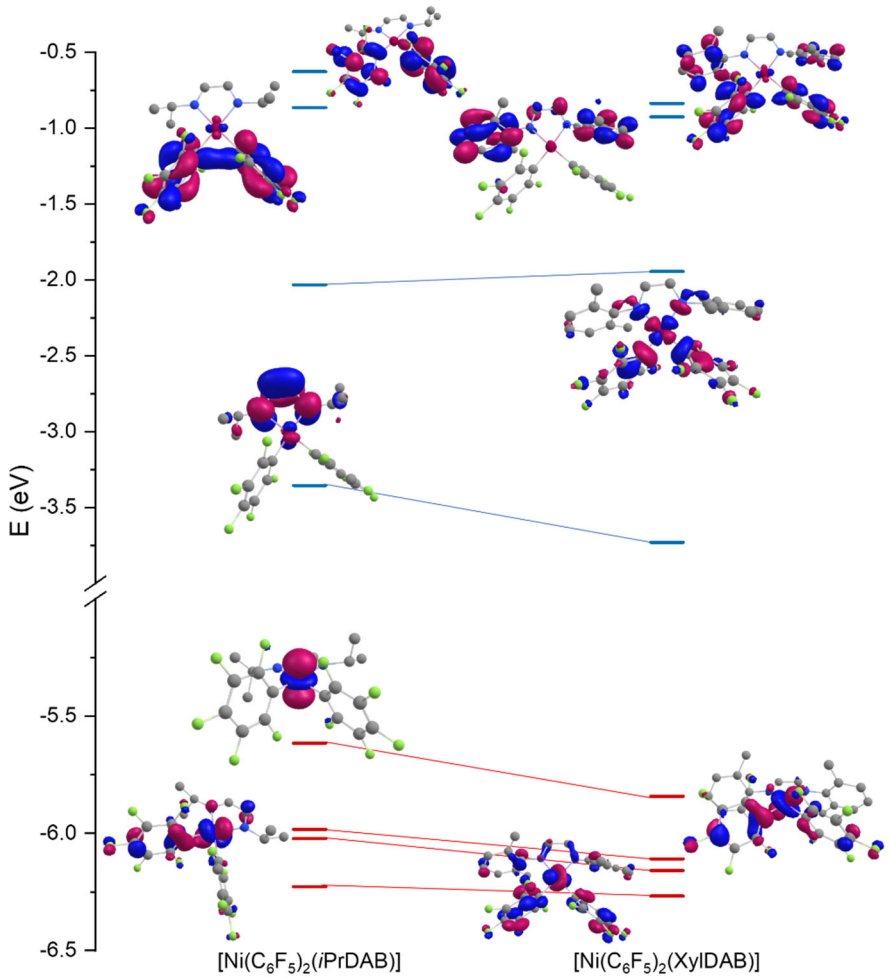

Figure S33. DFT-calculated frontier molecular orbital landscape of **5** and **6** using TPSSh/def2-TZVP/CPCM(THF).

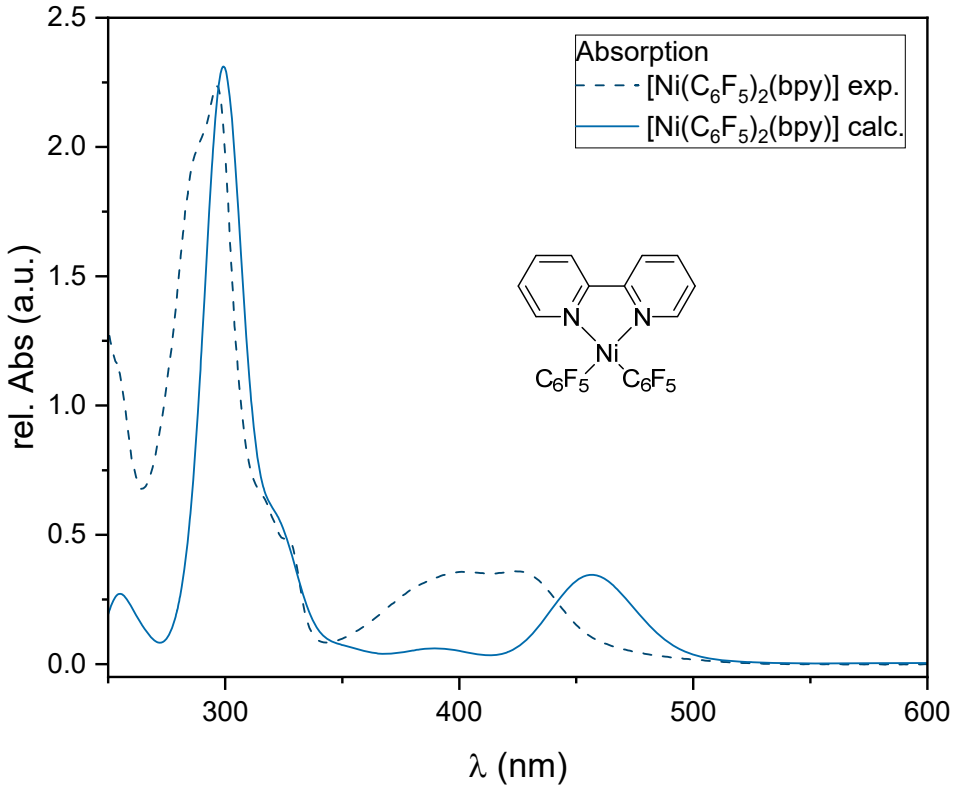

Figure S34. Experimental and DFT-calculated UV-vis absorption spectra of **1** in THF at 298 K.

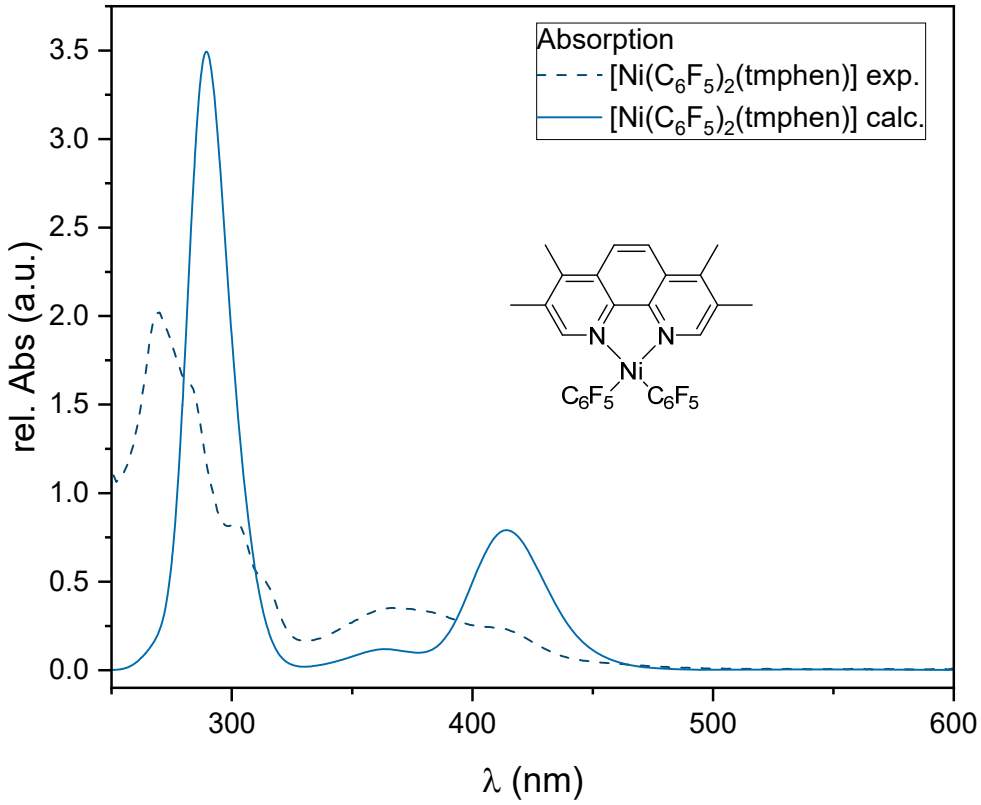

Figure S35. Experimental and DFT-calculated UV-vis absorption spectra of **2** in THF at 298 K.

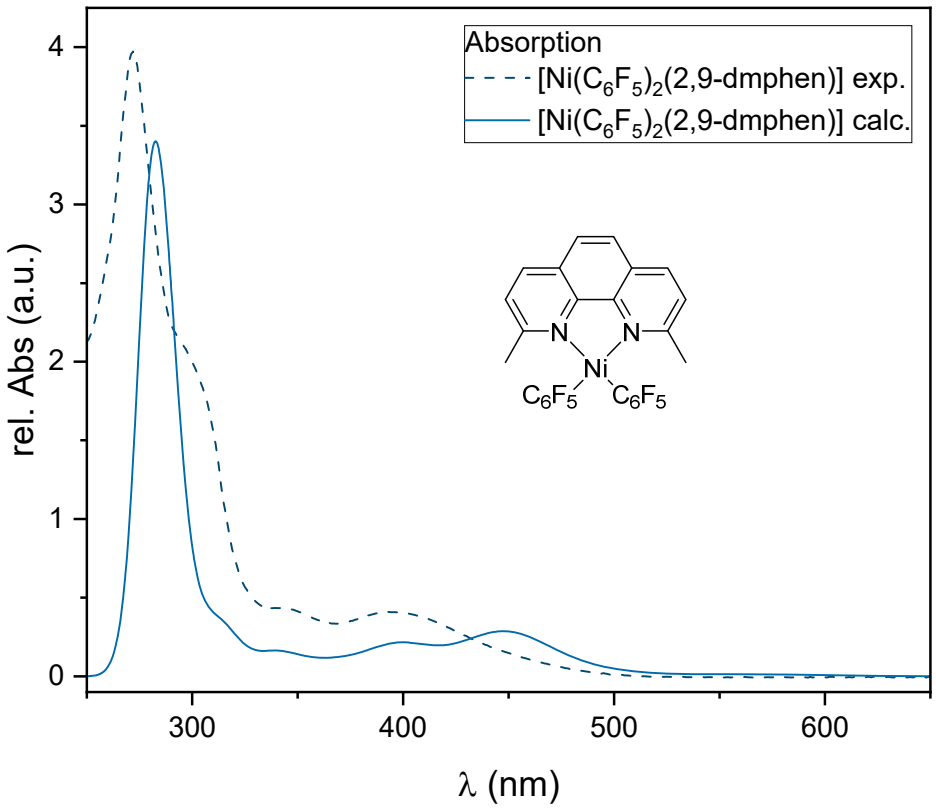

Figure S36. Experimental and DFT-calculated UV-vis absorption spectra of **3** in THF at 298 K.

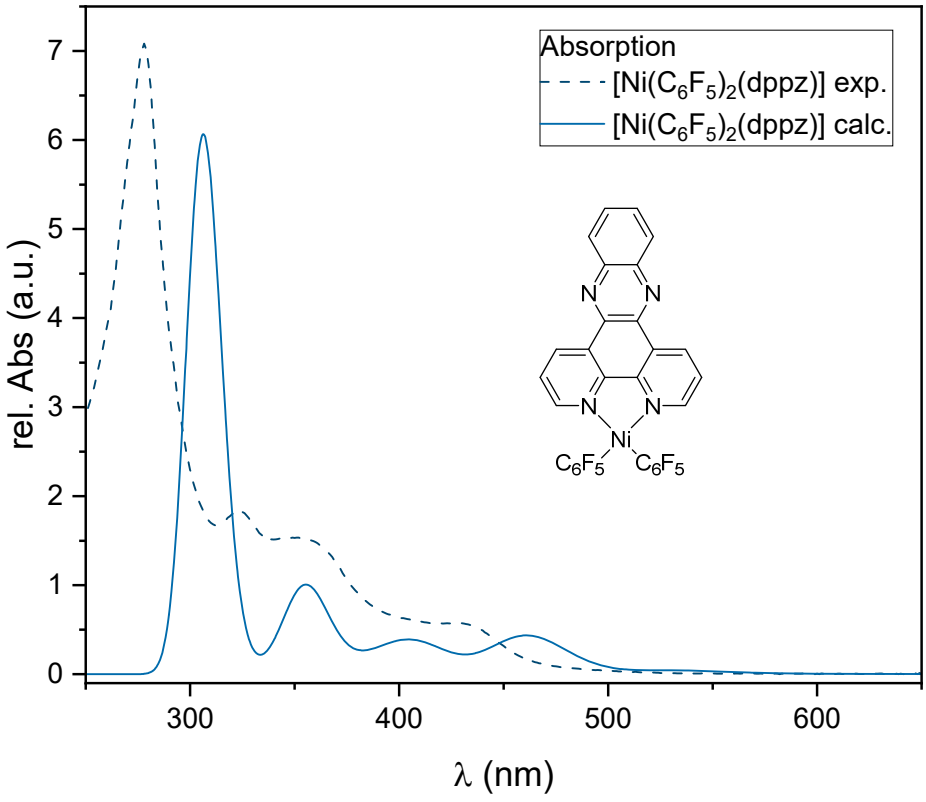

Figure S37. Experimental and DFT-calculated UV-vis absorption spectra of **4** in THF at 298 K.

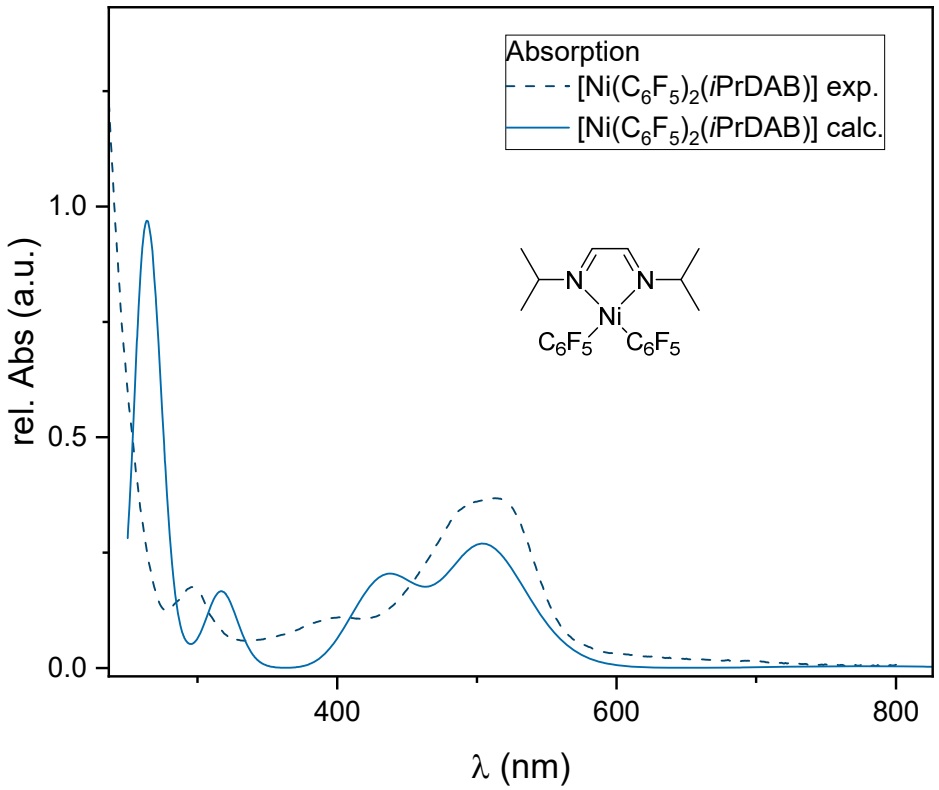

Figure S38. Experimental and DFT-calculated UV-vis absorption spectra of **5** in THF at 298 K.

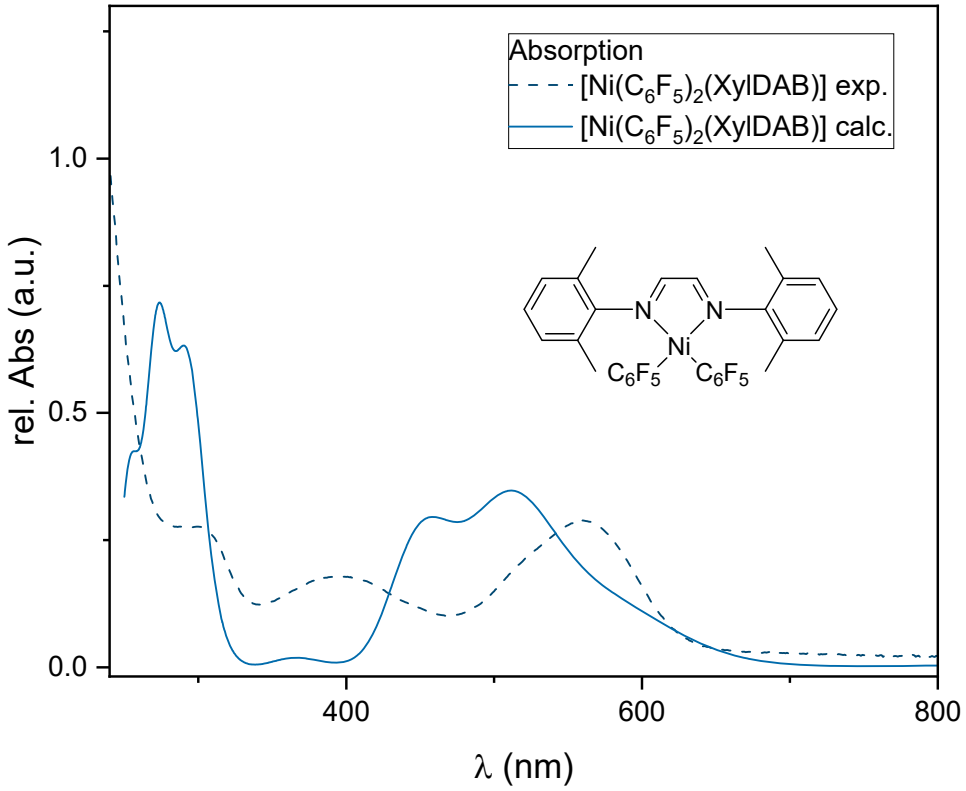

Figure S39. Experimental and DFT-calculated UV-vis absorption spectra of **6** in THF at 298 K.

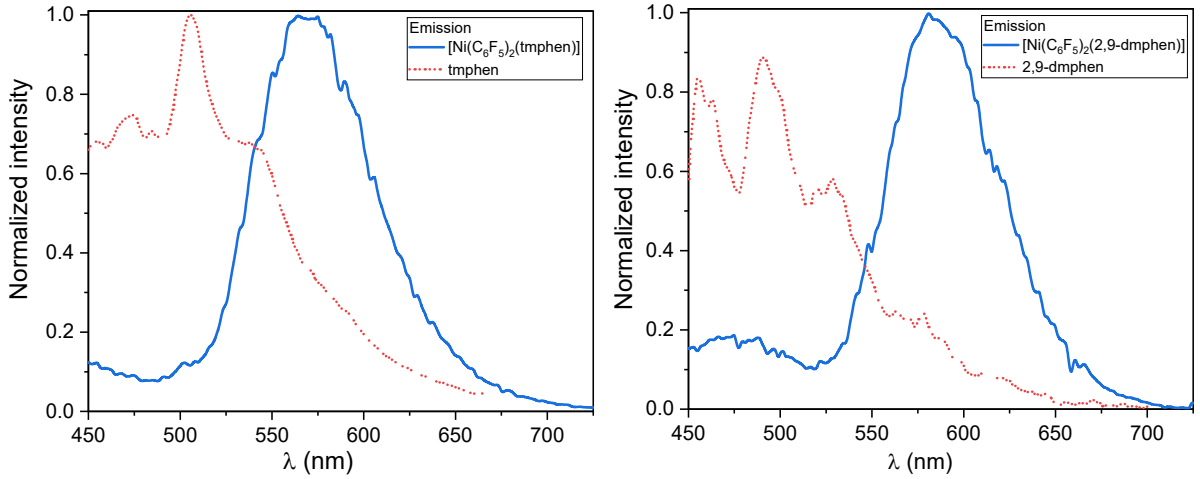

Figure S40. Photoluminescence spectra in 2-MeTHF glassy matrices at 77K of **2** (left) and **3** (right). In both cases λ_{ex} = 350. For comparison, tmphen and 2,9-dmphen are also shown under the same λ_{ex}.

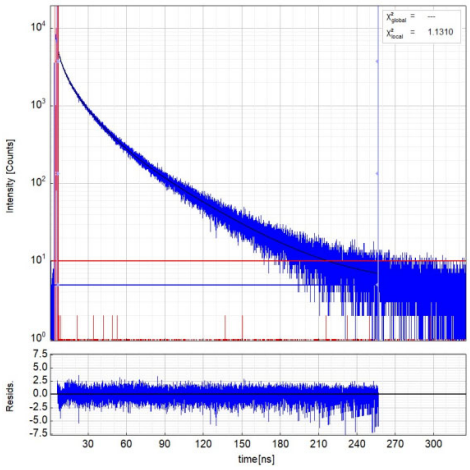

Parameter	Value	Δ	δ
A_1[kCnts/Chnl]	0.820	±0.038	4.6%
τ_1[ns]	42.14	±0.68	1.6%
I_1[kCnts]	2 160	±63	2.9%
A_{Rel1}[%]	12.6	±0.6	4.3%
I_{Rel1}[%]	41.2	±1.2	2.8%
A_2[kCnts/Chnl]	2.566	±0.056	2.2%
τ_2[ns]	14.59	±0.41	2.8%
I_2[kCnts]	2 339	±39	1.7%
A_{Rel2}[%]	39.2	±0.8	1.8%
I_{Rel2}[%]	44.6	±0.7	1.5%
A_3[kCnts/Chnl]	3.17	±0.12	3.6%
τ_3[ns]	3.78	±0.13	3.2%
I_3[kCnts]	747	±39	5.2%
A_{Rel3}[%]	48.4	±1.2	2.3%
I_{Rel3}[%]	14.3	±0.7	4.7%
$Bkgr_{Dec}$[kCnts]	0.0050	±0.0003	4.7%
$Bkgr_{IRF}$[Cnts/Chnl]	10.0000	---	---
$Shift_{IRF}$[ps]	1 190	±120	9.4%
τ_{AvInt}[ns]	24.39	±0.15	0.6%
τ_{AvAmp}[ns]	12.81	±0.17	1.3%

Figure S41. Left: Raw (experimental) time resolved photoluminescence decay of **2** in a frozen 2-MeTHF glassy matrix at 77 K (c = 10^{-5} M), including the residuals (λ_{ex} = 376 nm, λ_{em} = 580 nm), the instrument response function measured with Ludox is shown in red. Right: Fitting parameters including pre-exponential factors and confidence limits.

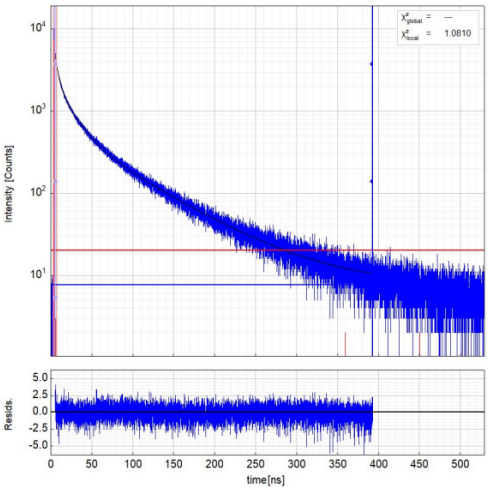

Parameter	Value	Δ	δ
A_1[kCnts/Chnl]	0.644	±0.019	2.8%
τ_1[ns]	72.6	±1.1	1.4%
I_1[kCnts]	1 459	±23	1.5%
A_{Rel1}[%]	10.9	±0.5	4.4%
I_{Rel1}[%]	49.4	±1.0	2.0%
A_2[kCnts/Chnl]	1.742	±0.060	3.4%
τ_2[ns]	19.03	±0.64	3.4%
I_2[kCnts]	1 036	±19	1.8%
A_{Rel2}[%]	29.3	±1.0	3.2%
I_{Rel2}[%]	35.1	±0.5	1.2%
A_3[kCnts/Chnl]	3.58	±0.23	6.3%
τ_3[ns]	4.13	±0.20	4.7%
I_3[kCnts]	461	±33	7.0%
A_{Rel3}[%]	60.0	±1.4	2.3%
I_{Rel3}[%]	15.6	±1.0	5.9%
$Bkgr_{Dec}$[kCnts]	0.0077	±0.0003	3.9%
$Bkgr_{IRF}$[Cnts/Chnl]	20.0000	---	---
$Shift_{IRF}$[ps]	690	±250	35%
A_{Scatt}[kCnts]	- 280	±110	36%
τ_{AvInt}[ns]	43.13	±0.48	1.1%
τ_{AvAmp}[ns]	15.87	±0.49	3.1%

Figure S42. Left: Raw (experimental) time resolved photoluminescence decay of **3** in a frozen 2-MeTHF glassy matrix at 77 K (c = 10^{-5} M), including the residuals (λ_{ex} = 376 nm, λ_{em} = 560 nm), the instrument response function measured with Ludox is shown in red. Right: Fitting parameters including pre-exponential factors and confidence limits.

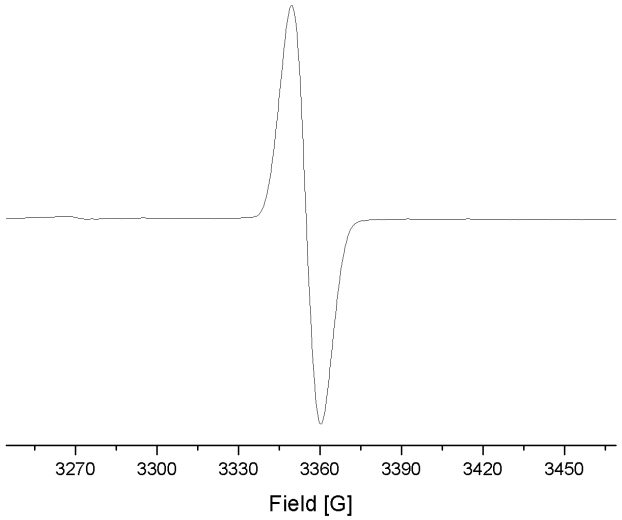

Figure S43. EPR spectrum of $[Ni(C_6F_5)_2(bpy)]^{\bullet-}$ ($\mathbf{1}^{\bullet-}$) obtained from electrochemical reduction of **1** in THF/nBu$_4$NPF$_6$ at 293 K.

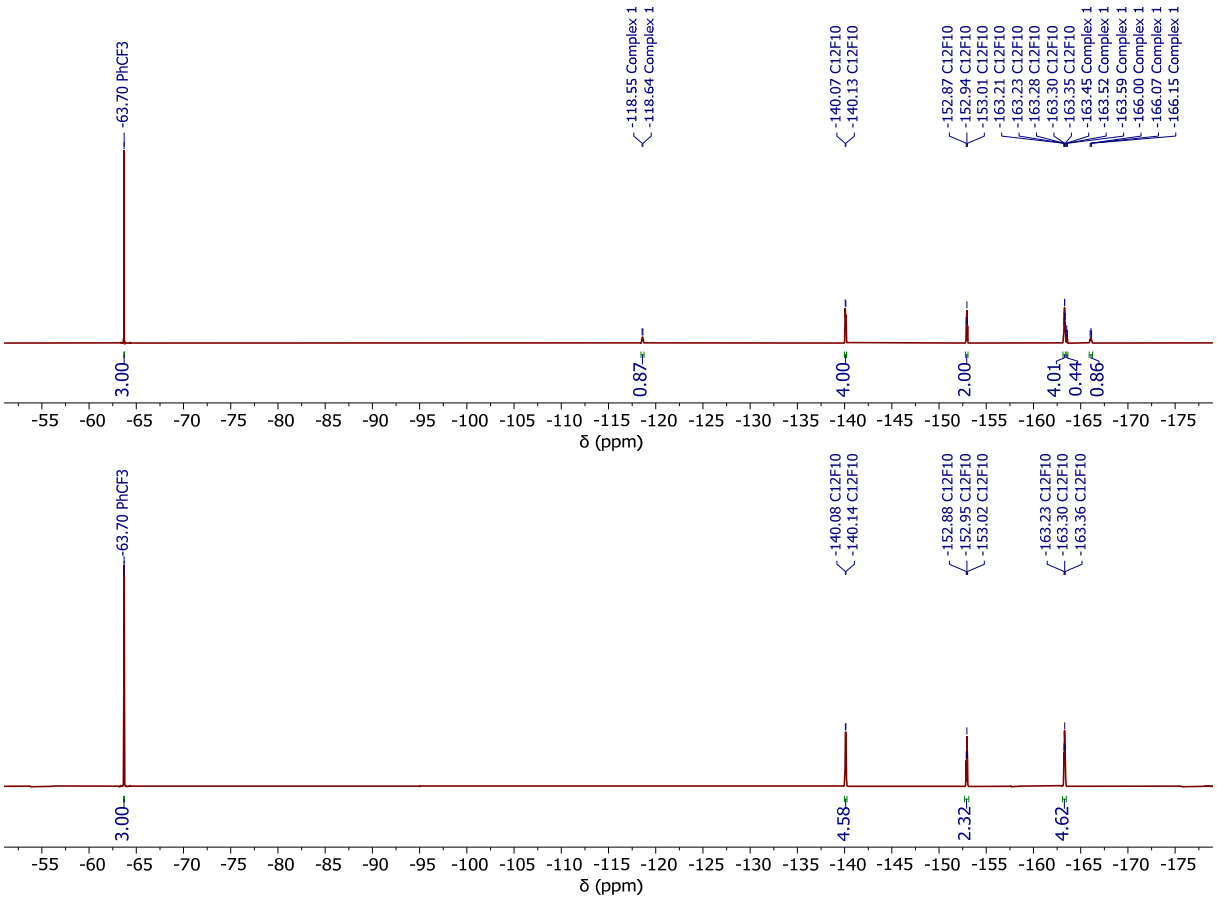

Figure S44. ^{19}F NMR (282 MHz, MeCN-d_3) measured immediately (top) and 9 h (bottom) after mixing of **1** and tris(4-bromophenyl)ammoniumyl hexachloroantimonate ("magic blue").

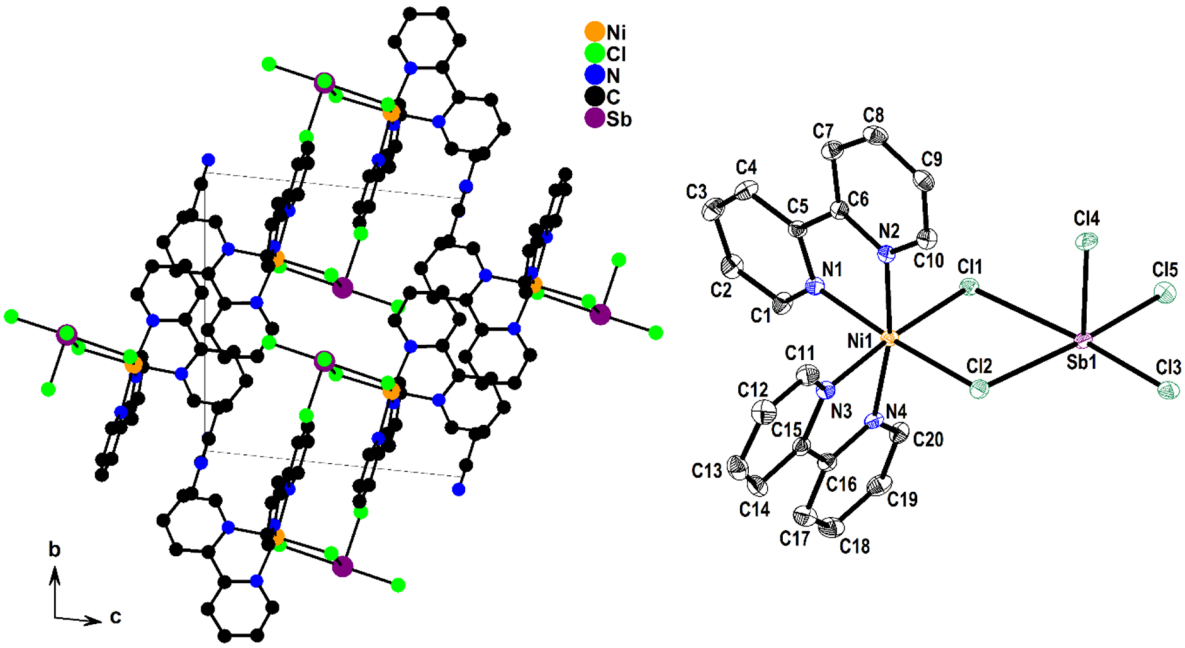

Figure S45. Crystal structure of $[Ni(bpy)_2Cl_2]\cdot SbCl_3\cdot MeCN$ viewed along the crystallographic *a* axis (left) and structure of $[Ni(bpy)_2Cl_2]\cdot SbCl_3$ from *sc*-XRD (right). Ellipsoids shown at 50% probability level, H atoms omitted for clarity.

References

(1) Spek, A. L. PLATON SQUEEZE: a tool for the calculation of the disordered solvent contribution to the calculated structure factors. *Acta Cryst. C – Struct. Chem.* **2015**, *C71*, 9–18. https://doi.org/10.1107/S2053229614024929

(2) Klein, A. Synthesis, Spectroscopic Properties, and Crystal Structure of 2,2'-Bipyridyldimesitylnickel(II). *Z. Anorg. Allg. Chem.* **2001**, *627*, 645–650. https://doi.org/10.1002/1521-3749(200104)627:4<645::AID-ZAAC645>3.0.CO;2-T

(3) Bour, J. R.; Camasso, N. M.; Meucci, E. A.; Kampf, J. W.; Canty, A. J.; Sanford, M. S. Carbon–Carbon Bond-Forming Reductive Elimination from Isolated Nickel(III) Complexes. *J. Am. Chem. Soc.* **2016**, *138*, 16105–16111. https://doi.org/10.1021/jacs.6b10350

(4) Alonso, P. J.; Arauzo, A. B.; García-Monforte, M. A.; Martín, A.; Menjón, B.; Conrado Rillo, C.; Tomás, M. Homoleptic Organoderivatives of High-Valent Nickel(III). *Chem.–Eur. J.* **2009**, *15*, 11020–11030. https://doi.org/10.1002/chem.200901259